

**STUDY OF POROUS MAGNETIC NANOCOMPOSITES
FOR BIO-CATALYSIS AND DRUG DELIVERY**

by

MANEEA EIZADI SHARIFABAD

A thesis submitted in partial fulfilment for the requirements for the degree
of Doctor of Philosophy at the University of Central Lancashire

November 2016

I declare that while registered as a candidate for the research degree, I have not been a registered candidate or enrolled student for another award of the University or other academic or professional institution. I declare that no material contained in the thesis has been used in any other submission for an academic award and is solely my own work.

Signature of Candidate : *Mancea Eizadi Sharifabad*

Date: *01/11/2016*

School of Physical Sciences and Computing

Dedicated to my beloved family; my mother, father, brother and my grandmothers.

ACKNOWLEDGMENT

It is great pleasure to finally present my research in the form of a doctoral thesis. Earning the doctoral degree is the outcome of determination and consistent effort through years of academic challenges and was only possible with the help of a number of wonderful and inspiring people who contributed in shaping my educational experience. I would like to take this opportunity to thank them all.

I would like to start my acknowledgment by thanking my supervisor Dr. Tapas Sen for his continuous support and belief in my abilities, which motivated me to stretch my limits and achieve excellence in research. I am thankful to Dr. Tim Mercer for being my co-advisor and guiding my research over the past three years. His insightful comments has pushed me to expand the depth of my knowledge in the area of magnetism. I would like to express my gratitude to Prof. Gray Bond for his kind support through writing my thesis.

I would also like to thank my examination committee members, Professor Waqar Ahmed and Professor Mike Anderson, for their detailed review, valuable discussion and constructive comments.

I am also thankful to Dr. Julie Shorrocks for providing help with the cellular studies and generously sharing her advice that facilitated my research. I am also thankful to Mrs. Tamar Garcia, Dr. Runjie Mao and Mr. Mansoor Ahmed for their help and support with the experimental works.

I would like to thank my colleagues at University of Central Lancashire: Dr. Ben Hodgson, Dr. Hajira Faki, Dr. Iftikhar Khan, Dr. Sundeep Kadam, Dr. Temba Mudariki and particularly, Dr. Vinod Vishwapathi their assistance and valuable guidance in my research and ingenious ideas during our discussions.

I would like to thank my friends, Dr. Ali Asadi, Dr. Robert Crewe, Dr. Hamidreza Soltani and Dr. Ilia Eizadi Sharifabad for their kind and generous help during this research project. I could not have done any of this without all my supportive, forgiving, generous, and loving friends. Their help in those moments which I was really disappointed and confused gave me the reason to continue.

Most importantly, I owe the deepest gratitude to my loving parents, Farida and Mohammad, my brother, Ilia, and my grandmothers, Nasrin and Fatemeh, for their unconditional love and prayer. They are always the reason of my happiness; no words can convey my gratitude toward them.

I would like to thank the University of Central Lancashire for the wonderful experience. This work was partially funded by University of Central Lancashire.

ABSTRACT

Despite advances in diagnostic procedures and treatments, the overall survival rate from cancer has not improved substantially over the past 30 years. One promising development is the encapsulation of toxic cancer chemotherapeutic reagents within biocompatible nanocomposite materials. The targeted stimuli triggered drug release restrict the toxic drugs to the tumour site, thereby reducing the effects of “free drug” on healthy tissues. One of the most versatile and safe materials used in medicine are iron oxide nanoparticles. This project describes the development of several formulations based on magnetite nanoparticles for drug delivery applications. Utilising magnetic nanoparticles in drug delivery systems allowed for the synergistic effects of hyperthermia and heat triggered drug released. The drug delivery systems developed in this project include magnetoliposomes, magnetic micelles, mesoporous silica-magnetite core-shell nanoparticles, liposome capped mesoporous silica-magnetite core-shell nanoparticles (protocells) and polymer capped mesoporous silica-magnetite core-shell nanoparticles.

The drug loading and release profiles of the developed nanomaterials were assessed using two different anticancer drugs; Mitomycin C (MMC) and Doxorubicin (DOX). The drug loading content and drug loading efficiency for different nanocomposites ranged from 0.48 to 10.30% and 16.16 to 85.85%, respectively. Drug release profiles were studied *in vitro* at 37°C at pH 5.5 and pH 7.4 and at hyperthermia elevated temperature of 43°C to evaluate the effects of pH and temperature on the release profiles. An AC magnetic field with frequency of 406 kHz and variable field of up to 200 G was used to induce magnetic heating and keep the temperature within hyperthermia treatment range. Compared to uncapped mesoporous silica nanoparticles capping the mesopores of the silica nanoparticles with liposome or polymer reduced the drug release by 52.7% and 41.5%, respectively.

The efficacy of doxorubicin-containing nanoparticles were evaluated *in vitro* against breast cancer and glioblastoma cell lines where different formulations demonstrated comparable or increased cytotoxicity compared to free drug. The cells treated with DOX loaded nanoparticles and hyperthermia demonstrated up to 89% lower viability compared to cells treated with free DOX.

Silica coated magnetic nanoparticles were also used as enzymes (Pseudomonas Fluorescens Lipase (PFL) and Candida Rugosa Lipase (CRL)) supports in catalysis reactions. The enzymes were immobilised onto nanoparticles through physical adsorption and chemical bonding. The immobilised lipases were used in hydrolysis of pNPP and hydrolysis of cis-3,5-diacetoxy-1-

cyclopentene to investigate the catalytic activity of the immobilized enzymes compared to free enzymes. The results indicated that free lipases provided slightly higher conversion than immobilised lipases in the first cycle however, the immobilised lipases were easily recycled and reused in sequential cycles which provides higher total yield per mg of lipase. The chemically immobilised lipase exhibited good reusability without loss of its activity in sequential cycles, however the physically adsorbed lipase showed reduced activity which could be explained by loss of enzyme during recycling between successive reactions. The CRL lipase activity were further assessed in the presence of an AC field where the results showed that exposure to the AC magnetic field resulted in increased lipase activity. The effect of reaction temperature on immobilised lipase activity were studied by performing the hydrolysis of cis-3,5-diacetoxy-1-cyclopentene at two temperatures of 25°C and 37°C where it was observed that both lipases exhibited higher activity at higher temperature which could be due to the fact that for PFL and CRL the optimum temperature is close to 37°C.

TABLE OF CONTENTS

DECLARATION	ii
DEDICATION	iii
ACKNOWLEDGMENT	iv
ABSTRACT	vi
TABLE OF CONTENTS	viii
LIST OF TABLES	xv
LIST OF FIGURES	xvii
LIST OF SCHEMES	xxviii
LIST OF ABBREVIATIONS	xxix
LIST OF SYMBOLS	xxxi
1 CHAPTER 1: INTRODUCTION.....	1
1.1 PROJECT MOTIVATION	2
1.2 AIMS AND OBJECTIVES OF THE PROJECT	2
1.3 NANOTECHNOLOGY AND ITS IMPORTANCE.....	5
1.4 MAGNETISM AND MAGNETIC NANOPARTICLES.....	6
1.5 SYNTHESIS OF MAGNETITE NANOPARTICLES.....	10
1.5.1 <i>Co-Precipitation</i>	13
1.5.2 <i>Thermal Decomposition</i>	13
1.6 GENERAL METHOD OF COATINGS.....	15
1.7 SILICA COATING ON MAGNETITE NANOPARTICLES AND ITS APPLICATIONS.....	19
1.7.1 <i>Stöber Method</i>	20
1.7.2 <i>Microemulsion Method</i>	20
1.7.3 <i>Templating method</i>	21
1.7.4 <i>Mesoporous Silica Coated Magnetite Nanoparticles for Drug Delivery</i>	24
1.8 LIPOSOME COATED MAGNETITE NANOPARTICLES: MAGNETOLIPOSOMES	28
1.9 POLYMER COATED MAGNETITE NANOPARTICLES: MAGNETOMICELLES	32
1.10 APPLICATIONS OF SUPERPARAMAGNETIC IRON OXIDE NANOPARTICLES (SPIONS) IN NANOMEDICINE	

1.10.1	<i>Magnetic Drug Targeting (MDT)</i>	39
1.10.2	<i>Magnetic Fluid Hyperthermia (MFH)</i>	41
1.11	INTRODUCTION TO BIO-CATALYSIS	45
1.11.1	<i>Lipase</i>	46
1.11.2	<i>Candida Rugosa Lipase (CRL)</i>	49
1.11.3	<i>Pseudomonas Fluorescens Lipase (PFL)</i>	51
1.12	ENZYME IMMOBILIZATION.....	52
1.12.1	<i>Enzymes Immobilisation on Mesoporous Silica Coated Magnetic Nanoparticles</i>	53
2	CHAPTER 2: MATERIALS AND METHODS	60
2.1	REAGENTS AND MATERIALS	61
2.2	SOLUTIONS AND BUFFERS	61
2.3	SYNTHESIS OF SUPERPARAMAGNETIC IRON OXIDE NANOPARTICLES (SPION's).....	63
2.3.1	<i>Co-precipitation of Iron Chlorides in Alkaline Media</i>	64
2.3.2	<i>Oxidative Hydrolysis of Iron Sulphate in Alkaline Media</i>	65
2.3.3	<i>Organic Phase Thermal Decomposition</i>	65
2.4	SYNTHESIS OF MESOPOROUS SILICA COATED MAGNETITE NANOPARTICLES.....	66
2.5	SYNTHESIS OF NON-POROUS SILICA COATED MAGNETITE NANOPARTICLES	67
2.6	PREPARATION OF HYDROPHOBIC SILICA COATED MAGNETITE	68
2.6.1	<i>Direct Etching Method</i>	68
2.6.2	<i>Surface Protected Etching</i>	69
2.6.3	<i>Direct Synthesis of Hydrophobic Mesoporous Silica Coated Magnetite</i>	69
2.7	SYNTHESIS OF POLY (ETHYLENE GLYCOL)- <i>B</i> -POLYCAPROLACTONE DIBLOCK COPOLYMER	70
2.8	SURFACE AMINE MODIFICATION OF THE SILICA COATED NANOPARTICLES	71
2.8.1	<i>Tri-phasic Reverse Emulsion (TPRE) Method</i>	71
2.8.2	<i>Water Method</i>	71
2.9	COLORIMETRIC ASSAY OF AMINE DENSITY	72
2.10	CONVERTING SURFACE AMINE GROUPS TO ALDEHYDES	73
2.11	ENZYME IMMOBILISATION ON SILICA COATED MAGNETITE NANOPARTICLES	74
2.11.1	<i>Covalent Enzyme Immobilisation on Nanoparticles</i>	74
2.11.1	<i>Physical Adsorption of Enzyme on Nanoparticles</i>	74
2.12	BRADFORD ASSAY.....	75
2.13	MODEL CATALYSIS REACTION, HYDROLYSIS OF PARA-NITROPHENYL PALMITATE (PNPP).....	75
2.13.1	<i>Immobilized Enzyme Activity at 25°C</i>	75
2.13.2	<i>Immobilized Enzyme Activity in Presence of an Alternating Current (AC)</i> <i>Magnetic Field</i>	76

2.14	DESYMMETRIZATION OF CIS-3,5-DIACETOXY-1-CYCLOPENTENE TO (1S,4R)-CIS-4-ACETOXY-2-CYCLOPENTEN-1-OL	76
2.15	SYNTHESIS OF LIPOSOME COATED MAGNETIC NANOPARTICLES: MAGNETOLIPOSOMES.....	77
2.16	DRUG LOADING OF MAGNETOLIPOSOMES	77
2.16.1	<i>Drug Loading Using an Incubation Method</i>	78
2.16.2	<i>Drug Loading Using Ultrasonication</i>	78
2.17	DRUG RELEASE FROM MAGNETOLIPOSOMES.....	78
2.17.1	<i>Drug Release at Body Temperature (37°C) and Room Temperature (23°C)</i>	78
2.17.2	<i>Drug Release in the Presence of an AC Magnetic Field</i>	79
2.18	DRUG LOADING OF THE MESOPOROUS SILICA COATED MAGNETIC NANOPARTICLES.....	79
2.18.1	<i>Mitomycin C (MMC) Loading of the Mesoporous Silica Coated Magnetic Nanoparticles</i>	79
2.18.2	<i>Doxorubicin (DOX) Loading of the Mesoporous Silica Coated Magnetic Nanoparticles</i>	79
2.19	DRUG RELEASE FROM MESOPOROUS SILICA COATED MAGNETIC NANOPARTICLES	80
2.19.1	<i>Drug Release at Body Temperature (37°C)</i>	80
2.19.2	<i>Drug Release in presence of an Alternating Magnetic Field</i>	80
2.20	DRUG LOADING OF THE LIPOSOME CAPPED MESOPOROUS SILICA COATED MAGNETIC NANOPARTICLES.....	80
2.21	DRUG RELEASE FROM THE LIPOSOME CAPPED MESOPOROUS SILICA COATED MAGNETIC NANOPARTICLES.....	81
2.22	PREPARATION OF POLYMERIC (PEG-PCL) MICELLES	82
2.22.1	<i>Preparation of PEG-PCL Magnetic Micelles</i>	82
2.23	CONVERSION OF DOX.HCL TO HYDROPHOBIC DOX.....	83
2.24	PREPARATION OF DRUG LOADED MAGNETIC MICELLES.....	83
2.25	PREPARATION OF DRUG LOADED PEG-PCL CAPPED SILICA COATED MAGNETITE NANOPARTICLES	83
2.26	CALCULATIONS OF THE DRUG LOADING CONTENT AND EFFICIENCY	84
2.27	<i>IN VITRO</i> DRUG RELEASE FROM PEG-PCL NANOCOMPOSITES	85
2.28	<i>IN VITRO</i> CELLULAR STUDY	85
2.28.1	<i>MCF7 Cell Line</i>	86
2.28.2	<i>U87 Cell Line</i>	86
2.28.3	<i>Thawing of Frozen Cells</i>	86
2.28.4	<i>Passaging the Cells</i>	86
2.28.5	<i>Cell Count</i>	87
2.28.6	<i>Cell Viability Assessment Using Trypan Blue</i>	87
2.28.7	<i>Growth Curve Preparation</i>	87

2.28.8	<i>Cytotoxicity Assay using Presto Blue</i>	88
2.29	<i>IN VITRO</i> CYTOTOXICITY STUDY OF THE PREPARED MATERIALS.....	89
2.29.1	<i>IC50 Determination</i>	89
2.30	EFFECT OF MAGNETIC HYPERTHERMIA ON CELL VIABILITY.....	90
2.31	STATISTICAL ANALYSIS.....	90
2.32	CHARACTERIZATION EQUIPMENT AND TECHNIQUES.....	90
2.32.1	<i>X-Ray diffraction (XRD)</i>	91
2.32.2	<i>Transmission Electron Microscopy (TEM)</i>	91
2.32.3	<i>Nitrogen Gas Adsorption-Desorption</i>	92
2.32.4	<i>Dynamics Light Scattering (DLS)</i>	92
2.32.5	<i>Vibration Sample Magnetometry (VSM)</i>	92
2.32.6	<i>Differential Scanning Calorimetry (DSC)</i>	93
2.32.7	<i>Scanning Column Magnetometry (SCM)</i>	93
2.32.8	<i>Contact Angle Measurements</i>	94
2.32.9	<i>Gas Chromatography (GC)</i>	94
2.32.10	<i>Fourier Transform Infrared Spectroscopy (FT-IR)</i>	94
2.32.11	<i>Small Angle X-Ray Scattering (SAXS)</i>	95
2.32.12	<i>Magnetic Heating Experimental Method and Procedure</i>	95
2.32.13	<i>Nuclear Magnetic Resonance (NMR) Spectroscopy</i>	95
2.32.14	<i>Energy Dispersive X-Ray Spectroscopy (EDS)</i>	96
3	CHAPTER 3: CHARACTERIZATION	97
3.1	INTRODUCTION.....	98
3.2	TRANSMISSION ELECTRON MICROSCOPY (TEM).....	98
3.2.1	<i>Magnetite Nanoparticles</i>	98
3.2.2	<i>Silica Coated Nanoparticles</i>	103
3.2.3	<i>Polymer Coated Nanoparticles</i>	108
3.3	NITROGEN GAS ADSORPTION-DESORPTION ISOTHERM AND BRUNAUER–EMMETT–TELLER (BET) SURFACE AREA ANALYSIS.....	109
3.4	X-RAY DIFFRACTION (XRD).....	113
3.5	SMALL ANGLE X-RAY SCATTERING (SAXS).....	115
3.6	ENERGY DISPERSIVE X-RAY SPECTROSCOPY (EDS).....	117
3.7	VIBRATING SAMPLE MAGNETOMETRY (VSM).....	117
3.8	SCANNING COLUMN MAGNETOMETRY (SCM).....	125
3.9	DYNAMIC LIGHT SCATTERING (DLS).....	131
3.10	DIFFERENTIAL SCANNING CALORIMETRY (DSC).....	136

3.11	CONTACT ANGLE MEASUREMENTS	137
3.12	NUCLEAR MAGNETIC RESONANCE SPECTROSCOPY (NMR)	138
3.13	FOURIER TRANSFORM INFRARED (FTIR) SPECTROSCOPY	140
3.14	MAGNETIC HEATING PROPERTIES OF THE NANOPARTICLES	144
3.14.1	<i>Neel and Brownian relaxation</i>	144
3.14.2	<i>Specific Power Absorption (SPA)</i>	146
3.14.3	<i>Intrinsic loss power (ILP)</i>	151
4	CHAPTER 4: CATALYSIS.....	153
4.1	INTRODUCTION	154
4.2	COLORIMETRIC ASSAY OF AMINE DENSITY	154
4.3	BRADFORD ASSAY FOR EVALUATING LIPASE IMMOBILISATION	157
4.4	BIO-CATALYTIC APPLICATION: HYDROLYSIS OF PNPP	159
4.5	EFFECTS OF AC MAGNETIC FIELD ON CATALYTIC ACTIVITY OF THE LIPASE.....	162
4.6	ENANTIOSELECTIVE DESYMMETRIZATION OF CIS-3,5-DIACETOXY-1-CYCLOPENTENE TO (1S,4R)-CIS-4-ACETOXY-2-CYCLOPENTEN-1-OL	164
4.6.1	<i>Effect of Temperature on Lipase Activity</i>	176
4.7	CONCLUSIONS.....	181
5	CHAPTER 5: DRUG LOADING AND RELEASE	183
5.1	INTRODUCTION	184
5.1.1	<i>Mitomycin C (MMC)</i>	186
5.1.2	<i>Doxorubicin (DOX)</i>	186
5.1.3	<i>Drug Loading</i>	187
5.2	MMC LOADED MESOPOROUS SILICA COATED NANOPARTICLES (ME32-ME33-ME16)	190
5.2.1	<i>Drug Loading</i>	191
5.2.2	<i>MMC Drug Release</i>	193
5.3	MMC LOADED MAGNETOLIPOSOMES.....	195
5.3.1	<i>Drug Loading</i>	196
5.3.2	<i>Drug Release</i>	197
5.3.3	<i>Hyperthermia triggered drug release</i>	198
5.4	ME60	200
5.4.1	<i>Drug Loading</i>	201
5.4.2	<i>pH Triggered Drug Release</i>	202
5.4.3	<i>Temperature Triggered Drug Release</i>	203
5.5	ME60-L	205
5.5.1	<i>Drug Loading</i>	207

5.5.2	<i>pH Triggered DOX Release</i>	207
5.5.3	<i>Temperature Triggered DOX Release</i>	209
5.6	ME55-PEG-PCL	211
5.6.1	<i>Drug Loading</i>	212
5.6.2	<i>pH Triggered Drug Release</i>	213
5.6.3	<i>Hyperthermia Triggered Drug Release</i>	214
5.7	DOX LOADING OF ME93-PEG-PCL AND ME94-PEG-PCL.....	217
5.7.1	<i>Drug Loading</i>	218
5.7.2	<i>pH Triggered Drug Release</i>	219
5.7.3	<i>Temperature Stimuli Drug Release</i>	221
5.8	SUMMARY	225
6	CHAPTER 6: CELL RESPONSE	227
6.1	INTRODUCTION TO CYTOTOXICITY STUDY.....	228
6.2	BREAST CANCER CELLS LINES (MCF7)	228
6.3	GLIOMA CELL LINE (U87)	229
6.4	GROWTH CURVES.....	229
6.5	BIOCOMPATIBILITY EVALUATION OF THE SYNTHESISED MATERIALS	231
6.5.1	<i>Data Analysis</i>	231
6.5.2	<i>ME53 (bare magnetite nanoparticles)</i>	232
6.5.3	<i>PEG-PCL</i>	234
6.5.4	<i>ME55-PEG-PCL</i>	236
6.5.5	<i>ME60</i>	238
6.5.6	<i>ME93-PEG-PCL and ME94-PEG-PCL</i>	240
6.5.7	<i>ME60-L</i>	243
6.5.8	<i>Summary</i>	244
6.6	IN VITRO CYTOTOXICITY STUDY OF DRUG LOADED NANOPARTICLES	247
6.6.1	<i>DOX Loaded ME55-PEG-PCL</i>	250
6.6.2	<i>DOX loaded ME93-PEG-PCL and ME94-PEG-PCL</i>	253
6.6.3	<i>DOX loaded ME60</i>	257
6.6.4	<i>DOX loaded ME60-L</i>	259
6.6.5	<i>Summary</i>	261
6.7	EFFECT OF MAGNETIC HYPERTHERMIA ON CELL VIABILITY	263
6.7.1	<i>ME53</i>	264
6.7.2	<i>ME55-PEG-PCL</i>	266
6.7.3	<i>ME93-PEG-PCL and ME94-PEG-PCL</i>	268

6.7.4	ME60	272
6.7.5	ME60-L	274
6.8	SUMMARY	276
7	CHAPTER 7: CONCLUSION AND FUTURE WORK	280
7.1	CONCLUSIONS	281
7.2	FUTURE WORK	285
8	REFERENCES	286
9	APPENDICES	321

LIST OF TABLES

TABLE 1-1.	A SUMMARY OF THE DIFFERENT TYPES OF MAGNETIC BEHAVIOUR	8
TABLE 1-2.	LIST OF METHODS COMMONLY USED TO SYNTHESISE MAGNETITE NANOPARTICLES.....	11
TABLE 1-3.	A LIST OF MATERIALS USED FOR COATING MAGNETITE NANOPARTICLES AND THEIR APPLICATIONS	16
TABLE 1-4.	A LIST OF MESOPOROUS SILICA BASED DRUG DELIVERY SYSTEMS.....	25
TABLE 1-5.	A LIST OF MAGNETOLIPOSOME BASED DRUG DELIVERY SYSTEMS.....	30
TABLE 1-6.	A LIST OF MAGNETIC MICELLES USED AS DRUG DELIVERY SYSTEMS.....	34
TABLE 1-7.	A LIST OF FDA APPROVED COMMERCIALISED IRON OXIDE NANOCOMPOSITES CURRENTLY USED IN NANOMEDICINE	38
TABLE 1-8.	A LIST OF THE LIPASES AND THEIR COMMON APPLICATION	48
TABLE 2-1.	DESCRIPTION, USAGE AND STORAGE INFORMATION OF SOLUTIONS AND BUFFERS USED IN THIS PROJECT.....	62
TABLE 2-2.	LIST OF MATERIALS USED AGAINST CELLS FOR CYTOTOXICITY STUDY	89
TABLE 3-1.	SUMMARY OF THE CHARACTERIZATION METHODS USED FOR DIFFRENT MATERIALS	99
TABLE 3-2.	SUMMARY OF THE SURFACE AREA OF THE MATERIAL	109
TABLE 3-3.	CONSTANTS USED FOR CALCULATIONS IN LANGEVIN EQUATION.....	120
TABLE 3-4.	THE SATURATION MAGNETIZATION FOR SILICA COATED NANOPARTICLES	121
TABLE 3-5.	VARIABLES USED IN POWER LOSS CALCULATIONS	145
TABLE 3-6.	LIST OF THE SOLVENTS SPECIFIC HEAT (C _s)	149
TABLE 3-7.	COMPARISON OF THE SAMPLES SAR AND ILP VALUES WITH THE LITERATURE. BLUE CELLS INDICATE THE MATERIALS SYNTHESISED IN THIS PROJECT.....	149
TABLE 4-1.	EQUIVALENT AMOUNT OF NANOPARTICLES TO OBTAIN 500 μG OF IMMOBILISED LIPASE 159	
TABLE 4-2.	ENANTIOMERIC EXCESS OF (1S, 4R)-CIS-4-ACETOXY-2-CYCLOPENTEN-1 USING IMMOBILIZED CRL AT DIFFERENT INTERVALS	174
TABLE 4-3.	ENANTIOMERIC EXCESS OF (1S, 4R)-CIS-4-ACETOXY-2-CYCLOPENTEN-1 USING IMMOBILIZED CRL AT DIFFERENT INTERVALS	180
TABLE 5-1.	A SUMMARY OF DRUG LOADING CONTENT AND DRUG LOADING EFFICIENCY OF THE DEVELOPED MATERIALS	190
TABLE 6-1.	IC ₅₀ FOR FREE DOX AT DIFFERENT INCUBATION TIMES	249
TABLE 6-2.	THE IC ₅₀ VALUES FOR DOX LOADED MAGNETIC MICELLES AGAINST MCF7AND U87.....	251
TABLE 6-3.	THE IC ₅₀ VALUES FOR DOX LOADED ME93-PEG-PCL AGAINST MCF7AND U87.....	256
TABLE 6-4.	THE IC ₅₀ VALUES FOR DOX LOADED ME94-PEG-PCL AGAINST MCF7AND U87.....	257
TABLE 6-5.	THE IC ₅₀ VALUES FOR DOX LOADED ME60 AGAINST MCF7AND U87	259

TABLE 6-6.	THE IC50 VALUES FOR DOX LOADED ME60-L AGAINST MCF7 AND U87	261
TABLE 6-7.	CALCULATED IC50 FOR DIFFERENT DOX ENCAPSULATED MATERIALS AGAINST U87 CELLS	263
TABLE 6-8.	CALCULATED IC50 FOR DIFFERENT DOX ENCAPSULATED MATERIALS AGAINST MCF7	263

LIST OF FIGURES

FIGURE 1-1 APPLICATIONS OF NANOPARTICLES	6
FIGURE 1-2. TYPICAL HYSTERESIS LOOP OF A FERROMAGNETIC MATERIAL.....	9
FIGURE 1-3. STRUCTURAL FORMULA AND (B) SPACE –FILLING MODEL OF SOY PC (AVATI POLAR LIPIDS, 2016) 29	29
FIGURE 1-4. (A) MAGNETOLIPOSOMES, AND (B) LIPOSOME CAPPED MESOPOROUS SILICA COATED MAGNETITE	32
FIGURE 1-5. (A) PEG-PCL MAGNETIC MICELLES, (B) PEG-PCL CAPPED MESOPOROUS SILICA COATED MAGNETITE, AND (C) PEG-PCL CAPPED MESOPOROUS SILICA COATED MAGNETITE.....	37
FIGURE 1-6. SCHEMATIC REPRESENTATION OF MAGNETIC NANOPARTICLE-BASED DRUG DELIVERY SYSTEM(PARK ET AL., 2010).	40
FIGURE 1-7. EPIDOXORUBICIN CHEMICALLY ATTACHED TO MAGNETIC NANOPARTICLES WERE ADMINISTERED TO CANCER PATIENTS, A PERMANENT MAGNETIC WAS PLACED IN THE WAY TO ASSURE THE DISTANCE LESS THAN 0.5 CM FROM THE TUMOUR SURFACE. THE MAGNETIC FIELD OF (0.5-0.8T) WAS REACHED (SHAPIRO ET AL., 2015).	41
FIGURE 1-8. AC MAGNETIC FIELD APPLICATOR (MFH300F, MAGFORCE® NANOTECHNOLOGIES GMBH, BERLIN). FOR COOLING PURPOSES, A CLOSED LOOP OF TUBES WITH CIRCULATING COLD WATER, IS PLACED AROUND THE PATIENT’S INNER THIGH, PERINEUM AND THE GROIN (JOHANNSEN ET AL., 2005B). 44	44
FIGURE 1-9. REACTIONS CATALYSED BY LIPASES (BARROS ET AL., 2010)	47
FIGURE 1-10. (3-AMINOPROPYL)-TRIETHOXSILANE (APTS).....	54
FIGURE 1-11. SURFACE FUNCTIONALISATION OF MESOPOROUS SILICA NANOPARTICLES, (A) GRAFTING METHOD FOR ORGANIC MODIFICATION OF MESOPOROUS SILICA MATERIAL WITH (R’O)3SIR. R= ORGANIC FUNCTIONAL GROUP, AND (B) CO-CONDENSATION METHOD (DIRECT SYNTHESIS) FOR THE ORGANIC MODIFICATION OF MESOPOROUS PURE SILICA PHASES. R=ORGANIC FUNCTIONAL GROUP(HOFFMANN ET AL., 2006).	55
FIGURE 1-12. GLUTARALDEHYDE MOLECULAR STRUCTURE	56
FIGURE 3-1. TEM IMAGE OF ME01, MAGNETITE NANOPARTICLES PREPARED BY OXIDATIVE HYDROLYSIS OF IRON SULPHATE IN ALKALINE MEDIA.....	101
FIGURE 3-2. TEM IMAGE OF ME18, MAGNETITE NANOPARTICLES PREPARED BY COPRECIPITATION OF IRON SALTS	101
FIGURE 3-3. TEM OF ME55, PREPARED BY OLEIC ACID FUNCTIONALISING THE MAGNETITE NANOPARTICLES PREPARED BY COPRECIPITATION OF IRON SALTS.....	102
FIGURE 3-4. TEM IMAGE OF ME59, OLEIC ACID COATED MAGNETITE NANOPARTICLES PREPARED BY THERMAL DECOMPOSITION OF FE (ACAC)3.....	102

FIGURE 3-5. TEM IMAGE OF ME16, CORE SHELL NANOPARTICLES.....	103
FIGURE 3-6. TEM IMAGE OF ME32, CORE SHELL NANOPARTICLES.....	104
FIGURE 3-7. TEM IMAGE OF ME33, MESOPOROUS CORE SHELL NANOPARTICLES	104
FIGURE 3-8. TEM IMAGE OF ME60, MESOPOROUS CORE-SHELL NANOPARTICLES.....	105
FIGURE 3-9. TEM IMAGE OF ME82, MESOPOROUS CORE-SHELL NANOPARTICLES.....	105
FIGURE 3-10. TEM IMAGE OF ME56, CORE SHELL PARTICLES.....	106
FIGURE 3-11. TEM IMAGE OF ME93, SILICA COATED MAGNETITE NANOPARTICLES PREPARED BY DIRECT COATING OF MAGNETITE NANOPARTICLES	106
FIGURE 3-12. TEM IMAGE OF ME80, HYDROPHOBIC SILICA COATED NANOPARTICLES.....	107
FIGURE 3-13. TEM IMAGE OF ME94, HYDROPHOBIC SILICA COATED CORE SHELL PARTICLES PREPARED BY PROTECTED ETCHING METHOD.....	107
FIGURE 3-14. TEM IMAGE OF ME94-I, PVP PROTECTED ETCHED SILICA NANOPARTICLES.....	108
FIGURE 3-15 TEM IMAGES OF PVP PROTECTED ETCHED SILICA NANOPARTICLES, (A) AFTER 20 MINUTES ETCHING, AND (B) AFTER 10 MINUTES ETCHING	108
FIGURE 3-16. TEM IMAGE OF ME55-PEG-PCL, POLYMER COATED MAGNETITE NANOPARTICLES.....	109
FIGURE 3-17. NITROGEN GAS ADSORPTION-DESORPTION ISOTHERM OF ME32, BET SURFACE AREA: 133.9683 ± 0.5248 M ² /G.....	110
FIGURE 3-18. NITROGEN GAS ADSORPTION-DESORPTION ISOTHERM OF ME33, BET SURFACE AREA: 1187.7596 ± 6.7348 M ² /G.....	111
FIGURE 3-19. NITROGEN GAS ADSORPTION-DESORPTION ISOTHERM OF ME33 AFTER CHEMICAL PFL IMMOBILIZATION. BET SURFACE AREA: 146.9339 ± 2.5072 M ² /G	111
FIGURE 3-20. NITROGEN GAS ADSORPTION-DESORPTION ISOTHERM OF THE ME60-BET SURFACE AREA: 358.0238 ± 0.5267 M ² /G.....	112
FIGURE 3-21. NITROGEN GAS ADSORPTION-DESORPTION ISOTHERM OF ME93, BET SURFACE AREA: 752.8064 ± 7.6538 M ² /G.....	113
FIGURE 3-22. BET ISOTHERM OF ME94 BET SURFACE AREA: 574.5482 ± 3.5390 M ² /G.....	113
FIGURE 3-23. XRD PATTERN OF BARE MAGNETITE (ME18)	114
FIGURE 3-24. XRD PATTERN OF SILICA COATED MAGNETITE (ME33).....	115
FIGURE 3-25. SAXS PATTERN OF ME32 (SILICA COATED MAGNETITE).....	116
FIGURE 3-26. SAXS PATTERN OF ME33 (SILICA COATED MAGNETITE).....	116
FIGURE 3-27. EDS SPECTRUM DATA OF ME33 (SILICA COATED MAGNETITE NANOPARTICLES)	117
FIGURE 3-28. MAGNETIC MEASUREMENTS OF BARE MAGNETITE NANOPARTICLES PREPARED BY OXIDATIVE HYDROLYSIS OF IRON SULPHATE IN ALKALINE MEDIA (ME01).....	118
FIGURE 3-29. MAGNETIC MEASUREMENTS OF BARE MAGNETITE NANOPARTICLES PREPARED BY COPRECIPITATION OF IRON SALTS (ME18).....	119
FIGURE 3-30. MAGNETIC MEASUREMENTS OF SILICA COATED MAGNETITE NANOPARTICLES (ME16)..	122
FIGURE 3-31. MAGNETIC MEASUREMENTS OF SILICA COATED MAGNETITE NANOPARTICLES (ME32)..	122
FIGURE 3-32. MAGNETIC MEASUREMENTS OF SILICA COATED MAGNETITE NANOPARTICLES (ME33)..	123
FIGURE 3-33. MAGNETIC MEASUREMENTS OF SILICA COATED MAGNETITE NANOPARTICLES (ME60)..	123
FIGURE 3-34. MAGNETIC MEASUREMENTS OF SILICA COATED MAGNETITE NANOPARTICLES (ME93)..	124

FIGURE 3-35. MAGNETIC MEASUREMENTS OF SILICA COATED MAGNETITE NANOPARTICLES (ME94) (THE OBSERVED NOISE ON THE SIGNAL IS DUE TO LOW SATURATION MAGNETIZATION VALUES FOR ME94)	124
FIGURE 3-36. SCM PROFILE OF THE BARE MAGNETITE (ME18)	126
FIGURE 3-37. SCM PROFILE OF THE OLEIC ACID FUNCTIONALISED MAGNETITE (ME55)	126
FIGURE 3-38. SCM PROFILE FOR SILICA COATED MAGNETITE (ME33)	127
FIGURE 3-39. IMAGE OF THE SCM COLUMN CONTAINING ME33 AFTER 40 MINUTES	127
FIGURE 3-40. SCM PROFILE FOR SILICA COATED MAGNETITE (ME60)	128
FIGURE 3-41. SCM PROFILE OF PEG-PCL COATED MAGNETITE NANOPARTICLES (ME55-PEG-PCL)	128
FIGURE 3-42. SCM PROFILE OF PEG-PCL CAPPED SILICA COATED NANOPARTICLES (ME93-PEG-PCL)	129
FIGURE 3-43. IMAGES OF ME93, (A) BEFORE POLYMER COATING, AND (B) AFTER POLYMER COATING (ME93-PEG-PCL)	129
FIGURE 3-44. SCM PLOT FOR LIPOSOME COATED MAGNETITE (MAGNETOLIPOSOMES-ME09)	130
FIGURE 3-45. SCM PROFILE OF THE LIPOSOME CAPPED SILICA NANOPARTICLES (PROTOCELLS-ME60-L)	130
FIGURE 3-46. DLS SIZE DISTRIBUTION PROFILE OF OLEIC ACID FUNCTIONALISED MAGNETITE NANOPARTICLES (ME55)	131
FIGURE 3-47. DLS SIZE DISTRIBUTION PROFILE OF MAGNETOLIPOSOMES (ME09)	132
FIGURE 3-48. DLS SIZE DISTRIBUTION PROFILE OF MMC LOADED MAGNETOLIPOSOMES	132
FIGURE 3-49. DLS SIZE DISTRIBUTION PROFILE OF PEG-PCL MICELLES	133
FIGURE 3-50. DLS SIZE DISTRIBUTION PROFILE OF PEG-PCL COATED MAGNETITE NANOPARTICLES (ME55-PEG-PCL)	133
FIGURE 3-51. DLS SIZE DISTRIBUTION PROFILE OF DOX LOADED PEG-PCL COATED MAGNETITE NANOPARTICLES (ME55-PEG-PCL)	134
FIGURE 3-52. DLS SIZE DISTRIBUTION PROFILE OF PEG-PCL CAPPED SILICA COATED MAGNETITE NANOPARTICLES (ME93-PEG-PCL)	134
FIGURE 3-53. DLS SIZE DISTRIBUTION PROFILE OF DOX LOADED PEG-PCL CAPPED SILICA COATED MAGNETITE NANOPARTICLES (DOX LOADED 93-PEG-PCL)	135
FIGURE 3-54. DLS SIZE DISTRIBUTION PROFILE OF LIPOSOME CAPPED SILICA COATED MAGNETITE NANOPARTICLES (PROTOCELLS-ME60-L)	135
FIGURE 3-55. DSC THERMOGRAMS OF COOLING STAGE OF PEG-PCL MICELLES	136
FIGURE 3-56. DSC THERMOGRAMS OF HEATING STAGE OF PEG-PCL MICELLES	137
FIGURE 3-57. MEASUREMENT OF STATIC CONTACT ANGLE OF A WATER DROPLET ON SILICA COATED NANOPARTICLES (ME60)	137
FIGURE 3-58. MEASUREMENT OF STATIC CONTACT ANGLE OF A WATER DROPLET ON HYDROPHOBIC SILICA COATED NANOPARTICLES (ME94)	138
FIGURE 3-59. MEASUREMENT OF STATIC CONTACT ANGLE OF A WATER DROPLET ON HYDROPHOBIC SILICA COATED NANOPARTICLES (ME93)	138
FIGURE 3-60. ¹ H-NMR SPECTRA OF PEG-PCL MICELLE DISSOLVED IN TWO D ₂ O	139
FIGURE 3-61. ¹ H-NMR SPECTRA OF PEG-PCL DISSOLVED IN IN CDCL ₃	140

FIGURE 3-62. FTIR SPECTRUM OF MAGNETITE NANOPARTICLES (ME18).....	141
FIGURE 3-63. FTIR SPECTRUM OF OLEIC ACID COATED MAGNETITE NANOPARTICLES (ME55)	141
FIGURE 3-64. FTIR SPECTRUM OF SILICA COATED MAGNETITE NANOPARTICLES (ME60).....	142
FIGURE 3-65. FTIR SPECTRUM OF PEG-PCL DIBLOCK COPOLYMER.....	142
FIGURE 3-66. FTIR SPECTRUM OF PEG-PCL COATED MAGNETITE NANOPARTICLES (ME55-PEG-PCL)	143
FIGURE 3-67. FTIR SPECTRUM OF PEG-PCL CAPPED SILICA COATED MAGNETITE NANOPARTICLES (ME93- PEG-PCL).....	144
FIGURE 3-68. TIME AND FIELD DEPENDENT TEMPERATURE CURVE OF ME18 UNDER THE AC MAGNETIC FIELD IRRADIATION.....	147
FIGURE 3-69. TIME AND FIELD DEPENDENT TEMPERATURE CURVE OF ME55 UNDER THE AC MAGNETIC FIELD IRRADIATION.....	147
FIGURE 3-70. TIME AND FIELD DEPENDENT TEMPERATURE CURVE OF ME33 UNDER THE AC MAGNETIC FIELD IRRADIATION.....	148
FIGURE 4-1. STANDARD CURVE OF 4-NITROBENZALDEHYDE DILUTIONS IN COUPLING SOLUTION (λ 282NM).	155
FIGURE 4-2. STANDARD CURVE OF 4-NITROBENZALDEHYDE DILUTIONS IN HYDROLYSIS SOLUTION (λ 282NM).	155
FIGURE 4-3. SURFACE AMINE DENSITY OF MESOPOROUS SILICA COATED MAGNETITE PREPARED FOLLOWING WATER METHOD. MEASURING IN COUPLING SOLUTION (A) AND MEASURING IN HYDROLYSIS SOLUTION (B). EACH COLUMN REPRESENTS AN INDEPENDENT EXPERIMENT AND ERROR BARS PRESENT STANDARD DEVIATION BETWEEN DIFFERENT SAMPLES IN EACH EXPERIMENT.....	156
FIGURE 4-4. SURFACE AMINE DENSITY OF MESOPOROUS SILICA COATED MAGNETITE PREPARED FOLLOWING TPRE METHOD. MEASURING IN COUPLING SOLUTION (A) AND MEASURING IN HYDROLYSIS SOLUTION (B). EACH COLUMN REPRESENTS AN INDEPENDENT EXPERIMENT AND ERROR BARS PRESENT STANDARD DEVIATION BETWEEN DIFFERENT SAMPLES IN EACH EXPERIMENT.....	156
FIGURE 4-5. CALIBRATION CURVE FOR PFL.....	157
FIGURE 4-6. CALIBRATION CURVES FOR CRL.....	158
FIGURE 4-7. THE AVERAGE ENZYME IMMOBILISATION PROFILES. VALUES ARE MEAN \pm STANDARD DEVIATION. ALL EXPERIMENTS ARE REPEATED AT LEAST 4 TIMES.	158
FIGURE 4-8. CALIBRATION CURVE FOR P-NITROPHENOL (PNP) IN A 1:1 MIXTURE OF REAGENT A: ISOPROPANOL	159
FIGURE 4-9. THE CATALYTIC ACTIVITY OF FREE, PHYSICALLY ADSORBED AND IMMOBILISED LIPASES TO PRODUCE PNP. (*AND ** STATISTICALLY SIGNIFICANT ($P < 0.05$) DIFFERENCE BETWEEN FREE CRL ACTIVITY AND IMMOBILISED CRL ACTIVITY)	160
FIGURE 4-10. THE REUSABILITY OF THE LIPASES OVER 4 SUCCESSIVE CYCLES.	161
FIGURE 4-11. MAGNETIC HEATING PROFILE OF THE ENZYME IMMOBILISED MAGNETIC NANOPARTICLES (ME33) CORRESPONDING TO FIELD FREQUENCY OF 406 KHZ.	162

FIGURE 4-12. HYDROLYSIS OF PNPP USING CHEMICALLY IMMOBILISED CRL UNDER INFLUENCE OF A MAGNETIC FIELD COMPARED WITH IN INCUBATOR AT 32°C.	163
FIGURE 4-13. HYDROLYSIS OF PNPP USING PHYSICALLY IMMOBILISED CRL UNDER INFLUENCE OF A MAGNETIC FIELD COMPARED WITH IN INCUBATOR AT 32°C.	163
FIGURE 4-14. SCANNED GC CHROMATOGRAMS OF THE REACTION USING PFL.	165
FIGURE 4-15. SCANNED GC CHROMATOGRAMS OF THE REACTION USING CRL.	166
FIGURE 4-16. CALIBRATION CURVES FOR (1S, 4R)-CIS-4-ACETOXY-2-CYCLOPENTEN-1-OL IN WATER. ...	167
FIGURE 4-17. CALIBRATION CURVES FOR CIS-4-CYCLOPENTENE-1,3-DIOL IN WATER.	167
FIGURE 4-18. CALIBRATION CURVE FOR CIS-3,5-DIACETOXY-1-CYCLOPENTENE IN HEXANE.	167
FIGURE 4-19. PERCENTAGE (%) OF UNREACTED CIS-3,5-DIACETOXY-1-CYCLOPENTENE AND THE CORRESPONDING PRODUCTS OF ENZYMATIC HYDROLYSIS OF CIS-3,5-DIACETOXY-1-CYCLOPENTENE USING CHEMICALLY IMMOBILISED PFL ON THE SURFACE OF THE NANOPARTICLES AT DIFFERENT TIME INTERVALS OF 1, 4, 24 AND 48 HOURS.	168
FIGURE 4-20. PERCENTAGE (%) OF UNREACTED CIS-3,5-DIACETOXY-1-CYCLOPENTENE AND THE CORRESPONDING PRODUCTS OF ENZYMATIC HYDROLYSIS OF CIS-3,5-DIACETOXY-1-CYCLOPENTENE USING PHYSICALLY IMMOBILISED PFL ON THE SURFACE OF THE NANOPARTICLES AT DIFFERENT TIME INTERVALS OF 1, 4, 24 AND 48 HOURS.	169
FIGURE 4-21. PERCENTAGE (%) OF UNREACTED CIS-3,5-DIACETOXY-1-CYCLOPENTENE AND THE CORRESPONDING PRODUCTS OF ENZYMATIC HYDROLYSIS OF CIS-3,5-DIACETOXY-1-CYCLOPENTENE USING FREE PFL AT DIFFERENT TIME INTERVALS OF 1, 4, 24 AND 48 HOURS.	169
FIGURE 4-22. COMPARISON BETWEEN FREE AND IMMOBILISED PFL LIPASES IN FORMING (1S, 4R)-CIS-4- ACETOXY-2-CYCLOPENTEN-1 DURING THE 48 HOURS REACTION PERIOD. AND CIS-4- CYCLOPENTENE-1,3-DIOL, RESPECTIVELY AVERAGE ACETOXY.	170
FIGURE 4-23. COMPARISON BETWEEN FREE AND IMMOBILISED PFL LIPASES IN FORMING CIS-4- CYCLOPENTENE-1,3-DIOL DURING THE 48 HOURS REACTION PERIOD.	171
FIGURE 4-24. REUSABILITY OF PFL IN PRODUCTION OF (1S, 4R)-CIS-4-ACETOXY-2-CYCLOPENTEN-1 OVER 3 CYCLES OF 24 HOURS REACTION AT 25°C. SINCE FREE ENZYME COULD NOT BE RECOVERED FROM THE REACTION MIXTURE, IT IS PRESENTED ONLY IN ONE CYCLE.	172
FIGURE 4-25. PERCENTAGE (%) OF UNREACTED CIS-3,5-DIACETOXY-1-CYCLOPENTENE AND THE CORRESPONDING PRODUCTS OF ENZYMATIC HYDROLYSIS OF CIS-3,5-DIACETOXY-1-CYCLOPENTENE USING CHEMICALLY IMMOBILISED CRL ON THE SURFACE OF THE NANOPARTICLES AT DIFFERENT TIME INTERVALS OF 1, 4, 24 AND 48 HOURS.	172
FIGURE 4-26. PERCENTAGE (%) OF UNREACTED CIS-3,5-DIACETOXY-1-CYCLOPENTENE AND THE CORRESPONDING PRODUCTS OF ENZYMATIC HYDROLYSIS OF CIS-3,5-DIACETOXY-1-CYCLOPENTENE USING PHYSICALLY IMMOBILISED CRL ON THE SURFACE OF THE NANOPARTICLES AT DIFFERENT TIME INTERVALS OF 1, 4, 24 AND 48 HOURS.	173
FIGURE 4-27. PERCENTAGE (%) OF UNREACTED CIS-3,5-DIACETOXY-1-CYCLOPENTENE AND THE CORRESPONDING PRODUCTS OF ENZYMATIC HYDROLYSIS OF CIS-3,5-DIACETOXY-1-CYCLOPENTENE FREE CRL AT DIFFERENT TIME INTERVALS OF 1, 4, 24 AND 48 HOURS.	173

FIGURE 4-28. COMPARISON BETWEEN FREE AND IMMOBILISED CRL LIPASES IN FORMING (1S, 4R)-CIS-4-ACETOXY-2-CYCLOPENTEN-1 DURING THE 48 HOURS REACTION PERIOD.	175
FIGURE 4-29. COMPARISON BETWEEN FREE AND IMMOBILISED PFL LIPASES IN FORMING CIS-4-CYCLOPENTENE-1,3-DIOL DURING THE 48 HOURS REACTION PERIOD.....	175
FIGURE 4-30. REUSABILITY OF CRL IN PRODUCTION OF (1S, 4R)-CIS-4-ACETOXY-2-CYCLOPENTEN-1 OVER 3 CYCLES OF 24 HOURS REACTION AT 25°C. SINCE FREE ENZYME COULD NOT BE RECOVERED FROM THE REACTION MIXTURE, IT IS PRESENTED ONLY IN ONE CYCLE	176
FIGURE 4-31. EFFECTS OF REACTION TEMPERATURE ON HYDROLYTIC ACTIVITIES PFL IN FORMING (1S,4R)- CIS-4-ACETOXY-2-CYCLOPENTEN-1-OL AT TWO DIFFERENT TEMPERATURES OF 25°C AND 37°C, OVER 48 HOUR PERIOD.....	177
FIGURE 4-32. REUSABILITY OF PFL IN PRODUCTION OF (1S, 4R)-CIS-4-ACETOXY-2-CYCLOPENTEN-1 OVER 3 CYCLES OF 24 HOURS REACTION AT 37°C. SINCE FREE ENZYME COULD NOT BE RECOVERED FROM THE REACTION MIXTURE, IT IS PRESENTED ONLY IN ONE CYCLE.....	178
FIGURE 4-33. EFFECTS OF REACTION TEMPERATURE ON HYDROLYTIC ACTIVITIES CRL IN FORMING (1S,4R)- CIS-4-ACETOXY-2-CYCLOPENTEN-1-OL AT TWO DIFFERENT TEMPERATURES OF 25°C AND 37°, OVER 48 HOUR PERIOD.....	179
FIGURE 4-34. . REUSABILITY OF CRL IN PRODUCTION OF (1S, 4R)-CIS-4-ACETOXY-2-CYCLOPENTEN-1 OVER 3 CYCLES OF 24 HOURS REACTION AT 37°C. SINCE FREE ENZYME COULD NOT BE RECOVERED FROM THE REACTION MIXTURE, IT IS PRESENTED ONLY IN ONE CYCLE.....	181
FIGURE 5-1. STRUCTURE OF MITOMYCIN C	186
FIGURE 5-2. DOX STRUCTURE.....	187
FIGURE 5-3. STANDARD CURVE OF DOX IN PBS	188
FIGURE 5-4. STANDARD CURVE OF DOX IN ACETATE BUFFER	188
FIGURE 5-5. STANDARD CURVE FOR MMC IN WATER	189
FIGURE 5-6. STANDARD CURVE FOR MMC IN PBS	189
FIGURE 5-7. MMC LOADING PROFILE OF ME16 AT DIFFERENT TEMPERATURES	191
FIGURE 5-8. MMC LOADING PROFILE OF ME32 AT DIFFERENT TEMPERATURES	192
FIGURE 5-9. MMC LOADING PROFILE OF ME33 AT DIFFERENT TEMPERATURES	192
FIGURE 5-10 RELATION BETWEEN SHELL THICKNESS AND DRUG LOADING CONTENT.	193
FIGURE 5-11. MMC RELEASE FROM ME16 IN PBS BUFFER AT BODY TEMPERATURE (37°C)	194
FIGURE 5-12. MMC RELEASE FROM ME32 IN PBS BUFFER AT BODY TEMPERATURE (37°C)	194
FIGURE 5-13. MMC RELEASE FROM ME33 IN PBS BUFFER AT BODY TEMPERATURE (37°C)	195
FIGURE 5-14. DRUG LOADING PROFILE OF MAGNETOLIPOSOMES OVER 48 HOURS.	197
FIGURE 5-15. MMC RELEASE PROFILE OF MAGNETOLIPOSOMES.....	198
FIGURE 5-16. HEATING PROFILE OF THE MAGNETOLIPOSOMES DURING HYPERTHERMIA TRIGGERED DRUG RELEASE USING AC MAGNETIC FIELD WITH FIELD STRENGTH OF 200 G AND FREQUENCY OF 406 KHZ.	199
FIGURE 5-17. IN VITRO DRUG RELEASE AT 37°C IN INCUBATOR AND UNDER MAGNETIC HYPERTHERMIA CONDITION.	199

FIGURE 5-18. DOX LOADING PROFILE FOR MESOPOROUS SILICA COATED MAGNETIC NANOPARTICLES	
201	
FIGURE 5-19. DOX RELEASE PROFILE INVESTIGATED AT PH=7.4 AND PH=5.5. MEASUREMENTS WERE PERFORMED AT 37°C .THE RELEASE RATE IS HIGHER AT LOWER PH.	202
FIGURE 5-20. MAGNETIC HEATING PROFILE OF ME60 WITH THE CONCENTRATION OF 10 MG/ML IN A VARIABLE MAGNETIC FIELD WITH MAXIMUM STRENGTH OF 200 G AND FREQUENCY OF 406 KHZ. THE FIELD WAS ADJUSTED IN THE WAY TO KEEP THE TEMPERATURE AT 43°C.....	204
FIGURE 5-21. ME60 IN VITRO DRUG RELEASE AT 37°C IN INCUBATOR AND UNDER MAGNETIC HYPERTHERMIA CONDITION	205
FIGURE 5-22. DOX RELEASE PROFILE OF ME60-L INVESTIGATED AT PH=7.4 AND PH=5.5. MEASUREMENTS WERE PERFORMED AT 37°C .THE RELEASE RATE IS HIGHER AT LOWER PH.....	208
FIGURE 5-23. MAGNETIC HEATING PROFILE OF ME60-L WITH THE CONCENTRATION OF 10 MG/ML IN A VARIABLE MAGNETIC FIELD WITH MAXIMUM STRENGTH OF 200 G AND FREQUENCY OF 406 KHZ. THE FIELD WAS ADJUSTED IN THE WAY TO KEEP THE TEMPERATURE AT 43°C.....	210
FIGURE 5-24. ME60-L IN VITRO DRUG RELEASE AT 37°C IN INCUBATOR AND UNDER MAGNETIC HYPERTHERMIA CONDITION	210
FIGURE 5-25. DOX RELEASE PROFILE FOR ME55-PEG-PCL, INVESTIGATED AT PH 7.4 AND PH 5.5. MEASUREMENTS WERE PERFORMED AT 37°C .THE RELEASE RATE IS HIGHER AT LOWER PH.	213
FIGURE 5-26. MAGNETIC HEATING PROFILE OF MAGNETIC MICELLES WITH THE CONCENTRATION OF 15.1MG/ML IN A VARIABLE MAGNETIC FIELD WITH MAXIMUM STRENGTH OF 200 G AND FREQUENCY OF 406 KHZ. THE FIELD WAS ADJUSTED IN THE WAY TO KEEP THE TEMPERATURE AT 43°C. 215	215
FIGURE 5-27. ME55-PEG-PCL IN VITRO DRUG RELEASE AT 37°C IN INCUBATOR AND UNDER MAGNETIC HYPERTHERMIA CONDITION	215
FIGURE 5-28. PH DEPENDANT DRUG RELEASE PROFILE FOR ME93-PEG-PCL	220
FIGURE 5-29. PH DEPENDANT DRUG RELEASE PROFILE FOR ME94-PEG-PCL	220
FIGURE 5-30. MAGNETIC HEATING PROFILE OF ME93-PEG-PCL AND ME94-PEG-PCL WITH THE CONCENTRATION OF 4 MG/ML IN A VARIABLE MAGNETIC FIELD WITH MAXIMUM STRENGTH OF 200 G AND FREQUENCY OF 406 KHZ. THE FIELD WAS ADJUSTED IN THE WAY TO KEEP THE TEMPERATURE AT 43°C.....	222
FIGURE 5-31. ME93 IN VITRO DRUG RELEASE AT 37°C IN INCUBATOR AND UNDER MAGNETIC HYPERTHERMIA CONDITION	223
FIGURE 5-32. ME94 IN VITRO DRUG RELEASE AT 37°C IN INCUBATOR AND UNDER MAGNETIC HYPERTHERMIA CONDITION	223
FIGURE 6-1. GROWTH CURVE OF U87, THE DAY 0 MEASUREMENTS WERE PERFORMED 3 HOURS AFTER SEEDING THE CELLS	230
FIGURE 6-2. GROWTH CURVE OF MCF7, THE DAY 0 MEASUREMENTS WERE PERFORMED 3 HOURS AFTER SEEDING THE CELLS.	230
FIGURE 6-3. CYTOTOXICITY OF UNCOATED MAGNETITE NANOPARTICLES (ME53) AGAINST U87 EACH BAR REPRESENTS THE MEAN OF THREE MEASUREMENTS (6 WELL EACH) WITH ERROR BARS	

INDICATING STANDARD DEVIATION. BARS MARKED WITH * SHOWED NO SIGNIFICANT DIFFERENCE COMPARED TO CONTROL SAMPLE (P>0.05)	232
FIGURE 6-4. CYTOTOXICITY OF UNCOATED MAGNETITE NANOPARTICLES (ME53) AGAINST U87 CELLS. 233	
FIGURE 6-5. CYTOTOXICITY OF UNCOATED MAGNETITE NANOPARTICLES (ME53) AGAINST MCF7 CELLS. EACH BAR REPRESENTS THE MEAN OF THREE MEASUREMENTS (6 WELL EACH) WITH ERROR BARS INDICATING STANDARD DEVIATION. BARS MARKED WITH * SHOWED NO SIGNIFICANT DIFFERENCE COMPARED TO CONTROL SAMPLE (P>0.05).	233
FIGURE 6-6. BIOCOMPATIBILITY OF THE PEG-PCL MICELLES AGAINST U87CELLS.	235
FIGURE 6-7. BIOCOMPATIBILITY OF THE PEG-PCL MICELLES AGAINST MCF7 CELLS.....	235
FIGURE 6-8. BIOCOMPATIBILITY OF THE PEG-PCL COATED MAGNETITE (ME55-PEG-PCL) AGAINST U87 CELLS. BARS MARKED WITH * SHOWED STATISTICALLY SIGNIFICANT DIFFERENCE COMPARED TO CONTROL SAMPLE (P<0.05).....	237
FIGURE 6-9. BIOCOMPATIBILITY OF THE PEG-PCL COATED MAGNETITE (ME55-PEG-PCL) AGAINST MCF7 CELLS. BARS MARKED WITH * SHOWED STATISTICALLY SIGNIFICANT DIFFERENCE COMPARED TO CONTROL SAMPLE (P<0.05).....	238
FIGURE 6-10. BIOCOMPATIBILITY OF THE MESOPOROUS COATED MAGNETITE (ME60) AGAINST U87 CELLS. BARS MARKED WITH * SHOWED STATISTICALLY SIGNIFICANT DIFFERENCE COMPARED TO CONTROL SAMPLE (P<0.05).....	239
FIGURE 6-11. BIOCOMPATIBILITY OF THE MESOPOROUS COATED MAGNETITE (ME60) AGAINST MCF7 CELLS. BARS MARKED WITH * SHOWED STATISTICALLY SIGNIFICANT DIFFERENCE COMPARED TO CONTROL SAMPLE (P<0.05).....	239
FIGURE 6-12. BIOCOMPATIBILITY OF THE POLYMER CAPPED MESOPOROUS COATED MAGNETITE NANOPARTICLES (ME93-PEG-PCL) AGAINST U87 CELLS.	241
FIGURE 6-13. BIOCOMPATIBILITY OF THE POLYMER CAPPED MESOPOROUS COATED MAGNETITE NANOPARTICLES (ME94-PEG-PCL) AGAINST U87 CELLS.	241
FIGURE 6-14. BIOCOMPATIBILITY OF THE POLYMER CAPPED MESOPOROUS COATED MAGNETITE NANOPARTICLES (ME93-PEG-PCL) AGAINST MCF7 CELLS.....	242
FIGURE 6-15. BIOCOMPATIBILITY OF THE POLYMER CAPPED MESOPOROUS COATED MAGNETITE NANOPARTICLES (ME94-PEG-PCL) AGAINST MCF7 CELLS.....	242
FIGURE 6-16. BIOCOMPATIBILITY OF THE SPC LIPOSOME CAPPED MESOPOROUS COATED MAGNETITE NANOPARTICLES (ME60-L) AGAINST U87 CELLS. BARS MARKED WITH * SHOWED STATISTICALLY SIGNIFICANT DIFFERENCE COMPARED TO CONTROL SAMPLE (P<0.05)	243
FIGURE 6-17. BIOCOMPATIBILITY OF THE SPC LIPOSOME CAPPED MESOPOROUS COATED MAGNETITE NANOPARTICLES (ME60-L) AGAINST MCF7 CELLS.....	244
FIGURE 6-18. BIOCOMPATIBILITY OF BARE MAGNETITE (ME53), SILICA COATED MAGNETITE (ME60) AND POLYMER COATED MAGNETITE (ME55-PEG-PCL) AGAINST U87 CELLS AFTER 24 HOURS OF INCUBATION.	245

FIGURE 6-19. BIOCOMPATIBILITY OF BARE MAGNETITE (ME53), SILICA COATED MAGNETITE (ME60) AND POLYMER COATED MAGNETITE (ME55-PEG-PCL) AGAINST U87 CELLS AFTER 24 HOURS OF INCUBATION.	245
FIGURE 6-20. BIOCOMPATIBILITY OF SILICA COATED MAGNETITE (ME60), LIPOSOME CAPPED SILICA NANOPARTICLES (ME60-L) AND POLYMER CAPPED SILICA NANOPARTICLES (ME93-PEG-PCL) AGAINST U87 CELLS AFTER 72 HOURS OF INCUBATION.	246
FIGURE 6-21. BIOCOMPATIBILITY OF SILICA COATED MAGNETITE (ME60), LIPOSOME CAPPED SILICA NANOPARTICLES (ME60-L) AND POLYMER CAPPED SILICA NANOPARTICLES (ME93-PEG-PCL) AGAINST MCF7 CELLS AFTER 72 HOURS OF INCUBATION.....	246
FIGURE 6-22. DOX INDUCED CYTOTOXICITY AGAINST U87 CELLS FOR VARIOUS INCUBATION TIME.....	247
FIGURE 6-23. DOX INDUCED CYTOTOXICITY AGAINST MCF7 CELLS FOR VARIOUS INCUBATION TIME...	248
FIGURE 6-24. DOX INDUCED CYTOTOXICITY AGAINST MCF7 CELLS AFTER 24 HOURS OF INCUBATION WITH 3RD DEGREE POLYNOMIAL TRENDLINE.....	249
FIGURE 6-25. CYTOTOXICITY OF DOX-LOADED MICELLES (ME55-PEG-PCL) AGAINST U87 CELLS. THE CELLS WERE INCUBATED WITH DOX-LOADED MICELLE WITH DOX CONCENTRATION UP TO 17.24 MM, FOR 3, 24, 48 AND 72H AT 37 °C	250
FIGURE 6-26. CYTOTOXICITY OF DOX-LOADED MICELLES (ME55-PEG-PCL) AGAINST MCF7 CELLS. THE CELLS WERE INCUBATED WITH DOX-LOADED MICELLE WITH DOX CONCENTRATION UP TO 17.24 MM, FOR 3, 24, 48 AND 72H AT 37 °C.....	251
FIGURE 6-27 THE OPTICAL MICROSCOPY OF U87 CELL LINE (LEFT) AS CONTROL CELLS AND DOX LOADED MAGNETIC MICELLE (ME55-PEG-PCL) TREATED CELLS (RIGHT).	253
FIGURE 6-28 MCF7 THE OPTICAL MICROSCOPY OF MCF7 CELL LINE (LEFT) AS CONTROL CELLS AND DOX LOADED MAGNETIC MICELLE (ME55-PEG-PCL) TREATED CELLS (RIGHT).....	253
FIGURE 6-29. CYTOTOXICITY OF DOX-LOADED POLYMER CAPPED NANOPARTICLES (ME93-PEG-PCL) AGAINST U87 CELLS. THE CELLS WERE INCUBATED WITH DOX-LOADED NANOPARTICLES WITH DOX CONCENTRATION UP TO 17.24 MM, FOR 3, 24, 48 AND 72H AT 37°C	254
FIGURE 6-30. CYTOTOXICITY OF DOX-LOADED POLYMER CAPPED NANOPARTICLES (ME93-PEG-PCL) AGAINST MCF7 CELLS. THE CELLS WERE INCUBATED WITH DOX-LOADED NANOPARTICLES WITH DOX CONCENTRATION UP TO 17.24 MM, FOR 3, 24, 48 AND 72H AT 37°C	255
FIGURE 6-31. CYTOTOXICITY OF DOX-LOADED POLYMER CAPPED NANOPARTICLES (ME94-PEG-PCL) AGAINST U87 CELLS. THE CELLS WERE INCUBATED WITH DOX-LOADED NANOPARTICLES WITH DOX CONCENTRATION UP TO 17.24 MM, FOR 3, 24, 48 AND 72H AT 37 °C.....	255
FIGURE 6-32. CYTOTOXICITY OF DOX-LOADED POLYMER CAPPED NANOPARTICLES (ME94-PEG-PCL) AGAINST MCF7 CELLS. THE CELLS WERE INCUBATED WITH DOX-LOADED NANOPARTICLES WITH DOX CONCENTRATION UP TO 17.24 MM, FOR 3, 24, 48 AND 72H AT 37°C	256
FIGURE 6-33. CYTOTOXICITY OF DOX-LOADED POLYMER CAPPED NANOPARTICLES (ME60) AGAINST U87 CELLS. THE CELLS WERE INCUBATED WITH DOX-LOADED NANOPARTICLES WITH DOX CONCENTRATION UP TO 17.24 MM, FOR 3, 24, 48 AND 72H AT 37°C	258

FIGURE 6-34. CYTOTOXICITY OF DOX-LOADED POLYMER CAPPED NANOPARTICLES (ME60) AGAINST MCF7 CELLS. THE CELLS WERE INCUBATED WITH DOX-LOADED NANOPARTICLES WITH DOX CONCENTRATION UP TO 17.24 MM, FOR 3, 24, 48 AND 72H AT 37°C	258
FIGURE 6-35. CYTOTOXICITY OF DOX-LOADED POLYMER CAPPED NANOPARTICLES (ME60-L) AGAINST U87 CELLS. THE CELLS WERE INCUBATED WITH DOX-LOADED NANOPARTICLES WITH DOX CONCENTRATION UP TO 17.24 MM, FOR 3, 24, 48 AND 72H AT 37 °C.....	260
FIGURE 6-36. CYTOTOXICITY OF DOX-LOADED POLYMER CAPPED NANOPARTICLES (ME60-L) AGAINST MCF7 CELLS. THE CELLS WERE INCUBATED WITH DOX-LOADED NANOPARTICLES WITH DOX CONCENTRATION UP TO 17.24 MM, FOR 3, 24, 48 AND 72H AT 37°C	260
FIGURE 6-37. CYTOTOXICITY OF DIFFERENT DOX LOADED MATERIALS TOWARD U87 CELLS AFTER 24 HOURS INCUBATION.	262
FIGURE 6-38. CYTOTOXICITY OF DIFFERENT DOX LOADED MATERIALS TOWARD MCF7 CELLS AFTER 24 HOURS INCUBATION.	262
FIGURE 6-39. EFFECTS OF HYPERTHERMIA ON U87 CELLS VIABILITY, THE VIABILITY OF CELLS INCUBATED WITH ME53 AND EXPOSED TO THE MAGNETIC FIELD WERE COMPARED TO WATER BATH HYPERTHERMIA TREATED CELLS (45 MINUTES TREATMENT).	264
FIGURE 6-40. EFFECTS OF HYPERTHERMIA ON MCF7 CELLS VIABILITY, THE VIABILITY OF CELLS INCUBATED WITH ME53 AND EXPOSED TO THE MAGNETIC FIELD WERE COMPARED TO WATER BATH HYPERTHERMIA TREATED CELLS (45 MINUTES TREATMENT).	265
FIGURE 6-41. EFFECTS OF HYPERTHERMIA ON U87 CELLS VIABILITY , THE VIABILITY OF CELLS INCUBATED WITH ME55-PEG-PCL (WITH AND WITHOUT DRUG) AND EXPOSED TO THE MAGNETIC FIELD WERE COMPARED TO WATER BATH HYPERTHERMIA TREATED CELLS (45 MINUTES TREATMENT).	267
FIGURE 6-42. EFFECTS OF HYPERTHERMIA ON MCF7 CELLS VIABILITY , THE VIABILITY OF CELLS INCUBATED WITH ME55-PEG-PCL (WITH AND WITHOUT DRUG) AND EXPOSED TO THE MAGNETIC FIELD WERE COMPARED TO WATER BATH HYPERTHERMIA TREATED CELLS (45 MINUTES TREATMENT).....	267
FIGURE 6-43. EFFECTS OF HYPERTHERMIA ON U87 CELLS VIABILITY , THE VIABILITY OF CELLS INCUBATED WITH ME93-PEG-PCL (WITH AND WITHOUT DRUG) AND EXPOSED TO THE MAGNETIC FIELD WERE COMPARED TO WATER BATH HYPERTHERMIA TREATED CELLS (45 MINUTES TREATMENT).	269
FIGURE 6-44. EFFECTS OF HYPERTHERMIA ON MCF7 CELLS VIABILITY , THE VIABILITY OF CELLS INCUBATED WITH ME93-PEG-PCL (WITH AND WITHOUT DRUG) AND EXPOSED TO THE MAGNETIC FIELD WERE COMPARED TO WATER BATH HYPERTHERMIA TREATED CELLS (45 MINUTES TREATMENT).....	270
FIGURE 6-45. EFFECTS OF HYPERTHERMIA ON U87 CELLS VIABILITY , THE VIABILITY OF CELLS INCUBATED WITH ME94-PEG-PCL (WITH AND WITHOUT DRUG) AND EXPOSED TO THE MAGNETIC FIELD WERE COMPARED TO WATER BATH HYPERTHERMIA TREATED CELLS (45 MINUTES TREATMENT).	270
FIGURE 6-46. EFFECTS OF HYPERTHERMIA ON MCF7 CELLS VIABILITY , THE VIABILITY OF CELLS INCUBATED WITH ME94-PEG-PCL (WITH AND WITHOUT DRUG) AND EXPOSED TO THE MAGNETIC FIELD WERE COMPARED TO WATER BATH HYPERTHERMIA TREATED CELLS (45 MINUTES TREATMENT).....	271

FIGURE 6-47. EFFECTS OF HYPERTHERMIA ON U87 CELLS VIABILITY , THE VIABILITY OF CELLS INCUBATED WITH ME60 (WITH AND WITHOUT DRUG) AND EXPOSED TO THE MAGNETIC FIELD WERE COMPARED TO WATER BATH HYPERTHERMIA TREATED CELLS (45 MINUTES TREATMENT).	273
FIGURE 6-48. EFFECTS OF HYPERTHERMIA ON MCF7 CELLS VIABILITY , THE VIABILITY OF CELLS INCUBATED WITH ME60 (WITH AND WITHOUT DRUG) AND EXPOSED TO THE MAGNETIC FIELD WERE COMPARED TO WATER BATH HYPERTHERMIA TREATED CELLS (45 MINUTES TREATMENT). 273	273
FIGURE 6-49. EFFECTS OF HYPERTHERMIA ON U87 CELLS VIABILITY , THE VIABILITY OF CELLS INCUBATED WITH ME60-L (WITH AND WITHOUT DRUG) AND EXPOSED TO THE MAGNETIC FIELD WERE COMPARED TO WATER BATH HYPERTHERMIA TREATED CELLS (45 MINUTES TREATMENT).	275
FIGURE 6-50. EFFECTS OF HYPERTHERMIA ON MCF7 CELLS VIABILITY , THE VIABILITY OF CELLS INCUBATED WITH ME60-L (WITH AND WITHOUT DRUG) AND EXPOSED TO THE MAGNETIC FIELD WERE COMPARED TO WATER BATH HYPERTHERMIA TREATED CELLS (45 MINUTES TREATMENT). 275	275
FIGURE 6-51. EFFECTS OF 45 MINUTES MAGNETICALLY INDUCED HYPERTHERMIA TREATMENT ON MCF7 CELLS VIABILITY.	277
FIGURE 6-52. EFFECTS OF 45 MINUTES MAGNETICALLY INDUCED HYPERTHERMIA TREATMENT ON U87 CELLS VIABILITY	277
FIGURE 6-53. CELLS VIABILITIES FOR MCF7 CELLS TREATED WITH DOX LOADED NANOPARTICLES WITH AND WITHOUT ADDITIONAL HYPERTHERMIA TREATMENT.....	278
FIGURE 6-54. CELLS VIABILITIES FOR U87 CELLS TREATED WITH DOX LOADED NANOPARTICLES WITH AND WITHOUT ADDITIONAL HYPERTHERMIA TREATMENT.....	279

LIST OF SCHEMES

SCHEME 1-1.	SYNTHETIC SCHEME OF PEG-PCL	36
SCHEME 1-2.	IMMOBILIZATION OF LIPASE ON MAGNETIC NANOPARTICLES (A) GLUTARALDEHYDE METHOD AND (B) ABSORPTION METHOD	57
SCHEME 1-3.	ENZYME-CATALYSED HYDROLYSIS OF MESO-CYCLOPENT-2-EN-1,4-DIACETATE).....	58
SCHEME 2-1.	THE CO-PRECIPIATION OF IRON (II) AND IRON (III) CHLORIDE (MASCOLO ET AL., 2013) 64	
SCHEME 2-2.	THE OXIDATIVE HYDROLYSIS OF IRON (II) SULPHATE HEPTAHYDRATE	65
SCHEME 2-3.	HYDROLYSIS AND CONDENSATION OF SILICA UNDER ALKALINE CONDITIONS (GIBSON, 2014) 66	
SCHEME 2-4.	SURFACE PROTECTED ETCHING OF SILICA COATED NANOPARTICLES AND SUBSEQUENT HYDROPHOBIC SILICA COATING.....	69
SCHEME 2-5.	SYNTHESIS PATHWAY OF THE PEG-PCL DIBLOCK COPOLYMER	70
SCHEME 2-6	SURFACE FUNCTIONALISATION OF THE SILICA COATED NANOPARTICLES	71
SCHEME 2-7.	SCHEMATIC REPRESENTATION OF THE 4-NBA COLORIMETRIC SURFACE ASSAY	72
SCHEME 2-8	CONVERSION OF SURFACE AMINE GROUPS TO ALDEHYDES USING GLUTARALDEHYDE.....	73
SCHEME 2-9.	SCHEMATIC DIAGRAM OF ENZYME IMMOBILISATION ON SURFACE FUNCTIONALISED CORE-SHELL SILICA-MAGNETITE NANOPARTICLES	74
SCHEME 2-10.	HYDROLYSIS OF MESO-CYCLOPENT-2-EN-1,4-DIACETATE.....	77
SCHEME 2-11.	THE PROCESS OF DOX LOADING OF THE LIPOSOME CAPPED SILICA MAGNETITE CORE-SHELL NANOPARTICLES	81
SCHEME 2-12.	THE PROCESS OF DRUG LOADING AND CAPPING OF THE SILICA MAGNETITE CORE-SHELL NANOPARTICLES	84

LIST OF ABBREVIATIONS

AC	ALTERNATING CURRENT
APTS	3-AMINOPROPYL TRIETHOXY SILANE
BET	BRAUNER-EMMETT TELLER
BSA	BOVINE SERUM WITH ALBUMIN
C	CARBON
CMC	CRITICAL MICELLAR CONCENTRATION
CTAB	CETYLTRIMETHYLAMMONIUM BROMIDE
CTAC	CETYLTRIMETHYLAMMONIUM CHLORIDE
CRL	CANDIDA RUGOSA LIPASE
DI	DEIONISED
DLS	DYNAMIC LIGHT SCATTERING
DMEM	DULBECCO'S MODIFIED EAGLE'S MEDIUM
DMSO	DIMETHYL SULFOXIDE
DNA	DEOXYRIBONUCLEIC ACID
DOX	DOXORUBICIN
EDTA	ETHYLENEDIAMINETETRAACETIC ACID
EDXS	ENERGY DISPERSIVE X-RAY SPECTROSCOPY
EMEM	EAGLE'S MINIMAL ESSENTIAL MEDIUM
EPR	ENHANCED PERMEABILITY AND RETENTION
FBS	FETAL BOVINE SERUM
FID	FLAME IONISATION DETECTOR
FT-IR	FOURIER TRANSFORM INFRARED
GC	GAS CHROMATOGRAPHY
GC-MS	GAS CHROMATOGRAPHY – MASS SPECTROMETRY
MEM	EAGLE'S MINIMAL ESSENTIAL MEDIUM
MLVS	MULTILAMELLAR VESICLE
MMC	MITOMYCIN C
MNP	MAGNETIC NANOPARTICLE
MRI	MAGNETIC RESONANCE IMAGING
MTT	3- (4,5-DIMETHYLTHIAZOL-2-YL)-2,5-DIPHENYL TETRAZOLIUM BROMIDE
NEAA	NON-ESSENTIAL AMINO ACIDS

NMR	NUCLEAR MAGNETIC RESONANCE
OA	OLEIC ACID
O-MSN	OCTYL MODIFIED MESOPOROUS NANOPARTICLES
OTS	OCTYLTRIETHOXY SILANE
PBS	PHOSPHATE BUFFERED SALINE
PCL	POLY CAPROLACTONE
PEG	POLYETHYLENE GLYCOL
PEO	POLYETHYLENE OXIDE
PFL	PSEUDOMONAS FLUORESCENS LIPASE
PMMA	POLYMETHYLMETHACRYLATE
PNP	P-NITROPHENOL
PNPP	P-NITROPHENYL PALMITATE
PPO	POLYPROPYLENE OXIDE
RT	RETENTION TIME
RES	RETICULOENDOTHELIAL SYSTEM
RPM	ROTATIONS PER MINUTE
RT	ROOM TEMPERATURE
SAXS	SMALL-ANGLE X-RAY SCATTERING
SCM	SCANNING COLUMN MAGNETOMETRY
SEM	SCANNING ELECTRON MICROSCOPY
SSC	BUFFER CONSISTING OF SODIUM CHLORIDE, SODIUM CITRATE AND WATER
SQUID	SUPERCONDUCTING QUANTUM INTERFERENCE DEVICE
SPC	SOYBEAN PHOSPHATIDYLCHOLINE
SPION	SUPERPARAMAGNETIC IRON OXIDE NANOPARTICLES
TEA	TRIETHYLAMINE
TEM	TRANSMISSION ELECTRON MICROSCOPY
TEN	BUFFER CONSISTING OF TRIS-HCL,EDTA, SODIUM CHLORIDE AND WATER
TEOS	TETRAETHYL ORTHOSILICATE
TGA	THERMOGRAVIMETRIC ANALYSIS
THF	TETRAHYDROFURAN
TPRE	TRI-PHASIC REVERSE EMULSION METHOD
TMAOH	TETRAMETHYLAMMONIUM HYDROXIDE
UV	ULTRAVIOLET
VSM	VIBRATING SAMPLE MAGNETOMETRY
XRD	X-RAY DIFFRACTION

LIST OF SYMBOLS

B	The magnetic field
C_{np}	The specific heat of the nanoparticles
C_s	The solvent specific heat
d	The particle diameter
e	The electron charge
ee	The enantiomeric excess
f	The field frequency
\hbar	The Dirac constant equal
h	Planck constant
H	The field intensity amplitude
I	Current
k	The Boltzmann's constant
m	The particle's magnetic moment
M_b	The saturation magnetization for bulk magnetite
M_s	Saturation magnetization of the nanoparticles
k_b	The Boltzmann constant
m_{np}	The mass of the nanoparticles
m_s	The mass of the liquid
μ_0	The permeability of the free space
P	The power loss
r	The radius of the particle
τ_0	The time constant
τ_B	The Brownian relaxation time
τ_N	The Neel relaxation time
M_r	The remnant magnetization
M_s	The saturation magnetization
T	Temperature
λ	The radiation wavelength
γ	The asphericity of the nanoparticles
η	The viscosity coefficient of the fluid
ρ	The density of material
σ	Standard deviation in the sample

τ	The magnetic relaxation time
V	The particle volume
ω	The measurement angular frequency

CHAPTER 1

INTRODUCTION

1.1 Project Motivation

Over the last few decades, extensive research has advanced the knowledge of physical and chemical properties of drug molecules along with mechanisms of cellular absorption and drug action resulting in numerous therapeutic strategies and pronounced improvements in pharmaceutical drug developments. However, in certain areas such as cancer treatments, existing therapy procedures mainly rely on the use of conventional cytotoxic drugs which only induce limited success and suffers from severe damaging side effects. Cancer is among the leading causes of morbidity and mortality worldwide. Over 338,000 people were diagnosed with cancer in 2012 in the UK which is about 928 people per day (UK, 2015). Numerous research studies have suggested that these problems could be resulting from insufficient targeting and target specificity of the current antitumor agents. The motivation for the first part of this project was to address some of the current challenges associated with drug delivery systems particularly in case of delivering toxic therapeutics agents for cancer therapy.

The cost of drugs form a significant proportion of the total expenditure of health authorities worldwide. For instance, the National Health Service (NHS) in England committed over 12% of their total budget (over £118 billion in 2014-2015) on drugs (Health, 2015). Despite such a significant financial contribution, the cost of many drugs remain prohibitive for a large number of patients. For example, Bevacizumab (Avastin), a first line treatment for patients with colorectal cancers is not available to English and Welsh patients through the NHS. The cost of Avastin as currently supplied by the manufacturer is £1,848.80 per month for a typical 70 kg patient (NewsMedical, 2014). An increase in efficiency and productivity of manufacturing process could result in lower drug cost. This could be achieved through the use of immobilized enzymes in multi-stepped drug syntheses. Repeated enzyme recycle/reuse will result in lower drug production cost and translate into significantly lower drug costs. Thus, developing the enzyme immobilisation support, which improves the enzyme activity and ease the separation and recycling/reusing of the enzymes i.e lipase, to overcome the above mentioned problems associated with pharmaceutical drug production inspired the second part of this project.

1.2 Aims and Objectives of the Project

The first aim of this project is to develop novel nanomaterials for drug delivery system (DDS). The success of such drug delivery system relies on many different factors as listed below:

1. The drug delivery system needs to be biocompatible.

This requirement was addressed by primarily using iron oxide nanoparticles (magnetite) which is shown to be biocompatible (Iron oxide nanoparticles are one of the few materials injected into the body that are easily incorporated into the body's natural metabolic

pathways) and was then further improved by applying additional biocompatible surface coatings of mesoporous silica, SPC lipid bilayers and PEG-PCL polymer.

The developed nanoparticles were tested against two cell lines of MCF7 and U87 to evaluate the cytotoxicity and biocompatibility of the developed materials as drug delivery systems.

2. The drug carriers should allow high drug loading and encapsulation capacities.

To achieve this requirement magnetic nanoparticles were coated with mesoporous silica shell with high surface area and mesoporous channels which enable high loading capacities.

The porosity and surface area of the core-shell nanomaterials were tested using nitrogen adsorption-desorption test using the well-known BET method.

The drug loading capacity of the materials were tested *in vitro* using Doxorubicin and Mitomycin C anticancer drugs.

3. The drug delivery system should have zero drug leaking/premature drug release before reaching the target tissue.

This issue was addressed by using the lipid bilayer (liposomes) and polymer micelle around mesoporous coated nanoparticles as capping materials to minimise the premature drug release. The capping enabled optimised drug delivery system and minimised the premature drug release however, “zero” drug leakage was not accomplished.

The drug release profile of the drug loaded nanoparticles were tested *in vitro* at body temperature (37°C) and hyperthermia temperature (43°C).

4. The drug delivery system should be able to target specific area or tissue.

The targeting ability of the drug delivery system was realised by using magnetic nanoparticles as drug carriers which can be directed to the target site using an externally applied magnetic field.

5. The drug delivery system should possess a controlled and triggered drug release profile.

Stimuli triggered drug release was achieved by applying an AC magnetic field triggered (magnetic hyperthermia) drug release strategy. Using magnetic iron oxide nanoparticles as core materials enables the materials to generate heat under the influence of an externally applied AC magnetic field. This strategy provides the advantage of synergistic effects of magnetic hyperthermia and chemotherapy.

Furthermore the drug release profiles were evaluated at different pH conditions (tumours exhibit a lower extracellular pH than healthy tissues, the pH of blood and normal tissues

are 7.4, but the extracellular pH in tumour tissues is about 6.8. Besides, endosome pH ranges from 4.5 to 6.5) and the nanoparticles exhibited an increase in the release rate with a decrease in pH value.

The second part of this project aimed to develop nanoparticles for efficient enzyme immobilisation and evaluated them by immobilization of CRL and PFL enzymes which are frequently used in pharmaceutical industry. Such materials for enzyme support should possess high surface area to maximise the enzyme immobilisation and should be easily separated from the reaction for recycle and reuse of the enzyme.

This goal was achieved by using high surface area mesoporous silica coated magnetic nanoparticles which were easily separated from the reaction by using an external magnetic field.

The immobilised enzyme was evaluated at different conditions and it was used in model catalysis reaction of hydrolysis of p-nitrophenyl palmitate and hydrolysis of pharmaceutically important chiral molecule “cis-3,5-diacetoxy-1-cyclopentene”, which demonstrated improved enzyme stability and activity with enhanced control over catalysis reaction.

The specific goals of this PhD. thesis were achieved as follows:

1. Synthesise different types of superparamagnetic iron oxide (magnetite) nanoparticles
2. Coating the nanoparticles with silica to produce mesoporous core-shell silica-magnetite nanoparticles
3. Coating the nanoparticles with liposomes to produce magnetoliposomes
4. Synthesis of thermosensitive polymer
5. Coating the nanoparticles with polymer to produce magnetic micelles
6. Development of polymer capped mesoporous silica coated magnetic nanoparticles
7. Development of liposome capped mesoporous silica coated magnetic nanoparticles
8. Characterization of the synthesised materials using different techniques to fully understand their physicochemical properties
9. Encapsulation of the drug molecules in the synthesised materials and study the drug loading and release profiles
10. Evaluation of the AC field induced heating profile of the nanoparticles and hyperthermia triggered drug release
11. Evaluation of the biocompatibility and cytotoxicity of the materials using cell lines

12. Evaluation of the efficiency of the drug delivery systems using cell lines under normal and hyperthermia conditions
13. Enzyme immobilisation (CRL and PFL) onto the nanoparticle by both chemical conjugation *via* the glutaraldehyde coupling and physical adsorption methods
14. Employment of the immobilised enzymes in catalysis reaction at different conditions to optimise the reaction condition
15. Investigation of the effects of an AC magnetic field on the catalytic activity of the immobilised lipase

1.3 Nanotechnology and Its Importance

Nanotechnology is defined as “understanding and control of matter with dimensions of 1 to 100 nanometres” (Medina et al., 2007). Nanotechnology is a multidisciplinary field which involves chemistry, biology, physics, optics, electronics, biomedical and materials sciences (Sabir et al., 2014). Nanotechnology is rapidly expanding in several directions such as nanodevices and nanosystems (Salata, 2004, Murray et al., 2000) with extensive ongoing research to provide pioneering solutions in various scientific fields.

Nanomaterials or nanoparticles exhibit size-dependant physical and chemical properties which could differ significantly from fine particles and bulk material (Tsuzuki, 2009, Salata, 2004). The size dependant properties of a material could appear continually over a range of size reduction or with an abrupt change below a critical size which is the key novelty of nanoscience (Cushen et al., 2012). Nanoparticles’ characteristics such as optical properties, fluorescence, electrical conductivity, magnetic permeability, and chemical reactivity change as a function of particles size (Nano, 2016). In principle, the so-called quantum effects phenomena and other physical effects such as extended surface area to volume, control the behaviour and characteristics of the nanoparticles (Nano, 2016, Gupta and Gupta, 2005).

Nanoparticles are of growing interest due to new or enhanced properties such as improved chemical reactivity and optical characteristics compared with bulk materials. For example, the antibacterial activity of silver nanoparticles, is a function of nanoparticles size e.g. smaller silver nuclei, shows higher antibacterial activity (Abou El-Nour et al., 2010). Similarly, zinc oxide become transparent at nanoscale and has been utilized in biosensors and cosmetics (Sabir et al., 2014). Nanoscale gold particles with confined electrons are emerging as promising cancer treatment agents and as photothermal agents, contrast agents and radio-sensitizers (Chakraborty et al., 2011). The tunability of nanomaterials enables researchers to change, control and tune the specific property of the nanoparticles (Nano, 2016).

Nanotechnology has advanced to develop engineered nanoparticles as a new class of materials with specially tailored properties to be used in various fields (Medina et al., 2007, Gupta and Gupta, 2005, Srivastava et al., 2013). Nanoparticles are used in diverse industrial and biomedical applications such as use of carbon nanotubes in cars, aircraft and space vehicles manufacturing (Gohardani et al., 2014, Kireitseu et al., 2007), use of silver nanoparticles as antibacterial agents in food packaging and water treatment (Sanguansri and Augustin, 2006, Cushen et al., 2012, Lv et al., 2009), use of copper nanoparticles as conductive inks and pastes for printing numerous electronic components (Youngil et al., 2008, Magdassi et al., 2010). A brief summary of the diverse applications of nanoparticles is presented in Figure 1-1.

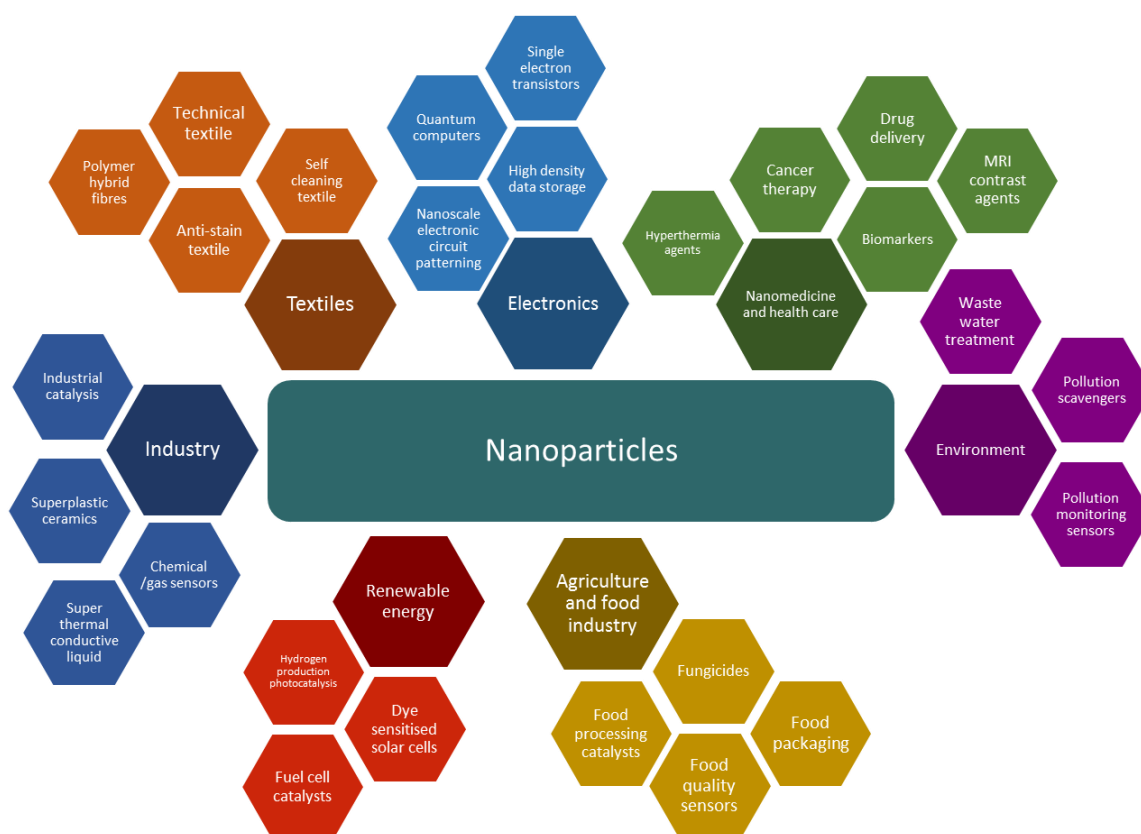


Figure 1-1 Applications of nanoparticles

Among all types of nanoparticles, magnetic nanoparticles attracted considerable interest due to their unique characteristics and have found applications in various industries. In the following, after briefly addressing the magnetic phenomena this chapter focuses mainly on developments in the synthesis of magnetic nanoparticles, and various strategies for nanoparticle coatings. Finally, application of magnetic nanoparticles in nanomedicine and catalysis will be extensively reviewed.

1.4 Magnetism and Magnetic Nanoparticles

Magnetism is a physical phenomenon generated by the movement of electrons within atoms. Magnetism arise from both electrons orbital angular velocity (ω) related to electrons circulating the nucleus and electron spin which is the electrons revolution against its axis. The orbital and the

spin movement independently generate a magnetic moment on each electron. The magnetic moment of a material is defined as the rotational force experienced by the material placed under a magnetic field of unit strength acting perpendicular to its magnetic axis (UCL, 2016). The magnetic moment caused by orbital motion is described as:

$$M_O = \mu_0 AI \quad \text{Equation 1-1}$$

Where A is the area circled by an electron, μ_0 is permeability in vacuum and I is the current created by the electron. By inserting $A = \pi r^2$ and $I = -\frac{e\omega}{2\pi}$ in Equation 1-1 it could be refined to

$$M_O = -\frac{\mu_0 e \omega r^2}{2} \quad \text{Equation 1-2}$$

Where ω is the angular velocity, r is the radius and e is the electron charge. Taking into account the quantization of angular momentum presented in Equation 1-3, the angular magnetic moment could be calculated from Equation 1-5:

$$p = m\omega r^2 = l\hbar \quad \text{Equation 1-3}$$

$$M_O = -\frac{\mu_0 e \hbar l}{2m} \quad \text{Equation 1-4}$$

$$\mu_B = \frac{\mu_0 e \hbar}{2m} \quad \text{Equation 1-5}$$

$$M_O = -\mu_B l \quad \text{Equation 1-6}$$

Where l is the angular momentum quantum number and \hbar is the Dirac constant equal to Planck constant h divided by 2π and the value can be calculated as 1.054×10^{-34} (J/s) and μ_B is Bohr magneton equal to 9.274×10^{-24} (Am²).

The magnetic moment created by electron spin momentum is given using spin angular momentum:

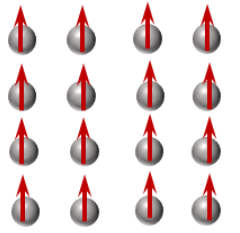
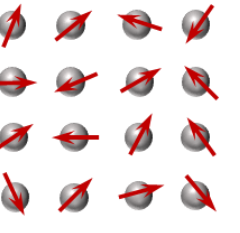
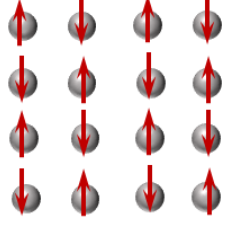
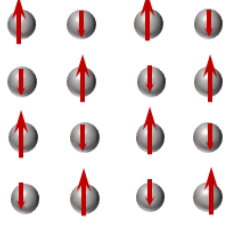
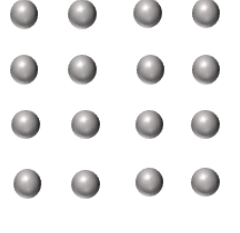
$$M_S = -\frac{\mu_0 e \hbar s}{m} \quad \text{Equation 1-7}$$

Therefore the total magnetic moment generated by an electron is

$$M = M_O + M_S \quad \text{Equation 1-8}$$

In most of the elements the total magnetism created by the electrons cancel out, however in magnetic materials the magnetic moments of the electrons are aligned, generating an integrated magnetic field. When a material is placed in an external magnetic field, it will experience a force trying to align its magnetic moments with the external field to create a net magnetic field. Magnetic materials can be classified in terms of their magnetic behaviour. A summary of the different types of magnetic behaviour is presented in Table 1-1.

Table 1-1. A summary of the different types of magnetic behaviour

Type of Magnetism	Characteristics	Magnetic moments
Ferromagnetic	Atoms hold parallel aligned magnetic moments. Molecular field within the material is enough to magnetise the material. Ferromagnetic materials possess a permanent magnetic field.	
Paramagnetic	Atoms possess randomly angled magnetic moments. Under the influence of a magnetic field the magnetic moments align to create a low magnetisation with similar direction as the applied field.	
Antiferromagnetic	Atoms hold antiparallel aligned magnetic moments. The magnetic fields counteract and the material behave similar to a paramagnetic material.	
Ferrimagnetic	Atoms possess mixed parallel and antiparallel aligned magnetic moments. These materials behave similar to ferromagnetic materials but show lower saturation magnetisations.	
Diamagnetic	Atoms have no net magnetic moment without an externally applied field. In the presence of externally applied field a magnetisation created in opposite direction of the applied field	

When a ferromagnetic or ferrimagnetic particle size is reduced to a value which is smaller than a critical size, it becomes single domain. Single domain magnetic nanoparticles could exercise a new type of magnetism called “Superparamagnetism”. This critical size could be calculated from Equation 1-9 (Lu et al., 2007a). Superparamagnetic particles are usually smaller than 100nm, without external field the net magnetic moment is zero and when the nanoparticle is placed in an external field magnetic it reacts similar to a paramagnetic particle.

$$d = \frac{18\sqrt{AK}}{\mu_0 M_s^2} \quad \text{Equation 1-9}$$

Where A is the exchange stiffness constant (which is typically 10^{-6} erg/cm in ferromagnetic materials (E.Y.Tsymbal, 2016)), K is the magnetic anisotropy of the nanoparticle, and M_s is saturation magnetization of the particles.

Hysteresis loop shows the magnetisation (M) of different types of magnetisms under the influence of a varying external magnetic field (H). A typical hysteresis loop of a ferromagnetic material is shown in Figure 1-2. Remanent magnetization or remanence is the remaining magnetization when the field is zero, and coercive field or coercivity is the reverse magnetic field required to further decrease the magnetization to zero. The area of the hysteresis loop indicates the energy dissipation upon reversal of the magnetic field, large hysteresis loop with high remanence is desirable for permanent magnets (Nave, 2016). For superparamagnetic materials the hysteresis loop is very small with negligible remanence and coercivity.

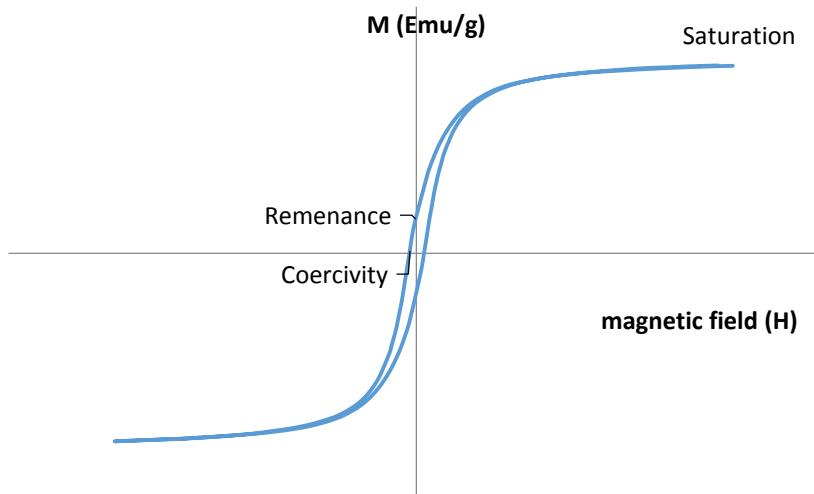


Figure 1-2. Typical hysteresis loop of a ferromagnetic material

Over the past decade iron oxide magnetic nanoparticles attracted considerable interest due to their superparamagnetic properties. Iron oxide is a mineral compound that shows different crystal structure and magnetic properties. The commonly used forms of iron oxides includes hematite (α - Fe_2O_3), magnetite (Fe_3O_4) and maghemite (γ - Fe_2O_3) (Babay et al., 2015). γ - Fe_2O_3 and Fe_3O_4 are easily magnetized and have very similar magnetic properties regarding saturation magnetization and superparamagnetism (Campos et al., 2015). Hematite possess much lower magnetic susceptibility at room temperature. Considering the relevance in this project the synthesis and characterization methods for magnetite nanoparticles are reviewed. Superparamagnetic iron oxide nanoparticles are candidates for wide range of applications including data storage (Reiss and Hutten, 2005, Natalie and Shouheng, 2010), catalysis (Sharifabad et al., 2014, Lu et al., 2004),

nanomedicine (Pankhurst et al., 2009, Frimpong and Hilt, 2010, Banerjee et al., 2010) and environmental remediation (Kong et al., 2013, Ravindra Kumar et al., 2015).

1.5 Synthesis of Magnetite Nanoparticles

Nanoparticles characteristics such as crystallinity, morphology and polydispersity are greatly influenced by the synthesis method and reaction parameters such as reaction temperature, pH, and ionic strength of the media. These characteristics have critical influence on electrical, mechanical, optical and magnetic properties of the nanoparticles and determine their behaviour in different applications (Gupta and Gupta, 2005).

Considerable research on synthesis and magnetic properties of iron oxides nanoparticles as ferrofluids was published during the last decades (Mahmoudi et al., 2011). A widely used well established synthesis method was introduced by Sugimoto and Matijević at 1980 (Sugimoto and Matijević, 1980). This method produced homogeneous spherical magnetite particles from iron salts by using potassium nitrate and potassium hydroxide following a co-precipitation method (Sugimoto and Matijević, 1980). Since then several strategies of synthesising magnetite nanoparticles have been developed aiming to control the shape, stability, size and polydispersity of iron oxide nanoparticles (Stanicki et al., 2015, Campos et al., 2015, Frimpong and Hilt, 2010). Some of the most commonly used strategies to synthesise magnetite nanoparticles are summarised in Table 1-2.

Table 1-2. List of methods commonly used to synthesise magnetite nanoparticles.

Synthetic method	Synthetic condition	references
Co-precipitation	Co-precipitation is a simple and convenient synthesis method using aqueous iron salt solutions with addition of a base under inert atmosphere at temperature ranging from room temperature up to 90°C. The resulting particles reported to be slightly polydisperse. This procedure provides high yield.	(Sen et al., 2006, Wu et al., 2007, Petcharoen and Sirivat, 2012)
Sonochemical	This method uses high-intensity, high energy ultrasonication. High energy ultrasonication generates acoustic cavitations which produce localised heat with a temperature of about 5000K. At this temperature, the formation and growth of nuclei occurs with the implosive collapse of bubbles. This method produce monodisperse nanoparticles in variety of shapes. This method lacks large scale production.	(Vijayakumar et al., 2000, Dang et al., 2008, Kim et al., 2005a)
Sol-gel combined with annealing	Sol-gel method includes multistep complicated procedure, followed by annealing under high temperature of 200 to 400°C. The particles size is controlled by annealing temperature. Particles with narrow size distribution could be prepared by this method.	(Xu et al., 2007, Hongzhang et al., 2010)
Thermal decomposition	Thermal decomposition method is performed under inert atmosphere at high temperature of 240 to 320°C. The particles size are monodisperse with a very narrow size range. The major disadvantage of this method is the synthesised nanoparticles are insoluble in water which limits the applications of the nanoparticles in biological field or necessitate the surface treatment after synthesis.	(Sun and Zeng, 2002, Sun et al., 2003, Park et al., 2004, Maityt et al., 2011)
Electrochemical deposition	Following this strategy, the anode is oxidised to metal ions in the solution followed by further reduction of metal ions to metal by the cathode in the presence of stabilisers. The particle size is controlled by regulating the electrochemical-oxidation current density or potential of the system. This method lacks large scale synthesis.	(Cabrera et al., 2008, Franger et al., 2004, Fajaroh et al., 2012)

Table 1-2. Continued

Synthetic method	Synthetic condition	references
Microemulsion	Microemulsion method uses water droplets as nano-reactors in an oil phase in the presence of surfactant molecules. Iron precursors reported to be precipitated as iron oxides in water phase inside the micelles core. Size of the synthesised nanoparticles is controlled by the size of micelles. The main disadvantage of this method is low yield. However using bi-continuous microemulsion method has reported to provide high yield.	(Liu et al., 2004c, Zhang et al., 2008a, Lee et al., 2005b, Mathew and Juang, 2007, Gobe et al., 1983, Koutzarova et al., 2006, Chin and Yaacob, 2007)
Hydrothermal	Hydrothermal procedure requires an autogenous pressure and relatively high temperature of 220°C. Hydrothermal method is based on a general phase transfer followed by a separation mechanism taking place at liquid, solid, and solution phase interfaces during the synthesis. In this method nanoparticles can be prepared in a very narrow size distribution.	(Wang et al., 2005, Kholam et al., 2002, Giri et al., 2005, Wang et al., 2009, Liang et al., 2010, Zheng et al., 2006)
Microwave assisted method	The microwave assisted method offers the advantages of rapid volumetric heating, high reaction rate, reduced reaction time, and increased product yield. This method reported to produce uniform nanoparticles with a narrow size distribution at large scale production.	(Kholam et al., 2002, Namboodiri and Varma, 2001, Wang et al., 2007, Komarneni, 2003)
Biomimetic	Biomimetic production of magnetic nanoparticles by magnetotactic bacteria has been known for a long time. Magnetotactic bacteria contain intracellularly produced crystals of magnetite (Fe_3O_4) and/or greigite (Fe_3S_4). Produced nanoparticles are reported to show species-specific morphology. The mineralization processes are regulated to form uniform magnetic nanoparticles. The method lacks large scale synthesis of monodisperse nanoparticles.	(Bharde et al., 2006, Klem et al., 2005, Matsunaga et al., 2004)

Co-precipitation and thermal decomposition methods were used in this project and will be discussed further in details.

1.5.1 Co-Precipitation

Inexpensive reagents and facile method have made coprecipitation the most common synthetic route of magnetite nanoparticles. In this method magnetite is synthesised through the coprecipitation of a mixture of iron salts in a basic aqueous medium (such as sodium hydroxide (NaOH) or ammonium hydroxide (NH₄OH)) under inert atmosphere (Lu et al., 2007a, Thanh, 2012). The size, shape and magnetic saturation of the magnetite prepared by this method is controlled by the reaction parameters including the type of iron salts (e.g. chlorides, sulphates, nitrates), the Fe²⁺/Fe³⁺ ratio, the reaction temperature and the pH of the reaction (Thanh, 2012, Lu et al., 2007a). Once the optimum parameters are finalised, the quality of the magnetite nanoparticles is fully reproducible. Particles from 5 to 50 nm in diameter can be prepared by this method, however the nanoparticles tend to be rather polydispersed (Lu et al., 2007a, Gupta and Gupta, 2005). It is established that a short burst of nucleation followed by a slow controlled growth is essential to produce nanoparticles of a controlled size and shape (Lu et al., 2007a).

The alkaline co-precipitation of ferrous and ferric salts for synthesis of iron oxide nanoparticles was originally reported by Massart at 1981 (Massart, 1981), in which the addition of base to an aqueous solution of ferrous and ferric ions in a 1:2 molar ratio in an oxygen free environment produced a black precipitate of spherical magnetite nanoparticles with uniform sizes. In the presence of oxygen magnetite can be oxidised further to produce ferric hydroxide, hence it is essential to have an oxygen free environment during the synthesis. Significant progress has been made in preparing magnetite nanoparticles *via* co-precipitation method by using organic additives such as polyvinyl alcohol as stabilizers and/or reducing agents (Lee et al., 1996). Bee *et al.* have reported the effect of citrate ions on growth of magnetite nanoparticles. They have synthesised 'Ultrafine' magnetite nanoparticles (diameter in the order of 2nm) by adding trisodium salt of citric acid, in an alkaline medium (Bee et al., 1995). Many researches have studied the effects of organic anions such as carboxylate on the formation of iron oxides (Ishikawa et al., 1992, Kandori et al., 1992, Ishikawa et al., 1993). Recent studies indicated oleic acid can effectively stabilize magnetite nanoparticles (Cushing et al., 2004, Willis et al., 2005, El-Boubbou et al., 2015). Effects of organic ions on the formation of magnetite nanoparticles can be explained by two competing mechanisms: chelation and adsorption. Chelation of metal ions can prevent nucleation which lead to the formation of larger particles. Alternatively, adsorption of additives on nuclei and growing crystals may inhibit the particle growth facilitating the formation of smaller particles (Varanda et al., 2011).

1.5.2 Thermal Decomposition

Monodisperse magnetic nanoparticles with small size can be synthesized *via* thermal decomposition of organometallic compounds. Some of the commonly used organometallic precursors include iron acetylacetonates (Sun and Zeng, 2002), iron carbonate (Narasimhan et al.,

2002), and carboxylate (William, 2004). In this method oleic acid, and hexadecylamine are often used as stabilizing surfactants resulting in hydrophobic nanoparticles (Sun and Zeng, 2002, Sun et al., 2003). The ratios of the starting reagents including organometallic compounds, surfactant, and solvent together with the reaction temperature, reaction time and aging period are crucial for the precise control of size and morphology (Sun and Zeng, 2002, Sun et al., 2003).

Preparation of monodisperse Fe_3O_4 via decomposition of $\text{Fe}(\text{acac})_3$ in the presence of 1,2-hexadecanediol, oleylamine, and oleic acid in phenol ether was reported for the first time by Sun and Zeng in 2002. This synthesis method resulted in monodisperse Fe_3O_4 nanocrystals, with variable sizes from 3 to 20 nm (Sun and Zeng, 2002, Sun et al., 2003). In this process the resulting magnetite nanoparticles were covered by long chain hydrocarbons which act as barriers that restrict the growth of particles and resulted in a well-controlled monodispersed nanoparticles (Sun and Zeng, 2002, Sun et al., 2003). Jana *et al.* have reported a general decomposition approach for the synthesis of size- and shape-controlled magnetic oxide nanocrystals based on pyrolysis of metal fatty acid salts in non-aqueous solutions (Jana et al., 2004).

Park *et al.* later reported the large scale synthesis (gram quantities) of monodisperse nanocrystals using inexpensive and non-toxic metal salts using a similar thermal decomposition approach (Park et al., 2004). They used iron (III) chloride and sodium oleate to produce an iron oleate complex in situ which was later decomposed at high temperatures between 240 and 320 °C in different solvents, such as 1-hexadecene, octyl ether, 1-octadecene, 1-eicosene, or trioctylamine. Particles size depend on the decomposition temperature and the aging period and were in the range of 5 to 22 nm (Lu et al., 2007a, Park et al., 2004).

A major disadvantage of thermal decomposition method is the production of organic solvent soluble nanoparticles which limits the application of the nanoparticles in biological field or requires further surface treatment after the synthesis. To overcome this problem, synthesis of water-soluble magnetite nanoparticles have been reported by different groups (Li et al., 2005, Maityt et al., 2011, Hu et al., 2006). Li *et al.* reported the synthesis of water soluble magnetite nanoparticles using $\text{FeCl}_3 \cdot 6\text{H}_2\text{O}$ as iron source and 2-pyrrolidone as coordinating solvent, under reflux at 245°C (Li et al., 2005). Hu *et al.* reported a one-pot synthesis process for water-soluble magnetite nanoparticles prepared under similar reaction conditions by the addition of α,ω -dicarboxyl- terminated poly (ethylene glycol) as a surface capping agent (Hu et al., 2006). Maityt *et al.* have reported one step synthesis of water dispersible magnetite nanoparticles by thermal decomposition of $\text{Fe}(\text{acac})_3$ (Maityt et al., 2011). Similarly Theppaleak *et al.* have reported synthesis of water dispersible magnetite nanoparticles (Fe_3O_4) by thermal decomposition of $\text{Fe}(\text{acac})_3$ in the presence of carboxylic acid-terminated poly (ethylene glycol) (mPEG acid), poly (vinyl alcohol) and NH_2 -containing polyether (Theppaleak et al., 2009). More recently, Zhao *et al.* have reported the synthesis of water-soluble magnetite nanoparticles with an average diameter

of 9.5 ± 1.7 nm by thermal decomposition of $\text{Fe}(\text{acac})_3$ in methoxy poly (ethylene glycol) as solvent, reducing agent and modifying agent (Zhao et al., 2012).

1.6 General Method of Coatings

There has been significant progress in synthesis of magnetic nanoparticles with different sizes, structures and properties. Maintaining the stability of these particles without agglomeration or precipitation and protection against oxidation or erosion by acidic or basic species is similarly important. Stabilization and protection of the particles are closely linked with each other and they are crucial requirements for almost all applications of magnetic nanoparticles. Therefore, it is important to develop efficient strategies to improve the chemical stability of magnetic nanoparticles. The most investigated strategy is to coat the nanoparticles with a protection layer. The coating layer could stabilise the nanoparticles and provide functional groups for the conjugation of small molecules and targeting ligands. In case of drug delivery applications the coating layer could be designed to limit non-specific cell interactions, reduce the toxicity of the bare magnetite nanoparticles and prolong the circulation time. Furthermore, it could add tailored drug loading and release behaviours.

These applied coating strategies can be categorized into two major groups of: organic shells, including surfactant and polymers, (Liu et al., 2004a, Hong et al., 2005) or inorganic shells, including silica (Kobayashi et al., 2003, Ito et al., 2005, Ding et al., 2012) and precious metals (Sobal et al., 2002) (Lu et al., 2007a). Surface modification of nanoparticles is performed either during the synthesis process or in a post-synthesis process. The most common materials used for in situ surface modification of magnetite nanoparticles are surfactants such as oleic acid, lauric acid, alkane sulphonic acids, and alkane phosphonic acids (Mamani et al., 2013). Citric acid has been used commercially for the stabilization of iron oxide nanoparticles, such as in the MRI contrast agent VSOP-C184 (Boyer et al., 2010). Surfactant mediated syntheses are mostly performed in organic solvents such as hexadecane, toluene and n-hexane, the hydrophobic hydrocarbon chain of the surfactant forms a shell around nanoparticles rendering the hydrophobic nanoparticles. The post-synthesis modification of magnetite nanoparticles, is mostly achieved using polymers, silica, liposomes and chitosan (Mahmoudi et al., 2011). Table 1-3 summarises examples of materials which have been used to coat magnetite nanoparticles to increase the material stability.

Table 1-3. A list of materials used for coating magnetite nanoparticles and their applications

Materials used	Applications	Advantages	Ref.
Polylactic acid (PLA)	Drug delivery, MR imaging agent, cell labelling and magnetic cell separation, tissue repair, and hyperthermia	Biodegradable, biocompatible, and hemocompatible	(Zhao et al., 2009, Wang et al., 2010b)
Polyvinyl alcohol (PVA)	Drug delivery and imaging contrast agent	Prevent aggregation and stabilised nanoparticles	(Mahmoudi et al., 2008, Chastellain et al., 2004)
Polyvinyl pyrrolidine (PVP)	Drug delivery and MR imaging contrast agent	Enhances the blood circulation time and stabilises the colloidal solution	(Liu et al., 2007, Lee et al., 2005a)
Polyacrylic acid (PAA)	Target thrombolysis with recombinant tissue plasminogen activator, Targeting drug resistance in mycobacteria	Increases the stability and biocompatibility of the particles and also helps in bio-adhesion	(Ma et al., 2009, Padwal et al., 2014)
Polystyrene	MR cellular imaging and DNA hybridisation	Stabilize nanoparticles	(Xu et al., 2009a, Lellouche et al., 2005)
Polymethyl methacrylate (PMMA)	DNA separation and amplification	Increases the stability, can be applied in automation systems to achieve high throughput detection of single nucleotide polymorphisms	(He et al., 2006, Zhang and O'Connor, 2007)
Dextran	Drug delivery, hyperthermia and MR imaging contrast agent	Biocompatible, increase stability, and prolong blood circulation time	(Jarrett et al., 2007, Lacava et al., 2001, Rodriguez-Luccioni et al., 2011, Estevanato et al., 2012)

Table 1-3. Continued

Materials used	Applications	Advantages	Ref.
Amorphous silica	Isolation and purification of DNA from soil samples, isolation of ultrapure plasmid DNA from bacterial cells, extraction of phenolic compounds from environmental water	Eliminates the need for the repeated centrifugation, vacuum filtration or column separation	(Sebastianelli et al., 2008, Zhao et al., 2008, Chiang et al., 2006)
Mesoporous silica	Controlled drug delivery, removal of mercury from industrial effluent, support for enzyme immobilisation for biocatalysis, fluorescence imaging, DNA extraction	High surface area with uniform pore size, and high pore volume	(Souza et al., 2009a, Qu and Tie, 2009, Sen and Bruce, 2009, Yang et al., 2009a, Kim et al., 2008)
Polyethylene glycol (PEG)	MR imaging contrast agent	Improves the biocompatibility, blood circulation time and internalization efficiency of the nanoparticles	(Sun et al., 2008, Lee et al., 2007)
Polyethylene glycol - Polyethylene imine (PEG-PEI)	DNA extraction, MR imaging contrast agent, drug delivery, and hyperthermia	Highly soluble and stable in water, biocompatible, hardly recognized by the macrophage system and prolong the circulation time	(Zhao et al., 2013c, Xie et al., 2015, Khalkhali et al., 2015)
poly (ϵ -caprolactone)-polyethylene glycol (PEL-PEG)	Drug and gene delivery, hyperthermia, MR imaging contrast agent	Highly soluble and stable in water, biocompatible, hardly recognized by the macrophage system and prolong the circulation time	(Khalkhali et al., 2015) (Cheng et al., 2011, Khoee et al., 2015)
Erythrocytes	MR imaging contrast agent, and drug delivery	Avoids the rapid clearance by the reticuloendothelial system (RES) and prolong blood circulation	(Antonelli et al., 2008, Brähler et al., 2006)

Table 1-3. Continued

Materials used	Applications	Advantages	Ref.
Polysaccharide	MR imaging agent, drug and gene delivery.	Biocompatible, the elimination by white corpuscles from liver would be avoided. Provides high stability and prevent agglomeration.	(Uthaman et al., 2015, Covaliu et al., 2011) (Saboktakin et al., 2009, Kim et al., 2003)
Chitosan	Water treatment and extraction of trace pollutants from environmental water, Tissue engineering, hyperthermia, agriculture and textiles industry	Biocompatible, increases the stability, hydrophilic	(Juang et al., 2010) (Bravo-Osuna et al., 2007, Zhang et al., 2010c, Kalkan et al., 2012, Tran et al., 2010) (Yu et al., 2007)
Lauric acid (LA)	Cellular tagging and MR imaging agents, enzyme immobilization in food industry	Biocompatible when use in low concentrations, stabilise colloidal suspension	(Zaloga et al., 2014, Mamani et al., 2013)
Citric acid (CA)	Cellular tagging, magnetic hyperthermia	Increases the stability, and biocompatible	(Răcuciu et al., 2006, de Sousa et al., 2013, Cheraghipour et al., 2012)
Liposome	MR imaging contrast agent, drug delivery, and hyperthermia	Increases blood circulating time	(Meincke et al., 2007, Pradhan et al., 2007, Fortin-Ripoche et al., 2006)
Albumin	Magnetic tagging and magnetically targeted therapy	Biocompatible	(Chunfu et al., 2004, Berry and Curtis, 2003, Berry et al., 2003)
Gelatin	Genomic DNA extraction from bacterial cells, drug delivery	Biocompatible natural polymer. Improves the efficiency of drug loading.	(Gaihre et al., 2009, Intorasoot et al., 2009)

Stabilisation strategies such as coating materials, coating thickness, hydrophobicity and surface charge can influence the characteristics of the magnetite nanoparticles in different ways (Duan et al., 2008, LaConte et al., 2007, Mahmoudi et al., 2011). For instance coating magnetite nanoparticles with diamagnetic materials results in decreased saturation magnetization (Lopez et al., 2010, Veiseh et al., 2010). Lopez *et al.* have reported a change in saturation magnetization from 0.067 emu/cm³ for as-synthesised water based magnetite nanoparticles to 0.335 emu/cm³ for the oleic acid kerosene based magnetite nanoparticles (Lopez et al., 2010). Voit *et al.* have reported decreased saturation magnetisation for polymer coated magnetite nanoparticles (Voit et al., 2001) and Sen and Bruce have observed similar reduction of saturation magnetisation for silica coated magnetite nanoparticles (Sen and Bruce, 2009). LaConte *et al.* reported that the coating thickness of magnetite nanoparticles can significantly influence the R2 and R1 relaxivity and consequently R2/R1 ratio of the MRI contrast agent. They have used a polyethylene glycol (PEG)-modified phospholipid coating, and observed that with an increases in coating thickness, the R2 decreases and the R1 increases (LaConte et al., 2007). In another study on magnetic nanoparticles with different coating, Duan *et al.* have shown polymer coatings with higher hydrophilicity (PEI versus octadecene coating) yield higher R2 relaxivities. They have suggested that these effects are the result of intrinsic surface spin disorders as well as rapid diffusion of water molecules between the bulk phase and the adjacent layer surrounding the particle surface (Duan et al., 2008, Veiseh et al., 2010). This demonstrates the importance of careful consideration in coating materials and the combinatorial effects of the coating on the final properties of the nanoparticle system. In the context of this project, in the following sections silica coatings, lipid coatings and polymer coatings are deliberated and explored.

1.7 Silica Coating on Magnetite Nanoparticles and Its Applications

Silica is one of the most promising and favourable coating material since it is biocompatible, it can protect magnetite core against oxidation and agglomeration at wide pH ranges and improves the chemical stability (Lu et al., 2007b). Silica is hydrophilic in nature and silica-coated core-shell nanoparticles are reported to be well dispersed in aqueous suspensions (Mahmoudi et al., 2011). Furthermore, the surface of silica is often finished with a silanol group, which can react with various chemicals and silane coupling agents to conjugate with a variety of biomolecules and specific ligands (Sonmez et al., 2015).

Currently the Stöber method (Stöber et al., 1968, Helmi Rashid Farimani et al., 2013) and microemulsion method (Narita et al., 2009, Ding et al., 2012, Lu et al., 2007c), are the most commonly used methods of preparing silica coated magnetite nanoparticles in which the former is applied to water soluble magnetite nanoparticles and the latter is an excellent alternative strategy for silica coating of non-polar solvent-dispersed magnetite (Mahmoudi et al., 2011).

Philipse *et al.* have reported the silica coating of magnetite nanoparticles for the first time at 1994 by a sol–gel method (Philipse *et al.*, 1994).

1.7.1 Stöber Method

In Stöber method the silica shells are formed *via* the hydrolysis and polycondensation of silica source such as tetraethyl orthosilicate (TEOS) in ethanol solution in the presence of water with ammonia as a catalyst (Van Ewijk *et al.*, 1999, Deng *et al.*, 2005, Stöber *et al.*, 1968). As a result of the high hydrolysis rate of TEOS, large aggregates and polydisperse product formation is inevitable in this method (Sonmez *et al.*, 2015). Many researchers have investigated modifications of Stöber method to improve the coating properties of the nanoparticles (Barnakov *et al.*, 2005). Deng *et al.* have reported a systematic study of the silica-coated core-shell magnetic nanoparticles formation *via* sol–gel method. Their results demonstrated that the reaction parameters such as alcohol type, volume ratio of alcohol to water, the amount of catalyst and the amount of precursor played an important role in the formation of nanoparticles. Furthermore, they have observed that the obtained silica-coated magnetite nanoparticles showed superparamagnetic property (Deng *et al.*, 2005).

Sun *et al.* have described an improved approach for the coating of magnetite nanoparticles to obtain stable core-shell colloid. In their method magnetite nanoparticles prepared by co-precipitation method were first modified with citric acid. The silica coating was controlled by a dilute silicate solution pretreatment and subsequent Stöber process directly in ethanol (Sun *et al.*, 2005). Gao *et al.* have reported the systematic investigation of the effects of the volume ratio of tetraethyl orthosilicate (TEOS) and magnetite colloid on the structural, morphological and magnetic properties of the composite nanoparticles. They have also shown that silica coating of magnetite nanoparticles improved the thermal stability of the magnetite nanoparticles (Gao *et al.*, 2011). Kulkarni *et al.* reported silica coating of magnetite nanoparticles prepared by co-precipitation method *via* modified stöber method their results showed that the silica coating prevents magnetic particles from aggregation and imparts excellent stability (Kulkarni *et al.*, 2014). Sonmez *et al.* have suggested that silica shells with the thickness from 5 to 200 nm can be formed by adjusting the ratio of tetraethoxysilane (TEOS) to water and ammonia concentration (Sonmez *et al.*, 2015).

1.7.2 Microemulsion Method

Microemulsion method could be used to coat the nanoparticles with a uniform layers of silica. This method contains three main components: water, oil and amphiphilic surfactant. In this method, micelles or reverse micelles formed by surfactant surround the nano-droplet shaping nano-reactors which controls the deposition of silica layer on magnetite nanoparticles. The advantage of the confined nano-reactor environment within the reverse micelle is the highly monodisperse yield. The size of the nano-droplets is controlled by the water to surfactant molar

ratio and is directly related to the size of the nanoparticles, and therefore it can be tuned in order to control the thickness of the silica layer. The reverse microemulsion method could be used to produce uniform silica shells as thin as 1 nm (Gupta and Wells, 2004). The advantage of this method is the readily controlled particle size by adjusting the molar ratio of water to surfactant, aging time, and reactant concentration. However, it is reported that the reverse microemulsion synthesis has low yield (Sonmez et al., 2015, Faraji et al., 2010). Furthermore, the use of surfactants and toxic organic solvents requires extensive washing before any biological applications, to avoid disruption or lyses of biomembranes by the surfactant molecules, rendering the process slow, expensive and less eco-friendly (Sonmez et al., 2015, Faraji et al., 2010).

Santra *et al.* applied the water-in-oil microemulsion strategy to prepare silica-coated iron oxide nanoparticles. They have used three different non-ionic surfactants of Triton X-100, Igepal CO-520, and Brij-97, and studied the effects of the different surfactants on the particle crystallinity, size, and the magnetic properties. They have obtained a uniform silica-magnetite core-shell nanoparticles with shell thickness of 1 nm. They have shown that adsorption of surfactant molecules on the nanoparticles' surface varies according to the chemical structure of the surfactant. Furthermore they showed the surfactant with higher hydrophobicity (Brij 97) yields a more ordered particle aggregation, which could be due to a strong hydrophobic-hydrophobic interaction between oleyl groups of the neighbouring nanoparticles (Santra et al., 2001). Lu *et al.* have reported the synthesis of uniform bifunctional silica –magnetite core-shell nanoparticles with (FITC)-incorporated silica shell with the thickness of 20 nm *via* microemulsion method that was used to efficiently label human mesenchymal stem cells (Lu et al., 2007c). Ding *et al.* have reported procedures for silica coating of magnetite nanoparticles by the reverse microemulsion method to obtain core-shell nanoparticles with a single magnetic core, controllable shell thicknesses, and without formation of core-free silica nanoparticles. Their results indicated that silica coating parameters should be selected considering the magnetite size, accordingly parameters suitable for certain size magnetite nanoparticles are not completely applicable to particles within different size ranges. They also reported that adjusting the amount of magnetite nanoparticles with aqueous domain is essential. They have observed that the small aqueous domain is suitable to prepare ultrathin silica shell, whereas larger aqueous domain is necessary for developing thicker shells. They suggested that formation of core-free silica nanoparticles could be avoided by forming thick silica shell *via* increasing the TEOS content through the consistently fractionated drops (Ding et al., 2012).

1.7.3 Templating method

To increase the surface area of silica coated nanoparticles, a number of different techniques have been implemented to coat iron oxide nanoparticles with porous silica structures. Silica coatings can be either amorphous or mesoporous. Amorphous silica coatings, which are non-porous and non-crystalline, were first reported by Philipse *et al.* in 1994 (Philipse et al., 1994) *via* the sol-gel

method. Amorphous coatings are produced if no templating systems are present in the coating process. In 1990 Yanagisawa *et al.* have reported the first mesoporous silica nanoparticles with uniform pore size of 2 to 4 nm and a long-range ordered pore structure using surfactants as structure-directing agents. The surface area of the nanoparticles were measured to be 900 m²/g. (Yanagisawa et al., 1990, Tang et al., 2012).

Currently, rapid progress has been achieved in synthesis and application of mesoporous nanoparticles in catalysis, adsorption, separation, sensing, and drug delivery. Many synthesis approaches have been successfully developed to fabricate mesoporous coated nanoparticles with core-shell structures. Some of these methods include, fast self-assembly, soft and hard templating, selective etching and modified aerogel approaches (Sonmez et al., 2015, Wu et al., 2013a). Among these synthesis strategies surfactants structure-directing methods and surface protected etching are used in this project.

1.7.3.1 Surfactants Structuring Template

In synthesis of mesoporous silica shell through surfactant templating method, a surfactant with a concentration higher than its critical micelle concentration (CMC) is added in the synthesis process. The surfactant would self-aggregate forming micelles and the silica precursor condensate around the template to generate a silica matrix. Surfactant templates could be removed by thermal calcination or solvent extraction resulting in mesoporous structure. The structure such as pore size, and pore direction is determined by the surfactant templates (Wu et al., 2013a, Slowing et al., 2007a). Numerous mesoporous structures with different pore arrangement and architecture have been developed using various types of surfactants (Tang et al., 2012).

In 2004 Wu *et al.* synthesized mesoporous magnetic silica nanocomposite for the first time. They used cetyltrimethylammonium chloride (CTAC) as a template to form mesoporous structure on micrometre-sized magnetite (Fe₃O₄) particles (Wu et al., 2004). Zhao *et al.* have synthesised uniform mesoporous magnetic nanocomposites spheres with a high surface area silica shell. The mesoporous silica layer was formed on a thin dense silica layer deposited on the surface of the magnetic particle by simultaneous sol-gel polymerization of tetraethoxysilane (TEOS) and n-octadecyltrimethoxysilane (C18TMS) followed by removal of the organic group (Zhao et al., 2005). Deng *et al.* have synthesised superparamagnetic high-magnetisation microspheres with a sandwich structure of a magnetite core, a nonporous silica layer in the middle, and an ordered mesoporous silica layer with cylindrical channels as the outer layer. They have used cetyltrimethylammonium bromide (CTAB) as template for formation of mesoporous shell (Deng et al., 2008). El-toni *et al.* have reported an optimization method for formation of mesoporous silica shell on magnetic nanoparticles for application in drug delivery. They have coated the Fe₃O₄ nanoparticles with a dense silica layer followed by co-structure directed mesoporous silica layer. They have proposed that co-structure directing agent assist the electrostatic interaction between

negatively charged silica layers and the negatively charged surfactant molecules (El-Toni et al., 2013b). Xue *et al.* have reported the synthesis of fluorescent mesoporous silica-coated iron oxide nanoparticles for magnetic resonance imaging, computed tomography, and fluorescence trimodal imaging by using cetyltrimethylammonium bromide (CTAB) as pore templating agent. They have prepared mesoporous silica-coated superparamagnetic iron oxide nanoparticles by growing fluorescent dye-doped silica onto superparamagnetic iron oxide nanoparticles directed by a CTAB template. Synthesised nanoparticles had a uniform size with 20 nm mesoporous silica shell. The mean pore size was reported to be 2.7 nm and the surface area was measured to be 692.06 m²/g (Xue et al., 2014).

1.7.3.2 Surface Protected Etching

Surface protected etching strategy consist of stabilization of the nanoparticle's surface using a protective layer (polymer ligands), and then selective etching of the interior to form hollow/rattle type mesoporous structures (Tang et al., 2012). Hollow / Rattle-Type mesoporous silica nanoparticles are a new type of mesoporous silica nanoparticles with special morphology. Hollow / rattle-type mesoporous nanoparticles have low density and high specific area, which are ideal as new-generation drug delivery systems with high loading capacity and possibility of co-delivery of different kinds of drugs. Recently, hollow and rattle-type nanomaterials have been actively explored for enzyme immobilization and confined-space catalysis (Lou et al., 2008, Liu et al., 2011, Chen et al., 2010c).

Ren *et al.* have established that alkaline treatment of cationic poly- (dimethyldiallylammonium chloride) (PDDA) pre-coated mesoporous silica spheres can form hollow microcapsule silica nanoparticles. It was suggested that the hydroxyl ions penetrate through the protecting PDDA layer and attack the interior silica sphere to create dissolved silicate oligomers under ammonia. The oligomers with negative charge tend to migrate and deposit onto the positively charged PDDA layer, which act as the scaffold for the formation of the final shell. Using this method a continuous and compact silica-PDDA complex shell is formed (Ren et al., 2005). Similarly, Zhang *et al.* have reported using poly (vinylpyrrolidone) (PVP) as surface protector and found that the solid silica sphere can be transferred to hollow / rattle-type structure under the treatment of NaBH₄ at relatively mild temperature. The mechanism was deduced to be a spontaneous dissolution-regrowth process (Zhang et al., 2008d). Same group later reported the conversion of sol-gel obtained silica nanoparticles into porous nanoparticles and multi-shell rattle structures using PVP protection layer followed by NaOH etching (Zhang et al., 2008c). Zhang *et al.* have reported using surface protected etching to form of SiO₂@SiO₂ core shell rattle type structures. They have used a PVP protecting layer on the surface of both core and shell in order to increase their relative stability against chemical etching. Upon reacting with etchant (NaOH), the silica between the two layers are removed, as a result the outer layer becomes a hollow shell since it is

protected by PVP. The core also maintains its original size due to the PVP protection layer on its surface. They have carried out the process at room temperature without additional templates (Zhang et al., 2010a).

1.7.4 Mesoporous Silica Coated Magnetite Nanoparticles for Drug Delivery

Mesoporous silica nanoparticles are promising candidate for drug delivery which can overcome the challenges in chemotherapy in a controllable and sustainable manner. They have the following advantages:

- Biocompatibility
- Large surface area and pore volume which offers pronounced potential for drug adsorption within the meso-channels
- Adjustable pore structure which allow control over drug loading and release kinetics
- Easily functionalised and modified surface which offers controlled and targeted drug delivery which in turn improves the drug therapeutic efficacy and reduces toxicity
- In combinations with magnetic nanoparticles allow simultaneous drug delivery and diagnostic imaging (Wang et al., 2015).

Table 1-4 highlight some of the recently developed mesoporous silica based drug delivery systems.

The major drawback related to mesoporous silica nanoparticles is related to the high surface density of silanol groups interacting with the red blood cell membrane's phospholipid leading to hemolysis. Another disadvantage is related to metabolic changes induced by porous silica nanoparticles (Bharti et al., 2015, Wang et al., 2015). These negative aspects of mesoporous silica nanoparticles could be avoided by surface modifications of nanoparticles such as lipid or polymer coatings.

In this project, mesoporous silica nanoparticles prepared by both template based strategy using CTAB as a template and protected surface etching strategy with PVP as a protecting agent. The nanoparticles were tested for drug delivery systems using Mitomycin C and Doxorubicin as model drugs. The detailed synthesis method is explained in Section 2.4.

Table 1-4. A list of mesoporous silica based drug delivery systems.

Nanoparticle structure	size	Model drug	results	ref
Mesoporous silica coated magnetite nanoparticles with PEG surface modification	53 and 45nm magnetite core with 15 and 22nm shell thickness	Doxorubicin	MCF7 cell line were used for cytotoxicity study and it was observed that cell viability and proliferation were not affected by nanoparticles up to a concentration 350µg/mL.	(Kim et al., 2008)
Mesoporous silica coated magnetite nanoparticles	208 nm magnetite core with 15 to 40 nm shell	Ibuprofen	High drug loading content of 954 mg/g where up to 81% of loaded drug was released after 72 hours. For cytotoxicity study 4 cell lines of MCF7, SKOV3, MRC-5, and IMR-90 were used and ~20% cytotoxicity after 48 hours of treatment with nanoparticles were observed.	(Uribe Madrid et al., 2015)
Rattle-type magnetic mesoporous silica, with PEG and folic acid (FA) surface modification	100 nm magnetite core with 35 nm shell	Docetaxel	Folic acid was used as targeting agent. Drug loading content of 180mg/g was achieved. HeLa and MCF7 cell lines were used for cytotoxicity study which showed around 20% cytotoxicity after 48 hours of treatment with 400µg/mL nanoparticles. Drug loaded nanoparticles exhibited significantly greater cytotoxicity than free drug.	(Wu et al., 2011)
Mesoporous silica coated magnetite nanoparticles with β-cyclodextrins on the outer surfaces surface	80 nm	Rhodamine	Sugar and pH dual-responsive biocompatible nanoparticles were obtained. Up to 25% toxicity for 100 µg/mL after 48 hours was observed against HEK293T. 70% release was achieved after 2 hours in pH=2.	(Qiu et al., 2015)

Table 1-4. Continued

Nanoparticle structure	size	Model drug	results	ref
Mesoporous silica coated magnetite nanoparticles	100 nm magnetite core with 50nm shell thickness	Doxorubicin	Loading content was 20.7%. Very slow release was observed in pH 7.4 and 43% release was observed within 24 hours in pH 5.5. Cytotoxicity was compared in HepG2 and HL-7702 cells. Higher doxorubicin content observed in HepG2 cells cytoplasm. Free dox showed higher cytotoxicity than dox loaded nanoparticles during the first 24 hours of treatment, however after 48 hours both group showed similar cytotoxicity.	(Shao et al., 2015)
Mesoporous silica coated magnetite nanoparticles with fluorescent polymer chain and folic acid surface modification	280 nm magnetite core and 25 nm mesoporous silica layer.	Doxorubicin	The folate moiety on the surface was used as targeting moiety while the iron oxide core and fluorescent polymer shell tracked the process. Drug loading content was 105 µg/mg and DOX release was 84% after 18 h at 37 °C and more than 90% within 100 hours.	(Chen et al., 2010a)
Hollow core/shell structured Mesoporous silica-magnetite nanoparticles	~100×200nm	Doxorubicin	Nanoparticles were developed for simultaneous MRI cell imaging and anticancer drug Delivery. Nanocapsules showed 20% drug loading content. The capability of the nanocapsules as MRI contrast agents was confirmed both <i>in vitro</i> and <i>in vivo</i> . The DOX loaded nanocapsules exhibited higher cytotoxicity than free DOX after 24 and 72 hours at DOX concentrations lower than 20 µg/mL.	(Chen et al., 2010d)

Table 1-4. Continued

Nanoparticle structure	size	Model drug	results	ref
Mesoporous silica coated magnetite nanoparticles with hydroxyapatite surface modification	20 nm magnetite core and total particle size of 85nm	Ibuprofen	pH responsive drug delivery system was developed. Drug loading content of 32.8% was obtained. Drug release from uncoated nanoparticles were rapid at both pH 4.5 and pH 7.4, reaching saturation at 10 hours. Fe ₃ O ₄ @mSiO ₂ -HAp did not show any substantial release after an initial release of about 10% at pH 7, 81.6% release was observed at pH 4.5 within the first 10 hours.	(Zhao et al., 2013b)
Mesoporous silica coated magnetite nanoparticles with disulfide gatekeepers	20 nm magnetite core and 20 nm shell thickness	Doxorubicin	Nanoparticles with enzyme-sensitive drug release were developed. Drug loading capacities of up to 2.16 ± 0.5 wt% was achieved. The <i>in vitro</i> release profile demonstrated that without GSH, less than 25% of drug was released. With the aid of GSH the release reached 45.16% after 4 hours and 94.89%, in about 24 hours. The cell viability was 86.14% after 24 hour incubation with 50µm/mL of nanoparticles. Non-cancerous cell line (HUVEC) incubated with Dox loaded nanoparticles showed low cell death (~28.40%) due to the lack of GSH to enhance DOX release.	(Yang et al., 2015)
Mesoporous silica coated magnetite nanoparticles with ZnO interlayer	170 nm magnetite core, 20 nm ZnO layer and 25 nm silica shell thickness	Etoposide (VP-16)	Microwave-triggered drug delivery system were developed with mesoporous silica shell, magnetite core and ZnO Interlayer. Drug release was less than 14% after 10 hours stirring, which was enhanced to 85% with discontinuous microwave irradiation.	(Qiu et al., 2014)

1.8 Liposome Coated Magnetite Nanoparticles: Magnetoliposomes

Incorporating liposomes with magnetic nanoparticles is an attractive approach to create multifunctional vesicles for a wide range of medical applications from drug delivery to diagnostic imaging agents. Liposomes are spherical vesicles formed by lipid bilayer membrane composed of natural or synthetic amphiphilic lipid molecules (Zhang and Granick, 2006, Torchilin, 2005a). Liposomes have been studied as pharmaceutical carriers for many years due to their unique properties to form different formulations with the required size and surface charge to encapsulated both hydrophilic and hydrophobic therapeutic agents. Liposomes can also protect the encapsulated “cargo” i.e. drug molecules from external conditions. Furthermore liposomes can be functionalised with targeting ligands or be coated with biocompatible polymers such as polyethylene glycol (PEG) to prolong their *in vivo* blood circulation half-life (Torchilin, 2005b, Moghimi and Szebeni, 2003). Liposomes were the first nanocarriers which succeeded in translating from bench to bedside with Doxil being first liposomal drug formulation approved by the Food and Drug Administration, USA (FDA) in 1995 for treatment of AIDS associated with Kaposi’s sarcoma (Zhang et al., 2008b, Monnier et al., 2014, Northfelt et al., 1998).

In 1988 De Cuyper and Joniau introduced the magnetoliposomes by adsorption of different types of phosphatidylglycerols onto superparamagnetic magnetite nanoparticles. Magnetoliposomes were formed by sonication of phospholipid vesicles in the presence magnetite nanoparticles. The inner phospholipids monolayer is adsorbed on the magnetite nanoparticles with their charged headgroup orientated towards the iron oxide surface (Cuyper and Joniau). Since the introduction of magnetoliposomes, it has attracted significant attention in nanomedicine due to the combination of the properties of liposomes and the magnetic nanoparticles therefore a significant progress have been made in their development.

The two common strategies to combine the magnetic nanoparticles with liposomes are either to encapsulate the magnetic nanoparticles directly within the liposome lumen (Beaune et al., 2008, Cintra et al., 2009a, Bothun and Preiss, 2011) or to embed them in between the lipid bilayer (Chen et al., 2010b, Amstad et al., 2011, Bonnaud et al., 2014, Monnier et al., 2014). The factors which could influence the formation of magnetoliposomes and affect lipid-nanoparticle interactions include the surface coating of the magnetite nanoparticles, the size of the nanoparticles, and the type of lipids. For instance the nanoparticles surface chemistry determine location of the nanoparticles within the liposome and changing the composition of the lipid bilayer by adding cholesterol, is shown to reduce the leakage of drug molecules from the liposomes by “tightening” the bilayer (Allen and Cullis, 2013).

Most of the research on magnetoliposomes are concentrated in their utility as MRI contrast agents (Martina et al., 2005, Fortin-Ripoche et al., 2006, Garnier et al., 2012) and in controlling the release of an encapsulated drug. One approach to design the controlled drug release is to choose

Table 1-5. A list of magnetoliposome based drug delivery systems

Core structure	size	Lipid composition	result	reference
Chitosan-coated magnetite	hydrodynamic diameter of 103.62	SPC	Enhanced magnetofection potential. Carrying and delivering genetic material. The <i>in vivo</i> studies revealed that lip-MNPs had a superior pharmacokinetic profile, compared to chi-MNPs. evasion of the RES.	(Linemann et al., 2013)
Dextran-coated iron oxide	range of 150–230 nm	DPPE:Chol	Thermosensitive magnetoliposomes synthesised for AMF-induced drug release	(Lin-Ai et al., 2009)
Fluidmag-hs	184 nm not loaded, 361 nm when loaded with doxorubicin	DPPE, DSPE-PEG	Folate receptor targeted thermosensitive magnetic liposomes. For use in magnetic hyperthermia-triggered drug release. calcein release of about 70% at 43 °C and less than 5% release at 37 °C .Folate-targeted magnetic liposomes showed encapsulation efficiencies of about 85% for doxorubicin with 52% doxorubicin release at 43°C	(Pradhan et al., 2010)
Hydrophobic magnetite nanoparticles	~200nm	DPPE	Thermosensitive magnetoliposomes synthesised for controlled drug release using alternating current electromagnetic fields (EMFs) operating at radio frequencies	(Chen et al., 2010b)
Dextran-coated magnetite nanoparticles	100 and 200 nm	POPC, DSPE-PEG:chol	Stable liposomal carriers as magnetic resonance imaging (MRI) contrast agents it was shown that magnetoliposomes produce a pronounced signal enhancement in MRI <i>in vitro</i> and <i>in vivo</i> .	(Frascione et al., 2012)
Magnetite nanoparticles	~80 nm	SPC	Stable liposomal carriers with high loading of mitomycin C anticancer drug (MMC) was developed. With the high loading of 10.9µg of MMC/mg of materials.	(Sen et al., 2012a)

Table 1-5. Continued

Core structure	size	Lipid composition	result	reference
Magnetite nanoparticles stabilized with tetramethylammonium hydroxide (TMAOH)	165 nm, 204 nm	SPC, SPC: chol	Enhanced magnetic resonance imaging (MRI) contrast. It was shown that SPC magnetoliposomes and SPC:Chol strongly alter the T2 weighted MRI image contrast.	(Faria et al., 2013)
Magnetic iron oxide	99.12 ± 0.11 nm, 95.06 ± 0.15 nm	SPC:chol, DPPC:chol	Thermosensitive and non-thermosensitive magnetoliposomes for delivery of artemisinin and transferrin. The drug loading efficiencies of artemisinin, transferrin in the magnetoliposomes were 89.11% ± 0.23, 85.09% ± 0.31. Thermosensitive formulation showed enhanced drug release at 42°C and exhibited high cytotoxicity against MCF7 and MDA-MB-231 cells in the presence of a magnetic field.	(Gharib et al., 2014)
Magnetite stabilized with anionic coating	200 nm	SPC	Magnetoliposomes were prepared for possible delivery of anti-inflammatory drugs. Magnetoliposomes presence in the exudates collected from the inflammation site and the iron biodistribution study in mice indicate that the magnetic nanoparticles accumulated mainly in the inflammation zone.	(Garcia-Jimeno et al., 2011)

architecture is an essential aspect affecting polymer aggregation, micelles formation and micelle size. Concerning di- and multi-block polymers, the functional block is usually kept rather short (several units) to prevent flocculation and adding several attachment points on a single chain can reduce the packing density (Boyer et al., 2010).

Magnetic polymer micelles have been explored to be used in different areas of nanomedicine such as multimodal imaging agents, targeting agents, delivery and triggered release of therapeutic agents such as peptides, proteins and DNA / RNA (Boyer et al., 2010, Torchilin, 2000, Lim et al., 2006, Hong et al., 2008b, Cuong et al., 2012). Some examples of polymer coated iron oxide nanoparticles which are already used in medicine includes INFeD (Watson Pharmaceuticals), Dexferrum (Luitpold Pharmaceuticals) which are dextran coated iron oxide and Feraheme (a.k.a. ferumoxytol, AMAG pharmaceuticals) which is superparamagnetic iron oxide nanoparticles and have been used as injectable material to treat iron anemia (Chen, 2010).

Temperature-sensitive polymers have been widely used in drug delivery systems to release drugs in response to a changes in the surrounding temperature (Glover et al., 2012, Silva et al., 2011, Brazel, 2009, Brazel, 2008). Similar to thermosensitive magnetoliposomes, temperature-sensitive polymers combined with superparamagnetic iron oxide nanoparticles can be designed to release the encapsulated cargo in the presence of alternating magnetic field and in response to the heat generated by the magnetic nanoparticles (Brazel, 2008). Sundaresan *et al.* have developed dual-responsive poly (N-isopropylacrylamide-acrylamide-chitosan) (PAC)-coated magnetic nanoparticles for controlled and targeted drug delivery and imaging applications. The PAC-MNPs showed dual-responsive drug release characteristics with the maximum release of drugs at 40 °C. They have conjugated prostate cancer-specific R11 peptides into the polymer shell which increased the uptake of PAC-MNPs by prostate cancer PC3 cells (Sundaresan et al., 2014). In another study Wadajkar *et al.* have developed Thermo-responsive poly (N-isopropylacrylamide-acrylamide-allylamine)-coated magnetic nanoparticles (PMNPs) conjugated with prostate cancer-specific R11 peptides for active targeting and imaging of prostate cancer. Their results indicated that R11-PMNPs decreased the magnetic resonance T2 signal intensity by 30% in tumours (Wadajkar et al., 2013). Ai *et al.* have developed poly (ϵ -caprolactone)-b-poly (ethylene glycol) coated magnetic nanoparticles as magnetic resonance imaging agents with remarkably high T2 relaxivity (Ai et al., 2005b). Change *et al.* reported the synthesis of 4 nm magnetite nanoparticles coated with amphiphilic block copolymers of poly (ethyl methacrylate)-b-poly (2-hydroxyethyl methacrylate) (PEMAb-PHEMA) for potential carriers of hydrophobic targeted drug delivery. The results showed that the amount of drug loaded into the core-shell Fe_3O_4 @PEMA-b-PHEMA depends on the length of hydrophobic segment of block copolymer (Chang et al., 2009). Some examples of application of magnetic micelles for drug delivery and hyperthermia are listed in Table 1-6.

Table 1-6. A list of magnetic micelles used as drug delivery systems.

Core structure	size	polymer composition	summary	reference
Oleic acid and oleyl amine modified magnetite	50-80nm	PEG-PCL	Magnetically triggered drug (Doxorubicin) delivery system for cancer therapy. Drug release was evaluated at physiological temperature (37 °C) and an elevated temperature (57 °C). Results indicated that the PEG-PCL micelles can be used as heat triggered drug release using a high frequency magnetic field.	(Glover et al., 2013)
Oleic acid modified magnetite	196.1 nm	Poly (HFMA-co-MOTAC)-g-PEGMA	Folate-bovine serum albumin functionalized micelles for tumour targeting and MR imaging. <i>In vivo</i> MRI of nude mice bearing the Bel-7402 xenografts after micelle administration revealed excellent tumour targeting and MRI capabilities.	(Li et al., 2015a)
Hydrophobic magnetite nanoparticles	40±8nm	PEG-PLA	Multifunctional Polymeric Micelles as Cancer-Targeted, MRI-Ultrasensitive Drug Delivery Systems. Doxorubicin were loaded at 2.7w/w% dox content. The presence of cRGD on the micelle surface resulted in the cancer-targeted delivery to $\alpha\beta3$ -expressing tumor cells.	(Nasongkla et al., 2006)
Oleic acid modified magnetite	265 nm	F127-PLA	Magnetic micelles was developed for dual targeted (folate-mediated and magnetic-guided) drug delivery. Doxorubicin was loaded into micelles at 1.8%.w/w ratio. Cellular uptake of the micelles <i>in vitro</i> and <i>in vivo</i> were enhanced by application a permanent magnet.	(Huang et al., 2012)
Oleic acid and oleyl amine modified magnetite nanoparticles	77 ± 3	PEG-PCL	Folate-functionalized micelles were developed as hepatic carcinoma-targeted, MRI-sensitive drug delivery system. Doxorubicin was loaded in micelles at 5.2%w/w ratio. Cellular uptake of the folate targeting micelle was increased about 2.5 fold. The MRI potential of micelles were assessed with a 1.5 T clinical MRI scanner which showed a significant decrease in T2 signal intensity.	(Hong et al., 2008b)

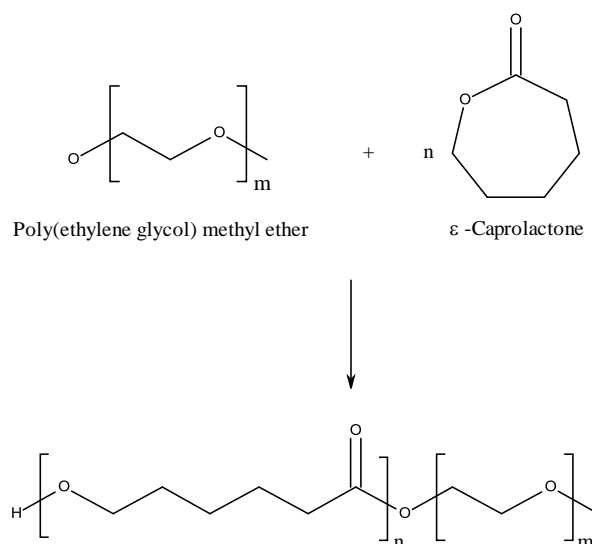
Table 1-6. Continued

Core structure	size	polymer composition	summary	reference
Oleic acid modified magnetite	150-300nm	(mPEG)-b-p (HPMAm-Lac2).	Thermosensitive, and biodegradable micelles were developed as MRI contrast agent with high magnetite loading of 40%. MRI scanning of the samples indicated that the micelles had high r_2 and r_2^* relaxivities. The micelles showed excellent stability under physiological conditions for up to 7 days.	(Talelli et al., 2009)
γ -Fe ₂ O ₃	43 nm	poly-n-isopropylacrylamide (PNIPAAm)	Thermosensitive micelles were developed for magnetic targeting with simultaneous hyperthermia and drug release. <i>In vitro</i> hyperthermia with 14.7% doxorubicin release was achieved in 47 min. <i>In vivo</i> magnetic targeting of micelles to hepatocellular carcinoma (HCC) in a rat model was confirmed by MRI and histology.	(Purushotham et al., 2009)
Oleic acid and oleyl modified magnetite nanoparticles	<200nm	PNIPAAm-co-AAm)-b-PCL	Thermosensitive micelles were developed for magnetic hyperthermia-mediated drug release and imaging agent was developed. Surface functionalization with the integrin β_4 (A9) antibody resulted in active targeting of head and neck carcinoma cells with over-express the A9 antigen. The LCST was adjusted to 43°C. Micelles demonstrated enhanced MRI contrast compared to free SPIONs.	(Kim et al., 2013)
Oleic acid and oleyl modified magnetite nanoparticles	44±3 nm	PEG-PCL	Folate-targeted micelles with high MRI sensitivity were developed. Compared to the magnetite nanoparticles the magnetic micelles showed a notably high r_2/r_1 ratio of up to 78. BEL-7402 cells over-expressing folate receptors show significant increase in micelles uptake. At 3 hours after intravenous injection of the micellar solution into mice bearing subcutaneous xenografts of human BEL-7402 hepatoma, a 41.2% signal intensity decrease was detected, signifying the effective accumulation micelles in the tumour tissue.	(Hong et al., 2012)

In this project thermosensitive PEG-PCL diblock copolymer was used for drug delivery systems with heat triggered drug release and applications in hyperthermia. PCL is biodegradable biocompatible polymer (Salgado et al., 2012) and Poly (ethylene glycol) (PEG) is nontoxic and FDA approved for internal use in the human body (Zhou et al., 2003). It is well established in the literature that surface modification of nanoparticles with polyethylene glycol (PEG), increases blood circulation times by reducing interactions with serum proteins and mitigating uptake by phagocytic cells (Ashley et al., 2011b).

The magnetic micelles were created by self-assembling of PEG-PCL polymer around the hydrophobic magnetite nanoparticles. The polymer was synthesised by the ring opening of ϵ -caprolactone and polymerization from the alcohol terminus of poly (ethylene glycol) monomethylether as shown in Scheme 1-1. In aqueous media, the PCL hydrophobic block forms the micelle core and the PEG hydrophilic block forms a shell that disperses the micelles. The micelle cores were loaded with oleic acid modified hydrophobic magnetite nanoparticles and anti-cancer drug Doxorubicin.

Since melting point for PCL is in the range of 40°C - 45°C (hyperthermia treatment range), heat generated by the magnetite core under the influence of an AC magnetic field leads to PCL melting. Unlike an lower critical solution temperature (LCST) polymer which release the drug following a discontinues phase change, in case of PEG-PCL micelles, melting the core of the polymeric micelle was used to release the drug by increased diffusivity of the drug (Glover et al., 2013, Glover et al., 2012)



Scheme 1-1. Synthetic scheme of PEG-PCL

Similar to liposomes, in this project polymers were also used to cap the mesopores of the silica coated nanoparticles. Figure 1-5 illustrates the schematic diagram of the polymeric micelles with magnetite nanoparticles and silica coated magnetite nanoparticles as core structures. To cap the silica nanoparticles with polymers the surface of the silica nanoparticles were modified to become

hydrophobic and then polymeric micelles were formed around the silica nanoparticles as core material.

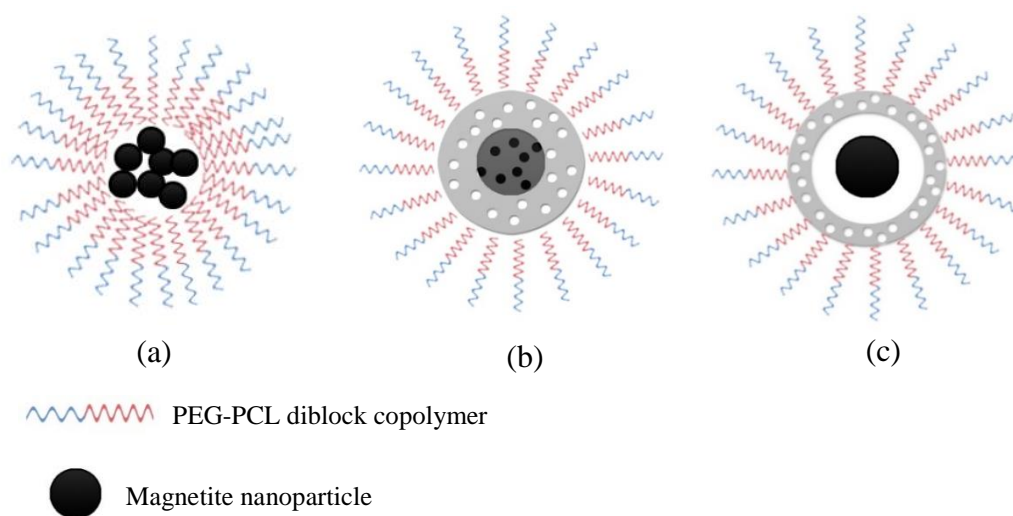


Figure 1-5. (a) PEG-PCL magnetic micelles, (b) PEG-PCL capped mesoporous silica coated magnetite, and (c) PEG-PCL capped mesoporous silica coated magnetite

1.10 Applications of Superparamagnetic Iron Oxide Nanoparticles (SPIONs) in Nanomedicine

Magnetic nanoparticles have shown great potential in nanomedicine. Current developments in the synthesis process of magnetic nanoparticles make it possible to develop nanoparticles with controllable size and biocompatible coatings which in turn make it feasible for the magnetic nanoparticles to interact with biological entities. Furthermore, the magnetic properties of these particles make it possible to manipulate them by means of an external magnetic field. These properties with the intrinsic permeability of magnetic fields into human tissue makes these nanomaterial ideal for a wide range of biomedical applications involving the transport or immobilization of magnetic nanoparticles or magnetically tagged biological units including delivery systems for therapeutic agents (Pankhurst et al., 2003a, McBain et al., 2008). Targeting allows localized delivery of the therapeutic agents, resulting in reduced required dosage, and consequently to less toxic side effects. These therapeutic agents either consist of therapeutic drug encapsulated nanoparticles or nanoparticles with therapeutic effects themselves. Typically these effects are toxic to healthy tissue as well, which make it essential to optimize the therapeutic window with low enough toxicity to result in minimal damage to surrounding tissue, yet toxic enough to eradicate the intended target. These parameters should be considered when designing a therapeutic iron oxide nanoparticle.

Table 1-7. A list of FDA approved commercialised iron oxide nanocomposites currently used in nanomedicine.

Commercial name	Nanoparticle drug component	Delivery route	Specific treatment	FDA approval	company
Feraheme (ferumoxytol)	Superparamagnetic iron oxide coated with polyglucose sorbitol carboxymethylether. The overall colloidal particle size is 17-31 nm	Intravenous injection	Iron deficiency anemia associated with chronic kidney disease. May also be useful as a diagnostic agent for vascular enhanced MRI	June 2009	AMAG
Injectafer	Iron carboxylate complex Ferric carboxymaltose	Intravenous injection	Iron deficiency anemia in patients undergoing chronic hemodialysis	July 2013	Luitpold Pharmaceuticals
Venofer	Iron sucrose	Intravenous injection	Iron deficiency anemia in patients undergoing chronic hemodialysis	2000	Luitpold Pharmaceuticals
Lumirem (GastroMAR K, ferumoxsil)	Silicone coated, superparamagnetic iron oxide (~400nm)	Oral or rectal administration	Enhances the contrast between the bowel and other abdominal structures and masses in MRI images.	1996	AMAG, Mallinckrodt (USA), Guerbet S.A (Europe)
Feridex, (Endorem in Europe)	Superparamagnetic iron oxide associated with dextran (120 to 180 nm)	Intravenous injection	contrast agent for magnetic resonance imaging (MRI) of liver lesions	1996	Berlex Laboratories (USA), Guerbet
Resovist, Ferucarbotran	Carboxydextrane-coated superparamagnetic iron oxide nanoparticles (between 45 and 60	Intravenous injection	Organ specific MRI contrast agent, used for the detection and characterization of especially small focal liver lesions.	Not approved in USA, approved in Europe at 2001.	Bayer Healthcare (Europe and Japan)

Superparamagnetic iron oxide nanoparticles themselves can act as therapeutic agents considering their hyperthermic qualities to kill cells. Magnetic nanoparticles respond to alternating magnetic fields resulting in energy generation and heating of the nanoparticles. Since many types of cancer cells are more sensitive to high temperatures than normal cells it is possible for magnetic nanoparticles to be used as hyperthermia agents for killing malignant cells while having no effect on the surrounding healthy tissue (Pankhurst et al., 2003b). Furthermore, iron oxide nanoparticles could be used as imaging agents. Iron oxide nanoparticles could effectively lower the T2 contrast signal of MR imaging and have been used as MRI contrasting agents (LaConte et al., 2007). Additionally, with appropriate coating and incorporating functional ligands, such as fluorophores or radioactive ions they can also be used for fluorescent imaging and PET imaging (Chen, 2010). Some examples of FDA approved commercialised iron oxide nanocomposites in nanomedicine are listed in Table 1-7.

1.10.1 Magnetic Drug Targeting (MDT)

The main disadvantage of most chemotherapeutic drugs is the nonspecificity in drug action which means the intravenously administered drug reach systemic distribution which results in harmful side effects such as bone marrow depression and reduced immunity, as the drug affects healthy cells as well as the targeted malignant cells. The use of magnetic carries to target specific site of the body was first proposed by Freeman *et al.* in 1960s (Freeman et al., 1960). The main objectives of the magnetic drug delivery system is to target the specific site and therefore reduce the systemic distribution and also reducing the required dosage of the toxic drug thus subsequently reducing the unwanted side effects (Pankhurst et al., 2003a, Wahajuddin and Arora, 2012). Over the last few decades, much research has been done on developing and optimizing magnetic drug delivery systems with improved magnetic properties, increased nanoparticles concentration in targeted tissue and reduced early detection and clearance from blood (Mahmoudi et al., 2011, Gupta and Gupta, 2005).

Magnetically targeting drug delivery system consist of a drug attached to biocompatible magnetic nanoparticles which could be inhaled or injected intravenously and be guided to concentrate at the target site through an external high gradient magnetic field. Schematic representation of magnetic targeted drug delivery system is shown in Figure 1-6.

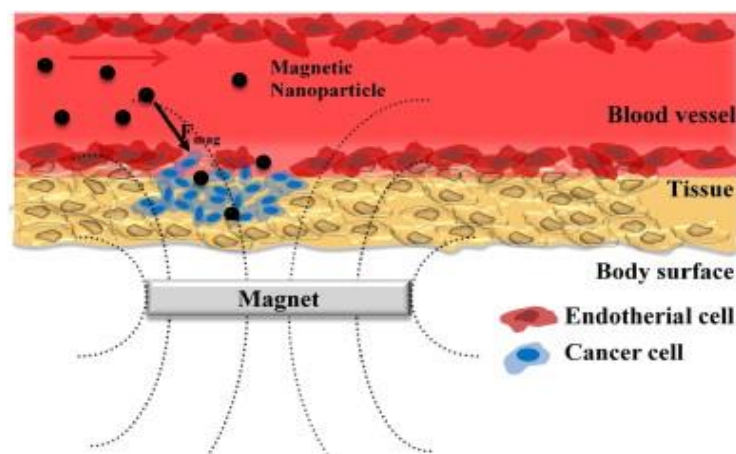


Figure 1-6. Schematic representation of magnetic nanoparticle-based drug delivery system (Park et al., 2010).

The physical concepts of magnetic targeting therapy are based on the magnetic force exercised by a magnetic nanoparticle under influence of a magnetic field gradient. The efficient magnetic targeting depends upon a number of physical parameters including the field strength, depth of the targeted tissue, magnetic moment of the nanoparticles, size and shape of the nanoparticles, blood flow rate, and ferrofluid concentration and viscosity (Sensenig et al., 2012, Chertok et al., 2010).

A number of magnetic targeting studies on small animals have already been reported (Alexiou et al., 2003, Nobuto et al., 2004, Chertok et al., 2010, Estelrich et al., 2015, Mody et al., 2014). Alexiou *et al.* have reported the treatment of squamous cell carcinoma in rabbits with mitoxantrone (MTX) bound to phosphate groups of magnetic particles coated with starch derivatives (FF-MTX). The FF-MTX was injected either *via* femoral artery or ear vein, while an external magnetic field was focused on the tumour. No negative side effects were observed and the intra artery FF-MTX administration produced a significant ($p < 0.05$), complete and permanent remission of the squamous cell carcinoma in comparison with both the control group and the intravenously administered group. The accumulation of magnetic particles in the tumour site were visualized both histologically and by magnetic resonance imaging (Alexiou et al., 2000). The same group reported another study in 2006 which further confirmed the efficiency of the magnetic targeting to concentrate the drug bounded to magnetic nanoparticles in peritumoral region and inside the tumour (Jurgons et al., 2006). Yanai *et al.* have demonstrated the feasibility of magnetic targeting in neurological tissue, by targeting stem cells magnetically to the upper hemisphere of the rodent retina. Rat mesenchymal stem cells magnetized by superparamagnetic iron oxide nanoparticles were injected *via* the tail vein of the rat model with a disc magnet placed outside the eye. Their results demonstrated that cells were localized to the inner retina in a tightly confined area corresponding to the position of the orbital magnet and stem cells retained their differentiation capabilities (Yanai et al., 2012).

Tietze *et al.* have reported a study comparing the *in vivo* distribution of free and magnetic nanoparticles bounded mitoxantrone (MTX). It was shown that while using magnetic targeting, 57.2% of the drug was accumulated in tumour region compared to only 0.7% for systemic

intravenous administration (Tietze et al., 2013). These studies showed the advantage of magnetically targeted chemotherapy over the conventional chemotherapy (Estelrich et al., 2015). However, due to the technical challenges such as weakening of magnetic field with the distance and depth of the target only few clinical trials have been reported and research is ongoing to optimise and overcome the problems.

The first Phase I clinical trial of magnetic drug targeting was conducted in 1996 with 14 unsuccessfully pre-treated cancer patients. In this study epirubicin chemically bound to 100 nm biocompatible starch coated iron oxide particles were used. This trial indicated that for half of the patients the drug was successfully guided to the target site using external magnetic field (Lubbe et al., 1996). Similar study was conducted in 2004 with 11 patients and the magnetic targeting was monitored with magnetic resonance imaging (MRI) which proved suitable to assess the success of the MDT. The study showed that about half of the particles were successfully guided and concentrated at the target site (Lemke et al., 2004). Figure 1-7 shows a magnetic targeted drug delivery system.



Figure 1-7. Epirubicin chemically attached to magnetic nanoparticles were administered to cancer patients, a permanent magnetic was placed in the way to assure the distance less than 0.5 cm from the tumour surface. The magnetic field of (0.5-0.8T) was reached (Shapiro et al., 2015).

In another study conducted in 2001-2002 Wilson *et al.* reported the use of metallic iron-activated carbon–doxorubicin (MTC-DOX) for treatment of inoperable hepatocellular carcinoma. Selective catheterization of hepatic artery was used to further optimize the delivery to the tumour and minimize delivery to normal tissue. MTC-DOX magnetic delivery to the hepatic artery was monitored by using MR imaging. The treated tumour section reported to be 0.64% to 0.91% of the tumour volume (Wilson et al., 2004).

Despite the fact that magnetic drug targeting procedure appears safe and feasible, improvements are essential to make it more effective. Currently the magnetic drug targeting is limited and have not yet passed regulatory approval for clinical use (Shapiro et al., 2015).

1.10.2 Magnetic Fluid Hyperthermia (MFH)

The National Cancer Institute of United States of America defines hyperthermia therapy as “A type of treatment in which body tissue is exposed to high temperatures to damage and kill cancer

cells or to make cancer cells more sensitive to the effects of radiation and certain anticancer drugs” (Bañobre-López et al., 2013). Hyperthermia therapy is commonly considered in two different temperature ranges, temperature rise between (41-46°C) which alters the intercellular structures and leads to cellular degradation and induce apoptosis (Deatsch and Evans, 2014). This type of hyperthermia is used in combination with chemotherapy or radiation (Overgaard et al., 2009). Hyperthermia with temperature rise above 46°C or thermoablation results in direct cell death by tissue necrosis or carbonization (Kumar and Mohammad, 2011, Deatsch and Evans, 2014).

Different tactics have been exploited to induce hyperthermia in cancerous tissue, such as laser, ionizing radiation, ultrasound and microwaves. Although these methods were able to raise the tissue temperature to hyperthermia treatment temperature, they were not able target heat specifically to cancer site and resulted in generating harmful side effects in the healthy tissues (Bañobre-López et al., 2013). This challenges encouraged the use of magnetic nanoparticles to induce hyperthermia.

Magnetically induce hyperthermia is based on the concept that placing a magnetic particle under influence of an alternating magnetic field (AMF) with sufficient field strength and frequency induce heating in the particles which subsequently raise the surrounding tissue temperature. The frequency of the field used in magnetic hyperthermia is between 100 kHz and 1 MHz (Bañobre-López et al., 2013) and Magnetite (Fe₃O₄) nanoparticles are the preferable heating source for magnetic hyperthermia (Motoyama et al., 2008b). The heat induced in magnetic particles is generated due to energy losses, namely Eddy current loss, hysteresis loss, Brownian rotational and Neel’s loss. The Eddy current loss is associated with currents generated due to material being exposed to an alternating magnetic field and is calculated from Equation 1-10.

$$P_{Eddy} = \frac{(\pi d f B)^2}{6k\rho D} \quad \text{Equation 1-10}$$

Where ρ (Ωm) is resistivity of the material, f (Hz) is the field frequency, B (T) is the magnetic field, d is the diameter of the particle, and D (kg/m^3) is the density of the material. As observed from the equation since the particles size is in the range of nanometre and frequencies are low for generation of Eddy current, the Eddy current loss is negligible (Pankhurst et al., 2003c). Furthermore, nanoparticles are mostly coated with biocompatible shells (e.g. polymers and lipids) which eliminate the setting up of current loops due to isolation or insulation.

Hysteresis loss is the energy loss associated with shifting domains in multi-domain magnetic particles and reversing the magnetization of the material. The hysteresis loss is calculated from the area enclosed by the hysteresis loop (Figure 1-2) (Motoyama et al., 2008a, Mornet et al., 2004).

$$P_H = \mu_0 f \oint H \cdot dM \quad \text{Equation 1-11}$$

Where H is the applied field, μ_0 is the permeability of the free space and f is the frequency of the applied field. Since both coercivity and remanence are negligible for superparamagnetic nanoparticles the hysteresis loss is insignificant and the heating is mostly the result of Neel and Brownian relaxations.

Relaxation losses are caused by the gradual alignment of the magnetic moments during the magnetization process in an AC magnetic field. The relaxation process of a ferrofluid may take place through two distinct mechanisms. Brownian motion of the magnetic nanoparticles consists of rotation of the single domain nanoparticle, itself in a fluid, resulting in friction and consequently, heating of the particles. The so-called Néel relaxation corresponds to reorientation of magnetization vector within the particle in order to stay aligned with the changing field direction. These two power losses are functions of the particle size. Ferrofluid can exhibit both of these mechanisms, each having the proper weight (Zhang et al., 2007, Behdadfar et al., 2012, Wang and Liu, 2011, Blanco-Mantecón and O'Grady, 2006).

The power loss corresponding to Néel and Brown relaxation can be calculated from Equation 1-12.

$$P = \frac{(mH\omega\tau)^2}{2\tau kT\rho V (1+\omega^2\tau^2)} \quad \text{Equation 1-12}$$

Where m is the particle's magnetic moment, τ is the magnetic relaxation time, ω is the measurement angular frequency, ρ the density of magnetic nanoparticles, H is the field intensity amplitude, k is the Boltzmann's constant, and V is the particle volume. It can be seen that temperature rise in the nanoparticles depends largely on the particles size, and magnetic saturation as well as the magnetic field frequency and amplitude.

The concept of magnetically induced hyperthermia for cancer treatment was first proposed by Gilchrist *et al.* at 1957. They established that lymph nodes could be heated to kill lymphatic metastases using an external magnetic field after the administration of magnetic particles. Fe_2O_3 particles were used in these experiments which generated a temperature rise of 14°C using 5 mg of Fe_2O_3 per gram of tissue while exposed to magnetic field 200-240 Oe (16-19.2 kA/m) (Gilchrist et al., 1957). In 1979, Gordon *et al.* reported inducing intracellular hyperthermia, by administering submicron magnetite nanoparticles intravenously to Sprague Dawley rats. They reported successful magnetic field induced heating and destruction of the tumours occurred in their *in vivo* experiments (Gordon et al., 1979).

Currently some research studies on magnetic nanoparticles based hyperthermia have entered animal experiments and clinical trials (Jordan et al., 2006, Kawai et al., 2006, Luo et al., 2014, Motoyama et al., 2008b). Johannsen *et al.* have reported the first clinical experiment of magnetic hyperthermia using magnetic nanoparticles. Hyperthermia sessions of 60 minutes were performed

once a week for 6 week on 67 year old patient with recurrent prostate cancer. Nanoparticle suspensions were injected transperineally into the prostate under transrectal ultrasound and fluoroscopy guidance. Computerized tomography (CT) of the prostate was used to plan the treatment, invasive thermometry of the prostate was implemented in the first and last hyperthermia treatment and additional CT-scans were carried out after first and last treatment to investigate the magnetic nanoparticles distribution in the prostate and monitor the location of the temperature control probes. The magnetic field was delivered using first magnetic field applicator for use in humans (MFH300F, MagForce® Nanotechnologies GmbH, Berlin). The magnetic field frequency was 100 kHz with variable field strength of up to 18 kA/m however it was kept less than 5 kA/m during treatment. Figure 1-8 shows the magnetic field applicator. The results of this study indicated that hyperthermia treatment using magnetic nanoparticles was feasible and well tolerated. A single intratumoural application of nanoparticles was required since particles remained in the prostate during the 6 weeks treatment period, allowing repeated hyperthermia treatments without the need for further application of magnetic fluid. The maximum and minimum intraprostatic temperatures measured were 48.5°C and 40.0°C during the first treatment and 42.5°C and 39.4°C during the sixth treatment, respectively (Johannsen et al., 2005b). These results encouraged the phase I clinical trial with 10 patients suffering from recurrence prostate cancer to investigate the feasibility, toxicity of magnetic induction hyperthermia. Same hyperthermia treatment with intraprostatic injection of nanoparticles were used and the maximum temperature of up to 55°C was achieved in the prostates. Prostate specific antigen (PSA) decreased in eight patients after treatment. No systemic toxicity was observed for 17.5 months of the median follow-up and indication. The results indicated that magnetic fluid hyperthermia of recurring prostate cancer is feasible and well tolerated and would not cause significant side effects (Johannsen et al., 2007).



Figure 1-8. AC magnetic field applicator (MFH300F, MagForce® Nanotechnologies GmbH, Berlin). For cooling purposes, a closed loop of tubes with circulating cold water, is placed around the patient's inner thigh, perineum and the groin (Johannsen et al., 2005b).

Wust *et al.* have performed magnetic fluid hyperthermia treatment on 22 patients suffering from recurring tumour entities to evaluate the feasibility and efficacy of MFH in combination with irradiation and / or chemotherapy. Magnetic nanoparticles were implanted with three different methods of infiltration under CT fluoroscopy, transrectal ultrasound guided implantation with X-ray fluoroscopy and operative infiltration with visual control. The temperature distribution in the tumour region is calculated based on direct temperature measurements. Magnetic field with strengths of 3.0-6.0 kA/m, >10.0 kA/m and 7.5 kA/m were used in the pelvis, head, and neck region, respectively. They have reported that the treatments were well tolerated without significant side effects. However they have reflected that improvement in temperature distribution is required (Wust *et al.*, 2006). Maier-Hauff *et al.* used magnetic hyperthermia treatment in combination with radiation therapy on 14 patients with recurring glioblastoma multiforme. The patient received 3D image guided intratumoral injection of magnetic nanoparticles planned in advanced using MRI. The nanoparticles distribution after injection was studied using CT-scans, and the data compared to pre-operative MRI data were used to calculate the expected heat distribution and the required magnetic field strength. Magnetic field with strength of 2.5–18 kA/m and frequency of 100 kHz was used to induce particles heating. The results indicated that median maximum temperature of 44.6°C (42.4°C-49.5°C) was reached in the tumour and the treatment was well tolerated by patients, and minor or no side effects were observed (Maier-Hauff *et al.*, 2007). Although there are still some challenges to overcome and optimize the effect of magnetic hyperthermia cancer therapy, magnetic nanoparticle based hyperthermia trials have passed the preclinical stages and received regulatory approval in 2010 as a new clinical therapy as “thermotherapy” (Asín *et al.*, 2012, Zhao *et al.*, 2013d). This approval follows successful completion of the conformity evaluation procedure of the NanoTherm® magnetic fluid by Medcert GmbH and of its NanoActivator® magnetic field applicator by Berlin Cert GmbH. NanoTherm™ is a aminosilane coated iron oxide nanoparticles with an average diameter of around 15 nm (MagForce, 2016).

Magnetic field parameters such as field strength and frequency are selected to be compliant with the approved protocols for MFH in Europe. For instance, for treatment of glioblastoma multiforme (MagForce, Berlin, Germany) magnetic field frequencies in the order of 100–200 kHz at around 20 mT are typically chosen (Monnier *et al.*, 2014).

1.11 Introduction to Bio-Catalysis

Enzymes are widespread natural proteins, although few are catalytic RNA molecules, which acts as catalysts with high activity, regioselectivity and enantioselectivity. Enzymes (like all catalysts) increase the reaction rate by reducing the reaction activation energy. Enzyme catalysed reactions mostly operate at near ambient condition and produce less waste and fewer by products (Rozzell and Lalonde, 2010). Enzymes are isolated from bacteria, moulds, yeasts, plants and animals

(Sinfelt and Cusumano, 1977). The catalytic function and selectivity of the enzyme is established by the unique active site architecture. The active site is made up of an array of amino acid residues in the polymeric peptide chain, of which only few are directly included in enzyme-substrate complex. Enzymes have been used in different applications such as food, pharmaceutical and chemical.

Considering pharmaceutical section, enzymatic processes are well established for synthesis of important drugs including penicillin, morphine, quinine, cyclosporin and paclitaxel (Yiu and Keane, 2012). For instance, Taxol (generic name paclitaxel), a widely used anti-cancer agent in the treatment of ovarian, breast and lung cancer is a natural product found in the bark of Pacific yews. Production process from natural resources is extremely expensive and unaffordable and synthetic production of Paclitaxel involves over 50 individual steps. In 1993 Bristol-Myers Squibb (BMS) adopted an enzymatic process of cytochrome P450 which can shorten the synthesis process to a 20-step procedure (Malik et al., 2011). The most widely used group of enzymes used in pharmaceutical industry are lipases, which are discussed in the following section.

1.11.1 Lipase

Lipases (triacylglycerol hydrolase, EC 3.1.1.3) signify one of the most important enzymes used in bio-catalysis systems. Lipase acts at oil-water interface and catalyse the hydrolysis of triglycerides into diglycerides, monoglycerides, glycerol and fatty acids, and under certain conditions the reverse reaction leads to esterification and formation of glycerides from glycerol and fatty acids. Therefore, lipases have important role in digest, transport and process fats, oils, triglycerides and other lipids. Lipases can have animal source (pancreatic, hepatic and gastric), microbial (bacterial, fungal and yeast) or vegetable origin, with variations in their catalytic properties (Barros et al., 2010). Depending on the nature of substrate and reaction conditions, lipases catalyse wide range of enantioselective and regioselective reactions. Figure 1-9 depicts the mechanisms of various lipase catalysed reactions. Acidolysis, Alcoholysis and Interesterification are classified as transesterification reactions.

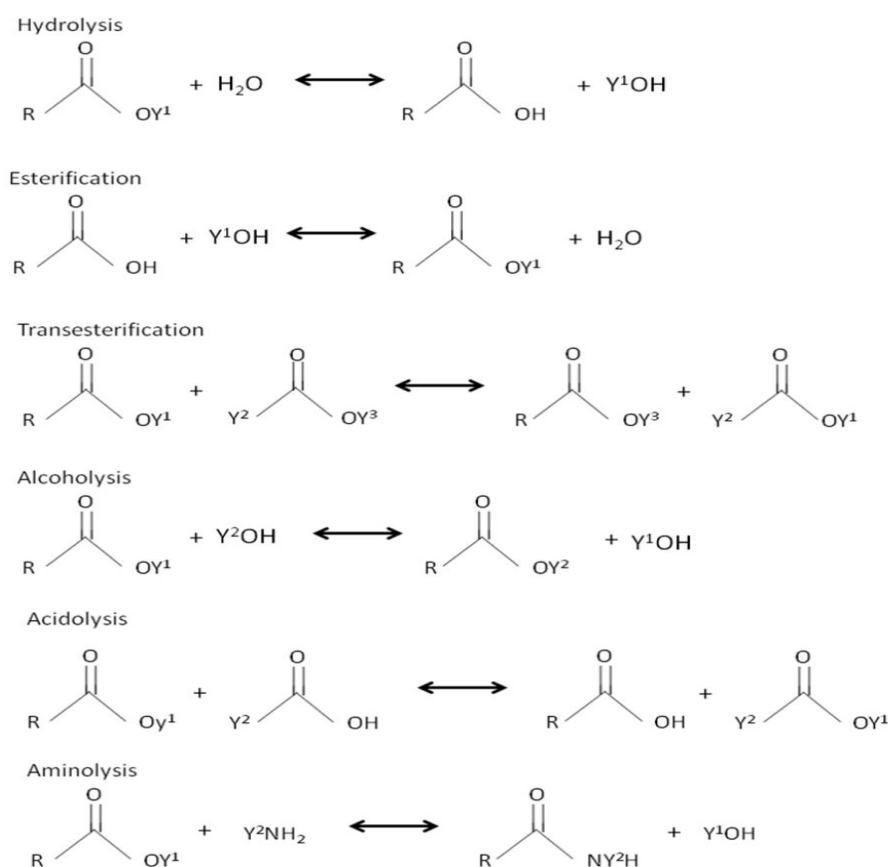


Figure 1-9. Reactions catalysed by lipases (Barros et al., 2010)

Most lipases are characterized by inclusion in their structure of a mobile domain, known as the “lid”, which consists of a single helix, two helices, or a loop region. In the absence of a lipid-water interface, the lid covers the active site, while the presence of an interface results in a rearrangement of the conformation of the enzyme that displaces the lid, thus making the catalytic site accessible to the substrate and the solvent (Borrelli and Trono, 2015). A simple model consists of two successive equilibrium defines the kinetics of lipase catalytic process at an interface. During the first equilibrium stage, the lipase is adsorbed reversibly to the interface ($E \rightleftharpoons E^*$), sequentially in the second stage the adsorbed enzyme (E^*) binds with a substrate molecule (S), forming the lipase-substrate complex (E^*S) which is equivalent to the Michaelis-Menten equilibrium of enzyme-substrate complex. When the lipase-substrate complex is formed the consequent catalytic steps occur after which the products are released and enzyme is restored at the interface adsorbed (E^*) form. In this model, the restored lipase remains adsorbed to the interface and is only released after several catalytic cycles (Houde et al., Reis et al., 2009).

Lipase catalysed reactions are easy to handle, do not need cofactors for lipase activation, and are commercially available, which make them attractive as industrial biocatalysts in pharmaceutical, food and cosmetics industries. Microbial lipases represent the most widely used class of enzymes in biotechnological applications due to their stability, selectivity and broad substrate specificity.

Microbial lipases sources includes bacteria, yeast, and fungi (Treichel et al., 2009). Some of the lipases and their application are summarised in Table 1-8.

Two particularly important lipases with respect to this project, are Candida Rugosa Lipase (CRL) and Pseudomonas Fluorescens Lipase (PFL).

Table 1-8. A list of the lipases and their common application

lipase	Application	Reference
Y. lipolytica lipase From Yarrowia lipolytica yeast	Used for bio-transformation of steroids and synthesis of pharmaceutical intermediates and fine chemicals, used in detergent industry for removal of oil-based stains.	(Fickers et al., 2011)
Geotrichum candidum	Used to synthesise lipophilic antioxidants and prepare chiral intermediates for pharmaceuticals	(Xu et al., 1995) (Ramos-Sánchez et al., 2015, Hasan et al., 2006)
Candida rugosa lipase	Used in reparation of highly pure unsaturated fatty acids such as oleic, linoleic, soap production and cheese production. Used in flavour development of concentrated milk and creams. Used for synthesise of lovastatin and Ezetimibe, drugs lowing serum cholesterol level. Used in biodiesel synthesis and paper industry. Used for preparation of The chiral compound intermediate for the synthesis of certain Hepatitis C virus protease inhibitors.	(Ramos-Sánchez et al., 2015, Anobom et al., 2014, Aravindan et al., 2007, Montero, 2011, Verma et al., 2012, Carvalho et al., 2015)
Lipases from Candida cylindracea,	Used in detergent industry for removal of oil-based stains, used in personal care products, bakery products. Used in pharmaceutical industry to resolve the enantiomers of flurbiprofen, naproxen, ibuprofen, suprofen and baclofen, and synthesise of lobucavir, hepatitis B antiviral and ribavarin antiviral	(Shay and Fisher, 1991, Vakhlu, 2006, Johnson, 2013, Sharma et al., 2011) (Ray, 2012)
Candida parapsilosis	Used in food industry for synthesis of food additives	(Ramos-Sánchez et al., 2015)

Table 1-8. Continued

lipase	Application	Reference
Candida antarctica lipase fraction B (CAL-B)	Used in synthesis of flavours and fragrance esters, surfactants, biodiesel, waxes, acylated flavonoids and modified glycerides. Used for esterification of free fatty acids in detergent industry for removal of oil-based stains. Used in synthesises processes of pharmaceutical intermediates such as anti-Alzheimer's drugs, flurbiprofen, naproxen, ibuprofen, suprofen and baclofen, lobucavir, hepatitis B antiviral and ribavarin antiviral.	(Larios et al., 2004, Hasan et al., 2006, Johnson, 2013, Sharma et al., 2011, Ray, 2012) (Tanino et al., 2009)
Serratia marcescens lipase	Used for synthesise of diltiazem hydrochloride, a coronary vasodilator.	(Matsumae et al., 1993)
Burkholderia cepacia (PS-30)	Used in pharmaceutical industry for synthesis of Taxane 5 and paclitaxel (an anti-cancer compound)	(Patel et al., 2003, Carvalho et al., 2015)
Lipase from Pseudomonas sp	Used in pharmaceutical industry for synthesis of paclitaxel and antidepressant agents.	(Patel et al., 1994, Yin et al., 2016, Carvalho et al., 2015)
Rhizomucor miehei lipase	Used for resolution of chiral compounds, and prepare anti-inflammatory drugs.	(Ray, 2012, Zullo and Ciafardini, 2008) (Ansorge-Schumacher and Thum, 2013)
Lipases from Pseudomonas fluorescens (PFL)	Used in pharmaceutical industry to synthesis the key intermediate of Prostaglandins, Prostacyclins, Thromboxane and Paclitaxel also to prepare Argatroban, an antithrombotic drug.	(Carvalho et al., 2015, Sharifabad et al., 2014)

1.11.2 Candida Rugosa Lipase (CRL)

Literature surveys reveal Candida Rugosa Lipase (CRL) as one of the most extensively studied enzymes due to its high activity and broad specificity (substrate, positional, fatty acid and stereopreference) (Benjamin and Pandey, 1998b, Yong et al., 2008). Candida Rugosa is a asporogenic, unicellular, non-pathogenic, mesophilic yeast (Wu et al., 2012, Benjamin and Pandey, 1998b) with a molecular weight of 45–60 kD and a molecular volume of $5 \times 4.2 \times 3.3 \text{ nm}^3$ (Gao et al., 2010). There have been contrasting reports on the number of CRL lipase isoforms;

two (Veeraragavan and Gibbs, 1989), three (Shaw et al., 1989, Wu et al., 1990) or five (Grochulski et al., 1993, Linko and Yan Wu, 1996, Rúa and Ballesteros, 1994). So far, six distinct isoforms in CRL lipases have been characterized (Chang et al., 2006, Lee et al., 2011, Xu et al., 2009b). Despite a high sequence similarity (over 80% amino acid homology) in these isoenzymes, individual CRL isoenzymes display obvious differences in their thermal stability and substrate preference (Zhang et al., 2016). For instance, LIP5 (fifth isoform) specificity on hydrolysis of amino acid-derivative substrates is shown to be the highest among other lipase isoforms, but it shown very weak preference on hydrolysing triacylglycerol substrates. LIP5 activity on hydrolysis of p-nitrophenyl (pNP) butyrate was optimal at 55 °C as compared with 37 °C of the commercial CRL lipase (Lee et al., 2011).

CRL has been used in a wide range of catalytic reactions in both aqueous and water-restricted environments which include non-specific and stereo-specific hydrolysis, reversal of hydrolysis *via* esterification, trans-esterification and inter-esterification (Benjamin and Pandey, 1998a, Jaeger et al., 1994, Macrae and Hammond, 1985). CRL is one of the enzymes most frequently used in bio-transformation and has the great advantage of being considered as safe for food applications (Ramos-Sánchez et al., 2015). CRL is used by Nippon Oils & Fats (Tokyo, Japan) for the preparation of highly pure unsaturated fatty acids (oleic, linoleic, linoleic, etc.), and is used by Miyoshi Yushi (Nagoya, Japan), to produce soap through lipase-based hydrolysis of oils and fats (Ramos-Sánchez et al., 2015).

CRL is also used in pharmaceutical industry for example to synthesize lovastatin, a drug lowering serum cholesterol level (Ramos-Sánchez et al., 2015). Singh have reported that CRL provides efficient enzymatic methods for the synthesis of enantiopure 3-[5- (4-fluorophenyl)-5 (S)-hydroxypentanoyl]-4 (S)-4-phenyl-1,3-oxazolidin-2-one ((S)-FOP alcohol) which is key intermediate of Ezetimibe drug used for lowering the blood cholesterol (Singh et al., 2013). Marszał have reported the kinetic resolution of an anti-inflammatory drug, (R,S)-ibuprofen using immobilized CRL (Marszał and Siódmiak, 2012).

Additionally, CRL lipase is used in the cheese manufacture (Kindstedt et al., 2004, Aravindan et al., 2007). The flavour development in concentrated milk and creams by microbial lipases was investigated, where it was reported that each lipase developed a characteristic flavour. CRL lipases were found as the most suitable for this purpose. CRL was selected to hydrolyze triacylglycerol for clinical lipid analysis and developed as a biosensor (Vakhlu, 2006, Sharma et al., 2011). CRL is also able to catalyze biodiesel synthesis (Borrelli and Trono, 2015, Montero, 2011).

Considering the occurrence of variable amounts of each isoforms in crude lipase, the preparations lead to a lack of reproducibility of bio-catalytic reactions. The expression of isoforms is directed by culture or fermentation conditions. Protein engineering of purified CRL isoforms allows the tailoring of enzyme function (Akoh et al., 2004, Borrelli and Trono, 2015), however purification

of the lipase results in higher costs. Furthermore free lipase is often unstable and possesses low activity in organic solvents or harsh environments such as high temperature or extreme pH (Wu et al., 2012).

To compensate the cost associated with CRL, enhance the operation stability and afford the recovery and reusability of the lipase, CRL could be used in immobilized form. Immobilization of CRL promotes the separation of products and lipases and improves catalytic activity, stability, and recyclability of immobilized lipase in continuous operations (Wu et al., 2012). CRL has been immobilised on different supports such as chitosan beads (Ting et al., 2006), glass beads (Yilmaz et al., 2011), magnetic beads (Marszał and Siódmiak, 2012), polymers (Yilmaz et al., 2009), epoxy supports (Mateo et al., 2003) and silica (Gao et al., 2010). Since lipases are not soluble in organic media, covalent linkages may not be necessary between the support and the lipase, and thus simple adsorption can be employed (Chang et al., 2007) (Khare and Nakajima, 2000).

1.11.3 *Pseudomonas Fluorescens* Lipase (PFL)

Pseudomonas Fluorescens Lipase (PFL) is produced from *Pseudomonas Fluorescens* bacterium (PFB). PFB is commonly isolated from soil, water, and the tissues of plants and animals (Son et al., 2012). PFL is a thermostable lipase which has high lipolytic activity for short- to medium-chain triacylglycerols (Kim et al., 2005b). PFL is shown to exist in two different states of bimolecular structure with a molecular weight of 66 kD (at moderate enzyme concentration to high concentration of lipase) an unimolecular structure with a molecular weight of 33 kD (at very low enzyme concentrations or in the presence of detergents). The two enzyme structures display different properties, the bimolecular structure is proved to be more stable than the unimolecular species, and the bimolecular structure demonstrated lower activity but higher enantioselectivity than the unimolecular structure (Fernández-Lorente et al., 2003). Lower activity of the bimolecular lipase structure is suggested to be due to the interaction between the hydrophobic areas of the lipase surface surrounding the active centre of lipase molecules in their open form, suggesting that interfacial activation competes with formation of the bi-molecular structure (Fernández-Lorente et al., 2003). Kim *et al.* have studied the purification and renaturation of solubilized PFL and reported that however lipases are generally stable in organic solvents, the cosolvents TFE and DMSO both destabilize PFL, and destroy its enzyme activity even at a low concentration of 2%. Nevertheless, Ca²⁺ stabilizes PFL in the presence of these cosolvents and, in particular, it extended the stability of PFL such that 50% of its lipase activity was retained in 16% TFE and 24% DMSO, respectively (Kim et al., 2005b). Cadirci *et al.* have studied the effect of different solvents on PFL. They have reported that PFL is stable in unpolar solvents such as benzene, styrene, toluene, hexane, and heptane, however, the enzyme is unstable in polar organic solvents such as acetone, methanol (Cadirci and Yasa, 2010). PFL is widely used in biotechnological application because of their potential in organic synthesis for highly valuable chemicals (Sharma and Kanwar, 2014).

Some of the applications listed for PFL in the literature includes, transesterification reaction for the production of biodiesel (Iso et al., 2001, Lima et al., 2015), Hydrolysis of racemic methyl-branched octanoic acids to determine stereoselective mechanism of action (Sonnet and Baillargeon, 1991), interesterification of butter fat (Kalo et al., 1989), conversion of microalgal lipids produce biodiesel (Guldhe et al., 2015), Regioselective deprotection of 3',5'-O-acylated pyrimidine nucleosides (Uemura et al., 1989), enzymatic synthesis of triacylglycerols of docosahexaenoic acid *via* transesterification of its ethyl esters with glycerol (Moreno-Perez et al., 2015). PFL is used in the synthesis of argatroban (an antithrombotic drug) with 99% enantioselectivity in forming (21S)-isomer, which is twice as potent as 21R (Carvalho et al., 2015). PFL is also used for enantioselective production of 4- (R)- hydroxycyclopent-2-en-1- (S)-acetate as a key intermediate in the synthesis of cyclopentenoid molecules with important biological activity, such as prostaglandins, prostacyclins and thromboxane (Sharifabad et al., 2014).

1.12 Enzyme Immobilization

Considering multi-step enzyme purification, application of enzyme in the reactions results in increased manufacturing costs and consequently increased product price. Enzyme immobilization on solid supports allows enzyme separation from the product with use of different means such as filtration. Enzyme immobilisation involves surface modification of the supports and enzyme incorporation which adds to the steps of the reaction and increase the costs of the process, however it is accepted that enzyme immobilization represents some advantages including possibility to recycle / reuse the enzyme which recover the costs, add the ability to control the reaction rate and possibility to increase the structural stability of the enzyme during the reaction. Additionally it is reported that compared to free enzymes, immobilised enzymes exhibit an increased tolerance toward organic solvents, temperature and pH (Yiu and Keane, 2012). Since most of natural enzymes are denatured and inactivated in the presence of organic solvents and high temperature, using free enzyme limits the catalytic reaction conditions to aqueous media and ambient temperature (Ogino and Ishikawa, 2001, Yiu and Keane, 2012) where many reactions necessitate organic solvents for the solvation of reactants or products. Furthermore, in some cases the immobilised enzymes outperformed the free enzymes (Chiou and Wu, 2004).

Different materials have been used as enzyme support including synthetic polymers (Cordeiro et al., 2011), TiO₂ membranes (Hou et al., 2014), zeolites (Corma et al., 2002), mesoporous silica nanoparticles (Carlsson et al., 2014, Corma, 1997) and magnetic nanoparticles (Sharifabad et al., 2014, Yiu and Keane, 2012).

Change *et al.* have reported the immobilization of *Candida rugosa* lipase on Celite *via* adsorption which resulted in a significantly improved enzyme performance, they have studied the various immobilisation conditions to optimise the lipase activity. The optimum immobilise lipase activity

was shown to be 34.1% of the free lipase (Chang et al., 2007). Ting *et al.* have reported the CRL lipase immobilized on chitosan beads and its catalytic efficiency in the hydrolysis of soybean oil. The authors have also investigated the pH and thermal stability, reusability and storage stability. The results indicated that under optimal conditions, 88% of the oil was hydrolysed after 5 hours and thermal stability of the lipase was improved by immobilization. The immobilised enzyme did not show reduced activity after 30 days storage at 4 °C. 80% relative activity was observed after six repeated cycles (Ting et al., 2006). Wu *et al.* have immobilised CRL on vesicular silica. The vesicular silica had unilamellar and multilamellar mesoporous structure. Interlamellar mesopores were 15-20 nm with a shell thickness of 5-15 nm. The lipase was immobilized through physical adsorption. The catalytic activity, thermal stability, and reusability of immobilized CRL were studied. They have established that immobilised enzyme show higher activities than of free lipases and it was shown that immobilized CRL demonstrated enhanced adaptability to higher pH range and exhibited increased thermal stability compared to free CRL. They have suggested that the enhanced enzyme activity may be explained by the porous structure which prevents enzyme denaturation and facilitates mass transport and substrate access to the immobilized enzyme (Wu et al., 2012). Dyal *et al.* have reported the stability and enzymatic activity of CRL immobilized on magnetic nanoparticles. They have used functionalized γ -Fe₂O₃ magnetic nanoparticles with the size of 20 ± 10 nm. The enzymatic activity of immobilized CRL reported to be lower than free enzyme. However immobilised CRL retained long-term stability with constant activity over one month. The enzyme–nanoparticle hybrid showed ~15% decrease in activity over that period probably due to desorption or denaturation (Dyal et al., 2003). In 2010 Gao *et al.* have investigated the effects of pore diameter of a mesoporous silica support and cross-linking method on CRL immobilization efficiency. SBA-15 with different pore-sizes of 6.8 nm, 9.1 nm, 13.2 nm, 15.6 nm and 22.4 nm were used as the support material. Their results indicated that the material with pore diameter of 15.6 nm was more suitable as immobilization support with the highest loading amount. They have used chitosan and glutaraldehyde to overcome the enzyme leaching problem. Their experimental results showed that the activities of the immobilized CRL were much higher than that of free lipase and remained 80.5% of the initial activity after 6 cycles in 48 hours (Gao et al., 2010).

The area which is most relevant to this project, is the use of mesoporous silica-coated magnetite nanoparticles as solid supports for lipase immobilisation.

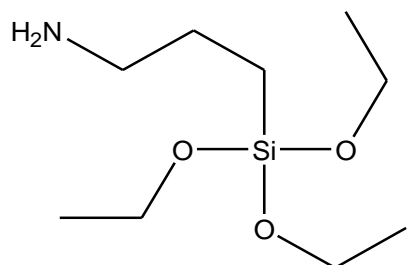
1.12.1 Enzymes Immobilisation on Mesoporous Silica Coated Magnetic Nanoparticles

Enzyme immobilization on magnetic iron oxide nanoparticles are of great interest since they facilitate enzyme recycling and separation and provide effective recovery of enzyme from product by using a magnetic field (Johnson et al., 2007). Furthermore recycling of enzymes immobilized on magnetic nanoparticles in a single reactor has far ranging advantages in fine chemical

production (Yiu and Keane, 2012). Magnetite nanoparticles with superparamagnetic properties are the most commonly used magnetic support for lipase immobilization. Having no permanent magnetic moment, these nanoparticles are readily suspended during the reaction and when separation is required, a magnetic field can be applied to recover the immobilised enzyme (Yiu and Keane, 2012).

The importance of mesoporous silica coated magnetic nanoparticles have raised from their large surface area which can be easily modified with various functionalities toward different applications (Hoffmann et al., 2006, Rath et al., 2014). This is due to the abundance of reactive silanol groups ($\equiv\text{Si-OH}$) on the surface of mesoporous silica materials owing to its amorphous wall structure (Hoffmann et al., 2006). This can be used to effectively immobilize organic functional groups onto a silica surface through either covalent bonding or hydrogen bonding. Functionalization through covalent bonding is preferred in most applications due to stronger bonds as hydrogen bonding usually results in undesired leaching problems due to weak interaction. The enzyme immobilization on the mesoporous silica nanoparticles are mostly performed by crosslinking of enzymes to supports *via* the enzyme's amino groups (Sen and Bruce, 2012a). For this purpose the surface of the mesoporous silica nanoparticles are selectively functionalised.

In the context of this work, aminosilanes in particular (3-aminopropyl)-triethoxysilane (APTS) surface functionalisation of silica-coated magnetic nanoparticles is explained (the detailed method is described in Section 2.8). Figure 1-10 present molecular structure of the APTS.



(3-aminopropyl)-triethoxysilane

Figure 1-10. (3-aminopropyl)-triethoxysilane (APTS)

Generally there are two well-established methods to surface functionalize mesoporous silica nanoparticles; the co-condensation or direct synthesis method and post-synthetic functionalization or grafting method. These two strategies are illustrated in Figure 1-11

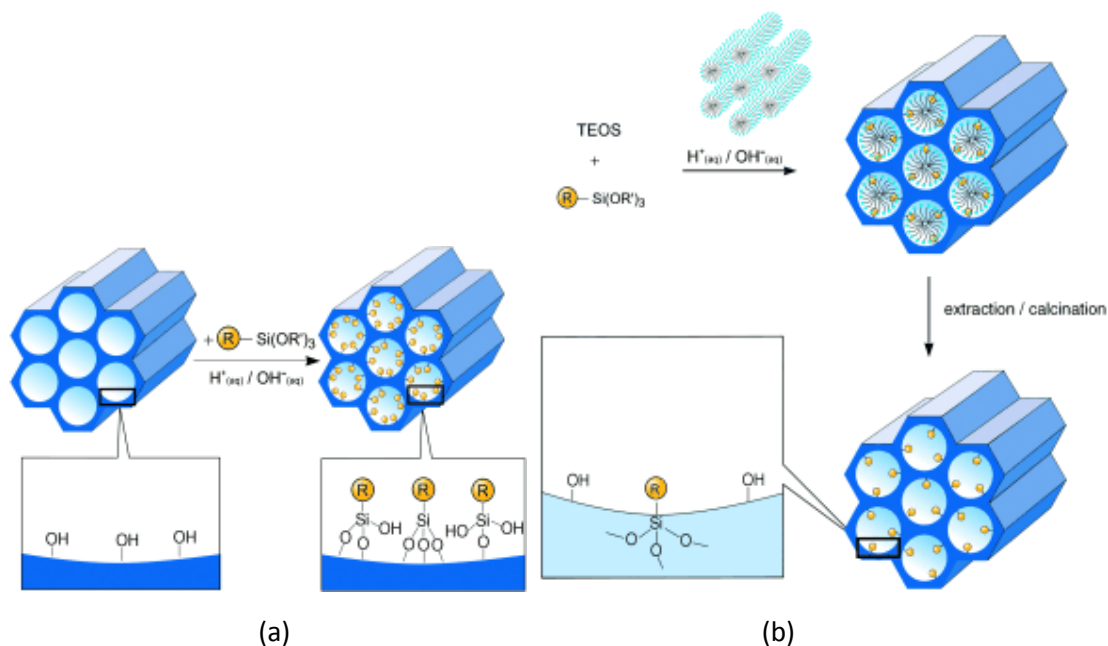


Figure 1-11. Surface functionalisation of mesoporous silica nanoparticles, (a) Grafting method for organic modification of mesoporous silica material with $(R'O)_3SiR$. R = organic functional group, and (b) Co-condensation method (direct synthesis) for the organic modification of mesoporous pure silica phases. R =organic functional group(Hoffmann et al., 2006).

As shown in Figure 1-11, in the co-condensation method, silica sources such as tetramethyl orthosilicate (TMOS) or tetraethyl orthosilicate (TEOS), and organosilanes are added together into the reaction mixture containing the structure-directing agent in either an acidic or basic environments. The organic functional group and the silica source co-condense to form the silica particles. Following this method, the organic functional groups are incorporated into the silica framework during the synthesis which is believed to result in a homogeneous distribution throughout the material. In addition, pore blocking is not an issue for materials prepared by this route, since the organosilanes are direct components of the silica matrix. However, an increase in the amount of organosilanes in the reaction may change the characteristic of the reaction and result in a change in pore structure and particles morphology. Therefore, in order to retain the pore structure, the synthesis conditions such as: chemical nature of the organosilanes, content of organic functionalities, and hydrolysis rate of organosilanes need to be thoroughly considered (Hoffmann et al., 2006). The main disadvantage of the co-condensation method may be the fact that some of organic functional groups may be inaccessible since they are embedded inside the silica matrix.

Post-synthetic functionalization is one of the most popular methods for surface modification of mesoporous silica. In post-synthetic functionalization or grafting strategy, the mesoporous silica nanoparticles are synthesised separately prior to surface functionalization. The process is performed by reaction of the organosilanes with surface silanol groups. The reaction conditions under which the organosilanes is added could affect the amount and network structure of the surface groups but the mesoporous structure and morphology of the starting silica nanomaterial

is usually remains unchanged, although the pore size might be reduced depending on the size of the organic groups and the degree of occupation (Hoffmann et al., 2006).

High quality research has been done to establish the possible binding method of 3-aminopropyltriethoxysilane (APTS) on silica gel in dependence of surface water, leading to the conclusion that polymerization of APTS takes place on the silica surface after adsorption of the silane molecules (Gartmann et al., 2010, Sen and Bruce, 2012a). Gartmann *et al.* have studied the effect of water on the reaction of APTS with mesoporous silica performing the APTS functionalisation reaction with in toluene containing various amounts of water. They have found that with increasing amount of water, clustering of APTS occurs, leading to a nonuniform distribution of the grafted amino groups and a scarcely functionalized pore body (Gartmann et al., 2010). Sen and Bruce have reported a nanoparticles' surface functionalisation strategy using a tri-phasic reverse emulsion (TPRE). The TPRE system were consisted of a solid phase (silica coated magnetite nanoparticles (solid phase), water phase (the water adsorbed on nanoparticles surface) and an organic phase (toluene), in the presence of Triton X-100 which is a bio-compatible, non-ionic surfactant. APTS was found to be soluble in toluene, but did not hydrolyse or self-condense. It was observed that having limited water on the surface of nanoparticles resulted in controlled polymerisation of APTS on the surface leading to an ordered and uniform amine layer on the surface. They have reported that functionalised nanoparticles prepared by this method demonstrated higher surface amine density (>80%) compared to those prepared using bulk water phase surface functionalisation (~20%) (Sen and Bruce, 2012b).

The enzyme immobilization on the surface functionalised nanoparticles are mainly performed *via* direct interaction of the enzyme with amine-functionalised nanoparticles or coupling agents such as glutaraldehyde (Rebelo et al., 2010). Glutaraldehyde molecular structure is presented in Figure 1-12.

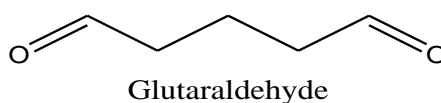
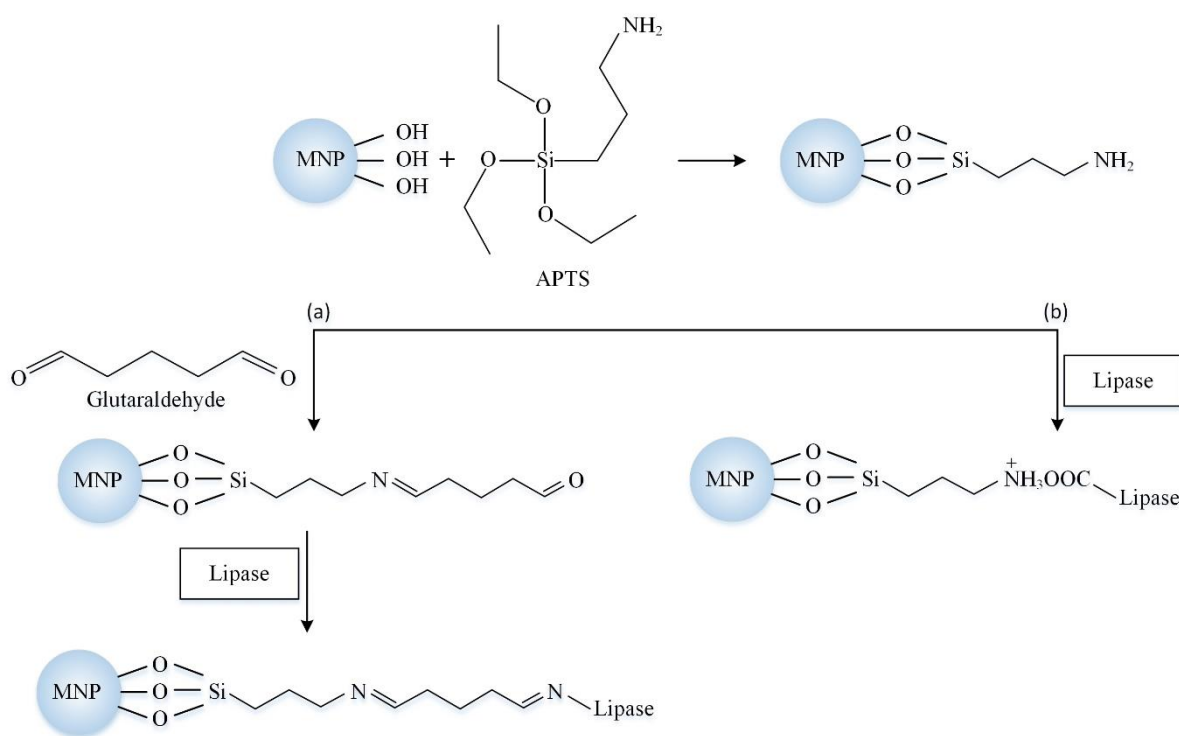


Figure 1-12. Glutaraldehyde molecular structure

Scheme 1-2 shows two common routes for the enzyme immobilization on the surface functionalised nanoparticles.



Scheme 1-2. Immobilization of lipase on magnetic nanoparticles (a) Glutaraldehyde method and (b) absorption method

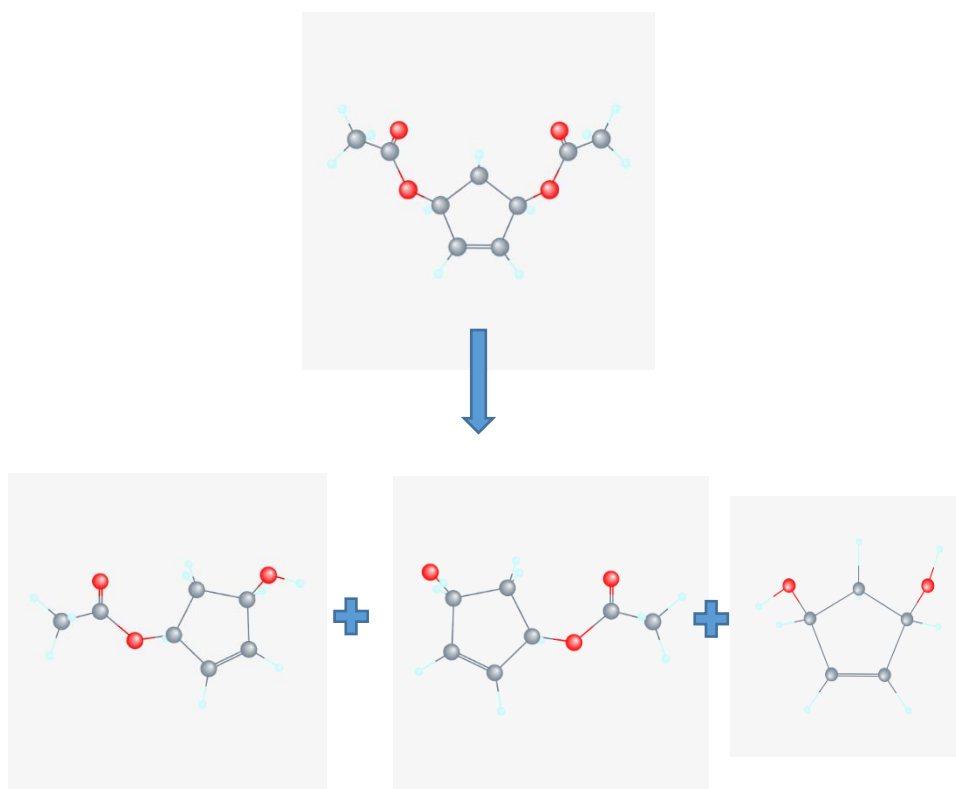
Coupling reagents are used to modify amino-functionalised surfaces to aldehyde functionality which allow the covalent cross-linking to other amino-groups. Among coupling agents, glutaraldehyde is the most popular and widely used reagent which holds unique characteristics that render it one of the most effective protein crosslinking reagents. Glutaraldehyde is a linear 5-carbon dialdehyde and is soluble in all proportions in water and alcohol, as well as in organic solvents. Glutaraldehyde is commercially available with low cost and show high reactivity. It reacts rapidly with amine groups at around neutral pH and is more efficient than other aldehydes in generating thermally and chemically stable crosslinks (Migneault et al., 2004).

Rebelo *et al.* have reported the immobilisation of Lipase from *Burkholderia cepacia* on superparamagnetic nanoparticles using three different methods of direct interaction of the enzyme with APTS functionalised nanoparticles, covalent attachment of lipase *via* modification of the APTS-functionalized nanoparticles with carboxybenzaldehyde, and by using glutaraldehyde as the coupling agent for making the covalent attachment of the lipase enzyme to the APTS functionalised nanoparticles. The transesterification reactions catalysed with *B. cepacia* lipase immobilized by the glutaraldehyde method showed the best results in terms of reusability, preserving the enzyme activity (conversion 50%, $E > 200$) for at least 8 successive cycles (Rebelo et al., 2010). Hu *et al.* have immobilised *Serratia marcescens* lipase on magnetic nanoparticles using glutaraldehyde as the coupling agent which was shown to deliver enantiomeric excess of more than 90% and retained still 59.6% of its initial activity after 11 cycles (totally 105 hours). They have observed a high immobilization rate of 35.2 mg/g. Immobilized lipase has displayed

improved thermal stability compared to free lipase, retaining over 60% activity after incubation at 40°C for 120 hours, while the free lipase was completely deactivated in same conditions (Hu et al., 2009).

The support structure such as the pore size of the mesoporous silica support could affect the enzyme loading capacity and the enzyme activity (Wu et al., 2012). It is established in the literature that the ideal pore size of a mesoporous support should be 3 to 5 times of the protein size (Gao et al., 2010). In fact, in materials with smaller pores only the external surface of the material is available for enzyme loading which result in low enzyme loading. Alternatively, in materials with larger pores the enzyme may leach out of the channels during the loading process or the reaction which consequently results in reduced enzyme activity (Gao et al., 2010, Serra et al., 2008, Salis et al., 2009).

Main reaction performed using the CRL and PFL immobilised nanoparticles in this project was hydrolysis of *cis*-3,5-diacetoxy-1-cyclopentene to obtain (1*S*,4*R*)-*cis*-4-acetoxy-2-cyclopenten-1-ol and its (1*R*,4*S*) enantiomer as illustrated in Scheme 1-3.



Scheme 1-3. Enzyme-catalysed hydrolysis of meso-cyclopent-2-en-1,4-diacetate).

The asymmetric hydrolysis of *cis*-3,5-diacetoxy-1-cyclopentene to the enantiomerically pure monoacetates is an important step in the synthesis of optically active cyclopentanoids such as prostaglandins, prostacyclins, and thromboxanes. Prostaglandins are hormone-like chemical messengers that regulate a broad range of physiological activities, including blood circulation, digestion and reproduction. Their biological activities and their complex molecular architectures have made prostaglandins popular targets for synthetic organic chemists for over 40 years.

Prostaglandin analogues are widely used as pharmaceuticals for instance latanoprost (Xalatan), which has been used to treat glaucoma has generated more than \$1.6 billion annually for Pfizer before it came off patent in 2011 (Coulthard et al., 2012).

Recent developments of physiologically highly potent prostaglandin prompted a great current interest in facile and economic routes to synthesise enantiomerically pure intermediates (Coulthard et al., 2012). Several esterases and lipases have been reported in the literature for the asymmetric hydrolysis of cis-3,5-diacetoxy-1-cyclopentene. Brüsehauer have reported a study on 83 enzymes for the asymmetric hydrolysis of cis-3,5-diacetoxycyclopent-1-ene (Brüsehauer et al., 2008).

CHAPTER 2

MATERIALS AND METHODS

2.1 Reagents and materials

All reagents employed in this study were commercially available, of highest purity grade and used as purchased used without further purification, unless otherwise stated.

Specialist reagents were obtained as follows: 3-aminopropyl tri-ethoxysilane (APTS), Pluronic® F-127, Hexadecyltrimethylammonium bromide (CTAB), Benzyl ether, Polyethylene glycol monomethyl ether (mPEG), ϵ -Caprolactone (CL), Gum arabic, Dibutyltin dilaurate, Iron (III) chloride hexahydrate ($\text{FeCl}_3 \cdot 6\text{H}_2\text{O}$), iron (II) chloride tetrahydrate ($\text{FeCl}_2 \cdot 4\text{H}_2\text{O}$), Iron (II) sulphate heptahydrate ($\text{FeSO}_4 \cdot 7\text{H}_2\text{O}$), Iron (III) acetylacetonate ($\text{Fe}(\text{acac})_3$), 1,2-Dodecanediol, Ammonium hydroxide solution, Oleylamine, Oleic acid (OA), Octyltriethoxy silane (OTS), Ammonium nitrate, Triethylamine (TEA), Sodium hydroxide (NaOH), Diethyl ether, Tetraethyl orthosilicate (TEOS), tetrahydrofuran (THF), toluene, Acetic acid (glacial), Lipases [Candida Rugosa (CRL) and Pseudomonas Fluorescens (PFL)], mitomycin C (MMC), triton X-100, Dimethyl sulfoxide (DMSO), Bradford reagent, glutaraldehyde solution (Grade I, 25% in H_2O), 4-nitrobenzaldehyde (4-NBA), *p*-nitrophenyl palmitate (pNPP), *p*-nitrophenol (pNP), and chiral reagents [*cis*-3,5-dihydroxycyclopentene, *cis*-3,5-diacetoxy-1-cyclopentene, (1S,4R)-*cis*-4-acetoxy-2-cyclopenten-1-ol and (1R,4S)-*cis*-4-acetoxy-2-cyclopenten-1-ol] were all purchased from Sigma-Aldrich, UK. Methanol (HPLC grade), Ethanol (Absolute, 99.8%, HPLC grade) and Cyclohexane were purchased from Fisher Scientific (Loughborough, UK). Doxorubicin hydrochloride (DOX) was purchased from Cayman Chemical. U87 and MCF7 Cell lines were kindly provided by UCLan tissue culture lab. PrestoBlue Cell Viability reagent was purchased from Invitrogen. Eagle's Minimum Essential Medium (EMEM) and Dulbecco's Modified Eagle Medium (DMEM), Fetal bovine serum (FBS), L-glutamine, Non Essential Amino Acids (NEAA), and Sodium Pyruvate were purchased from Lonza.

2.2 Solutions and Buffers

A list of the stock solutions and buffers used in this project and their preparation is summarised in Table 2-1. All the solutions were made up using E-pure deionised water supplied from a Thermo Scientific Barnstead Nanopure Water Deionisation System unless otherwise stated. Where necessary solutions were sterilised by autoclaving for 25 minutes at 120°C.

Table 2-1. Description, usage and storage information of solutions and buffers used in this project.

Solution	Description	Use	Storage
Coupling solution	1 litre of solution was prepared containing 0.8% w/v acetic acid (glacial) in methanol	UV-Visible colorimetric assays and storage of NH ₂ modified nanoparticles	Capped clear glass bottle at 25°C
Hydrolysis solution	1:1 mixture of methanol and water containing 0.15% acetic acid (glacial)	UV-Visible colorimetric assays	Capped clear glass bottle at 25°C
4-NBA solution (700 µg/ml)	7 mg of 4-NBA was dissolved in 10 ml coupling solution	UV-Visible colorimetric assays	Centrifuge tubes at 4°C in the dark (used on the day of production)
Glutaraldehyde solution (5% w/v)	10 ml stock solution was typically prepared containing 1.886 ml glutaraldehyde and 8.114 ml 20×SSC buffer	Conversion of surface amine groups to aldehydes	Centrifuge tubes at -18°C
20×SSC stock buffer	Stock solution was made by dissolving 175.3 g NaCl and 88.2 g sodium citrate in 1 L water. The pH was adjusted to 7.4	Conversion of surface amine groups to aldehydes.	Capped clear glass bottle at 25°C
1×SSC and 13×SSC buffer solutions	20×SSC stock buffer solution was diluted respectively to produce 1× and 13×SSC buffers	Conversion of surface amine groups to aldehydes.	Capped clear glass bottle at 25°C
Reagent A	Gum Arabic (0.0667g), sodium deoxycholate (0.267g), Tris-HCl (12 mL, 250 mM) was added to 48 mL deionised water	Hydrolysis of PNPP reaction solvent in 1:1 mixture with isopropanol	Capped clear glass bottle at 25°C
PBS Buffer	1×PBS tablet (136 mM NaCl, 3 mM KCl, 10 mM Na ₂ HPO ₄ , 2 mM KH ₂ PO ₄) dissolved in 200mL water	Washing and storage of immobilised lipase materials.	Capped clear glass bottle at 25°C

Table 2-1. Continued

Solution	Description	Use	Storage
Sterile PBS Buffer	1×PBS tablet dissolved in 200mL water	Drug loading and release study cellular study for washing the cells	Capped in glass bottle and sterilised by autoclaving. Then kept at 2°C
Acetate buffer	~350mL of 0.1M acetic acid was added to ~650 mL of 0.1M sodium acetate to make pH 5.5	Drug release study	Capped clear glass bottle at 25°C
Growth medium to expand U87 cells	EMEM + 10 % (v/v) FBS + 2mM L-glutamine (5ml) 1% Non Essential Amino Acids (NEAA- 5ml) 1mM Sodium Pyruvate (5ml) 1% penstrep (5ml)	Cell growth media	Stored at 2 °C. warmed in water bath at 37 °C for 15 min to 30 min before use.
Growth medium to expand MCF7 cells	EMEM + 10 % (v/v) FBS + 2mM L-glutamine (5ml) 1% Non Essential Amino Acids (NEAA- 5ml) 1mM Sodium Pyruvate (5ml) 1% penstrep (5ml)	Cell growth media	Stored at 2 °C. warmed in water bath at 37 °C for 15 min to 30 min before use.
DOX.HCl solution	1.8 mg DOX dissolved in 10ml PBS	Drug loading	Stored at 2 °C-in dark
DOX hydrophobic solution	2 mg DOX was deprotonated in TEA and 10 ml DMSO (pH 9.6)	Drug loading	Stored at 2 °C in dark

2.3 Synthesis of Superparamagnetic Iron Oxide Nanoparticles (SPION's)

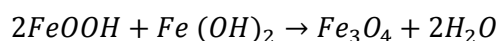
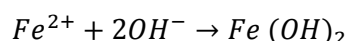
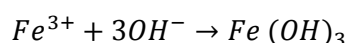
Potential applications of magnetic nanoparticles, particularly iron oxide nanoparticles, in medicine, biological science and technology, led to the development of a number of different techniques to synthesize γ -Fe₂O₃ and Fe₃O₄ nanoparticles in a range of sizes and shapes with

different properties as previously described in Section 1.5. Among these techniques for synthesizing iron oxide nanoparticles, co-precipitation and thermal decomposition methods were used in this project. Co-precipitation strategy was used because of its simplicity and capacity to produce high quantity of superparamagnetic iron oxide nanoparticles of reasonable sizes. Moreover, this technique is compatible with different approaches for functionalizing the nanoparticles with organic surfactants. Organic-phase thermal decomposition synthesis was used where monodisperse nanoparticles with smaller diameter were needed.

2.3.1 Co-precipitation of Iron Chlorides in Alkaline Media

In this method magnetite nanoparticles were synthesized by co-precipitation of ferrous and ferric chloride in alkaline media according to procedures previously reported (Sen et al., 2006). Iron (III) chloride hexahydrate ($\text{FeCl}_3 \cdot 6\text{H}_2\text{O}$, 22.95 g, 0.08 mol) and iron (II) chloride tetrahydrate ($\text{FeCl}_2 \cdot 4\text{H}_2\text{O}$, 8.46 g, 0.04 mol) was dissolved in 500 mL of degassed deionised water under nitrogen environment. Nitrogen was used in preparations to prevent oxidation of the iron species in aqueous environments. Generally, the reaction is performed under an inert (N_2 or Ar) atmosphere using degassed solutions to avoid uncontrollable oxidation of Fe^{2+} into Fe^{3+} (Mascolo et al., 2013). In the presence of dissolved oxygen molecules, the resulting magnetic colloids are usually reddish brown indicating contamination of the colloids with other iron oxides ($\gamma\text{-Fe}_2\text{O}_3$) as a result of strong oxidation of magnetite (Tresilwised et al., 2005, Liu et al., 2004b). The orange solution was heated to 80°C whilst stirring under nitrogen. Aqueous ammonium hydroxide (50 mL, 25% w/v NH_4OH) was added drop wise to the mixture over a 30 minutes period. The reaction was allowed to proceed for further one hour then the reaction mixture was transferred to a conical flask, and was allowed to rest on a magnet. The black product was washed to neutral pH with distilled, deionised water *via* magnetic separation. The final product has pH~7. This method of preparation produced ultra-small spherical nanoparticles with the size of 10 to 15 nm (TEM images are presented in Section 3.2.1). The material was labelled as ME18.

The overall reaction may be written as follows:



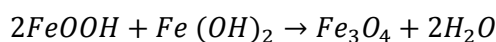
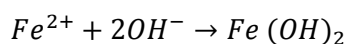
Scheme 2-1. The co-precipitation of iron (II) and iron (III) chloride (Mascolo et al., 2013)

Synthesise of hydrophobic magnetite nanoparticles was carried on by adding oleic acid to the synthesis process (Xu et al., 2006). Iron (III) chloride hexahydrate ($\text{FeCl}_3 \cdot 6\text{H}_2\text{O}$, 22.95 g, 0.08 mol) and iron (II) chloride tetrahydrate ($\text{FeCl}_2 \cdot 4\text{H}_2\text{O}$, 8.46 g, 0.04 mol) was dissolved in 500

mL of degassed deionised water under nitrogen environment. The mixture was heated to 80°C whilst stirring under nitrogen. Aqueous ammonium hydroxide (50mL, 25% w/v NH₄OH) was added drop wise to the mixture. The colour of the solution turned to black immediately. After 30 minutes oleic acid (3.76 g, 0.013 mol) was added to the reaction. The reaction was kept at 80°C for 1 hour, then it was transferred to a conical flask and washed to neutral pH with distilled, deionised water *via* magnetic separation. This method produced hydrophobic spherical nanoparticles. The material was labelled ME55.

2.3.2 Oxidative Hydrolysis of Iron Sulphate in Alkaline Media

In this method magnetite was prepared by oxidative hydrolysis of iron (II) sulphate heptahydrate as the iron source in alkaline media as previously reported (Sugimoto and Matijevic, 1980, Sen et al., 2006). Iron (II) sulphate heptahydrate (FeSO₄·7H₂O, 7.1 g, 0.025 mol) was dissolved in 1L of degassed deionised water in a three-necked round-bottomed flask equipped with a magnetic stirrer, a nitrogen inlet, a condenser and a thermometer. The solution was heated to 90°C whilst stirring under nitrogen. Subsequently potassium nitrate (KNO₃, 20.4 g, 0.20 mol) and potassium hydroxide (KOH, 3.3 g, 0.058 mol) were added to the solution and the reaction was allowed to proceed for further 4 hours while stirring at 90°C under nitrogen. The black mixture was then transferred to a conical flask and allowed to cool down to room temperature. Obtained material were washed several times with 1L of deionised water using magnetic separation until it reached neutral pH. This material was labelled as ME01. Due to the large size of magnetite produced by this method (average diameter of 25 nm, see the TEM image in 3.23.2.1) this material was not used for further applications. The possible reaction for formation of Fe₃O₄ by this method is represented by Scheme 2-2:



Scheme 2-2. The oxidative hydrolysis of iron (II) sulphate heptahydrate

2.3.3 Organic Phase Thermal Decomposition

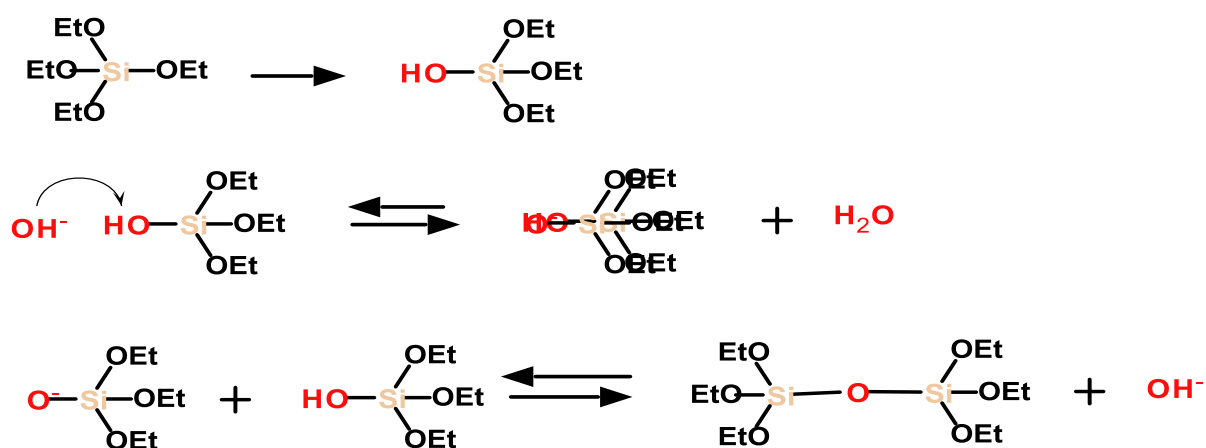
In this method magnetite was prepared by high-temperature solution phase reaction of iron (III) acetylacetonate (Fe (acac)₃), as iron source in the presence of oleic acid and oleylamine which leads to monodisperse magnetite (Fe₃O₄) nanoparticles. The synthesis was carried out following the procedure developed by Sun *et al.* (Sun and Zeng, 2002, Sun et al., 2003).

Iron (III) acetylacetonate (Fe (acac)₃, 706 mg, 2 mmol), 1,2-dodecanediol (2.02 g, 10 mmol), oleic acid (1.69 g, 6 mmol), oleylamine (1.604 g, 6 mmol) and benzyl ether (20 mL) were mixed in a round-bottomed flask equipped with a magnetic stirrer, a nitrogen inlet, a condenser and a

thermometer. The solution was heated to 200°C for 2 hours whilst stirring under nitrogen environment. Subsequently, the temperature was raised to 300°C and stirred for a further one hour, then the reaction was allowed to cool down to room temperature. Ethanol (40 mL) was added to the mixture and the obtained material was separated *via* centrifugation (4000 rpm, 20 minutes) and dispersed in hexane. The black-brown hexane dispersion was characterised and found to range from 7 to 9 nm. Fe₃O₄ nanoparticles produced following this method was labelled as ME59 (TEM images are presented in Figure 3-4).

2.4 Synthesis of Mesoporous Silica Coated Magnetite Nanoparticles

Mesoporous silica coating of magnetic nanoparticles was carried out through surfactant-templating approach *via* hydrolysis and condensation mechanism. Reaction scheme is shown in Scheme 2-3.



Scheme 2-3. Hydrolysis and condensation of silica under alkaline conditions (Gibson, 2014)

Method A) Tetraethyl orthosilicate (TEOS, 3.78 g, 18.14 mmol) was added to 45 mL of a solution containing sodium hydroxide (0.22 M) and cetyltrimethyl ammonium bromide (CTAB, 17.8 g, 49 mmol) and stirred to mix. Magnetite nanoparticles (ME18, 225 mg) and deionised water were added to the mixture to make the total volume of 300 mL. The mixture was stirred for 5 minutes followed by adding HCl (2 M) drop-wise to adjust the pH from 12.5 to ~7. The reaction mixture was stirred further for 30 minutes at room temperature, after which the mixture was left unstirred for further 2 hours. The product was collected and washed twice with 500 mL of 1:1 mixture of deionised water and ethanol to remove the surfactant from the mesopores. The material was subsequently washed with deionised water. The material produced following this methods was labelled as ME16.

Method B) As synthesised magnetite nanoparticles (480 mg of ME18) were dispersed in 200 mL of ethanol: water solution (4:1, V/V) and subsequently ammonium hydroxide (NH₄OH, 14 mL) was added to the mixture and stirred for 5 minutes. Afterward cetyltrimethyl ammonium bromide (CTAB, 10 g, 27.43 mmol) was added to the solution and the suspension was homogenized by

ultrasonic vibration for 15 minutes. The mixture was then placed on the stirrer and Tetraethyl orthosilicate (TEOS, 6 mL) was added drop wise to the reaction under vigorous stirring. The reaction was allowed to proceed for further 24 hours. Final reaction product was isolated from the reaction mixture using magnetic separation. The product was rinsed 3 times with acidic ethanol using ultrasonic bath and then twice with 500 mL of 1:1 mixture of deionised water: ethanol to remove the surfactant from the mesopores. The silica coated nanoparticles were subsequently washed with deionised water until reached pH~7. The materials were fully characterised and found to be mesoporous silica coated core-shell nanoparticles. The material produce following this method was labelled as ME33. ME33 was later for enzyme immobilization and drug delivery.

Same method was optimized to make mesoporous silica coated magnetite nanoparticles with reduced shell thickness and enhanced magnetic heating properties and used for drug delivery applications. These materials was labelled as ME60 and ME32.

Method C) In this method oleic acid modified magnetite ME55 (0.6 mL of 11.2 mg/mL) was dispersed in chloroform. CTAB (1.01 g, 2.77 mmol) was added to water (10 mL) and stirred till dissolved, and afterward added to the magnetite mixture. A turbid brown solution was obtained which is believed to be due to formation of an oil-in-water microemulsion. The mixture was then, heated up to 60°C and stirred for 10 minutes to evaporate the chloroform, resulting in a clear black solution. After 10 minutes, water (100 mL), NaOH (0.6 mL of 2 M solution), and TEOS (1 mL) was added to the mixture and stirred for another 3 hours. The silica coated nanoparticles were collected magnetically and washed with water and acidic ethanol to remove the surfactant as described in methods A and B. The material produced following this method was labelled as ME82. Following characterisation of ME82 it was found that the material possess low surface area therefore, mesoporous silica coated magnetite nanoparticles produced *via* this method were not used for further applications in drug delivery or enzyme immobilisation. TEM images of ME82 are presented in Chapter 3, Figure 3-9.

2.5 Synthesis of Non-porous Silica Coated Magnetite Nanoparticles

Magnetic silica coated core shell nanoparticles with amorphous silica shell were synthesized by a water-in-oil reverse micelle method as reported by Lu *et al.* (Lu et al., 2006) . Monodisperse hydrophobic magnetite (ME55) was used as core material.

Magnetite nanoparticles (ME55, 50 mg) were dispersed in cyclohexane (585 mL). Triton X-100 (200 mg, 320 µmol), hexanol (160 mL), and H₂O (34 mL) were added to the nanoparticles and stirred to generate the microemulsion system. Subsequently, tetraethoxy orthosilicate (TEOS, 4 mL) was added to the mixture and the reaction was allowed to proceed for further three hours. After three hours, an aqueous ammonia (28%, 10 mL) solution was introduced to initiate the TEOS hydrolysis and the reaction was left to continue for further 20 hours. Ethanol was added

after 20 hours in order to destabilize the microemulsion system. Silica coated core-shell nanoparticles were isolated and washed in sequence with ethanol and DI water to remove the surfactant and unreacted reactants. The nanoparticles produced following this method were labelled as ME56. The material were characterised (the TEM images of the ME56 are presented in Figure 3-10) and found to have average particle size of 67 nm. The ME56 was further used to obtain hydrophobic silica shell (see Section 2.6).

2.6 Preparation of Hydrophobic Silica Coated Magnetite

The surface of the silica coated magnetite nanoparticles were modified to enhance their drug loading and release performance. This was achieved by initially modifying the surface of the nanoparticles with octyl groups and subsequently, the hydrophobic organosilane surface of the mesoporous silica nanoparticles were coated with a polymer. Hydrophobic silica coated magnetite nanoparticles were prepared following three different strategies. In the first two approaches the nonporous silica coated nanoparticles (ME56) were used as starting materials.

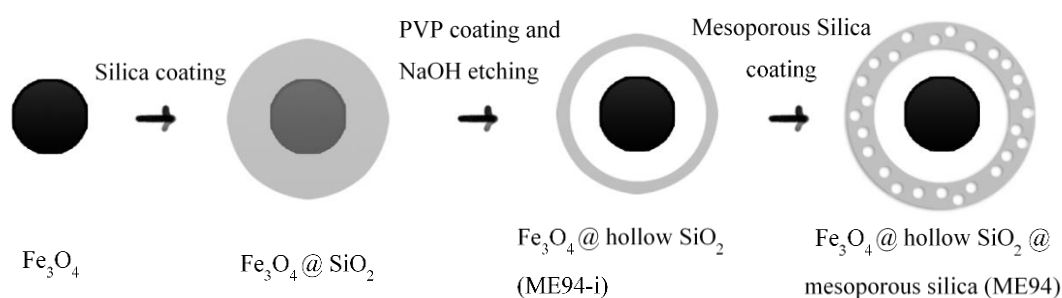
2.6.1 Direct Etching Method

This approach aims to gently etch the silica coatings to convert the dense silica shell to a mesoporous silica shell and add an additional hydrophobic layer of mesoporous silica on top of the nanoparticle so it can later be capped with the polymer. CTAB and pluronic F127 were used as the templates. CTAB (1 g, 2.74 mmol) and pluronic F127 (25 mg) were added to DI water (480 mL) and stirred till they were completely dissolved. ME56 (50 mL, suspension density of 1 mg/mL) was added to the solution whilst stirring in an oil bath at 80°C. TEOS (0.5 mL) was added to the solution and left stirring for another 10 minutes. After 10 minutes sodium hydroxide (1.5 mL of 0.5 M) and ammonium hydroxide (0.5 mL of 28% NH₄OH) were added to the reaction and left stirring for another 20 minutes. To prepare the octyl containing shell, octyltriethoxysilane (OTS, 1 mL) was dissolved in THF (50 mL) and slowly added to the reaction mixture. The mixture was further stirred for 3 hours after which the reaction mixture was allowed to cool down to the room temperature and particles were collected by centrifugation at 4000 rpm for 40 minutes. The nanoparticles were washed twice with ethanol followed by 30 minutes stirring in ethanolic ammonium nitrate (20 g/L) at 60°C to remove the surfactant molecules. Nanoparticles were further washed with ethanol before storage. The material was labelled as ME80. ME80 was characterised as presented in Chapter 3. It was found that ME80 possess comparable size with the starting material (ME56) and relatively low surface area which is consistent with the literature (Yildirim et al., 2013). The surface protected etching was used to increase the surface area.

2.6.2 Surface Protected Etching

In this method a polymer coating process is performed prior to the etching step to protect the outer layer of the material, the process is illustrated in Scheme 2-4. Polyvinylpyrrolidone (PVP) is used as protecting layer over the silica layer (Zhang et al., 2009, Zhang et al., 2008c) to increase the stability against chemical etching due to the hydrogen bonding interaction between the carbonyl group and the hydroxyls on the silica surface. The PVP protects the outer layer of the nanoparticles from the etching while the inner silica is etched to form porous structure.

Monodisperse silica coated magnetic nanoparticles (ME56, suspension density of 50 mL) were mixed with PVP (5 mg) and left stirring for 3 hours refluxing in an oil bath set at 100°C. After 3 hours, the reaction was allowed to cool down to room temperature. The nanoparticles were then collected using centrifuge at 4000 rpm for 50 minutes and redispersed in water using sonication for 5 minutes. The nanoparticles were labelled as ME94-i. Octyl modified nanoparticles were prepared following the same protocol as described earlier in Section 2.6.1. The etching time was optimized to 15 minutes with 0.08 mL of 2 M sodium hydroxide, and 0.5 mL of OTS in 20 mL THF where 50 mg of ME94-i was used.



Scheme 2-4. Surface protected etching of silica coated nanoparticles and subsequent hydrophobic silica coating

As shown in Scheme 2-4 upon reacting with NaOH, the PVP protected outer silica layer undergoes partial etching as the interior is removed to make hollow structure (ME94-i). The original particle size remains the same during the etching and an extra hydrophobic layer is formed over the surface. The material was labelled as ME94.

2.6.3 Direct Synthesis of Hydrophobic Mesoporous Silica Coated Magnetite

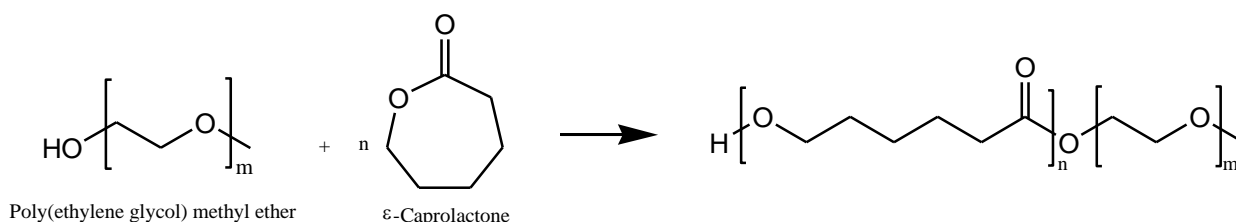
In this process hydrophobic mesoporous coating of magnetite nanoparticles was performed by adding OTS together with TEOS as silica sources, to magnetite nanoparticles. Magnetite nanoparticles (ME53) were used as starting material. Magnetite nanoparticles (ME53, suspension density of 22.8 mg/mL, 22 mL) were added to DI water (540 mL) and placed in an oil bath at 80°C. CTAB (1.02 g) and pluronic F127 (25.5 mg) were added to the nanoparticles and stirred

until completely dissolved. Afterward NaOH (3.5 mL of 2 M) was added and the mixture was stirred for 5 minutes. After 5 minutes, TEOS (5 mL) was added under vigorous stirring and left for further 90 minutes at 80°C. An OTS (1.25 mL) solution in THF (50 mL) was added to the reaction mixture and left stirring for further 3 hours. Subsequently nanoparticles were collected using centrifugation (40 minutes at 4000 rpm) and washed with ethanolic ammonium nitrate and ethanol. The particles were dried over night at 50°C. The material produced following this method was labelled as ME93.

2.7 Synthesis of Poly (ethylene glycol)-*b*-polycaprolactone diblock copolymer

Diblock copolymer was prepared by the tin catalysed ring-opening polymerization of ϵ -caprolactone from the alcohol terminus of poly (ethylene glycol) monomethyl ether following the procedure reported by Glover *et al.* (Glover et al., 2012). The ratio of the number of moles of ϵ -caprolactone to poly (ethylene glycol) monomethylether was 1:20 and dibutyltin dilaurate was used as catalyst.

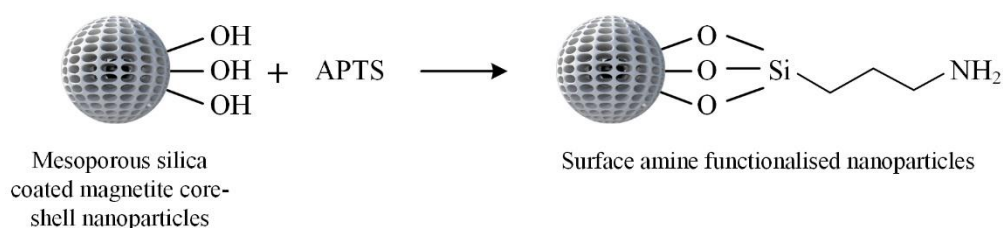
Poly (ethylene glycol) monomethyl ether (17.17 g, 8.6 mmol), ϵ -caprolactone (19.59 g, 172 mmol), and dibutyltin dilaurate (0.2 mL) were added to a round-bottom flask equipped with a condenser, a magnetic stirrer, and a nitrogen inlet and placed in an oil bath. The mixture was heated to 140°C and allowed to stir for 3 hours. After 3 hours the reaction mixture was allowed to cool down to room temperature. The synthesised polymer was dissolved in warm acetone to give a homogeneous solution and then hexane was added until the polymer began to precipitate. The solution was then placed in a freezer (-20°C) till further use. Before use, the polymer was rinsed with hexane by suction filtration and allowed to dry. Synthesised polymer was dissolved in CDCl₃ and ¹H NMR was performed to study the polymer formation (NMR spectrum is presented in Chapter 3, Figure 3-61). The synthesis pathway of the copolymer is presented in Scheme 2-5.



Scheme 2-5. Synthesis pathway of the PEG-PCL diblock copolymer

2.8 Surface Amine Modification of the Silica Coated Nanoparticles

The procedures for surface functionalisation of the silica coated nanoparticles is presented in Section 1.12.1.



Scheme 2-6 surface functionalisation of the silica coated nanoparticles

2.8.1 Tri-phasic Reverse Emulsion (TPRE) Method

In this method surface activation (salinization) of nanoparticles was performed using the novel tri-phasic reverse emulsion (TPRE) method recently reported by our group (Sen and Bruce, 2012a, Sharifabad et al., 2014). In the actual method, as-synthesised mesoporous silica coated nanoparticles (ME33, 150 mg) were collected using magnetic separation and redispersed in toluene (30 mL). Triton-X100 (5 g) was added to the mixture and shaken to form a tri-phasic reverse emulsion. (3-Aminopropyl) triethoxysilane (APTS) was added to the emulsion to a final concentration of 2% (w/v) and kept at 50°C on an end over end rotator at 40 rpm for 24 hours. After 24 hours reaction, surface functionalised mesoporous magnetic nanoparticles were collected by magnetic separation and washed 3 times with 10 mL of coupling solution [0.8% (v/v) glacial acetic acid in methanol] and redispersed in 10 mL of the coupling solution for storage at 4°C till further use. It was observed that surface amine density decreased after prolonged storage, consequently the amine functionalised nanoparticles were disposed after 1 month and new batch was produced for further use. The surface amine density was measured by an established colorimetric assay using 4-nitrobenzaldehyde (Moon et al., 1996, Bruce and Sen, 2005).

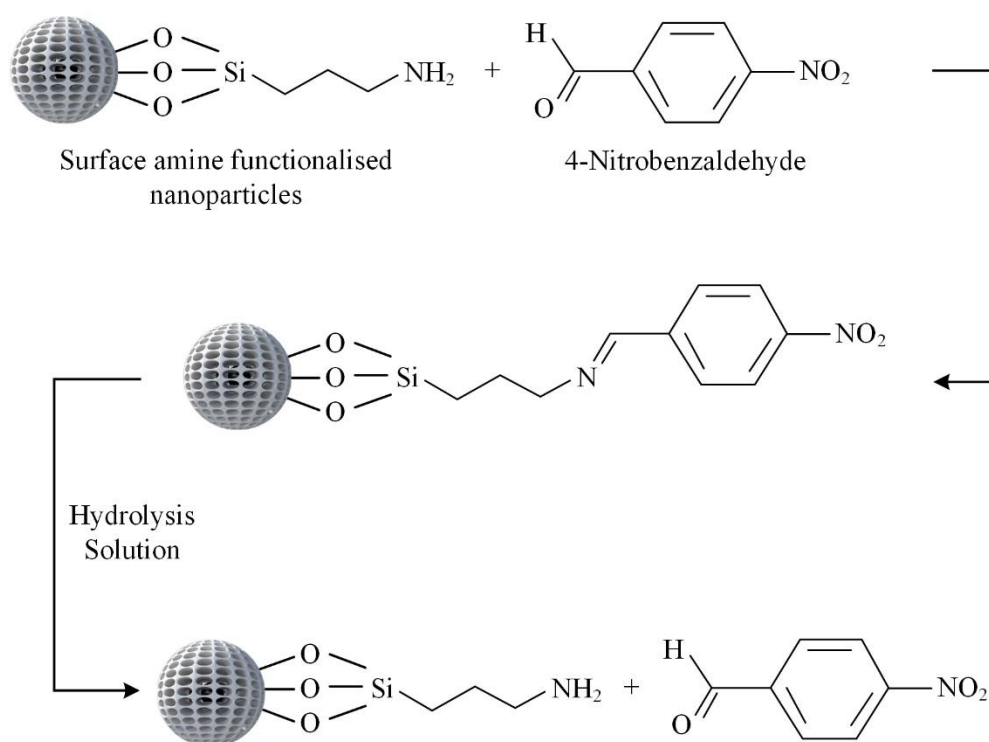
2.8.2 Water Method

Surface functionalization of silica coated magnetite nanoparticles by water method was performed following a modified strategy from the previously reported method by Bruce *et al.* (Bruce and Sen, 2005). Silica coated magnetite nanoparticles (ME33, 150 mg) were collected using magnetic separation and redispersed in a (3-Aminopropyl) triethoxysilane (APTS) in water solution (30 mL, 2% (w/v)). The mixture was kept in an incubator at 50°C on end over end rotator at 40 rpm for 24 hours. Surface functionalised magnetic nanoparticles were collected by magnetic separation and washed 3 times with 10 mL of coupling solution [0.8% (v/v) glacial acetic acid in methanol] and redispersed in 10 mL of the coupling solution for storage at 4°C till further use.

The surface amine density was determined by colorimetric assay using 4-nitrobenzaldehyde (Moon et al., 1996, Bruce and Sen, 2005) and compared with the results from TPPE surface functionalization method (results are presented in Section 4.2).

2.9 Colorimetric Assay of Amine Density

Colorimetric assay was used to determine the density of amine groups on the surface of the amine functionalised silica coated magnetite nanoparticles. This method was performed according to the protocol described first by Moon *et al.* (Moon et al., 1996) for flat surface NH₂ groups and later modified by Bruce and Sen (Bruce and Sen, 2005). In this method 4-Nitrobenzaldehyde was reacted with amine functionalized nanoparticles followed by removal of conjugated 4-Nitrobenzaldehyde by hydrolysis. The amount of 4-Nitrobenzaldehyde in the solution was analysed using UV-Visible spectrophotometry by measuring the absorbance value at $\lambda_{282\text{nm}}$. The assay is illustrated by Scheme 2-7



Scheme 2-7. Schematic representation of the 4-NBA colorimetric surface assay

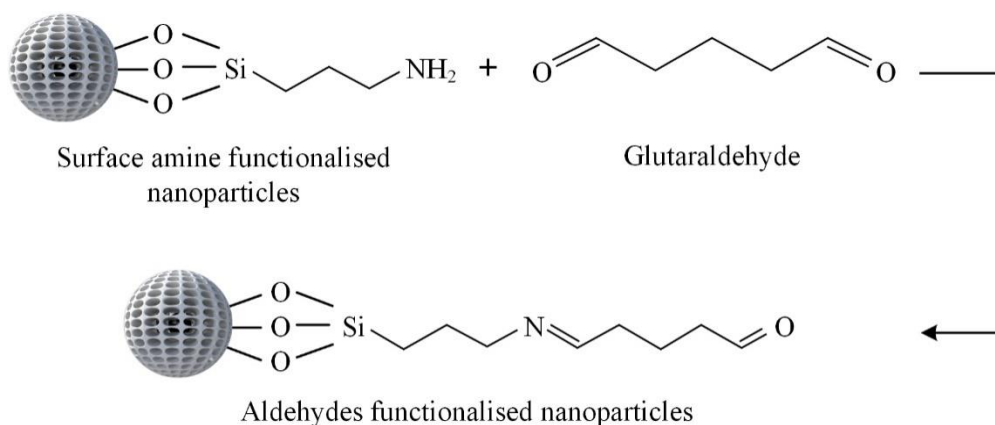
Surface functionalised nanoparticles (5 mg) were placed in a 1.5 mL eppendorf tube and washed four times with coupling solution [0.8% (v/v) glacial acetic acid in methanol] by magnetic separation. Afterward nanoparticles were redispersed in 1 mL of 4-nitrobenzaldehyde in coupling solution (0.7 mg/mL) and placed on end over end rotator in an incubator at 25°C for 3 hours so that 4-nitrobenzaldehyde react with the amine group of surface functionalised nanoparticles. After 3 hours, the supernatant was collected by magnetic separation and absorbance at λ_{282} was

measured by UV-Visible spectroscopy. After removal of the supernatant, nanoparticles were washed again with coupling solution (4×1 mL) and redispersed in 1 mL of hydrolysis solution (75 mL water: 75 mL methanol: 0.2 mL glacial acetic acid). The reaction mixture was then placed in an incubator at 25°C on end over end rotator at 40 rpm for further 1 hour. The supernatant was collected using magnetic separation and absorbance at λ_{282} was measured again. The amount of 4-nitrobenzaldehyde detected in the hydrolysis solution indicates the amount of amine groups present on the surface of the nanoparticles. The surface amine density was calculated using a calibration curve of standard solutions of 4-nitrobenzaldehyde in coupling and hydrolysis solution.

2.10 Converting Surface Amine Groups to Aldehydes

Conversion of surface amine groups to aldehydes was performed using glutaraldehyde reaction as reported earlier (Nimni et al., 1987).

Sodium chloride (NaCl, 175.3 g, 3 mol) and sodium citrate (88.2 g, 0.3 mol) were dissolved in water (1 L) to make SSC buffer (20 \times) with the final pH of 7.4 and subsequently it was diluted to prepare dilute SSC buffer (1 \times). Surface amine functionalized nanoparticles (50 mg of surface functionalized ME33) in coupling solution were washed 3 times with 10 mL of SSC (1 \times) buffer and the supernatant was removed. Glutaraldehyde solution (4 mL, 5% (w/v) in 20 \times SSC buffer) was added to the nanoparticles and the suspension was placed in an incubator at 18°C for 3 hours with end-over-end rotation (40 rpm). After 3 hours, the nanoparticles were collected magnetically and washed 3 times with 5 mL of SSC (1 \times) buffer followed by 3 washes with 5 mL of PBS buffer. Nanoparticles were then redispersed in PBS buffer and kept at 4°C till further use. The procedure of converting surface amine groups to aldehydes using glutaraldehyde is presented in Scheme 2-8.



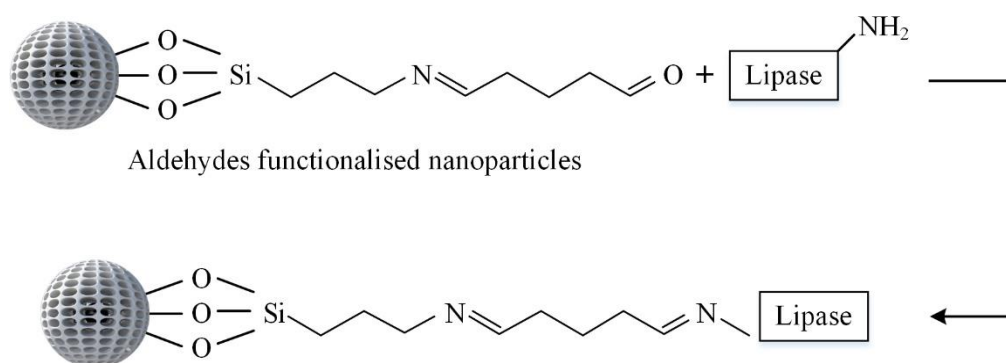
Scheme 2-8 Conversion of surface amine groups to aldehydes using glutaraldehyde

2.11 Enzyme Immobilisation on Silica Coated Magnetite Nanoparticles

Enzyme was immobilised into nanoparticles following two strategies of chemical bonding and physical adsorption.

2.11.1 Covalent Enzyme Immobilisation on Nanoparticles

Silica-coated glutaraldehyde-modified magnetic nanoparticles (glutaraldehyde-modified ME33, 50 mg) were magnetically collected from PBS buffer and added to lipase solution (CRL or PFL, 4 mL, 1 mg/mL, in PBS buffer). The mixture was placed in an incubator at 18°C with constant rotation at 40 rpm for 20 hours. After 20 hours of reaction, the enzyme immobilised nanoparticles were separated using magnetic separation. The supernatant was used for measuring the amount of enzyme loaded into nanoparticles. The enzyme concentration was measured following Bradford assay by measuring absorption at $\lambda_{595\text{nm}}$ by UV spectrophotometry (Bradford, 1976). The enzyme immobilized nanoparticles were redispersed in PBS buffer and kept at 4°C until further use. The procedure for enzyme immobilisation is demonstrated in Scheme 2-9.



Scheme 2-9. Schematic diagram of enzyme immobilisation on surface functionalised core-shell silica-magnetite nanoparticles

2.11.1 Physical Adsorption of Enzyme on Nanoparticles

Mesoporous silica coated nanoparticles (not-functionalised ME33, 50 mg) were used for physical absorption of the lipase. The nanoparticles were washed with PBS buffer and collected magnetically. Lipase solution (CRL or PFL, 4 mL, 1 mg/mL lipase in PBS) were added to the nanoparticles and the mixture was placed on an end to end rotator at 40 rpm and incubated at 18°C for 20 hours. After incubation, the enzyme adsorbed nanoparticles were magnetically separated and the amount of enzyme immobilised was calculated by determining the amount of lipase left in the supernatant using Bradford assay by measuring absorption at $\lambda_{595\text{nm}}$ using UV spectrophotometry. The enzyme immobilized nanoparticles were redispersed in PBS buffer and kept in fridge (at 4°C) until further use.

2.12 Bradford Assay

Bradford Coomassie brilliant blue G-250 assay is a spectroscopic analytical procedure used to quantify the concentration of protein available in a solution. Bradford assay is the most commonly used assay since it enables rapid and simple protein quantification in cell lysates, cellular fractions, or recombinant protein samples (Bradford, 1976, Ernst and Zor, 2010).

The Bradford assay is performed by adding Bradford reagent (1 mL) to the lipase solution (1 mL) and mix completely followed by measuring the absorbance at $\lambda_{595\text{nm}}$. The amount of lipase available in the solution is then calculated using a calibration curve prepared using a range of lipase concentrations.

2.13 Model Catalysis Reaction, Hydrolysis of para-nitrophenyl palmitate (pNPP)

2.13.1 Immobilized Enzyme Activity at 25°C

Immobilized enzyme activity was measured by employing the routine para-nitrophenyl palmitate assay (Gupta et al., 2002, Sen et al., 2010). The basis of this assay is the colorimetric estimation of concentration of 4-nitrophenol released in the reaction mixture as a result of enzymatic hydrolysis of pNPP by measuring the absorbance at $\lambda_{410\text{nm}}$.

Lipase (0.5 mg of CRL or PFL) either free or immobilised (chemically bonded or physically adsorbed into nanoparticles) was added to the pNPP solution (1 mL, 3.74 $\mu\text{mol/mL}$). The pNPP solution was prepared in a 1:1 mixture of isopropanol and reagent A. Reagent A was prepared by adding Gum Arabic (0.0667 g), Tris-HCl buffer (12 mL, 250 mM, pH 7.8) and sodium deoxycholate (0.267 g) and deionised water (48 mL). The hydrolysis reaction was placed on an end over end rotator at 40 rpm in incubator at 25°C for 1 hour. The nanoparticles were then magnetically collected and UV-Visible spectrophotometry at $\lambda_{410\text{nm}}$ was used to measure the concentration of para nitrophenol. In order to test the immobilisation efficiency and reusability of the immobilised enzyme, the enzyme-immobilised nanoparticles were collected after the reaction, washed 3 times with PBS buffer and further used in 3 more identical cycles for hydrolysis of pNPP.

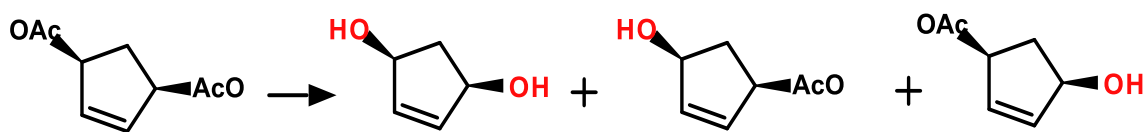
2.13.2 Immobilized Enzyme Activity in Presence of an Alternating Current (AC) Magnetic Field

Hydrolysis of pNPP was performed *for the first time* as per our knowledge under influence of an alternating magnetic field (AC) to evaluate the effect of an AC field on the enzymatic activity of the immobilized enzyme. To perform the hydrolysis reaction under alternating magnetic field, lipase (0.5 mg of CRL) either free or immobilised (covalently immobilised or physically adsorbed into nanoparticles), was added to the ester solution (1 mL, 3.74 $\mu\text{mol/mL}$) in a glass vial. The ester solution was prepared same as described in 2.13.1. The hydrolysis reaction was exposed to an alternating magnetic field applied by a DM2-nb nanoscale biomagnetics AC applicator. The reaction was performed under stirring at 40 rpm using an overhead stirrer. Control reaction was performed simultaneously in an incubator at 32°C. An aliquot of the reaction mixture was withdrawn during the reaction at different time intervals and analysed with UV-Visible spectrophotometry at $\lambda_{410\text{nm}}$ in order to determine the concentration of para nitrophenol in solution. The enzyme-immobilised nanoparticles were then washed 3 times with PBS buffer and further used for 2 more identical cycles of pNPP hydrolysis for reusability evaluation.

2.14 Desymmetrization of cis-3,5-Diacetoxy-1-cyclopentene to (1S,4R)-cis-4-acetoxy-2-cyclopenten-1-ol

Desymmetrization of meso-cyclopent-2-en-1,4-diacetate by enzymatic hydrolysis was performed according to our recently published report (Sharifabad et al., 2014) by adding cyclopent-2-en-1,4-diacetate (50 μmol) to the mixture of hexane: water (1 mL, 4:1) followed by the addition of lipases (0.5 mg of free or equivalent amount of immobilised lipase on nanoparticle support). The reaction mixture was placed on an end to end rotator (40 rpm) and incubated at 25°C for 48 hours. Since the reaction products such as meso-cyclopent-2-en-1,4-diol, (1S,4R)-cis-4-acetoxy-2-cyclopenten-1-ol and its enantiomer (1R,4S)-cis-4-acetoxy-2-cyclopenten-1-ol are soluble in water, during the reaction, a 5 μL aliquot of the reaction mixture (water layer) was withdrawn at different time intervals (1 hour, 4 hours, 24 hours and 48 hours) and analysed using gas chromatography for determination and quantification of each product. The hexane layer was analysed for determination of initial concentration of cis-3,5-diacetoxy-1-cyclopentene. The amount of the products were calculated using pre-constructed calibration curves of standard solutions of meso-cyclopent-2-en-1,4-diol, (1S,4R)-cis-4-acetoxy-2-cyclopenten-1-ol and its enantiomer (1R,4S)-cis-4-acetoxy-2-cyclopenten-1-ol in water and meso-cyclopent-2-en-1,4-diacetate in hexane. After the 48 hours reaction, the enzyme immobilized nanoparticles were washed 3 times with 1 mL PBS buffer and the experiment was repeated under identical conditions to test the stability and reusability of the immobilized enzyme. The reaction scheme is presented in Scheme 2-10.

This reaction was repeated at 37°C to evaluate the effect of the temperature on the immobilised lipase activity in hydrolysis of the meso-cyclopent-2-en-1,4-diacetate.



Scheme 2-10. Hydrolysis of meso-cyclopent-2-en-1,4-diacetate

2.15 Synthesis of Liposome Coated Magnetic Nanoparticles:

Magnetoliposomes

Magnetoliposomes were prepared by using the synthesised ultra-small magnetite nanoparticles (ME18) as core with multilamellar liposomes (MLVs) shell. Liposomes were resized to reduce the size using high energy ultrasonication as published earlier (Sen et al., 2012a).

Liposomes were prepared by dissolving soyabean phosphatidylcholine (SPC, 1321 mg) and cholesterol (680 mg) in chloroform (50 mL) within a 500 mL round bottom flask. The flask containing the phospholipid solution was placed on a rotary evaporator (Buchi Rotavapor R-114, Buchi, Switzerland) and immersed in a 41°C water bath for 2 hour. Upon evaporation of chloroform, a thin film of lipid formed on the inner wall of the flask. The film was hydrated with 200 mL of deionized water and shaken manually for 15 min followed by 2 hours annealing at room temperature. After 2 hours, magnetite nanoparticles (ME18, 1 mL, 22 mg/mL in water) were added to the liposome solution (40 mL) and the mixture underwent strong ultrasonic vibration using a titanium horn (Vibra cell sonicator, Sonics, Sonics & Materials, Inc.) for 12 minutes (3×4 minutes with 1 min rest in between in order to avoid excessive heat generation). The mixture was kept in an ice bath during the sonication in order to avoid excessive heat generation.

Empty magnetoliposomes were used as control samples in order to compare the effect of the drug loading on liposomes size. (Dynamic light scattering (DLS) results are presented in Figure 3-47).

2.16 Drug Loading of Magnetoliposomes

Mitomycin C (MMC) is a powerful water-soluble antibacterial and antitumor antibiotic agent but the dose-limiting toxicity, subacute and cumulative myelosuppression, and nephrotoxicity limit its therapeutic efficacy. The clinical use of MMC is significantly hindered due to the rapid elimination from the body with a low plasma level around the effect-relevant sites *in vivo*, which increase the importance of new strategies for delivery of MMC (Li et al., 2014b).

Loading of the MMC drug into the liposome-coated magnetite nanoparticles was carried out by two different methods.

2.16.1 Drug Loading Using an Incubation Method

Drug loading using incubation method was performed following the method recently reported by our group (Sen et al., 2012a). To load the anticancer drug MMC into the liposome coated magnetic nanoparticles, firstly the density of the magnetoliposomes were determined by drying 3×1 mL of the mixture at 50°C overnight which measured to be 10.8 mg/mL. MMC solution (1 mL, 0.08 mg/mL in water) was added to the magnetoliposome solution (1 mL, 10.8 mg/mL) and kept in an incubator at 10°C for 48 hours. During this time, an aliquot was taken in different time intervals (30 minutes, 1 hour, 3 hours, 24 hours and 48 hours) and the MMC concentration was determined by measuring the UV absorption at $\lambda_{365\text{ nm}}$. Drug loaded nanoparticles were separated from the solution and washed with deionized water prior to use in the drug release study.

2.16.2 Drug Loading Using Ultrasonication

In this method strong ultrasonic vibration was applied to the MMC containing magnetoliposome solution (10 mL of 0.08 mg/mL MMC solution and 10 mL of 10.8 mg/mL of liposome solution) using titanium horn for 8 minutes and the drug loading content was calculated by measuring the MMC concentration left in the solution using UV absorption at $\lambda_{365\text{ nm}}$. The concentration values were calculated using a pre-established standard curve of MMC in water. MMC-loaded nanoparticles were separated from the solution by magnetic separation and washed with deionized water and kept at 4°C until their further use in the drug release study.

2.17 Drug Release from Magnetoliposomes

Drug release study was carried out in PBS at different conditions such as room temperature (23°C), body temperature (37°C) and under the influence of an AC magnetic field.

2.17.1 Drug Release at Body Temperature (37°C) and Room Temperature (23°C)

The MMC release from magnetoliposomes were evaluated in PBS buffer (pH=7.4) at two different temperatures; body temperature (37°C) and room temperature (23°C). To determine the drug release performance of the magnetoliposomes, the drug loaded magnetoliposome solution (1 mL) was kept in an incubator at constant temperature of 37 or 23°C, on an end over end rotator

(40 rpm) for 48 hours. During this period aliquots were taken using magnetic separation at different time intervals and the drug content was calculated by measuring the absorbance at $\lambda_{365 \text{ nm}}$. The drug concentration was calculated by using pre-established standard curve of MMC in PBS buffer.

2.17.2 Drug Release in the Presence of an AC Magnetic Field

Drug release study was carried out under alternative magnetic field to evaluate the feasibility of the MMC loaded magnetoliposomes to be used together with hyperthermia cancer treatment and to test the stimuli triggered drug release performance. To study the drug release performance under alternative magnetic field the drug loaded magnetoliposomes (2 mL in PBS buffer) were placed in an AC field applicator with a frequency of 406 KHz and a 40 rpm overhead rotator for 30 minutes. The drug release profile was determined by measuring UV absorbance at $\lambda_{365 \text{ nm}}$ and comparing the results with the pre-established standard curve of MMC in PBS buffer.

2.18 Drug Loading of the Mesoporous Silica Coated Magnetic Nanoparticles

Drug loading into mesoporous silica core-shell nanoparticles was performed both with MMC and Doxorubicin (DOX).

2.18.1 Mitomycin C (MMC) Loading of the Mesoporous Silica Coated Magnetic Nanoparticles

MMC loading of the magnetic nanocomposites were performed in water. Mesoporous silica coated magnetite nanoparticles (ME16, ME32 and ME33, 4 mg) were placed in 1.5 mL Eppendorf tubes and incubated with aqueous MMC solution (1 mL, 118 $\mu\text{g/mL}$) at 10°C with end over end rotation for 48 hours. The amount of MMC loaded into the nanomaterials were determined at different time intervals by measuring the UV absorption at $\lambda_{365\text{nm}}$. The concentration of MMC encapsulated into the nanoparticles were calculated by comparing the absorption values with a pre-established standard curve of MMC in water.

The experiment was repeated at 18°C to evaluate the effect of temperature on drug loading profile of the materials. MMC-loaded nanoparticles were separated from the solution by magnetic separation and washed with deionised water before the release study.

2.18.2 Doxorubicin (DOX) Loading of the Mesoporous Silica Coated Magnetic Nanoparticles

Doxorubicin (DOX) loading of the magnetic nanocomposites was performed in PBS buffer. DOX solution (10 mL, 0.18 mg/mL) was added to the mesoporous silica coated magnetite nanoparticles

(ME60, 10 mg) and underwent ultrasounication to obtain a homogeneous solution. The mixture was then stirred for further 48 hours and the loading profile was accessed at different time intervals by measuring the UV absorption at $\lambda_{485\text{nm}}$. The samples were magnetically collected, washed with PBS and freeze dried to be used drug release and in cellular study.

2.19 Drug Release from Mesoporous Silica Coated Magnetic Nanoparticles

2.19.1 Drug Release at Body Temperature (37°C)

Release of MMC from silica coated magnetite nanoparticles was studied in PBS buffer (pH 7.4). The drug loaded nanoparticles were washed 3 times after drug loading to remove the unloaded drug from the surface of the nanoparticles. Washed nanoparticles were redispersed in 1 mL of PBS buffer and placed in incubator at 37°C on an end over end rotator for 48 hours. An aliquot was taken at different time intervals and used for measuring the concentration of MMC released into the solution. The concentrations of MMC in the solution were determined by comparing the absorption values with a pre-established standard curve of MMC in PBS buffer.

Same process was performed to study the DOX release from the mesoporous silica coated magnetic nanoparticles at body temperature. DOX release from silica coated nanoparticles were also studied at pH=5.5 (acetate buffer) to evaluate the effect of pH change on drug release profile of the nanoparticles.

2.19.2 Drug Release in presence of an Alternating Magnetic Field

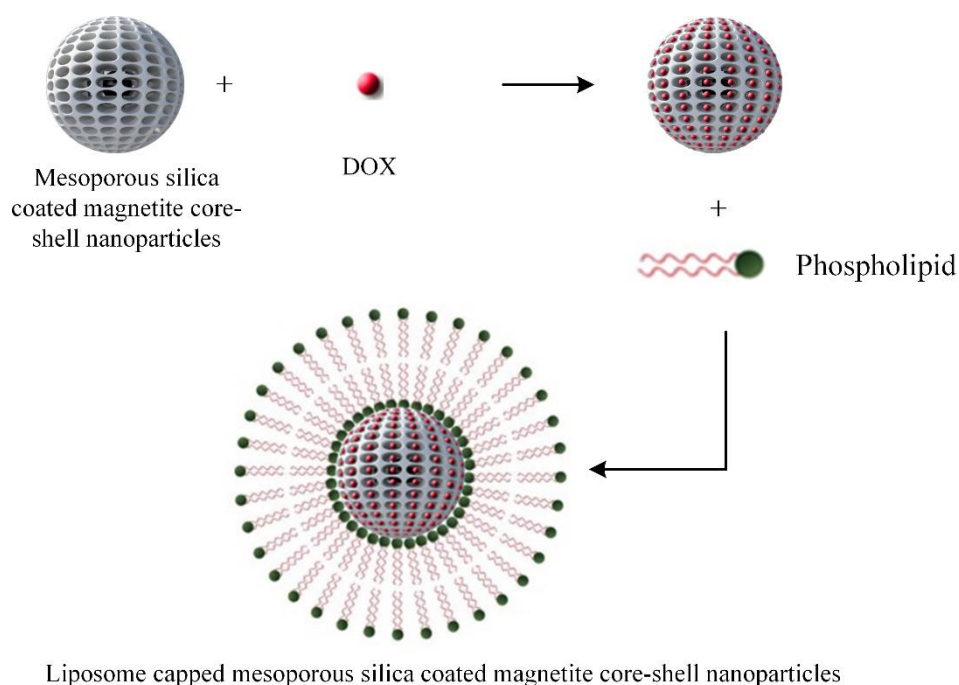
The DOX release was further studied in the presence of an AC magnetic field. DOX loaded magnetic nanoparticles (0.1 mg drug equivalent/1 mL in PBS buffer) were placed in an AC field with the frequency of 406 kHz and 40 rpm overhead rotator. The drug release profile was quantified by measuring UV absorbance at $\lambda_{485\text{nm}}$ and comparing the results with the standard curve of DOX in PBS buffer. As a control experiment, samples were placed in an incubator at 43°C and the drug release was assessed to determine the effects of the increased temperature and AC field exposure on drug release profile.

2.20 Drug Loading of the Liposome Capped Mesoporous Silica Coated Magnetic Nanoparticles

The mesochannels of the mesoporous silica coated nanoparticles were capped with liposomes to reduce the drug leakage into the solution and improve the control over the release profile. DOX

loading and liposome capping of the mesoporous magnetic nanocomposites are illustrated in Scheme 2-11.

Mesoporous silica coated magnetic nanoparticles (ME60, 10 mg) were washed with PBS buffer before drug loading and redispersed in DOX solution (10 mL, 0.18 mg/mL). After 4 hours the liposome solution (2.5 mL, 4 mg/mL, prepared as explained before in 2.15) was added to the drug mixture and underwent ultrasounication (using titanium horn sonicator while the sample was placed in ice bath to protect it from overheating) to obtain a homogeneous solution. The mixture was then placed in an incubator at 18°C, on end over end rotator for further 48 hours. The drug loading profile was evaluated at different time intervals by measuring UV absorption at $\lambda_{485\text{nm}}$. The drug loaded nanoparticles were collected and freeze dried to be used further in drug release and cellular study.



Scheme 2-11. The process of DOX loading of the liposome capped silica magnetite core-shell nanoparticles

2.21 Drug Release from the Liposome Capped Mesoporous Silica Coated Magnetic Nanoparticles

In vitro release profile of DOX from the liposome capped nanoparticles was investigated in PBS buffer (pH 7.4) at two different temperatures of 37°C and 42°C to evaluate and confirm the hyperthermia triggered drug release. DOX release from liposome capped mesoporous silica

coated magnetic nanoparticles were also studied at pH 5.5 (acetate buffer) at 37°C to evaluate the effect of pH change on drug release profile of the nanoparticles.

DOX-loaded freeze-dried nanocomposites were dissolved in PBS buffer (0.1 M, 3 mL, pH 7.4), covered with aluminium foil and placed in an incubator at 37°C on an end over end rotator (40 rpm) for 48 hours. At different time intervals, 0.1 mL of the solution was withdrawn (using magnetic separation) for UV-Visible analysis. The DOX concentration was calculated based on comparing the absorbance at $\lambda_{485\text{nm}}$ to a pre-established standard curve of DOX prepared in the same solution. Same process was repeated in an incubator at 42°C.

To study the release profile under alternative magnetic field, DOX loaded nanoparticles in PBS buffer solution were placed in an AC magnetic field with magnetic field strength of up to 200 G and the frequency of 406 kHz and an overhead rotator (40 rpm). The concentration of the DOX released into the solution was calculated by measuring UV absorbance at $\lambda_{485\text{nm}}$ and comparing the results with the standard curve of DOX in PBS buffer.

2.22 Preparation of Polymeric (PEG-PCL) Micelles

Biodegradable PEG-PCL polymeric micelles (self-assembled from PEG-PCL copolymer) were prepared to achieve hyperthermia stimuli triggered delivery of doxorubicin (DOX). Magnetite nanoparticles were encapsulated inside the micelle core following the method reported by Hong *et al.* (Hong *et al.*, 2008b).

The micellar solution was prepared by adding PEG-PCL copolymer (10 mg) to THF (2.0 mL). The mixture was stirred till the polymer completely dissolved, after which deionized water (10 mL) was added dropwise under stirring. The resulting solution was kept at room temperature overnight to allow the evaporation of THF. The micellar solution was characterized by dynamic light scattering (DLS) to determine the micelle size (the results are presented in Figure 3-49) and ^1H NMR to study the micelles formation (the results are presented in Figure 3-61).

2.22.1 Preparation of PEG-PCL Magnetic Micelles

PEG-PCL copolymer (120 mg) and magnetite nanoparticles (ME55, 30 mg) were added to THF (30 mL) and stirred for 30 minutes, afterward PBS (130 mL) was added to the mixture under sonication. The resulting solution was stirred at room temperature for further 3 hours. Magnetic micelles were magnetically collected and washed with PBS and subsequently filtered through a 0.22 μm membrane to remove the aggregates. The micellar solution was characterized and freeze dried for further use in cytotoxicity studies.

2.23 Conversion of DOX.HCl to Hydrophobic DOX

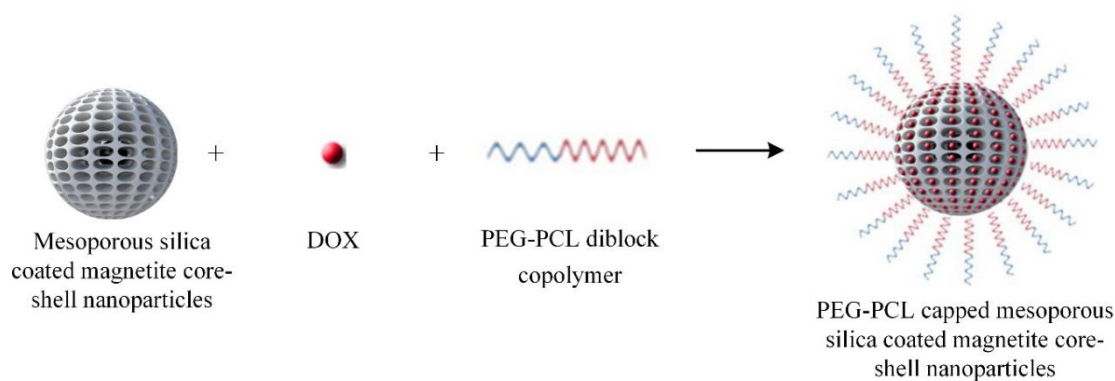
Doxorubicin hydrochloride (DOX.HCl, 25 mg) was deprotonated by dissolving it in a mixture of triethylamine (TEA, 0.05 mL, 0.358 mmol) and Dimethyl sulfoxide (DMSO, 7.5 mL). The mixture was sonicated in a water bath sonicator for 5 minutes and then placed in an incubator at 18°C over night. The container was covered with aluminium foil to protect DOX from light.

2.24 Preparation of Drug Loaded Magnetic Micelles

PEG-PCL copolymer (120 mg) and hydrophobic magnetic nanoparticles (ME55, 30 mg) were added to THF (30 mL). Next the drug containing solution (10 mg of drug) was added to the polymer solution and stirred till completely mixed. To form the micelles, PBS buffer (130 mL) was added to the mixture under ultrasonic agitation. The mixture was stirred for 3 hours in dark to allow the formation of DOX loaded micelles. The drug loaded micelles were collected through magnetic separation and the supernatant was used to determine the remaining drug in the solution in order to calculate the drug loading content. The drug loaded magnetic nanoparticles were washed with PBS solution in order to remove the organic solvent and loosely bounded surface DOX. The drug loaded magnetic nanoparticles were filtered through a 0.22 µm membrane to remove large aggregates. The drug loaded micelles were freeze dried to be used later in drug release and cellular studies. To further confirm the drug loading content 1 mg of the drug loaded nanoparticles were dissolved in DMSO under ultrasonication and the drug content was confirmed using UV-visible at $\lambda_{485\text{nm}}$.

2.25 Preparation of Drug Loaded PEG-PCL Capped Silica Coated Magnetite nanoparticles

To prepare the PEG-PCL capped silica coated magnetite nanoparticles, PEG-PCL copolymer (120 mg) was dissolved in THF (30 mL). Hydrophobic silica coated magnetite nanoparticles (ME93 or ME94, 30 mg) were added to the polymer mixture and sonicated for 5 minutes followed by 15 minutes of stirring. PBS (130 mL) was then added to the mixture and stirred for further 3 hours to form the micelles around the hydrophobic silica core. The materials were labelled as ME93-PEG-PCL and ME94-PEG-PCL. The process of drug loading and capping of the silica coated nanoparticles are presented in Scheme 2-12.



Scheme 2-12. The process of drug loading and capping of the silica magnetite core-shell nanoparticles

To prepare the drug loaded PEG-PCL capped silica coated magnetite nanoparticles, PEG-PCL copolymer (120 mg) was dissolved in THF (30 mL). Subsequently, hydrophobic silica coated magnetite nanoparticles (ME93 or ME94, 30 mg) were added to the polymer mixture and sonicated for 5 minutes. After that the drug containing solution (10 mg of drug, prepared as explained in Section 2.23) was added to the mixture. The mixture was stirred for 15 minutes before adding PBS buffer (130 mL) to form the micelles around the hydrophobic silica core. The mixture was stirred for further 3 hours in dark. The drug loaded magnetic nanocomposites were separated magnetically (the supernatant was collected and UV absorbance was measured to determine the drug loading content) and washed with PBS buffer to remove the organic solvents and unencapsulated DOX from the nanoparticles. The nanoparticles solution was filtered through a 0.45 μm membrane to remove large aggregates. The drug loaded micelles were freeze dried for drug release and cytotoxicity studies.

2.26 Calculations of the Drug Loading Content and Efficiency

Drug loading efficiency (DLE) is defined as the weight percentage of the drug encapsulated into the nanoparticles compared to the initial feeding amount. The drug loading content (DLC) is calculated from the mass of incorporated drug divided by the weight of nanoparticles.

$$DLE = \frac{\text{initial weight of drug} - \text{weight of drug in supernatant solution}}{\text{initial weight of drug}} \times 100\% \quad \text{Equation 2-1}$$

$$DLC = \frac{\text{initial weight of drug} - \text{weight of drug in supernatant solution}}{\text{weight of nanoparticles}} \times 100\% \quad \text{Equation 2-2}$$

After drug loading and before washing the drug-loaded nanoparticles, the solution was placed on magnetic stand and supernatant was removed. The UV absorbance of the supernatant was measured to determine the amount of unencapsulated drug remained in the solution. The values were used to calculate the DLC and DLE.

To further confirm the DLE and DLC of the magnetic micelles, the lyophilized micelles were weighed and dissolved in a mixture of chloroform and DMSO (1mL, 1:1, v/v) by ultra-sonication. After which the solution was kept on a magnet to eliminate the magnetite nanoparticles. An

aliquot of the solution was taken and used for the UV–Vis measurement. DOX concentrations were quantified using a pre-established calibration curve of DOX in same solution.

2.27 *In vitro* Drug Release From PEG-PCL Nanocomposites

In vitro DOX release profiles of PEG-PCL magnetic micelles and PEG-PCL capped nanoparticles were investigated in PBS buffer (pH 7.4) at both body temperature (37°C) and hyperthermia treatment temperature (42°C). The drug release was also investigated in acetate buffer (pH 5.5) to ensure the intracellular drug release due to a pH decrease around cancerous tissue and inside the endosomes/lysosomes of the cells.

To determine the drug release performance of the PEG-PCL capped nanoparticles, DOX-loaded freeze-dried nanoparticles, equivalent of 0.3 mg of free DOX (calculated from drug loading measurements) were dispersed in PBS buffer (0.1 M, 3 mL, pH 7.4) or acetate buffer solution (3 mL, 0.10 M, pH 5.5) and covered with aluminium foil. The reaction mixture was placed in an incubator at 37°C on an end over end rotator stirring at 40 rpm for 48 hours. Using magnetic separation, 0.1 mL of the buffer solution was withdrawn at different time intervals for UV-Vis analysis. DOX concentration was calculated based on comparing the absorbance at $\lambda_{485\text{nm}}$ to a pre-established standard curve of DOX in the same solution.

Drug release profile of the PEG-PCL capped nanoparticles was also evaluated under the influence of an AC magnetic field to study the feasibility of the DOX loaded magnetic nanoparticles to be used together with hyperthermia cancer treatment and to test the stimuli triggered drug release performance. To study the drug release performance under alternative magnetic field the drug loaded nanoparticles (0.1 mg drug equivalent of drug loaded nanoparticles/1 mL in PBS buffer) were placed in an AC magnetic field with maximum magnetic field strength of 200 G and frequency of 406 kHz and stirred at 40 rpm using an overhead stirrer. The concentration of the drug released into the solution was determined by measuring UV absorbance at $\lambda_{485\text{nm}}$ and comparing the results with standard curve of DOX in PBS buffer. Control tests were performed in an incubator at 43°C to study the differences in drug release profiles in incubator and under AC magnetic field.

2.28 *In vitro* Cellular Study

Cell culture is a useful tool in drug development research as it can provide excellent model systems for studying the effect of drugs on physiology and biochemistry of cells. The major advantage of using cell culture for research applications is the consistency and reproducibility of results that can be obtained from using a batch of clonal cells. Two cell lines of MCF7 and U87 were used in this study.

2.28.1 MCF7 Cell Line

MCF7, human breast adenocarcinoma cell line, was used for the cell culture experiments. To grow the MCF7 cells the ATCC (American type culture collection) complete growth medium (Eagle's Minimum Essential Medium (EMEM)+10% (v/v) Fetal Bovine Serum (FBS)) was used with the addition of, Non-Essential Amino Acids Solution (NEAA, 1%), Sodium Pyruvate (1%), Penicillin Streptomycin (Pen Strep, 1%) and L-Glutamine (1%). The seeding density of MCF7 was about 5×10^4 cells/cm² in T-75 flask containing 10 mL of the growth medium as recommended by the ATCC (ATCC, 2015).

2.28.2 U87 Cell Line

U87 is a glioblastoma, astrocytoma cell line derived from human malignant gliomas classified as grade IV as of 2007. To grow the U87 cells the ATCC complete growth medium (Eagle's Minimum Essential Medium (EMEM)+10% (v/v) FBS) were used with the addition of, Non-Essential Amino Acids Solution (NEAA, 1%), Sodium Pyruvate (1%), Penicillin Streptomycin (Pen Strep, 1%) and L-Glutamine (1%). The seeding density of U87 cells was about 4×10^4 cells/cm² in T-75 flask containing 10 mL of the growth medium as recommended by ATCC (ATCC, 2016).

2.28.3 Thawing of Frozen Cells

Thawing of frozen cells were performed according to ATCC protocols. To prepare the cells from frozen state first the appropriate complete growth medium for each cell line was prepared and placed in the 37°C water bath. The cryovials containing the frozen cells were retrieved from liquid nitrogen and placed in a water bath at 37°C with gentle swirling to speed the thawing process. It is important that this step performed rapidly, within 2 minutes. Complete growth medium (9 mL of the pre-warmed medium) was added to a centrifuge tube and the cells were transferred to this medium and resuspended. The cell solution was centrifuged at 1000 rpm for 5 minutes and subsequently, the medium was discarded and the cell pellet was resuspended in 10 mL of growth media. An aliquot was taken for cell count. After cell count the cells were placed in T-25 flasks with appropriated cell density (5×10^4 cell/cm² for MCF7 and 4×10^4 cell/cm² for U-87). Flasks containing the cells were kept in an incubator at 37°C \pm 1°C in 5% CO₂. Cells were monitored and passaged when needed (at 70% to 80% confluent).

2.28.4 Passaging the Cells

Cells were passaged at 70-80% confluence. Trypsin was used as dissociation reagent. To passage the cells, the media was aspirated from the culture flask (Serum was removed from the cells as it inactivates trypsin), and cells were washed with pre-warmed PBS buffer (5 mL for 75 cm² T-flask). After the PBS was removed from the flask, pre-warmed trypsin solution was added to the

flask (2 mL for 75cm² T-flask) and kept in an incubator at 37°C ± 1°C in 5% CO₂ for 3 to 5 minutes till the cells are detached. After that the growth medium was added to the flask (2 mL for 75cm² T-flask) and cells were dispersed by pipetting the medium over the cell layer several time. The cell suspension was then transferred to a 15 mL centrifuge tube and centrifuged for 5 minutes at 1000 rpm. Afterward supernatant was extracted, leaving a small amount of medium above the cell pellet. The cell pellet was redispersed in 3 mL of pre-warmed growth medium and an aliquot was taken for cell count using hemocytometer. The cells were then transferred to new flasks containing growth media (10 mL for 75cm² T-flask) and placed in an incubator at 37°C with 5% CO₂.

2.28.5 Cell Count

Cell counts were performed using a Hemocytometer. To determine number of the cells in the cell suspension for calculating the seeding density a coverslip was placed on hemocytometer and 10 µL of the cell solution was added to the hemocytometer and visualised using a microscope. The average number of cells per large square used to calculate the number of cells per mL of cell solution.

2.28.6 Cell Viability Assessment Using Trypan Blue

Trypan Blue Solution, 0.4%, is frequently used as a cell stain to assess cell viability using the dye exclusion test. Trypan Blue cell viability test is usually performed with the hemocytometer cells counting routine. The dye exclusion test is based upon the concept that viable cells do not take up Trypan Blue, but dead cells are permeable and take up the dye. Cell viability is calculated as:

$$\text{Cell viability} = \frac{\text{Number of viable cells}}{\text{Total number of cells}} \quad \text{Equation 2-3}$$

Viability assessment using Trypan Blue was performed by mixing the cell suspension (100 µL) and Trypan blue (100 µL) in an Eppendorf tube. 10 µL of this suspension was added to one of the hemocytometer chambers and cell count was performed. The dead cells adsorbed the dye and appeared blue.

2.28.7 Growth Curve Preparation

The growth curves of U87 and MCF7 cell lines were established to evaluate the growth characteristics for each cell line. The cell growth curves are commonly used to determinate the best time range for evaluating the effects of the biological compounds on the cells.

After reseeding the cells into the fresh medium, cells require some time to recover from the trypsinization, adjust to the new environment, and to secrete an extracellular matrix that facilitates the linkage between the cells and their proliferation. This is called “Lag phase”, in this period

cellular metabolism is accelerated, but cells are not able to replicate so there is no increase in the cell number. Subsequently, the cells enter into an exponential growth phase, known as “log-phase”. During this phase, the growth medium is consumed at a maximal rate, the culture reaches the maximum growth rate and the number of cells increase exponentially. The time needed for cells to double in number is known as the generation time or population doubling time (PDT). The effects of drugs and biologicals agents that stimulate or inhibit cellular growth is mostly studied in this phase (Rubio-Pino, 2013). Finally as the cell population grows, the nutrients in the growth medium are metabolised and as a result waste materials, toxic metabolites and inhibitory compounds accumulate, which create an unfavourable environment for the cell growth. This leads to a stationary phase. In this phase reproduction rate slows down, until it completely stops and the cell population is constant. Finally exhaustion of the nutrients and the subsequent build-up of metabolic waste products and other toxic materials in the cell media cause cell death. In death phase, cells loses their ability to reproduce and begin to die.

On day 0, standard 96-well plates were seeded with MCF7 cells at a concentration of 2×10^3 cells per well (the surrounding outer wells were filled with growth medium to minimise the variation in cell growth between wells at the edge compared with those in the middle). The plates were placed in an incubator at 37°C under 5% CO₂. After 3 hours the medium was removed from the first plate and replaced with 100 µL of medium and 10 µL of the PrestoBlue reagent. The plate was covered with aluminium foil and incubated for 30 minutes at 37°C under 5% CO₂ in a humidified incubator. Fluorescence was measured from the bottom of the plate with excitation at 535 nm and emission at 612 nm using the Tecan Genius Pro Plate Reader. The process was repeated every 24 hours for 8 days to generate the growth curve.

To obtain the growth curve for U87 cells, the same process was performed with the cell seeding concentration of 4×10^3 cells per well.

2.28.8 Cytotoxicity Assay using Presto Blue

PrestoBlue (PB) is a ready to use cell permeable resazurin-based solution that functions as a cell viability indicator by using the reducing power of living cells to quantitatively measure the proliferation of cells. When added to cells, the PrestoBlue® reagent is modified by the reducing environment of the viable cells and turns red in colour, becoming highly fluorescent. This colour change can be detected using fluorescence or absorbance measurements (life-technologies, 2014, Boncler et al., 2014, Lall et al., 2013).

Cytotoxicity assessments using PrestoBlue reagent were performed according to the manufacturer's protocol. Typically for cells seeded in 96 well plates, PrestoBlue reagent (10 µL) was added to each well containing 100 µL of growth media. The plates were covered with foil and incubated for 30 minutes. The fluorescence was measured using excitation at 535 nm and emission at 612 nm using the Tecan Genius Pro Plate Reader.

2.29 *In vitro* cytotoxicity Study of the Prepared Materials

PrestoBlue (PB) assay was used to determine the influence of synthesised materials on the proliferation of cells, and to indicate the applicable dosage of each material which induce minimal cytotoxicity. To achieve this cells were harvested at the logarithmic growth phase and seeded in 96 well plates with a seeding density of 3×10^3 cells per well (except for surrounding wells which were filled with media). Cells were maintained in complete growth medium (100 μ L of the growth media per well) and incubated for 24 hours at 37 °C in a humidified atmosphere with 5% CO₂. After 24 hours the medium was removed and replaced with 100 μ L of media containing different concentrations of a synthesised material. Subsequently, the cell viability was measured at different periods of up to 72 hours using PrestoBlue assay as explained before.

The materials used against cells in cytotoxicity studies are listed in Table 2-2. The concentration range of different materials (without drug) were chosen based on the related literature and the test concentrations of the drug loaded materials were chosen based on the DLC calculations. Free DOX with the same concentrations were used as control samples.

Table 2-2. List of materials used against cells for cytotoxicity study

Material ID	Material composition
ME53	Uncoated magnetite
ME60	Mesoporous silica coated magnetite
ME111	PEG-PCL micelles
ME55-PEG-PCL	PEG-PCL coated magnetite
ME93-PEG-PCL	PEG-PCL capped Mesoporous silica coated magnetite
ME94-PEG-PCL	PEG-PCL capped Mesoporous silica coated magnetite
ME60-L	Liposome capped Mesoporous silica coated magnetite

2.29.1 IC₅₀ Determination

Half maximal inhibitory concentration (IC₅₀) is a measure of the effectiveness of a substance in inhibiting a specific biological or biochemical function by half. Commonly, it is used to evaluate the efficiency and *in vitro* potency and performance of a drug or substance. IC₅₀ is determined by exposure of the cells to a series of different concentration of a drug (Sebaugh, 2011).

IC₅₀ of DOX-loaded materials were calculated from the viability tests performed using different concentration of DOX-loaded nanoparticles and it was compared with the IC₅₀ obtained for free DOX. The initial dosages used in this study were selected based on the reported IC₅₀ of DOX (approximately 0.1 μ M (Fornari et al., 1994)) in the literature.

2.30 Effect of Magnetic Hyperthermia on Cell Viability

Cells were collected at 70% confluence and seeded into T-25 flasks and incubated with 5 mL of growth media at $37^{\circ}\text{C} \pm 1^{\circ}\text{C}$ in 5% CO_2 for 2 days. After 2 days the medium was removed and replaced with different magnetic nanoparticles with various concentrations. The concentration of magnetic nanoparticles were calculated based on the drug loading content and the cell viability tests in presence of the drug loaded nanoparticles. Cells were incubated with the nanoparticles for further 24 hours. After 24 hours, the media containing nanoparticles was removed and replaced with fresh media. Cells were then exposed to an AC magnetic field for 45 minutes whilst measuring the medium temperature (the field strength was adjusted to maintain the temperature 43°C with). After that, cells were placed back in the incubator at $37^{\circ}\text{C} \pm 1^{\circ}\text{C}$ in 5% CO_2 . The cell viability was measured 2 hours and 24 hours post magnetic hyperthermia treatment using PrestoBlue assay.

Same process was repeated for the drug loaded nanoparticles in the presence of the AC magnetic field to examine the efficiency of the magnetic hyperthermia to increase the cell death.

As the third part of the experiment, cells were treated with nanoparticles for 24 hours (with and without drug) were placed in water bath for 45 minutes at 43°C and then placed back in the incubator at $37^{\circ}\text{C} \pm 1^{\circ}\text{C}$ in 5% CO_2 . The cell viability was measured after 2 and 24 hours in order to compare the cell viability after treatment with water bath hyperthermia and AC magnetic field induce hyperthermia.

2.31 Statistical Analysis

All the results are reported as mean (average) of at least three independent experiments with error bar presenting the standard deviation (SD).

In case of tissue culture experiments, each experiment was repeated at least 3 times and was measured using no less than six wells per experiment.

Statistical analysis were performed by t test where P values less than 0.05 were considered to be statistically significant.

2.32 Characterization Equipment and Techniques

Nanoparticles' characteristics such as size, morphology, surface area, saturation magnetisation, and dispersion stability have significant influence on their performance in different applications. Following techniques were used in this project for characterisation of nanomaterials.

2.32.1 X-Ray diffraction (XRD)

X-ray diffraction is a common technique to study the crystal structures and atomic spacing of the materials. It is based on interference of monochromatic X-rays and a crystalline sample. The X-ray is generated by bombarding a metal target (usually Cu or Mo) with a beam of electrons emitted from a hot filament (usually tungsten). The interaction of the incident rays with the sample produces a diffracted ray which satisfies the Bragg's Law ($n\lambda = 2d \sin \theta$, where n is an integer, λ is the wavelength of the X-ray radiation, and θ is the angle at which the scattered beam was observed). This law relates the wavelength of electromagnetic radiation to the diffraction angle and the lattice spacing in a crystalline sample.

X-ray diffraction (XRD) was used to confirm the identity of magnetite and silica-coated magnetite nanoparticles. The X-ray diffraction patterns were obtained with a Inel Equinox 2000 powder diffractometer equipment using $\text{CuK}\alpha$ radiations (1.5418 \AA). The samples were dried overnight in an oven set at 80°C . The dry samples were ground into a fine powder and packed into X-ray sample holder ensuring smooth surface with no visible cracks.

2.32.2 Transmission Electron Microscopy (TEM)

Transmission Electron Microscopy (TEM) is a common technique to study the morphology and size of nanoparticles. Electron beams are used in TEM to illuminate the specimen and consequently creates an image. TEM consists of an electron gun (usually a tungsten filament) which produces electron beam which are then accelerated by a voltage in the anode, a condenser system (magnetic coils) that focus the beam onto the specimen, objective lenses which focus the electrons passing through the sample to form a magnified image and a fluorescent screen and a digital camera for viewing the image. A higher anode voltage will give the electrons a higher speed.

TEM images of the samples were recorded using a JEOL JEM2000EX (JEOL, Japan) instrument operating at an accelerating voltage of 200 kV. The micrographs were recorded using digital camera and Gatan Digital Micrograph software. 400 mesh carbon coated copper grids (Agar Scientific, UK) were used. TEM samples were prepared by placing approximately $5 \mu\text{L}$ of diluted nanoparticles suspension on the carbon coated copper grid. The grids were left to dry in air at room temperature.

The TEM images were processed using ImageJ software 1.50b and Gatan Digital micrograph 3.01.598 to obtain average particle sizes. Examples of the processed images are shown in Appendix A.

2.32.3 Nitrogen Gas Adsorption-Desorption

Gas adsorption-desorption analysis is commonly used to evaluate the surface area and porosity of the materials. The Brunauer, Emmet and Teller (BET) technique is the most common method for determining the surface area of the powders and porous materials. Nitrogen gas is commonly used as the probe molecule. The material is exposed to the nitrogen at liquid nitrogen conditions (i.e. 77 K). The surface area of the solid is calculated considering the amount of gas used to form the monolayer on the solid surface as well as the dimensions and the number of the molecules (Naderi, 2015). Adsorption isotherm is obtained measuring the amount of gas adsorbed onto the solid sample across a range of relative pressure. The type of the isotherms indicate the pore types in the materials.

To perform the surface area evaluation of the nanoparticles, nanoparticles were dried overnight in an oven at 50°C. Prior to analysis, the nanoparticles were degassed at 100°C for 24 hours. Analysis was performed using a Micromeritics ASAP 2010 Autopore, USA (Accelerated Surface Area and Porosimetry System). The Micromeritics ASAP 2010 software was used to perform automatic BET analysis.

2.32.4 Dynamics Light Scattering (DLS)

Dynamic light scattering (DLS) is typically used for sizing of nanoparticles dispersed or dissolved in a liquid. DLS principle is based on the fact that small particles in a suspension experience random thermal motion known as Brownian motion. The sample is illuminated by a laser beam, the Brownian motion of particles in a suspension causes laser light to be scattered at different intensities. The fluctuations of the scattered light are detected at a known scattering angle θ by a fast photon detector. This random motion is used for particle sizing using the Stokes-Einstein equation.

DLS was performed to estimate the particles size (mostly for polymeric micelles and liposomal formulations) using a Zetasizer Nano, Malvern Instruments, UK at 23°C. Nanoparticles were suspended in water at a dilute concentration, consequently, 1 mL of the nanoparticle suspension were placed in a 12 mm (OD) square polystyrene cuvettes for measurements.

2.32.5 Vibration Sample Magnetometry (VSM)

Vibrating Sample Magnetometer (VSM) is commonly used to measure the magnetic properties of a material as a function of magnetic field. VSM operates based on Faraday's Law of Induction, which states that a changing magnetic field will produce an electric field. In the measurement setup, the sample is fixed to the sample rod which is connected to an oscillator. The oscillator provides a sinusoidal signal that is translated by the transducer assembly into a vertical vibration. The sample rod is placed at the centre of two pole pieces of an electromagnet that generates a

magnetic field and, stationary pickup coils are mounted on the poles of the electromagnet. When a magnetic sample is placed under the magnetic field, the magnetic domains will be aligned with the field which creates a magnetic field around the sample. Since the sample moves vertically in the field, the magnetic field generated by the sample changes as a function of time and can be sensed by the pickup coils. This alternating magnetic field causes an electric field in the pick-up coils which is proportional to the magnetization of the sample.

VSM measurements were performed at room temperature using a 7 kOe vibrating sample magnetometer and data were collected using a home built computer software. The samples were prepared by drying and grinding of nanocomposites into a fine powder. The powder was then packed into plastic tubes with length of 10 mm and internal diameter of approximately 2 mm.

2.32.6 Differential Scanning Calorimetry (DSC)

Differential scanning calorimetry (DSC) is a thermoanalytical technique which monitors the heat effects related with phase transitions of a sample as a function of temperature. The main application of DSC is in studying melting point, crystallisation and glass transitions. A DSC measuring cell consists of a furnace and an integrated sensor with designated positions for the sample and reference pans and the sensors are connected to thermocouples. The basic principle underlying this technique is that, when the sample undergoes a physical transformation such as phase transitions, the heat flow to the sample is affected and is higher or lower than the reference sample depending on whether the process is exothermic or endothermic.

The melting temperature of the polymer was measured using DSC Nano, TA instruments under a flow of nitrogen at a scanning rate of 5°C/min. The thermograms covered from -20 to 60°C. Samples were prepared by placing the solid sample in a hermetic aluminium DSC pan and sealing the lids using an encapsulating press, an empty pan was sealed and used as reference sample.

2.32.7 Scanning Column Magnetometry (SCM)

Scanning column magnetometer (SCM) is used to measure concentration profiles of columns of magnetic dispersions and stability of the magnetic suspensions. The SCM plots the changes in the frequency (Δf) as a function of distance from the bottom of the column. The principle underlying this technique is that changes in the inductance of a coil in an LC oscillatory circuit result in corresponding changes in the frequency. On that basis a column containing magnetic dispersion is driven through the core of the detection coil, which is a part of a Colpitts oscillatory circuit. The inductance of the coil is directly related to the concentration of the magnetic suspension, as a result variation in the suspension concentration is translated to a change in induction and consequently a change in the oscillator frequency.

SCM measurements were performed using a built in-house SCM with a sample-free frequency of 1MHz. The LabVIEW software is used for operating the system. The samples for the SCM were

prepared by sonication of the magnetic suspension using titanium horn sonicator for 4 minutes followed by placing up to 10 mL of the suspension into the SCM column.

2.32.8 Contact Angle Measurements

Contact angle measurement is performed to determine the hydrophilicity of a sample. Contact angle is conventionally measured through the liquid, where a liquid–vapor interface encounters a solid surface. The wettability of a solid surface is quantified by the Young equation (Yuan and Lee, 2013).

Contact angle measurements were performed by using a FTA contact angle/surface tension at room temperature. Samples were packed to small tablets with smooth surface with no visible cracks. A drop of Milli-Q water was placed on the sample surface and the evolution of the droplet shape was recorded with a video camera. An image analysis software (drop Shape Analysis v2) was used to determine the contact angle.

2.32.9 Gas Chromatography (GC)

Gas chromatography (GC) is an analytical technique that measures the content of various components in a sample. A GC consist of a mobile phase (Helium or nitrogen is commonly used as the carrier gas.) and a stationary phase. When a sample is injected into the GC, it instantaneously vaporized at the column inlet. Mobile phase then carry the vaporized sample through the column. Passing through the column, each component in the sample is adsorbed or partitioned to the stationary phase according to its characteristic. Identification of the compounds is based on the strengths of this interactions between the compounds and the stationary phase. Stronger interaction translate to longer time required for the compound to migrate through the column which in turn result in longer retention time. A detector at the end of the column measures the quantity of the components as they exit the column.

Gas chromatography (GC) was used to identify and quantify the products of the catalytic hydrolysis of cis-3,5-diacetoxy-1-cyclopentene. Analysis was performed by injecting a 1 μ L aliquot of the reaction mixture into a Varian Inc CP-3380 Gas Chromatograph with nitrogen as the carrier gas. Chromatograms were interpreted using Varian Star Integrator software version 4.51. Temperature program was set to start at 50°C and increase to 200°C at a 10°C per minute rate. A Supelco β -DEX 110 fused silica capillary column specifically designed to separate chiral compounds with the length of 30 m, internal diameter of 0.25 mm and film thickness of 0.25 μ m was used (Sigma-Aldrich, 2016).

2.32.10 Fourier Transform Infrared Spectroscopy (FT-IR)

Fourier transform infrared spectroscopy (FT-IR) is commonly used to identify the presence of certain functional groups in a molecule by monitoring the bond vibration. FT-IR operates based

on the principle that when an IR radiation is passed through a sample, some of the infrared radiation is absorbed by the sample. The probability of a particular IR frequency being absorbed depends on the actual interaction between this frequency and the molecule. In general, a frequency will be strongly absorbed if its photon energy coincides with the vibrational energy levels of the molecule. This absorption corresponds specifically to the bonds present in the molecule. The frequency range are measured as wave numbers typically over the range 4000 to 350 cm^{-1} . The resulting spectrum represents the molecular absorption and transmission, creating a molecular fingerprint of the sample.

Infrared spectra of the samples were recorded over the frequency range of 350 to 4000 cm^{-1} using a JASCO FT/IR 410 Fourier transform infrared spectrophotometer, where the dry samples were directly cast over the FT-IR diamond crystal for analysis. To analyse the liquid samples, 10 μL of sample was cast over a low-e slides and left to dry overnight in room temperature after which it was placed directly against the FT-IR diamond crystal and analysed.

2.32.11 Small Angle X-Ray Scattering (SAXS)

Small Angle X-ray Scattering (SAXS) measurements were performed using S3-Micro, HECUS X-RAY SYSTEMS, GMBH GRAZ instrument with Geni Xenocs software in order to investigate structure of the particles. The powdered samples were packed in a 1.5 mm diameter quartz capillaries. Scattering curves were monitored in a q -range from 0.01 to 0.5 \AA^{-1} .

2.32.12 Magnetic Heating Experimental Method and Procedure

Magnetic heating, specific power absorption (SPA) and Intrinsic loss power (ILP) of the nanoparticles were evaluated using a commercial AC field applicator, DM2, with a system controller DM100 by nB nanoscale Biomagnetics, Spain. All the experiments were performed at frequency of 406 kHz and the temperature was monitored using a fibre optic temperature sensor and controlled by adjusting the magnetic field strength. The maximum field strength was 15.8 kA/m. System embedded software, MaNiAC, was used to control the experiments and collect the data. Experiments were performed by placing 1 ml of a magnetic suspension in a glass vial in the centre of the DM2 applicator coil. Experiments using cells were performed by placing the T-25 flask directly in the DM2 field applicator.

2.32.13 Nuclear Magnetic Resonance (NMR) Spectroscopy

Nuclear Magnetic Resonance (NMR) spectroscopy is based on the nuclear magnetic resonance phenomenon. The NMR is a characteristic of the nucleus of an atom, related to the nuclear spin (I), the intramolecular magnetic field around an atom in a molecule changes the resonance frequency, consequently providing information about the molecular structure. The NMR

spectroscopy can determine an entire structure of an organic compound using one set of analytical tests (RSC, 2016).

¹H-NMR spectra were obtained using a Bruker fourier 300 (300MHz) spectrometer with CDCl₃ and D₂O as solvents at 25°C. The 5 mm outer diameter NMR tubes were used with and polyethylene cap.

2.32.14 Energy Dispersive X-Ray Spectroscopy (EDS)

Energy dispersive X-ray spectroscopy (EDS or EDX) is an analytical technique used to study the elemental composition of a sample. EDS is commonly combined with imaging tools such as scanning electron microscopy (SEM) or TEM. The EDS is based on interactions of the X-ray and a sample, where the impact of the electron beam on the sample produces x-rays. When the electron beam reaches the sample, electrons are ejected from the atoms leaving vacancies, these vacancies are subsequently filled by electrons from a higher state, resulting in an x-ray emission to balance the energy difference between the two electrons' states. Each element emits a unique set of peaks on its X-ray emission spectrum during bombardment by an electron beam. EDS can be used to determine the elemental composition of individual points or to map the distribution of elements in a sample (EAG, 2016).

The EDS analysis was performed to investigate the existence and distribution of elements in nanocomposites. Measurements were carried out by moving the electron beam to different positions and examine different particles. An Oxford Instruments INCA X-Sight EDS combined with TEM, operating on Microanalysis Suite, INCA version 4.15 were used for elemental analysis of the samples. The samples were prepared using 400 mesh carbon coated copper grids.

CHAPTER 3

CHARACTERIZATION OF THE SYNTHESISED NANOPARTICLES

3.1 Introduction

Different characterization techniques such as TEM, VSM, BET and SCM were used in order to evaluate the synthesised nanomaterials. Characterization techniques employed for each material were chosen according to the methods suggested in literature.

Sample preparation for each measurement and the equipment specifications are explained in Section 2.32. A list of the characterization methods used for the synthesised materials are summarized in Table 3-1.

Materials were chosen for further use in drug delivery or catalysis applications based on the characterization results described in this chapter.

3.2 Transmission Electron Microscopy (TEM)

Transmission electron microscopy (TEM) was used to study the size and morphology of the nanoparticles. The sample and TEM grid preparations were performed according to methods explained in Section 2.32.2. The statistical analysis of the images were performed using the GATAN DigitalMicrograph software version 3.01.598.0 and ImageJ software 1.50b as described in 2.32.2.

3.2.1 Magnetite Nanoparticles

Magnetite nanoparticles were prepared by the methods explained in Section 2.3 and evaluated using TEM as the initial step to assess the shape and size of the nanoparticles.

Figure 3-1 shows the TEM images of magnetite nanoparticles prepared by oxidative hydrolysis of iron sulphate (ME01). From the TEM images it is observed that the nanoparticles exhibited rhombic and spherical morphologies. The statistical analysis of the nanoparticles indicated that nanoparticles were in the size range from 8 to 45 nm with an average size of 25 nm. The particles were similar to those reported by Sen *et al.* (Sen et al., 2006). Since these nanoparticles were observed to be within a large size distribution range and of different shapes they were not used in further applications. However, their magnetic curves were evaluated for comparison to other particles.

Table 3-1. Summary of the characterization methods used for different materials

Material ID	Material description	TEM	BET	XRD	VSM	NMR	SCM	DCS	DLS	EDAX	SAXS	FT-IR	Contact angle
ME01	Magnetite nanoparticles	✓			✓								
ME16	Mesoporous silica coated magnetite nanoparticles	✓	✓		✓								
ME18	Ultra-small magnetite nanoparticles	✓		✓	✓		✓					✓	
ME32	Mesoporous silica coated magnetite nanoparticles	✓	✓		✓						✓		
ME33	Mesoporous silica coated magnetite nanoparticles	✓	✓	✓	✓		✓			✓	✓		
ME55	Ultra-small hydrophobic magnetite nanoparticles	✓			✓		✓					✓	
ME56	silica coated magnetite nanoparticles	✓	✓		✓								
ME59	Ultra-small hydrophobic magnetite nanoparticles	✓			✓								

Table 3-1. Continued

Material ID	Material description	TEM	BET	XRD	VSM	NMR	SCM	DCS	DLS	EDAX	SAXS	FT-IR	Contact angle
ME60	Mesoporous silica coated magnetite nanoparticles	✓	✓		✓		✓					✓	✓
ME55-PEG-PCL	Polymer coated hydrophobic magnetite (Magnetic micelles)	✓					✓		✓			✓	
ME82	Mesoporous silica coated magnetite nanoparticles	✓	✓										
ME93	Mesoporous silica coated magnetite nanoparticles	✓	✓										✓
ME94	Mesoporous silica coated magnetite nanoparticles	✓	✓										✓
PEG-PCL	Poly ethyleneglycol-b-polycaprolactone					✓		✓	✓			✓	
ME09	Magnetoliposomes						✓		✓				
ME60-L	Liposome coated mesoporous silica coated magnetite nanoparticles						✓		✓			✓	

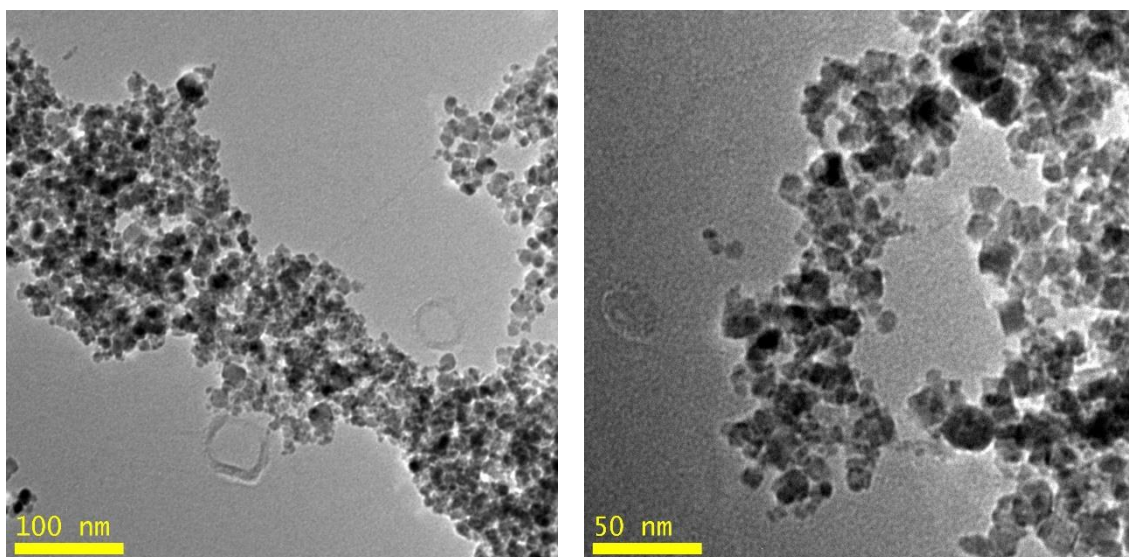


Figure 3-1. TEM image of ME01, magnetite nanoparticles prepared by oxidative hydrolysis of Iron Sulphate in alkaline media

The magnetite nanoparticles prepared by coprecipitation of ferrous and ferric chloride solutions in alkaline media (ME18) are shown in Figure 3-2.

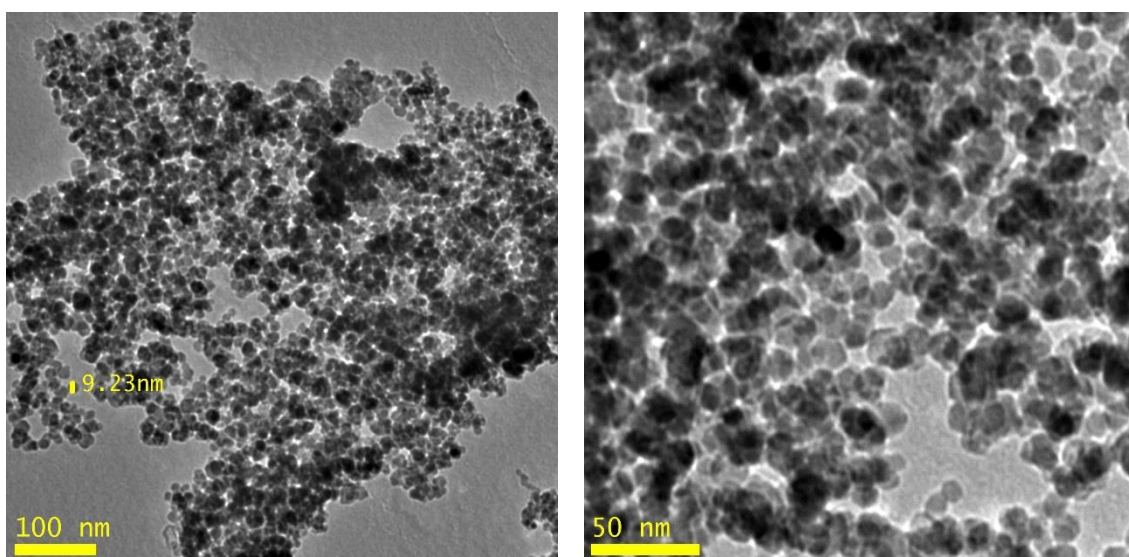


Figure 3-2. TEM image of ME18, magnetite nanoparticles prepared by coprecipitation of iron salts

The nanoparticles (ME18) were found to be spherical in the size range of 8 to 15 nm and average diameter of 13 nm. The size and shape are in close agreement with the reported literature (Sen et al., 2006, Massart, 1981). These nanoparticles were further characterized by VSM and XRD and used in drug delivery and catalysis applications with silica or liposome coatings.

Figure 3-3 shows the magnetite nanoparticles prepared by the coprecipitation method and functionalised with oleic acid (ME55) as explained in Section 2.3.1

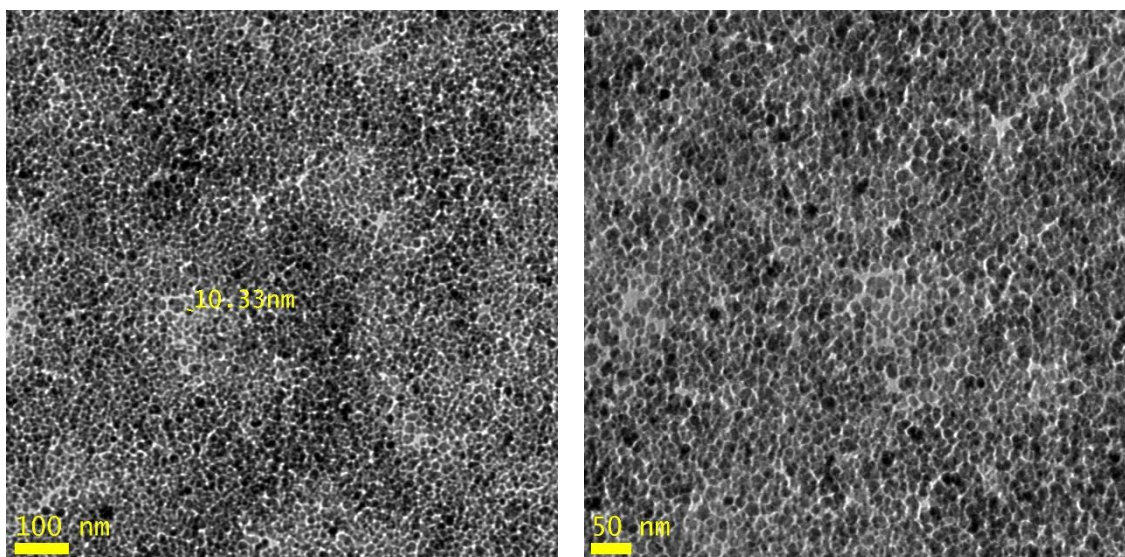


Figure 3-3. TEM of ME55, prepared by oleic acid functionalising the magnetite nanoparticles prepared by coprecipitation of iron salts

It was observed that the nanoparticles were monodispersed with similar size and shape as the as-prepared magnetite nanoparticles (ME18, before surface functionalising the particles). However, the nanoparticles were highly hydrophobic. These nanoparticles were further tested in an AC magnetic field to measure the AC field induced heating. These nanoparticles were coated with polymer and silica and used in drug delivery applications, the performance of these drug delivery systems are evaluated in Chapter 5.

Figure 3-4 shows the magnetite nanoparticles prepared through high temperature $\text{Fe}(\text{acac})_3$ reaction followed by the method first reported by Sun and Zeng (Sun and Zeng, 2002) and explained in Section 2.3.3.

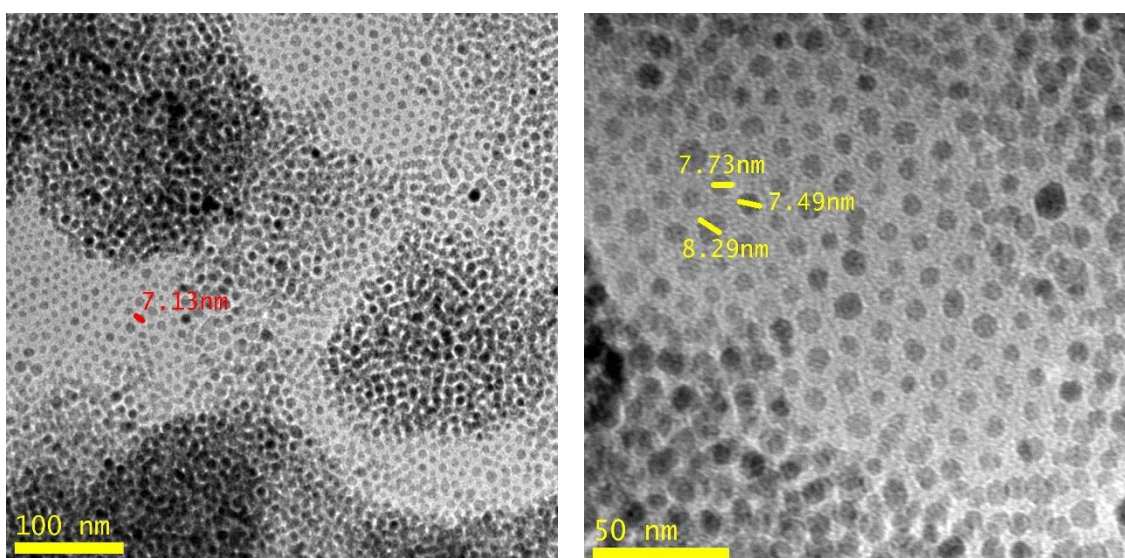


Figure 3-4. TEM image of ME59, oleic acid coated magnetite nanoparticles prepared by thermal decomposition of $\text{Fe}(\text{acac})_3$

The nanoparticles were spherical and monodisperse with size range of 7 to 9 nm. This is in good agreement with the literature (Sun and Zeng, 2002, Sun et al., 2003, Sun et al., 2007).

3.2.2 Silica Coated Nanoparticles

Figure 3-5 shows TEM image of mesoporous silica coated magnetite nanoparticles (ME16) prepared as described in Section 2.4. The particles were prepared by coating the hydrophilic ultra-small magnetite nanoparticles (ME18). The silica coating was performed following the method described in Section 2.4 Method A, which produced mesoporous silica coatings. As observed from the TEM images, materials exhibited core-shell structure with a single magnetite core particle and they were uniformly coated with a thin mesoporous shell. The composite nanoparticles have an average size of 30 nm with ~5 nm of silica coating. These nanoparticles were further tested with VSM and BET to evaluate the magnetic response and surface area properties.

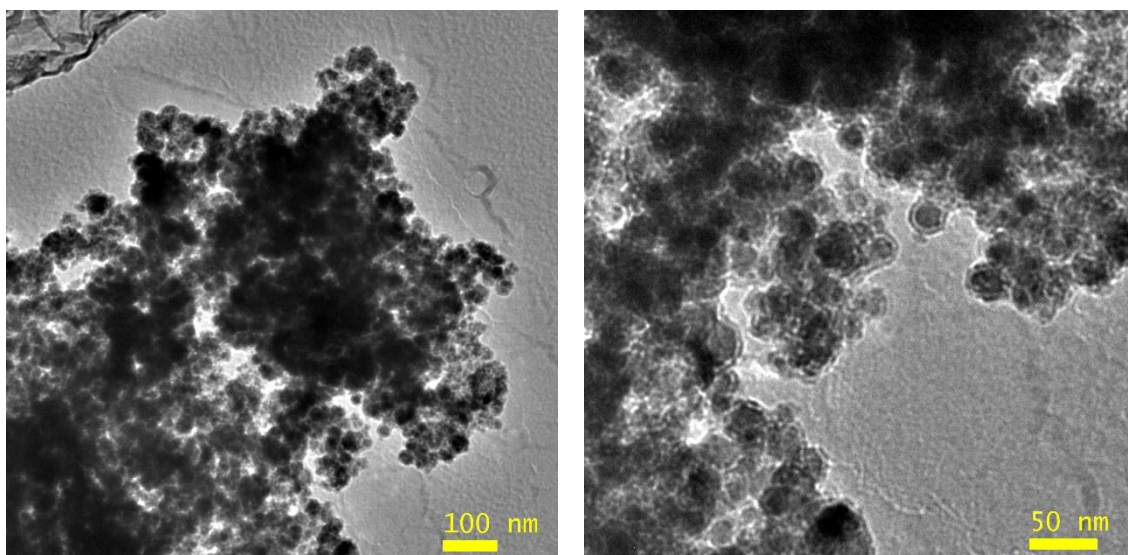


Figure 3-5. TEM image of ME16, Core shell nanoparticles

The mesoporous silica nanoparticles prepared following the second method described in Section 2.4 (Method B) are shown in Figure 3-6, Figure 3-7 and Figure 3-8. All the nanoparticles prepared by this method (ME32, ME33 and ME60) showed multi core nanoparticles with mesoporous structure which could be observed in the TEM images. The nanoparticles showed aggregation.

As seen in Figure 3-6, ME32 particles possess mesoporous structure with an average size of 40 nm, however the nanoparticles were not homogenous i.e. it was a mixture of core shell structure and pure silica nanoparticles.

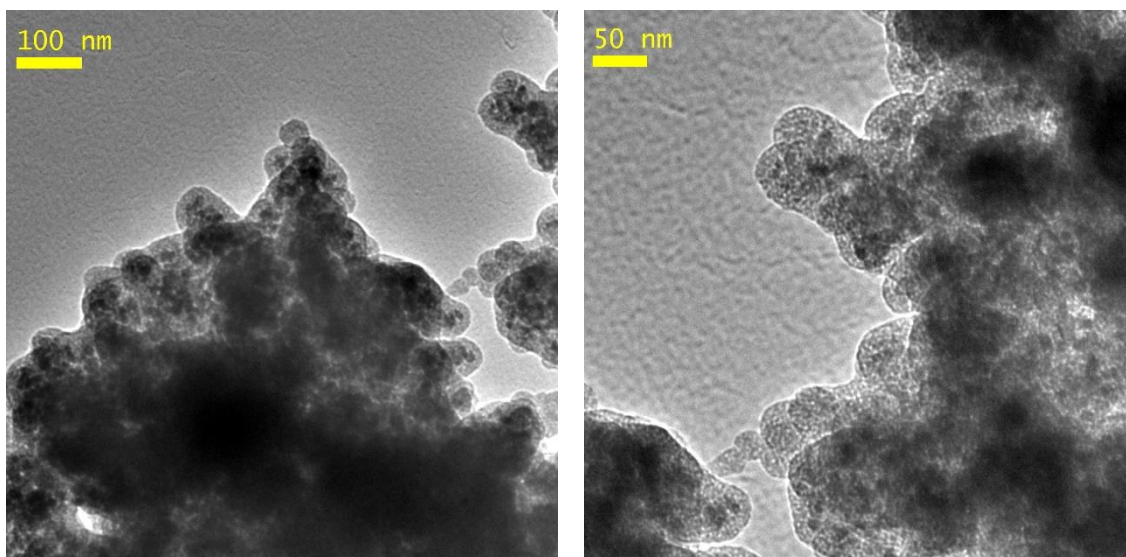


Figure 3-6. TEM image of ME32, Core shell nanoparticles

Figure 3-7 and Figure 3-8 show the mesoporous silica structure prepared by the second method (Method B) described in Section 2.4. As shown in the figures multi core mesoporous silica coated nanoparticles of different sizes could be prepared by this method. ME33 contained nanoparticles with average diameter of about 150 nm. These nanoparticles were used in catalysis. The nanoparticles prepared by the optimized method to obtain smaller size nanoparticles (ME60) are shown in Figure 3-8. These nanoparticles have an average size of 80 nm.

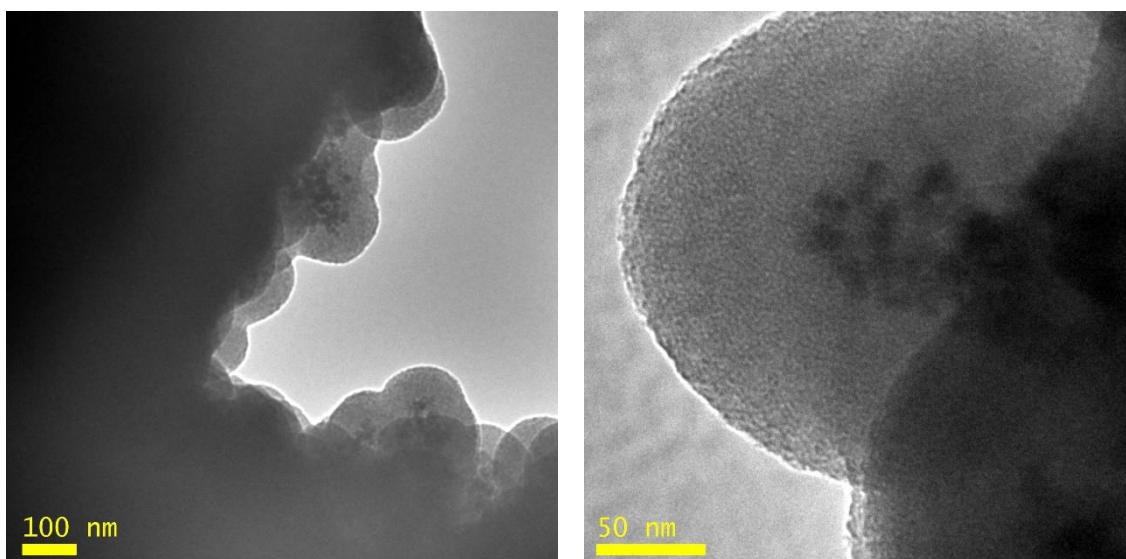


Figure 3-7. TEM image of ME33, mesoporous Core shell nanoparticles

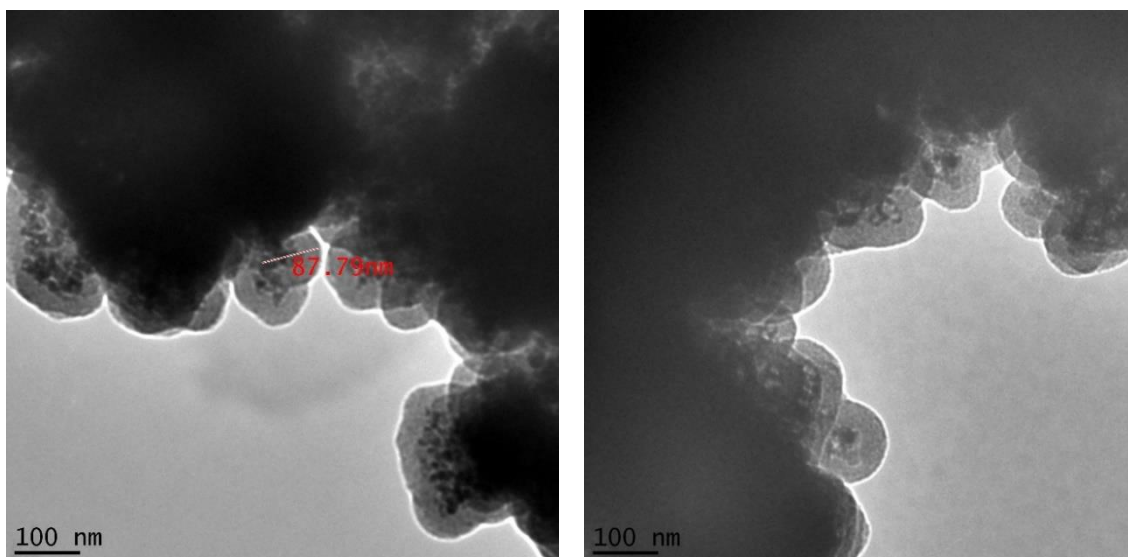


Figure 3-8. TEM image of ME60, mesoporous core-shell nanoparticles

The core shell nanoparticles (ME82) made by Method C in Section 2.4 is shown in Figure 3-9. The materials made by this method observed to be in the size range of 20 to 30 nm with mostly single magnetite core structure. The core magnetite nanoparticles used for the synthesis of these nanoparticles were oleic acid functionalised hydrophobic particles (ME55).

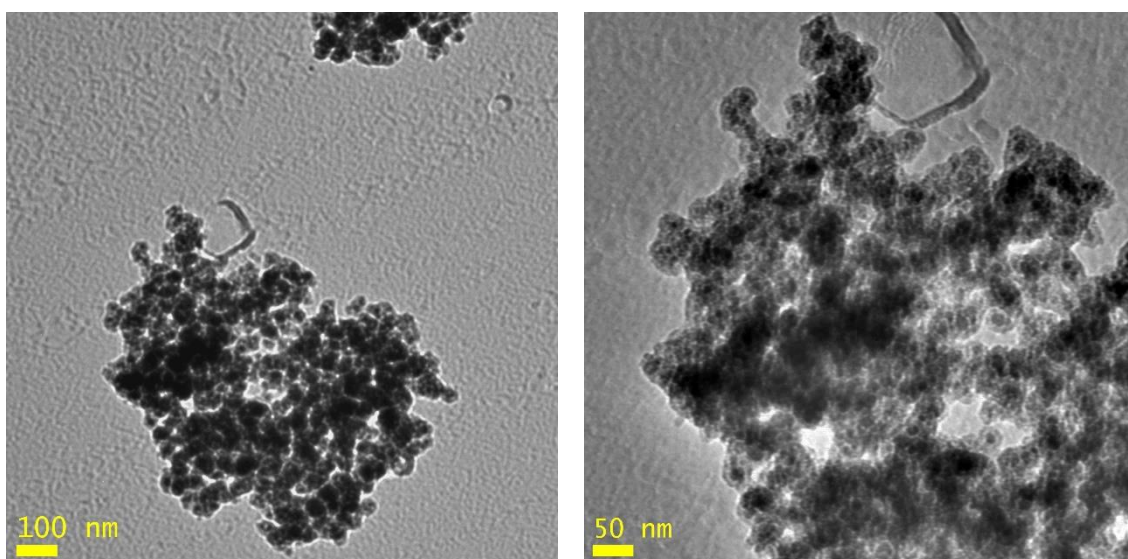


Figure 3-9. Tem image of ME82, mesoporous core-shell nanoparticles

Figure 3-10 shows the silica coated magnetite nanoparticles prepared by a water in oil reverse micelle method (ME56), following the protocol reported by Lu *et al.* (Lu et al., 2006) as described in Section 2.5. The hydrophobic nanoparticles ME55 and ME59 were used to prepare these nanoparticles. The materials made using ME55 demonstrated higher magnetic heating and therefore were used to prepare ME94 with further application as drug delivery systems. As observed from the images the nanoparticles exhibited monodisperse core-shell structure with an average size of 67 nm.

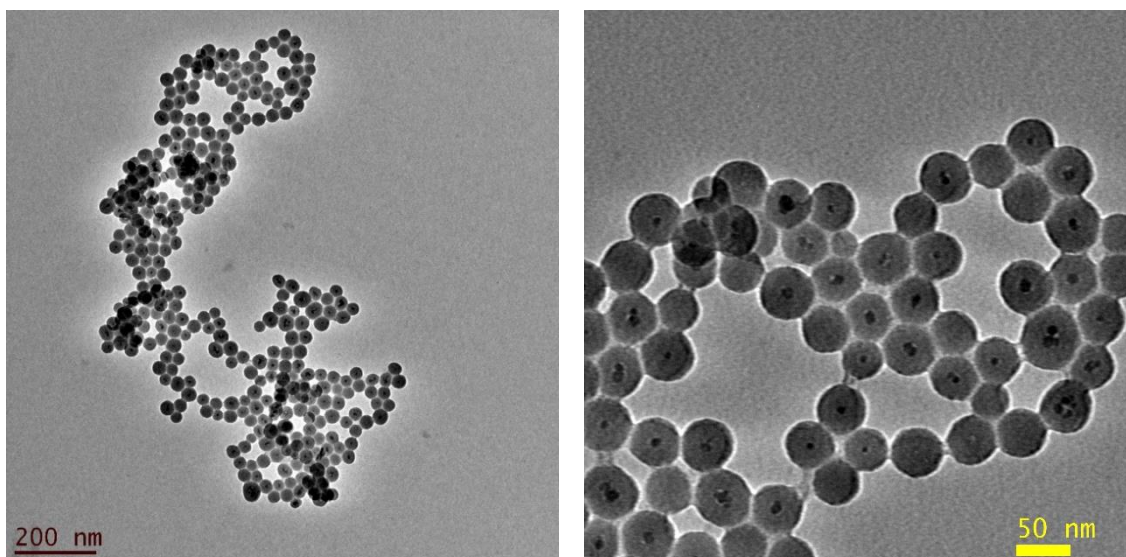


Figure 3-10. TEM image of ME56, Core shell particles

Hydrophobic silica core shell nanoparticles were prepared by three different methods as described in Section 2.6. Figure 3-11 shows the hydrophobic silica coated magnetite nanoparticles (ME93) prepared by direct coating of magnetite nanoparticles (see Section 2.6.3). Hydrophilic magnetite nanoparticles (ME18) were used as the core magnetite nanoparticles. As seen in the images, the nanoparticles exhibited spherical morphology with core-shell structure. The material possess mesoporous structure containing multiple magnetite nanoparticle cores. The nanoparticles were measured to be in the size range of 80 to 120 nm.

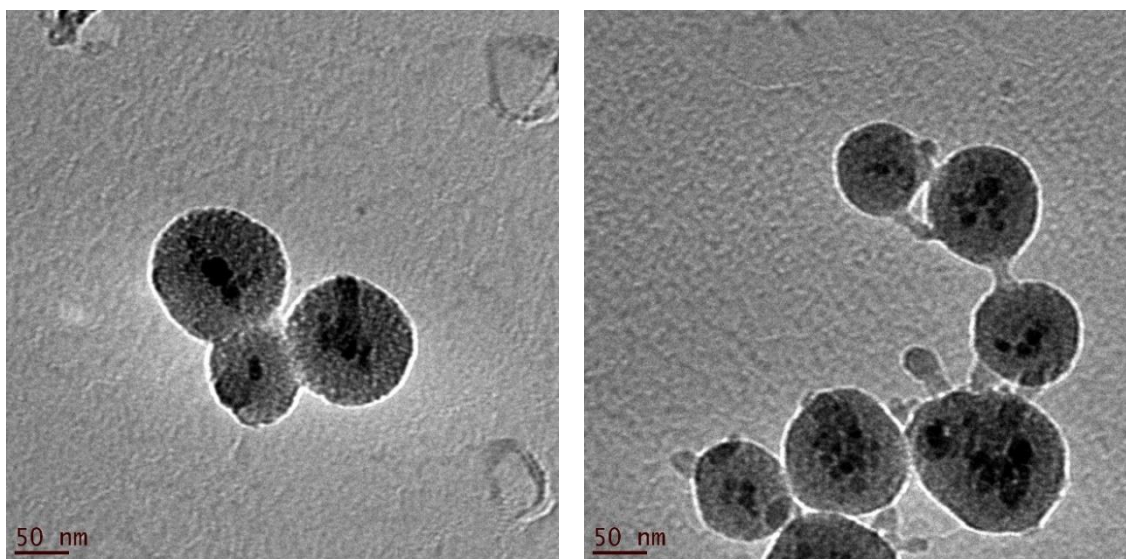


Figure 3-11. TEM image of ME93, silica coated magnetite nanoparticles prepared by direct coating of magnetite nanoparticles

Figure 3-12 shows the hydrophobic silica-magnetite core-shell nanoparticles developed by direct etching of the silica layer of ME56 followed by the OTS silica coating of the nanoparticles (ME80). Core-shell silica coated magnetite nanoparticles ME56 were used as starting materials. As seen in the images, the nanoparticles exhibited porous structure however; the pore structure is random in size and shape. The nanoparticles were in the size range of 70 to 80 nm.

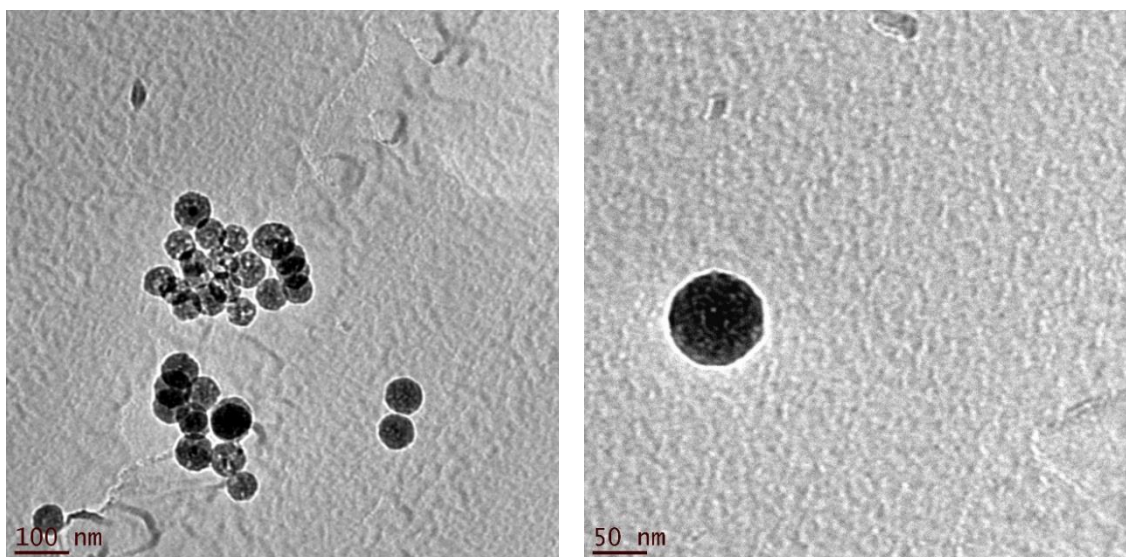


Figure 3-12. TEM image of ME80, hydrophobic silica coated nanoparticles

Figure 3-13 shows the hydrophobic silica coated magnetic nanoparticles (ME94). These nanoparticles were prepared by PVP protected etching of the silica coated nanoparticles (ME56) followed by an additional silica coating of the surface with OTS silica source to obtain hydrophobic nanoparticles. Figure 3-14 shows the nanoparticles after protected etching and before the final silica coating. As seen in the images the protected etching resulted in hollowed shaped nanoparticles with the magnetite core inside. The final nanoparticles are monodisperse with average size of 100 nm. The etching time was optimized to be 15 minutes since it was observed that the longer etching time breaks the silica layer and shorter etching times result in incomplete etching and dense silica layer. The silica nanoparticles underwent protected etching for 20 and 10 minutes are illustrated Figure 3-15, (a) and (b).

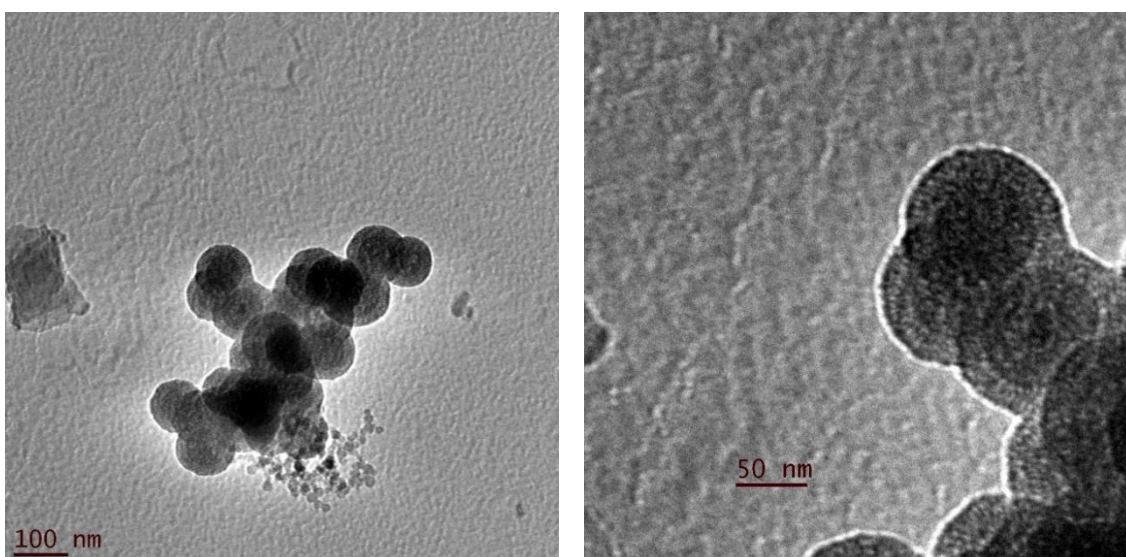


Figure 3-13. TEM image of ME94, Hydrophobic Silica coated core shell particles prepared by protected etching method.

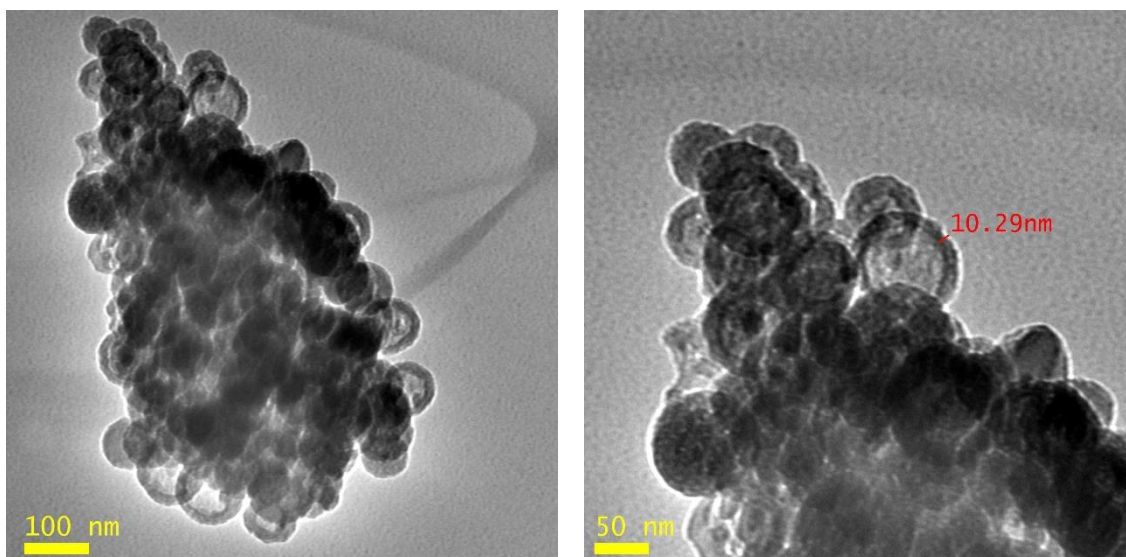


Figure 3-14. TEM image of ME94-I, PVP protected etched silica nanoparticles

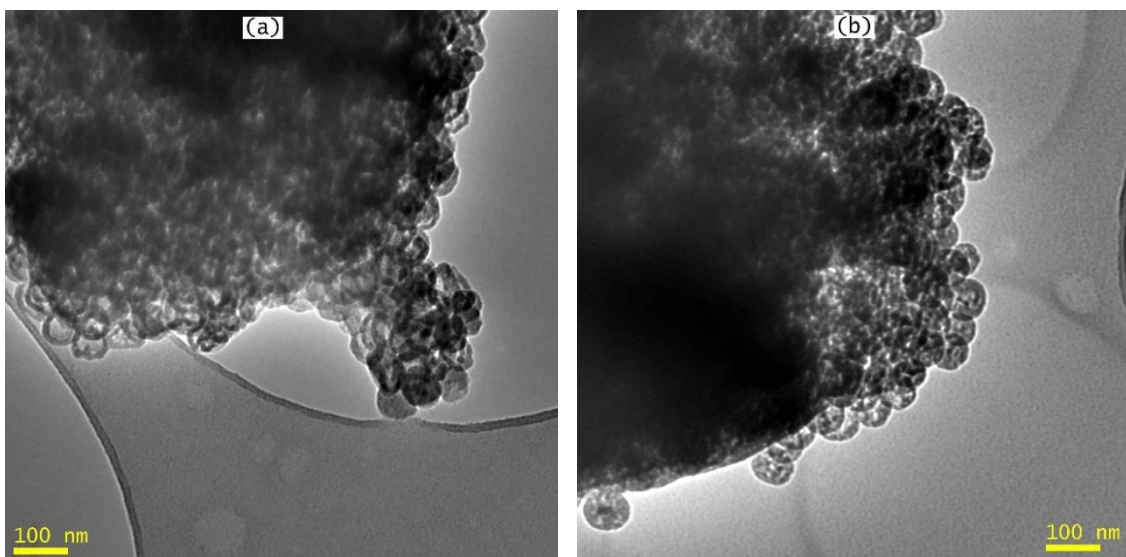


Figure 3-15 TEM images of PVP protected etched silica nanoparticles, (a) after 20 minutes etching, and (b) after 10 minutes etching

3.2.3 Polymer Coated Nanoparticles

Figure 3-16 presents the PEG-PCL coated magnetic nanoparticles (ME55-PEG-PCL). The magnetic micelles are seen as separate groups of magnetite which clearly differs from uncoated magnetite particles shown in Figure 3-3. The overall size of the magnetic micelles measured from the TEM images were in the range of 100 to 130 nm which is in agreement with DLS size measurements. The micelles shown similar morphology to those reported by Nasongkla *et al.*, they have suggested that since the polymer does not significantly attenuate the electron beams of TEM the magnetic micelles can be seen as isolated magnetite clusters (Nasongkla *et al.*, 2006).

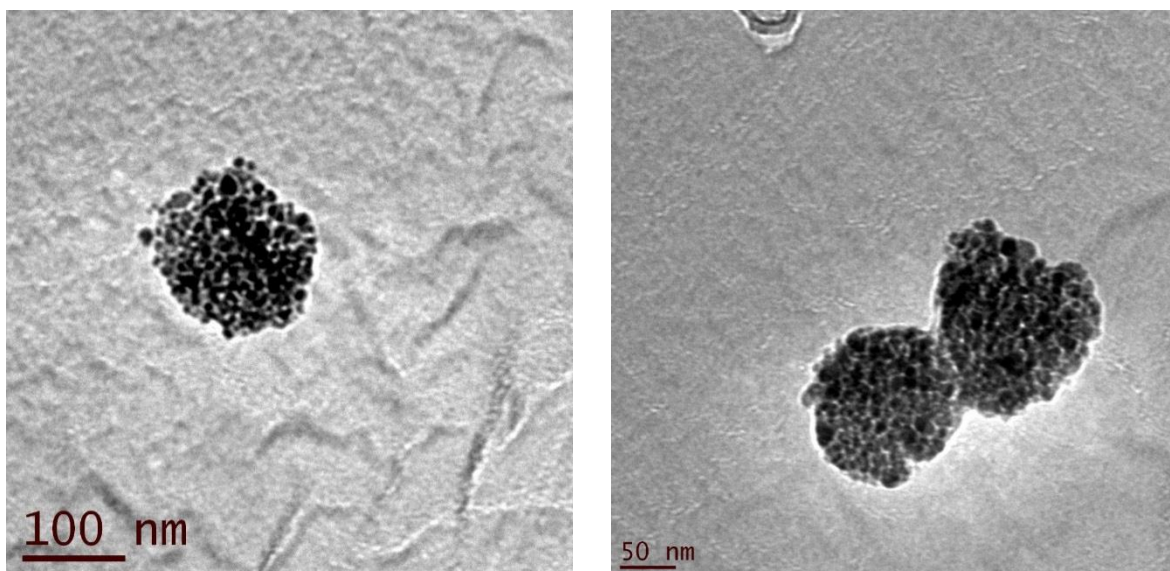


Figure 3-16. TEM image of ME55-PEG-PCL, polymer coated magnetite nanoparticles

3.3 Nitrogen Gas Adsorption-Desorption Isotherm and Brunauer–Emmett–Teller (BET) Surface Area Analysis

Surface area of the different synthesised materials were determined using nitrogen adsorption – desorption test. BET analysis of adsorption isotherm determines the specific surface area of the powder sample by physical adsorption of nitrogen on the sample surface. Measurements were performed according to methods described in Section 2.32.3. The data was considered acceptable if the correlation coefficient was greater than 0.9975 (Naderi, 2015). Surface area of the different materials are summarised in Table 3-2.

Table 3-2. Summary of the surface area of the material

Material ID	Surface area (m ² /g)
ME32	133.9683 ± 0.5248
ME33	1187.7596 ± 6.7348
ME56	38.2521 ± 0.6845
ME60	358.0238 ± 0.5267
ME93	752.8064 ± 7.6538
ME94	574.5482 ± 3.5390

Figure 3-17 presents the Nitrogen gas adsorption-desorption isotherm of mesoporous silica coated magnetic nanoparticles (ME32). The BET plot is classified as type IV isotherm which is associated with mesoporous structures. The isotherm displayed a H1 hysteresis loop within the relative pressure range of 0.6 to 1 indicating the presence of agglomerates in the sample (Haul, 1982). The BET specific surface area was measured to be 133.96 m²/g. The presence of porous structures and agglomerates were consistent with the TEM images (see Figure 3-6).

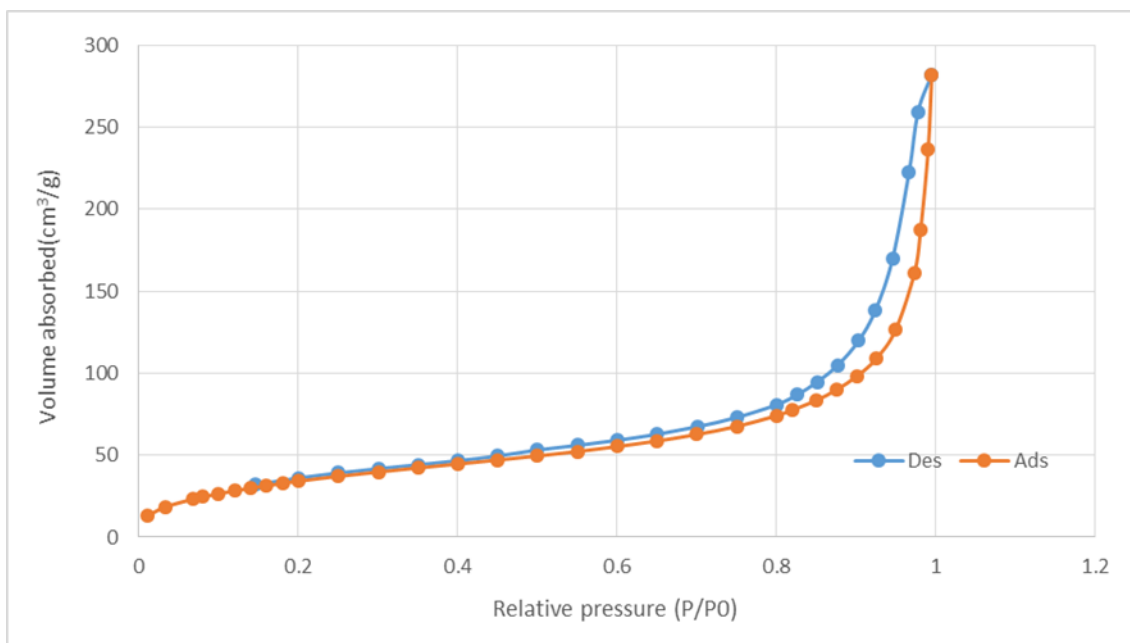


Figure 3-17. Nitrogen gas adsorption-desorption isotherm of ME32, BET Surface Area: 133.9683 ± 0.5248 m^2/g

Figure 3-18 shows the Nitrogen gas adsorption-desorption isotherm of the mesoporous silica coated magnetite (ME33). This material exhibited a type IV isotherm indicating the mesoporous structure. The hysteresis loop observed between relative pressures of 0.4 to 0.8 could be categorized to be type H2 indicating non-uniform shapes and sizes of mesopores (Haul, 1982). The BET surface area of the material was measured to be $1187.8 \text{ m}^2/\text{g}$ which is exceptionally high. This presents the potential of this material to be used in drug loading or enzyme immobilisation. The average pore diameter was measured to be around 4 nm which is expected from the porous structures generated using CTAB as pore templates (Lieberman et al., 2014).

The surface area measurement was repeated after the enzyme immobilisation on ME33 to study the effects of the enzyme on the surface area of the material. The BET results after enzyme immobilisation shows a surface area of $146.93 \text{ m}^2/\text{g}$ for chemically immobilised PFL and $51.27 \text{ m}^2/\text{g}$ after chemical immobilisation of CRL. The drastic decrease observed in the surface area of the material confirms the presence of the enzyme molecules inside the pores. The BET isotherm for PFL immobilised nanoparticles are shown in Figure 3-19.

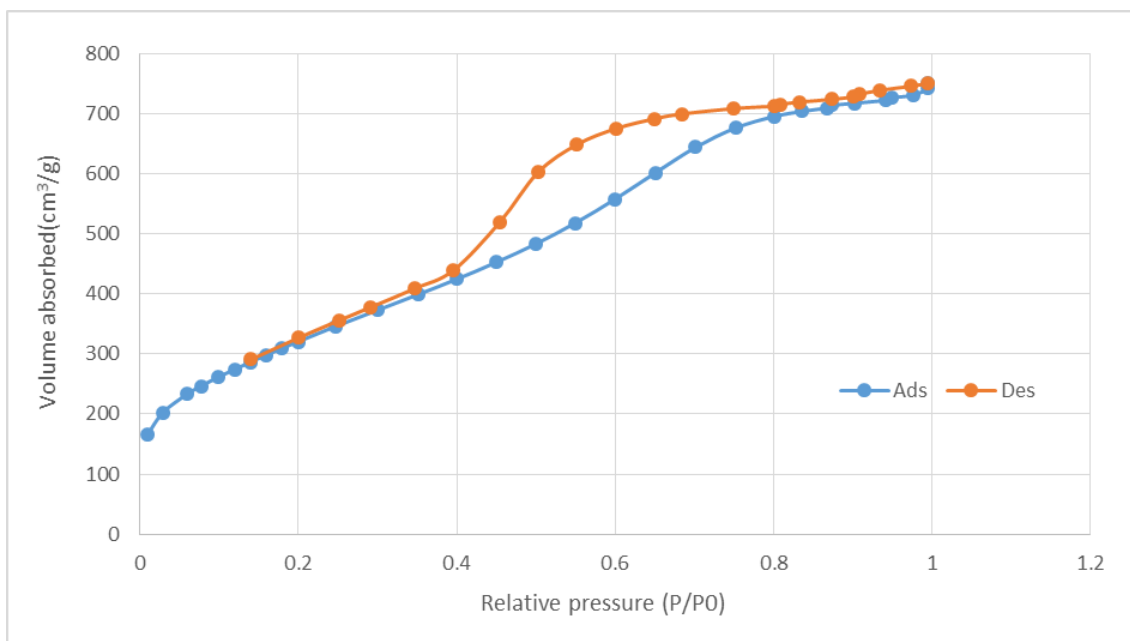


Figure 3-18. Nitrogen gas adsorption-desorption isotherm of ME33, BET Surface Area: $1187.7596 \pm 6.7348 \text{ m}^2/\text{g}$

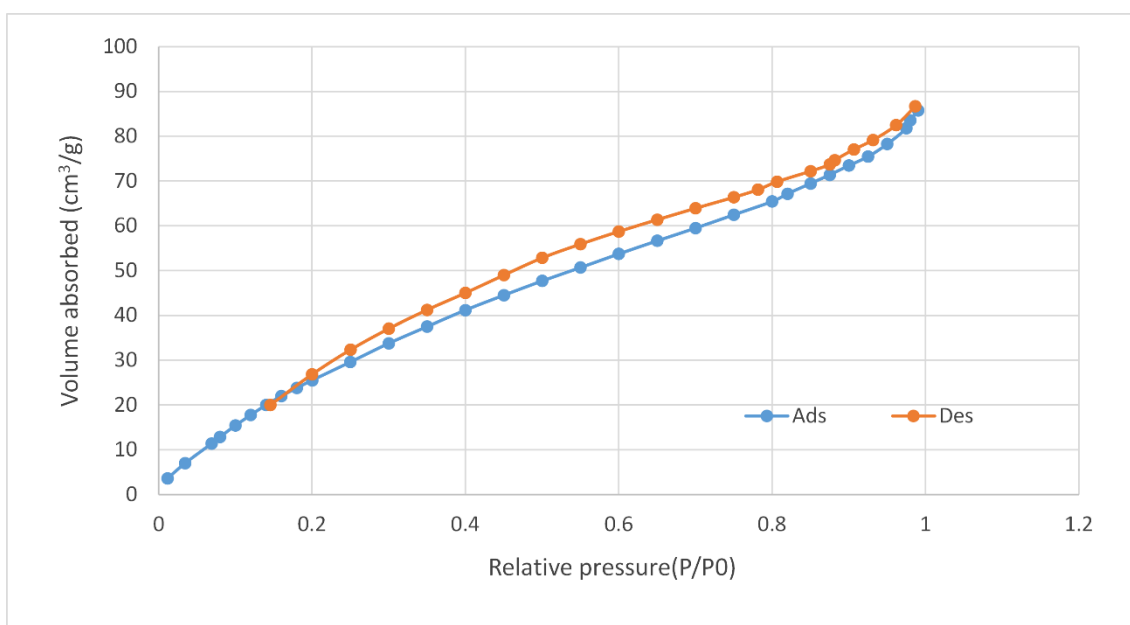


Figure 3-19. Nitrogen gas adsorption-desorption isotherm of ME33 after chemical PFL immobilization. BET Surface Area: $146.9339 \pm 2.5072 \text{ m}^2/\text{g}$

The nitrogen gas adsorption-desorption isotherm of mesoporous silica coated magnetic nanoparticles (ME60), is presented in Figure 3-20. The BET plot shows Type IV isotherm and H2 hysteresis loop which is similar to the results obtained for ME33. The similar results was expected since ME60 was synthesised following the same method as ME33 with slight modification in synthesis method to reduce the size of the nanoparticles in order to make them suitable for drug delivery applications. The BET specific surface area of ME60 was measured to be $358 \text{ m}^2/\text{g}$ which is much lower in value compared to ME33. This could be the result of relatively thin silica shell of ME60.

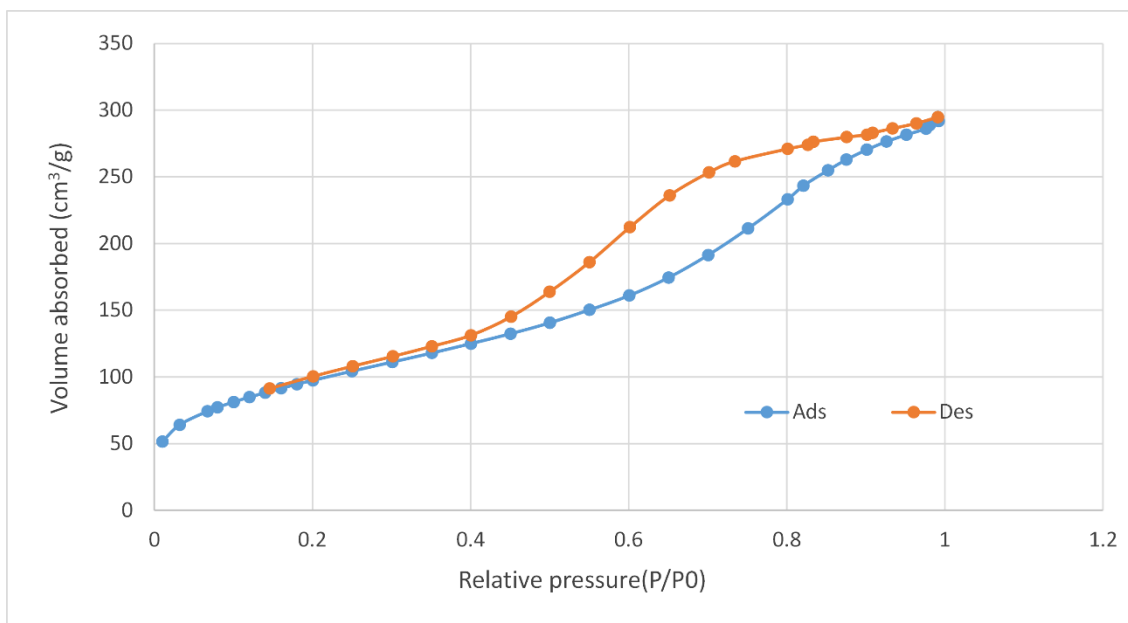


Figure 3-20. Nitrogen gas adsorption-desorption isotherm of the ME60-BET Surface Area: 358.0238 ± 0.5267 m^2/g

Figure 3-21 presents the nitrogen gas adsorption-desorption isotherm of ME93. A type IV isotherm was obtained from nitrogen gas adsorption-desorption isotherm plot for ME93 indicating mesoporous structure. The nitrogen adsorption-desorption isotherm exhibits a linear increase in the volume of adsorbed nitrogen at low relative pressure ($P/P_0 < 0.2$), which can be assigned as the mono-layer adsorption of nitrogen on the sample surface. The sharp inflection in the volume of adsorbed nitrogen between relative pressures 0.2 and 0.4 could be the result of nitrogen capillary condensation inside the mesopores. The hysteresis loop observed for ME93 between relative pressure 0.3 and 1 could be classified as type H4 indicating the presence of narrow slit-shaped pores (Haul, 1982, Ursachi et al., 2011a). The BET surface area of the material was measured to be $752.80 m^2/g$. The high surface area indicates that ME93 is suitable to be used in drug delivery applications. The average pore diameter was measured to be 3 nm which is lower than pore size generated by either CTAB or Pluronic F127 templates. The lower pore diameter could be the result of OTS surface functionalization which is consistent with the results reported by Yildirim *et al.* (Yildirim et al., 2013).

The nitrogen gas adsorption-desorption isotherm of ME94 is shown in Figure 3-22. ME94 established a type IV isotherm indicating mesoporous structure. The vertical hysteresis loop observed between relative pressures 0.4 and 1 could be categorised to be a type H1 which could be obtained from either agglomerates (in case of ME32) or spherical nanoparticles with fairly uniform size (Haul, 1982) which is consistent with the TEM images of ME94 (Figure 3-13). The surface area of the material was measured to be $574.5 m^2/g$. The high surface area of the material suggests the potential of this material to be used for drug delivery applications. The average pore diameter was measured to be 6.3 nm which is consistent with pores generated using CTAB and triblock polymers together as network structuring templates (Lieberman et al., 2014).

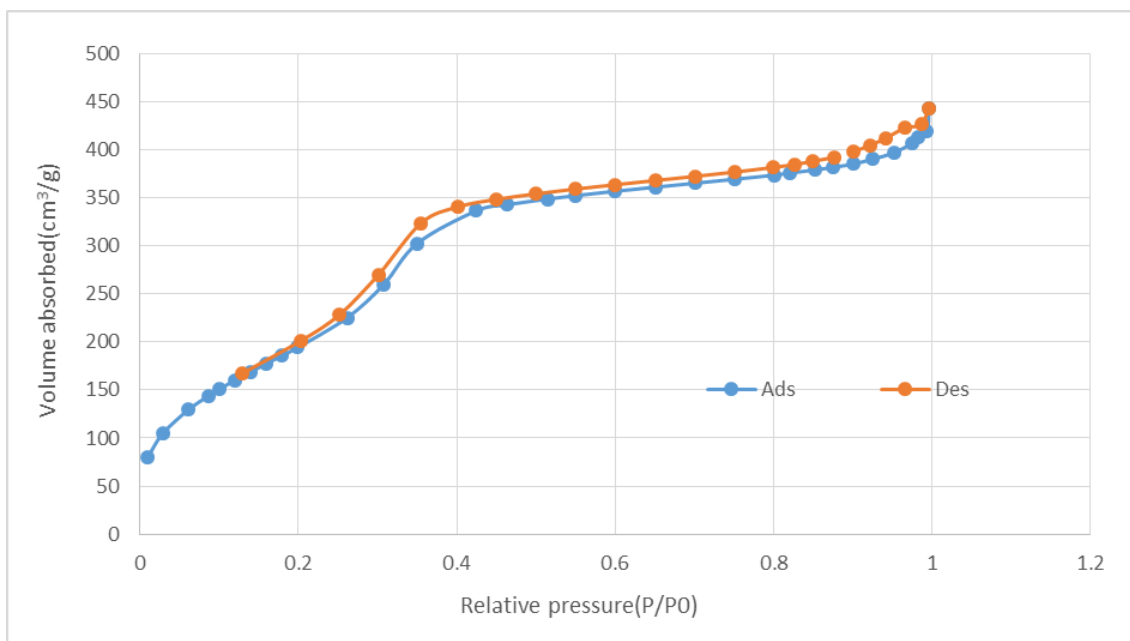


Figure 3-21. Nitrogen gas adsorption-desorption isotherm of ME93, BET Surface Area: 752.8064 ± 7.6538 m^2/g

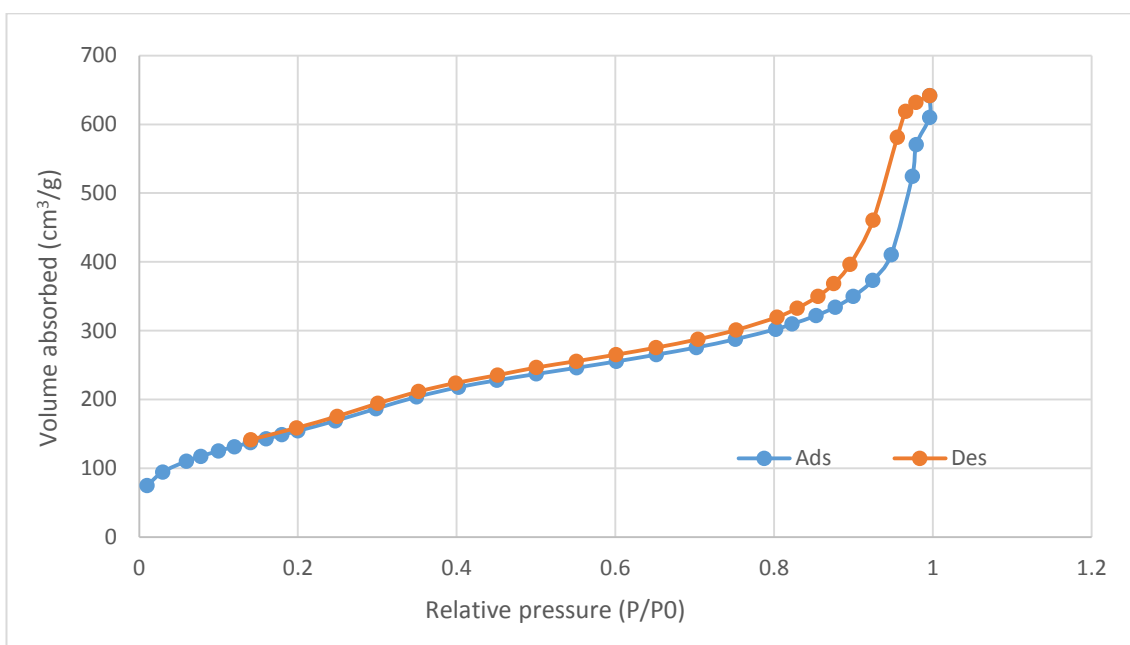


Figure 3-22. BET isotherm of ME94 BET Surface Area: 574.5482 ± 3.5390 m^2/g

The surface area measurement was performed for the starting material for development of ME94 (ME56) before etching process which demonstrated a low surface area of 38.25 m^2/g .

3.4 X-Ray Diffraction (XRD)

X-ray diffraction (XRD) was used to confirm the crystalline structure of the magnetite nanoparticles. Samples for X-ray diffraction analysis were prepared according to methods described in Section 2.32.1.

Figure 3-23 shows the XRD pattern of ME18 (bare magnetite nanoparticles). The powder X-ray diffraction of magnetite nanoparticles exhibited multiple peaks with miller indices of 220, 311, 400, 422, 511, and 440 similar to the fingerprint of pure magnetite (Fe_3O_4) (JCPDS No. 19-0629) in the 2θ range of 20 to 70 (Sen et al., 2006, Sun et al., 2004).

While the patterns of Fe_3O_4 (JCPDS No. 19-0629) and $\gamma\text{-Fe}_2\text{O}_3$ phases (JCPDS No. 39-1346) are rather similar (Todaka et al., 2003) some peaks corresponding to $\gamma\text{-Fe}_2\text{O}_3$ phase, such as (210) and (211) peaks, were not present in the XRD pattern of ME18 indicating that the synthesized nanoparticles were in Fe_3O_4 phase. The black colour of the powder further verifies that it contains mainly magnetite nanoparticles.

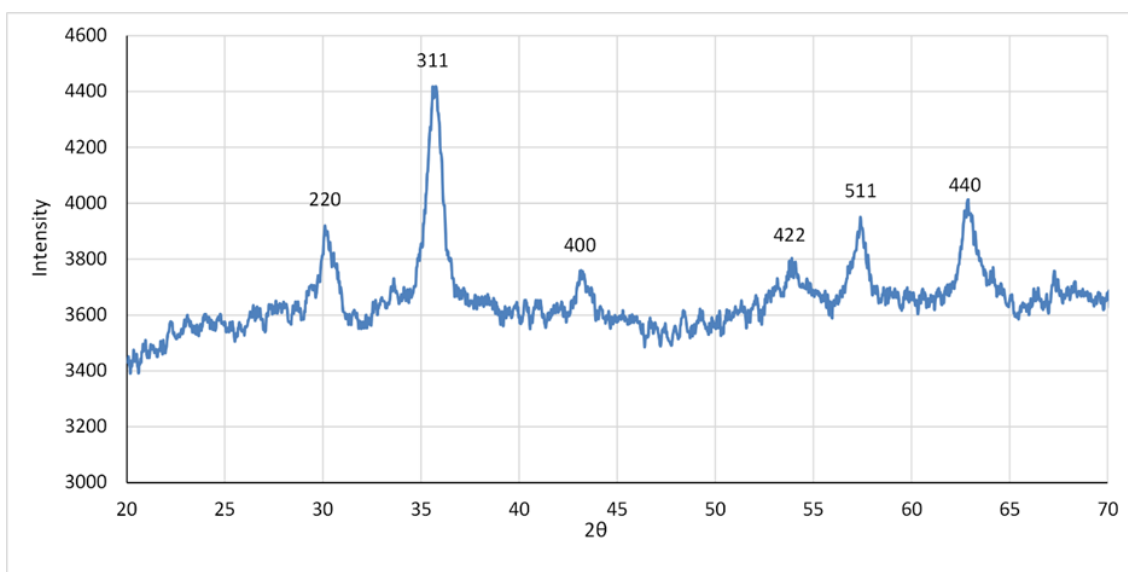


Figure 3-23. XRD pattern of bare magnetite (ME18)

The low intensity of the peaks could be an indication of ultra-small size of magnetite nanoparticles. The average particle diameters were calculated from the XRD pattern according to the linewidth of the (3 1 1) plane refraction peak using Scherrer equation as presented in Equation 3-1 (Sun et al., 2004, Schwertmann and Cornell, 2007)

$$D = \frac{k\lambda}{b \cos \theta} \quad \text{Equation 3-1}$$

The equation uses the reference peak width at angle θ , where λ is the X-ray wavelength (1.5418 Å), b is the width of the XRD peak at half height and K is a shape factor (about 0.9 for magnetite). The calculated diameter of ME18 was about 10.4 nm which is consistent with the TEM images (see Figure 3-2).

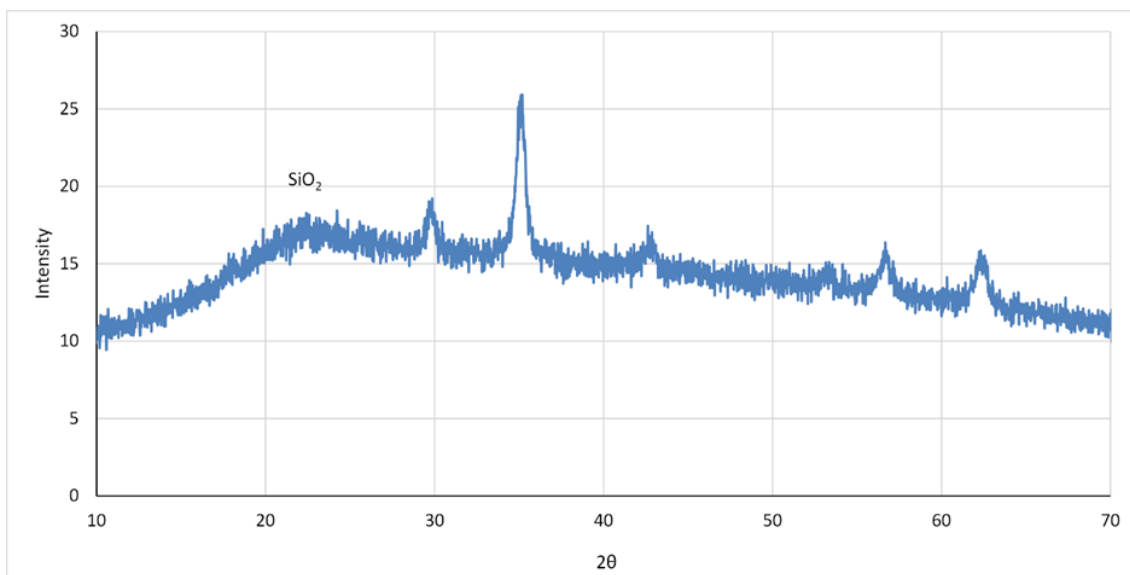


Figure 3-24. XRD pattern of silica coated magnetite (ME33)

Figure 3-24 shows the XRD pattern of mesoporous silica coated magnetite nanoparticles in the wide angle region. As seen in the image the XRD pattern of silica coated nanoparticles has similar diffraction peaks to uncoated magnetite nanoparticles, which suggests the magnetite nanoparticles were conserved during mesoporous silica coating. The broad peak observed in mesoporous silica coated nanoparticles at around $2\theta = 22^\circ$ corresponds to the presence of amorphous silica (JCPDS No. 29-0085) (Souza et al., 2008, Souza et al., 2009b, Ursachi et al., 2011a)

3.5 Small angle X-ray scattering (SAXS)

SAXS measurements were performed in order to further investigate the structure and the morphology of the nanoparticles. Scattering curves were monitored in a 2θ range from 0.08 to 8° . The pore size were calculated according to the Bragg's equation:

$$n\lambda = 2d \sin \theta \quad \text{Equation 3-2}$$

Where n is an integer, λ is the wavelength of the X-ray radiation (1.5418 \AA), and θ is the angle at which the scattered beam was observed.

Figure 3-25 presents the SAXS pattern of ME32. SAXS pattern exhibit apparent diffraction peak at about 2θ of 1.3° corresponding to the (1 0 0) diffraction peak which is characteristic for hexagonal mesopores (Corma, 1997). However, the broad (1 0 0) peak could indicate limited pore ordering (El-Toni et al., 2013a). The pore size were calculated to be around 5.7 nm .

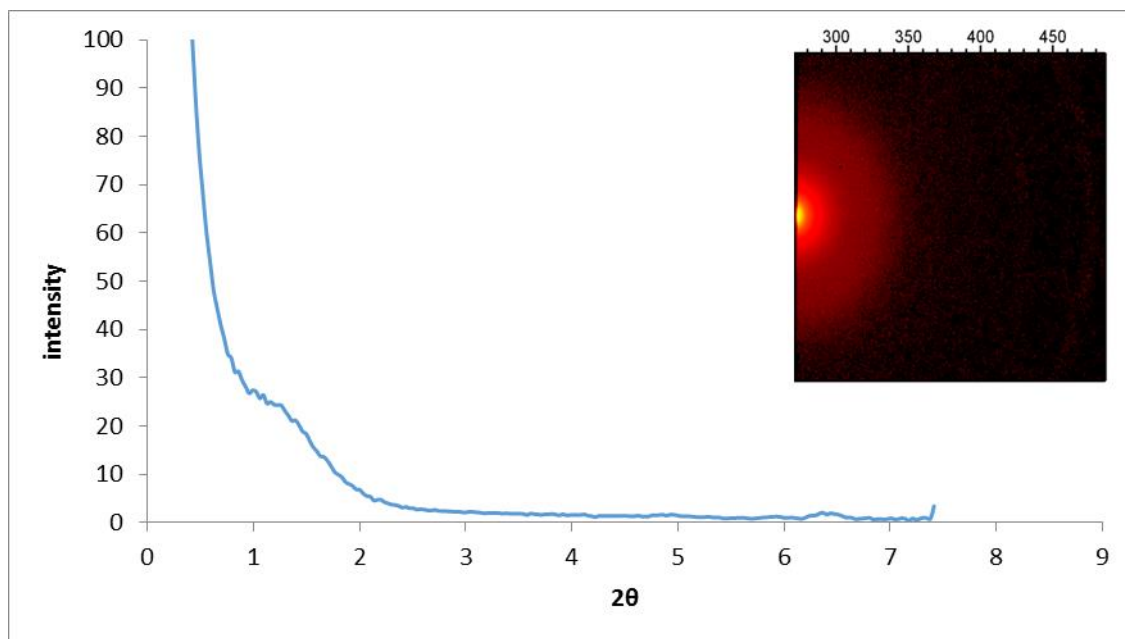


Figure 3-25. SAXS pattern of ME32 (silica coated magnetite)

Figure 3-26 presents the SAXS pattern of ME33 indicating the appearance of a single peak which could be assigned to the miller plane (1 0 0). The observed diffraction peak could be indexed to a 2D hexagonal structure that suggest reasonably ordered mesoporous shell similar to MCM-41 material (El-Toni et al., 2013a, Ursachi et al., 2011b). However, the absence of other hexagonal peaks, (1 1 0) or (2 0 0), could be attributed to a certain extent to the distortion from a perfect 2D hexagonal mesostructure, due to the packing of the radially oriented mesopores in the spherical shell (El-Toni et al., 2013a). The pore size were calculated according to Bragg's equation to be around 3.7 nm which is consistent with the BET analysis.

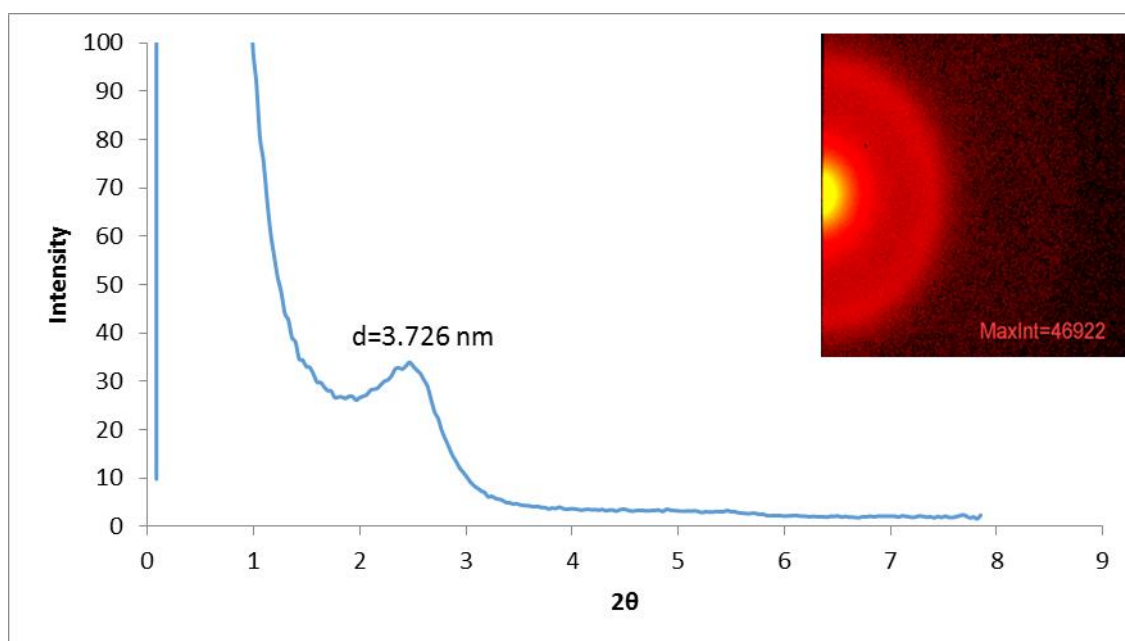


Figure 3-26. SAXS pattern of ME33 (silica coated magnetite)

3.6 Energy Dispersive X-ray Spectroscopy (EDS)

The energy dispersive X-ray Spectroscopy (EDS) was performed to investigate the existence and distribution of elements in the magnetic nanocomposites. Samples were prepared as explained in Section 2.32.14. Measurements were carried out parallel to TEM by moving the sample to examine different parts of the grid. The high amount of copper observed in the sample is from the TEM grids (copper grids were used).

Figure 3-27 illustrates the EDS spectrum of core-shell nanocomposites (ME33) with the atomic fractions (weight %) of Si and Fe in the nanoparticle. The EDS spectra shows multiple peaks corresponding to presence of Si, Fe and O in the sample which indicated that there was no impurity in the sample and as expected, the surfactant molecules were completely removed from the sample.

The measurements were performed on four different sections of the sample on TEM grids which confirmed the homogenous distribution of the core-shell structure of the nanocomposites.

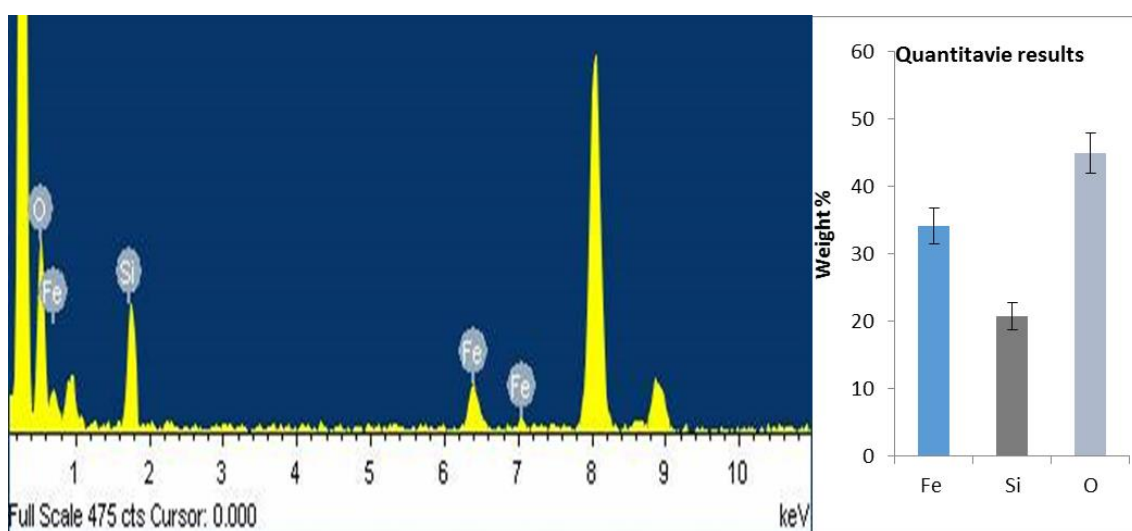


Figure 3-27. EDS spectrum data of ME33 (silica coated magnetite nanoparticles)

3.7 Vibrating Sample Magnetometry (VSM)

Vibrating sample magnetometry (VSM) was used to evaluate magnetic properties of different materials such as susceptibility and saturation magnetization (M_s). The VSM operates on Faraday's Law of Induction; a changing magnetic field will induce an electric field in a conductor. Samples were placed in an oscillating sample holder. As the magnetic sample vibrates along the Z axis perpendicular to the magnetic field it induces an AC voltage of the amplitude that is proportional to the magnetic moment of the test sample. The samples for VSM were prepared as explained in Section 2.32.5.

The magnetic measurements (M-H hysteresis measurements) were performed for bare and silica coated magnetite as shown in the following graphs. All measurements were performed at room

temperature and samples exhibited typical hysteresis curves of superparamagnetic materials with negligible coercivity. It is of utmost importance that the final nanocomposites exhibit sufficient magnetic characteristics to be used in the targeted applications.

Figure 3-28 presents the VSM hysteresis curves for bare magnetite nanoparticles prepared by oxidative hydrolysis of iron sulphate in alkaline media (ME01). The VSM analysis indicated that the nanoparticles were superparamagnetic with small hysteresis. The saturation magnetization (M_s) was measured to be 50.98 emu/g which is lower than the literature reported value of 92 emu/g for pure magnetite (Qu and Tie, 2009). The lower value of saturation magnetization could be due to the reduced size of the nanoparticles (Sato et al., 1987, Qu and Tie, 2009, Santra et al., 2001). The magnetization of ferromagnetic materials is highly dependent on the size and structure of the sample and the magnetization decreases with a decrease in particle size especially when the particles size is reduced to single domain and the material reach a superparamagnetic state the exchange interaction between the particles is decreased resulting in reduced magnetization (Santra et al., 2001).

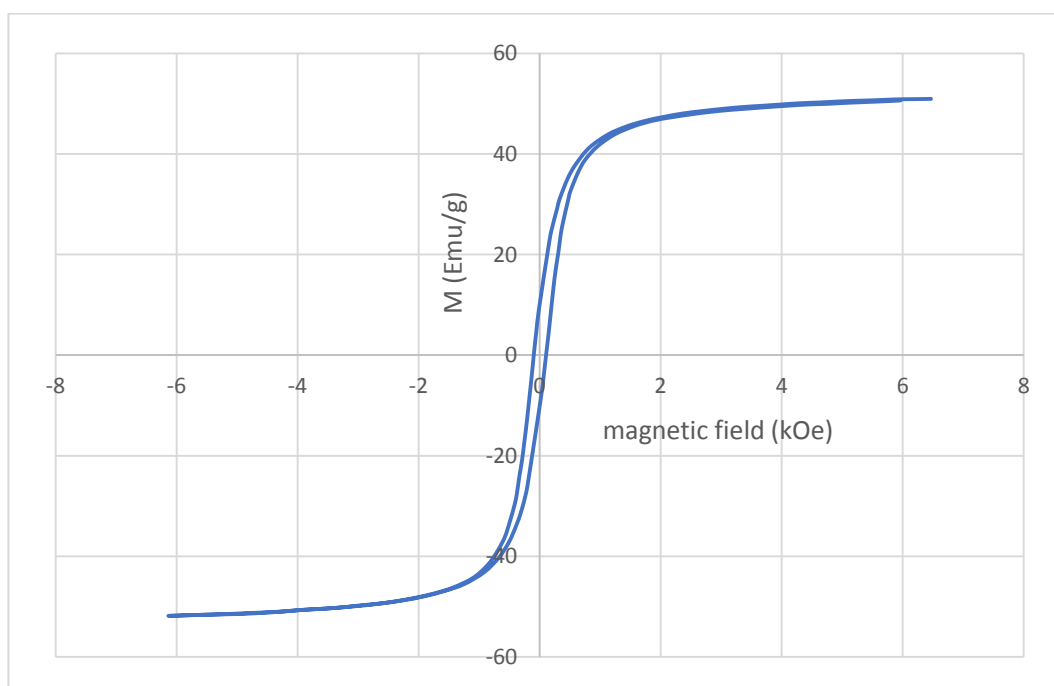


Figure 3-28. Magnetic measurements of bare magnetite nanoparticles prepared by oxidative hydrolysis of iron sulphate in alkaline media (ME01)

Figure 3-29 shows the hysteresis curves of bare magnetite nanoparticles prepared by coprecipitation of ferrous and ferric chloride in alkaline media (ME18). The VSM analysis indicated that the nanoparticles were superparamagnetic with small hysteresis. The saturation magnetization (M_s) was measured to be 66.94 emu/g which is higher than the values observed for magnetite synthesised by hydrolysis of iron sulphate, this could be due to presence of more uniform nanoparticles in the ME18. However similar to ME01 the saturation magnetization value is lower than reported saturation magnetization for bulk material. As observed from the hysteresis

curves for bare magnetite nanoparticles, both materials reached saturation at the low applied field of around 2 kOe.

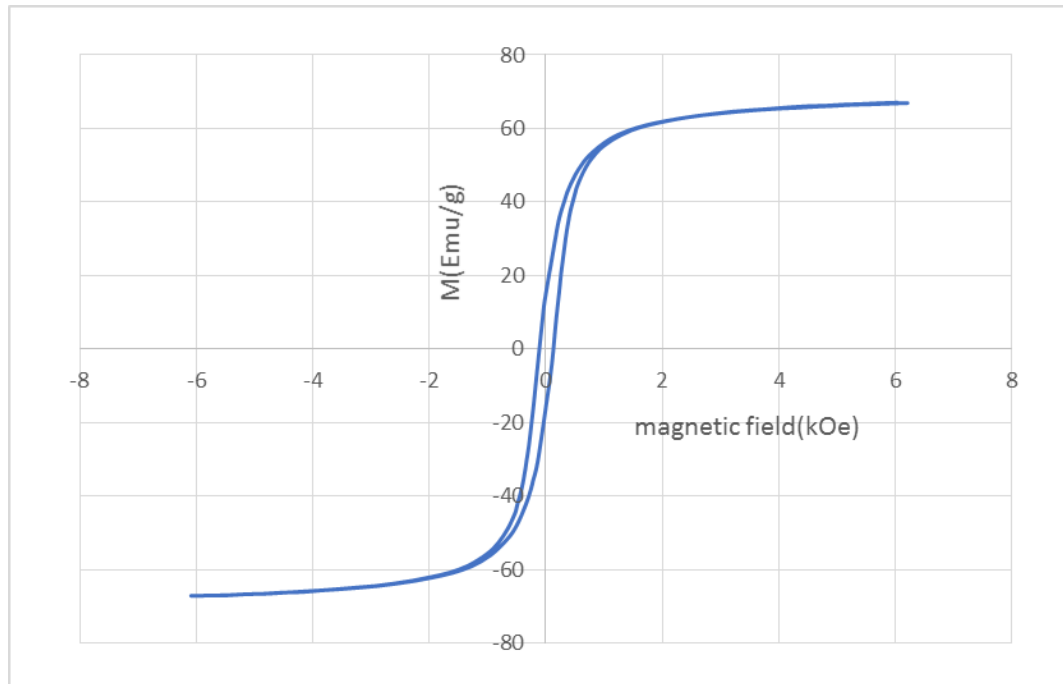


Figure 3-29. Magnetic measurements of bare magnetite nanoparticles prepared by coprecipitation of iron salts (ME18)

The magnetization can be fitted using Langevin equation (Rovers, 2010):

$$M = M_s \left(\coth \left(\frac{mH}{k_b T} \right) - \frac{k_b T}{mH} \right) \quad \text{Equation 3-3}$$

Where m is the magnetic moment and can be calculated from Equation 3-4.

$$m = \frac{\pi \mu_0 M_b d^3}{6} \quad \text{Equation 3-4}$$

Where M_s and M_b are saturation magnetization of the nanoparticles and the saturation magnetization for bulk magnetite, respectively, μ_0 is the permeability of free space, k_b is the Boltzmann constant, and d is the particle diameter.

Which in strong field limit by replacing magnetic moment in equation it reduce to (Rovers, 2010)

$$M = M_s - \alpha \frac{1}{H} \quad \text{Equation 3-5}$$

Where

$$\alpha = \frac{6 M_s k_b T}{\pi \mu_0 M_b d^3} \quad \text{Equation 3-6}$$

For weak magnetic field the initial susceptibility of the nanoparticles can be calculated from Langevin equation (Rovers, 2010).

$$\chi = \frac{\pi\mu_0 M_b M_s d^3}{18k_b T} \quad \text{Equation 3-7}$$

By fitting the magnetization curve using the Langevin equation the coefficient α and consequently magnetic size of the nanoparticles could be calculated:

$$d = \sqrt[3]{\frac{6M_s K_b T}{\pi\mu_0 M_b \alpha}} \quad \text{Equation 3-8}$$

The magnetic moment and susceptibility for ME01, was calculated from the magnetization curve to be to be 4.26×10^{-25} (Am²) and 8.73 respectively. The magnetic moment, the coefficient α and susceptibility for ME18 was calculated to be 6.24×10^{-25} (Am²), 2.32×10^9 and 16.82.

The calculated magnetic particle sizes for ME01 and ME18 were 11.20 nm and 12.73 nm, respectively which are smaller than the average sizes measured using TEM images. The constant values which were used in the calculations are listed in Table 3-3.

Table 3-3. Constants used for calculations in Langevin equation

Saturation magnetization for bulk magnetite	M_b	4.6×10^5 A/m
Permeability of free space	μ_0	$4\pi \times 10^{-7}$ H/m
Boltzmann constant	k_b	1.3807×10^{-23} m ² kg/s ² K
Temperature	T	300°K
Magnetite density	ρ	5000 kg/m ³

The coercivity values of $H_c=0.1015$ kOe and $H_c=0.1199$ kOe were observed for ME01 and ME18 which are very low compared to the bulk material and are acceptable for superparamagnetic nanoparticles (Ammar et al., 2007). According to Néel, dissymmetry of atomic layers of magnetic nanoparticles could lead to an increase in demagnetizing field which results in increased coercivity (Néel, 1953). The coercive field due to shape anisotropy effect of the aspherical nanoparticles could be calculated based on (Ammar et al., 2007)

$$H_c = \frac{2(\gamma-1)M_s}{5\mu_0} \quad \text{Equation 3-9}$$

Where γ is the asphericity of the nanoparticles. For ME01 and ME18 the coercivity was very low which indicated monodisperse spherical nanoparticles which is in agreement with TEM images.

The remanent magnetization (M_r) values for ME01 and ME18 were calculated to be 10.15 emu/g and 15.41 emu/g. The squareness value ($S = M_r/M_s$) for bare magnetite nanoparticles were calculated to be 0.19 for ME01 and 0.26 for ME18 which indicate the presence of pseudosingle-domain (PSD) particles. The squareness values can range from 0.1 to 0.5 for pseudosingle-domain (PSD) particles (Dunlop, 1990, Ursachi et al., 2011b, Ursachi et al., 2011a). PSD particle may

consist of only one or two domains, indicating that the material might possess same magnetic properties as of SD and MD structures simultaneously (Ursachi et al., 2011b).

Figure 3-30 to Figure 3-35 present the magnetisation M-H plot for silica coated nanoparticles. ME16, ME32, ME33, ME60 and ME93 are core-shell nanoparticles synthesised using ME18 as magnetic core and coated with different thickness of mesoporous silica layer whereas ME94 was prepared by using ME55 as magnetic core. The saturation magnetization and coercive field for these nanoparticles are listed in Table 3-4.

Table 3-4. The saturation magnetization for silica coated nanoparticles

Material	Saturation magnetization (M_s) emu/g	Coercivity (H_c) kOe	Squareness (M_r/M_s)
ME16	30.43	0.142	0.20
ME32	10.78	0.0136	0.028
ME33	14.23	0.095	0.22
ME60	16.48	0.045	0.13
ME93	14.83	0.045	0.12
ME94	4.60	0.025	0.07

All silica coated nanoparticles displayed superparamagnetic characteristics with very low or negligible remanence and coercivity as observed from the plots. As expected the saturation magnetization value of the silica coated nanoparticles was found to be lower than uncoated magnetite nanoparticles (Qu and Tie, 2009). It is suggested in the literature that at any given field the saturation magnetization of uncoated magnetite is always higher than that of the silica coated materials (Qu and Tie, 2009, Santra et al., 2001).

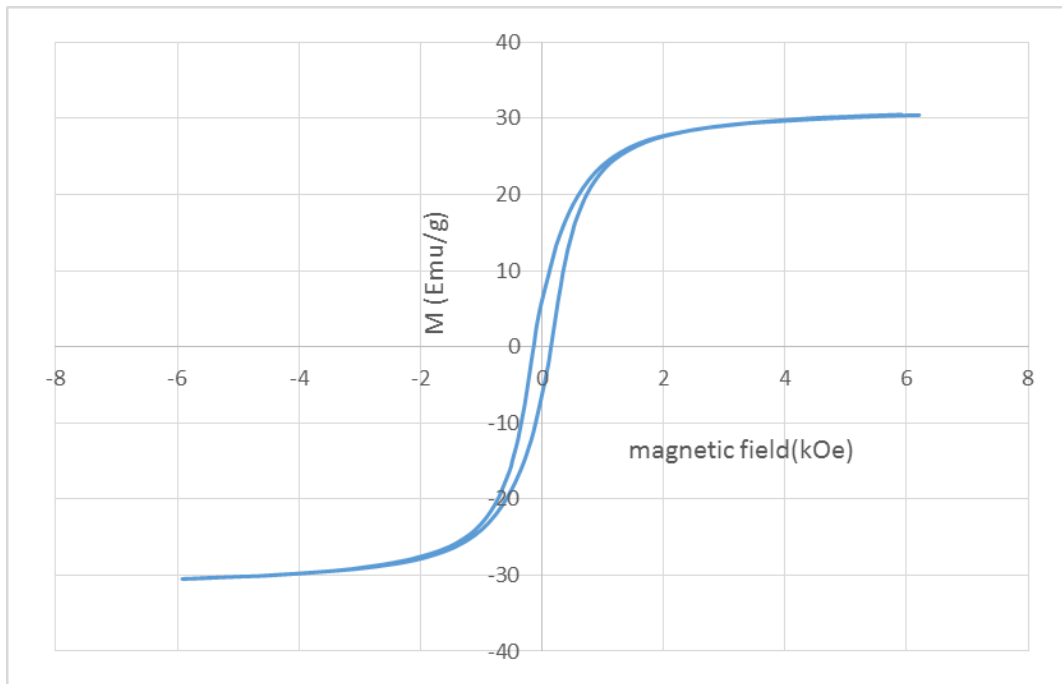


Figure 3-30. Magnetic measurements of silica coated magnetite nanoparticles (ME16)

Figure 3-30 presents the VSM obtained M-H plot for ME16. The saturation magnetization and the coercive field were measured to be 30.43 emu/g and 142 Oe. The remanent magnetization of the silica coated nanoparticles was calculated to be 6.15 emu/g.

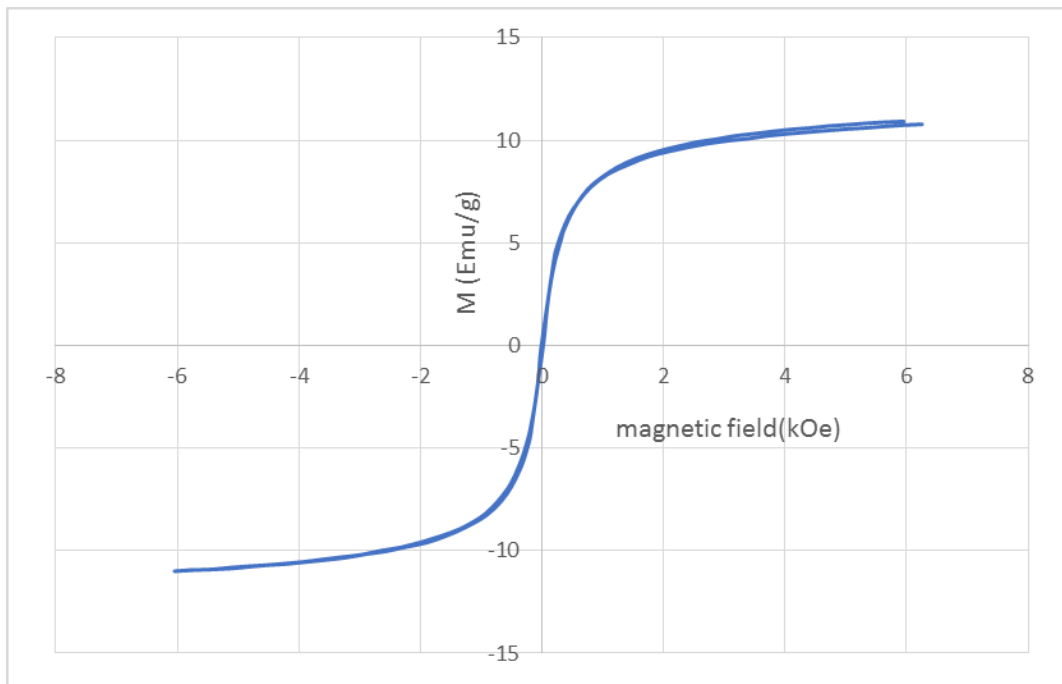


Figure 3-31. Magnetic measurements of silica coated magnetite nanoparticles (ME32)

Figure 3-31 presents the VSM obtained M-H plot for ME32. The saturation magnetization and the coercive field values were measured to be 10.78 emu/g and 13.6 Oe. The remanent magnetization of the silica coated nanoparticles was calculated to be 0.309 emu/g.

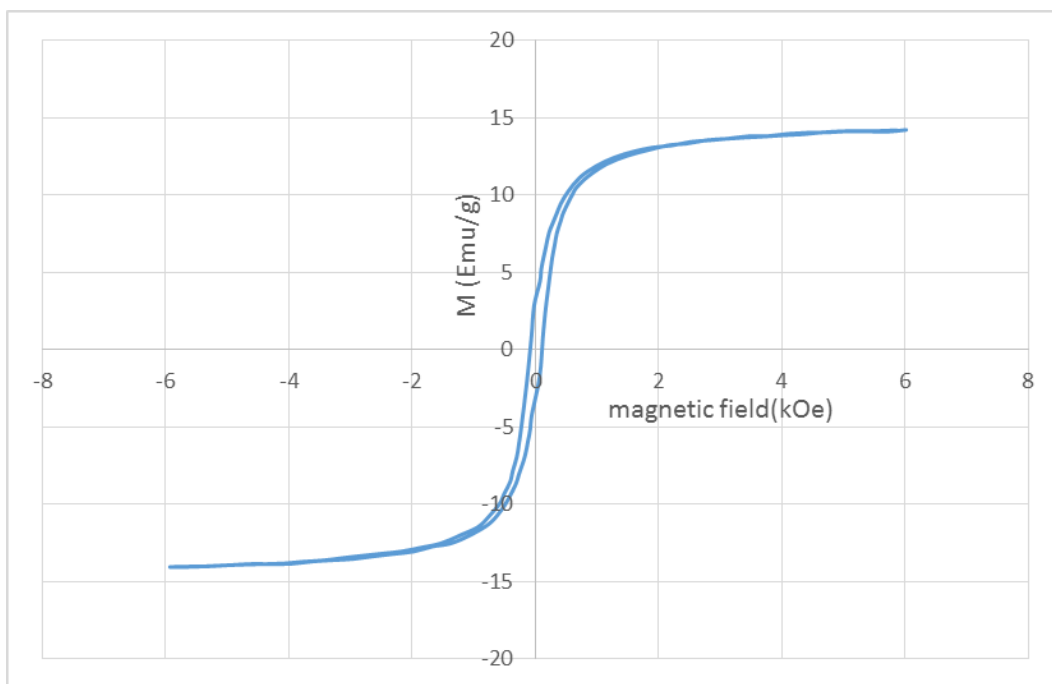


Figure 3-32. Magnetic measurements of silica coated magnetite nanoparticles (ME33)

Figure 3-32 presents the VSM obtained M-H plot for ME33. The saturation magnetization and the coercive field were measured to be 14.23 emu/g and 95 Oe. The remanent magnetization of the silica coated nanoparticles was calculated to be 3.18 emu/g.

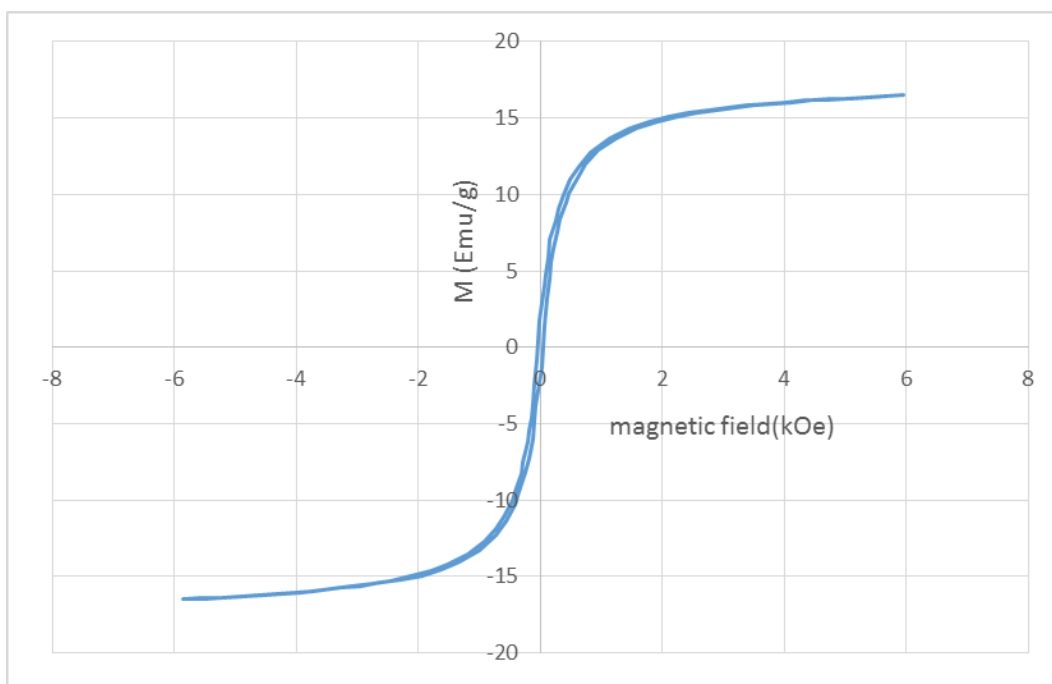


Figure 3-33. Magnetic measurements of silica coated magnetite nanoparticles (ME60)

Figure 3-33 presents the VSM obtained M-H plot for ME60. The saturation magnetization and the coercive field were measured to be 16.48 emu/g and 45.8 Oe. The remanent magnetization of the silica coated nanoparticles was calculated to be 2.15 emu/g.

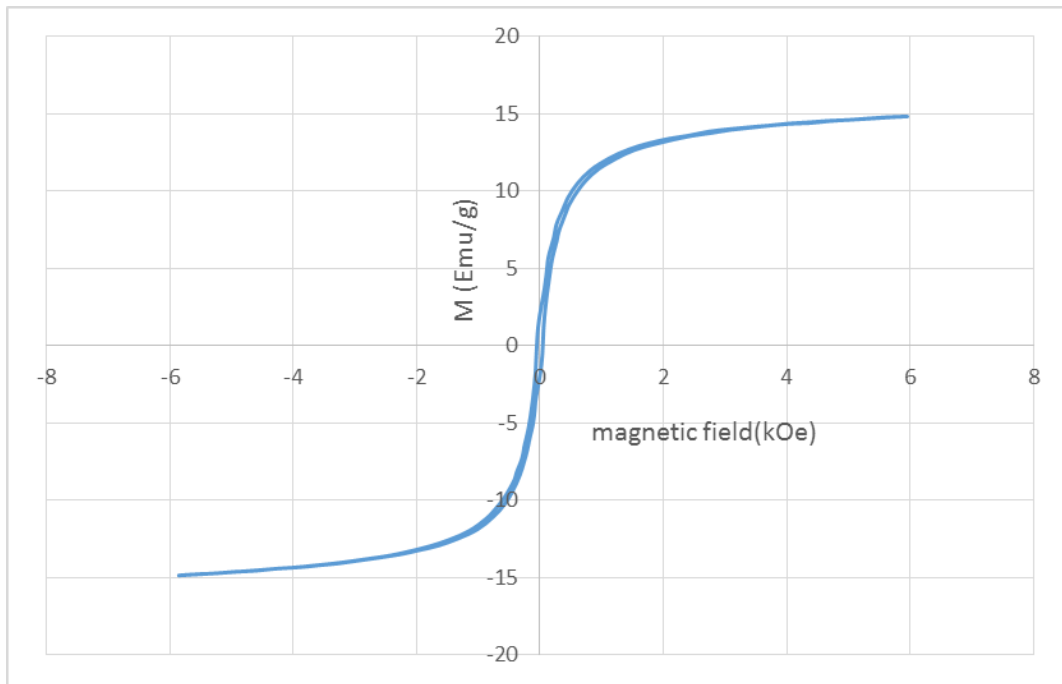


Figure 3-34. Magnetic measurements of silica coated magnetite nanoparticles (ME93)

Figure 3-34 presents the VSM obtained M-H plot for ME93. The saturation magnetization and the coercive field were measured to be 14.84 emu/g and 45.1 Oe. The remanent magnetization of the silica coated nanoparticles was calculated to be 1.88 emu/g.

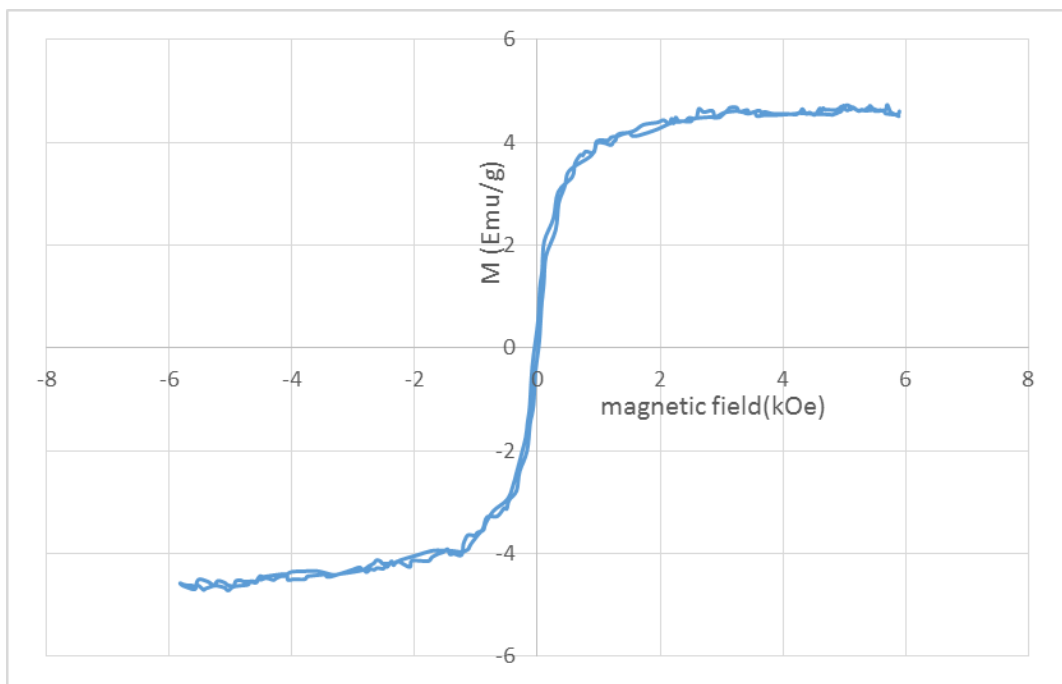


Figure 3-35. Magnetic measurements of silica coated magnetite nanoparticles (ME94) (the observed noise on the signal is due to low saturation magnetization values for ME94)

Figure 3-35 presents the VSM obtained M-H plot for ME94. The saturation magnetization and the coercive field were measured to be 4.6 emu/g and 79.2 Oe. The remanent magnetization of the silica coated nanoparticles was calculated to be 0.365 emu/g.

As seen in the plots the magnetic field required for coated material to reach saturation magnetisation is higher than uncoated magnetite. This could be explained by the restrained interparticle interactions due to magnetic isolation of nanoparticles caused by silica coatings. Therefore, depending on the silica layer thickness the saturation becomes more difficult (Ammar et al., 2007). Furthermore, the diamagnetic characteristic of the silica layer affect the saturation magnetization of the nanocomposites lowering the saturation magnetization of the nanoparticles. It was observed from the VSM results that the saturation magnetization decreases with the increase in silica shell thickness. This could be clearly observed from saturation magnetization for ME33 and ME60 which are 14.43 and 16.28 emu/g. These two material were prepared following same method with different silica shell thickness.

The magnetic characteristics of the nanoparticles were identified from the M-H hysteresis loop of the nanoparticles. According to literature the squareness value larger than 0.5 indicates single domain (SD) nanoparticles, the values between 0.1 to 0.5 indicates pseudosingle domain (PSD) nanoparticles and values less than 0.1 specifies multi domain (MD) nanoparticles (Ursachi et al., 2011b, Dunlop, 1990). As summarized in Table 3-4 the nanoparticles in sample ME16, ME33, ME60 and ME93 demonstrate PSD type characteristic ($0.1 < S < 0.5$) which is in agreement with hysteresis observed for the core material used (ME18). However, ME32 and ME94 show a multi domain behaviour ($S < 0.1$).

3.8 Scanning Column Magnetometry (SCM)

Scanning Column Magnetometry (SCM) was used to study the stability of the nanoparticles in suspension. In this method a column of magnetic dispersion is driven through the core of a coil that forms part of an oscillatory circuit. The sedimentation of the material during the experiment would change the material concentration over the column length, which would result in a change in output frequency over time this change in frequency over time is used to produce a magnetic particle concentration profile over column height (Mercer et al., 1999, Sollis et al., 1998, Mercer and Bissell, 2013). The particles sedimentation is usually described by Stokes' law which calculates the speed of the particles moving in a viscous fluid, however in the magnetic suspension, sedimentation could be hindered as a result of particle interactions.

Figure 3-36 presents the SCM profile of the bare magnetite (ME18) over the period of 2 hours. The change in the profile after 1 hour indicates the sedimentation of the sample in the column. Since the output frequency is directly related to the concentration of the magnetic particles in the column, the large increase in frequency over time in the lower part of the column, indicate high concentration of the magnetic material settled in the bottom of the column (Mercer et al., 2002). The sharp peak in the profile indicates the build-up of magnetic particles at the bottom of the column by the end of 1 hour. This change in the frequency demonstrate the nanoparticles are not

stable in aqueous medium and emphasises the need for coatings over bare magnetite nanoparticles to increase the particles stability.

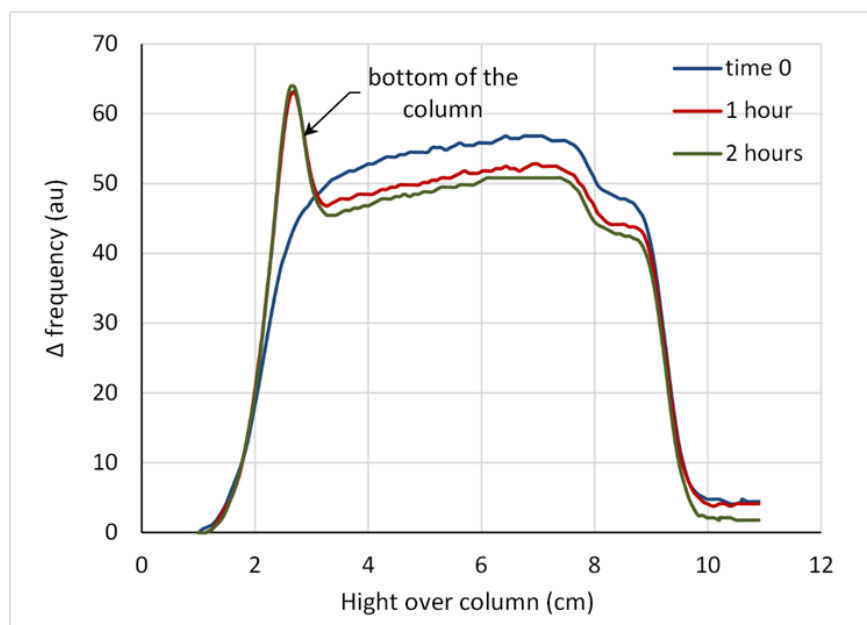


Figure 3-36. SCM profile of the bare magnetite (ME18)

Figure 3-37 shows the oleic acid functionalised magnetite in cyclohexane after 24 hours. As seen in the plot the nanoparticles are very stable and no obvious changes in the frequency was observed after 24 hours.

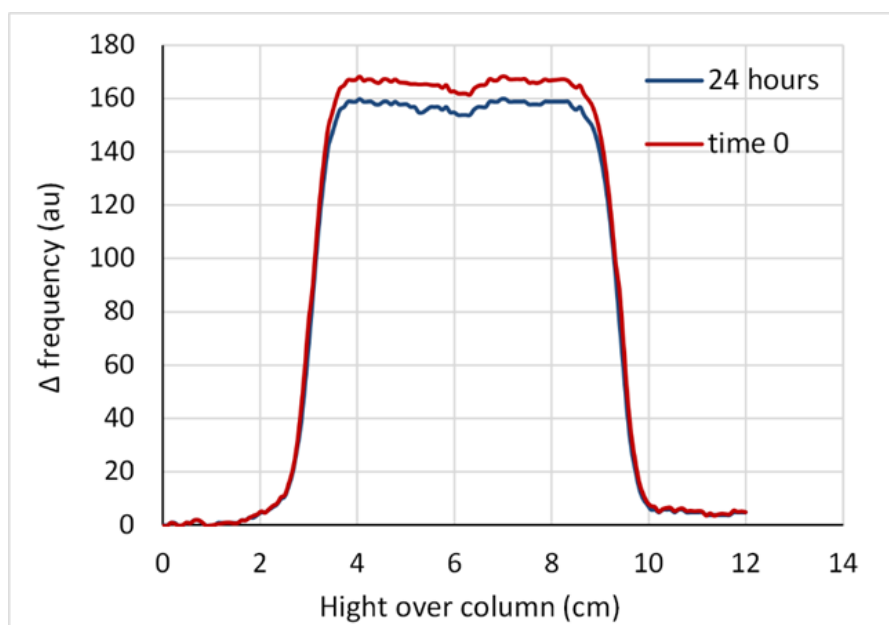


Figure 3-37. SCM profile of the oleic acid functionalised magnetite (ME55)

Figure 3-38 presents the SCM profile for ME33 over the period of 1 hour. The SCM plot shows the change in material concentration in the column over time. Compare to uncoated magnetite nanoparticles the silica coated particles show more stable profile however there is visible sedimentation in the column after 40 minutes as shown in Figure 3-39.

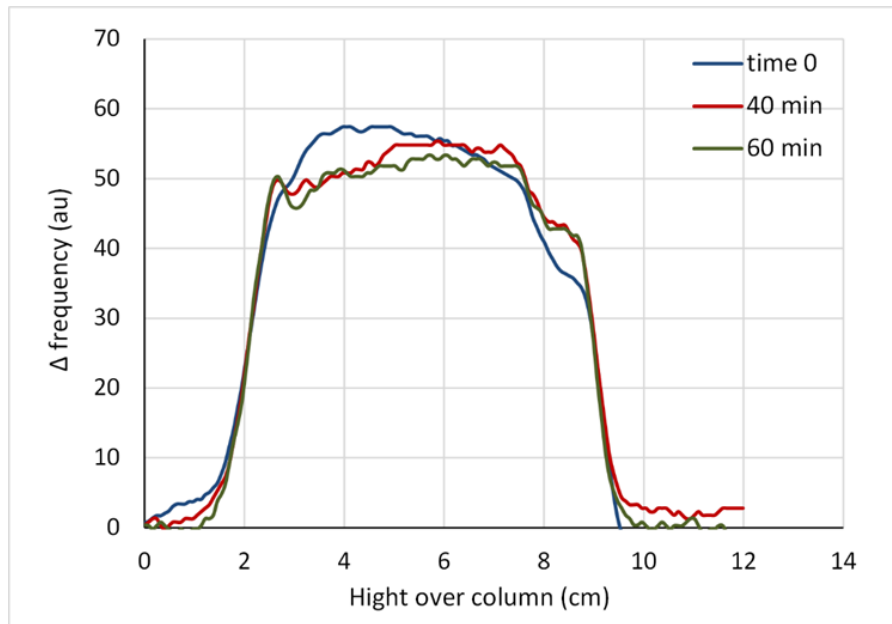


Figure 3-38. SCM profile for silica coated magnetite (ME33)



Figure 3-39. Image of the SCM column containing ME33 after 40 minutes

Figure 3-40 shows the SCM profile for ME60 over 90 minutes. The SCM plot shows clear change in material concentration over the column length with time. At 40 minutes, a peak was observed corresponding to the material build up at the bottom of the column which is associated with the increased magnetic susceptibility in the end of the column. It was observed that the initial peak intensity increased with time indicating an increase in the density of the magnetic material settled in the end of the column. The step observed in the profile near the top of the suspension column could be due to the different speed of the particles descend (Mercer and Bissell, 2013). The silica coating clearly increase the stability of the magnetite nanoparticles however it was not enough to make the material stable over long period of time.

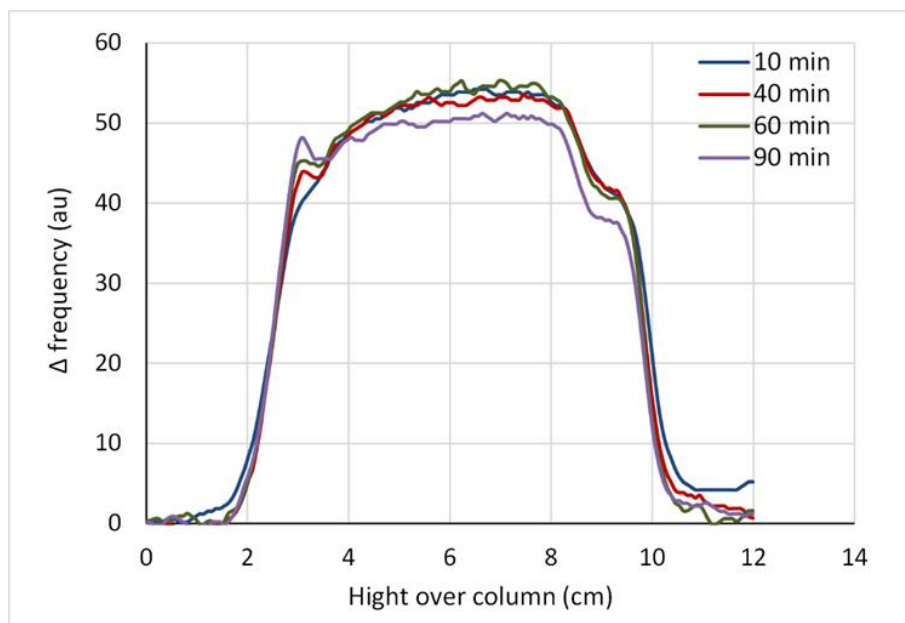


Figure 3-40. SCM profile for silica coated magnetite (ME60)

Figure 3-41 shows the SCM profile for ME55-PEG-PCL over the period of 4 hours. The SCM plot shows no obvious change in the profile over time which indicates that the material was stable over the measurement period, and there was no sedimentation in the column. The results shows that polymer coating of the magnetite nanoparticles could be more effective than silica coating in increasing the stability of the nanoparticles.

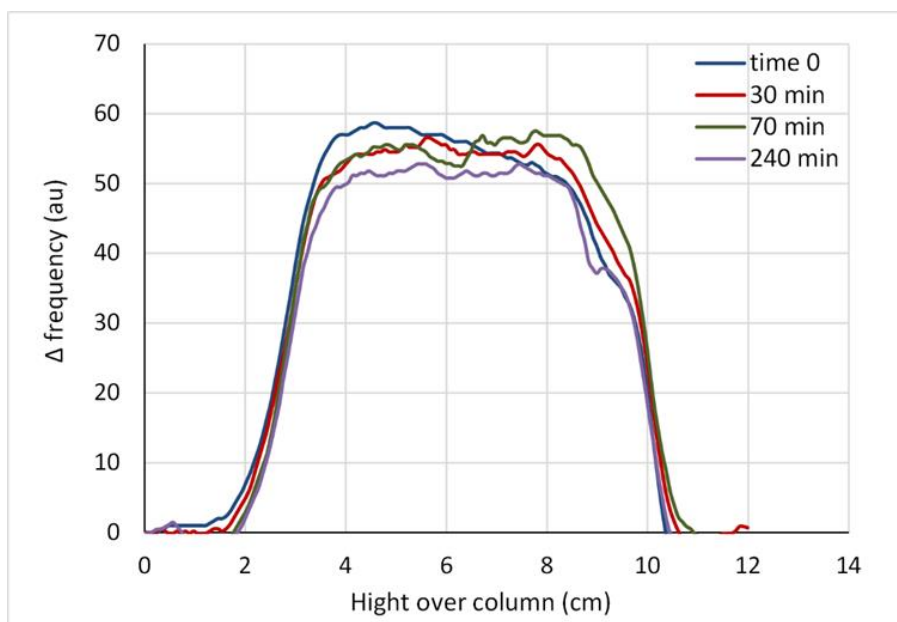


Figure 3-41. SCM profile of PEG-PCL coated magnetite nanoparticles (ME55-PEG-PCL)

Figure 3-42 presents the SCM profile for ME93-PEG-PCL over the period of 4 hours. The plot shows no obvious change in the profile over time which indicates the material was stable over the measurement period and there was no sedimentation in the column. The results show that polymer coating of the silica coated magnetite nanoparticles could increase the stability of the nanoparticles. Figure 3-43 presents the image of the ME93 before and after polymer coating. As

observed from the image ME93 is highly hydrophobic and insoluble in water, however after polymer coating it became hydrophilic and stable in water.

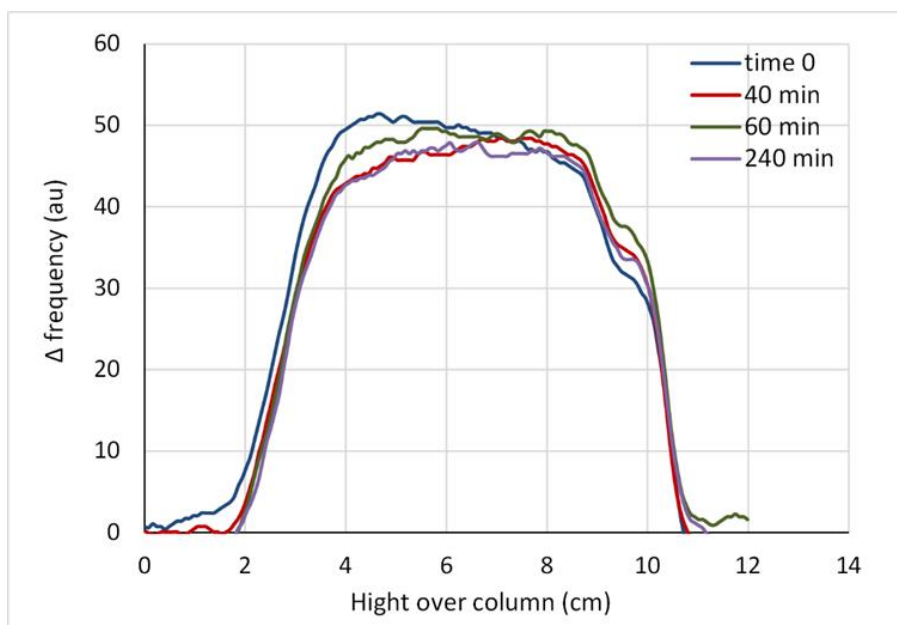


Figure 3-42. SCM profile of PEG-PCL capped silica coated nanoparticles (ME93-PEG-PCL)

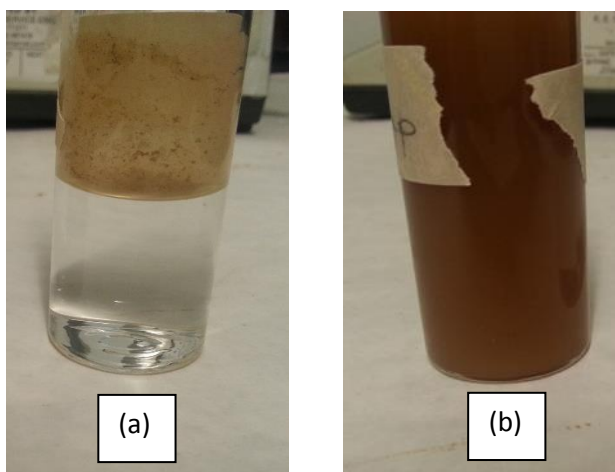


Figure 3-43. Images of ME93, (a) before polymer coating, and (b) after polymer coating (ME93-PEG-PCL)

Figure 3-44 presents the SCM profile for liposome coated magnetite (magnetoliposomes) over the period of 30 hours. The SCM profile demonstrates that the liposome coated magnetite nanocomposites suspension generated only a slight frequency change over a long period of time (over 30 hours). This confirms the stability of the sample compared to bare magnetite (see Figure 3-36).

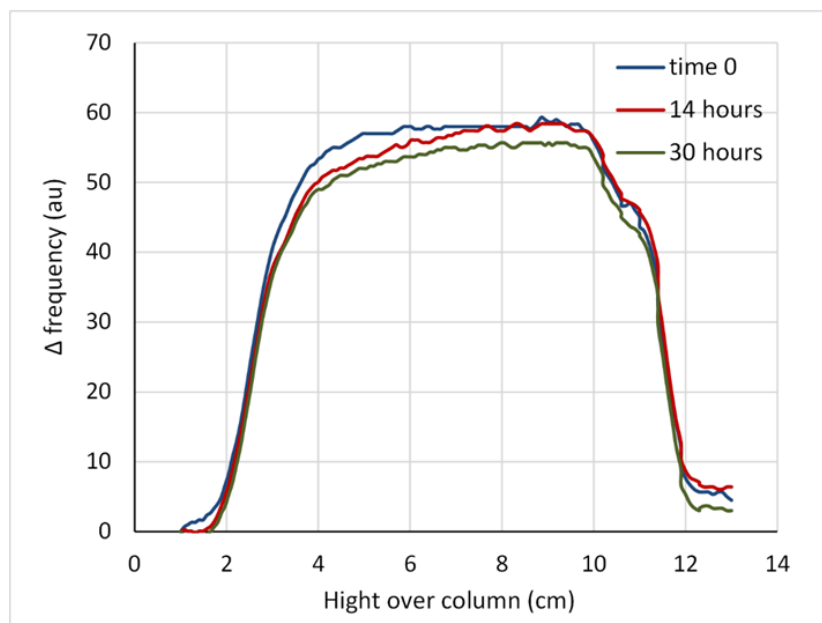


Figure 3-44. SCM plot for liposome coated magnetite (magnetoliposomes-ME09)

Figure 3-45 presents the SCM profile for ME60-L (protocells) over the period of 4 hours. The plot shows no obvious changes in the profile over time which indicates that the material was stable over the measurement period and that there was no sedimentation in the column. The step observed in the SCM plot for other materials was not observed here which could be associated with homogenous monodisperse nanoparticle suspension with no separation of the aqueous media on top of the column. The results shows that liposome coating of the silica coated magnetic nanoparticles could effectively increase the stability of the silica coated nanoparticles.

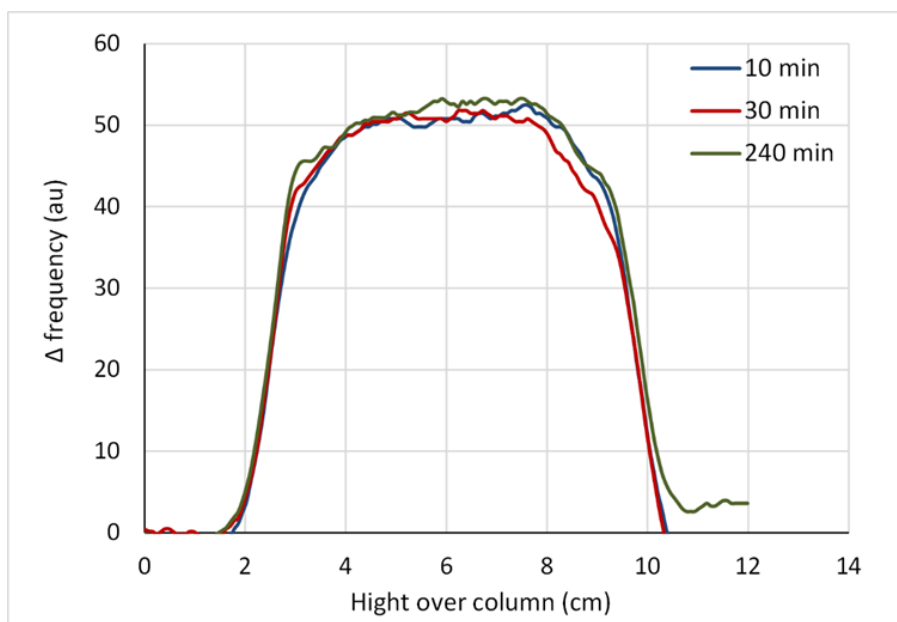


Figure 3-45. SCM profile of the liposome capped silica nanoparticles (protocells-ME60-L)

3.9 Dynamic Light Scattering (DLS)

Dynamic light scattering (DLS) was used to measure the hydrodynamic size of the nanoparticles. The measurements performed using a Zetasizer as described in Section 2.32.4. Since this measurement technique requires a completely stable sample during measurements and diffusion be the only cause of motion in the sample (Kätzel, 2007), the samples which were less stable (i.e. bare magnetite nanoparticles) and show sedimentation could not be characterized using this method. Auto-Correlation Function (ACF) and the polydispersity index were checked to confirm the accuracy of data. Data with y-intercept higher than 0.8 and PDI values lower than 0.7 (based on ISO13321) was considered acceptable (Malvern, 2011, Kätzel, 2007). Samples with lower intercepts were diluted to reduce the multiple scattering, and the particles size were measured again. Additionally Malvern Zetasizer's software includes a built in function which evaluates a number of different parameters to determine the confidence in the reliability of the data (nanoComposix, 2012). As advised by ISO 13321, the Z-Average size (harmonic intensity averaged particle diameter) was reported as average size of the nanoparticles (Malvern, 2011).

Figure 3-46 shows the DLS determined hydrodynamic number average size distributions of oleic acid functionalized magnetite nanoparticles. The average hydrodynamic diameter of the particles was determined to be 15 nm with a polydispersity (PDI) index of 0.27. The particles size measured using DLS were slightly higher than the size measured from TEM images.

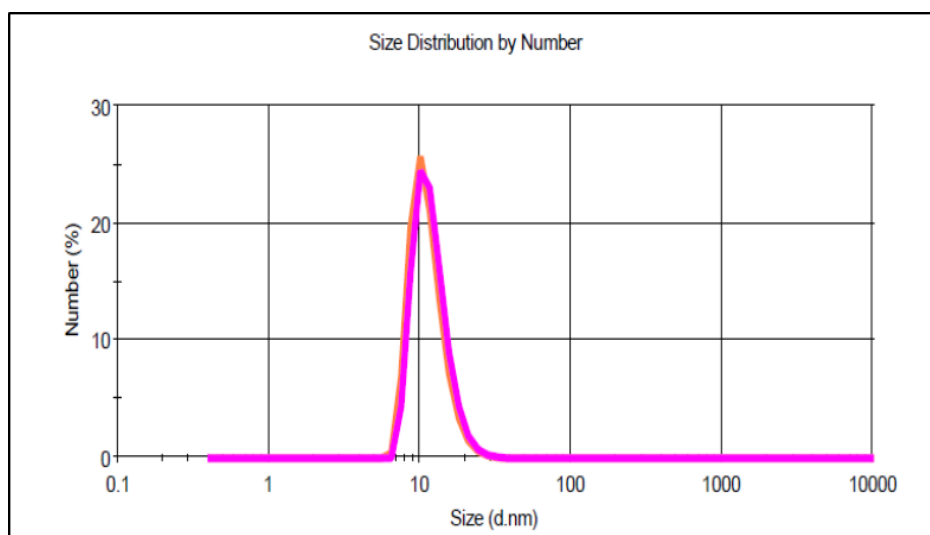


Figure 3-46. DLS size distribution profile of oleic acid functionalised magnetite nanoparticles (ME55)

Figure 3-47 shows the hydrodynamic number average size distributions of the magnetoliposomes after 12 minutes of sonication and before drug loading. The average hydrodynamic diameter of the particles was determined to be 104 nm with a polydispersity (PDI) index of 0.27. The peaks observed were at 68.4 and 198 nm with volume weighted percentage of 89.3 and 10.7%. The initial size of the magnetoliposomes before sonication was measured to be around 1685 nm with PDI of 0.47. The results indicates the effect of sonication time on the size distribution of the

magnetoliposomes. It was observed increasing the sonication periods more than 12 minutes did not affect the particles size. Similarly Cintra *et al.* have reported magnetoliposomes with initial size of 1000 nm and polydispersity of 0.891, changed to particles with sizes ranging from of 30 to 300 nm with PDI reduced to 0.266 after 10 minutes of sonication (Cintra et al., 2009b).

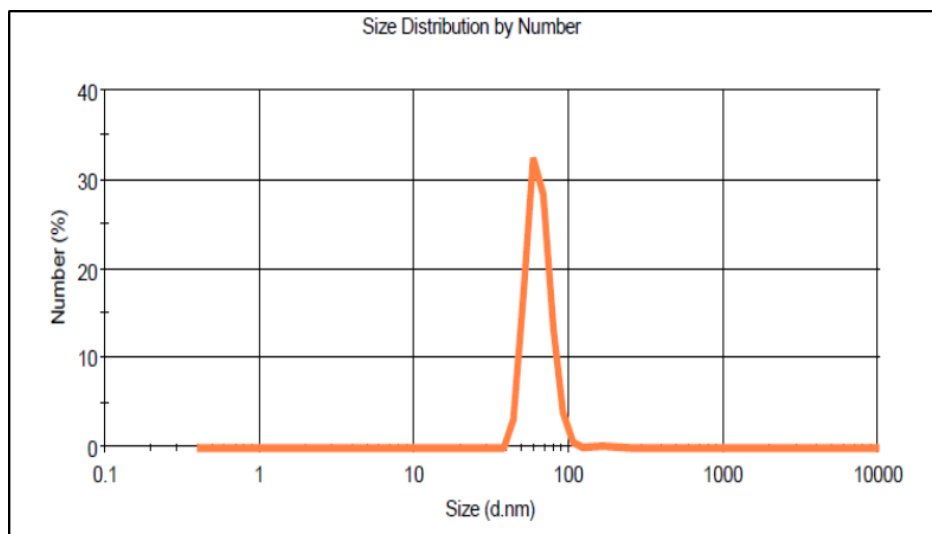


Figure 3-47. DLS size distribution profile of magnetoliposomes (ME09)

Figure 3-48 shows the size distribution of the magnetoliposomes after drug loading (MMC loaded magnetoliposomes). It was observed that the average particle size was slightly increased after drug loading to be 134 nm and the peaks were observed to move to higher values of 77.97 and 251 nm. The polydispersity index was 0.267. The standard deviation in the sample could be calculated from the PDI and average size diameter based on

$$\sigma = \sqrt{PDI \times d^2} \quad \text{Equation 3-10}$$

Where d is the Z-average diameter of the nanoparticles. The standard deviation was calculated to be 69.2 for drug-loaded magnetoliposomes.

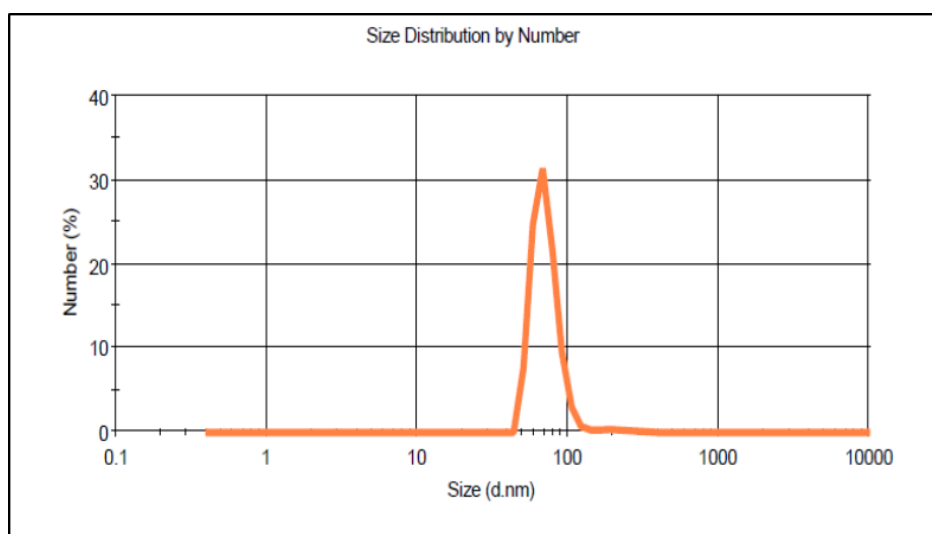


Figure 3-48. DLS size distribution profile of MMC loaded magnetoliposomes

Figure 3-49 presents the hydrodynamic number average size distributions of the PEG-PCL micelles after sonication. The average hydrodynamic diameter of the particles was determined to be 60.34 nm and the PDI index was 0.36.

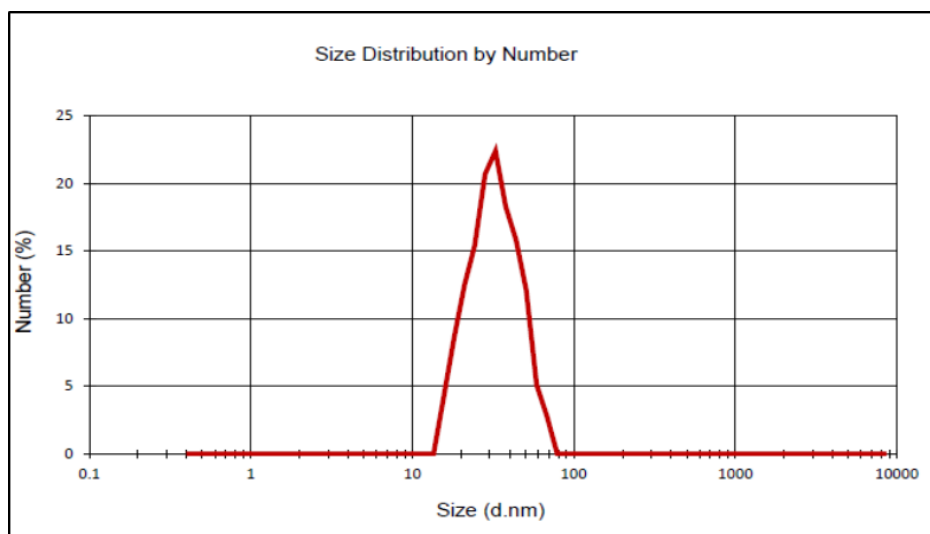


Figure 3-49. DLS size distribution profile of PEG-PCL micelles

Figure 3-50 presents the hydrodynamic number average size distributions of the PEG-PCL coated magnetite after sonication and before drug loading. The average hydrodynamic diameter of the particles was determined to be 76.34 nm and the PDI index was 0.6. The peaks observed were at 76.34 and 1124 nm with number percentage of 99.4 and 0.6%. Since the polydispersity index is larger than 0.3, and more than 90% of the %Number data are observed to be in same peak, the mean number distribution data were used instead of the Z-Average cumulants fit (nanoComposix, 2012).

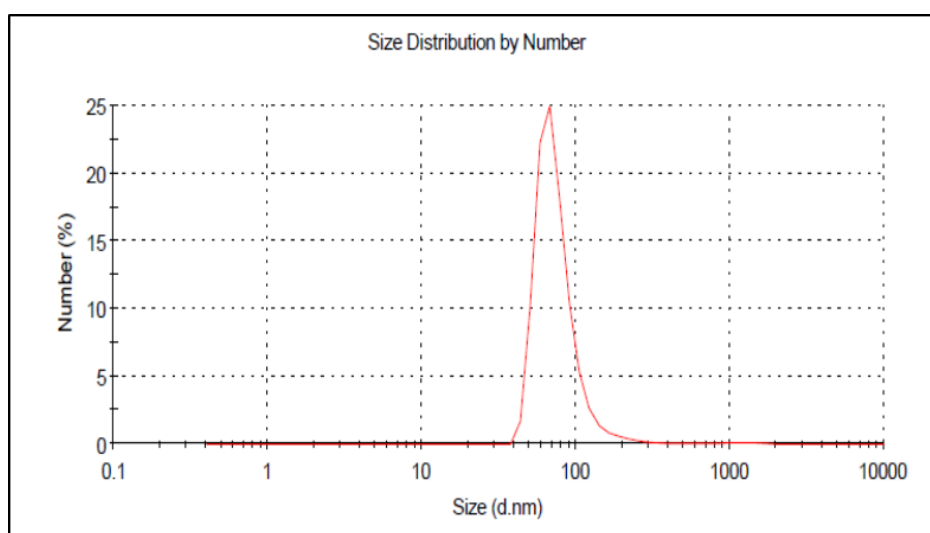


Figure 3-50. DLS size distribution profile of PEG-PCL coated magnetite nanoparticles (ME55-PEG-PCL)

Figure 3-51 presents the hydrodynamic number average size distributions of the PEG-PCL coated magnetite after drug loading (drug loaded ME55-PEG-PCL). As presented in Figure 3-51, similar to magnetoliposomes the average particle size of the polymer coated magnetite nanoparticles were

increased after drug loading. The average particles size was measured to be 106 nm with PDI index of 0.27. The increase in micelle size after drug loading is in agreement with the reported literature (Cuong et al., 2012, Mohan and Rapoport, 2010). The increase in the micelle size after drug loading could be associated to the interactions of hydrophobic DOX molecules, hydrophobic magnetite core, and hydrophobic PCL segment of the micelles (Cuong et al., 2012).

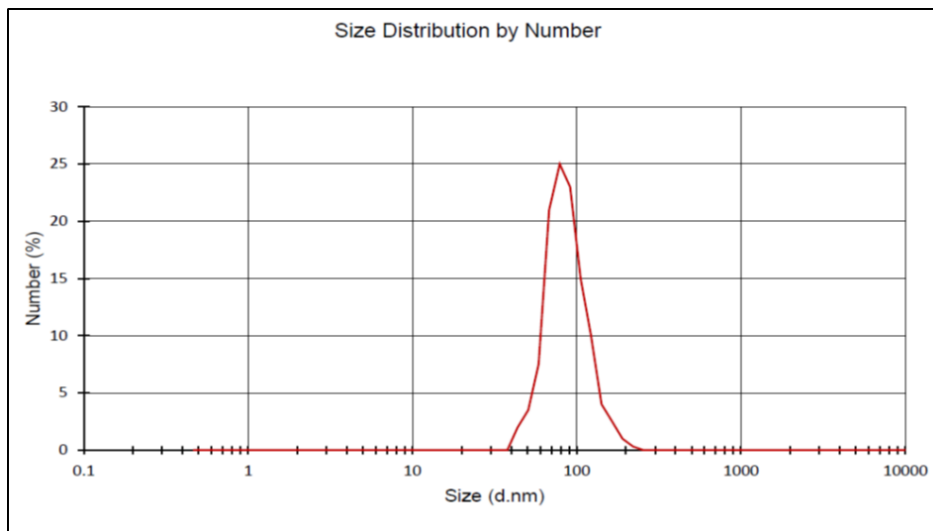


Figure 3-51. DLS size distribution profile of DOX loaded PEG-PCL coated magnetite nanoparticles (ME55-PEG-PCL)

Figure 3-52 shows the hydrodynamic number average size distributions of the PEG-PCL capped silica coated nanoparticles (ME93-PEG-PCL) before drug loading. The average hydrodynamic diameter of the particles was determined to be 165 nm with a polydispersity (PDI) index of 0.28. The hydrophobic silica nanoparticles before polymer coatings were water insoluble therefore it is not possible to measure their hydrodynamic size however their size was measured using TEM to be 100 nm. From the DLS measurements and the TEM images the thickness of the PEG-PCL layer is determined to be around 32.5 nm. similarly an increase in the size of the nanoparticles (45 nm thickness) was reported by Liu *et al.* for PEGylated silica nanoparticles (Liu et al., 2014a).

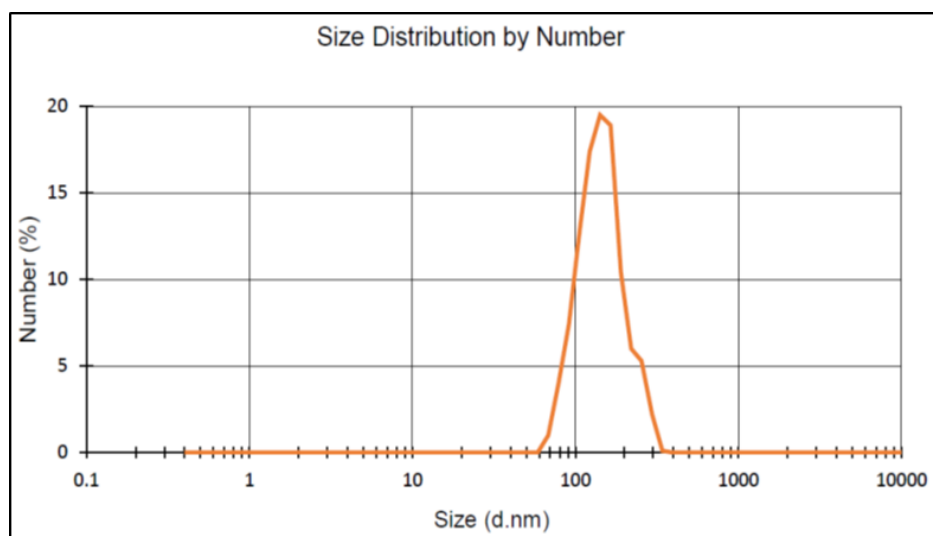


Figure 3-52. DLS size distribution profile of PEG-PCL capped silica coated magnetite nanoparticles (ME93-PEG-PCL)

Figure 3-53 presents the size distribution of the ME93-PEG-PCL after drug loading (DOX loaded PEG-PCL capped silica coated nanoparticles). It was observed that the average particle size was slightly increased after drug loading to be 170 nm. A very small increase in PEG-PCL micelles size after DOX loading is in agreement with reported literature (Shuai et al., 2004, Sanson et al., 2010).

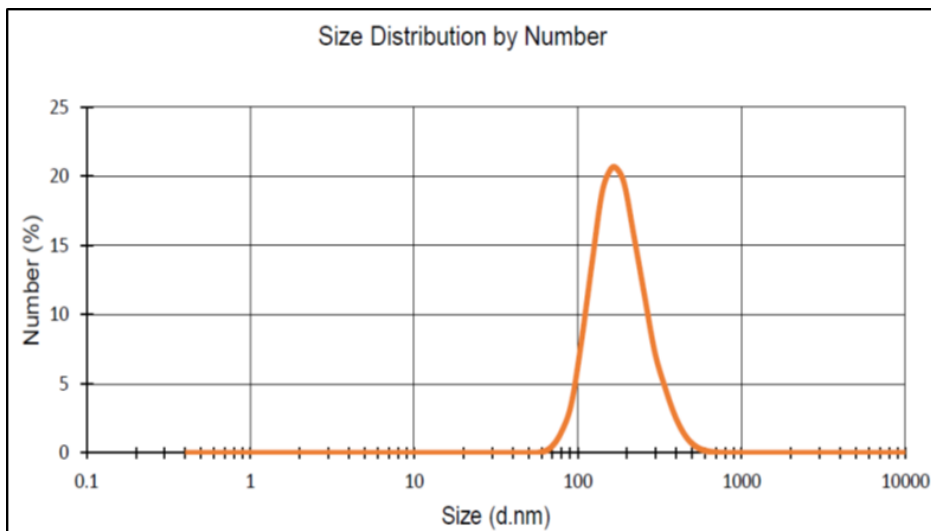


Figure 3-53. DLS size distribution profile of DOX loaded PEG-PCL capped silica coated magnetite nanoparticles (DOX loaded 93-PEG-PCL)

Figure 3-54 presents the hydrodynamic number average size distributions of the protocells (ME60-L) before drug loading. The average hydrodynamic diameter of the particles was determined to be 147 nm with a polydispersity (PDI) index of 0.32. The average particle size were slightly increased after drug loading to be 150 nm. The TEM images of the ME60 shows that the size of the core particles were around 80 nm.

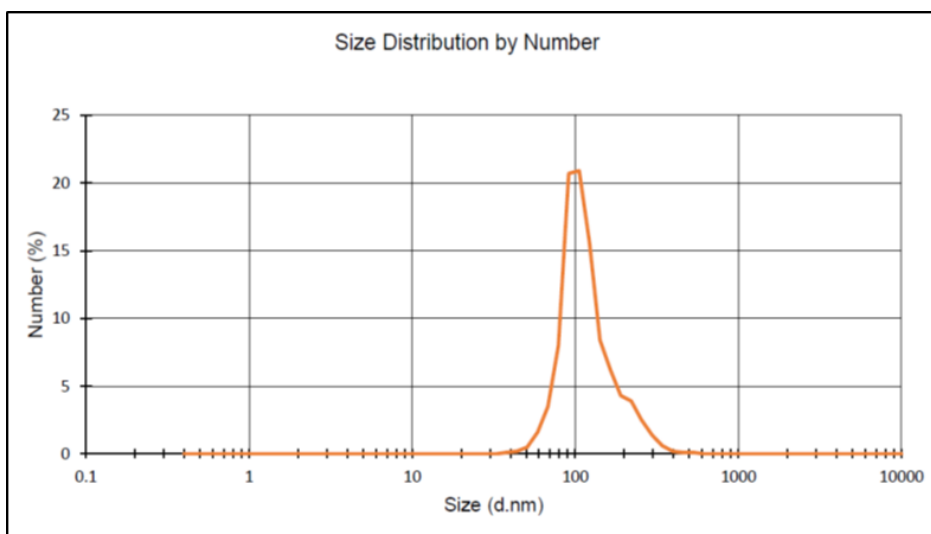


Figure 3-54. DLS size distribution profile of liposome capped silica coated magnetite nanoparticles (protocells-ME60-L)

3.10 Differential Scanning Calorimetry (DSC)

Differential scanning calorimetry (DSC) was used to characterize the thermal properties of the block polymers. The sample were prepared and measurements performed according to methods explained in Section 2.32.6.

Figure 3-55 and Figure 3-56 present the DSC thermograms of the PEG-PCL diblock copolymer. The sample were initially heated to 60°C to erase the previous thermal history and cooled to -20°C and reheated to 60°C.

The melting temperature (T_m) and the crystallisation temperature (T_c) of the copolymer was observed from the DSC curves. The PEG-PCL polymer exhibited a crystallisation exotherm at around 32.1°C and a two melting endotherm at 35.7°C and 44.8°C. Occurrence of more than one melting peak for PEG-PCL dilocks is in agreement with the literature (Glover et al., 2012, Sosnik and Cohn, 2003). Both the melting temperature and crystallization temperature of the copolymer is lower than the melting temperature and crystallization temperature for PCL which could be associated with the PEG in the diblock molecule and indicates that the PEG-PCL diblock copolymer is formed (Glover et al., 2012, Sosnik and Cohn, 2003). The crystallisation temperature is higher than reported T_c for PEG segment which suggests that the PEG chain in the copolymer was unable to crystallise (Sosnik and Cohn, 2003). The melting temperature of the material proved its potential to be used in hyperthermia applications.

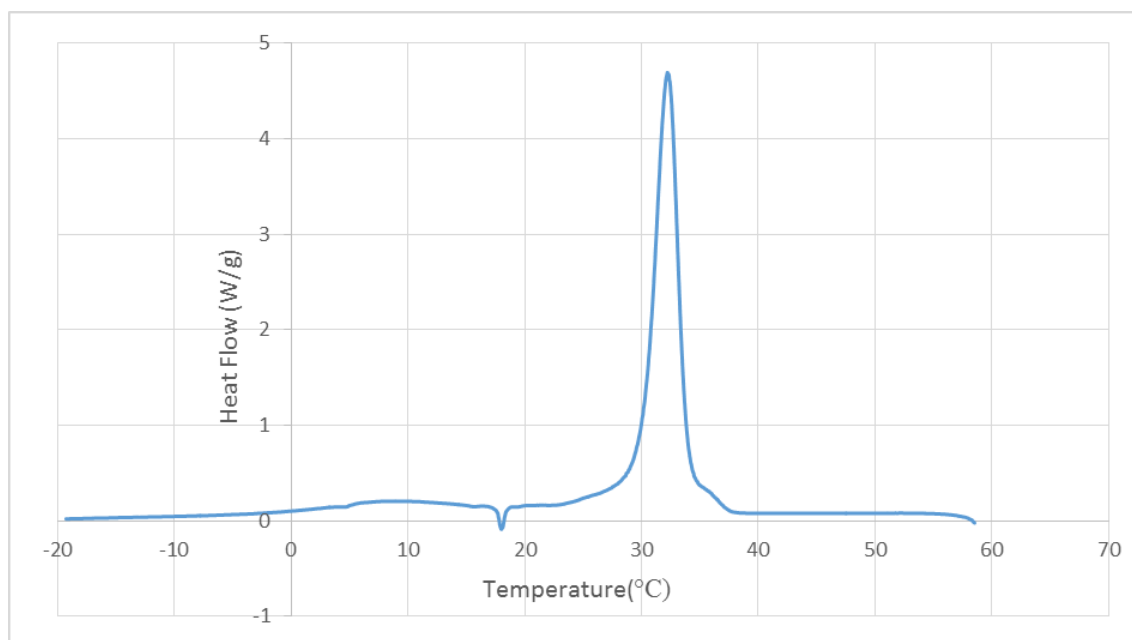


Figure 3-55. DSC thermograms of cooling stage of PEG-PCL micelles.

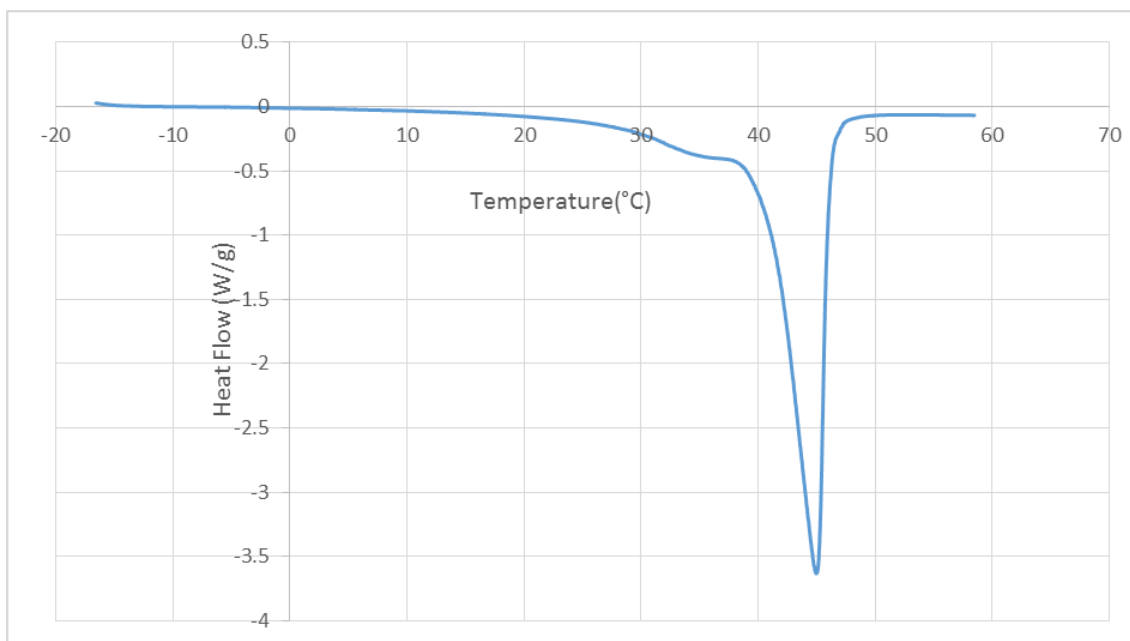


Figure 3-56. DSC thermograms of heating stage of PEG-PCL micelles

3.11 Contact Angle Measurements

Contact angle measurements were performed to measure the hydrophobicity of the nanoparticles. The samples were prepared and measurements were performed according to methods described in Section 2.32.8. Contact angle measurement was performed by measuring the angle of a water droplet on the sample surface.

Figure 3-57 shows an image of the water droplet on the silica coated nanoparticles (ME60). The low contact angle indicates that the sample is hydrophilic and water is spread over the top of the sample.

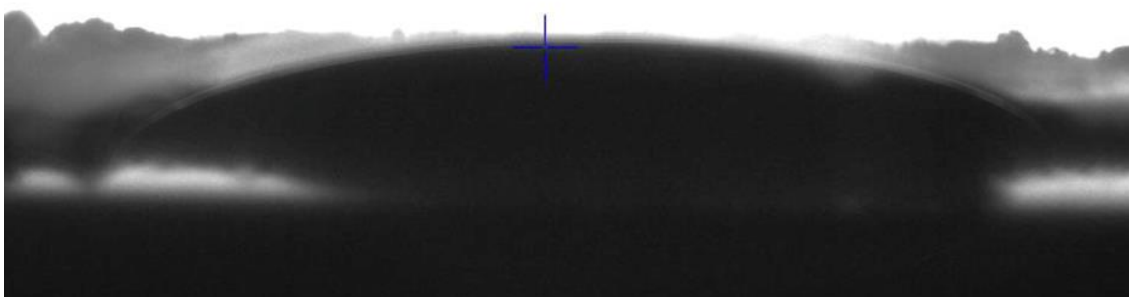


Figure 3-57. Measurement of static contact angle of a water droplet on silica coated nanoparticles (ME60)

Figure 3-58 and Figure 3-59 present the image of the hydrophobic magnetic nanocomposites (ME93 and ME94). From the images it was observed that the contact angle of the water droplet with the nanocomposites (θ) is greater than 90° which indicates that both samples were hydrophobic in nature suggesting the successful surface functionalization of the silica coted

nanoparticles. However, ME93 showed larger contact angle indicating higher hydrophobicity of the sample.



Figure 3-58. Measurement of static contact angle of a water droplet on hydrophobic silica coated nanoparticles (ME94)



Figure 3-59. Measurement of static contact angle of a water droplet on hydrophobic silica coated nanoparticles (ME93)

3.12 Nuclear Magnetic Resonance Spectroscopy (NMR)

Formation of the PEG-PCL diblock copolymer and the degree of polymerization was evaluated using $^1\text{H-NMR}$. The samples for NMR were prepared according to methods described in Section 2.32.13.

Figure 3-60 presents the $^1\text{H-NMR}$ spectra of the PEG-PCL diblock copolymer in deuterated water (D_2O). Since the micelles would not be dissolved in D_2O , it was selected as solvent to determine formation of the micelle. A single peak was observed at $\delta = 3.6 \text{ ppm}$ in $^1\text{H-NMR}$ spectra of the PEG-PCL in D_2O which could be assigned to the segments of PEG (s, 4H, $-\text{OCH}_2\text{CH}_2-$). The absence of the peaks from the PCL segment of the copolymer confirms the formation of micelles as hydrophobic PCL positioned at the core of the micelles which is insoluble in D_2O (Cuong et al., 2012, Cuong et al., 2010a).

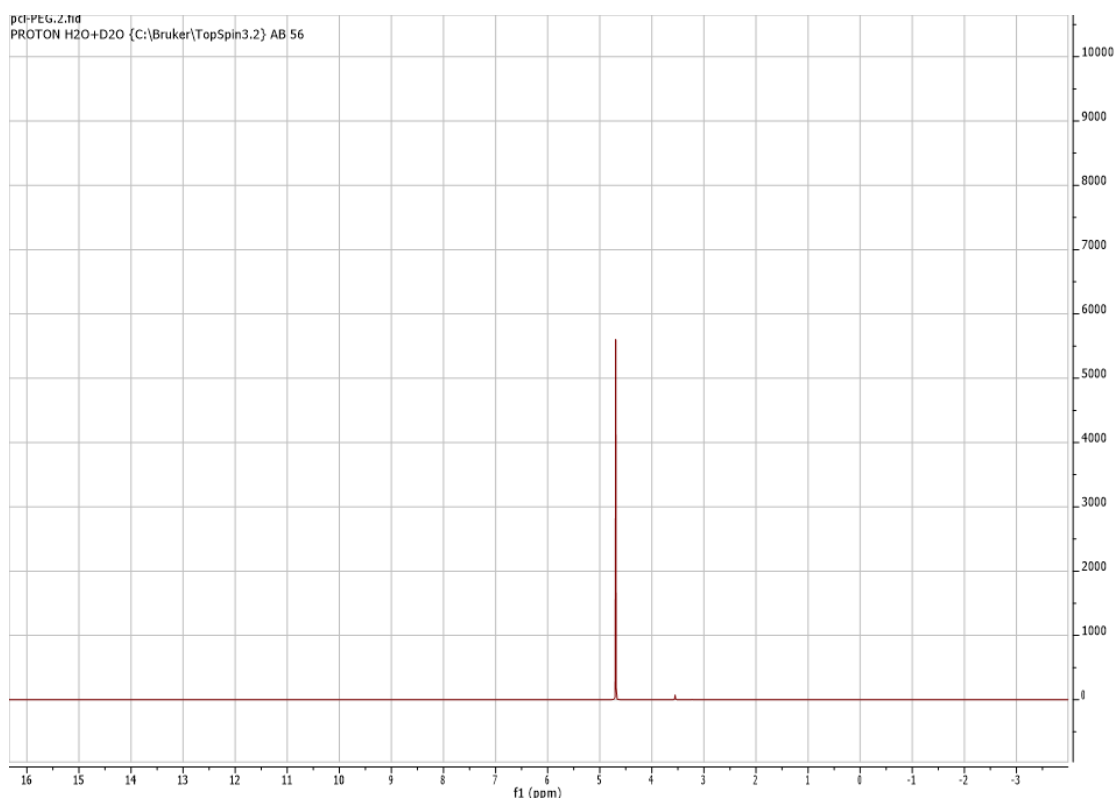


Figure 3-60. $^1\text{H-NMR}$ spectra of PEG-PCL micelle dissolved in two D_2O .

Figure 3-61 presents the $^1\text{H-NMR}$ spectra of the PEG-PCL diblock copolymer in CDCl_3 . The characteristic signals of both PEG and PCL were observed in $^1\text{H-NMR}$ spectra of the PEG-PCL in CDCl_3 . The peaks observed at δ 1.35 (m, 2H, $-\text{OCH}_2\text{CH}_2\text{CH}_2\text{CH}_2\text{CH}_2\text{O}-$), 1.60 (m, 4H, $-\text{OCH}_2\text{CH}_2\text{CH}_2\text{CH}_2\text{CH}_2\text{CH}_2\text{O}-$), 2.27 (t, 2H, $-\text{OCH}_2\text{CH}_2\text{CH}_2\text{CH}_2\text{CH}_2\text{O}$) and 4.02 (t, 2H, $-\text{OCH}_2\text{CH}_2\text{CH}_2\text{CH}_2\text{CH}_2\text{O}-$) are assigned to the PCL unit.

The peaks present at δ 4.19 (t, 2H, $-\text{OCH}_2\text{CH}_2-$) and 3.64 (s, 4H, $-\text{OCH}_2\text{CH}_2-$) in $^1\text{H-NMR}$ spectra are assigned to be the methylene protons from the PEG segment of the diblock copolymer which confirms the formation of the copolymer (Glover et al., 2012, Gao et al., 2013, Gou et al., 2008, Khoee et al., 2015). The peak observed at δ 3.38 (m, 3H, $-\text{OCH}_3-$) is assigned to PEG end terminal of the copolymer (Hong et al., 2012, Cuong et al., 2012).

The ratio of the PEG/PCL is calculated based on integration of the PEG peak at δ 4.19 ppm and the PCL peak at δ 4.02 ppm. The ratio of the PCL to PEG segment in the diblock copolymer was calculated to be 92% PCL to 8% PEG.

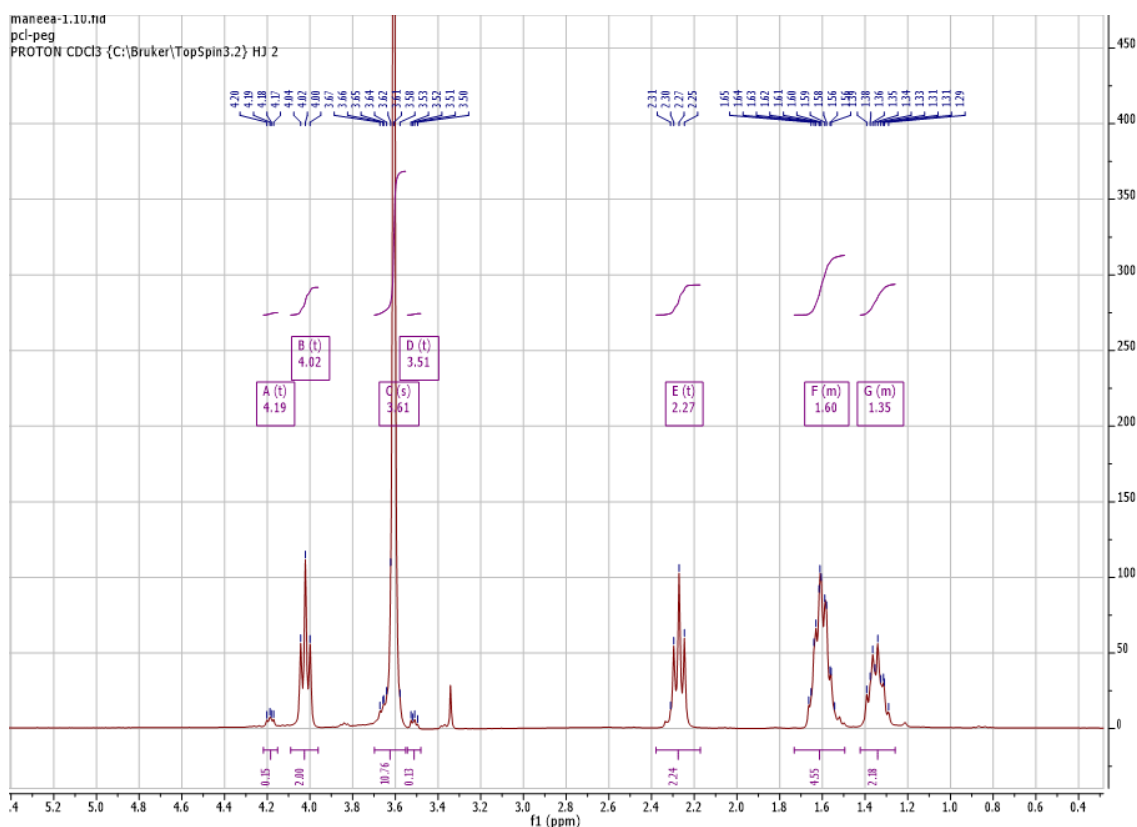


Figure 3-61. $^1\text{H-NMR}$ spectra of PEG-PCL dissolved in CDCl_3 .

3.13 Fourier Transform Infrared (FTIR) Spectroscopy

Fourier transform infrared (FTIR) spectroscopy was used to study the chemical structures, bonds and functional groups of synthesised nanoparticles. The samples were prepared as explained in Section 2.32.10.

Figure 3-62 and Figure 3-63 present the FTIR spectra of the bare and oleic acid coated magnetite nanoparticles. The peaks observed at 576 cm^{-1} and 439 cm^{-1} were assigned to the Fe–O bond of Fe_3O_4 nanoparticles and the peaks observed at 3409 cm^{-1} were assigned to O–H, bending vibration and stretching vibration, respectively (Ma et al., 2003, Chen et al., 2009b).

Similarly the peaks observed in Figure 3-63 at 578 cm^{-1} and 444 cm^{-1} were assigned to be due to presence of Fe–O bond of Fe_3O_4 nanoparticles and peaks at 3409 cm^{-1} were assigned to be due to stretching vibration of OH groups. The additional strong absorption peaks observed at 2852 and 2923 cm^{-1} were assigned to symmetric and asymmetric stretching of C–H bonds in the oleyl chains (Lu et al., 2012, Ma et al., 2003).

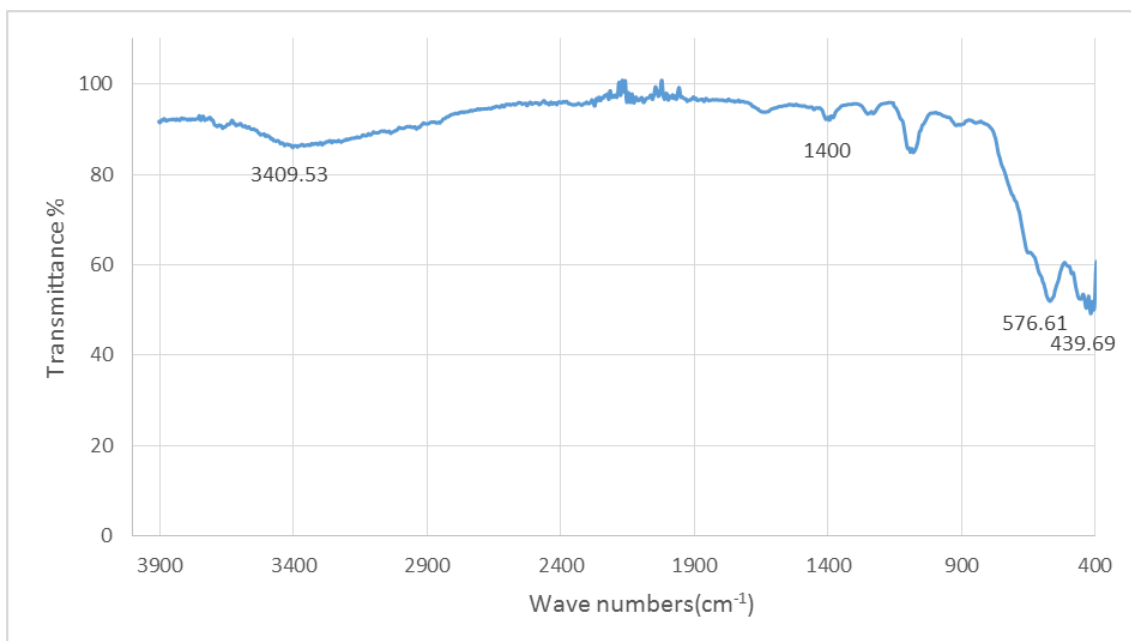


Figure 3-62. FTIR spectrum of magnetite nanoparticles (ME18)

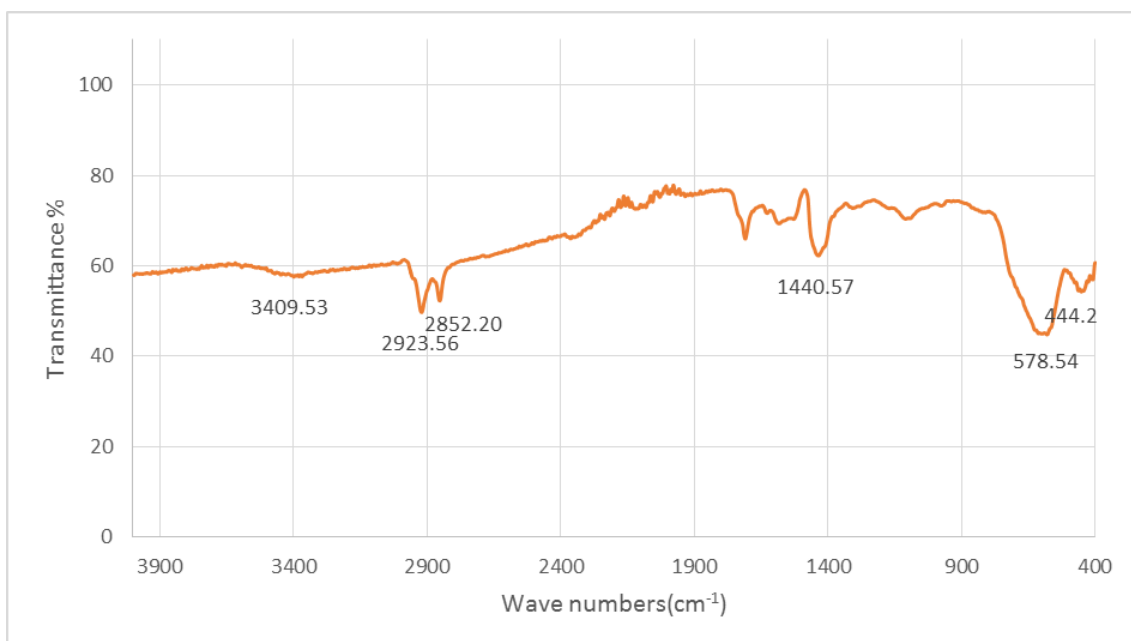


Figure 3-63. FTIR spectrum of Oleic acid coated magnetite nanoparticles (ME55)

Figure 3-64 presents the FTIR spectra of the silica coated magnetite nanoparticles (ME60). The peaks observed at 443 cm^{-1} , 798 cm^{-1} , 1052 cm^{-1} were assigned to Si–O bending, Si–O–Si bending and Si–O–Si stretching, respectively (Zou et al., 2014). The broad high intensity peak at 1052 cm^{-1} could be due to asymmetric stretching of Si–O–Si, while the peak at 798 cm^{-1} is associated with Si–O–Si symmetric stretch. The peak at 958 cm^{-1} was assigned to the Si–O symmetric stretch (Chen et al., 2009b).

The peak observed at 570 cm^{-1} was assigned to vibration of Fe–O bond of core particles (Zou et al., 2014) which compared to bare magnetite nanoparticles the intensity of the peak is lowered. The FTIR spectrum indicates the successful silica coating of the magnetite nanoparticles.

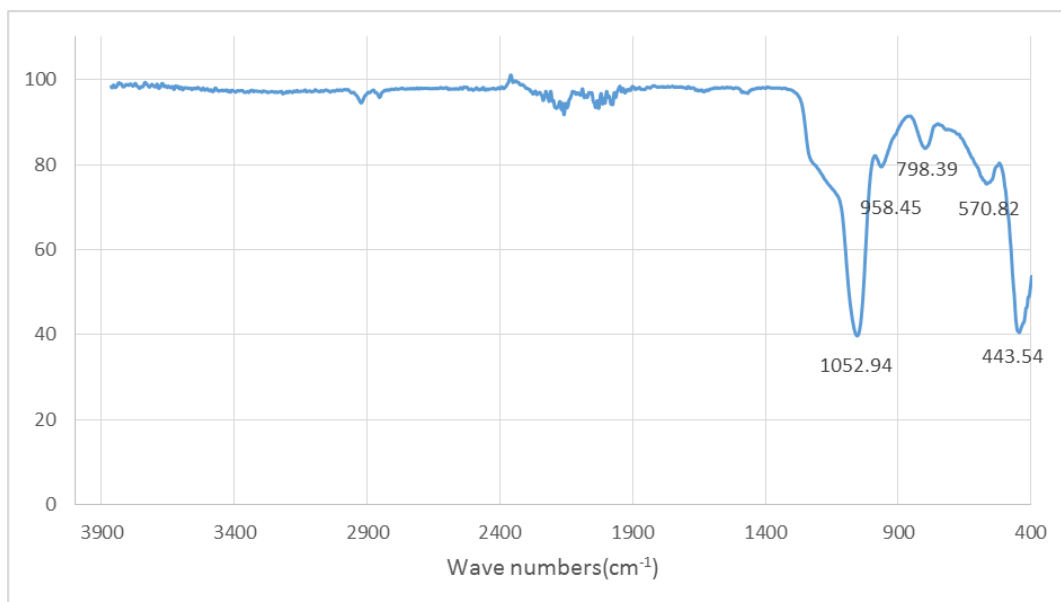


Figure 3-64. FTIR spectrum of silica coated magnetite nanoparticles (ME60)

Figure 3-65 presents the FTIR spectra of the PEG-PCL diblock copolymer. Presence of the characteristics peaks of both PEG and PCL in the FTIR spectrum indicates that the PEG-PCL copolymer was formed. The absorption band appeared at 1722 cm^{-1} was attributed to the C=O stretching bond of the PCL ester carbonyl group, and the absorption band at 1240 cm^{-1} was attributed to the -COO- stretching bond. The peak appeared at 1103 cm^{-1} was attributed to C-O etheric bond. The peaks observed at 2985 cm^{-1} and 2862 cm^{-1} were assigned to C-H stretching bonds. The wide absorption band in the 3485 cm^{-1} was assigned to terminal OH groups (Khoee et al., 2015, Danafar et al., 2014, Zhou et al., 2003).

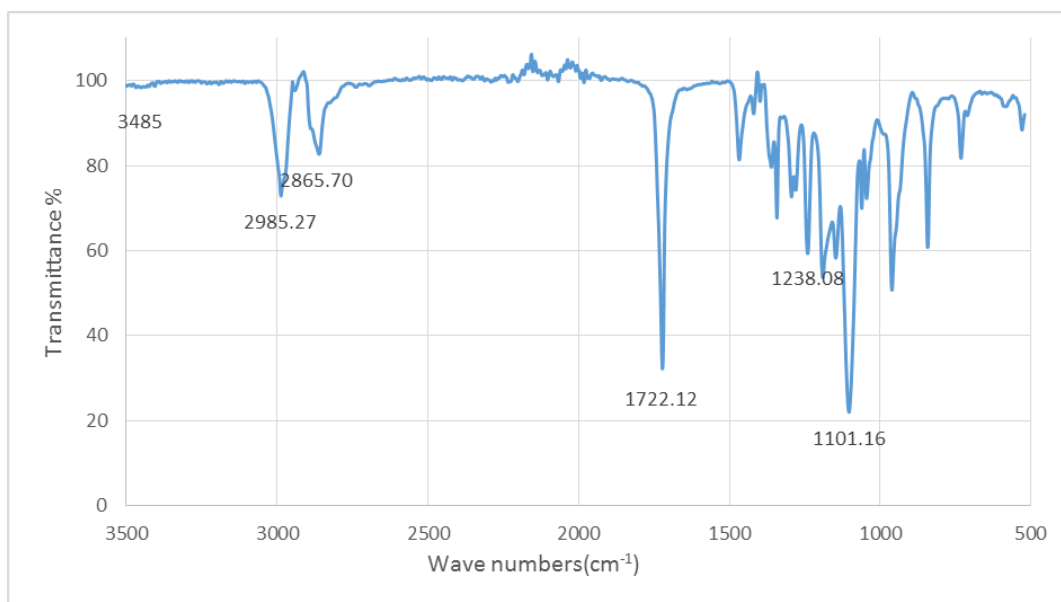


Figure 3-65. FTIR spectrum of PEG-PCL diblock copolymer

Figure 3-66 presents the FTIR spectra of PEG-PCL magnetic micelles. All the peaks from the PEG-PCL copolymer were observed in the FTIR spectra. The additional peak at 580 cm^{-1} is attributed to the Fe-O indicating the presence of the magnetite nanoparticles.

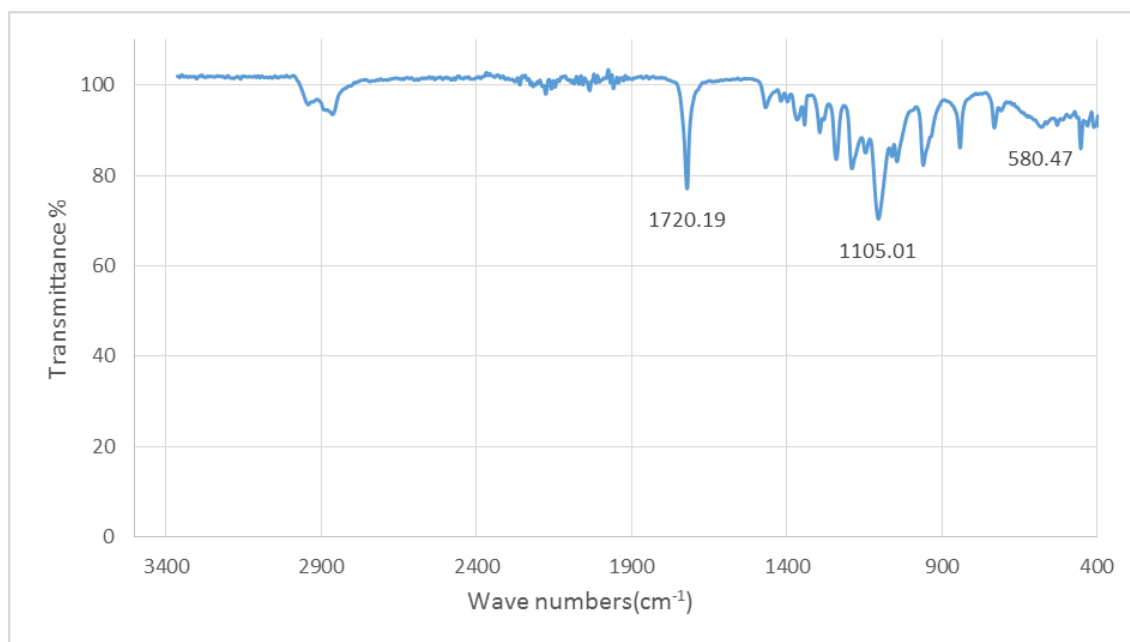


Figure 3-66. FTIR spectrum of PEG-PCL coated magnetite nanoparticles (ME55-PEG-PCL)

Figure 3-67 presents the FTIR spectra of PEG-PCL capped silica coated magnetic nanoparticles (ME93-PEG-PCL). The absorption band observed at 1722 cm^{-1} was attributed to C=O stretching bond of the PCL segment of the copolymer. The broad peak observed between 1050 cm^{-1} and 1200 cm^{-1} was attributed to the overlay of the C-O from the polymer and the Si-O-Si stretching of the silica shell of the nanoparticles. The peak appeared at 1238 cm^{-1} was attributed to the -COO- stretching bond. The peaks observed at 453 cm^{-1} and 809 cm^{-1} were assigned to Si-O bending, Si-O-Si bending, respectively (Zou et al., 2014). The peaks observed at 2900 cm^{-1} and 2987 cm^{-1} were assigned to C-H stretching bonds. The peak observed at 578 cm^{-1} was assigned to the Fe-O bond of core nanoparticles. The presence of the characteristic peaks of both silica coated magnetite core-shell nanoparticles and the copolymer, indicates the successful coating of the polymer over the nanoparticles.

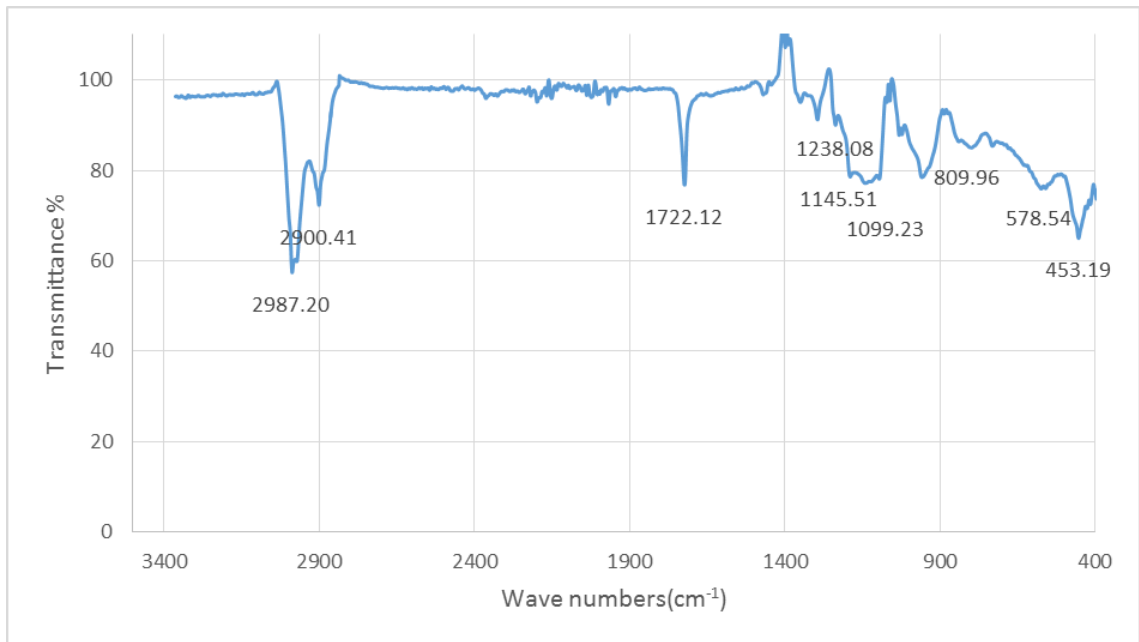


Figure 3-67. FTIR spectrum of PEG-PCL capped silica coated magnetite nanoparticles (ME93-PEG-PCL)

3.14 Magnetic Heating Properties of the Nanoparticles

Magnetic nanoparticles with various diameters and structure were prepared and characterised as explained in Chapter 2. The magnetic heating of the nanoparticles will be discussed in this Section. For application of the nanoparticles in magnetic inductive hyperthermia (MIH) the heating efficiency of the nanoparticles should be optimized.

For nanoparticles to be suitable for hyperthermia applications a relatively small amount of nanoparticles under specific magnetic field could be able to rise the temperature. Hyperthermia is a well-known clinical procedure in which temperature of the tumor tissue is raised from the physiological temperature (37 °C) to temperatures up to 46 °C or higher to kill the tumor cells.

As described before in case of superparamagnetic nanoparticles relaxation mechanisms are the main sources of power loss.

3.14.1 Neel and Brownian relaxation

The power loss corresponding to Néel and Brown relaxation can be calculated from Equation 3-11.

$$P = \frac{(mH\omega\tau)^2}{2\tau kT\rho V (1+\omega^2\tau^2)} \quad \text{Equation 3-11}$$

Where m is the particle magnetic moment, τ is the magnetic relaxation time, ω is the measurement angular frequency, ρ the density of magnetic nanoparticles and H is the field intensity amplitude. The effective relaxation time is given by

$$\frac{1}{\tau} = \frac{1}{\tau_B} + \frac{1}{\tau_N} \quad \text{Equation 3-12}$$

Where τ_B is The Brownian relaxation time and τ_N is the Neel relaxation time calculated from Equation 3-13 and Equation 3-14, respectively.

$$\tau_B = \frac{4\pi\eta r^3}{kT} \quad \text{Equation 3-13}$$

$$\tau_N = \tau_0 \exp \frac{KV}{kT} \quad \text{Equation 3-14}$$

Where η is the viscosity coefficient of the fluid, r is the hydrodynamic radius of the particle, k is the Boltzmann's constant, τ_0 is the time constant, V is the particle volume, and K is the magnetocrystalline anisotropy energy density. The variables used in the above equations are summarized in Table 3-5.

Table 3-5. Variables used in power loss calculations

Parameters	Values
f	406 kHz
ω	255×10^4 /s
ρ	5170 kg/m ³
k	$1.3806488 \times 10^{-23}$ m ² kg/ s ² K
H	15.89 kA/m
K	1.35×10^4 J/m ³
T	293 K
τ_0	10×10^{-9} s
η	10^{-3}

In Equation 3-11 the measurement frequency defines the so called critical particle volume for which $\omega\tau = 1$ and P will reach maximum value. Measuring frequency of 406 kHz, $\omega = 255 \times 10^4$ in room temperature (20° C) were used in this study which leads to calculated particle size of 15.0 nm for $\omega\tau_N = 1$ and maximum power loss corresponding to Néel relaxation.

For magnetite nanoparticles (ME18) with the average particle size of 13 nm from the TEM images, the τ_N and $\omega\tau_N$ where calculated to be 4.64×10^{-8} s and 0.11, respectively. In comparison for ME59 with the particle size of 8 nm the τ_N and $\omega\tau_N$ where calculated to be 2.44×10^{-9} s and $0.006 \ll 1$. These results indicate that the Neel loss for ME59 is comparatively lower than that of ME18 in the same applied frequency.

From the Equation 3-13 the particle size, which makes $\omega\tau_B = 1$ and therefore $P_{Brownian}$ reach a maximum was calculated to be around 10 nm. The $\omega\tau_B$ for ME59 was calculated to be 0.5 which

is much higher than $\omega\tau_N$ of the same nanoparticles, indicating that the heat produced by ME59 is mostly due to Brownian motion.

As observed from the magnetization curves and the power loss calculation the homogenous narrow size distributed magnetite nanoparticles synthesised by thermal decomposition method did not exhibit high power loss in the measurement frequencies and therefore they were not used further in hyperthermia applications.

3.14.2 Specific Power Absorption (SPA)

The nanoparticles efficiency to generate heat from the magnetic coupling between the magnetic moment of nanoparticles and the applied alternate magnetic field could be assessed from specific power absorption (SPA) calculations (also known as specific power losses SPL), which is the power absorbed per unit mass of magnetic nanoparticles.

The correlation between the magnetic parameters of the nanoparticles and their efficiency for power absorption magnetization could be evaluated from magnetic hysteresis curves. Magnetic hysteresis measurements were performed using a vibrating sample magnetometer (VSM) as described in Section 3.7. Hysteresis losses of the particles, coercivity (H_c) and saturation magnetization (M_s) values were determined from magnetisation curves at room temperature.

As illustrated in the magnetization curves the nanoparticles were superparamagnetic at room temperature. The calculated saturation magnetizations of sample shown in Table 3-4. The saturation magnetization (M_s) of the synthesised nanoparticles are in agreement with the literature reported values for magnetite particles of similar size and coatings (Gonzalez-Fernandez et al., 2009).

In order to develop direct measure of magnetic heat generated by the nanoparticles, time dependent calorimetric measurements were performed. The measurements were achieved by determining the ratio of temperature increase in the ferrofluid placed in the centre of a coil. The coil generates a maximum AC-magnetic field of 15.8 kA/m at a frequency of 406 kHz. Magnetic induction heating experiments were performed using DM100 and DM2 as described in previous chapters. Temperature data was collected using a fibre optic temperature probe.

Figure 3-68 shows the time and field dependent temperature curve of ME18 under the AC magnetic field irradiation. The magnetic field was varied to keep the maximum temperature at 55°C. The maximum field was 200 G and the frequency was set as constant 406 kHz.

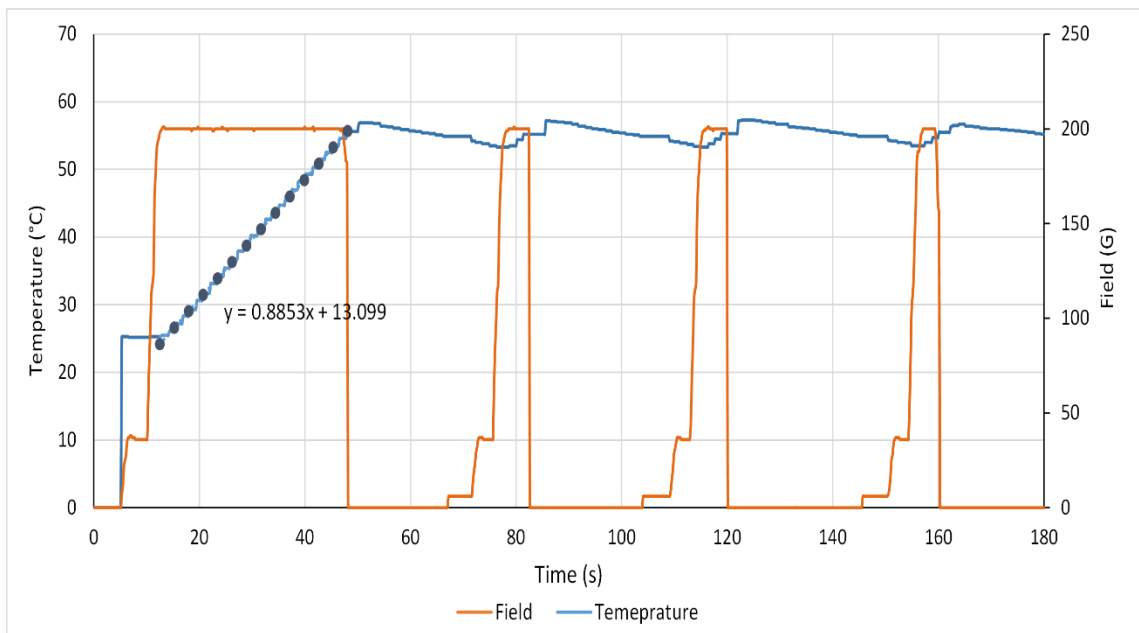


Figure 3-68. Time and field dependent temperature curve of ME18 under the AC magnetic field irradiation

Figure 3-69 shows the time and field dependent temperature curve of ME55 under the AC magnetic field irradiation.

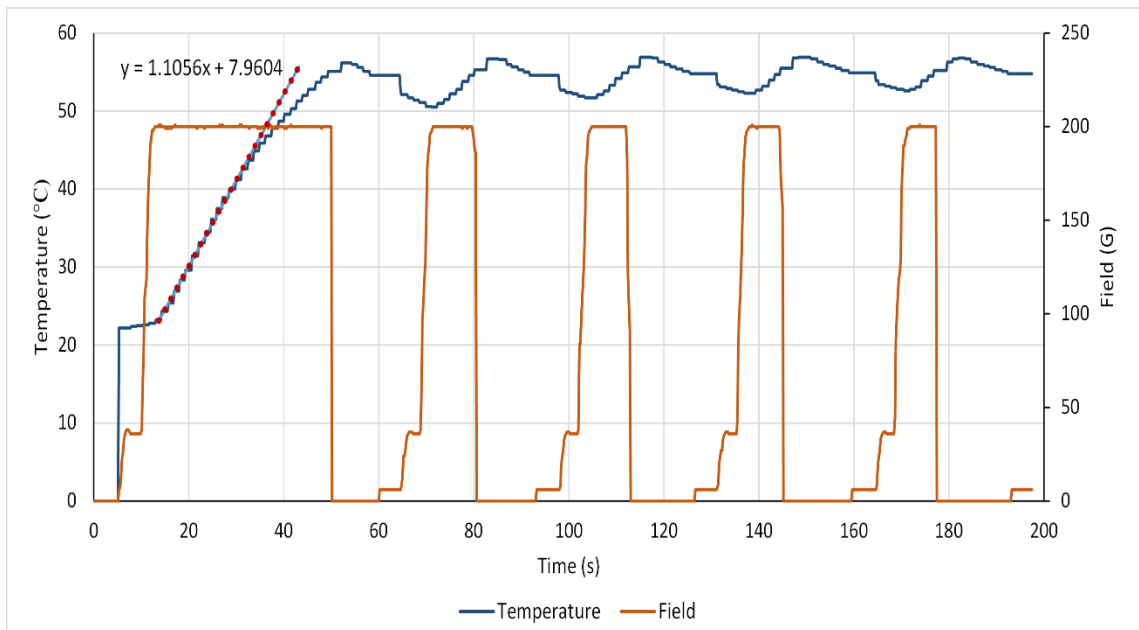


Figure 3-69. Time and field dependent temperature curve of ME55 under the AC magnetic field irradiation.

Figure 3-70 shows the time and field dependent temperature curve of ME33 under the AC magnetic field irradiation. Compare to ME18 and ME55 the temperature increase with lower rate which could be explain by existence of the silica shell on the nanoparticles. However, to compare the heating rate of different samples, the weight of the sample and the heating capacity of the sample should be accounted.

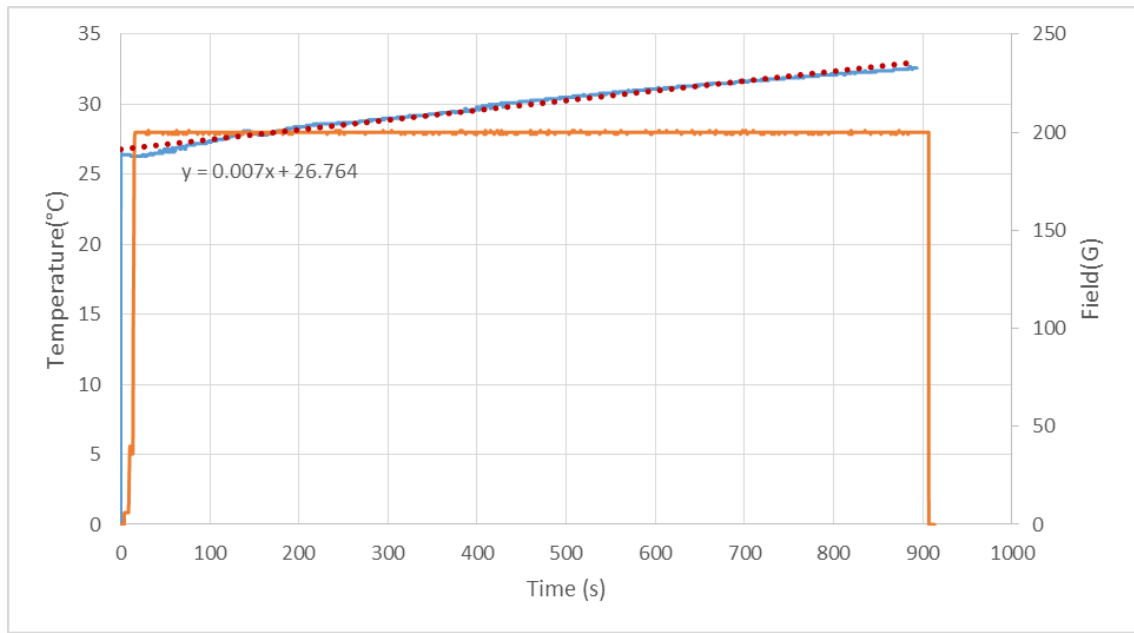


Figure 3-70. Time and field dependent temperature curve of ME33 under the AC magnetic field irradiation.

The SPA (W/g) can be calculated by Equation 3-15 (Motoyama et al., 2008a):

$$SPA = \frac{m_{np}C_{np} + m_s C_s}{m_{np}} \times \frac{\Delta T}{\Delta t} \quad \text{Equation 3-15}$$

Where m_{np} is the mass of the nanoparticles (g), m_s is the mass of the liquid (g), C_{np} is the specific heat of the nanoparticles (j/gK), C_s is the specific heat of the liquid (j/gK), and the $\frac{\Delta T}{\Delta t}$ is the initial slope of the time-dependent magnetic heating curve (K/s). As demonstrated in the figures above under a constant magnetic field, there is a linear relation in the first rising of the temperature. It is important to notice that all temperature vs. time heating curves display the maximum slope of $\frac{\Delta T}{\Delta t}$ in the first few seconds after the magnetic field is turned on.

The heat capacity for magnetite C_{np} is negligible due to its low contents in the samples and therefore the Equation 3-15 is replaced with the Equation 3-16 (Motoyama *et al.*, 2008).

$$SPA = \frac{C}{m_{np}} \times \frac{\Delta T}{\Delta t} \quad \text{Equation 3-16}$$

Where C is the sample-specific heat capacity which is calculated as a mass weighed mean value of sample. The solvent specific heat (C_s) of the different solvents used in this study is summarized in Table 3-6.

The SPA values for synthesized magnetic nanoparticles were calculated based on the equations above and was in the range of 5.2 to 175 W/g which is comparable to previously reported SPA values. The SPA values of the samples compared to the values reported in the literature are summarized in Table 3-7.

Table 3-6. List of the solvents specific heat (C_s)

Material	Specific heat (j/gK)
Cyclohexane	1.8
Hexane	2.26
Water	4.19
Magnetite	0.841

Table 3-7. Comparison of the samples SAR and ILP values with the literature. Blue cells indicate the materials synthesised in this project.

Material	Average core size (nm)	H (kA/m)	f (kHz)	SPA (W/g)	ILP (nHm ² /kg)	Reference
Magnetite	7.5	32.5	80	15.6	0.184	(Ma et al., 2004)
Magnetite	13	32.5	80	39.4	0.466	(Ma et al., 2004)
Magnetite	8.4	6	330	10.86	0.9	(Behdadfar et al., 2012)
Magnetite	9.5	6	330	111.76	9.4	(Behdadfar et al., 2012)
Dextran-coated magnetite	18	15.91	55	57	4.09	(Zhang et al., 2007)
Magnetite	50	15.91	55	4.5	0.32	(Zhang et al., 2007)
Dextran coated magnetite	3.3	13.2	520	120	1.32	(Jordan et al., 1996)
Aminosilan coated magnetite	13.1	13.2	520	146	1.61	(Jordan et al., 1996)
Magnetic iron oxide	13.2	11	410	87	1.75	(Müller et al., 2005)

Table 3-7. Continued

Material	Average core size (nm)	H (kA/m)	f (kHz)	SPA (W/g)	ILP (nHm ² /kg)	Reference
Magnetic iron oxide	9.2	11	410	1.7	0.034	(Müller et al., 2005)
Maghemite	25	12	300	2.8	0.064	(Baker et al., 2006)
Silica-coated magnetite	45 (shell thickness of 4.5nm)	12	260	45	1.2	(Gonzalez-Fernandez et al., 2009)
Silica-coated magnetite	110 (shell thickness of 15 nm)	12	260	1.74	0.046	(Gonzalez-Fernandez et al., 2009)
Liposome coated magnetite	120	32.5	200	4.18	0.019	(Motoyama et al., 2008a)
PEG-PCL coated magnetite	6 (total size of 78nm)	82.7	266	0.82	45e-5	(BENNETT, 2012)
Liposome coated magnetite	35	30	118	96	0.90	(Le et al., 2001)
ME18	13	15.8	406	176.546	17.2	Present study
ME33	13	15.8	406	10.684	1.04	Present study
ME55	13	15.8	406	128.001	12.5	Present study
ME59	8	15.8	406	37.590	3.67	Present study
ME60	29 (shell thickness of 29 nm)	15.8	406	10.800	1.05	Present study
ME60-L	29	15.8	406	1.319	0.129	Present study
ME55-PEG-PCL	13	15.8	406	8.796	0.858	Present study
ME93-PEG-PCL	40	15.8	406	3.352	0.327	Present study
ME94-PEG-PCL	30	15.8	406	2.011	0.196	Present study

3.14.3 Intrinsic loss power (ILP)

The direct comparison of the calculated SPA data with the reported literature is difficult due to different AC field frequencies and the field intensities used in each measurements. Intrinsic loss power (ILP), allows more direct evaluations to be made between experiments performed in different laboratories under different AC field strength and frequency conditions (Behdadfar et al., 2012, Kallumadil et al., 2009).

Intrinsic loss power (ILP) is calculated using Equation 3-17.

$$ILP = \frac{SAR}{H^2 f} \quad \text{Equation 3-17}$$

This equation is valid under frequencies of up to several MHz which covers the range for hyperthermia applications. SPA and the ILP were calculated for synthesised materials under magnetic field with 406 kHz frequency and 200 G magnetic field strength.

For the magnetic heating measurements magnetite nanoparticles prepared by thermal decomposition method (ME59) with monodisperse size of 8 nm were dispersed in cyclohexane to achieve a final concentration of 39 mg/mL solution. The SPA and ILP was calculated to be 37.59 W/g and 3.67 nHm²/kg, respectively.

Magnetite nanoparticles prepared by coprecipitation method (ME18 and ME55) were dispersed in water and hexane to the final concentration of 21 mg/mL and 12 mg/mL, respectively. ME55 was prepared by coprecipitation method and it was oleic functionalised post synthesised. The size range for ME18 and ME55 was in the range of 8-15 nm. The calculated SPA and ILP from the AC field measurements showed that the SPA and ILP of the material prepared by coprecipitation method was much higher than the monodisperse material prepared by thermal decomposition method.

Silica coated and polymer coated magnetic nanoparticles were also investigated for their magnetic heating abilities. The comparative results of SPA measurements between bare and coated nanoparticles demonstrated a decrease of SPA with the increase in nanoparticles size. Coated nanoparticles displayed smaller SPA values than the corresponding uncoated ones. The SiO₂ shell thickness was found to play an important role in the heating efficiency. This variance could be related to the insulating nature of the silica coating, which could be shielding the heat from the magnetic nanoparticle and consequently decreasing the heating efficiency (Gonzalez-Fernandez et al., 2009). The calculated ILP was reduced from 17.2 nHm²/kg for uncoated magnetite to 1.05 nHm²/kg for silica coated magnetite. This indicates that the silica coating of the nanoparticles should be designed to be the minimum necessary for the related application.

Similarly for polymer coated magnetite the coating reduced the calculated heat efficiency from 12.5nHm²/kg for bare magnetite to 0.858 nHm²/kg for magnetic micelles. It is concluded that a

compromise between good heating efficiency, surface functionality and surface area for biomedical purposes can be attained by making the biocompatible coating as thin as possible.

Liposome coated and polymer capped silica coated nanoparticles were also developed for magnetic hyperthermia applications. The heating performance of this material is significantly affected by the silica thickness and hydrodynamic size of the particles. The polymer capped silica nanoparticle (ME93-PEG-PCL) showed ILP value of 0.327 nHm²/kg and the liposome capped silica coated nanoparticles (ME60-L) exhibited and ILP value of 0.129 nHm²/kg.

Table 3-7 shows comparison between heating efficiencies of the synthesised nanocomposites and some of the material reported in the literature. The highest ILPs between commercial ferrofluids belong to Micromode and Bayer-Schering (Bayer-Schering's Resovist is medically approved ferrofluid) ferrofluids which are 3.12 and 3.1 nHm²/kg with particle sizes of 11.8 and 10.5 nm, respectively. Comparing our results with the results in that report shows that the calculated intrinsic loss power (ILP) of most of the synthesised nanocomposites are in similar range or higher than the literature and the commercially available ferrofluids (Kallumadil et al., 2009). These results indicates that the synthesised material have great potential to be used in magnetic hyperthermia applications.

CHAPTER 4

CATALYSIS

4.1 Introduction

The focus of this chapter is the evaluation of the synthesised magnetic nanocomposites as enzyme supports. This was achieved by quantifying the amount of lipase (*Candida Rugosa* lipase (CRL) and *Pseudomonas Fluorescens* Lipase (PFL) immobilised on the nanocomposite support followed by assessing the catalytic activity of the immobilised lipase compared to the free lipase.

The first part of this chapter presents the data and discusses the results on the lipase immobilisation by assessing the surface amine density, followed by Bradford assay to quantify the immobilized enzyme (both physically adsorbed and chemically bonded lipase).

The second part of this chapter aims to examine the catalytic activity of the immobilized lipase using two lipase catalysed reactions. The first reaction used was the widely known model reaction of hydrolysis of p-nitrophenyl palmitate (pNPP) to palmitic acid and p-nitrophenol (pNP). This reaction was repeated in presence of an AC field to evaluate the activity of the immobilized enzyme in the presence of an AC field. The hydrolysis of pNPP has been commonly used as a model reaction since it can be readily monitored using UV-Visible spectrophotometry by measuring the absorbance at $\lambda_{410\text{nm}}$ (Teng and Xu, 2007, Gupta et al., 2002, Leis et al., 2015). The second catalytic application was the hydrolysis of cis-3,5-diacetoxy-1-cyclopentene to produce the chiral optical isomers (1S,4R)-cis-4-acetoxy-2-cyclopenten-1-ol and its enantiomer.

Mesoporous silica coated magnetic core-shell nanoparticles (ME33) were used for enzyme immobilisation through covalent bonding and physical adsorption. The nanoparticles were prepared following the method described in Section 2.4. The nanomaterials were characterized using various techniques such as transmission electron microscopy (TEM), X-ray diffraction (XRD), small angle X-ray scattering, infrared spectroscopy (FT-IR), vibrating sample magnetometer (VSM), scanning column magnetometry (SCM) and Energy-dispersive X-ray analysis (EDAX) as described in Chapter 3.

4.2 Colorimetric Assay of Amine Density

The lipase was immobilized on the magnetic nanoparticles covalently, as well as *via* physical adsorption. To immobilise the lipase on nanoparticles surface *via* chemical bonding, the magnetic nanoparticles were modified by amine surface functionalization which was then activated by glutaraldehyde as explained in Section 2.8 and 2.10.

Physical and chemical properties of amine functionalised nanoparticles can be determined by the density of the amine groups. The surface amine density was measured following the process explained in Section 2.9. Generally, the aminosilane layer was allowed to react with 4-nitrobenzaldehyde, a UV-sensitive molecule, followed by UV-Visible spectroscopy at $\lambda_{282\text{nm}}$ to confirm the formation of the corresponding imines. Subsequently the imines were hydrolysed to

regenerate the amine groups on the surface of the nanoparticles. The density of the amine groups were quantified by measuring the amount of 4-nitrobenzaldehyde available in the solution and comparing it to the initial concentration. The amount of the 4-nitrobenzaldehyde present in solution was calculated based on the pre-established standard curve.

Standard curves of 4-nitrobenzaldehyde in coupling and hydrolysis solution was prepared by measuring the absorbance of series of dilutions of 4-nitrobenzaldehyde in hydrolysis and coupling solution. Figure 4-1 and Figure 4-2 present typical standard curve for dilutions of 4-nitrobenzaldehyde in hydrolysis and coupling solution.

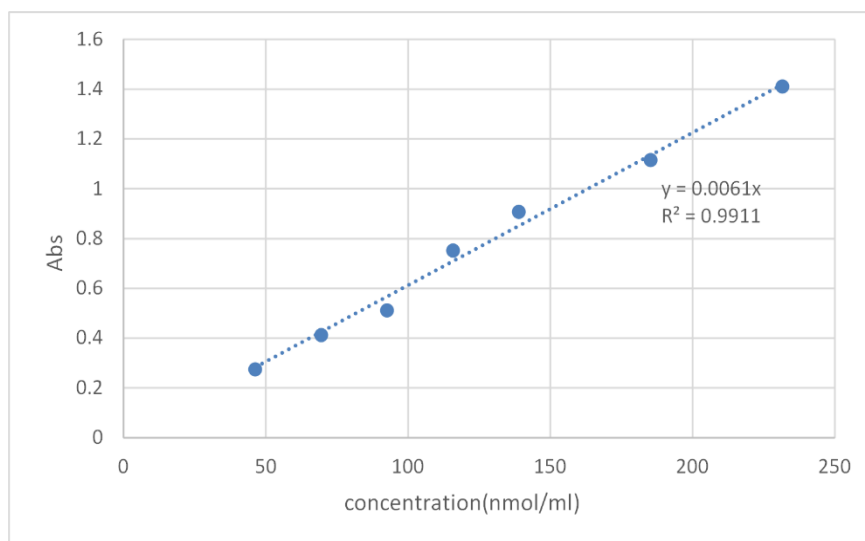


Figure 4-1. Standard curve of 4-nitrobenzaldehyde dilutions in coupling solution (λ_{282nm}).

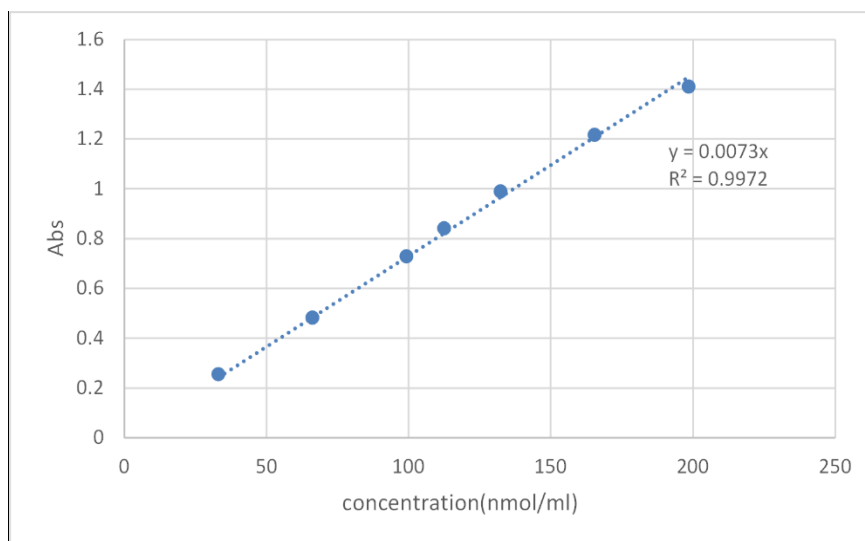


Figure 4-2. Standard curve of 4-nitrobenzaldehyde dilutions in hydrolysis solution (λ_{282nm}).

As shown in Figure 4-1 and Figure 4-2, a linear trend was observed at the concentration range of 0 to 240 nmol/mL. The initial concentration of 4-nitrobenzaldehyde was 0.7 mg/mL which was not in the range of acceptable UV-visible readings, consequently, all the absorbance including the initial readings were recorded on 20 times diluted samples. Standard curves were reproduced

every six months using fresh samples to maintain the measurements reliability and reproducibility.

Results of both the water method and TPRE method of amine functionalisation are shown in Figure 4-3 and Figure 4-4. The measurements were performed in coupling solution by measuring the amount of unbounded 4-nitrobenzaldehyde left in the solution and comparing that with initial values and it was then confirmed by measuring the amount of 4-nitrobenzaldehyde present in the solution after hydrolysis.

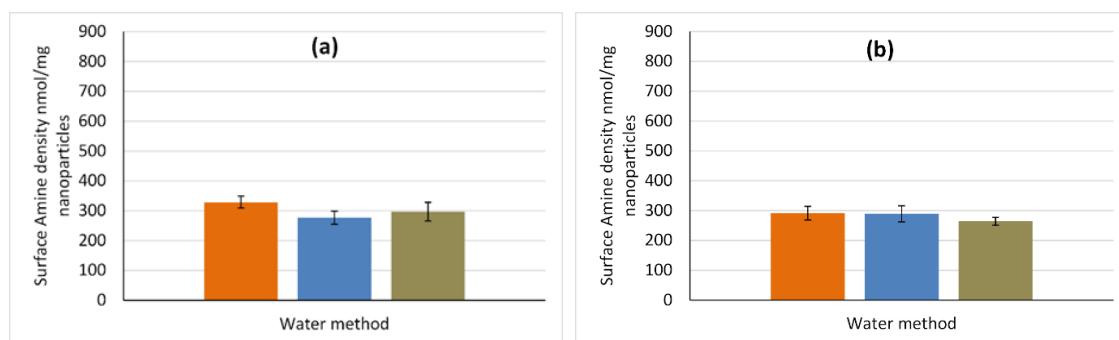


Figure 4-3. Surface amine density of mesoporous silica coated magnetite prepared following water method. Measuring in coupling solution (a) and measuring in hydrolysis solution (b). Each column represents an independent experiment and error bars present standard deviation between different samples in each experiment

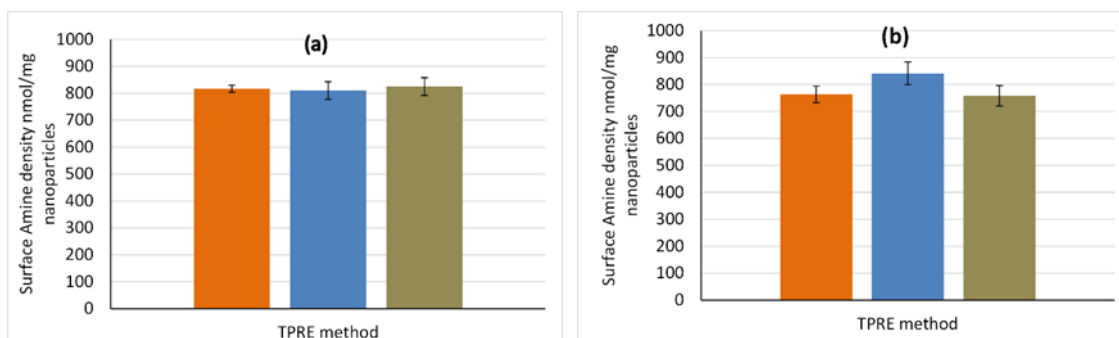


Figure 4-4. Surface amine density of mesoporous silica coated magnetite prepared following TPRE method. Measuring in coupling solution (a) and measuring in hydrolysis solution (b). Each column represents an independent experiment and error bars present standard deviation between different samples in each experiment

Surface amine density ($\text{molecules}/\text{nm}^2$) was calculated by integrating the amine values obtained from the colorimetric assay and the surface area of the mesoporous silica coated nanoparticles obtained from nitrogen adsorption-desorption (BET) test. Surface amine density was calculated to be around $0.152 \text{ molecule}/\text{nm}^2$ ($0.300 \text{ mmol}/\text{g}$) for water method and $0.414 \text{ molecule}/\text{nm}^2$ ($0.817 \text{ mmol}/\text{g}$) for TPRE method. It is clear from the figures that TPRE method leads to higher surface amine density which is consistency with the literature (Gartmann et al., 2010, Sen and Bruce, 2012a). Higher surface amine density attained by TPRE method could be due to limited water in the system which controls the surface condensation of the aminosilane and leads to uniform amine distribution on the surface. It is well established that water promotes the interaction

of the amino groups with the surface, by proton transfer from the surface silanols to the amino moieties and subsequent electrostatic interaction. The resulting orientation of the amino groups toward the silica surface provides accessible triethoxysilyl moieties for cross-linking, ultimately leading to the formation of clusters. The presence of such clusters can also make pores partially inaccessible for additional APTES molecules and result in a lower amine groups density (Gartmann et al., 2010).

4.3 Bradford Assay for Evaluating Lipase Immobilisation

Lipase immobilisation was performed following the method explained in Section 2.11. After the lipase was immobilised on nanoparticles the quantification of the immobilised lipase was performed using Bradford assay (Bradford, 1976, Ernst and Zor, 2010, Sen et al., 2010). In this method magnetic nanoparticles were separated from the solution using a permanent magnet and the amount of free enzyme remained in the supernatant was measured by adding equal amount of Bradford reagent and measuring the UV absorbance at $\lambda_{595\text{nm}}$. The lipase concentration was then calculated using the prepared standard curves. Standard curves of PFL and CRL were prepared in PBS solution by measuring the absorbance of series of dilutions of lipase. Figure 4-5 and Figure 4-6 show the standard curves for PFL and CRL in PBS solution.

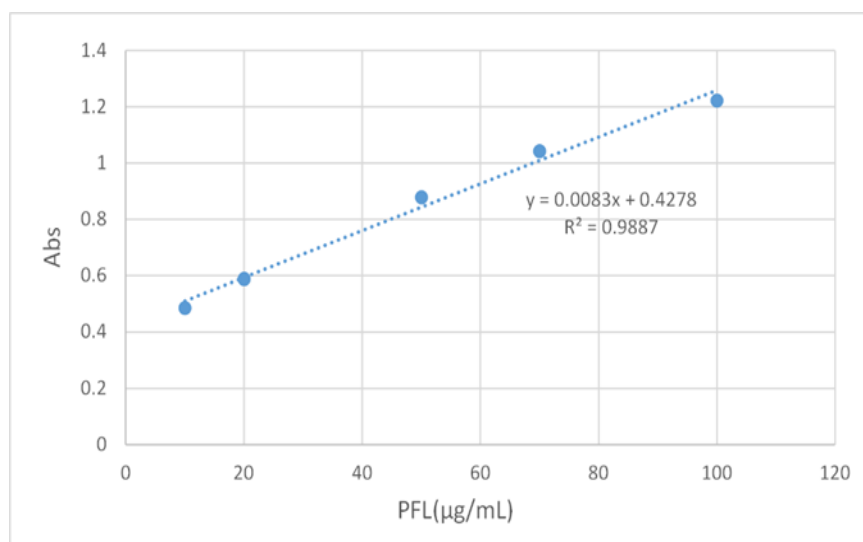


Figure 4-5. Calibration curve for PFL

In case of PFL the standard curve showed non-linear behaviour over the higher lipase concentration range therefore the standard curve was conducted in low lipase concentration and during the measurements where required the samples were diluted to fit in the calibration range.

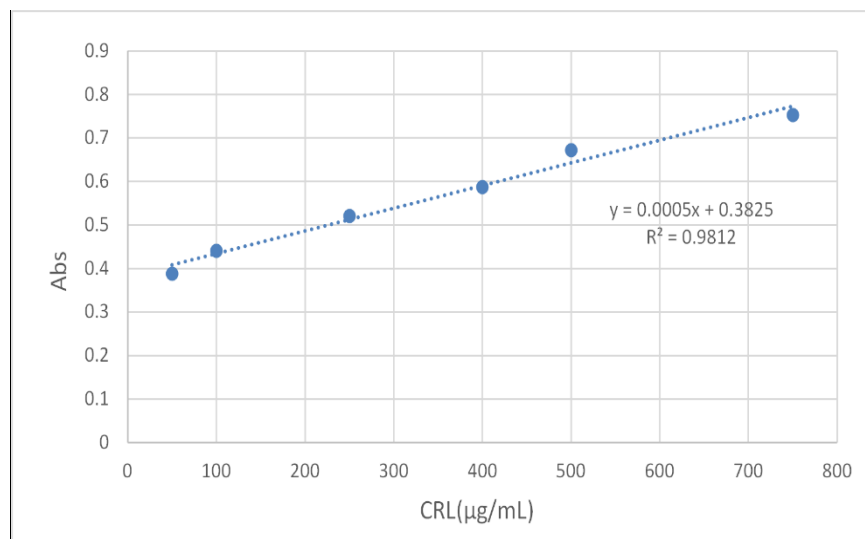


Figure 4-6. Calibration curves for CRL

Since the materials functionalised using TPPE method showed higher amine density they have been used further in enzyme immobilisation. Figure 4-7 shows the average enzyme immobilisation profile calculated using Bradford assay.

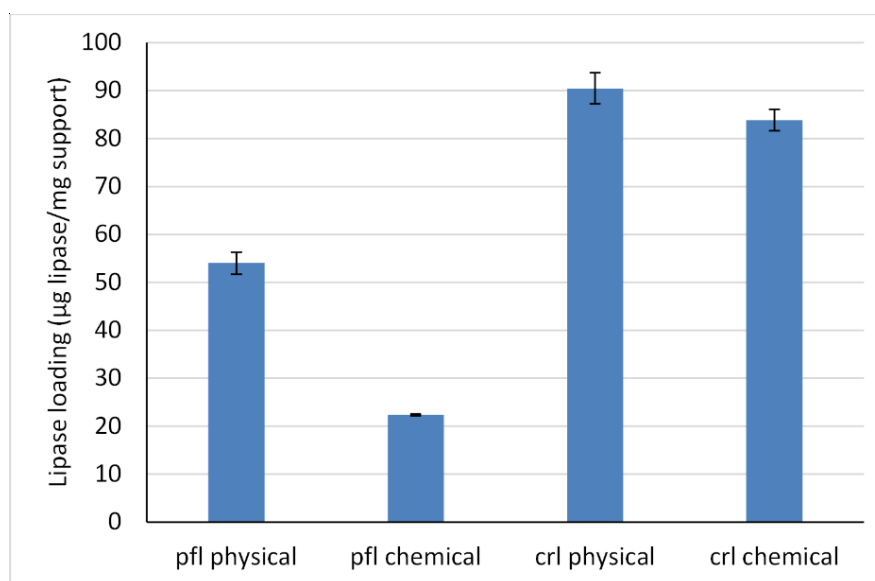


Figure 4-7. The average enzyme immobilisation profiles. Values are mean \pm standard deviation. All experiments are repeated at least 4 times.

From Figure 4-7, it is seen that CRL showed a higher immobilisation rate. It is also observed that both in case of CRL and PFL, physically adsorbed lipase showed higher loading capacity, which could be explained by the possibility of the pores of the surface functionalise nanoparticles being blocked by the functional groups. However, it was observed and will be discussed in the following sections that the physically immobilised enzymes tend to leak into the solution and result in enzyme loss and consequently decreased catalytic activity after reuse in few cycles.

4.4 Bio-Catalytic Application: Hydrolysis of pNPP

The activity of lipases are commonly assessed using the para-nitrophenyl palmitate (pNPP) assay. This assay is based on the colorimetric assessment of yellow chromogen para-nitrophenol (pNP) introduced in to the solution as the consequence of enzymatic hydrolysis of pNPP (Gupta et al., 2002). In this project the model catalysis reaction of pNPP hydrolysis to produce palmitic acid and pNP was used to evaluate the activity of lipase immobilised onto the nanoparticles. pNP has a strong absorption at $\lambda_{410\text{nm}}$ which allows for an easy and reliable means to measure reaction rates by UV-visible spectroscopy.

Standard curve of pNP were prepared using a sequence of pNP dilutions in a 1:1 mixture of reagent A (Gum Arabic, sodium deoxycholate and Tris-HCl as explained in Section 2.13) and isopropanol. Figure 4-8 presents the calibration curve of pNP. As seen in Figure 4-8 good linearity between UV-Absorption and pNP concentration was observed in the range of 0 to 27 $\mu\text{mol/mL}$.

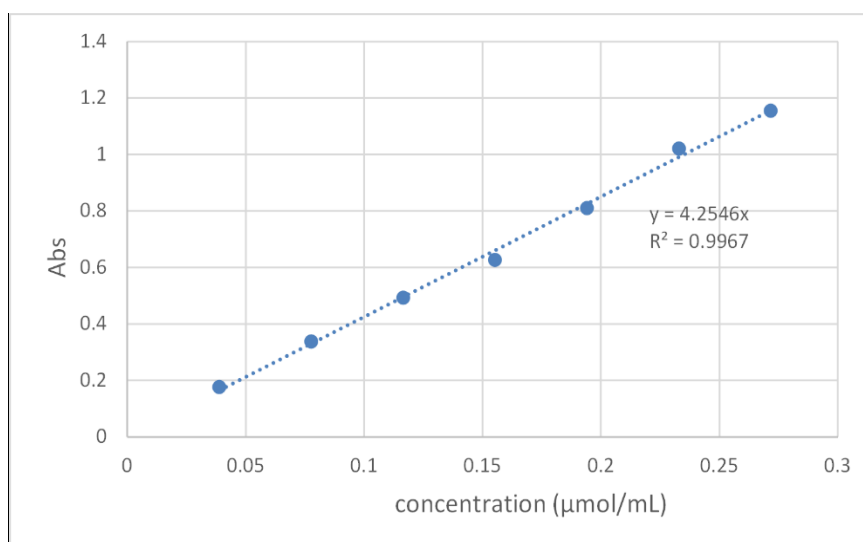


Figure 4-8. Calibration curve for p-nitrophenol (pNP) in a 1:1 mixture of reagent A: Isopropanol

The hydrolysis of para-nitrophenyl palmitate was carried out according to the method described in Section 2.13. To perform this reaction an equivalent amount of 500 μg lipase either in immobilised form or in free form was used. The actual mass of particles used in each case is calculated based on the results from the Bradford assay and is given in Table 4-1.

Table 4-1. Equivalent amount of nanoparticles to obtain 500 μg of immobilised lipase

Immobilisation technique	PFL immobilised nanoparticles (mg)	CRL immobilised nanoparticles (mg)
Physical adsorption	9.25	5.52
Chemical bonding	22.36	5.96

The catalytic activity of free, physically adsorbed and chemically conjugated lipases to hydrolyse pNPP is demonstrated in Figure 4-9.

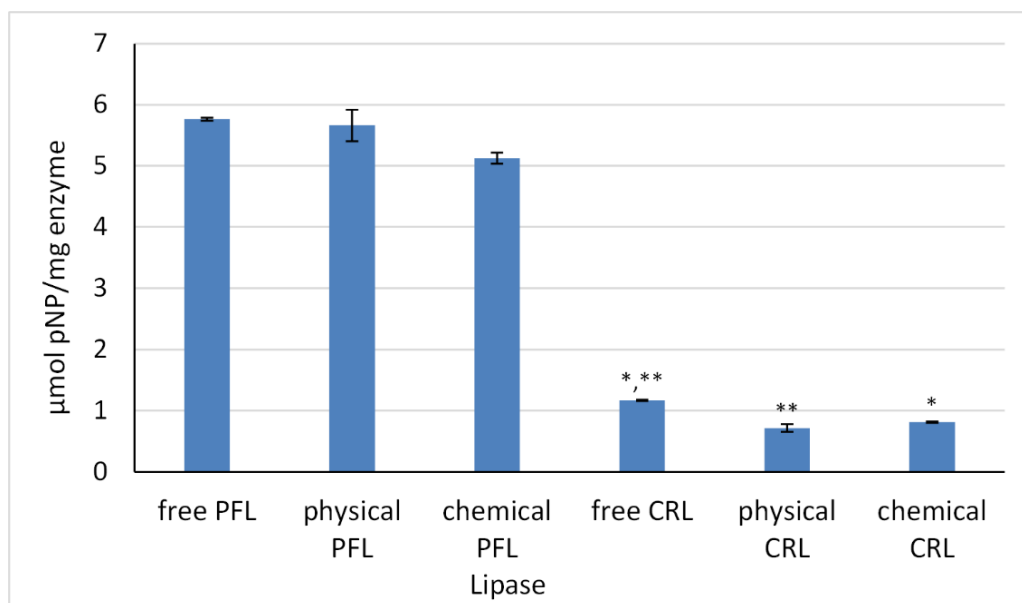


Figure 4-9. The catalytic activity of free, physically adsorbed and immobilised lipases to produce pNP. (*and ** statistically significant ($P < 0.05$) difference between free CRL activity and immobilised CRL activity)

The results indicate that the PFL lipase either in free form or immobilised form display higher activity in hydrolysis of pNPP compare to CRL lipase. In this reaction free PFL showed 5 times higher activity than free CRL. Immobilised and free PFL did not show significant difference in catalytic activity, however the chemically conjugated lipase showed the lowest activity compare to free and physically adsorbed lipases. Chemically immobilised PFL maintained 88% and physically immobilised PFL maintained 98% of it activity.

In case of CRL lipase, free CRL showed higher activity and there was a significant difference between catalytic activity of free and immobilised lipase, however there was no significant difference in hydrolytic activity of physically and chemically immobilised lipases. Chemically immobilised CRL maintained 69% and physically immobilised CRL maintained 61% of it activity.

After the hydrolysis reaction, the immobilised enzymes were collected using a permanent magnet and washed with PBS buffer and used again in the same reaction to assess the reusability of the immobilised lipase. The immobilised enzymes were used in 4 consecutive cycles. Similarly for reactions performed with free enzyme, the enzyme was recycled using centrifugation and washed and reused in another cycle. The results for reusability evaluation of the immobilised lipases are shown in Figure 4-10.

As shown in Figure 4-10 due to difficulties during isolation and recycling of the free lipase from the reaction mixture, which resulted in losing the lipase, it was not possible to use the free lipase in more than two successive cycles.

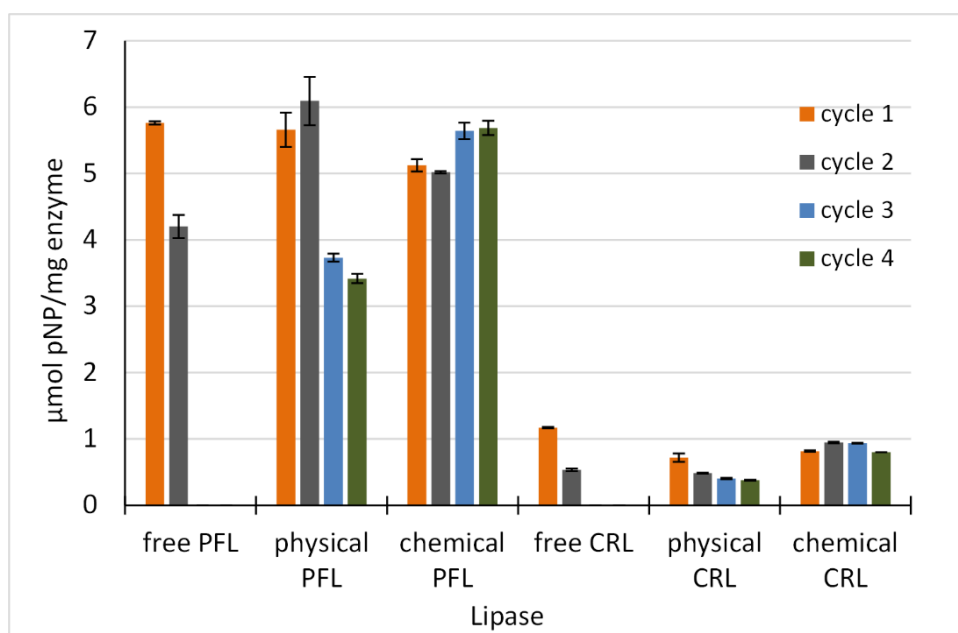


Figure 4-10. The reusability of the lipases over 4 successive cycles.

The results indicated that compared to chemically immobilised lipases, physically adsorbed lipases initially showed higher catalytic activity, however for both lipases there was a decrease in lipase activity after each cycle which could be due to lipase leaching into the solution and consequently less available lipase in the subsequent cycle (Sen et al., 2010). An exception was observed for physically adsorbed PFL which showed an initial increase in activity in the first reuse cycle (second cycle). After four consecutive cycles the PFL physical maintained 60% of its initial activity and CRL physical maintained 52% of its initial activity. In case of chemically immobilised lipases there were no significant decrease in lipases activity where chemically immobilised CRL maintained 98% of its activity after four cycles, and interestingly the chemically immobilised PFL showed even higher activity after 4 cycles (110%). The increased activity for PFL after the first cycle is suggested to be a result of lipase activation and aggregation of PFL. In moderate to high concentrations PFL tends to auto assemble into bimolecular structure which shows lower activity (Fernández-Lorente et al., 2003). High loading of PFL in mesochannels leads to formation of bimolecular form of PFL. In bimolecular form of PFL the active sites of both lipase molecules are intimately associated leading to a reduction in activity of the lipase with competition between neighbouring PFL active sites (Fernández-Lorente et al., 2003). During the first catalysis cycle some of the adsorbed PFL leach into the solution increasing the accessibility of the remained lipase, which consequently lead to an increase in lipase activity. However, after second cycle the amount of lipase lost in the reaction is dramatically increased resulting in lower activity. Similarly for chemically immobilised enzyme the increased activity after initial cycle could be explained by enzyme activation and better accessibility of the lipase active sites.

4.5 Effects of AC Magnetic Field on Catalytic Activity of the Lipase

Magnetic fields are known to influence the enzyme activity however, previous studies into the influence of magnetic fields on the activity of immobilised enzymes, particularly enzymes immobilised on magnetic supports, are somewhat controversial as some reports claim enzyme activation while others reports deactivation (Klyachko et al., 2012, Willner and Katz, 2003, Golovin et al., 2014a, Møller and Olsen, 1999). Nonetheless previous studies have focused on the low frequency range of <100 Hz (Suzuki et al., 2015) while the results reported in this thesis are significantly different due to measurements being in high frequency of 406 kHz.

The effect of magnetic field on the course of the reaction is evaluated by exposing the reaction to a magnetic field for different time frames. The hydrolysis of para-nitrophenyl palmitate was performed under influence of a magnetic field using an equivalent amount of 500 µg CRL lipase in immobilised form. The actual amount of nanoparticles used in each case is calculated based on the results from Bradford assay and is given in Table 4-1.

A magnetic field with the field strength of up to 200 G and frequency of 406 kHz was used for these experiments. The field strength was set variable in the way to keep the temperature constant at 32°C. The heating profile of CRL lipase immobilised nanoparticles in presence of the magnetic field is shown in Figure 4-11.

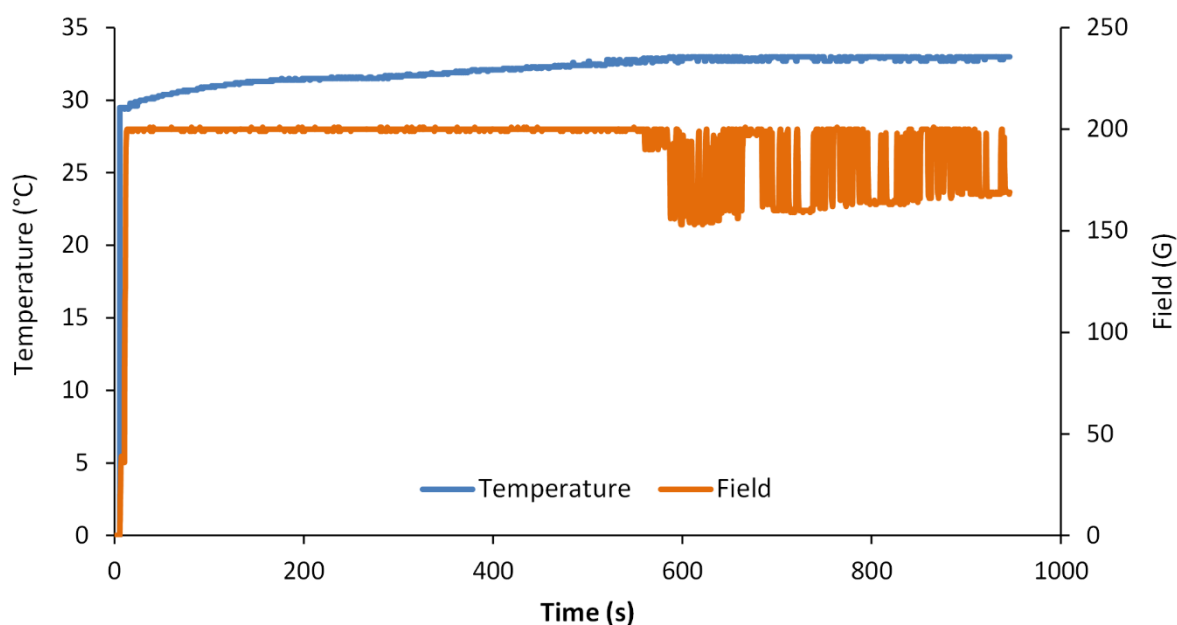


Figure 4-11. Magnetic heating profile of the enzyme immobilised magnetic nanoparticles (ME33) corresponding to Field frequency of 406 kHz.

To account for the magnetic heating of the magnetic nanoparticles and effects of the heat on the lipase activity, the control reaction was performed simultaneously in an incubator at 32°C. The activity of the CRL lipase in presence of a magnetic field is presented in Figure 4-12 and Figure 4-13.

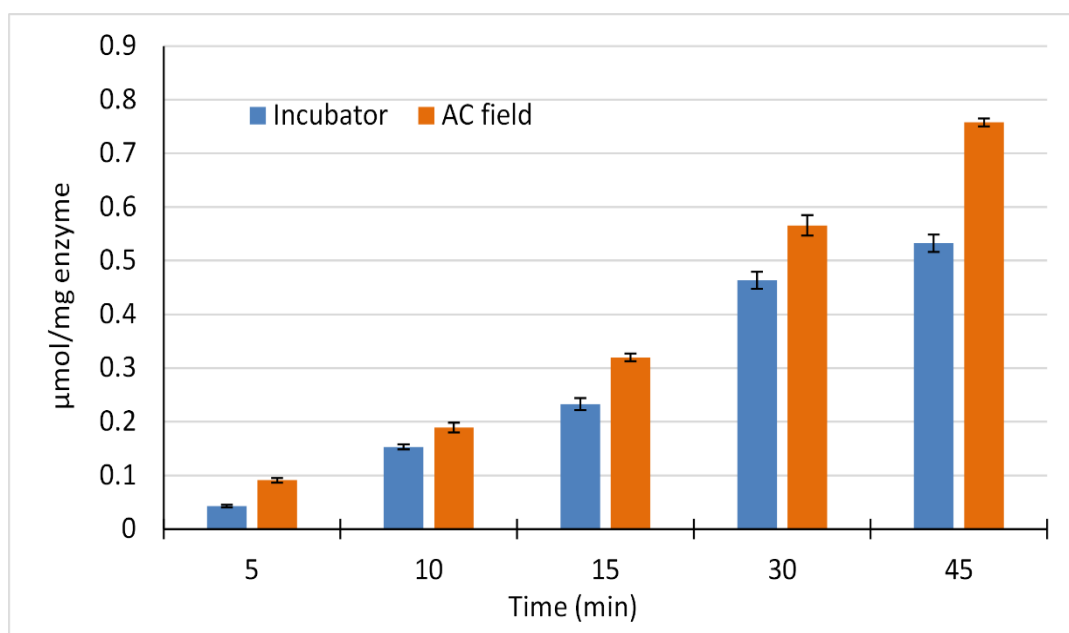


Figure 4-12. Hydrolysis of pNPP using chemically immobilised CRL under influence of a magnetic field compared with in incubator at 32°C.

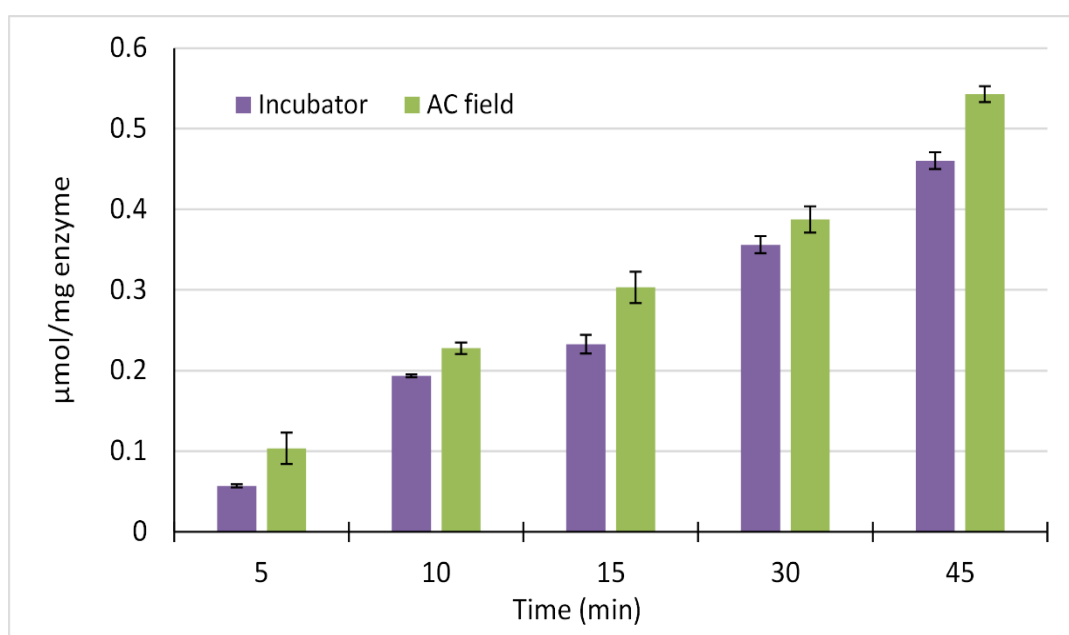


Figure 4-13. Hydrolysis of pNPP using physically immobilised CRL under influence of a magnetic field compared with in incubator at 32°C.

As seen in Figure 4-12 and Figure 4-13 exposure of the lipase to the magnetic field increased the reaction rate of both physically adsorbed and chemically bonded lipase. The increased lipase activity is suggested to be a result of conformational changes in the lipase structure in a way which lead to variations in the interatomic distances in the active sites and increased lipase activation (Golovin et al., 2014b). On the other hand the increased lipase activity could be attributed to the local heat generated by the magnetic support as suggested by Suzuki *et al.* (Suzuki et al., 2015). Suzuki *et al.* have studied the effect of an AC magnetic field with frequency of 340 kHz, and amplitude of 30 kA/m on activities of α -amylase immobilized on ferromagnetic particles and reported an increased activity which was suggested to be the result of activation of the enzyme

by magnetic heating of the nanoparticles (Suzuki et al., 2015). Mizuki *et al.* have reported an increase in activity of α -amylase and lipase immobilized on superparamagnetic particles under influence of magnetic field. However they have used rotational magnetic field with a very low frequency in the range of 0 to 30 Hz (Mizuki et al., 2010, Mizuki et al., 2013). Klyachko *et al.* have studied the effect of magnetic field on the enzyme immobilized on copolymer-magnetic nanoparticle and reported a decrease in enzyme activity which was attributed to conformational changes in the enzymes induced by realignment of magnetic nanoparticles rather than the heat generation of the particles (Klyachko et al., 2012).

To be certain that the increased enzyme activity was not due to enzyme leaching into the solution and acting as free lipase, the immobilised lipases were exposed to the magnetic field for an hour. After which nanoparticles were separated from the solution *via* magnetic separation and Bradford assay was performed on the supernatant. The assay for chemically bonded lipase indicated that there was no lipase in the solution. However, as it was expected, it was observed that the physically adsorbed lipase was leaked out into the solution. The reaction was repeated for 3 consecutive cycles which at the end of the third cycle the chemically immobilised lipase retained 83% of its activity.

4.6 Enantioselective Desymmetrization of cis-3,5-Diacetoxy-1-cyclopentene to (1S,4R)-cis-4-acetoxy-2-cyclopenten-1-ol

Significance of (1S,4R)-cis-4-acetoxy-2-cyclopenten-1-ol is in the synthesis of biologically active cyclopentenoid natural products such as prostaglandins, prostacyclins and thromboxanes, and some anti-HIV drugs. The importance of these products and the great market demand for high cost chiral intermediates have led to development of various synthesis methods. Most commonly used methods are; enzymatic desymmetrization of meso-cyclopenten-1,4-diol by transesterification, and enzymatic hydrolysis of the diacetate (Ghorpade *et al.*, 1999, Kalkote *et al.*, 2000, Sharifabad *et al.*, 2014). With regard to desymmetrization of cis-3,5-diacetoxy-1-cyclopentene *via* enzymatic hydrolysis, most of the efficient enzymes reported, (except Pig liver esterase (PLE)) have shown pro-S preference which necessitates additional chemical steps to convert the (4S)-hydroxy enantiomer to get the (4R)-hydroxy configuration (Ghorpade et al., 1999, Kalkote et al., 2000).

The hydrolysis of cis-3,5-diacetoxy-1-cyclopentene was performed according to the method described in Section 2.14. To conduct this reaction an equivalent amount of 500 μ g lipase (both PFL and CRL) either in immobilised form or in free form was used. The actual amount of particles used in each case is calculated based on the results from Bradford assay and is given in Table 4-1.

Gas Chromatography (GC) has been used to verify and quantify the reaction products. To achieve this, gas chromatography were performed for commercially available pure materials ((1S,4R)-

cis-4-acetoxy-2-cyclopenten-1-ol (Sigma-Aldrich cat. No. 446041), (1R,4S)-cis-4-acetoxy-2-cyclopenten-1-ol (Sigma-Aldrich cat. No. 00848), cis-3,5-Diacetoxy-1-cyclopentene (Sigma-Aldrich cat. No. 31481) and cis-4-cyclopentene-1,3-diol (Sigma-Aldrich cat. No. 29823)) to recognize the retention time (RT) of each material. Based on the chromatograms, the peak at 10.53 minutes corresponded to cis-4-cyclopentene-1,3-diol, the peak at 11.04 minutes corresponded to (1S,4R)-cis-4-acetoxy-2-cyclopenten-1-ol, the peak at 11.18 minutes corresponded to (1R,4S)-cis-4-acetoxy-2-cyclopenten-1-ol, and the peak at 12.26 minutes corresponded to cis-3,5-diacetoxy-1-cyclopentene

AS an example of GC chromatograms, Figure 4-14 and Figure 4-15 present scanned GC chromatograms of the reaction products using PFL and CRL lipases after 48 hours.

The peak observed at 3.46 could be attributed to the formation of acetic acid as a by-product of the reaction resulting from further hydrolysis of the hydrolysed acetoxy groups. The increasing concentration of acetic acid in the reaction mixture could result in further acid-catalysed hydrolysis of the mono-acetoxy to the dihydroxy product.

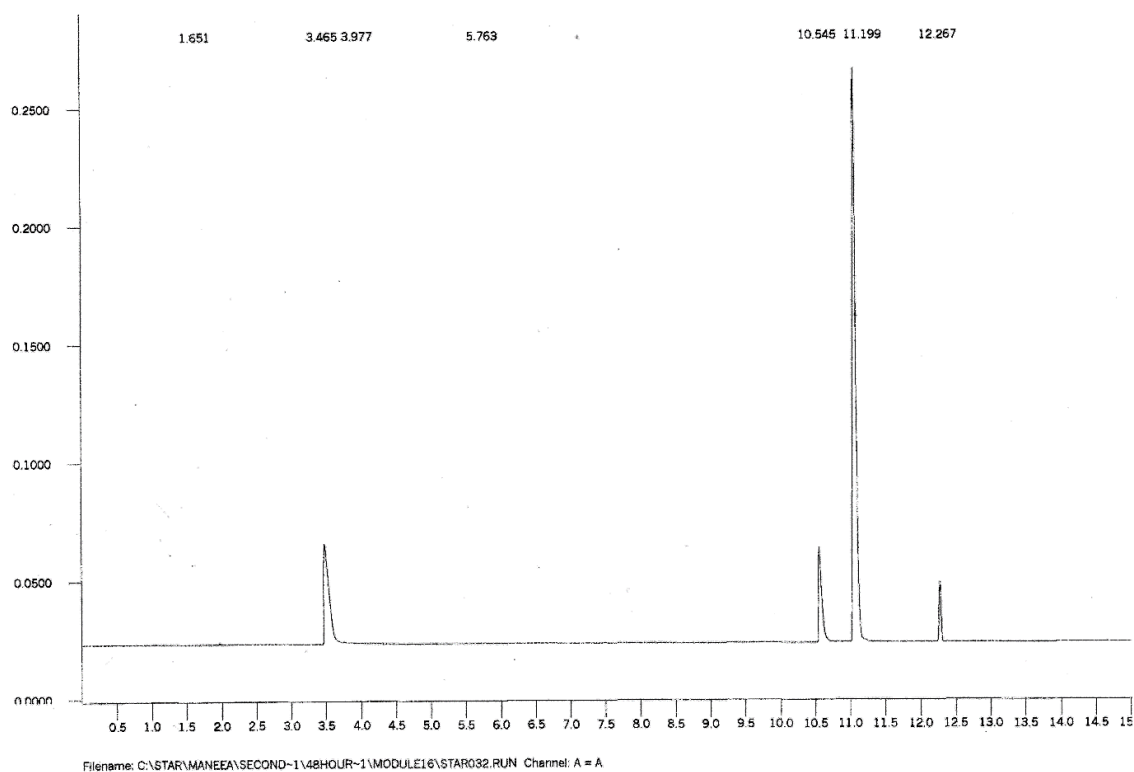


Figure 4-14. Scanned GC chromatograms of the reaction using PFL.

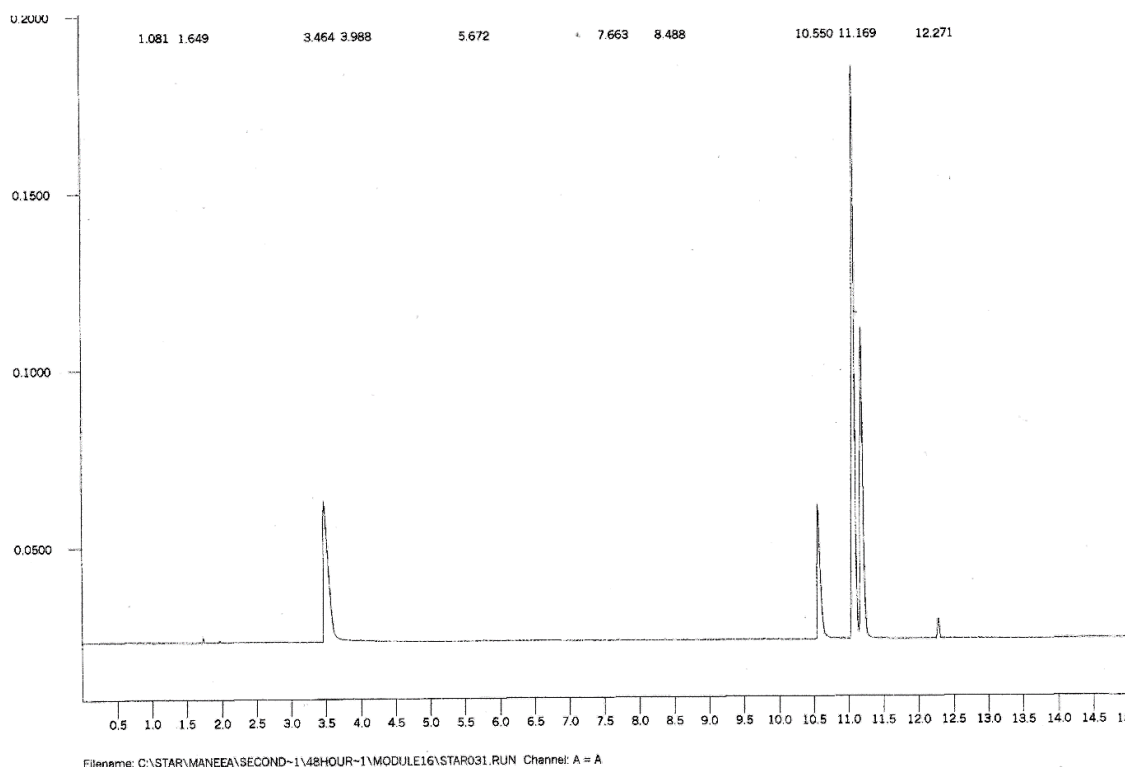


Figure 4-15. Scanned GC chromatograms of the reaction using CRL

The quantity of products were calculated based on the pre-established standard curves which were prepared from integration of the peak area of GC graphs of a range of diluted pure materials. Considering the reaction conditions the standard curves of the products were prepared either in hexane or water. Since (1S,4R)-cis-4-acetoxy-2-cyclopenten-1-ol and cis-3,5-dihydroxycyclopentene are insoluble in hexane their standard curves were prepared in water. Calibration curve for cis-3,5-diacetoxy-1-cyclopentene was prepared in hexane to calculate the exact amount of starting material and monitor the conversion. The calibration curves are shown in Figure 4-16, Figure 4-17 and Figure 4-18. Since equal amount of (1S,4R)-cis-4-acetoxy-2-cyclopenten-1-ol and its enantiomer showed equal peak area, the standard curve of (1S,4R)-cis-4-acetoxy-2-cyclopenten-1-ol was used for (1R,4S)-cis-4-acetoxy-2-cyclopenten-1-ol. As seen in the figures linearity with high confidence regression values were observed in all standard plots.

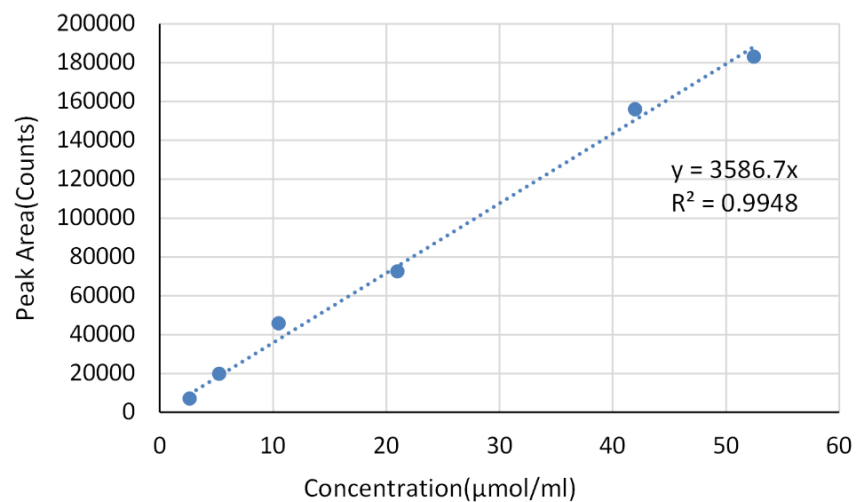


Figure 4-16. Calibration curves for (1s, 4R)-cis-4-acetoxy-2-cyclopenten-1-ol in water.

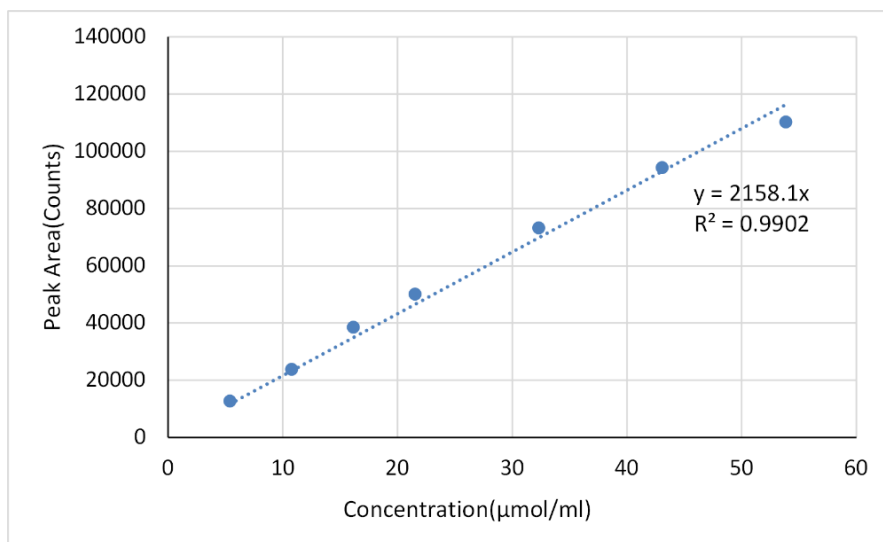


Figure 4-17. Calibration curves for cis-4-cyclopentene-1,3-diol in water.

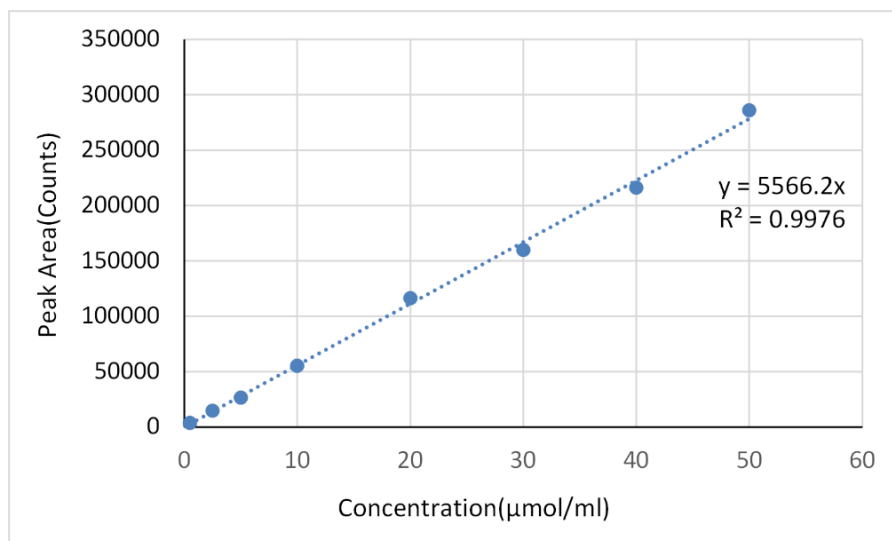


Figure 4-18. Calibration curve for cis-3,5-diacetoxy-1-cyclopentene in hexane

As described in Section 2.14. The reaction was performed in a biphasic condition with a solvent mixture of hexane: water with ratio of 4:1. The biphasic solvent was used in order to ease the product separation since the (1S,4R)-cis-4-acetoxy-2-cyclopenten-1-ol and (1R,4S)-cis-4-acetoxy-2-cyclopenten-1-ol are water soluble and insoluble in hexane, while the reactant is mostly soluble in hexane. Furthermore as established by Hodgson (Hodgson, 2014) biphasic system of hexane and water enhance the activity of free CRL and PFL lipases in transesterification reactions. The reaction was placed in an incubator at 25°C on end-over-end rotation (40 rpm).

The reaction was monitored by quantifying the products present in the water layer *via* injecting 1 µL of the water layer into the GC at different time intervals. Analysing the reaction rate was attained using only water layer since using the hexane layer proved difficult as a result of slight evaporation of hexane during the reaction.

The activity of free and immobilized PFL in the hydrolysis of cis-3,5-diacetoxy-1-cyclopentene and formation of the products are calculated based on the standard curves and presented in Figure 4-19, Figure 4-20, and Figure 4-21.

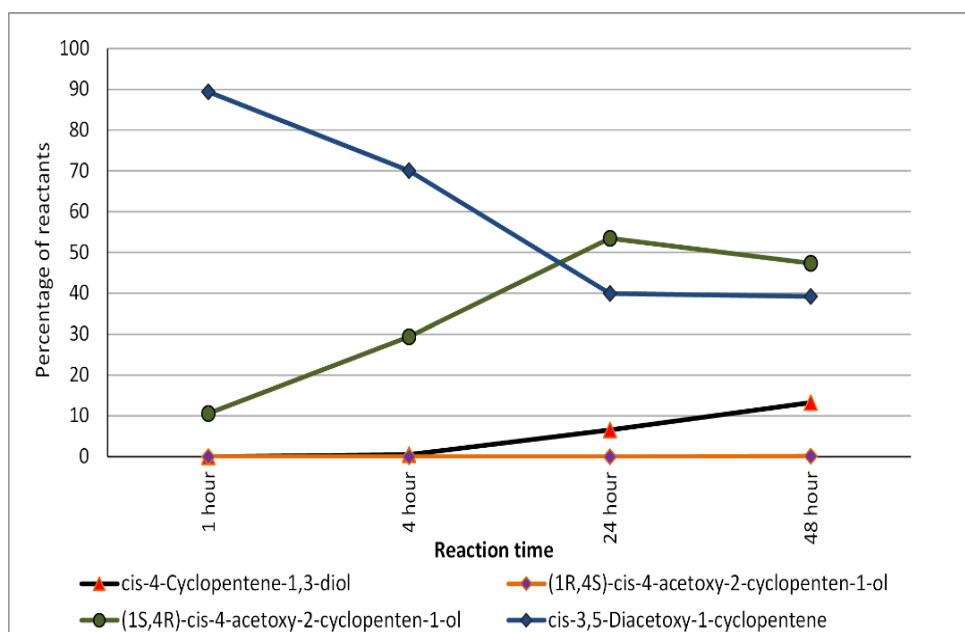


Figure 4-19. Percentage (%) of unreacted cis-3,5-diacetoxy-1-cyclopentene and the corresponding products of enzymatic hydrolysis of cis-3,5-Diacetoxy-1-cyclopentene using chemically immobilised PFL on the surface of the nanoparticles at different time intervals of 1, 4, 24 and 48 hours

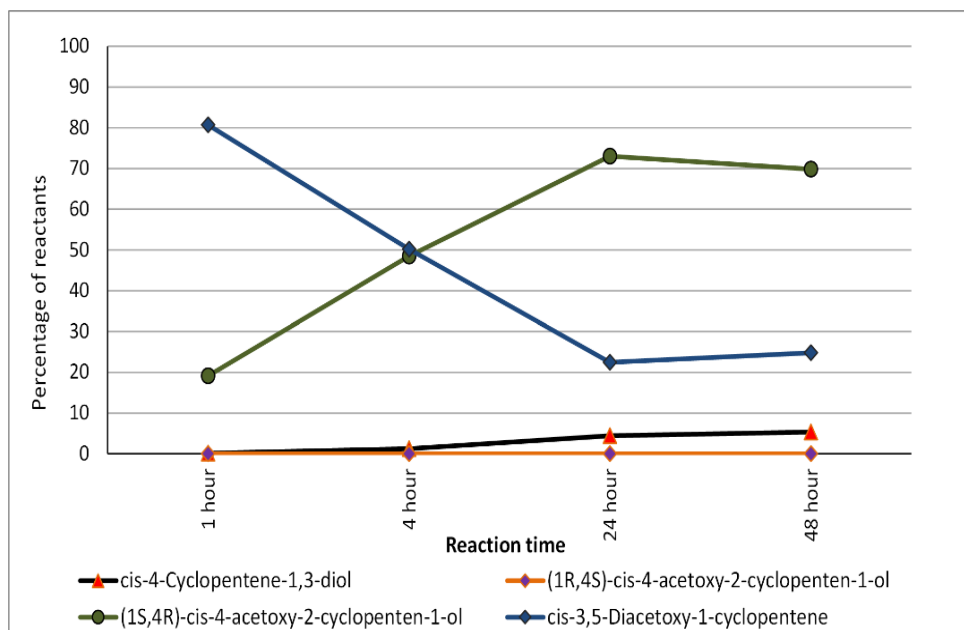


Figure 4-20. Percentage (%) of unreacted *cis*-3,5-Diacetoxy-1-cyclopentene and the corresponding products of enzymatic hydrolysis of *cis*-3,5-Diacetoxy-1-cyclopentene using physically immobilised PFL on the surface of the nanoparticles at different time intervals of 1, 4, 24 and 48 hours

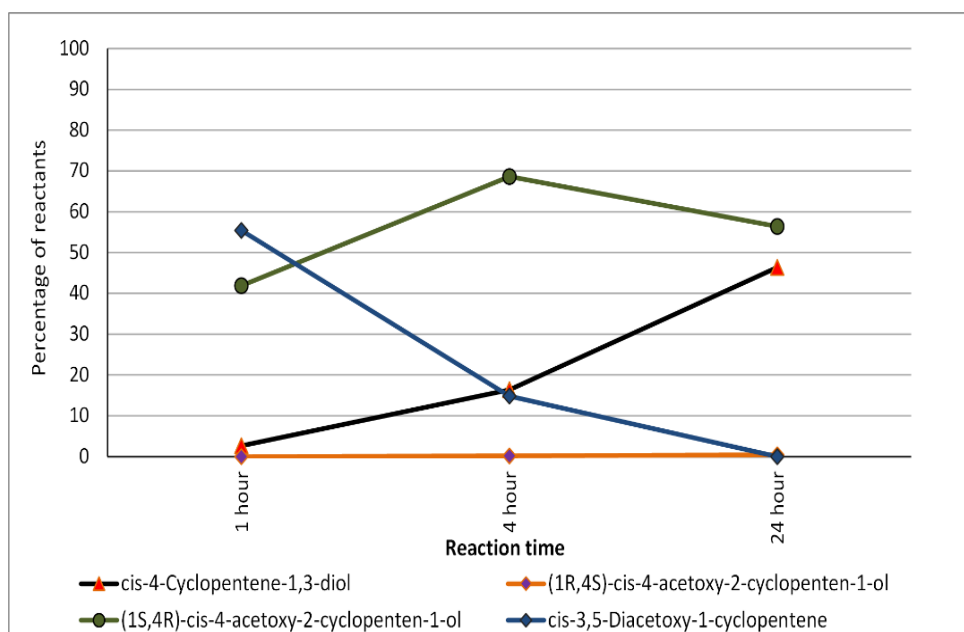


Figure 4-21. Percentage (%) of unreacted *cis*-3,5-Diacetoxy-1-cyclopentene and the corresponding products of enzymatic hydrolysis of *cis*-3,5-Diacetoxy-1-cyclopentene using free PFL at different time intervals of 1, 4, 24 and 48 hours

As observed from the figures when either free PFL or immobilized PFL were used as the catalyst in the reaction it produced (1S, 4R)-*cis*-4-acetoxy-2-cyclopenten-1 without the formation of its enantiomer, (1R, 4S)-*cis*-4-acetoxy-2-cyclopenten-1. At the end of 24 hours the free PFL have completed the conversion (1 μ mol of reactant per 10 μ g of enzyme) while the immobilized enzyme (physically or chemically) accomplished relatively lower conversion values. After 48 hours the physically adsorbed PFL materials achieved about 75% conversion of reactant

(0.75 μmol of reactant per 10 μg of enzyme) and the chemically bonded PFL materials attained about 60% conversion of reactant (0.60 μmol of reactant per 10 μg of enzyme).

In both cases of free and immobilised lipase, the conversion of the reactants to different products were increased with increasing the reaction time from 1 hour to 48 hours. However increasing the reaction time resulted in further hydrolysis of the acetate group of (1S, 4R)-cis-4-acetoxy-2-cyclopenten-1 to increase the concentration of unwanted cis-4-cyclopentene-1,3-diol product. Particularly in case of free lipase the amount of (1S, 4R)-cis-4-acetoxy-2-cyclopenten-1 decreased from 68% after 4 hours to 19% by the end of 48 hours reaction. The high quantity of the dihydroxy by-product produced in the reactions can be attributed to the relatively high water content in the reaction and the increasing concentration of acetic acid in the reaction mixture which could result in acid-catalysed hydrolysis of the newly formed mono-acetoxy products to the dihydroxy.

Figure 4-22 and Figure 4-23 present the comparison between free and immobilised lipase in forming (1S, 4R)-cis-4-acetoxy-2-cyclopenten-1 and cis-4-cyclopentene-1,3-diol, respectively.

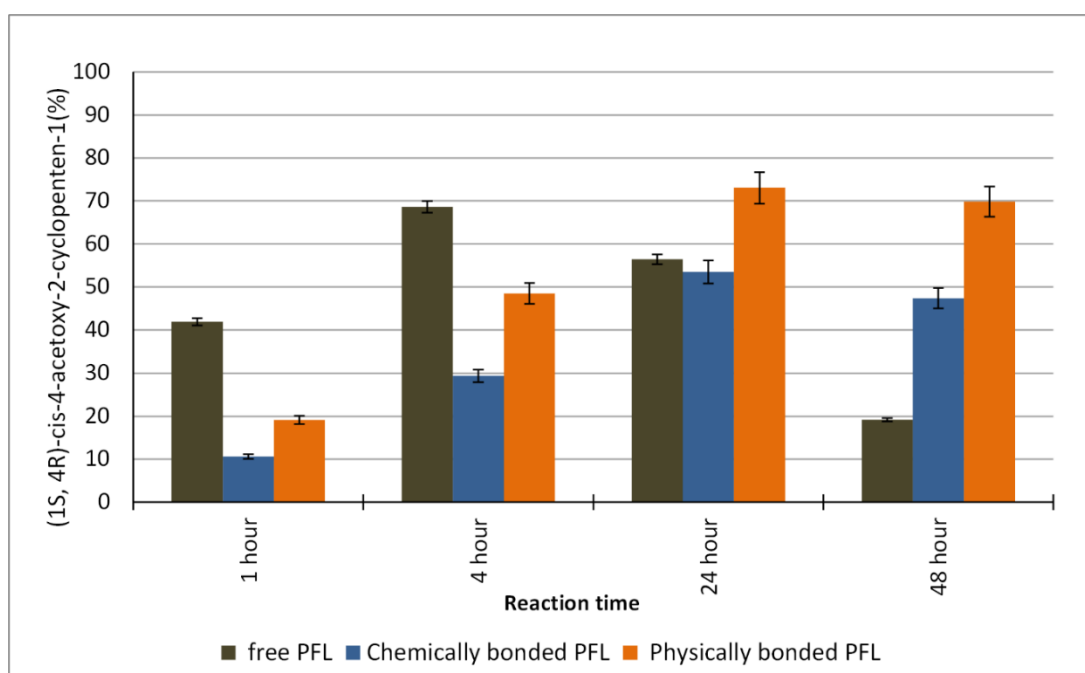


Figure 4-22. Comparison between free and immobilised PFL lipases in forming (1S, 4R)-cis-4-acetoxy-2-cyclopenten-1 during the 48 hours reaction period. and cis-4-cyclopentene-1,3-diol, respectively average acetoxy

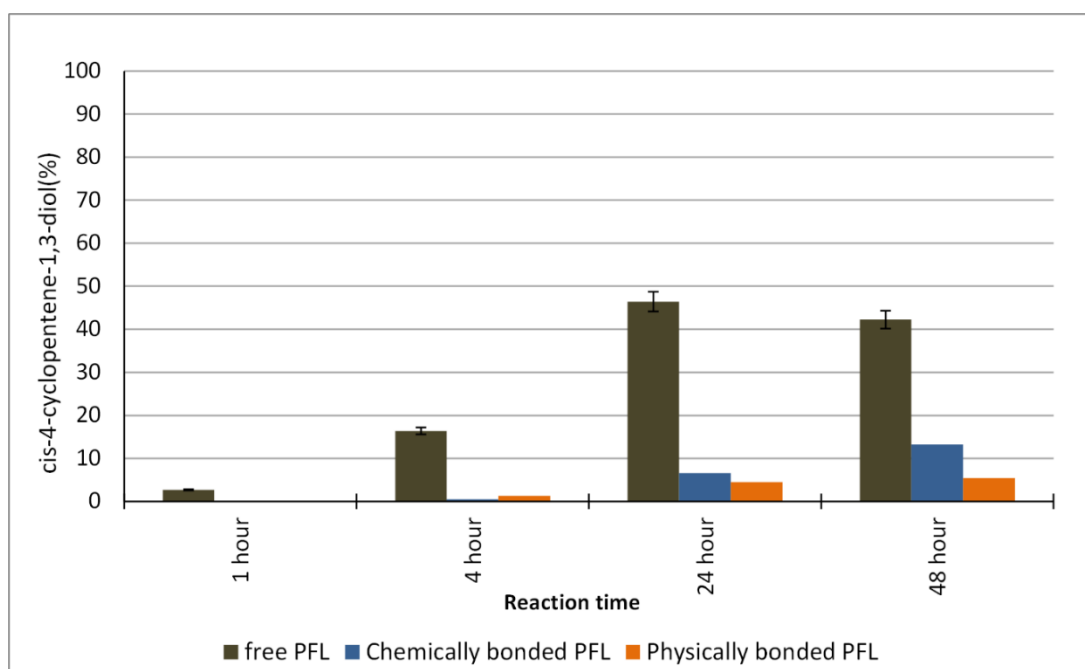


Figure 4-23. Comparison between free and immobilised PFL lipases in forming *cis*-4-cyclopentene-1,3-diol during the 48 hours reaction period.

It was observed that the initial conversion to desired products using free PFL is much higher than immobilised PFL, with the optimum conversion of 68% after 4 hours. However as shown in the figures physically adsorbed PFL affords higher conversion of reactant to desired product with 73% conversion over 24 hours. Nevertheless when physically adsorbed lipase was reused as the catalyst in the second cycle the conversion reduced to less than 36% which suggest that physically adsorbed PFL was not stable and leached into the reaction. With regard to chemically immobilized PFL, the lipase exhibited an increased catalytic activity in the second cycle which could be the result of enzyme activation as discussed in Section 4.4.

In order to evaluate the reusability of the immobilised lipase, after the experiment enzyme was recycled and reused in successive reactions. Figure 4-24 presents the percentage of (1*S*, 4*R*)-*cis*-4-acetoxy-2-cyclopenten-1 produced during the reusability test (3 cycles). Free enzyme could not be recovered from the reaction mixture hence presented only in the first cycle.

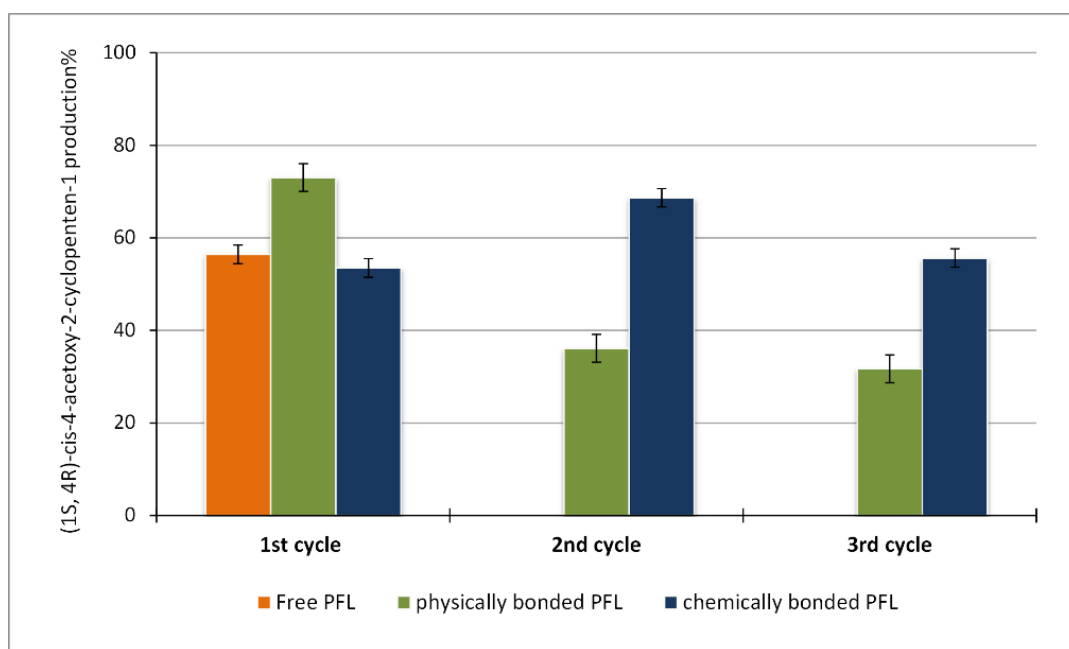


Figure 4-24 Reusability of PFL in production of (1S, 4R)-cis-4-acetoxy-2-cyclopenten-1 over 3 cycles of 24 hours reaction at 25°C. Since free enzyme could not be recovered from the reaction mixture, it is presented only in one cycle

The activity of free and immobilized CRL in the hydrolysis of cis-3,5-diacetoxy-1-cyclopentene and formation of the products were evaluated over 48 hours reaction. The quantity of the products were calculated based on the standard curves presented in Figure 4-25, Figure 4-26 and Figure 4-27.

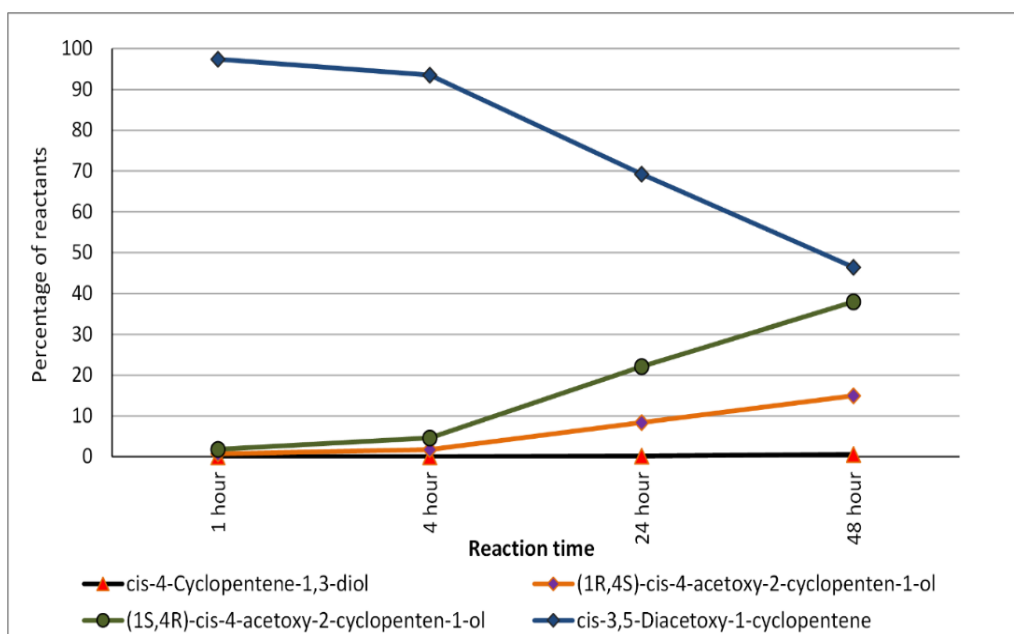


Figure 4-25. Percentage (%) of unreacted cis-3,5-Diacetoxy-1-cyclopentene and the corresponding products of enzymatic hydrolysis of cis-3,5-Diacetoxy-1-cyclopentene using chemically immobilised CRL on the surface of the nanoparticles at different time intervals of 1, 4, 24 and 48 hours

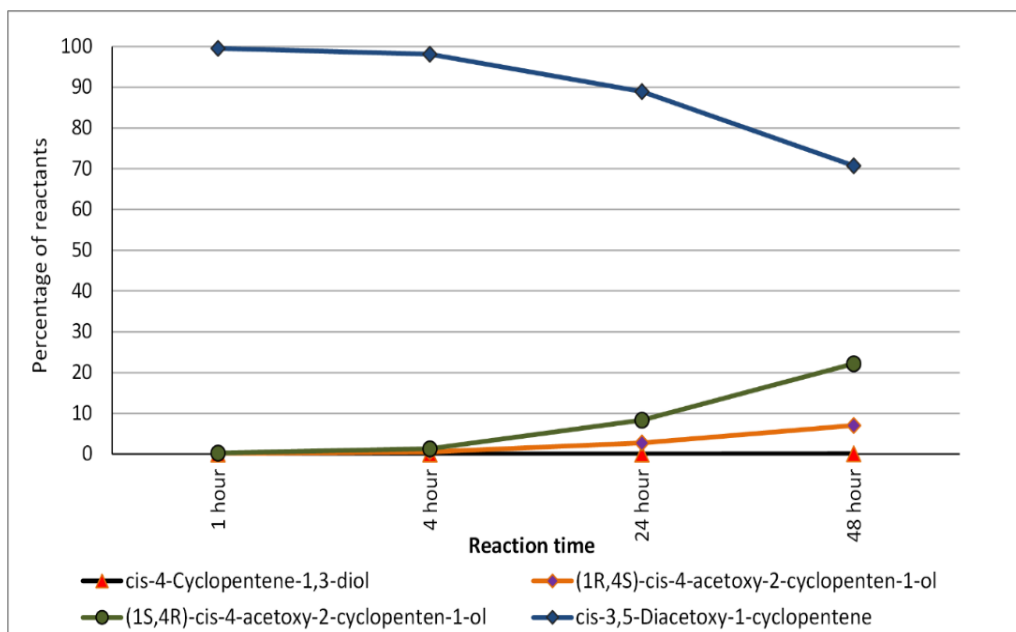


Figure 4-26. Percentage (%) of unreacted *cis*-3,5-Diacetoxy-1-cyclopentene and the corresponding products of enzymatic hydrolysis of *cis*-3,5-Diacetoxy-1-cyclopentene using physically immobilised CRL on the surface of the nanoparticles at different time intervals of 1, 4, 24 and 48 hours

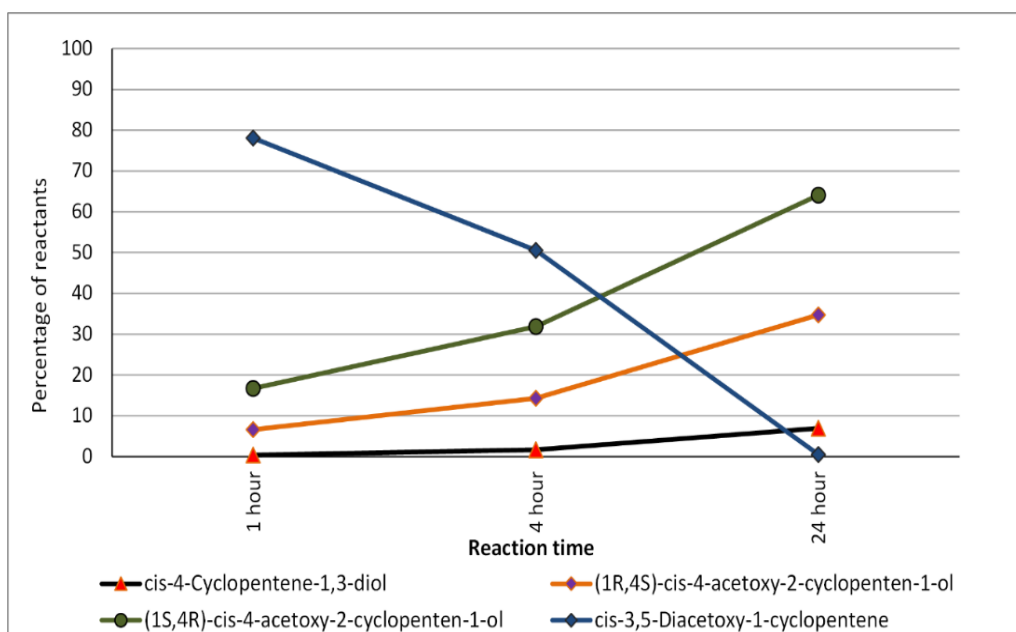


Figure 4-27. Percentage (%) of unreacted *cis*-3,5-Diacetoxy-1-cyclopentene and the corresponding products of enzymatic hydrolysis of *cis*-3,5-Diacetoxy-1-cyclopentene free CRL at different time intervals of 1, 4, 24 and 48 hours

As observed from the figures when either free CRL or immobilized CRL were used as the catalyst in the reaction, they produced both optical isomers, (1S, 4R)-*cis*-4-acetoxy-2-cyclopenten-1 and its enantiomer, (1R, 4S)-*cis*-4-acetoxy-2-cyclopenten-1, plus a negligible amount of unwanted *cis*-4-cyclopentene-1,3-diol. By the end of 24 hours the free CRL have completed the conversion (1 μ mol of reactant per 10 μ g of enzyme) while the immobilized enzyme (physically or chemically) accomplished relatively lower conversion values with physically adsorbed lipase affording the lowest conversion. After 48 hours the physically adsorbed CRL materials achieved

about 29% conversion of reactant (0.29 μmol of reactant per 10 μg of enzyme) and the chemically bonded CRL materials attained about 53.6% conversion of reactant (0.53 μmol of reactant per 10 μg of enzyme).

The ratio of (1S, 4R)-cis-4-acetoxy-2-cyclopenten-1 to (1R, 4S)-cis-4-acetoxy-2-cyclopenten-1 in the product mixture and the enantiomeric ratio (E) of the reaction was calculated based on Equation 4-1 (Fernández-Lorente et al., 2003, Chen et al., 1982). The enantiomeric ratio using CRL as the catalyst was calculated to be around 1.64 for free CRL, 3.58 for chemically immobilised CRL and 6.28 for physically adsorbed lipase.

$$E = \frac{\ln[1-c(1+ee)]}{\ln[1-c(1-ee)]} \quad \text{Equation 4-1}$$

Where c is the conversion and ee is the enantiomeric excess which can be calculated as Equation 4-2:

$$ee = \frac{A-B}{A+B} \quad \text{Equation 4-2}$$

Calculation of enantiomeric ratio (E) provides an indication of the interrelationship between enantiomeric excess (ee) and the conversion rate which helps to determine when to terminate the reaction to obtain specific enantiomeric excess of the desired product. The enantiomeric excess of (1S, 4R)-cis-4-acetoxy-2-cyclopenten-1 calculated at different intervals during the reaction are summarised in Table 4-2.

Table 4-2. Enantiomeric excess of (1S, 4R)-cis-4-acetoxy-2-cyclopenten-1 using immobilized CRL at different intervals.

Time (hours)	Physically adsorbed		Chemically immobilized		Free lipase	
	Yield (%)	ee (%)	Yield (%)	ee (%)	Yield (%)	ee (%)
1	0.30	0.29	1.87	0.44	16.71	0.43
4	1.32	0.43	4.64	0.45	31.84	0.38
24	8.34	0.50	22.12	0.45	64.06	0.29
48	22.17	0.51	37.97	0.43	63.80	0.25

From Table 4-2 it was observed that in the course of the reaction the free lipase showed decreased ee value which corresponds to reduced specificity toward formation of (1S, 4R)-cis-4-acetoxy-2-cyclopenten-1 where in case of chemically immobilised lipase the ee value is almost constant indication enhanced control over the reaction. In the case of physically immobilised lipase the increase in ee could be explained by the sustained leaching of the free lipase into the solution.

As seen from the graphs in both cases of free and immobilised lipase, with increasing the reaction time from 1 hour to 48 hours the conversion of the reactants to different products were increased. However in case of free lipase increasing the reaction over 24 hours resulted in further hydrolysis of the acetate group of (1S, 4R)-cis-4-acetoxy-2-cyclopenten-1 and its enantiomer to increase the concentration of unwanted cis-4-cyclopentene-1,3-diol product. Figure 4-28 and Figure 4-29 present the comparison between the free and immobilised lipase in forming (1S, 4R)-cis-4-acetoxy-2-cyclopenten-1 and cis-4-cyclopentene-1,3-diol, respectively.

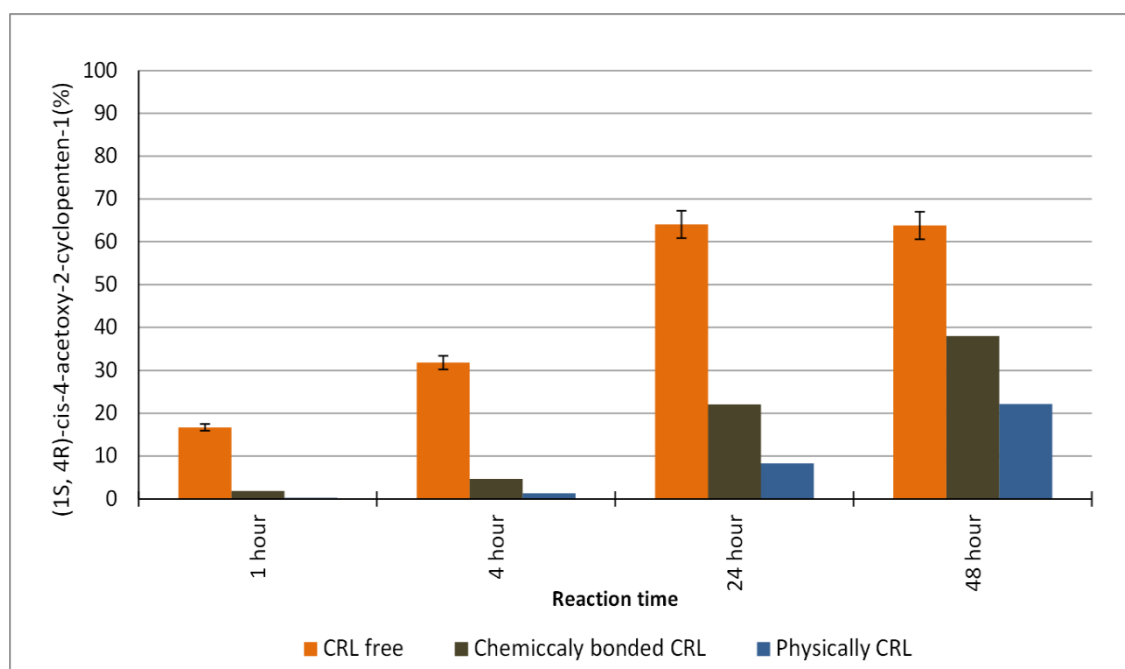


Figure 4-28. Comparison between free and immobilised CRL lipases in forming (1S, 4R)-cis-4-acetoxy-2-cyclopenten-1 during the 48 hours reaction period.

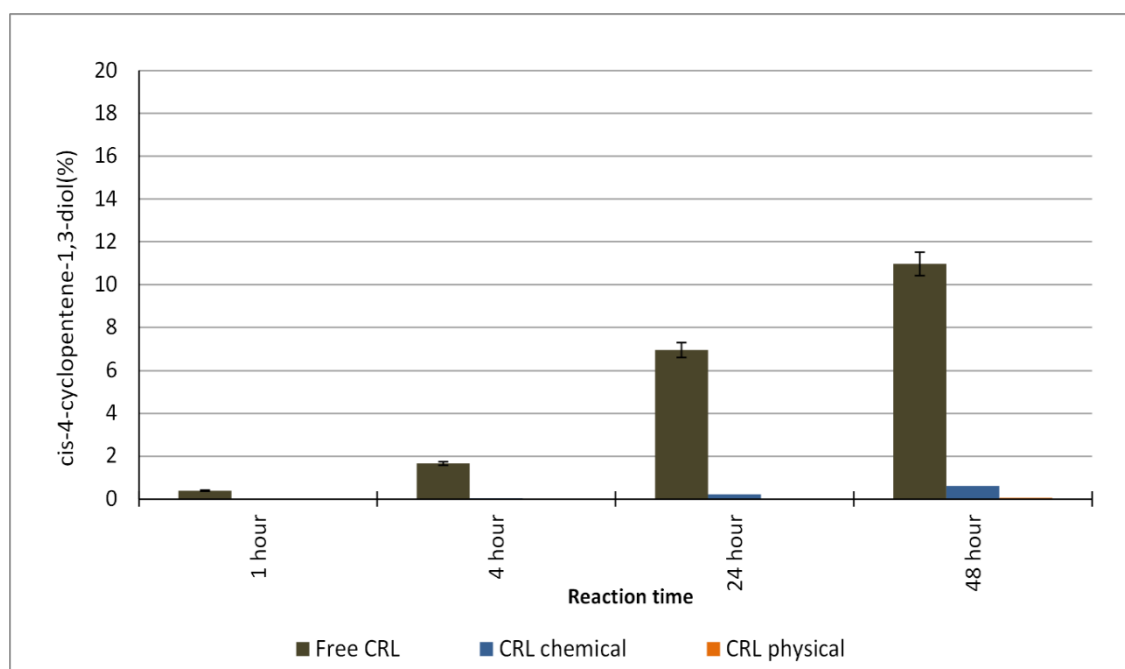


Figure 4-29. Comparison between free and immobilised PFL lipases in forming cis-4-cyclopentene-1,3-diol during the 48 hours reaction period.

It was observed that the free CRL showed higher conversion of cis-3,5-diacetoxy-1-cyclopentene to desired product compared to immobilised lipase with the optimum of 64% after 24 hours. Physically adsorbed CRL affords the lowest conversion of reactant to desired product with 22% conversion over 48 hours.

In order to evaluate the reusability of the immobilised lipase, after the experiment enzyme was recycled and reused in successive reactions. Figure 4-30 presents the percentage of (1S, 4R)-cis-4-acetoxy-2-cyclopenten-1 produced during the reusability test (3 cycles). Free enzyme could not be recovered from the reaction mixture hence presented only in the first cycle. As seen in the figure the catalytic activity of the lipase remained unchanged during the reusability study indicating no loss of enzymes after the 1st cycle even for the physically adsorbed lipase. Chemically immobilised CRL affords 22% of (1S,4R)- cis-4-acetoxy-2-cyclopenten-1-ol in the first cycle, 23% in second cycle and 27% in third cycle.

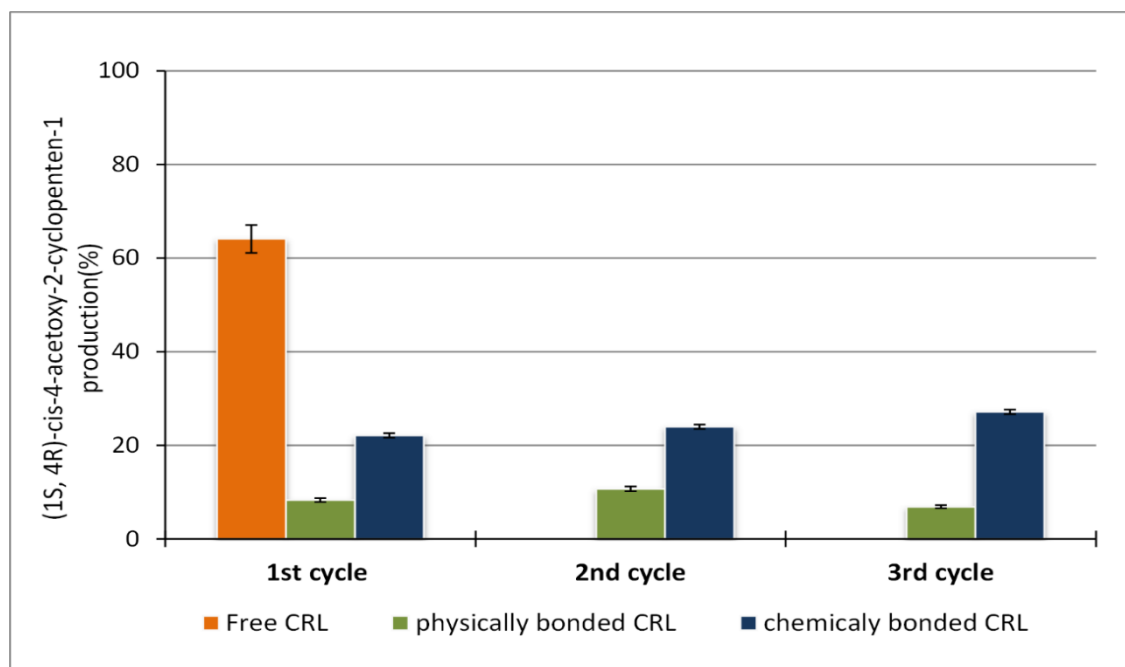


Figure 4-30. Reusability of CRL in production of (1S, 4R)-cis-4-acetoxy-2-cyclopenten-1 over 3 cycles of 24 hours reaction at 25°C. Since free enzyme could not be recovered from the reaction mixture, it is presented only in one cycle

4.6.1 Effect of Temperature on Lipase Activity

Lipases have received much attention due to their broad applications particularly CRL is well established as a result of its applications in pharmaceutical industry and biodiesel production from vegetable oils. An increase in the optimum temperature of immobilized lipase is important for industrial applications, since it allows reduced microbial contamination and reduced viscosity of oil and greases, which consequently increases the process yield (Miranda et al., 2011).

Enzymes are often immobilized onto solid supports to enable their recoverability and increase their thermal stability. The effects of temperature on activity of both free and immobilized PFL

and CRL lipases were studied by repeating the reaction at 37°C. This temperature was chosen based on the literature which suggest maximum activity of the free lipase for PFL is achieved between 30 and 50°C (Fox and Stepaniak, 1983, Boscolo et al., 2010, Chakraborty and Paulraj, 2009, Aysun Adan GÖKbulut, 2013) and maximum activity of the CRL occurs between 37 to 40°C (Santos et al., 2007, Miranda et al., 2011).

Figure 4-31 presents the activity of PFL in forming (1S,4R)- cis-4-acetoxy-2-cyclopenten-1-ol at two different temperatures of 25°C and 37°C.

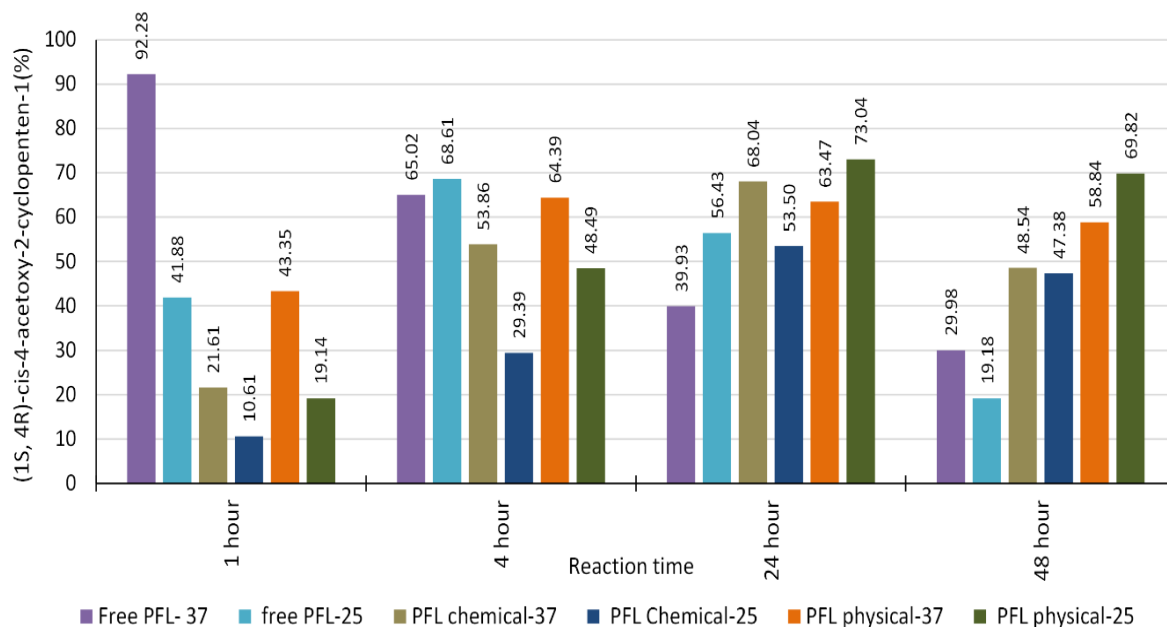


Figure 4-31. Effects of reaction temperature on hydrolytic activities PFL in forming (1S,4R)- cis-4-acetoxy-2-cyclopenten-1-ol at two different temperatures of 25°C and 37°C, over 48 hour period

Increasing the reaction temperature resulted in a raise in reaction rate. Free PFL produced maximum (1S,4R)- cis-4-acetoxy-2-cyclopenten-1-ol during the first hour of the reaction with the production rate of 92%. Similarly the reaction rate was increase for immobilised lipase. At 37°C, using the physically adsorbed PFL the maximum quantity of the desired product was produced in 4 hours where at 25°C it took 24 hours to maximise the desired product. The chemically immobilised lipase reached maximum production in 24 hours at both temperatures, however the product quantity was higher at 37°C.

Similar to the reaction performed at 25°C, free PFL exhibits high initial conversion to the desired product, however with increasing the reaction time an increasing amount of undesired dihydroxy was formed, which eventually became the dominant product in the reaction mixture. Increasing the reaction temperature resulted in even faster hydrolysis of the acetate group of (1S,4R)- cis-4-acetoxy-2-cyclopenten-1-ol to increase the concentration of unwanted cyclopent-2-en-1,4-diol product to 70% over 48 hours. The final concentration of (1S,4R)- cis-4-acetoxy-2-cyclopenten-

1-ol after 48 hours using free PFL was decreased to 29%. The increased PFL lipase activity in 37°C is in agreement with the literature (Aysun Adan GÖKbulut, 2013).

In order to compare the reusability of the immobilised lipase at 37°C and 25°C, after the experiment enzyme was recycled and reused in three successive reactions. Figure 4-32 presents the percentage of (1S, 4R)-cis-4-acetoxy-2-cyclopenten-1 produced during the reusability test. Free enzyme could not be recovered from the reaction mixture hence presented only in the first cycle. As seen in the figure the catalytic activity of the chemically immobilised lipase remained unchanged during the reusability study, however the physically immobilised lipase showed significant decrease in activity in each cycle.

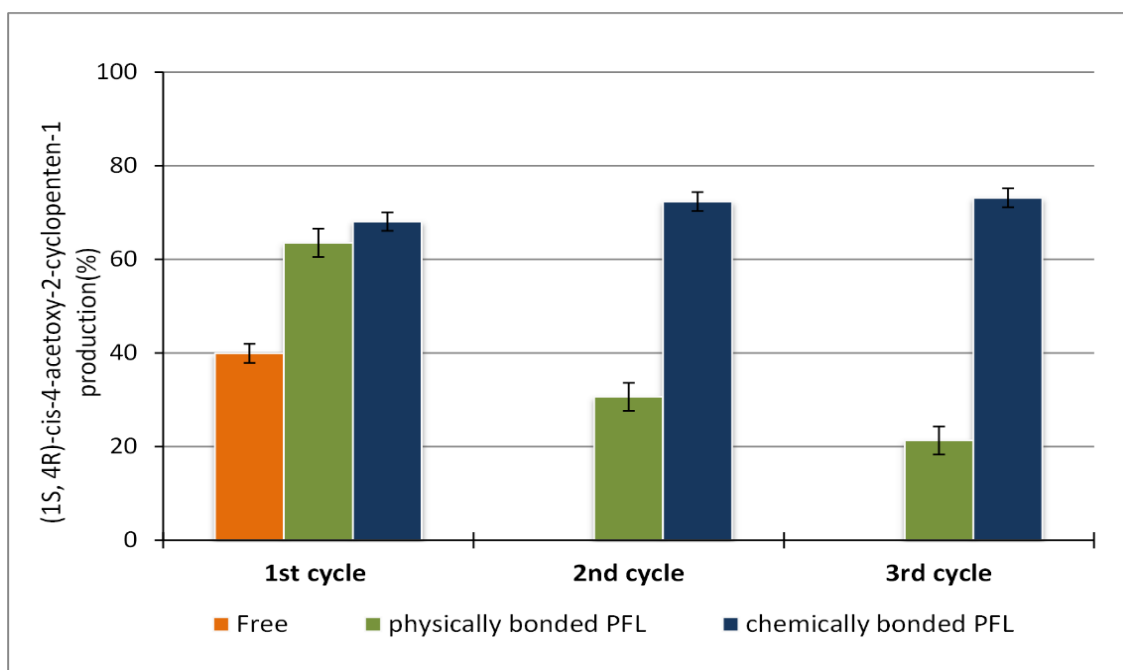


Figure 4-32. Reusability of PFL in production of (1S, 4R)-cis-4-acetoxy-2-cyclopenten-1 over 3 cycles of 24 hours reaction at 37°C. Since free enzyme could not be recovered from the reaction mixture, it is presented only in one cycle.

Figure 4-33 presents the CRL activity in forming (1S,4R)- cis-4-acetoxy-2-cyclopenten-1-ol at two different temperatures of 25°C and 37°C.

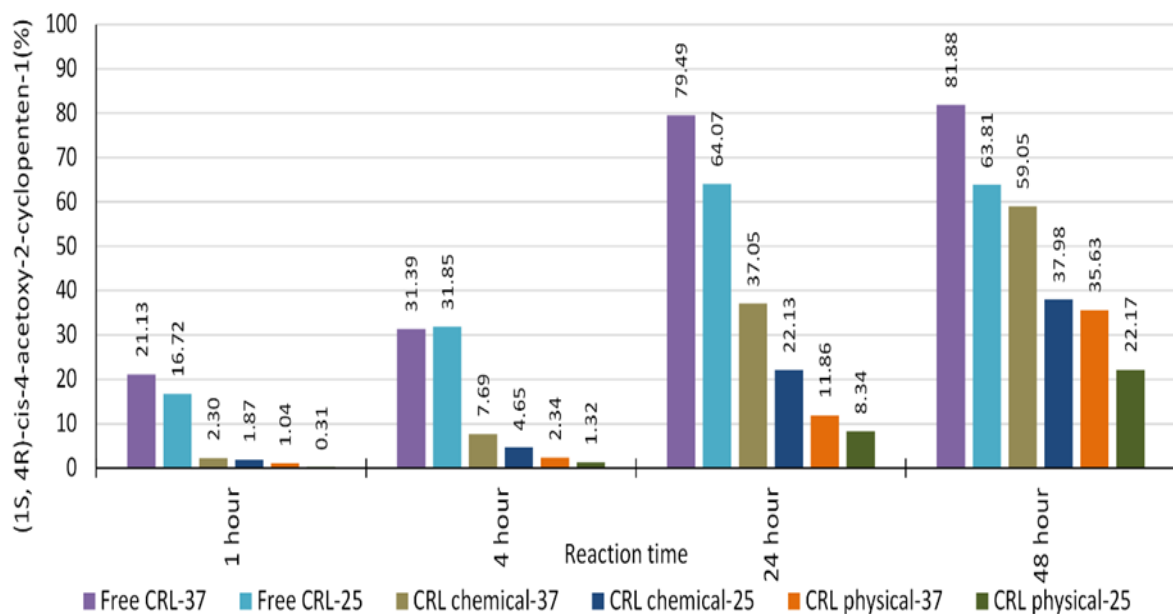


Figure 4-33. Effects of reaction temperature on hydrolytic activities CRL in forming (1S,4R)- cis-4-acetoxy-2-cyclopenten-1-ol at two different temperatures of 25°C and 37°, over 48 hour period

Similar to what observed for the reaction at 25°C, CRL lipase produced both optical isomers, 4-(R)-hydroxycyclopent-2-en-1- (S)-acetate and its enantiomer, 4- (S)-hydroxycyclopent-2-en-1- (R)-acetate and a negligible amount of unwanted cyclopent-2-en-1,4-diol. Compared to the reaction at 25°C the conversion rate was increased at 37°C. However, the activity ratio of the CRL lipase during the reaction was similar at both temperatures with free CRL exhibiting 25% of its activity in the first hour which indicates an increased lipase activity at higher temperature.

During the entire reaction free CRL affords higher conversion compared to immobilised lipase. Maximum production of 4- (R)-hydroxycyclopent-2-en-1- (S)-acetate was achieved in 48 hours reaction, where free lipase afforded 81%, chemically bonded lipases afforded 59% and physically adsorbed lipase afforded 35% yield. With regard to forming dihydroxy by-product, much higher values were obtained at 37°C (19% for free CRL) compared to 25°C (10.9% for free CRL) which could be due to higher lipase activity and reaction speed.

The increased CRL activity with the temperature is in agreement with the literature which suggests that for free CRL the maximum lipase activity is around 37 to 40°C (Santos et al., 2007, Miranda et al., 2011), for physically absorbed CRL is around 45°C (Milašinović et al., 2014) and for chemically bonded is around 45 to 55°C (Miranda et al., 2011, Pereira et al., 2003). The increase in the optimum temperature of the immobilized lipase could be attributed to the change in the conformational integrity of the lipase structure upon attachment to the support (Miranda et al., 2011). The lower activity of the immobilised lipase may be due to the higher optimum temperature of the immobilised lipase.

The enantiomeric excess of (1S, 4R)-cis-4-acetoxy-2-cyclopenten-1 at 37°C is calculated at different intervals during the reaction and summarised in Table 4-3 and Table 4-2. As seen from Table 4-2 and Table 4-3 the temperature of the reaction did not affect the *ee* values.

Table 4-3. Enantiomeric excess of (1S, 4R)-cis-4-acetoxy-2-cyclopenten-1 using immobilized CRL at different intervals.

Time (hours)	Physically adsorbed		Chemically immobilized		Free lipase	
	Yield (%)	<i>ee</i> (%)	Yield (%)	<i>ee</i> (%)	Yield (%)	<i>ee</i> (%)
1	1.04	0.30	2.30	0.43	21.13	0.42
4	2.34	0.32	7.69	0.47	31.39	0.38
24	11.86	0.50	37.05	0.44	79.49	0.30
48	35.63	0.54	59.05	0.44	81.88	0.28

In order to evaluate the reusability of the immobilised lipase at 37°C, after the experiment enzyme was recycled and reused in three successive reactions. Figure 4-34 presents the percentage of (1S, 4R)-cis-4-acetoxy-2-cyclopenten-1 produced during the reusability test over three consecutive cycles. Free enzyme could not be recovered from the reaction mixture therefore it was presented only in the first cycle. As seen in the figure the catalytic activity of the chemically immobilised lipase decreased slightly in each cycle, where the physically immobilised lipase showed significant decrease in lipase activity indicating the lipase loss during the reaction and the recycling process.

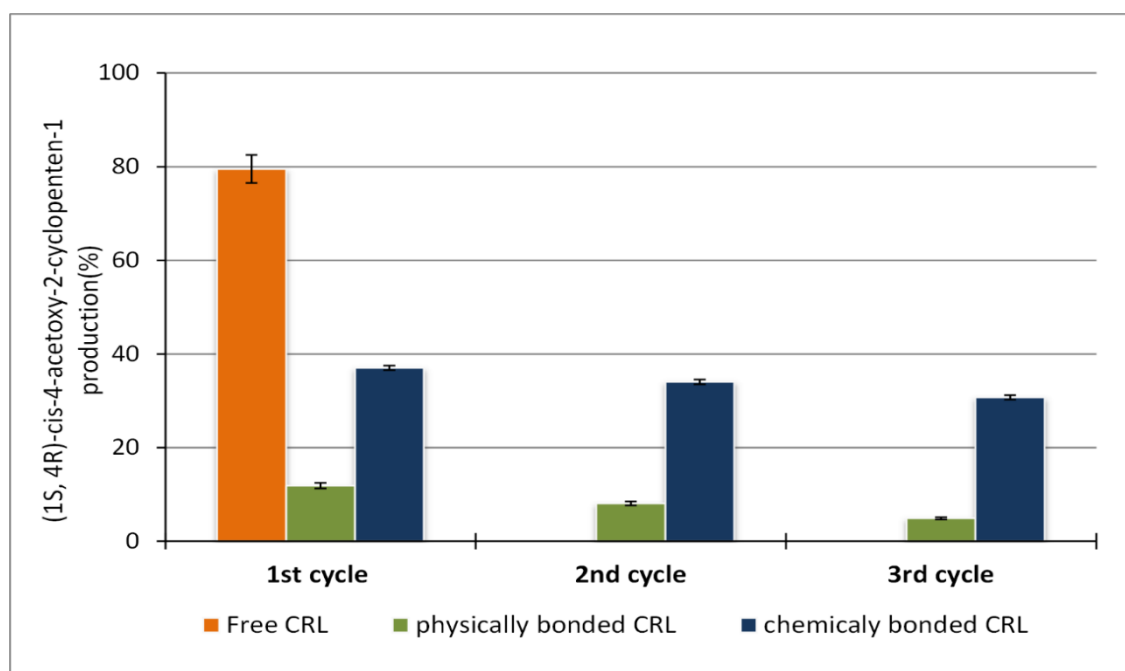


Figure 4-34. Reusability of CRL in production of (1S, 4R)-cis-4-acetoxy-2-cyclopenten-1 over 3 cycles of 24 hours reaction at 37°C. Since free enzyme could not be recovered from the reaction mixture, it is presented only in one cycle.

Comparing the enzymatic activity of CRL and PFL in hydrolysis of meso-cyclopent-2-en-1,4-diacetate, in both cases free lipases offer complete conversion in the first 24 hours of the reaction at 25°C and 37°C. Since 37°C is in the optimum activity range of the free lipase and close to optimal range for immobilised lipases, both lipases exhibited an increased activity with the raise in temperature (both free and immobilised lipase). PFL (both free and immobilised) offered an enantiomeric excess of 100% for the desired product while producing high amounts of the undesired dihydroxy by-product, whereas CRL (both free and immobilised) produced both enantiomers with lower quantity of the dihydroxy by-product. The highest conversion to the desired products for CRL is achieved using free CRL for 48 hours at 37°C with 81% conversion and for PFL the highest conversion occurs after 1 hour in 37°C using free lipase.

4.7 Conclusions

The catalytic activity of the enzymes immobilized on high surface area silica coated magnetite nanoparticles were investigated and compared with free enzyme in two different reactions. The results indicated that immobilised lipases (both CRL and PFL) retained their activity after immobilisation. In case of hydrolysis of pNPP the free lipases provided slightly higher conversion than immobilised lipases in the first cycle. The chemically immobilised lipase exhibited good reusability without loss of its activity in four sequential cycles, however the physically adsorbed lipase showed reduced activity which could be explained by loss of enzyme during recycling between successive reactions.

The CRL lipase (free or immobilised) activity in the presence of an AC field were accessed by hydrolysis of pNPP and the results were compared with the lipase activity in similar temperature using an incubator. The results indicated that the lipase retained its activity under influenced of a magnetic field and even produced higher yield compared to the control reaction at same temperature in the incubator.

With regard to hydrolysis of cis-3,5-diacetoxy-1-cyclopentene, the free lipase showed higher total conversion rate compared to immobilised lipases, however the immobilised lipases afford higher ratios of the desired product of (1S,4R)-cis-4-acetoxy-2-cyclopenten-1-ol which conclude that the immobilised lipases provide enhanced control over the formation of the desired products. Particularly in case of PFL, the free lipase reached its maximum conversion to desired product during the initial 4 hours of the reaction at 25°C or initial hour at 37°C, after which the dihydroxy by-product is formed in an excess amount as the dominant product.

The immobilised lipases were used in three successive cycles to evaluate the reusability of the immobilised lipase. Both chemically immobilised lipases retained their activity during recycling while physically adsorbed lipase displayed a decreased activity in each consecutive cycle indicating lipase loss during the reaction and recycling process.

The lipase activity were examined in an increased temperature of 37°C for both free and immobilised lipases. As expected, from the literature, it was observed that both lipases exhibited higher activity at this temperature which could be due to fact that for PFL and CRL the optimum temperature is close to 37°C. At 37°C similar to 25°C the free lipases showed higher conversion compared to immobilised lipase.

CHAPTER 5

DRUG LOADING AND RELEASE

5.1 Introduction

Since most of the commonly used anticancer agents induce serious side effects to healthy cells and tissues before reaching the target cancer cells, the main challenge in cancer treatment is to deliver the therapeutic agents directly to cancerous tissue and modifying the release kinetics of the therapeutic agents from their carrier system. Additionally, many of the therapeutic agents suffer from short half-life and low solubility, especially for hydrophobic drugs, which require them to be injected in doses higher than required (Daglar et al., 2014, Nicolas et al., 2013). Furthermore, in many cases tumour cells develop multidrug resistance (MDR) which lead to therapeutic failure and death in patients suffering from cancer (Kievit et al., 2011, Tsubaki et al., 2014, Wang et al., 2014, Cuong et al., 2010b).

Nanoparticle-based drug delivery systems offer numerous advantages including low toxicity, controlled cargo release, and the targeting ability (Knezevic and Lin, 2013, Wang et al., 2014). Nanoparticulate drug carriers afford higher accumulation of drug in tumour cells *via* enhanced permeability and retention (EPR) (Cuong et al., 2010b). Furthermore encapsulation of the drugs in nanoparticles could bypass the efflux action of P-glycoprotein which has been proven to be a promising approach to overcome the drug resistance (Wang et al., 2014, Meng et al., 2013, Zeng et al., 2014). P-glycoprotein (Pgp) is an energy-dependent drug efflux pump which actively pumps the drug out of cells causing reduced intracellular drug concentrations and decreased therapeutic efficacy (Huang et al., 2011, Gottesman et al., 2002) Among different nanoparticle-based drug delivery systems, biocompatible mesoporous silica nanoparticles with large surface area offer many advantages as efficient drug delivery systems. Wang *et al.* among others have confirmed the ability of mesoporous silica nanoparticles as nanocarriers to sidestep drug resistance mechanisms (Wang et al., 2014). Mesochannels of the mesoporous silica nanoparticles enable encapsulation of large dosage of drugs and protects the drugs from hydrolysis and enzymatic degradation. Recently mesoporous silica based nanoparticles have been used in various nanomedicine applications such as fluorescent markers (Lu et al., 2010b, Rosenholm et al., 2010b), drug and gene delivery (Chen et al., 2009a, Yiu et al., 2011, Meng et al., 2013), and MRI contrast agents (Nakamura et al., 2015, Sahoo et al., 2014, Lee et al., 2010, Julian-Lopez et al., 2007).

Utilisation of mesoporous silica-based drug delivery systems are facing some challenges, for instance there is limited control over drug release kinetics from uncapped mesoporous nanoparticles which could result in premature drug release. Additionally mesoporous silica nanoparticles have low dispersibility and could aggregate under physiological conditions (Wang et al., 2010a). Different strategies have been reported in the literature to overcome these challenges including surface functionalization (Knezevic and Lin, 2013, Sardan et al., 2014) and surface coatings (Mal et al., 2003, Nguyen et al., 2005). Capping the mesopores with stimuli-

responsive materials may facilitate a new generation of smart delivery systems. Stimuli-responsive materials could deliver therapeutic agents at the targeted tissue, minimizing the systemic delivery of drug and protecting the healthy cells from the toxic side effects of the drugs. Physicochemical properties or structural conformations of stimuli-responsive materials could be altered using external or internal stimuli to trigger the cargo release (Daglar et al., 2014, Dong et al., 2013). In This project the change in pH and the temperature were studied as internal and external release triggers.

Since tumors exhibit a lower extracellular pH than healthy tissues, pH triggered drug release is extensively studied. The pH of blood and normal tissues is 7.4, but the extracellular pH in tumour tissues is about 6.8 and, endosome's pH ranges from 4.5 to 6.5. These pH differences could be used to trigger drug release in cancer site (Daglar et al., 2014). Additionally pH-sensitive drug release could overcome the Pgp-mediated multidrug resistance by releasing the drug in endosomes (Wang et al., 2014).

Another method to induce drug release is temperature triggered release. Application of an external AC magnetic field to magnetic nanoparticles causes localized temperature rise, hyperthermia, which could be used to kill the cancer cells. This temperature rise could also be used to modify the characteristic of the drug delivery system and trigger the drug release. Using this thermal energy as stimuli to release drugs, make it possible to gain the synergistic effect of hyperthermia and chemotherapy agents to kill cancer cells (Glover et al., 2013).

In this project different magnetic nanocomposites were developed as nano carriers for drug delivery systems based on magnetite core-shell structure. Two different model drugs were used to explore the ability of the synthesised nanoparticles for loading and release of the chemotherapeutic agents. The drug delivery systems were first evaluated by using hydrophilic chemotherapy drug mitomycin C (MMC). Then the drug delivery systems were optimized by capping the mesopores of the silica nanoparticles with heat sensitive polymer or liposomes. The optimized system were tested using Doxorubicin (DOX) as model drug. Coating the silica nanoparticles with polymeric micelles or liposomes have various advantages in drug delivery applications including preventing the entrapped drug in the silica mesopores from dissociation upon dilution in the blood stream after intravenous injection and facilitating their extravasations at tumour sites by avoiding renal clearance and non-specific reticuloendothelial uptake (Shuai et al., 2004). The drug release was assessed under both pH and temperature stimuli conditions.

The cytotoxic effects of the developed drug delivery systems were studied *in vitro* against breast cancer cell lines (MCF7) and glioblastoma cancer cell lines (U87). It is the utmost importance that the drug delivery system without the drug have no cytotoxic effects and are biocompatible. Therefore the nanoparticles were tested *in vitro* against the cell lines with and without the drug. Generally, nanoparticles with and without drug were added into the cell culture and proliferation

and viability of the cells were monitored and compared with control cells without drug and free drug control cells. The results are presented in Chapter 6.

5.1.1 Mitomycin C (MMC)

Mitomycin or Mitomycin C (MMC) is a water-soluble antibiotic and anticancer drug widely used in first-line treatment for a wide range of cancers (Verweij and Pinedo, 1990, Cummings et al., 1998, Tomasz, 1995). Mitomycin C (MMC) is commonly used in chemotherapy regimens for treatments in various tumour types such as gastric cancer, pancreatic cancer, breast cancer, non-small cell lung cancer, cervical cancer, prostate cancer, liver cancer and bladder cancer (Slowing et al., 2007b). MMC cytotoxicity mechanism is related to DNA cross-linking, and free radical-induced DNA strand breakage (Cummings et al., 1998). MMC is a very poor substrate for Pgp and maintains its activity against many types of Pgp-mediated MDR tumour phenotype (Gabizon et al., 2006, Li et al., 2014a, Gontero et al., 2002) (Yi et al., 2014, Matsumoto et al., 1986).

Therapeutic effect of MMC is limited due to the dose-limiting toxicity and serious side effects such as subacute and severe myelosuppression, gastrointestinal complications and nephrotoxicity, and rapid elimination from the body (Li et al., 2014a, Yi et al., 2014). Different strategies have been developed in the literature to overcome these drawbacks including encapsulation of the MMC in liposomes (Sen et al., 2012b) or polymeric carriers (Yi et al., 2014). Figure 5-1 shows the MMC structure.

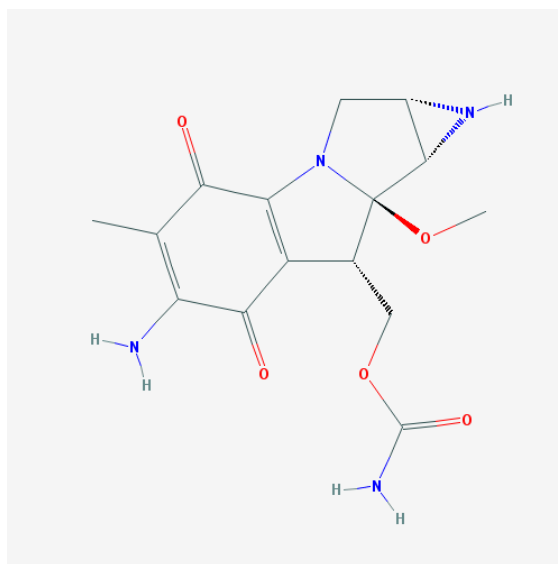


Figure 5-1. Structure of Mitomycin C

5.1.2 Doxorubicin (DOX)

Doxorubicin (DOX) was chosen as a model hydrophobic anticancer drug to load in synthesised nanoparticles. DOX is a highly potent anthracycline used in the treatment of numerous malignancies including bladder cancer, breast cancer, stomach cancer, lung cancer, ovarian cancer, thyroid cancer, neuroblastoma, and multiple myeloma and other cancer types (Mohan and

Rapoport, 2010). However, the therapeutic efficacy of DOX is limited by its poor solubility, low bioavailability, short-plasma half-life, and its life-threatening side effects including cardiotoxicity and bone marrow suppression (Cuong et al., 2010a, Greene et al., 1983). In addition, DOX is a substrate for ABC-mediated drug efflux. Overexpression of various members of the superfamily of adenosine triphosphate binding cassette (ABC)-transporters has been shown to promote the efflux of a broad class of hydrophobic drugs including DOX from cancer cells and cause the multidrug resistance (MDR) phenotype (Wang et al., 2014, Kievit et al., 2011, Szakacs et al., 2006).

The high therapeutic index, but poor efficacy of doxorubicin makes it essential to explore new approaches to improve the therapeutic efficacy of DOX and overcome the drug resistance. A novel approach to address cancer drug resistance is to take advantage of the ability of nanocarriers to sidestep drug resistance mechanisms by endosomal delivery of chemotherapeutic agents (Kievit et al., 2011, Tsubaki et al., 2014, Wang et al., 2014, Cuong et al., 2010b). Figure 5-2 presents the DOX structure.

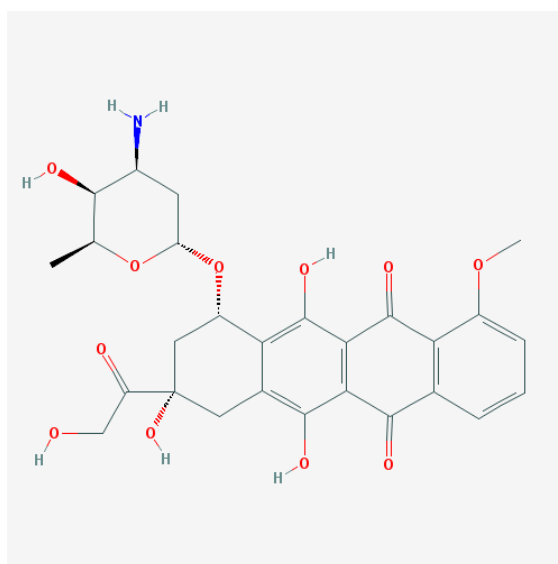


Figure 5-2. DOX structure

5.1.3 Drug Loading

The Drug loading content (DLC) and drug loading efficiency (DLE) were calculated based on Equation 2-1 and Equation 2-2 in Section 2.26.

DLC was quantified indirectly by determining the absorbance of the supernatant (at $\lambda_{485\text{nm}}$ for DOX and $\lambda_{365\text{nm}}$ for MMC) after magnetically separation of the nanoparticles and comparing the drug concentration with the initial drug in the solution or directly by dissolving the lyophilized micelles in a mixture of DMSO and chloroform.

The drug loading efficiency was calculated by comparing the weight percentage of drug loaded into the nanoparticles with the initial amount of drug available in the solution.

DOX concentrations were quantified using a pre-established calibration curve of DOX in PBS and acetate solutions. The DOX standard curves are presented in Figure 5-3 and Figure 5-4. The calibration curve was obtained by preparing DOX solutions of various concentrations and measuring the UV-absorptions of the solution.

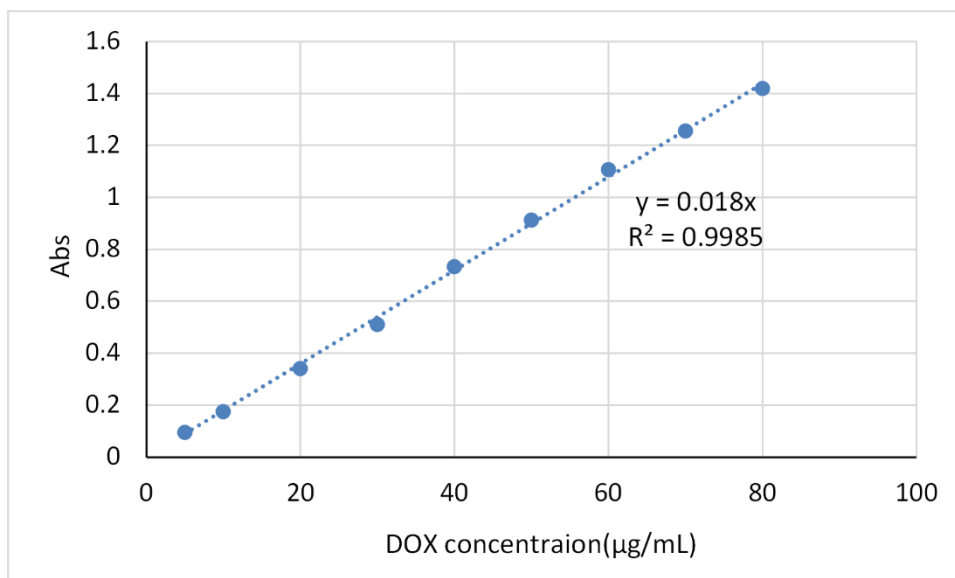


Figure 5-3. Standard curve of DOX in PBS

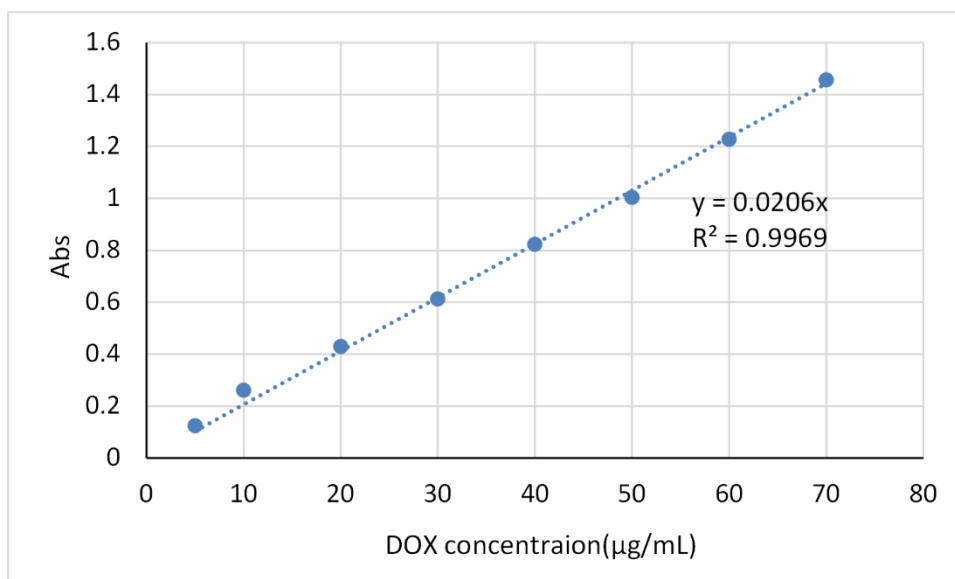


Figure 5-4. Standard curve of DOX in acetate buffer

The DOX loading content and DOX loading efficiency for different nanocomposites were ranged from 3.75 to 10.30% and 57 to 85%, respectively.

Similarly the MMC encapsulations were quantified using a pre-established calibration curve of MMC in water or buffer. The standard curves for MMC are shown in Figure 5-5 and Figure 5-6. Since the MMC loading was performed in water and the MMC release study was performed in PBS, the MMC standard curves were prepared both in water and PBS.

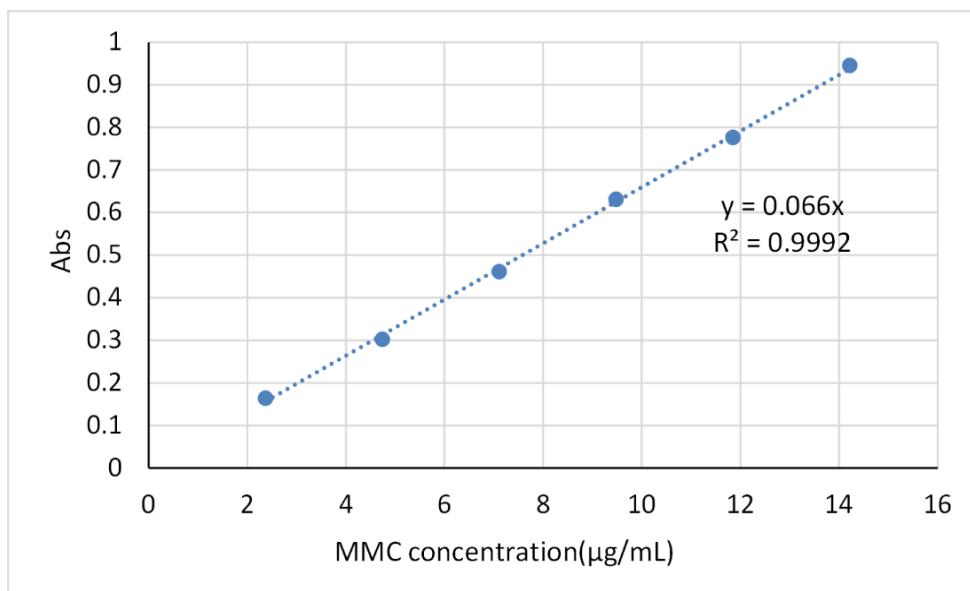


Figure 5-5. Standard curve for MMC in water

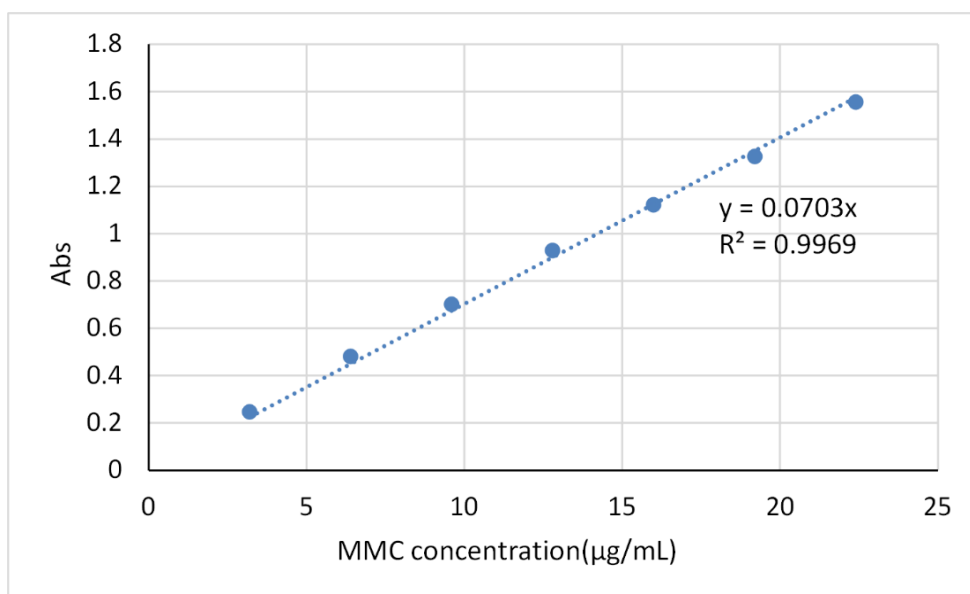


Figure 5-6. Standard curve for MMC in PBS

The DLC and DLE of the different materials were calculated and summarised in Table 5-1.

Table 5-1. A summary of drug loading content and drug loading efficiency of the developed materials

Material	Drug used	DLC (mg drug/mg material)%	DLE%
ME55-PEG-PCL	DOX	6.91	74.86
ME93-PEG-PCL	DOX	7.92	85.85
ME94-PEG-PCL	DOX	6.20	67.21
ME60	DOX	10.3	57.60
ME60-L	DOX	5.9	65.8
ME16	MMC	0.48	16.16
ME32	MMC	0.66	22.35
ME33	MMC	0.90	30.42
Magnetoliposomes	MMC	0.46	68.80

5.2 MMC Loaded Mesoporous Silica Coated Nanoparticles (ME32-ME33-ME16)

Silica nanoparticles have shown great potential as drug delivery systems. The biodegradable and biocompatible mesoporous silica nanoparticles with high surface area and pore volume have great drug loading capacities. Furthermore the easily achieved surface functionalization would enhance the cellular uptake and make them suitable for targeted drug delivery applications (Kapse-Mistry et al., 2014, Rosenholm et al., 2010a). The drawbacks of MMC could be overcome by using the silica nanoparticles as drug carriers to localise the cytotoxicity of the drug to cancerous tissue and minimize the necessary drug dosage.

The silica nanoparticles were prepared as described in Section 2.4. The shell thickness of the core-shell silica coated nanoparticles were controlled through the reaction time and the amount of the TEOS silica source. The pores in the mesoporous silica nanoparticles were prepared by using CTAB as template. The template was removed using acidic ethanol. The prepared mesoporous silica nanoparticles were characterized using TEM and VSM for morphological study and magnetic evaluation as shown in Chapter 3. The surface area of the nanoparticles were measured using nitrogen adsorption-desorption test where a clear relation between the mesoporous shell thickness and the surface area of the nanoparticles was observed.

Three different mesoporous silica coated nanoparticles were tested for MMC drug delivery applications; ME16, ME32 and ME33.

5.2.1 Drug Loading

Drug loading efficiency and drug loading content was determined by measuring the UV absorbance of the supernatant at $\lambda_{365\text{nm}}$ and quantifying it using the pre-established standard curve of MMC in water (the standard curve of MMC in water is shown in Figure 5-5). The drug loading content was measured at two different temperatures of 18°C and 10°C and at different intervals of up to 48 hours. The drug loading performance of different samples are shown in Table 5-1.

Figure 5-7 shows the drug loading profile of ME16. The MMC loading content and efficiency were calculated to be 0.46% and 15.52% at 18°C and 0.47% and 16.16% at 10°C. The maximum drug loading was observed in the first 12 hours of the drug loading process at 18°C after which the drug loading content was only slightly increased with increased time. However at 10°C the maximum drug loading was achieved in the first 3 hours and after that drug loading efficiency was only increased by 2%. The drug loading content after 3 hours loading at 10°C was close to drug loading content measured at 18°C after 48 hours.

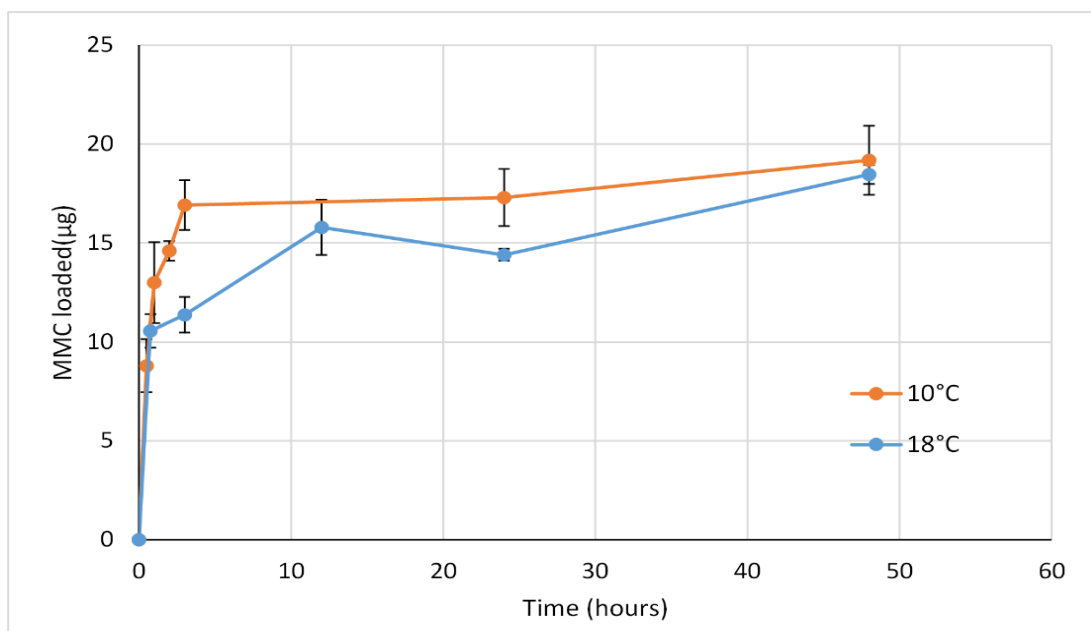


Figure 5-7. MMC loading profile of ME16 at different temperatures

Figure 5-8 shows the drug loading profile of ME32. The MMC loading content and efficiency were calculated to be 0.60% and 20.42% at 18°C and 0.66% and 22.35% at 10°C. The drug loading profile of ME32 shows maximum loading of MMC in the initial 3 hours of the incubation process for both temperatures. The drug loading content shows a decrease after reaching the maximum at initial 3 hours. This decrease in drug content could be due to leakage of the drug from the mesopores back into the solution. The drug loading profiles indicate an increase in drug loading content with the decrease in incubation temperature during the drug loading process.

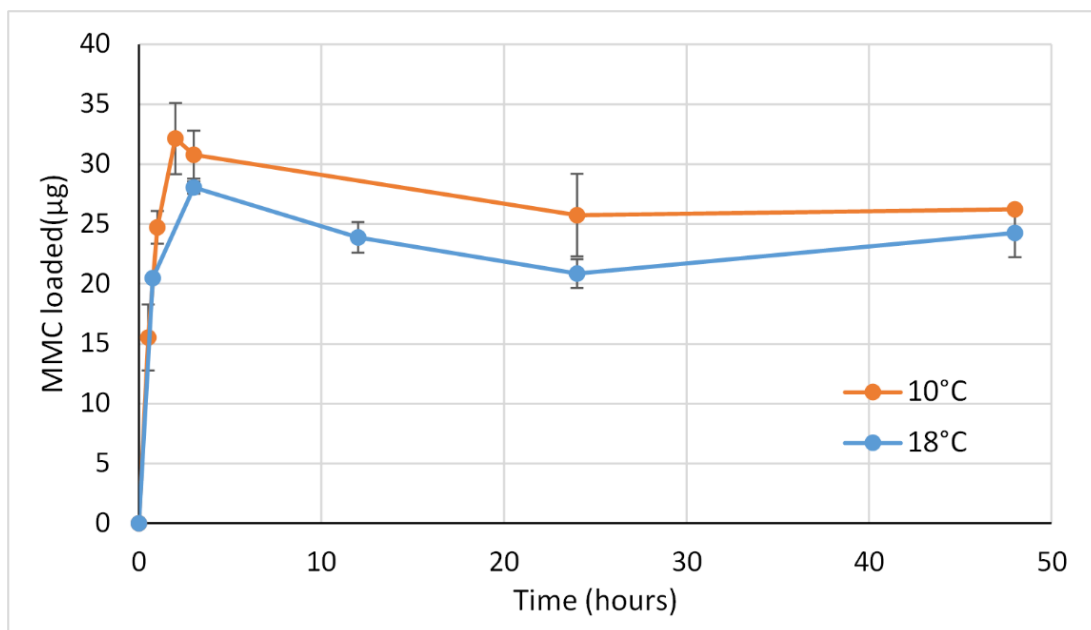


Figure 5-8. MMC loading profile of ME32 at different temperatures

Figure 5-9 presents the drug loading profile of ME33. The MMC loading content and efficiency were calculated to be 0.71% and 24.03% at 18°C and 0.90% and 30.42% at 10°C. The drug loading profile of ME33 shows maximum loading of MMC in the initial 3 hours of incubation at 18°C and maximum loading of MMC after 6 hours of incubation at 10°C. The drug loading content was decreased with increased incubation time which could be explained by leaking the drug from the uncapped mesopores back to into the solution. The drug loading profiles indicate an increase in drug loading content with the decrease in the incubation temperature during the drug loading process.

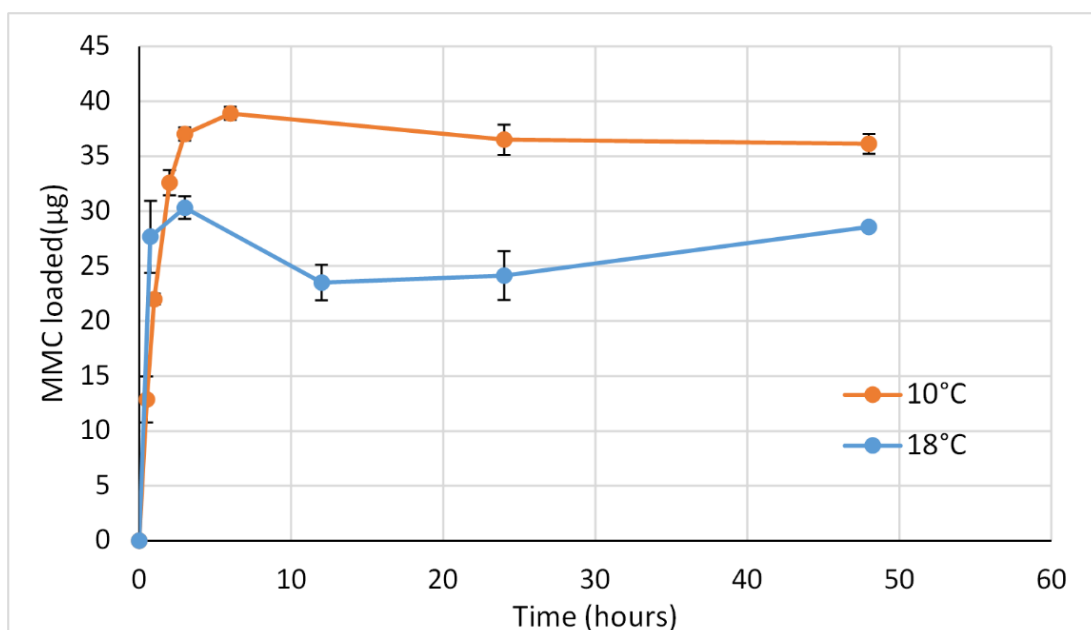


Figure 5-9. MMC loading profile of ME33 at different temperatures

All the samples demonstrated increased drug loading efficiency with the decreased incubation temperature. The maximum drug loading was observed for ME33 with around 40 μg drug loaded which was about 30.5% of the available drug in solution. The higher drug loading performance of the ME33 compared to ME16 and ME32 could be due to higher shell thickness and higher surface area of ME33. Figure 5-10 presents the relation between shell thickness and drug loading content based on ME16, ME32 and ME33.

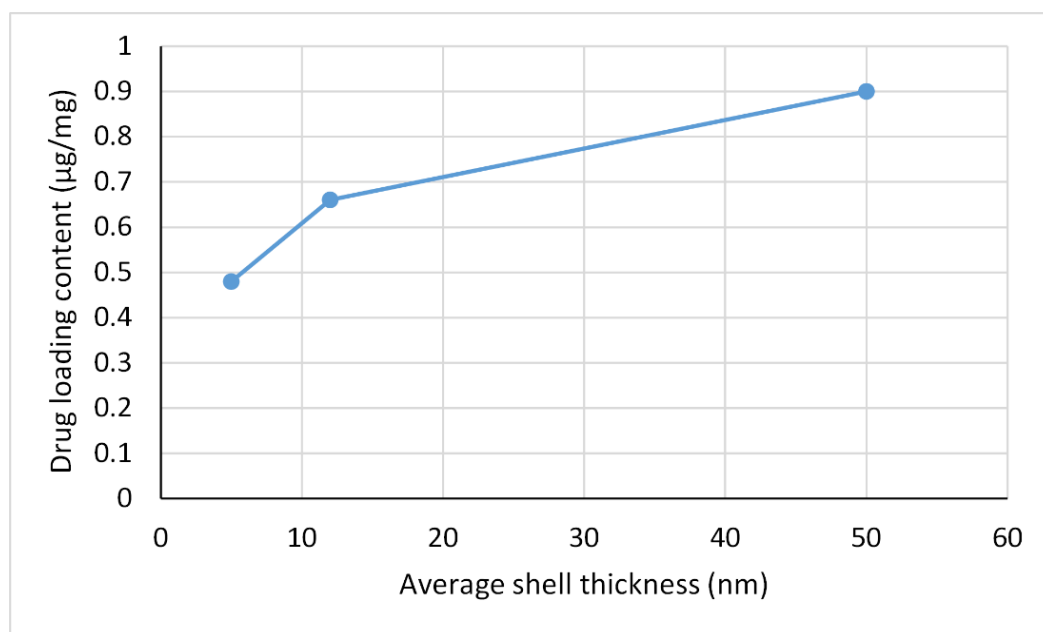


Figure 5-10 Relation between shell thickness and drug loading content.

5.2.2 MMC Drug Release

The MMC release from silica coated magnetic nanoparticles were studied in PBS buffer at body temperature. MMC-loaded nanoparticles were magnetically collected at different time intervals and the drug content of the solution was measured using UV absorbance at $\lambda_{365\text{nm}}$. The concentration of MMC in the solution were determined by comparing the absorption values with a pre-established standard curve of known MMC concentrations in PBS buffer (see Figure 5-6).

Figure 5-11 presents the MMC release profile of ME16 in PBS buffer at body temperature (37°C). The release profile indicates a burst release of the drug in the first initial hour of incubation. The drug released reached a plateau in about 15 hours and did not change significantly over next 30 hours of experiment. The final drug released from the nanoparticles were around 5.2% of the loaded drug. The initial burst release could be due to diffusion of the MMC absorbed on or near the external surface of the nanoparticles.

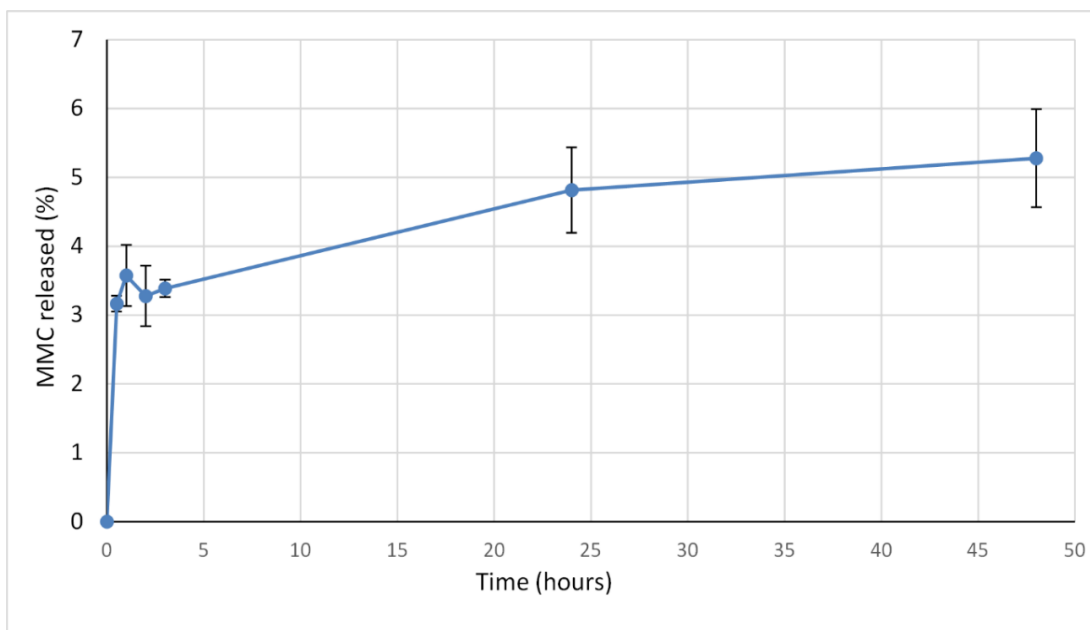


Figure 5-11. MMC release from ME16 in PBS buffer at body temperature (37°C)

Figure 5-12 presents the MMC release profile of ME32 at body temperature. The release study indicates a burst release at the initial 4 hours followed by reaching a plateau with no significant increase in drug release. After 48 hours the cumulated drug release was reached the maximum of 6.7%.

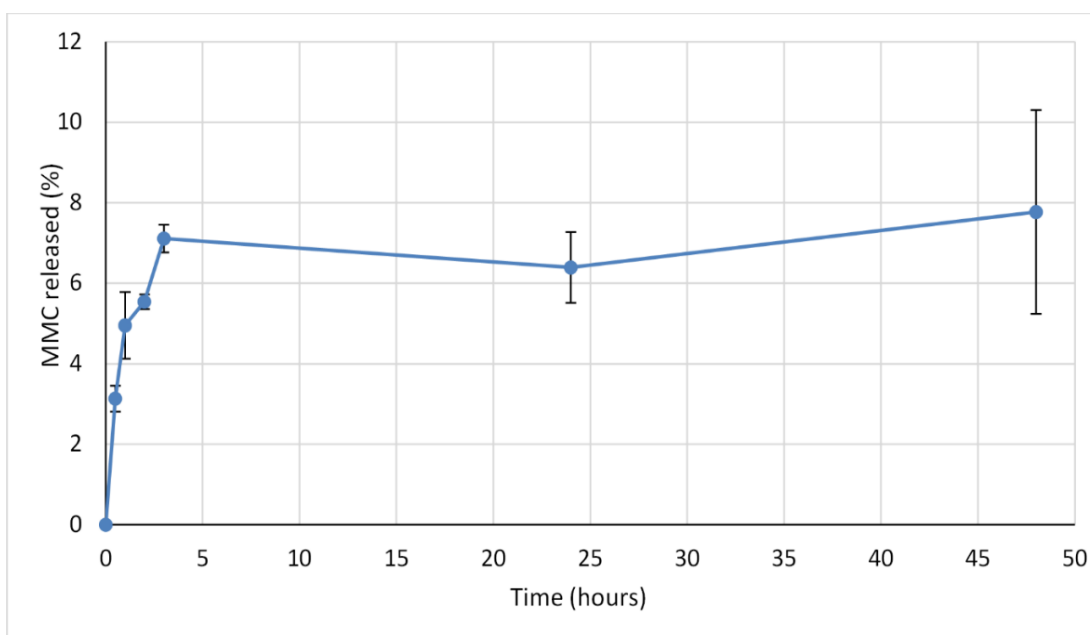


Figure 5-12. MMC release from ME32 in PBS buffer at body temperature (37°C)

Figure 5-13 presents the MMC release profile of ME33. The MMC release profile indicates an initial burst release of the drug in the first 3 hours of incubation followed by a sustained release for the next 48 hours. The total drug release from the nanoparticles reaches 9.7% after 48 hours of incubation. The slow continues drug release from the silica nanoparticles is in agreement with reported literature (Yi et al., 2014).

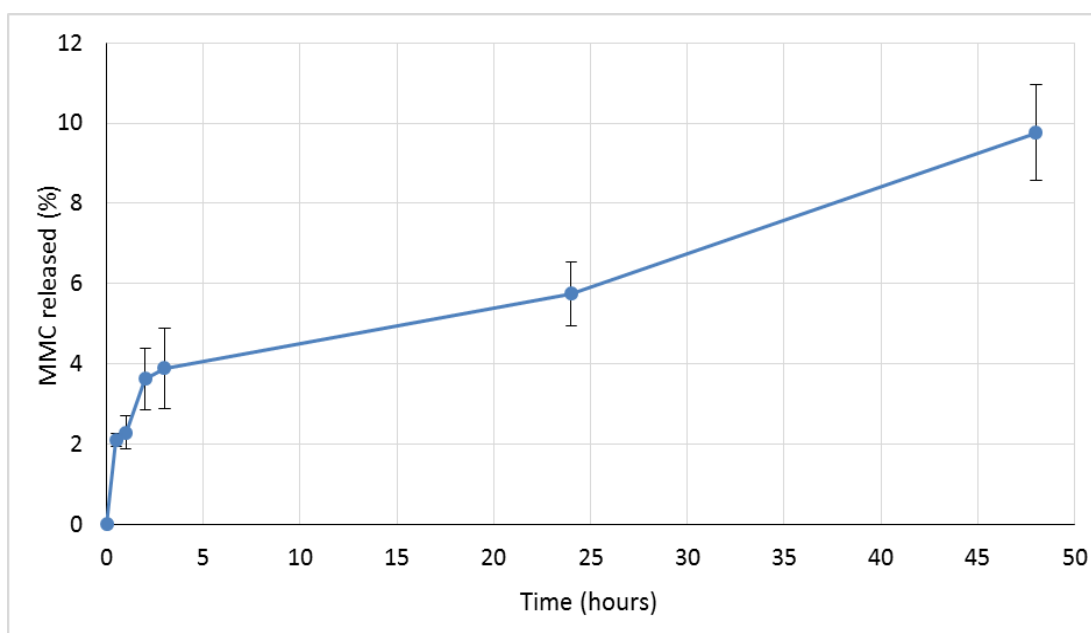


Figure 5-13. MMC release from ME33 in PBS buffer at body temperature (37°C)

Evaluation of MMC loading and release of from silica coated nanoparticles show that the nanoparticles are capable of loading large amount of drug molecules however the drug release from the nanoparticles was observed to be very low and almost 90% of the encapsulated drug was not recovered. Since the drug loading was performed by physical diffusion of the drug molecules into the mesochannels of the nanoparticles, low drug release could be explained by the water soluble nature of the MMC drug and uncapped mesopores of the nanoparticles. Furthermore UV measurements were performed during the washing of the drug loaded nanoparticles prior to release studies, which indicated drug loss during washing and storage of the nanoparticles. Nevertheless the released drug was around 0.88 $\mu\text{g}/\text{mg}$ material after 48 hours for ME33.

5.3 MMC loaded Magnetoliposomes

Contributions of several researchers over past 50 years have led to significant advances and initial success with different liposome based drug delivery systems. Liposomes are now considered clinically established drug delivery systems for cytotoxic anticancer drugs (Nappini et al., 2010, Torchilin, 2005a, Li et al., 2015b). Recently there were some liposomal formulations approved for clinical applications such as DaunoXome, Myocet and Doxil which proved to be successful in improvement of survival rates (O'Shaughnessy, 2003, Torchilin, 2005a). Liposomes are attractive drug delivery systems since they are biocompatible and they are able to encapsulate both hydrophilic and hydrophobic drugs, in the aqueous core and within the lipid bilayer, respectively. The encapsulated drug would be protected from deactivating effect of external conditions. Additionally liposomes could deliver the anti-cancer agents inside cells, or individual cell compartments (Torchilin, 2005a). However, the drug release from liposomes are usually slow and not controlled (Podaru et al., 2014).

Combination of liposomes with magnetic nanoparticles known as magnetoliposomes could create multifunctional drug carriers for controlled drug delivery, hyperthermia and MR imaging (Monnier Christophe et al., 2014, Podaru et al., 2014). Magnetic nanoparticles placed in a magnetic field could produce enough heat to alter the liposome membrane diffusion properties and render it permeable for the encapsulated drug. This could combine the effect of magnetic hyperthermia and targeted drug delivery (Monnier Christophe et al., 2014, Nappini et al., 2010, Hsu and Su, 2008). Encapsulating the MMC inside magnetoliposomes could address the rapid elimination of MMC from the body (Li et al., 2014a).

Magnetoliposomes were prepared using lipid film hydration method, followed by ultra-sonication and filtration as explained Section 2.15. Liposomes were prepared by evaporation of chloroform from the lipid solution followed by the hydration of the dry lipid film and addition of magnetic nanoparticles. The liposomes were prepared using soybean phosphatidylcholine (SPC) and cholesterol. The hydrophilic magnetite nanoparticles prepared by coprecipitation were used as magnetic cores of the liposomes. The DLS experiments were used to indicate the size of the magneto liposome as presented in Figure 3-47. The stability of the magneto liposomes were evaluated using SCM as shown in Figure 3-44.

5.3.1 Drug Loading

Drug loading of the magnetoliposomes were performed by ultra-sonication and incubation of the liposomes with the MMC for up to 48 hours. Drug loading efficiency and the drug loading content for both methods were established by magnetic separation of the magnetoliposomes and measuring the UV absorbance of the supernatant at $\lambda_{365\text{nm}}$. Drug loading content were quantified using the pre-established standard curve of MMC in water (the standard curve of MMC in water is shown in Figure 5-5). The drug loading content was measured at 10°C at different intervals of up to 48 hours.

Figure 5-14 presents the drug loading profile of the magnetoliposomes for over 48 hours period. The MMC loading content and efficiency were calculated to be 0.46% and 68.80%, respectively. The drug loading content and efficiency for the samples loaded using ultra-sonication method were calculated to be 0.16% and 19.82% which is much lower than the drug loading using incubator. The drug loaded nanoparticles prepared *via* incubation was further used in the release experiments. The maximum drug loading was obtained after 24 hours of incubation and did not increase after that. Similar results in the range of 0.1 to 10 μg of MMC per milligrams of nanoparticles have been reported in the literature (Sen et al., 2012a, Yi et al., 2014, Li et al., 2014a). However Yi *et al.* have reported an increased drug loading efficiency of up to 94.5% for MMC encapsulated by polymer-lipid nanoparticles prepared by a reverse micelle–solvent evaporation technique (Yi et al., 2014).

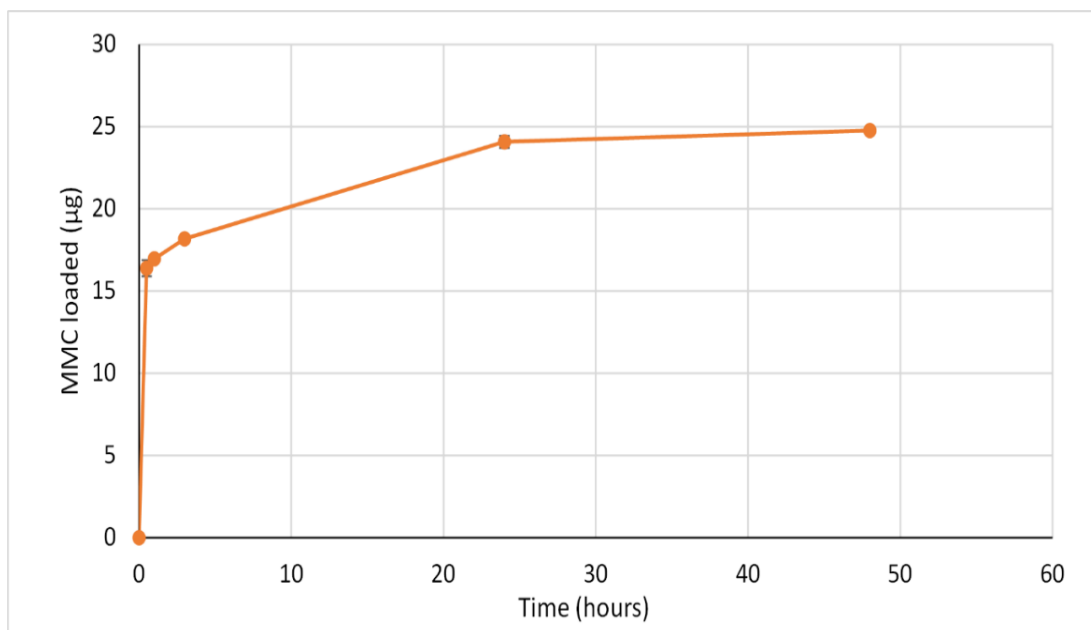


Figure 5-14. Drug loading profile of magnetoliposomes over 48 hours.

5.3.2 Drug Release

Mitomycin C release from magnetoliposomes were studied in PBS buffer at room temperature (23°C), body temperature (37°C) and hyperthermia conditions. MMC-loaded magnetoliposomes were magnetically collected at different time intervals and the drug content of the solution was measured using UV absorbance at $\lambda_{365\text{nm}}$. The concentrations of MMC in the solution were determined by comparing the absorption values with a pre-established standard curve of known MMC concentrations in PBS buffer (Figure 5-6).

Figure 5-15 presents the MMC release profile of magnetoliposomes in PBS buffer at two different temperatures. The release profiles indicate a burst release of the drug in the first initial hours for both temperatures, followed by a slow release over 48 hours. The final drug released from the nanoparticles were around 45% of the loaded drug at body temperature and 29% of the loaded drug at room temperature. Similarly, Yi *et al.* have reported between 30 to 50% MMC drug release from liposomes in the initial 12 hours of the measurements followed by slow release over following 80 hours (Yi et al., 2014). Li *et al.* have reported 50% drug release after around 48 hours which only increased to 60% over 170 hours of measurements (Li et al., 2014a).

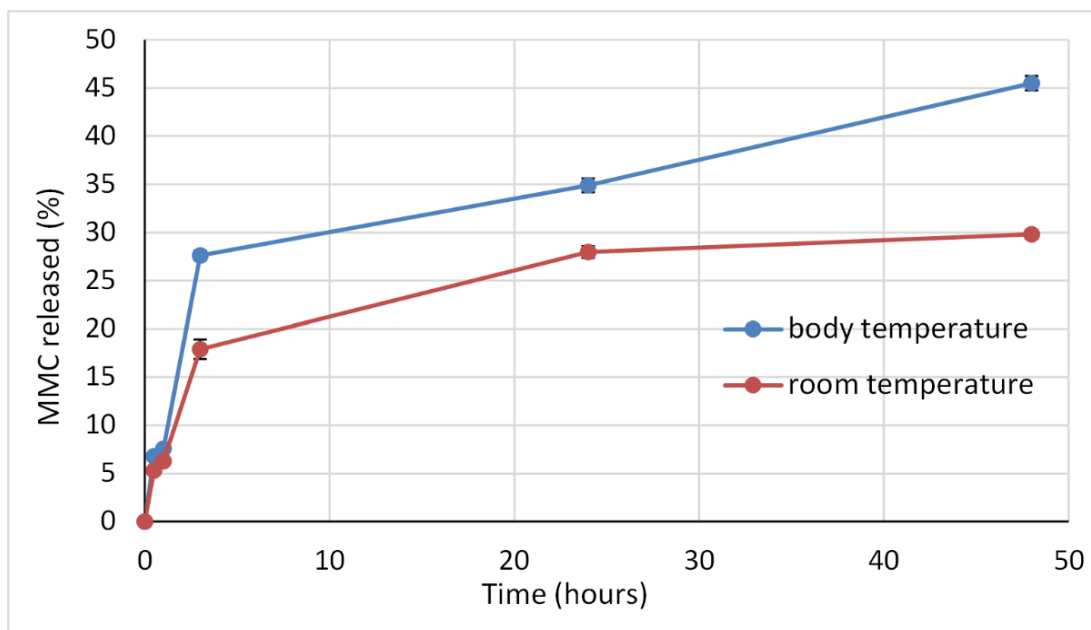


Figure 5-15. MMC release profile of magnetoliposomes.

5.3.3 Hyperthermia triggered drug release

The Magnetic heating of the magnetoliposomes were verified using the magnetic hyperthermia unit as described in Section 3.14. Magnetic heating of the magnetoliposomes was used to generate time and field dependent temperature data which were used to define the specific power absorption (SPA) as shown in Section 3.14.2.

Magnetoliposomes were dispersed in phosphate buffer solution and placed in an AC field with the magnetic field strength of 200 G and frequency of 406 kHz for 30 minutes. The heating profile of the magnetoliposomes during hyperthermia triggered drug release is shown in Figure 5-16. The starting temperature for the release experiments was set as 37 °C similar to normal physiological conditions. As demonstrated from the heating profile of the magnetoliposomes, they were heated effectively in the AC field and were able to increase the temperature of the solution to reach hyperthermia condition.

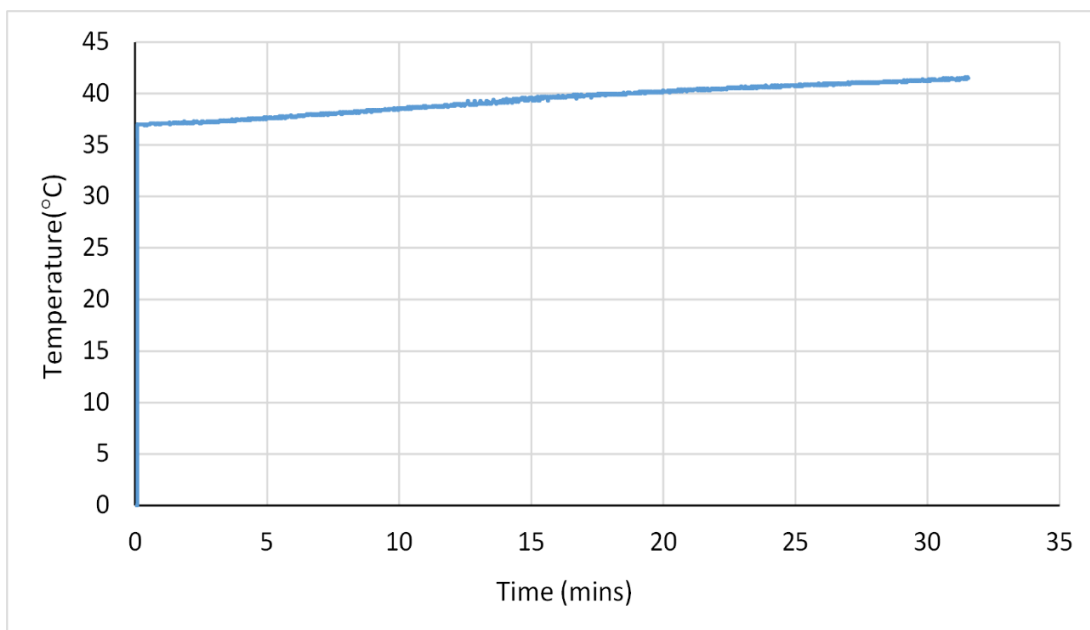


Figure 5-16. Heating profile of the magnetoliposomes during hyperthermia triggered drug release using AC magnetic field with field strength of 200 G and frequency of 406 kHz.

Figure 5-17 illustrates the *in vitro* magnetic field heating activated drug release profile of magnetoliposomes over 30 minutes. The drug release at 37°C in incubator is shown in the figure to compare the drug release rate.

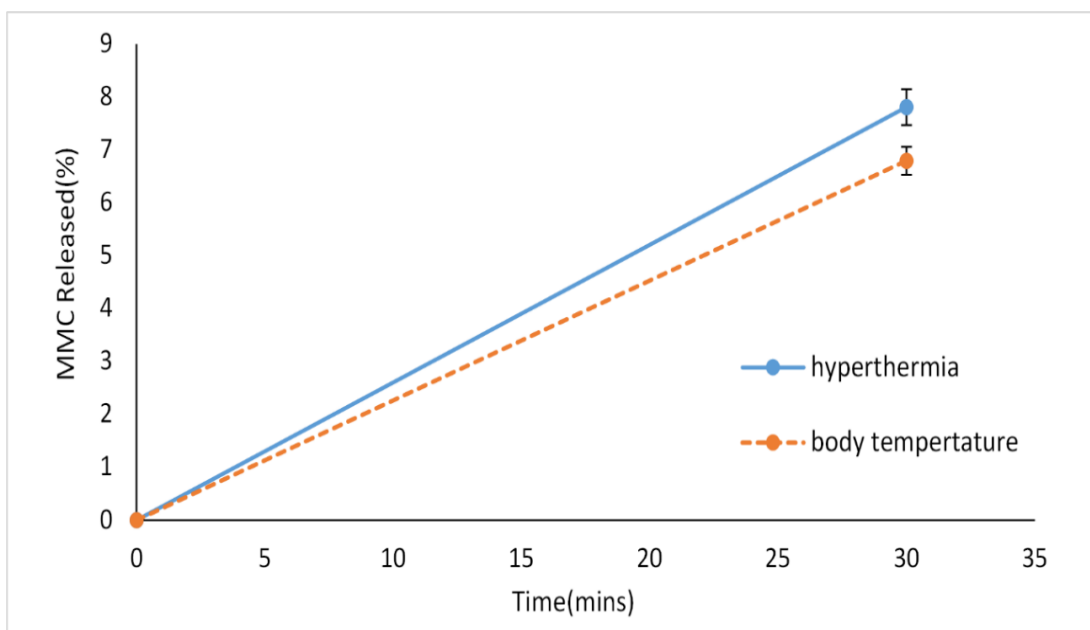


Figure 5-17. *In vitro* drug release at 37°C in incubator and under magnetic hyperthermia condition.

MMC release rate was increased under AC magnetic field induced hyperthermia condition. The increased drug release indicates the MMC loaded magnetoliposomes could be thermally triggered to release the drug under influence of the magnetic field. The drug release from magnetoliposomes under AC field was around 7.8% after 30 minutes. The increased drug release from magnetoliposomes could be due to heating of magnetite core of the magnetoliposomes under the magnetic field which could change the diffusion properties of the lipid bilayer and lead to an

increased drug release (Kulshrestha et al., 2012). Podaru *et al.* have reported increased drug release from magnetoliposomes under pulsed magnetic field without temperature rise, which was suggested to be a result of the liposomes rupture due to ultrasound generated from the pulsed magnetic field (Podaru et al., 2014).

The observed heating properties of the magnetoliposomes together with the increased drug release in presence of the AC field, indicate that synergistic effect of hyperthermia and cytotoxic chemotherapeutic drugs may be realized by incorporating magnetite nanoparticles into the liposomes. In addition to therapeutic applications, superparamagnetic nanoparticles are well recognised as excellent MRI probes. Magnetite nanoparticles encapsulated in liposomes, with high stability have proved to be effective as MRI T2 contrasts (Faria et al., 2013).

5.4 ME60

Mesoporous silica based nanoparticles possess excellent biocompatibility (Lu et al., 2010a, He et al., 2010) with unique structural features including a large surface area, great number of mesochannels and tuneable pore size in the range of 2 to 15 nm (Rosenholm et al., 2010b, Rosenholm et al., 2011, Liu et al., 2012). These structures make it possible to reach high drug-loading capacity and could also protect the encapsulated drugs in the mesopores from undesired enzymatic degradation due to the inaccessibility of the inner surface to the enzymes in blood or tissue plasma (Gao et al., 2009). Additionally *in vivo* and *in vitro* studies have proved DOX encapsulated within mesoporous silica nanoparticles could overcome drug resistance in the human cancer cells by bypassing the efflux action of P-glycoprotein and avoiding the activation of efflux pumps in these cells (Wang et al., 2014, Zeng et al., 2014, Meng et al., 2013, Huang et al., 2011).

Silica coated magnetic nanoparticles (ME60) were synthesised by using magnetite nanoparticles prepared by coprecipitation method as core material, TEOS as silica source and CTAB as pore templates as explained in Section 2.4. The mesoporous silica –magnetite core shell nanoparticles were characterised using transmission electron microscopy (TEM), and N₂ adsorption-desorption test as shown in Figure 3-8 and Figure 3-20, respectively. The porous structure observed in TEM images are supported by N₂ adsorption-desorption isotherms. The Brunauer-Emmett-Teller (BET) measurements indicated mesochannels with high surface area of 358 m²/g which is advantageous for adsorption of drug molecules. In addition, the size distribution of nanoparticles exhibit average value of 80 nm, which make it possible for the nanoparticles to escape from vasculature into tumour *via* enhanced permeability and retention effect (EPR) (Liu et al., 2012, Iyer et al., 2006).

5.4.1 Drug Loading

DOX loading was performed by adding nanoparticles to DOX solution in PBS. The mixture was placed on an end to end rotator at 25°C for 48 hours in dark. During this 48 hours the supernatant was taken at different intervals using magnetic separation to evaluate the drug loading performance. The drug concentration in supernatant compared to the initial drug concentration was used to determine the amount of DOX loaded into nanoparticles. Subsequently after 48 hours the drug-loaded nanoparticles were collected and washed with DI water to remove the unencapsulated DOX from the external surfaces. The nanoparticles were then freeze dried to be used in drug release and cytotoxicity studies.

The drug loading study was performed at neutral pH (7.4) which was chosen based on results reported by Wang and colleagues. They have reported a pH dependant drug loading profile for rod-like mesoporous nanoparticles, the drug entrapment efficiency of their samples were increased from 25.2% at pH 5.4 to 94% at pH 7.4 (Wang et al., 2014). However the maximum drug loading efficiency obtained in this study was 54%.

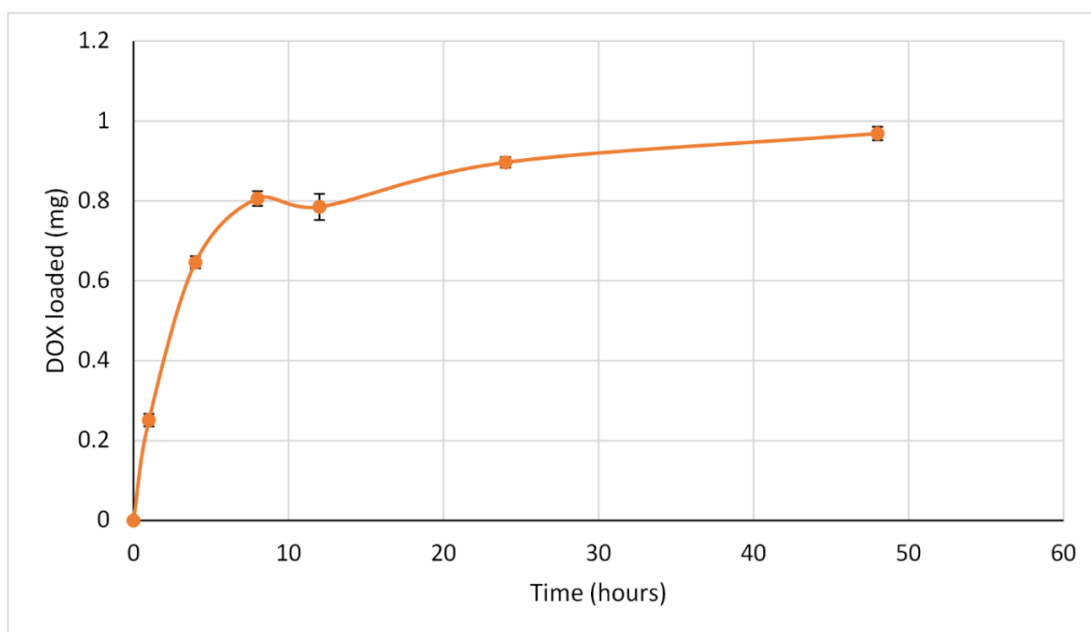


Figure 5-18. DOX loading profile for mesoporous silica coated magnetic nanoparticles

Figure 5-18 presents the drug loading profile of ME60 nanoparticles during 48 hours drug loading process. The graph implies a typical loading behaviour, with initial increase for the first 8 hours followed by reaching a plateau after 24 hours. Strong increase of absorbed drug in the first few hours indicates diffusion and transport of the drug molecules into mesopores.

Maximum drug loading achieved after 48 hours was 0.96 mg with the DLC and DLE of 10.3 and 57.6%, respectively. Similar results were observed by Sahoo *et al.*, they have reported DOX loading content and encapsulation efficiency of 11.3% and 60.4% for mesoporous silica-coated superparamagnetic nanoparticles with manganese ferrite (MnFe_2O_4) as magnetic core (Sahoo et

al., 2014). It is suggested that DOX loading into mesoporous nanoparticles occurred through physical diffusion (Sahoo et al., 2014).

5.4.2 pH Triggered Drug Release

The DOX release profile was investigated *in vitro* in physiological condition (in PBS, at pH 7.4) and acidic conditions (pH 5.5). The results are presented in Figure 5-19. The drug release measurements were performed at body temperature (37°C).

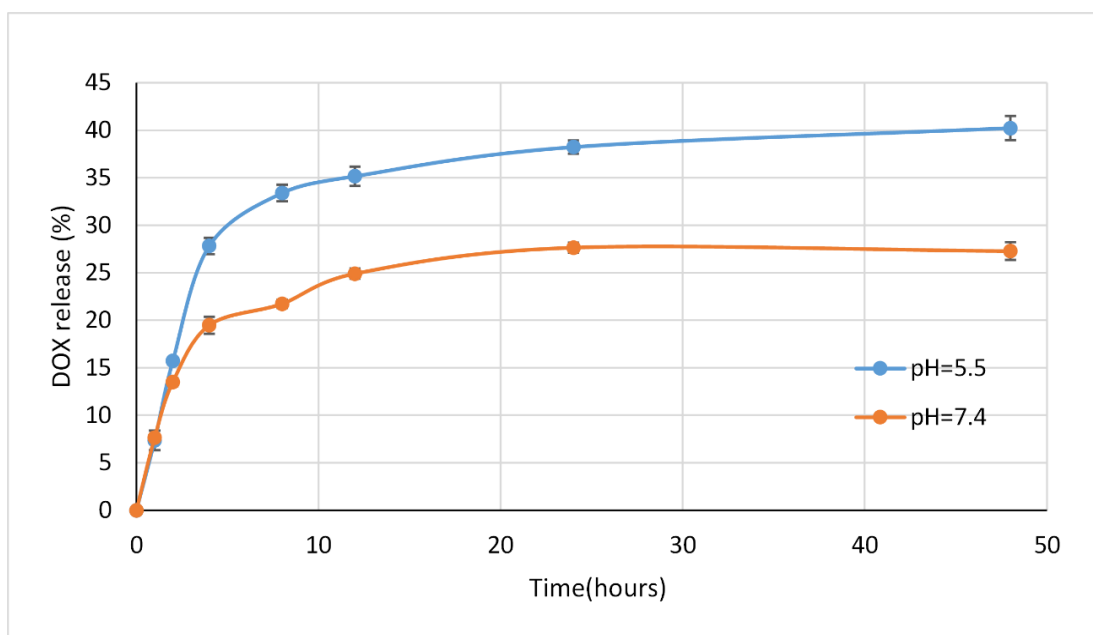


Figure 5-19. DOX release profile investigated at pH=7.4 and pH=5.5. Measurements were performed at 37°C. The release rate is higher at lower pH.

The drug release profile, at both pH values, showed an initial burst release for the first 4 hours followed by slow gradual release in following 44 hours. The initial fast release could be explained by the rapid diffusion of the drug molecules adsorbed near the mesochannels openings, while the drug stored in the inner surface diffuse into the solution with slower rate (Gai et al., 2011). Additionally, interactions of the drug molecules and the hydrogen bonds of silica surface could lead to slow release of DOX (Gai et al., 2011, Liu et al., 2012).

As evident from Figure 5-19, DOX release ratio was higher in the acidic pH condition compared to the physiological pH condition. At physiological pH (pH 7.4), nanoparticles demonstrated slow DOX release rate, while at pH 5.5 DOX release was higher. The total drug release reached 40.23% at pH 5.5 and 23.2% at pH 7.4. It is clear that DOX was released more readily at lysosomal pH condition rather than physiological blood plasma pH condition. Similar trends of drug release from mesoporous silica have been observed by other groups (Wang et al., 2014, Sahoo et al., 2014, Nakamura et al., 2015, Yildirim et al., 2013, Xie et al., 2014). For instance, Wang *et al.* have observed nearly 25% drug release at physiological pH which was increased to 46.1% at pH 5.6 (Wang et al., 2014). Similarly, Tang *et al.* have reported DOX release of 8% at physiological pH which was doubled to 16% at acidic pH of 5.5 over 24 hours (Tang et al., 2011). The

accelerated drug release at pH 5.5 suggest that the surrounding pH affects the electrostatic interactions between the nanoparticles and the drug. Furthermore, at lower pH (pH 5.5), DOX molecules could become protonated and get released into the solution (Sahoo et al., 2014).

These results suggested that the mesoporous based drug delivery systems were promising for DOX release at acidic conditions similar to tumour microenvironment or endosomal/lysosomal compartment of cells (pH 4-6). DOX release in endosomal/lysosomal compartment of cells could also protect DOX from drug efflux (Wang et al., 2014, Sahoo et al., 2014, Nakamura et al., 2015). Furthermore, sustained DOX release could be beneficial in treatment plans which includes killing tumour cells by an initial burst release to insure the required drug dosage and followed by a continued slow DOX release (Gai et al., 2011).

5.4.3 Temperature Triggered Drug Release

Magnetic properties of the mesoporous magnetic nanocomposites were characterised based on magnetic hysteresis loops using (VSM) and magnetic heating induced by an AC field as explained before in Section 3.14. The saturation magnetization was lower than pure magnetite which could be explained by the silica coating of the magnetite nanoparticles. However the nanocomposites showed superparamagnetic characteristics with acceptable saturation magnetization.

To study the magnetically induced heating of the nanocomposites, 10 mg of the nanoparticles were dispersed in 1 mL of DI water and placed under influence of the AC field for 45 minutes. The magnetic field was variable to attain constant temperature and the field frequency was 406 kHz. The temperature was set to 43°C which is suitable for hyperthermia (Kobayashi, 2011). The profile of the magnetic heat generated by nanoparticles is demonstrated in Figure 5-20. The SPA calculation are demonstrated in Section 3.14.2.

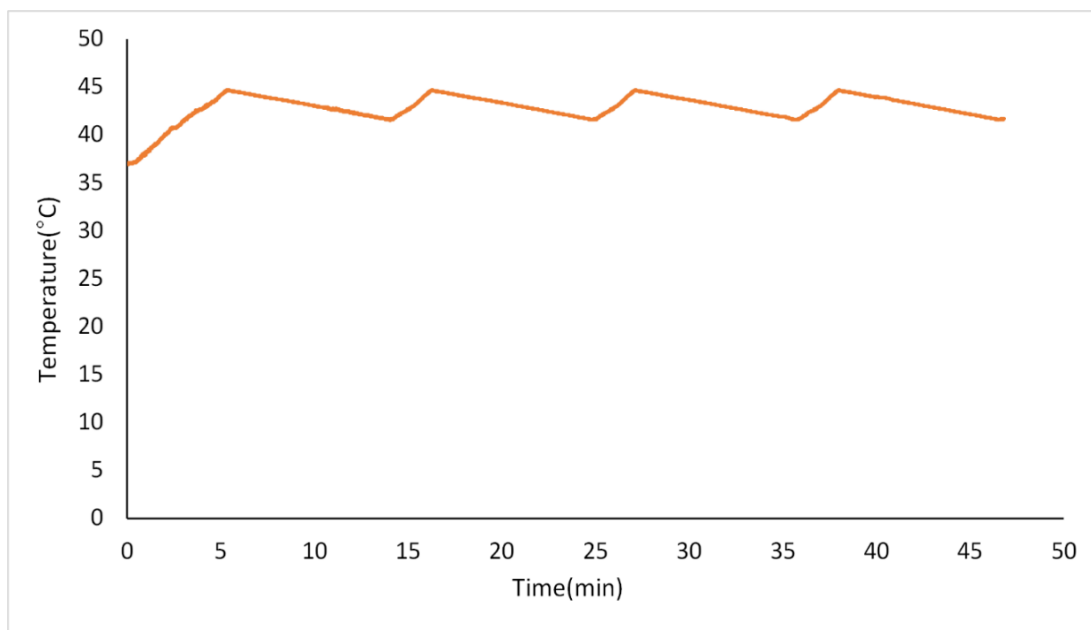


Figure 5-20. Magnetic heating profile of ME60 with the concentration of 10 mg/mL in a variable magnetic field with maximum strength of 200 G and frequency of 406 kHz. The field was adjusted in the way to keep the temperature at 43°C

As shown in Figure 5-20, the mesoporous magnetic nanoparticles were heated efficiently in the presence of a high frequency magnetic field. The time dependent temperature profile of the ME60 demonstrated that the nanoparticles were effective heating source and were suitable for hyperthermia cancer treatment applications. The solution temperature reached hyperthermia condition in about 4 minutes. Temperature of the nanoparticle suspension was kept in the range of 41.5 to 44.6 which is in the suggested range for hyperthermia cancer treatments (Bae et al., 2009, Reddy et al., 2012, Kobayashi, 2011). Similar heating profiles for magnetic mesoporous nanocomposites have been reported by other groups (Azevedo et al., 2014, Julian-Lopez et al., 2007, Souza et al., 2009b). For instance, Azevedo *et al.* have reported 37 degree increase in temperature of aqueous solution of 20 mg/mL mesoporous coated magnetite nanoparticles by applying an alternating magnetic field of 13.37 kA/m at frequency of 222 kHz for 30 minutes (Azevedo et al., 2014). Similarly Souza *et al.* have reported 21 degree temperature raise for 20 mg/mL of SBA-15/magnetite nanocomposites under magnetic field of 13.37 kA/m at frequency of 198 kHz (Souza et al., 2009b).

DOX release was studied under hyperthermia condition to investigate the feasibility of the synthesised nanoparticles to be used in simultaneous hyperthermia and drug delivery applications for cancer treatment. Temperature triggered DOX release were evaluated both in incubator and under AC magnetic field induced heating.

The starting temperature for the release studies were set at 37 °C similar to body temperature. Heat activated drug release profiles are shown in Figure 5-21. Drug release was assessed at an elevated temperature of 43°C, for up to 45 minutes.

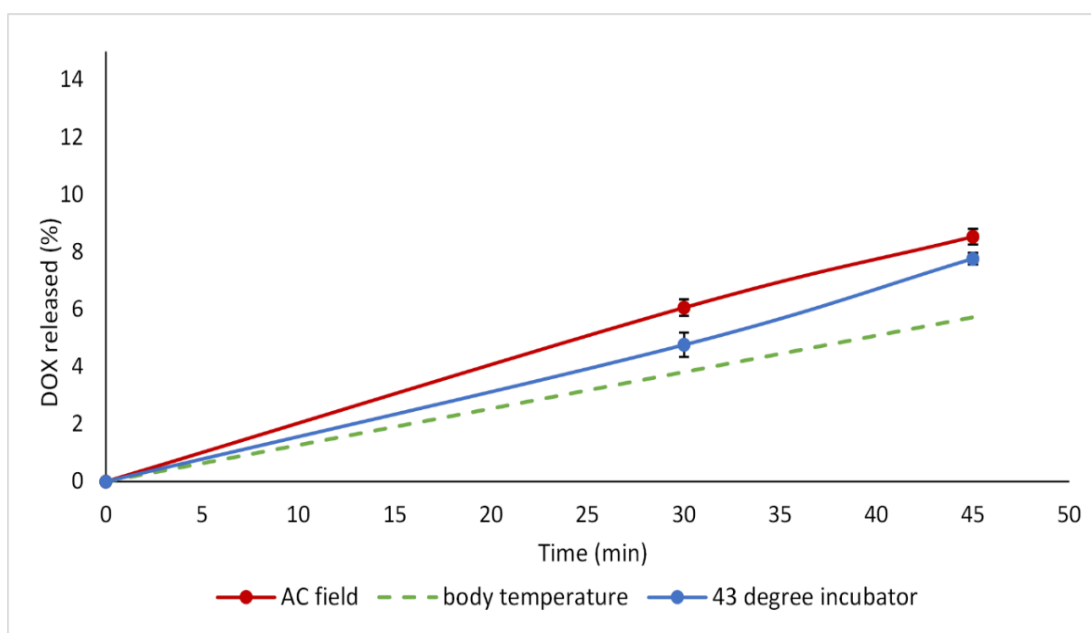


Figure 5-21. ME60 in vitro drug release at 37°C in incubator and under magnetic hyperthermia condition

As seen in Figure 5-21, only slight increase (about 3%) in drug release was detected under elevated temperature both in incubator and under AC field. Similarly less than 5% increase in drug release from mesoporous nanoparticles was reported by Liu *et al.* when the temperature raised from 37 to 40°C (Liu et al., 2014a). Since the drug release from mesoporous silica is mostly based on physical diffusion, it is suggested that the slight increase in drug release with increased temperature could be due to temperature dependence of the diffusion coefficient (Liu et al., 2014a).

The results indicate that the synthesised mesoporous magnetic nanoparticles are suitable for hyperthermia application and drug encapsulation however, appropriate capping is required to improve the control over drug release.

5.5 ME60-L

As explained before encapsulating the drugs within nanoparticles can overcome the difficulties presented by the ‘free’ drug *via* improving the solubility and stability, and increased selectivity towards targeted tissues, which results in decreased toxicity toward healthy cells and reduced necessary drug dosage to eliminate malignant cells (Ferrari, 2005). Mesoporous Silica nanoparticles (MSN) are very attractive as potential drug delivery systems due to their biocompatibility, high surface area, and tuneable particle size and pore diameters which attribute to high drug loading capacity and low cytotoxicity (Lu et al., 2007d, Vogt et al., 2010, Slowing et al., 2007b, Wu et al., 2013b, Vallet-Regi et al., 2001, Liu et al., 2009a, Yang et al., 2010).

Recently, the feasibility of the mesoporous silica based nanoparticles to deliver extensive range of drugs and therapeutic agents have been widely explored (Lingjie et al., 2015, Sahoo et al.,

2014, Meng et al., 2013, Rosenholm et al., 2010b). Mostly the cargo is loaded in mesoporous silica nanoparticles through simple electrostatic interactions or physical absorption (Nakamura et al., 2015, Rosenholm et al., 2011, Lu et al., 2010b).

It is of significant importance that the loaded drugs remain in the particles and be protected from metabolites/ions in the body fluid before reaching the targeted tissues to minimize the toxicity towards healthy cells. The release profiles of mesoporous nanoparticles could be partly adjusted by altering the pore size and pore surface chemistry (Liu et al., 2009b). However, drugs loaded into the accessible pores through electrostatic interactions or physical adsorption, could easily leach out into the blood stream resulting in premature drug release. Additionally mesoporous nanoparticles low dispersibility and aggregation under physiological condition, and their nonspecific binding in protein containing solutions limit their applications in biomedicine (Wang et al., 2010a).

To address these challenges different strategies have been reported in the literature including molecular-gating and surface functionalization (Mal et al., 2003, Nguyen et al., 2005). Two different approaches were examined in this project firstly the nanoparticles were coated with phospholipids and secondly polymer coating of mesoporous nanoparticles, as will be explained in Section 5.7.

Liposomes have been extensively investigated as drug carriers due to their high biocompatibility (Li et al., 2012a, Li et al., 2015b). Most recently, a new type of nanoparticles based on integration of porous nanoparticle as support for lipid bilayers (protocells) have been reported (Pan et al., 2011, Liu et al., 2009a, Liu et al., 2009b, Wu et al., 2013b, Mornet et al., 2005). Fusing liposomes on mesoporous silica surface could obtain combined properties of lipid bilayers and mesoporous particles. High surface area of the mesoporous nanoparticles results in higher capacity for loading of the therapeutic agents compare to the same size liposomes (Ashley et al., 2011a). On the other hand liposome coating of mesoporous silica nanoparticles enhance the stability of the nanoparticles in body fluid and minimize the premature drug release (Wu et al., 2013b, Ashley et al., 2011a). Furthermore liposome coatings on hydrophilic mesoporous silica nanoparticles could suppresses the bilayer fluctuations reducing the bilayer defects which leads to better stability than similar unsupported lipid bilayers (Liu et al., 2009a) (Ashley et al., 2011a, Komura et al., 2006). Additionally it is demonstrated in the literature that introducing of a lipid layer coating on mesoporous silica nanoparticles could increase the biocompatibility and the cellular uptake of the nanoparticles (Yang et al., 2010). Ashley *et al.* have reported 10^6 times improvement in killing a drug-resistant human hepatocellular carcinoma cell by using protocells over similarly sized liposomes (Ashley et al., 2011a).

Protocells were synthesized by coating liposomes over magnetic mesoporous nanoparticles. The mesoporous magnetic core shell nanoparticles (ME60) were used as core material to provide high drug loading capacity. Synthesis and characterization of magnetic mesoporous nanoparticles have

been described in previous chapters. Natural phospholipid (soy phosphatidylcholine, SPC) was used to prepare the lipid bilayer. The use of SPC instead of the commonly used synthetic phospholipids such as dioleoyl phosphatidylethanolamine (DOPE) and dipalmitoyl phosphatidylcholine (DPPC) leads to much lower cost and better serum stability (Wu et al., 2013b). Cholesterol was added to phospholipids to increase the lipid packing density and decrease the drug diffusion across the bilayer (Drummond et al., 1999). Liposomes were prepared by hydration of lipid films as explained in Section 2.15. The mesoporous nanoparticles were preloaded with drug by immersion in DOX solution and then the liposome solution were added to the drug loaded mesoporous nanoparticles. The mixture underwent probe sonication to prepare a homogenous solution and placed in the incubator to complete the liposome coatings and drug loading of the nanoparticles.

The stability of the mesoporous silica nanoparticles after lipid coatings were measured using SCM. Improved stability of the nanoparticles after liposome coating prove the presence of lipid bilayers on the nanoparticles surface. The size of the nanocomposites was estimated from DLS measurements to be around 165 nm (Figure 3-52).

5.5.1 Drug Loading

The drug loading content and efficiency were assessed after incubation of the drug loaded mesoporous core-shell nanoparticles with liposome mixture. The nanoparticles were separated by centrifuge and the UV absorbance of the supernatant at $\lambda_{485\text{nm}}$ was measured and compared with the previously established standard curve of DOX in PBS (as shown in Figure 5-3) to quantify the amount of the drug loaded into the nanoparticles.

The DOX loading content and DOX loading efficiency are calculated to be 5.9 and 65.8%, respectively (see Table 5-1). The results indicate that the liposome capped mesoporous nanoparticles are capable of encapsulating large amount of drug effectively which could be explained by large surface area of the core mesoporous particles. Similarly Wu *et al.* have reported 47.8% DOX loading efficiency and 2.9% DOX loading content for Protocells containing porous silica core and copolymer-liposome coating (Wu et al., 2013b). It is suggested in the literature that, due to high surface area of the porous silica core of the protocells they could load up to 1,000 times more DOX than similar size liposomes (Fritze et al., 2006, Ashley et al., 2011a).

5.5.2 pH Triggered DOX Release

DOX release from liposome capped nanoparticles (ME60-L) was studied *in vitro* in physiological condition (in PBS, at pH 7.4) and acidic conditions (pH 5.5). The results are shown in Figure 5-22. The pH dependant drug release experiments were performed at body temperature (37°C).

The drug release profile, at pH 7.4, showed no initial burst release of DOX confirming that sustained release could be obtained by liposome coating of nanoparticles. Indeed, after liposome

coating of the mesoporous nanoparticles the DOX release at physiological pH was reduced by 53% compare to uncoated particles. Similarly Liu *et al.* have observed 55% reduction of calcein release from DOPS bilayer coated mesoporous particles (Liu et al., 2009a).

DOX release profile at acidic condition shows a fast release in the initial 8 hours which could be due to disruption of the lipid bilayer caused by the acidic pH.

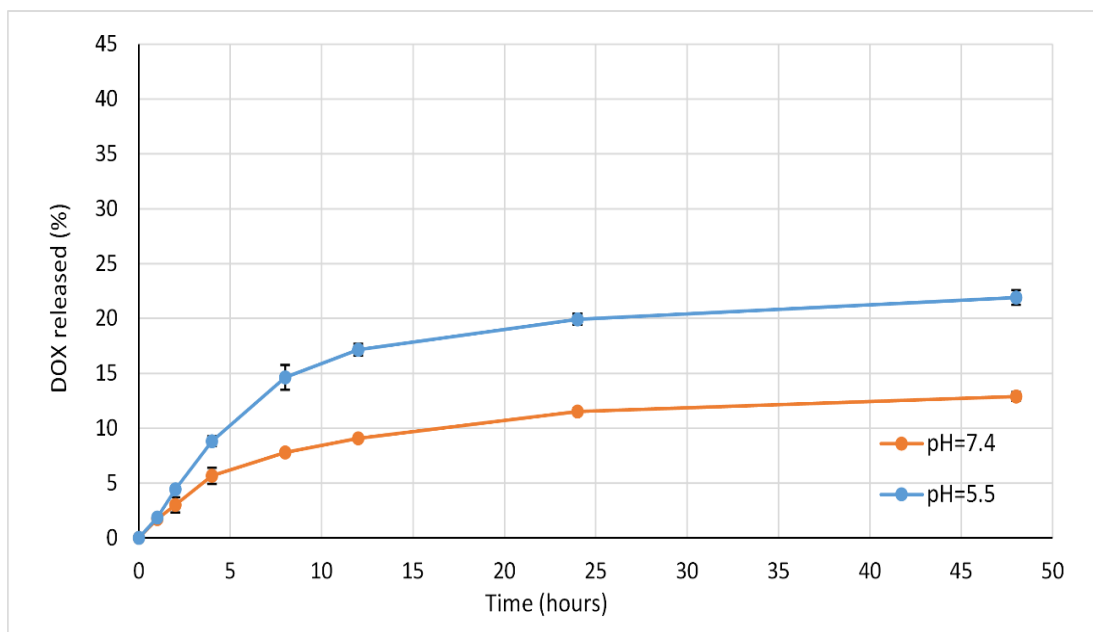


Figure 5-22. DOX release profile of ME60-L investigated at pH=7.4 and pH=5.5. Measurements were performed at 37°C. The release rate is higher at lower pH.

As shown in Figure 5-22, DOX release rate was higher in the acidic condition than in physiological pH condition. At physiological pH (pH 7.4), nanoparticles demonstrated a slow release of DOX, while at pH 5.5, DOX release was higher. The overall drug release after 48 hours reached 21.9% at pH 5.5 and 12.89% at pH 7.4. It is clear that DOX was released more readily at Endosome/lysosomal pH condition rather than physiological blood plasma pH condition. It is suggested that the acidification destabilizes the lipid bilayer enabling DOX to diffuse out of the nanocomposites (Ashley et al., 2011a). However the DOX release was not drastically increased by changes in pH which suggest that the interaction of drug molecules with hydrogen bonds of the silica surface and slow diffusion of DOX from inner mesochannels could have slowed the DOX release from the porous core of the protocells (Gai et al., 2011, Liu et al., 2012) (Yang et al., 2010). Capping the mesopores of the silica nanoparticles reduce the drug release (at 37°C after 48 hours) by 52.7% compared to uncapped nanoparticles.

It is established in the literature that liposomes made from SPC experience pH-sensitivity and upon acidification, a fraction of liposome population gets disrupted resulting in making the liposome unstable which consequently increase the permeability of the membrane leading to faster release of the encapsulated cargo (Li et al., 2015b, Baptista et al., 2003). Similar trends have been observed by Ashley *et al.* for DOPC protocells when exposed to simulated body fluid

(pH7.4) the protocells release 20% of the cargo in 20 days which was increased to 99% cargo release in 12 hours at pH 5 buffer (Ashley et al., 2011a). Similarly Liu *et al.* have reported 7 times increase in calcein release from DOTAP protocells when the pH was changed from 8 to 5 (Liu et al., 2009b).

These results demonstrated that the protocells based on mesoporous silica and SPC phospholipids exhibit enhanced drug loading capacity and long-term stability compared to uncapped mesoporous silica nanoparticles. Furthermore developed protocells showed promising potential for a DOX delivery system with increased release rate at acidic condition similar to tumour microenvironment or endosomal/lysosomal compartment of cells (pH 4-6) (Liu et al., 2009b).

5.5.3 Temperature Triggered DOX Release

Magnetic heating properties of the protocells were characterised using an AC field induced heating as explained in Section 3.14. The heat generated by the liposome capped nanoparticles under the influence of the AC field was observed to be lower than the heat generated by the polymer coated mesoporous silica nanoparticles.

Figure 5-23 shows the magnetic heating profile of the liposome capped mesoporous silica nanoparticles (ME60-L). The magnetic induced heating of the nanocomposites were evaluated by dispersing 10 mg of the nanoparticles in 1 mL of DI water which was then placed in the AC field for 45 minutes. The temperature was set at 43°C which is suitable for hyperthermia treatment (Kobayashi, 2011). The field frequency was 406 kHz and the magnetic field strength was variable between 0 to 200 G to attain constant temperature. The SPA of the nanoparticles were calculated as demonstrated in Section 3.14.2.

Temperature triggered DOX release were evaluated both in an incubator and under an AC magnetic field. Starting temperature for the release studies were set at 37 °C similar to body temperature. Drug release profiles were studied at an elevated temperature of 43°C, for up to 45 minutes.

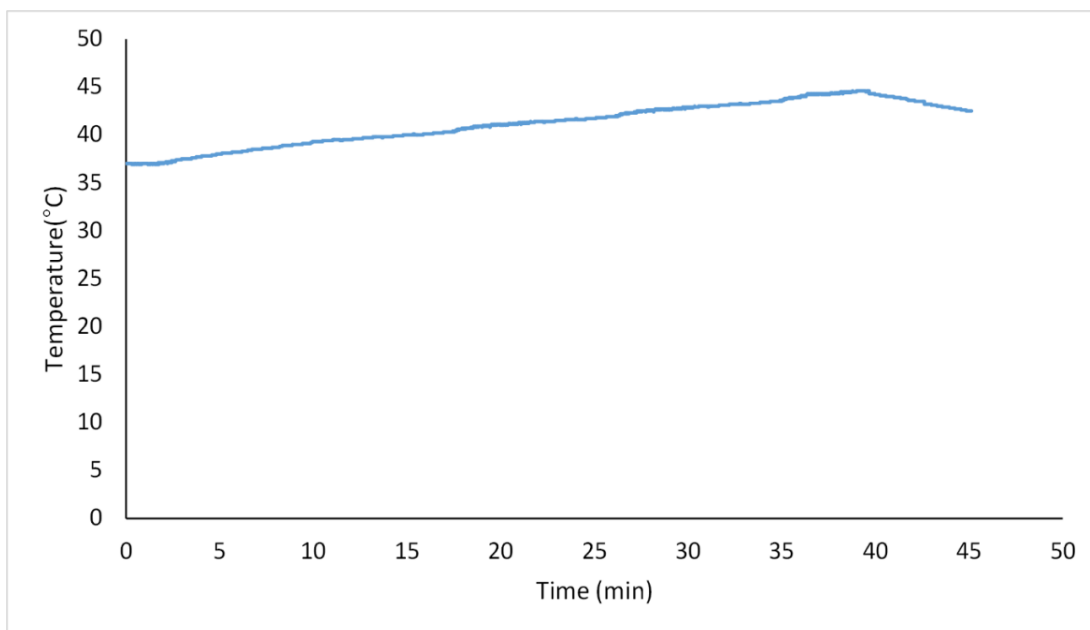


Figure 5-23. Magnetic heating profile of ME60-L with the concentration of 10 mg/mL in a variable magnetic field with maximum strength of 200 G and frequency of 406 kHz. The field was adjusted in the way to keep the temperature at 43°C

As presented in Figure 5-23, the protocells were able to produce sufficient heat for hyperthermia treatment, however the heating process took 30 minutes to reach hyperthermia temperature of 43°C in presence of 406 kHz magnetic field. The maximum temperature reached 44.6°C.

DOX release was studied under hyperthermia condition to investigate the extent of heat triggered DOX release from the synthesised nanoparticles and evaluate their feasibility for use in simultaneous hyperthermia and drug delivery applications for cancer treatment. The results are illustrated in Figure 5-24.

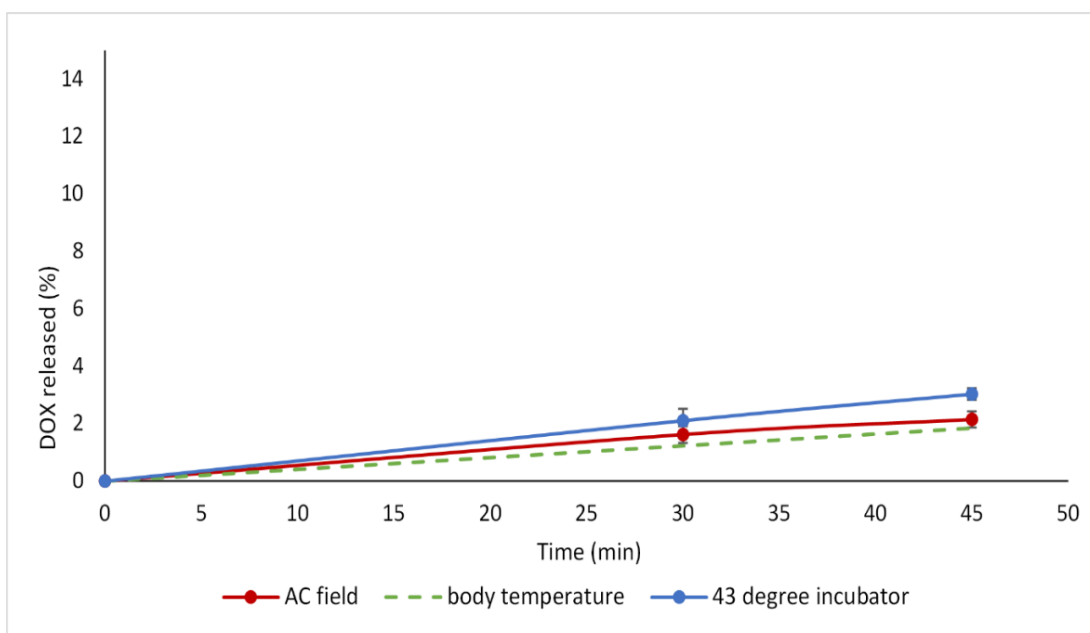


Figure 5-24. ME60-L in vitro drug release at 37°C in incubator and under magnetic hyperthermia condition

As shown in Figure 5-24, only slight change in drug release was observed under elevated temperature both in incubator and under AC field. The low increase in drug release with increase in temperature could be due to the fact that the slight change in the temperature was not enough to affect the structure of the capping liposomes (Li et al., 2015b).

The results indicate that the synthesised protocells are suitable for hyperthermia application and drug encapsulation independently however appropriate changes in capping material is required to improve the control over drug release. Wu *et al.* have suggested the use of copolymer–liposome structure as coating material for mesoporous silica nanoparticles to increase the pH and thermo-sensitivity of the protocells (Wu et al., 2013b).

5.6 ME55-PEG-PCL

Nanoparticles composed of poly (ϵ -caprolactone) (PCL) and poly (ethylene glycol) (PEG) have shown great potential for drug delivery systems (Glover et al., 2012). PCL is a biodegradable, biocompatible and nontoxic thermoplastic polyester (Sinha et al., 2004, Cuong et al., 2010b). PEG is known to reduce the adhesion of plasma proteins, and stabilize and improve solubility of particles and it is frequently used for the hydrophilic outer shell of nanocomposites (Cuong and Hsieh, 2009, Shuai et al., 2003, Cuong et al., 2012, Cuong et al., 2010a). Additionally, polymeric nanoparticles with hydrophilic PEG outer shell can potentially prevent recognition by reticuloendothelial system (RES) after intravenous injection and increase the circulation time (Nasongkla et al., 2006, Zahr et al., 2006, Otsuka et al., 2003). Furthermore, since PCL melting temperature is in the range of 40 °C to 45 °C (which is the range for hyperthermia cancer therapy) it could offer temperature triggered drug release under elevated hyperthermia temperature where the encapsulated drug diffuse out the melted PCL core (Glover et al., 2013).

Hydrophobic monodisperse magnetite nanoparticles and biodegradable thermally responsive polymer based on PCL hydrophobic and PEG hydrophilic segments were synthesised as explained in Section 2.7. Polymerization was performed *via* ring opening of ϵ -caprolactone (CL) and initiated by the alcohol terminus of polyethylene glycol (mPEG) with dibutyltin dilaurate as a catalyst. The molecular characteristics of diblock copolymers were studied by ^1H NMR as shown in Figure 3-61. Differential scanning calorimetry (DSC) was used to evaluate the thermal properties of the synthesised polymer as shown in Figure 3-56 and Figure 3-55.

Magnetite nanoparticles and DOX were loaded into the polymeric micelles at 25% and 8.3% w/w initial feed rate ratio, respectively. To increase the DOX loading content, DOX was first neutralized before micelle preparation by using an excess amount of TEA in DMSO. The encapsulation of magnetite nanoparticles and DOX inside the micelle cores were performed following the method described in Section 2.22. Similar methods have been reported in the

literature (Shuai et al., 2004, Nasongkla et al., 2006, Hong et al., 2008a). The amphiphilic copolymers self-assembled in PBS solution to encapsulate the magnetic particles and DOX.

5.6.1 Drug Loading

Micellar solution was stirred for 3 hours in dark after which DOX loaded micelles were collected using magnetic separation and drug loading content and efficiency were measured. The drug loaded micelles were freeze dried to be used in drug release studies. Drug loading efficiency and the drug loading content was determined by measuring the UV absorbance of the supernatant at $\lambda_{485\text{nm}}$ and quantifying it using the standard curve of DOX in PBS (as shown in Figure 5-3). The drug loading content was confirmed by measuring the UV absorbance after dissolving the freeze dried nanoparticles in Chloroform and DMSO under sonication.

The DOX loading content and DOX loading efficiency were calculated to be 6.91 and 74.86%, respectively (see Table 5-1). The results indicated that the copolymer micelles with hydrophobic PCL segment could efficiently encapsulate hydrophobic drugs in the micelle core. DOX encapsulation in the micelle core could be affected by several factors such as hydrophobic interaction of drug with the PCL segment of the micelle and the interaction of hydrogen bonding, the volume of the hydrophobic core, PCL crystallinity and the water solubility of the drug (Cuong et al., 2012, Shuai et al., 2004). Zhang *et al.* and Shuai *et al.* suggested while the long PCL blocks with increased hydrophobicity favour DOX encapsulation in the micelles, long PCL segments results in a higher crystallinity, and result in a decrease in drug loading content of the micelles (Zhang et al., 2010b, Shuai et al., 2004).

Hydrodynamic size of the prepared micelles (magnetic micelles and drug loaded magnetic micelles) were measured using DLS. The average size of magnetic micelles and DOX loaded micelles were measured to be around 76 nm and 106 nm, respectively, as shown in Figure 3-50 and Figure 3-51. The average particle size of the DOX and magnetite encapsulated micelles increased slightly comparing to that of the magnetic micelles. The increase in micelle size after drug loading could be due to interaction of hydrophobic PCL core of the micelle, hydrophobic magnetite and DOX (Zhang and Zhuo, 2005). Similar results have been reported by other groups (Cuong et al., 2010a, Zhang and Zhuo, 2005, Shuai et al., 2004, Hong et al., 2008a). Hong *et al.* observed that the PEG-PCL micelles' size increased around 10 nm upon loading of SPIONs into the micelles core (Hong et al., 2012). Hsieh group have also reported around 10 nm increase in PEG-PCL micelles size after drug loading, the initial micelles size were reported to be 148 nm with DLE of 5.8% (Cuong et al., 2012). Similarly Cuong *et al.* have reported a 6 nm increase in PEG-PEG-PCL micelles' size with the drug loading content 8.5% (Cuong et al., 2010b).

The results indicated that the diblock copolymer self-assembled into nanoscale micelles with insoluble PCL blocks as the core and soluble PEG blocks as the shell. Hydrophobic DOX and

magnetite nanoparticles were physically encapsulated into polymeric micelles core due to the hydrophobic interaction with PCL segment.

Furthermore the low water solubility of DOX was improved by encapsulation in the polymeric micelles. The stability of the nanoparticles were tested using SCM which was found to be soluble and stable in aqueous solution as shown in Figure 3-41.

5.6.2 pH Triggered Drug Release

Figure 5-25 demonstrate the *in vitro* release profile of DOX from magnetic micelles in PBS (pH=7.4) and acetate buffer solutions (pH=5.5) at 37°C. The results displayed an initial burst release of DOX followed by a sustained release during 48 hours for both pH values. The initial burst release of DOX from micelles in the first few hours could be attributed to the diffusion of DOX adsorbed near the surface of particles or trapped inside the hydrophilic shell (Cuong et al., 2010a, Cuong et al., 2012). After 48 hours the overall DOX release reached 32.7% and 56% of the total encapsulated DOX at pH 7.4 and 5.5, respectively.

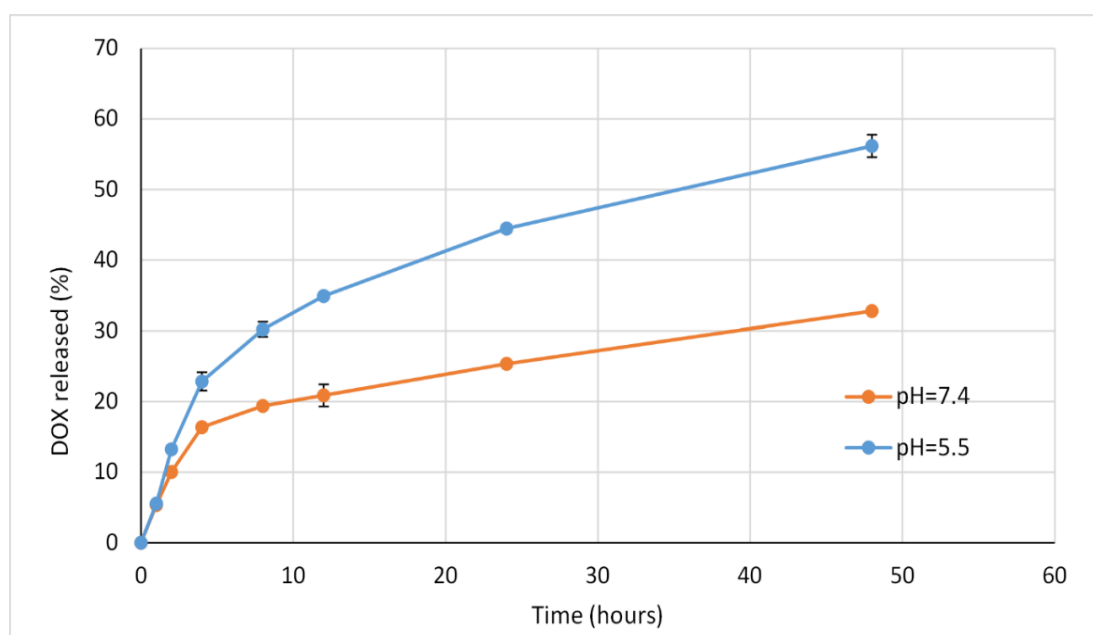


Figure 5-25. DOX release profile for ME55-PEG-PCL, investigated at pH 7.4 and pH 5.5. Measurements were performed at 37°C. The release rate is higher at lower pH.

The results showed higher DOX release rate at acidic condition with pH value of 5.5. The relatively slow DOX release rate of nanoparticles at pH 7.4 could be due to strong interaction of drug molecules and hydrophobic core of the micelles and the short incubation period (Cuong et al., 2010a). It is suggested that the slow DOX release at pH 7.4 could be due to DOX being in non-ionized state and hydrophobic form which consequently result in strong hydrophobic interactions between DOX and the core of the micelle. The relatively fast DOX release rate at pH 5.5 could be attributed to the re-protonation (ionization) of the amino group of DOX which causes weaker interaction of DOX molecules and hydrophobic core of the micelle. In addition the

degradation of the micelle core is increased at lower pH values (Cuong et al., 2012, Zhang et al., 2010b, Shuai et al., 2004, Liu et al., 2012).

Similar patterns have been observed by others (Hsieh et al., 2008). Cuong *et al.* reported the release rate of 25% and 37% for pH 7.4 and 5.4 after 48 hours, for PEG-PCL-PEG triblock copolymer micelles (Cuong et al., 2010a). Nasongkla *et al.* reported up to 80% release of DOX from PEG-PLA micelles at pH 5.0 after 10 days comparing to 30% release at pH 7.4 in the same period (Nasongkla et al., 2006). Cuong group reported total release rates of 78% and 42% at pH values of 5.4 and 7.4 after 156 hours from PEG-PCL micelles (Cuong et al., 2012). Similarly Gao *et al.* reported 60% and 40% DOX release at pH 5.5 and 7.4 from star shaped PEG-PCL micelles over 48 hours period which was increased to 80% and 60% over 96 hours (Gao et al., 2013).

From the pH dependent release profile it is expected that most of the hydrophobic drug remain in the micelle core after intravenous injection in plasma at normal physiological conditions which potentially increase DOX retention time in the blood circulation. Additionally, faster release may occur at acidic pH surrounding the tumour site or inside the endosome/ lysosome of tumour cells after internalization inside the cells by endocytosis (Zhang et al., 2010b). The pH dependant release profile and high DOX loading content suggest great potential for nanoparticles in cancer chemotherapy applications. The DOX release rate may be improved by modifying the composition of the copolymer, incubation time, and pH of media (Cuong et al., 2012).

5.6.3 Hyperthermia Triggered Drug Release

Magnetic heating of the magnetic micelles were verified by magnetic hyperthermia unit as explained in Section 3.14 with magnetic field strength and frequency of 200 G and 406 kHz. Specific power absorption (SPA) was calculated based on the magnetic heating of the micelles and time and field dependent temperature data.

Magnetic micelles were dispersed in phosphate buffer solution and place in the AC field for 45 minutes. The heating profile of the micelles during hyperthermia triggered drug release is shown in Figure 5-26. The starting temperature for the release experiments were set at 37 °C similar to normal physiological conditions. The micellar solution concentration of 15 mg/ml was used for *in vitro* release tests which is lower than reported literature (Johannsen et al., 2005a, Purushotham et al., 2009)

Figure 5-27 illustrates the *in vitro*, magnetic field heating activated drug release profile. Drug release was conducted at an elevated temperature up to 43°C, for 45 minutes. These conditions were selected according to hyperthermia treatment conditions (Reddy et al., 2012). The same experiments were performed in incubator at 43°C to investigate the effect of AC field induced magnetic heating.

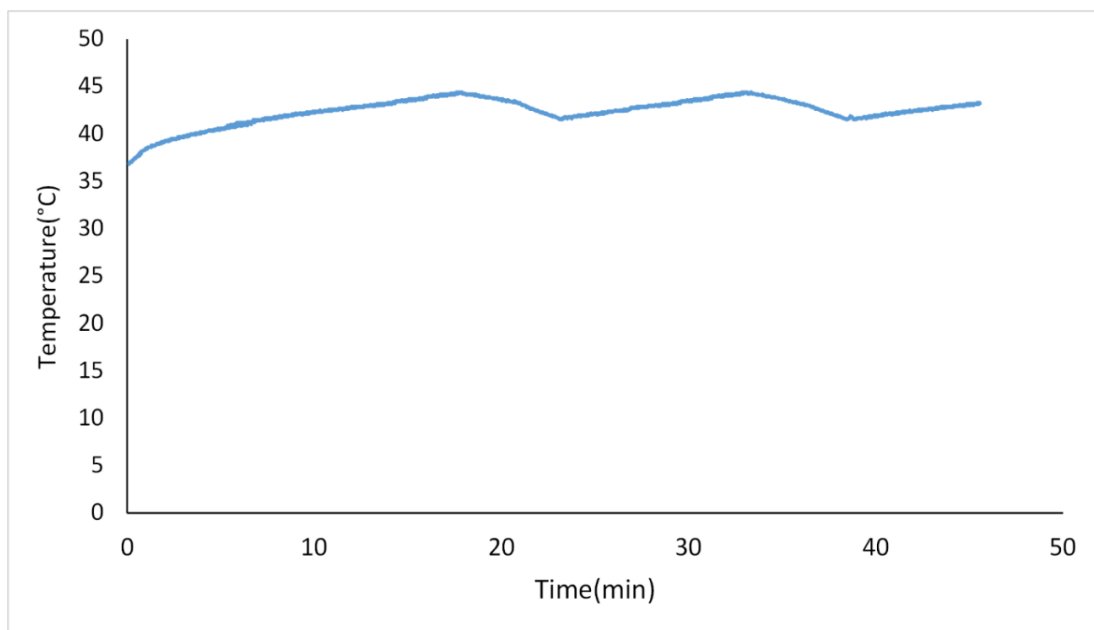


Figure 5-26. Magnetic heating profile of magnetic micelles with the concentration of 15.1mg/mL in a variable magnetic field with maximum strength of 200 G and frequency of 406 kHz. The field was adjusted in the way to keep the temperature at 43°C.

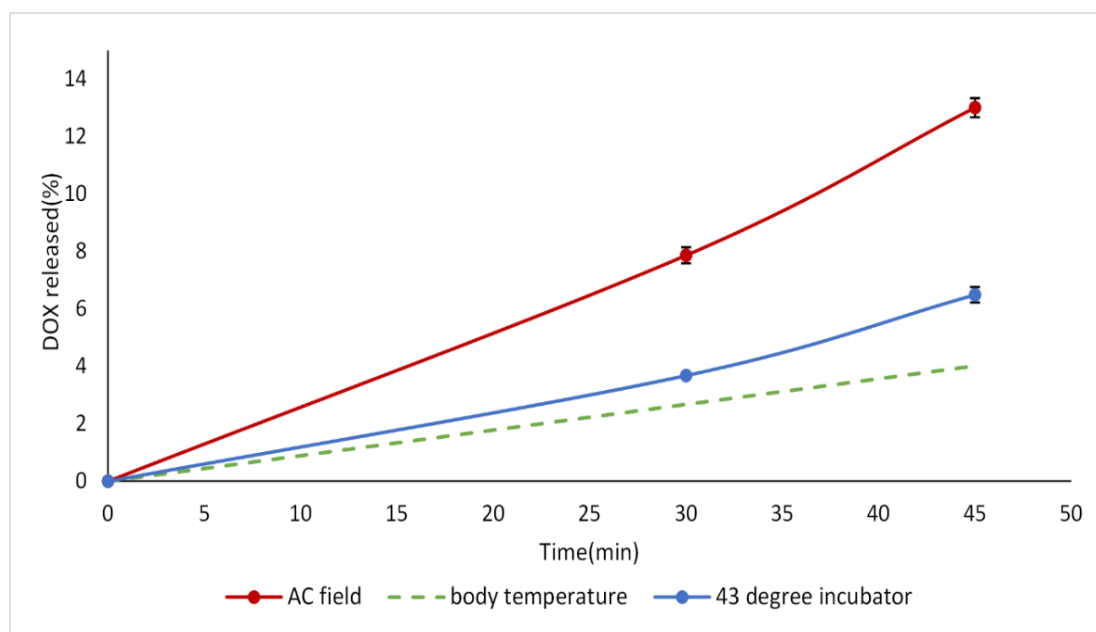


Figure 5-27. ME55-PEG-PCL in vitro drug release at 37°C in incubator and under magnetic hyperthermia condition

The magnetic nanoparticles were heated successfully in high frequency magnetic field and were able to increase the temperature of the micellar solution to reach hyperthermia conditions in about 5 minutes. Glover *et al.* have reported a time lag of around 2 minutes, observed by infrared camera, in the temperature raise of magnetic micelles during the magnetic heating experiments. They have suggested it might be due to the thermal energy needed to melt PCL micelle cores prior to gain functional energy to increase the solution temperature (Glover et al., 2013). However no lag time was observed in this experiment which could be due to different method of temperature measurements.

Doxorubicin release rate was faster at higher temperature over the measurement period (45 minutes). Which indicates the PEG-PCL magnetic micelle system can be thermally triggered to release the drug. Furthermore, drug release from magnetic micelles were enhanced in the presence of the magnetic field. The total drug release reached 13% and 6.48% for AC field heating and incubation, respectively.

These results suggested that the heat generated in the magnetic core upon application of the AC field is conducted from the magnetic core to the surrounding PCL micelle core and raised the temperature of the drug-loaded micelle. Upon heating, (the melting point for PCL is in the range of 40 °C–45 °C), when the temperature of the polymer solution reaches above the melting point of the micelle core, the core become molten and due to greater diffusivity of the molten core, DOX release is accelerated. The increased release rate is suggested to be proportional to the void space within the micelle core and the concentration gradient with surrounding fluid (Glover et al., 2012, Glover et al., 2013).

Glover *et al.* have performed series of temperature dependent critical micelle concentration (CMC) and temperature dependent dynamic light scattering measurements and observed that the micelles remained intact at temperatures above the melting point of the PCL core (Glover et al., 2012). Purushtham *et al.* have observed similar DOX release trend from thermoresponsive polymer poly-n-isopropylacrylamide at elevated temperature, in presence of magnetic field with 14.7% drug release after 47 minute at hyperthermia temperature (Purushotham et al., 2009).

The observed heating properties of the magnetic micelles together with rapid release of doxorubicin from magnetic micelles under hyperthermia condition indicate that a synergistic effect of hyperthermia and cytotoxic chemotherapeutic drugs may be realized by incorporating magnetite nanoparticles into the PEG-PCL diblock copolymer micelles. Application of high frequency AC magnetic field will heat the particles by magnetic induction, allowing hyperthermia and simultaneous drug release (Brazel, 2009). Additionally, magnetic nanoparticles can overcome the drawbacks of conventional hyperthermia through magnetic targeting and localized heating (Purushotham et al., 2009, Shah et al., 2015).

In addition to therapeutic applications, superparamagnetic nanoparticles are well recognised as excellent MRI probes. SPIONs encapsulated in polymeric micelles, with high monodispersity and stability in aqueous solution, could be used as ultrasensitive MRI T_2 contrast agent with longer blood half-life and improved biocompatibility (Ai et al., 2005a, Hong et al., 2012, Hong et al., 2008a). Hong *et al.* have observed that compared to the water soluble SPIONs, SPIONs encapsulated PEG-PCL micelles could simultaneously increases transverse (r_2) and decreases longitudinal (r_1) magnetic resonance relaxivities of water proton in micelle solution, leading to remarkably high r_2/r_1 ratio of up to 78, which makes a highly sensitive MRI T_2 contrast agent (Hong et al., 2012). Similarly, Ai *et al.* reported clusters of hydrophobic SPIONs encapsulated

into the core of PEG-PCL micelle could result in an ultrasensitive MRI T_2 contrast agent (Ai et al., 2005a).

5.7 DOX Loading of ME93-PEG-PCL and ME94-PEG-PCL

It is suggested in the literature that drug encapsulated mesoporous silica nanoparticles could overcome drug resistance mechanisms (Wang et al., 2014). Although mesoporous silica nanoparticles are unable to deliver drugs in a targeted and controlled manner, without appropriate surface modification to cap the pores, inevitable premature drug release occurs during blood circulation (Tang et al., 2011, Aznar et al., 2009, Liu et al., 2014a, Chang et al., 2011, Slowing et al., 2007b).

Polymer capped mesoporous silica magnetite core-shell nanoparticles (MSMNs) were synthesised as DOX nanocarriers for cancer therapy. These nanocomposites were developed based on mesoporous silica coated magnetite combined with thermally responsive PEG-PCL copolymer. The magnetite core of the nanocomposites could be used to induce localized heating under alternating current (AC) field for heat triggered drug release and parallel hyperthermia treatment (Azevedo et al., 2014).

The mesochannels of the mesoporous silica nanoparticles were capped using the synthesised amphiphilic diblock copolymer to improve the control over release profiles and decrease the drug leakage. Furthermore the PEG-PCL coating could enhance the aqueous stability and cellular uptake of the nanoparticles. Additionally, PEG segments on the hydrophilic outer shell are known to prolong the circulation time. (Kwon, 2003, Otsuka et al., 2003, Shuai et al., 2004, Nasongkla et al., 2006, Cuong et al., 2012) (Ferlay et al., 2015).

For this purpose, the surface of the mesoporous silica coated nanoparticles were octyl modified to give covalent anchorage on the silica surface. Subsequently the hydrophobic, octyl-modified mesoporous silica coated nanoparticles were coated with amphiphilic diblock copolymer. Octyl modified water insoluble mesoporous silica magnetite core-shell nanoparticles (OMSMNs) were synthesized following two different methods as explained in Section 2.6.

ME93 was developed by using a one-pot respective condensation method. Tetraethyl orthosilicate (TEOS) molecules were condensed under basic conditions to make initial mesoporous coating shell on the magnetite nanoparticles then, octyl triethoxysilane (OTS) molecules were added to the reaction mixture to coat the nanoparticles with a hydrophobic octyl layer.

ME94 was produced by using the silica coated nanoparticles developed following the method explained in Section 2.6.2 as starting material. Surface protected etching technique was then used to produce mesoporous silica structure followed by adding octyl triethoxysilane (OTS) to modify the nanoparticles with a hydrophobic octyl shell.

As-prepared OMSMNs are insoluble in water (Figure 3-43, a) due to the hydrophobic octyl groups on the surface. After the addition of PEG-PCL diblock copolymer, the polymer self-assembles on the OMSMNs due to hydrophobic interactions between alkyl chains of OMSMNs and PCL segment. Functionalization with amphiphilic polymer renders the water dispersible magnetic nanocomposites by providing hydrophilic PEG on the outer shell of the nanocomposites. (Figure 3-43, b).

TEM images of ME94 and ME93 are shown in Figure 3-11 and Figure 3-13. Successful octyl coating of nanoparticles were evaluated by using contact angle measurements as shown in Figure 3-58 and Figure 3-59. Hydrophobic surface were clearly observed for both samples, however ME93 demonstrated higher contact angle and higher hydrophobicity. The improved stability of the polymer capped mesoporous magnetic nanocomposites were evaluated using SCM. The results (as presented in Figure 3-42) indicated that the polymer coated particles are water soluble and stable for long duration.

5.7.1 Drug Loading

OMSMNs were loaded with hydrophobic DOX molecules and coated with amphiphilic polymer by ultrasonication and stirring at room temperature in dark condition for 3 hours. DOX loaded micelles were collected using a magnet and lyophilised to be used later in drug release and cytotoxicity studies.

Drug loading efficiency and the drug loading content were determined by measuring the UV absorbance of the supernatant after 3 hours loading process at $\lambda_{485\text{nm}}$ and calculated to be 7.92 and 85.85% for ME93-PEG-PCL and 6.2 and 67.21% for ME94-PEG-PCL (see Table 5-1).

Higher drug loading content of ME93 compared to ME94 could be due to higher surface area (BET graphs presented in Figure 3-21 and Figure 3-22) of the ME93 as well as higher hydrophobicity of the ME93 surface which could affect the electrostatic interaction of the drug and silica surface (He et al., 2013). The higher hydrophobicity of the core in case of ME93 could influence the drug loading content as it is suggested in the literature that physical entrapment of the hydrophobic drugs is driven by interactions between hydrophobic segments of the nanoparticles and the drug (Shuai et al., 2004, Cuong et al., 2012). He *et al.* have observed that compared to PEG capped mesoporous silica nanoparticles, PEG-PCL capped particles have shown an increased drug loading efficiency. They have suggested that it could be due to hydrophobic PCL chains (He et al., 2013).

The drug loading content of mesoporous silica nanoparticles (ME60) were slightly higher than octyl modified nanoparticles which could be attributed to higher surface area of the unmodified mesoporous silica nanoparticles. Yildirim *et al.* have reported similar tendency for mesoporous

silica nanoparticles and surface modified nanoparticles with drug loading values of 15.3 $\mu\text{g}/\text{mg}$ and 11.5 $\mu\text{g}/\text{mg}$, respectively (Yildirim et al., 2013)..

A decrease in DOX loading content and efficiency was observed when DOX loading was performed under acidic conditions with hydrophilic DOX. DLC and DLE were decreased to 2.0% and 11%, respectively. Since DOX encapsulation into mesoporous silica matrix is mainly based on the physical adsorption mechanism it is suggested that at higher pH, the electrostatic repulsion between the adsorbed DOX molecules would decrease and consequently DOX molecules could be absorbed close to each other in the mesochannels with higher encapsulation efficiency (Chang et al., 2011, Tang et al., 2011). Tang *et al.* have reported high pH dependency of DOX loading into chitosan/poly (methacrylic acid) coated mesoporous silica nanoparticles with drug loading content of 22.3% at pH 8 (Tang et al., 2011). Similarly, Chang *et al.* have observed the pH dependent drug loading behaviour for poly (N-isopropylacrylamide-co-methacrylic acid) coated magnetic mesoporous silica nanoparticles with an increase in drug loading content from 0.9 wt% to 21% with pH change from 5.1 to 10.0 (Chang et al., 2011).

The size distribution of nanoparticles measured by dynamic light scattering indicated that polymer coated ME93 nanoparticles (ME93-PEG-PCL) showed slightly smaller size than drug loaded polymer capped nanoparticles. It is suggested that the particles size might be dependent upon hydrophobicity of the core material (Sardan et al., 2014). An increased electrostatic interaction on the surface of the material could result in dense packing of the polymeric shell which consequently result in smaller particles.

5.7.2 pH Triggered Drug Release

The *in vitro* drug release profiles were studied at 37°C under neutral physiological condition (pH 7.4) and acidic condition (pH 5.5) to simulate the normal physiological environment and tumour cell environment. The results are presented in Figure 5-28 and Figure 5-29 for ME93 and ME94, respectively.

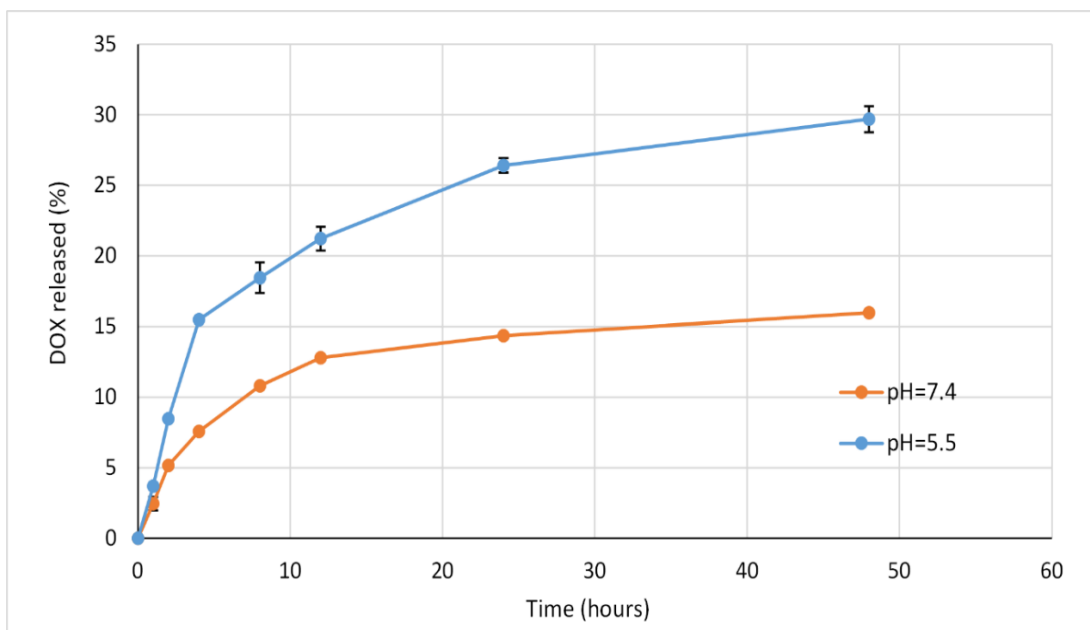


Figure 5-28. pH dependant drug release profile for ME93-PEG-PCL

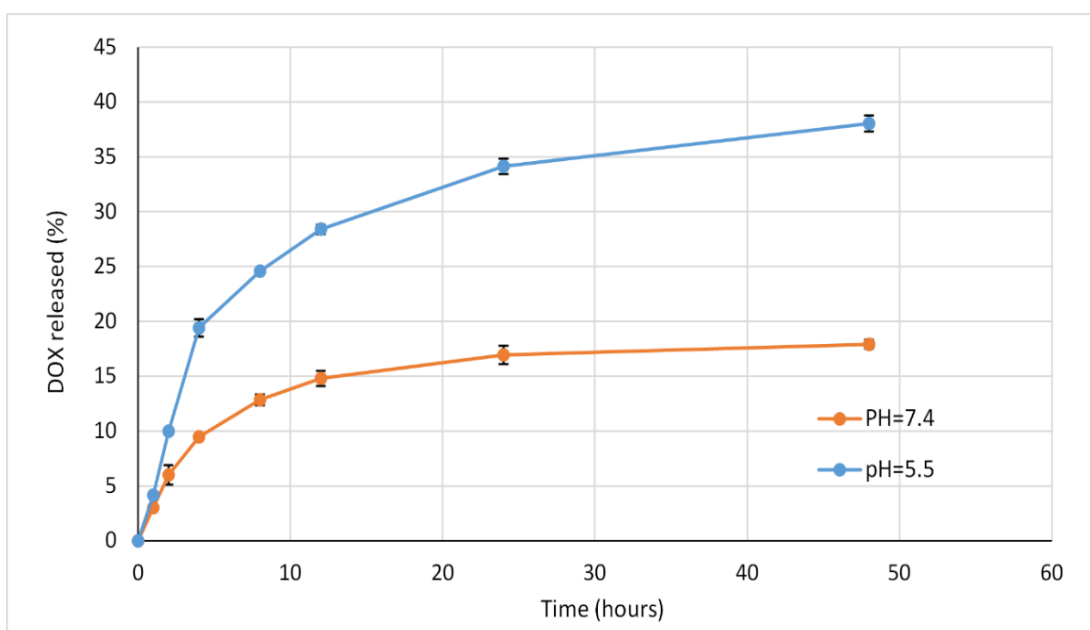


Figure 5-29. pH dependant drug release profile for ME94-PEG-PCL

The DOX release profile of polymer capped nanoparticles compare to un-capped nanoparticles showed that the initial burst release which was detected for mesoporous silica nanoparticles (ME60) was suppressed by polymer capping of the mesopores. Capping the mesopores of the silica nanoparticles reduced the drug release (at 37°C after 48 hours) by 41.5%. This results indicated that the PEG-PCL polymer layer has covered the pore openings and could effectively preserved the encapsulated drug and reduce the drug release from mesoporous silica structure at pH 7.4. Similar results were observed by Yildirim *et al.* where they have used F127 polymer to coat the mesoporous silica nanoparticles. They have reported 30% decrease in drug release from nanoparticles by capping the mesoporous silica nanoparticles with the F127 polymer (Yildirim *et al.*, 2013).

As it is shown in Figure 5-28 and Figure 5-29 both samples exhibited a pH dependant drug release profile with the total drug release of 29.6% and 15.9% at pH 5.5 and 7.4 for ME93 and 38.04% and 17.93% for ME94 after 48 hours. Similar pH dependant drug release profiles have been reported in the literature. Tang *et al.* have reported a similar pH dependant release profile for chitosan/poly (methacrylic acid) coated mesoporous silica nanoparticles with an increase from 18% release at pH 7.4 to 70% release at pH 5.5 during a 24 hours period (Tang et al., 2011). Similarly, Chang *et al.* have reported a pH responsive poly (*N*-isopropylacrylamide-*co*-methacrylic acid) coated magnetic mesoporous silica nanoparticles. They have observed 80.2% drug release at pH 5 while the drug release was reduced to 7.2% at pH 7.4 over the same time period (Chang et al., 2011). He *et al.* have reported 20% and 30% DOX release at pH 7.4 and 5.0 within 36 hours for PEG-PCL capped nanoparticles *via* disulfide bonds (He et al., 2013).

It is suggested that the drug release is significantly affected by the electrostatic attraction between DOX and the nanoparticles. The pH decrease would make DOX became more water soluble due to the protonated daunosamine group (Liu et al., 2014b) and consequently, the reduced electrostatic interaction between the drug molecules and the silica shell would facilitate the DOX release (He et al., 2013) (Chang et al., 2011) (Tang et al., 2011).

It is proposed that the slight difference in DOX release profile between ME93 and ME94 could be due to the differences in the pore structure, as it is observed by several groups that modulating the pore size and structure could affect both the drug loading and release profiles (Zhang et al., 2009).

The drug release profiles clearly indicated the role of polymer coatings on the mesoporous silica nanoparticles in controlling the diffusion behaviour of DOX from the nanoparticles and minimising the drug leakage during blood circulation. Additionally the pH responsive drug release with increased drug release in acidic condition means accelerated drug release rate inside the endosome/lysosome after cellular uptake which is an advantageous for cancer therapy (Chang et al., 2011, Medeiros et al., 2011, He et al., 2013).

5.7.3 Temperature Stimuli Drug Release

Magnetic properties of the nanocomposites were evaluated based on magnetic hysteresis loops obtained by vibrating sample magnetometry (VSM) and magnetic heating using nanoscale biomagnetics hyperthermia unit as explained before in Section 3.14. It was observed that compared to bare magnetite nanoparticles and silica coated core-shell nanoparticles, the saturation magnetization was reduced due to the additional polymer coating of the silica coated nanoparticles. However the nanocomposites have shown superparamagnetic characteristics with acceptable saturation magnetization according to the literature (Lien and Wu, 2008, Zhu et al., 2007).

To study the magnetic field induced hyperthermia characteristics of the materials, the magnetic nanocomposites were dispersed in phosphate buffer solution and placed in the AC field for 45 minutes. The heating profiles for ME93-PEG-PCL and ME94-PEG-PCL are shown in Figure 5-30. The field strength was variable between 0 to 15.8 kA/m (200 G) in the way to reach hyperthermia temperature (43°C) and then keep the temperature constant. The AC field frequency was constant at 406 kHz. Specific power absorption (SPA) of the nanoparticles were calculated based on the magnetic heating profile as shown in Section 3.14.2.

As shown in Figure 5-30, magnetic nanoparticles were heated successfully in high frequency magnetic fields. The temperature of the solution reached hyperthermia conditions in about 8 minutes and 15 minutes for ME93-PEG-PCL and ME94-PEG-PCL, respectively. It is worth noting that hyperthermia recommended temperature rise should be between 4 to 8°C to avoid damages to healthy cells (Reddy et al., 2012, Kobayashi, 2011). The nanoparticle suspension offered a ΔT of 5°C in around 10 minutes for ME93-PEG-PCL and 16 minutes for ME94-PEG-PCL which are in the recommended range for hyperthermia treatments (Bae et al., 2009, Reddy et al., 2012). However higher magnetic heating of $\Delta T=32$ degree was observed by Azevedo *et al.* for SBA-16/Fe₃O₄/P (N-iPAAm) at a concentration of 20 mg/mL while applying an alternating magnetic field of 13.37 kA/m at frequency of 222 kHz for 30 minutes in aqueous medium (Azevedo et al., 2014). The lower temperature raise observed here could be due to lower magnetite nanoparticle concentration in the solution. The lower heating properties of ME94-PEG-PCL compare to ME93-PEG-PCL is consistent with its lower magnetite content in a single nanoparticle and its lower saturation magnetization (M_s) as observed using VSM data (see Figure 3-35).

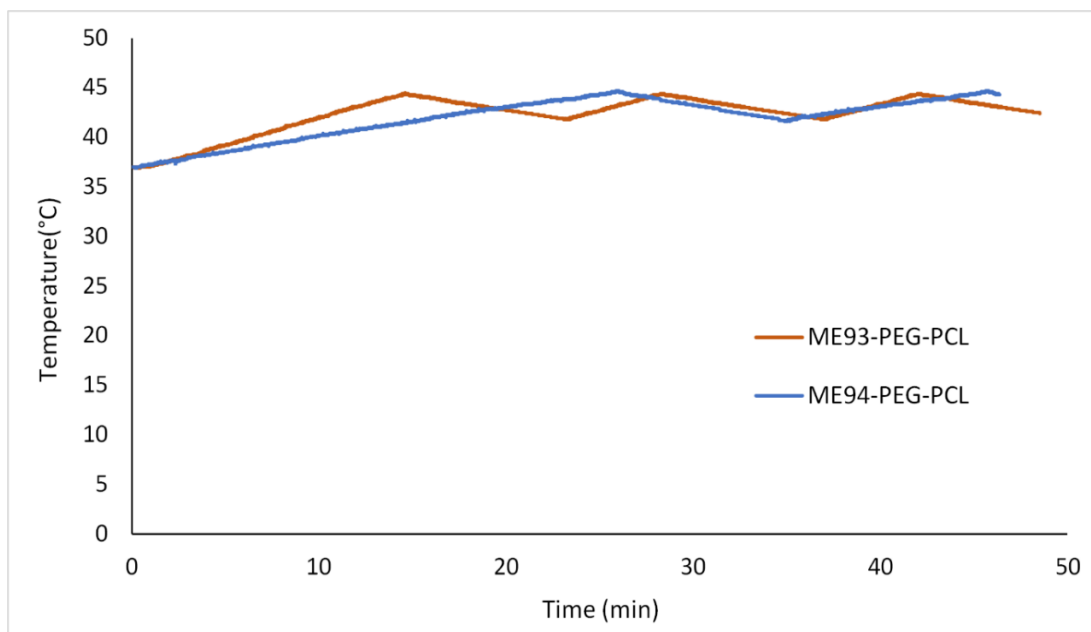


Figure 5-30. Magnetic heating profile of ME93-PEG-PCL and ME94-PEG-PCL with the concentration of 4 mg/mL in a variable magnetic field with maximum strength of 200 G and frequency of 406 kHz. The field was adjusted in the way to keep the temperature at 43°C

Temperature triggered DOX release were studied both in an incubator and under magnetic field induced heating. The starting temperature for the release studies were set at 37 °C similar to body temperature. Heat activated drug release profiles are shown in Figure 5-31 and Figure 5-32. Drug release was assessed at an elevated temperature of 43°C, for up to 45 minutes.

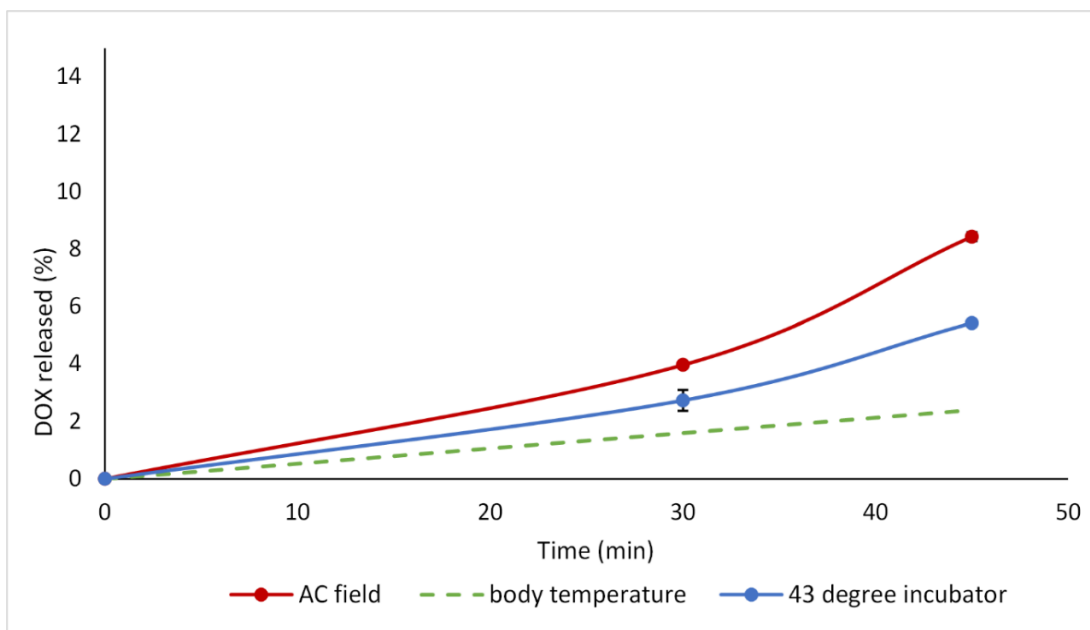


Figure 5-31. ME93 In vitro drug release at 37°C in incubator and under magnetic hyperthermia condition

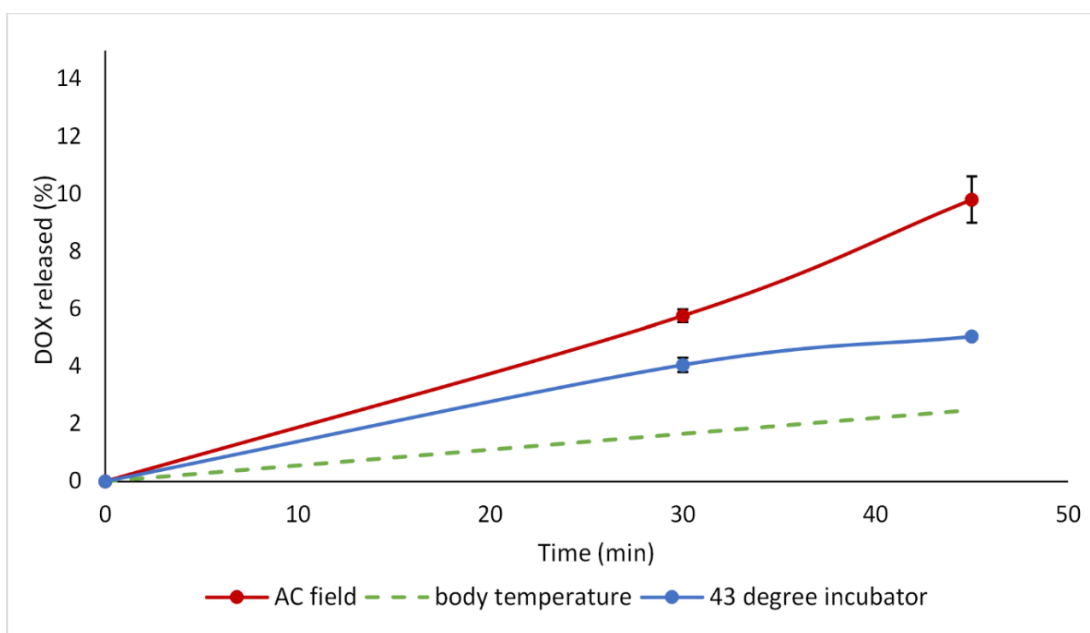


Figure 5-32. ME94 In vitro drug release at 37°C in incubator and under magnetic hyperthermia condition

Doxorubicin release rate were increased with the temperature rise. The enhanced release profile suggested that the PEG-PCL polymer capped nanoparticles could be thermally stimulated to release the drug. Additionally, as illustrated in the graphs the drug release was higher when activated by AC field rather than high temperature in the incubator. The accumulated drug release for ME93-PEG-PCL after 45 minutes of heating reached 8.4% and 5.4% in presence of AC field

and in incubator, respectively which is much higher compare to 2.3% drug release at 37°C. Similarly for ME94-PEG-PCL the drug release reached 9.8% and 5.0% under hyperthermia condition induced by the AC field and in the incubator. Liu *et al.* have studied the hyperthermia drug release using 1-tetradecanol (TD) as gatekeeper. They have achieved low drug release of less than 4% at 37°C after 96 hours while at 40°C TD molecules were melted to release the drug, however TD molecules stayed within the pores and hindered the DOX molecules diffusion into the solution (Liu et al., 2014a).

It is observed that once the silica coated magnetic nanoparticles combined with thermally responsive PEG-PCL polymer, is placed in an AC magnetic field, magnetic cores can be used to produce localized heating. Since the melting temperature of the PCL segment is in the range of 40 to 45°C the induced heating could cause the PCL segments of the polymer to melt and allow enhanced diffusion and subsequently increase the drug release (Glover et al., 2012). Additionally, Wu *et al.* have suggested that the heat could dissociate the strong interactions between the DOX and mesoporous silica which could result in an increased drug release with an increase in temperature (Liu et al., 2014b, Lingjie et al., 2015).

Furthermore, the increase in drug release under hyperthermia condition in presence of the AC field could be explained by increase in the Brownian motion of the nanoparticles, which could in turn lead to an increased drug release from the mesopores of the nanoparticles (Lingjie et al., 2015, Chon et al., 2005).

PEG-PCL copolymer demonstrated promising characteristics to be used in hyperthermia triggered drug release compare to other polymers reported in the literature. Zhu *et al.* described synthesis of a thermally responsive drug delivery system based on ordered mesoporous silica SBA-15 with magnetic particles and poly (N-isopropyl acrylamide) (PNIPA). They have observed thermally activated release. However, the system showed very low saturation magnetization and in addition drug release reached its maximum at temperatures between 15 to 20°C, which is much lower than body temperature making the material unsuitable for thermally controlled drug release (Zhu et al., 2007). Lien and Wu reported synthesis of nanoparticles containing thermosensitive polymer poly (N-isopropylacrylamide) grafted onto the surfaces of silica coated magnetite nanoparticles. However, these multifunctional nanoparticles demonstrated a phase transition at temperatures around 34° to 36 °C which is again lower than body temperature (Lien and Wu, 2008).

The AC field induced heating of the PEG-PCL magnetic nanocomposites together with increased doxorubicin release rate under hyperthermia condition would effectively release the drug in cancer cells and establish a synergistic effect for killing cancer cells with significant enhancement in cancer therapy.

The results demonstrated that the PEG-PCL capped magnetic silica nanocomposites have successfully encapsulated DOX as model drug with efficient drug loading content and achieved a controllable drug release, triggered by pH and magnetic induced heating.

5.8 Summary

Different drug delivery systems based on magnetic nanoparticles were developed to address the challenges in cancer therapy. The drug delivery systems were evaluated *in vitro* to test the drug loading and release performance of the developed systems and assess the feasibility of the synthesised material to be used as drug delivery systems.

The developed materials included mesoporous silica coated magnetic nanoparticles, magnetoliposomes, liposome capped mesoporous silica coated magnetic nanoparticles, magnetic micelles, and polymer capped mesoporous silica coated magnetic nanoparticles.

The developed materials were drug loaded using two different anticancer drugs MMC and DOX which both are commonly used for cancer therapy however, they both induce strong toxic side effects.

MMC loading into silica nanoparticles and magnetoliposomes showed that mesoporous nanoparticles are able to encapsulate more drug than magnetoliposomes however uncapped mesoporous silica coated nanoparticles lose most of the drug during washing process before drug release experiments. Maximum drug release from silica nanoparticles after 48 hours at body temperature reached 12% but for magnetoliposomes drug release reached up to 45%.

DOX loading into developed nanoparticles showed that mesoporous nanoparticles were able to encapsulate large amount of DOX and the polymer and liposome capping of the mesochannels were able to decrease the drug leakage from the nanoparticles.

DOX release from nanoparticles was studied under pH and temperature triggered conditions. The results indicated that all the developed materials are suitable to be used in hyperthermia treatments however polymer coated materials showed a higher increase in drug release with the temperature rise compared to liposome coated material. All the developed materials showed pH responsive release profiles with increased drug release at lower pH.

The DLC of the materials were decreased with polymer capping and liposome capping of the material which could be explained by the increase weight of the nanoparticles due to the capping material which would decrease the drug to nanoparticles ratio (w/w).

The results confirmed that the nanoparticles are able to produce sufficient heat for hyperthermia treatments and either increased temperature or change in pH could trigger the drug release from

the nanoparticles, which indicates the developed nanoparticles have great potential for applications in drug delivery and cancer therapy.

CHAPTER 6

CELL RESPONSE

6.1 Introduction to cytotoxicity study

A drug delivery system is required to be non-cytotoxic and biocompatible (Cuong and Hsieh, 2009, Gao et al., 2013). Cytotoxicity is among the main concerns regarding the application of nanoparticles in nanomedicine. Cytotoxicity is defined as the toxic effect of materials on viable cells (Daglar et al., 2014). Commercial cell lines are usually used as the first tool to evaluate the biocompatibility of a drug delivery system. Generally, nanoparticles are added into the cell-culture and viability, proliferation and differentiation of the cells are compared to control cells. Flow cytometry, confocal microscopy, optical microscopy, transmission electron microscopy, and cell viability assays could be used to monitor the cells.

This chapter presents the results of *in vitro* biocompatibility and efficiency tests of the drug loaded nanoparticles evaluated against two commercial cell lines; MCF7 and U87.

Since Doxorubicin (DOX) is commonly used in breast cancer chemotherapy the efficacy of the developed drug loaded nanoparticles were assessed against breast cancer cells lines (MCF7). In addition to MCF7 the cytotoxicity of the nanoparticles were measured against glioblastoma cell lines (U87) as DOX is used to treat glioblastoma due to its preserved efficacy in extreme metabolic conditions (Rittierodt and Harada, 2003). Cytotoxicity of the developed nanoparticles were evaluated through PrestoBlue assay according to the procedure explained in Section 2.28.8. The cells viability were monitored for up to 72 hours in presence of nanoparticles to evaluate the effect of nanoparticles on cell viability.

6.2 Breast Cancer Cells Lines (MCF7)

Breast cancer is currently the second most widespread cancer, with around 1.7 million new cases diagnosed every year (Ferlay et al., 2015), around one in every 10 Western women will develop breast cancer at some time in their life (Ferlay et al., 2010). Despite all available treatments including radical mastectomy approximately one third of affected women die. Breast cancer is ranked as fifth cause of cancer death (Ferlay et al., 2015). Currently, chemotherapy including adjuvant and neoadjuvant treatments is the main action for breast cancer. Although chemotherapy improves survival rates in the adjuvant setting, around 50% of all treated patients will relapse. The major reason for therapeutic failure and progression of the tumour is associated with overexpression of inhibitors of apoptosis proteins (IAPs) such as multidrug resistant P-glycoprotein (Pgp) (Wang et al., 2014, Liu et al., 2010). Nanoparticle based drug delivery shown to be able to sidestep the MDR1 in MCF7 breast cancer cells by endosomal delivery of the chemotherapeutic agents (Wang et al., 2014).

6.3 Glioma Cell Line (U87)

U87 is a frequently studied grade IV glioma cell line also called glioblastoma multiforme (GBM). Glioblastoma is the most common primary malignant brain tumor which accounted for 256,000 new cases and 189,000 deaths in 2012 (1.8% of new cancers) with the highest incidence and mortality rates in more developed regions (Ferlay et al., 2015). While the number of cases is relatively small, GBMs have a one-year survival rate of only 29.6%, which makes it one of the most deadly types of cancer (Clark et al., 2010). The standard of treatment of newly diagnosed glioblastoma patients is surgical resection to the extent feasible, followed by adjuvant treatment of Carmustine implants or temozolomide chemotherapy with radiotherapy (Stupp et al., 2005, UK, 2013).

Nanoparticle based drug delivery could improve the treatment efficacy in glioblastoma. Similar to breast cancer cells, the lack of chemotherapeutic success in glioblastoma is associated with MDR1. Due to diverse metabolic and protective tasks of the blood-brain barrier, there is a relatively high P-gp expression under physiological conditions (Rittierodt and Harada, 2003).

6.4 Growth Curves

The growth characteristics are different for each cell line. Growth curve are established in order to evaluate the growth characteristics of a cell line. From growth curve, the lag time, exponential growth phase (log phase), population doubling time (PDT), and saturation density can be obtained (Jennie P. Mather, 2007). The effects of drugs and biological agents that stimulate or inhibit the cellular growth is mostly studied in log phase (Rubio-Pino, 2013, Assanga and Lujan, 2013), which is determined by the growth curve .

Growth curves were obtained using PrestoBlue viability assay following the method explained in Section 2.28.7. The growth curves for U87 and MCF7 are shown in Figure 6-1 and Figure 6-2, respectively. The cells were seeded in 96 well plates with the seeding density of 2×10^3 for MCF7 and 4×10^3 for U87 cell lines.

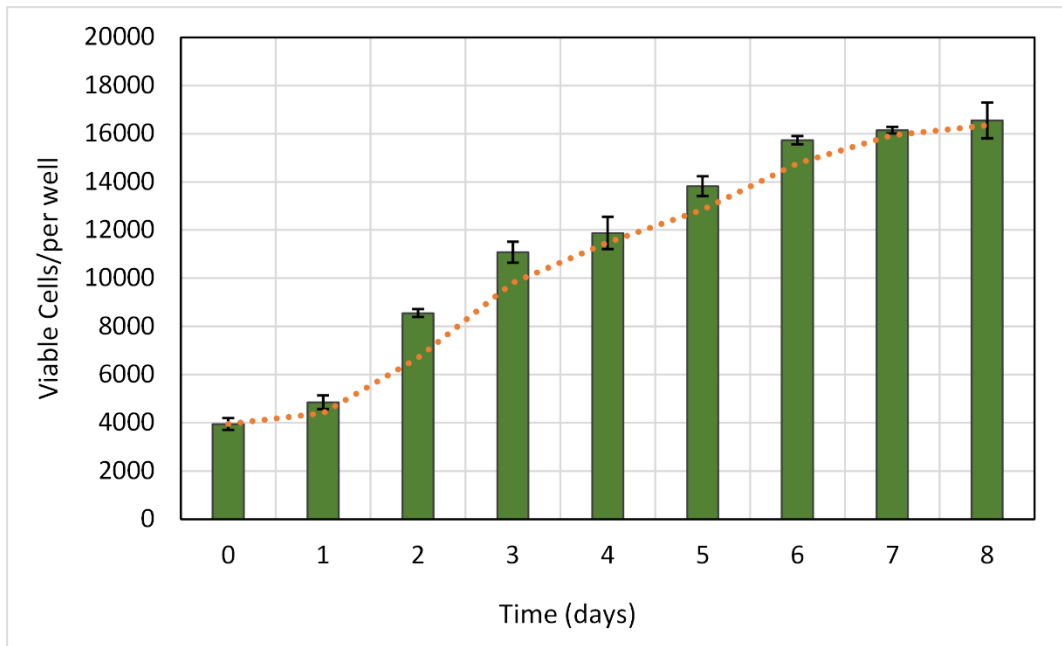


Figure 6-1. Growth curve of U87, the day 0 measurements were performed 3 hours after seeding the cells

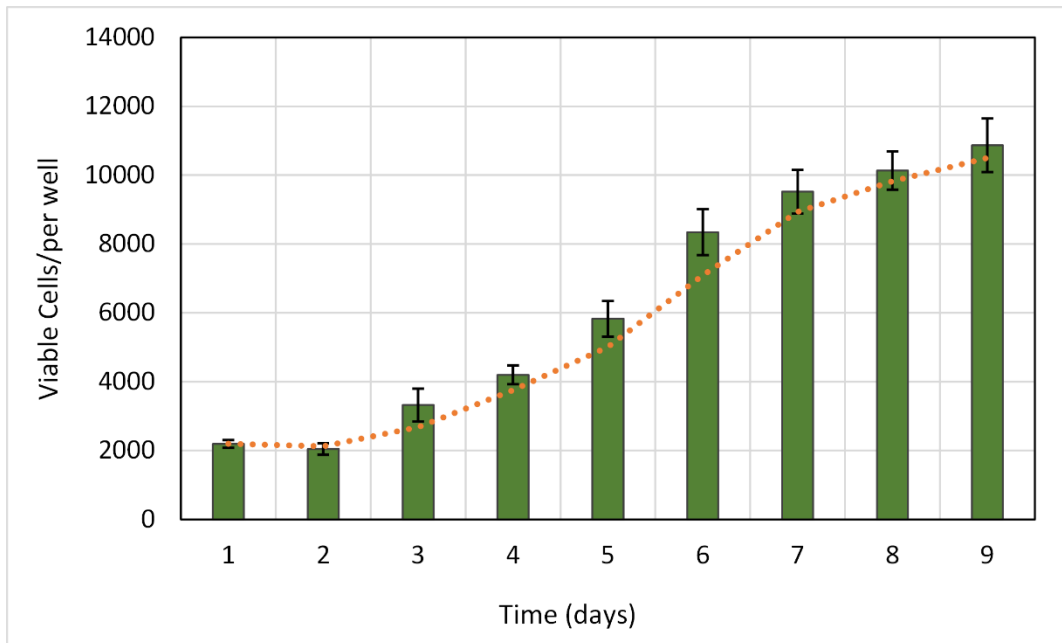


Figure 6-2. Growth curve of MCF7, the day 0 measurements were performed 3 hours after seeding the cells.

The first measurements were performed 3 hours after seeding the cells. The lag phase was observed to be around 20 hours for U87 and 48 hours for MCF7. Subsequently, the cells entered into exponential growth phase. For biocompatibility tests the nanoparticles with or without drug were added to culture media during this phase.

Population doubling time (PDT) was calculated based on

$$PDT = t \times \frac{\ln 2}{\ln \frac{C_e}{C_b}} \quad \text{Equation 6-1}$$

Where t is the incubation time, C_e is the cell population at the end of incubation time and C_b is the cell population at the beginning of the incubation time. The PDT was calculated to be 44 hours for MCF7 and 40 hours for U87. The stationary saturation phase was observed after 6 days for U87 and 8 days for MCF7. American Type Culture Collection (ATCC) suggest the PDT of 38 hours for MCF7 and 34 hours for U87 (ATCC, 2012).

6.5 Biocompatibility Evaluation of the Synthesised Materials

Biocompatibility of therapeutic nanoparticles with biological tissue is necessary to avoid possible side effects. The *in vitro* methods are extremely valuable for biocompatibility assessments of nanoparticles as they can produce specific and measureable toxicity evaluations inexpensively and without use of animals. Nanoparticles effect on cells' metabolic activity, membrane integrity, apoptosis, and proliferation could be studied *in vitro* cell culture (Lei et al., 2013).

MCF7 and U87 cell lines were cultured for biocompatibility experiments. Both cell lines were grown in Eagle's Minimum Essential Medium (EMEM) with 10% fetal bovine serum (FBS) , 1% Non-Essential Amino Acids Solution (NEAA), 1% Sodium Pyruvate, 1% L-Glutamine and 1% Penicillin/Streptomycin and maintained at 37°C in a humidified 5% CO₂ atmosphere. The cells were subcultured every 2 to 3 days when they have reached 70 to 80% confluence. Cells were maintained in 96 well plates for cytotoxicity studies. MCF7 and U87 cell lines were treated with a range of concentrations of control empty nanoparticles to assess the biocompatibility of the synthesised materials. It is suggested that materials which could maintain cell viability of more than 80% to be considered biocompatible (Mahmoudi et al., 2009).

Since it is suggested in the literature that incubation periods longer than 72 hours will not make significant difference in cell viability against different tested materials the cytotoxicity tests were performed for up to 72 hours incubation (Cuong et al., 2010b).

6.5.1 Data Analysis

Each experiment was measured using six wells per concentration and at least three independent identical experiments were performed. Data is presented as mean with error bars showing the standard deviation. Viability of each group was demonstrated as percentage of untreated control group which was considered to be 100%. T-test (two tailed distribution, two sample with unequal variances) was used for statistical analysis where P values less than 0.05 were considered to be statistically significant.

6.5.2 ME53 (bare magnetite nanoparticles)

Magnetic nanoparticles are one of the significant pioneering nanomaterials that can be used across a range of biomedical applications (Balasubramanian et al., 2014). Magnetite nanoparticles compare to other iron oxide exhibit better biocompatibility (Baba et al., 2012). Currently, great attention has been paid to biocompatibility of SPIONs in the human body. Many studies have evaluated the cytotoxic effects of different types of SPIONs with different coatings which demonstrated that, SPIONs at doses of up to 100 $\mu\text{g/mL}$ are biocompatible or may induce low cytotoxicity (Lei et al., 2013). The SPIONs biocompatibility was observed to be dependent on several factors such as surface coatings and oxidation state of iron in SPIONs (Singh et al., 2010).

Magnetite nanoparticles were synthesised following coprecipitation method as explained in Section 2.3.1. Synthesised bare magnetite nanoparticles were washed with sterile PBS buffer and redispersed in the EMEM medium with the final concentration of 1 mg/mL. This solution was then diluted to different concentration of nanoparticles (0.1 mg/mL, 0.25 mg/mL, 0.5 mg/mL, 0.75 mg/mL and 1 mg/mL) for treatment in 96-well plates cell culture. The viability of the cells after adding the SPIONs were studied using PrestoBlue assay at different time intervals of 3, 24, 48 and 72 hours. The cultures without nanoparticles were used as control experiments. The results are illustrated in Figure 6-3 and Figure 6-5 for U87 and MCF7 cell lines, respectively.

As seen in the figures the viability assay showed a concentration dependent cell toxicity. The cytotoxicity of the nanoparticles increased with increasing nanoparticles concentration.

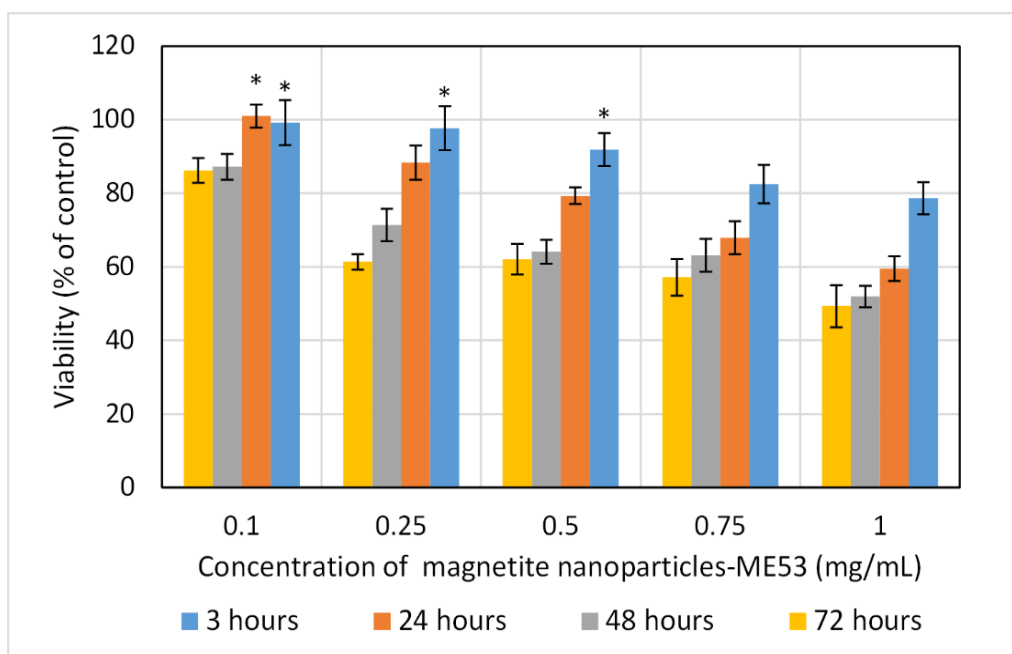


Figure 6-3. Cytotoxicity of uncoated magnetite nanoparticles (ME53) against U87. Each bar represents the mean of three measurements (6 well each) with error bars indicating standard deviation. Bars marked with * showed no significant difference compared to control sample ($P > 0.05$)

There was no significant difference in U87 cell viability for 0.1 mg/mL SPIONs in the first 24 hours ($P=0.82$) however magnetite nanoparticles (ME53) induced cell toxicity in 48 hours ($P<0.05$ for over 48 hours). The concentrations of up to 0.5 mg/mL did not show significant toxicity for the first 3 hours of treatment. The cytotoxicity data can also be presented in a time dependant cytotoxicity plot. Cytotoxicity of ME53 at concentrations of 0.25, 0.50 and 1 mg/mL against U87 cells is presented in Figure 6-4 as an example.

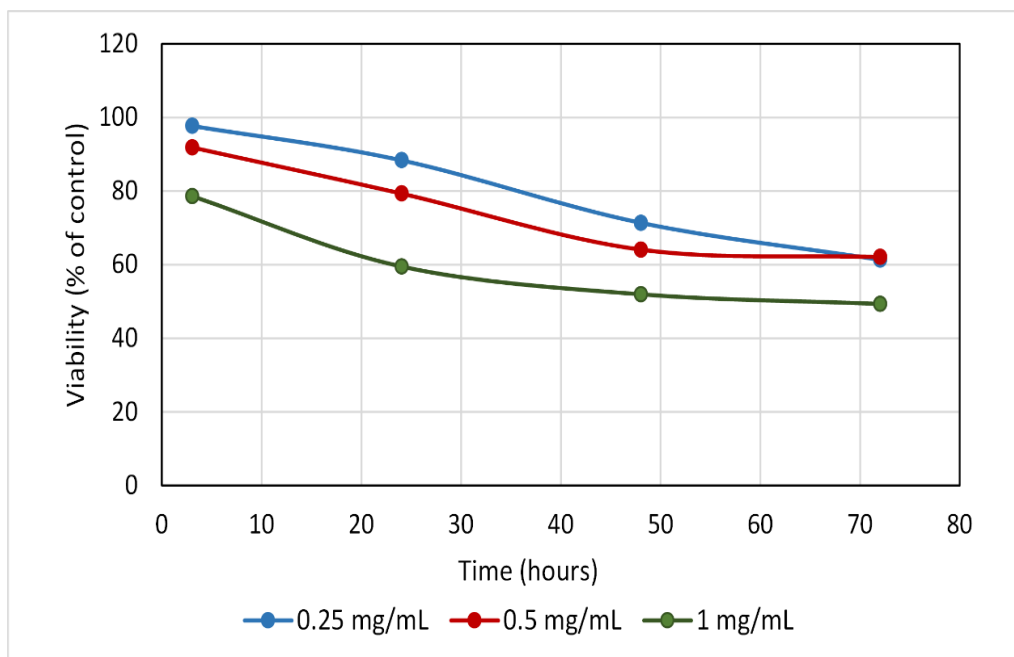


Figure 6-4. Cytotoxicity of uncoated magnetite nanoparticles (ME53) against U87 cells.

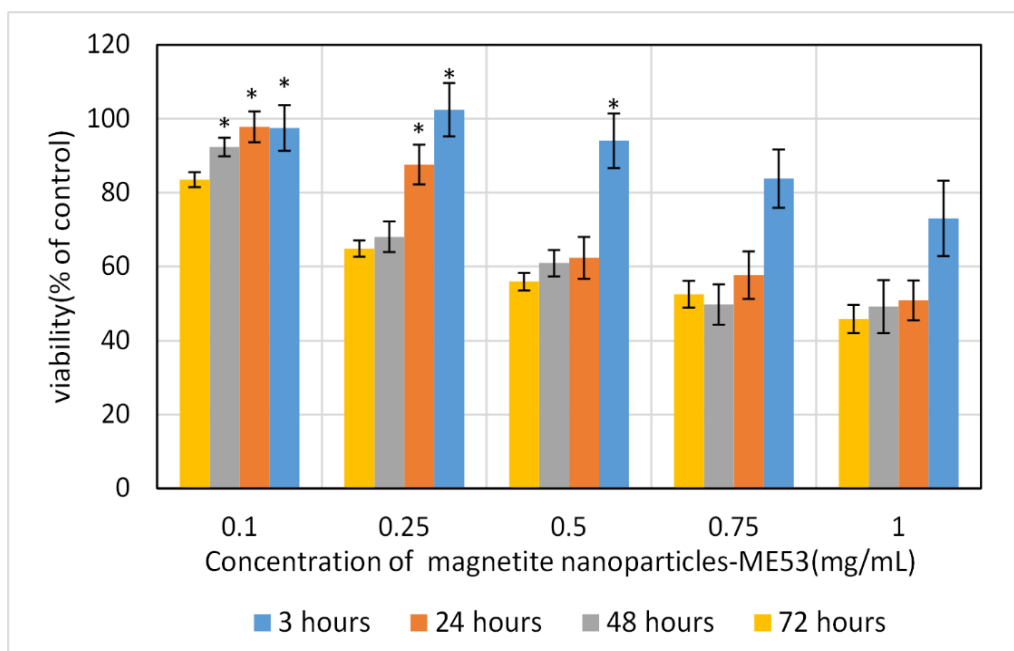


Figure 6-5. Cytotoxicity of uncoated magnetite nanoparticles (ME53) against MCF7 cells. Each bar represents the mean of three measurements (6 well each) with error bars indicating standard deviation. Bars marked with * showed no significant difference compared to control sample ($P>0.05$).

There was no significant difference in viability of MCF7 cells treated with magnetite nanoparticles (ME53) with concentration of 0.1 mg/ml for 48 hours ($P=0.17$). However magnetite nanoparticles induced cell toxicity in 72 hours ($P<0.05$ for over 72 hours). Cell viability for MCF7 was reduced to 87% after 24 hours of incubation with 0.25mg/ml of SPIONs. The lowest concentration tested were 0.1 mg/mL which did not induce significant toxicity after 48 hours of incubation.

It was observed that magnetite nanoparticles (ME53) with concentration less than 0.1 mg/mL were biocompatible while treating the cells with ME53 at the highest concentration of 1 mg/mL, for 24 hours resulted in reduced viability of 59% for U87 and 50% for MCF7. Similarly, Balasubramanian *et al.* have reported 80% viability for 0.1 mg/mL bare magnetite and reduced viability of 53% for 1 mg/mL bare magnetite after 24 hours (Balasubramanian *et al.*, 2014).

It is suggested that the cytotoxicity induced by the magnetite nanoparticles is due to their physicochemical properties. Magnetite nanoparticles present a large surface area for the generation of free radicals. Consequently, the reactive oxygen species (ROS), including superoxide anions, hydroxyl radicals and nonradical hydrogen peroxide, are moved inside the cells where they can produce oxidative stress by activating transcription factors for pro-inflammatory mediators. Additionally, ROS reacts with macromolecules and damage the cells by peroxidizing lipids, changing proteins, disrupting DNA, and interfering with signalling functions, and subsequently cause cell death (Mahmoudi *et al.*, 2011).

6.5.3 PEG-PCL

Self-assembled polymeric micelles are one of the most promising drug delivery systems since they could improve bioavailability, solubility, and retention time of drugs and also could overcome MDR effect (Cuong *et al.*, 2012, Kedar *et al.*, 2010). Particularly nanoparticles composed of biodegradable, biocompatible poly (ϵ -caprolactone) (PCL) and poly (ethylene glycol) (PEG) have demonstrated great potential for drug delivery systems (Cuong *et al.*, 2010b, Sosnik and Cohn, 2003). Therapeutic activity and stability of PCL is reasonably higher than other polymers such as PLGA in nanomedicine. PCL (poly- ϵ -caprolactone) is biodegradable by hydrolysis of its ester linkages in physiological conditions (Kumari *et al.*, 2010). Additionally hydrophilic PEG shell is known to enhance the solubility in water and reduce the adhesion of plasma proteins which could potentially increase the circulation time of drugs and can prevent recognition by reticuloendothelial system (RES) after intravenous injection (Cuong *et al.*, 2010b).

PEG-PCL polymer was synthesised as explained in Section 2.7. Biocompatibility and safety of the copolymer was evaluated *in vitro* before loading of drug molecules. The *in vitro* cytotoxicity studies were performed by PrestoBlue assay as explained before in Section 2.28.8.

MCF7 cells and U87 cells were seeded in 96-well plate and incubated at 37 °C under a humidified atmosphere containing 5% CO₂ for 24 hours. After which the media was replaced with fresh media containing different concentration of the copolymer (0.25 mg/mL, 0.5 mg/mL, 0.75 mg/mL and 1 mg/mL). The cells were further incubated for up to 72 hours. The cell viability (%) were determined as the ratio of the living cells compare to untreated control cells at 3, 24, 48 and 72 hours.

Figure 6-6 and Figure 6-7 show the viability when cells were treated with PEG-PCL copolymer where the highest concentration of the copolymer was 1 mg/mL.

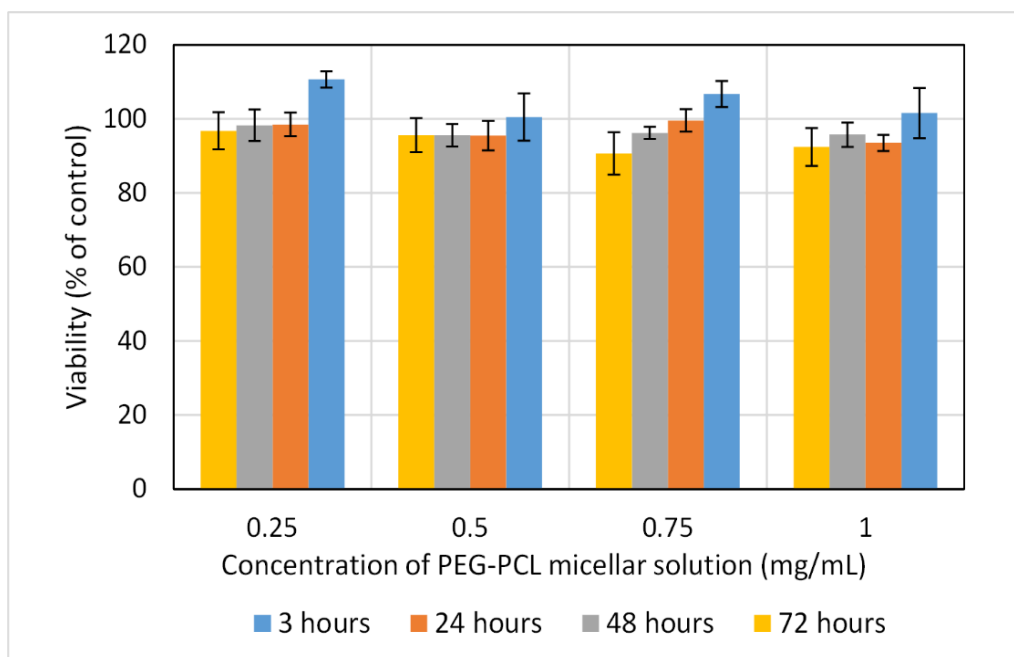


Figure 6-6. Biocompatibility of the PEG-PCL micelles against U87cells.

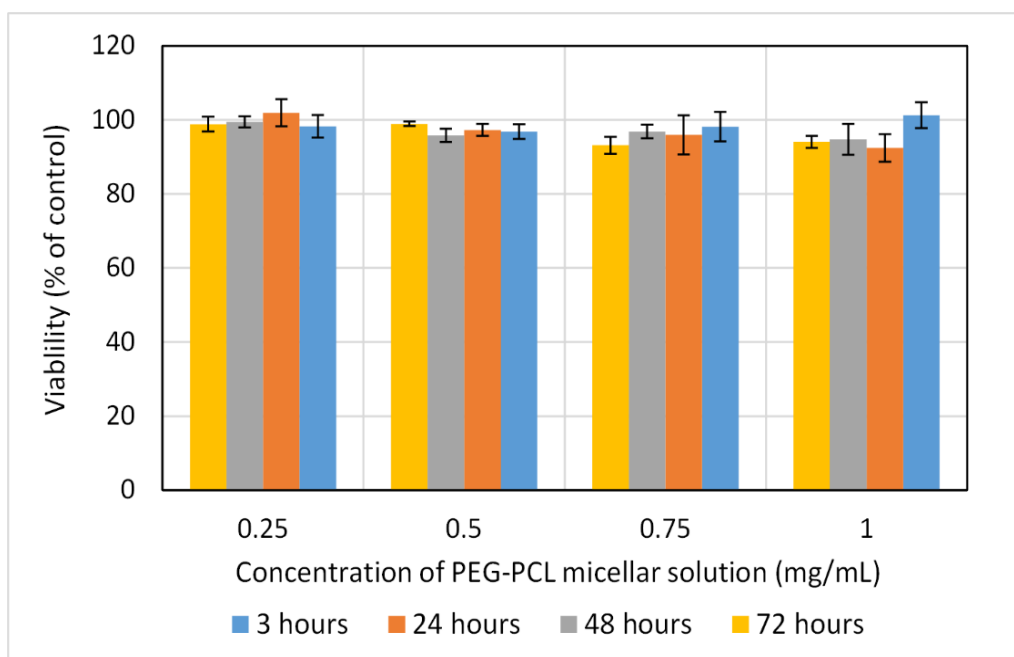


Figure 6-7. Biocompatibility of the PEG-PCL micelles against MCF7 cells.

The cellular viability tests shows that the viability of the either cell lines were not significantly affected by PEG - PCL copolymer. However the viability was concentration dependant. The lowest cell viability after 72 hours of incubation with highest polymer concentration was 94% for MCF7 and 92% for U87. Which indicates that the PEG-PCL copolymer is biocompatible and generated very low toxicity toward MCF7 and U87 cell lines even at high concentration of 1 mg/mL.

Similar results were observed by other groups. Nguyen group have reported a polymer concentration dependant viability for MCF7 cells with cell viability of approximately 92% for 1.0 mg/mL concentration of star-shaped FOL-PEG-PCL micelle after 48 hours treatment (Cuong et al., 2012). Cuong *et al.* have reported 89% viability for MCF7 cell lines after 24 hours of treatment with 1 mg/mL of PEG-PCL-PEG triblock copolymer (Cuong et al., 2010b). Similarly Gao *et al.* have reported around 90% viability of HEK293 cell line (human embryonic kidney) after 48 hours treatment with star shaped PEG-PCL micelles (Gao et al., 2013). Zhao *et al.* have reported around 95% viable Eahy.926 (umbilical vein cell line) cells after 24 hours treatment with 0.83 mg/mL of PEG-PCL micelles (Zhao et al., 2013a).

The observed cells viability results confirmed the biocompatibility and low cytotoxicity of the synthesised PEG-PCL diblock copolymer and its potential to be used in nanomedicine and drug delivery systems.

6.5.4 ME55-PEG-PCL

Uncoated magnetite nanoparticles have very low dispersibility that can lead to precipitation and a high rate of agglomeration under physiological conditions which could limit the efficiency of these nanoparticles (Lei et al., 2013). Surface modification of nanoparticles and appropriate coatings can improve magnetite stability, prevent the aggregation, reduce toxicity, and reduce nonspecific protein adsorption as well as prolonging the nanoparticles *in vivo* circulation time (Häfeli et al., 2009). Among all, polymer coatings containing PEG polymer has been extensively used in drug delivery applications, since it is biocompatible and improves hydrophilicity of the nanoparticles and minimizes their aggregation (Häfeli et al., 2009, Hong et al., 2012, Li et al., 2012b).

The PEG-PCL magnetic micelles were prepared by polymer coating of oleic acid functionalized magnetite nanoparticles as explained in Section 2.22.1. The polymer coating clearly enhanced the stability of the nanoparticles as shown in Section 3.8. The Biocompatibility and safety of the copolymer was evaluated *in vitro* using PrestoBlue assay.

Cells were treated with PEG-PCL coated magnetite nanoparticles (ME55-PEG-PCL) with the different concentrations of 0.25 mg/mL, 0.5 mg/mL, 0.75 mg/mL and 1 mg/mL and the viability was measures after 3, 24, 48 and 72 hours. The results are presented in Figure 6-8 and Figure 6-9

as cell viability percentage compare to control untreated cells. As observed from the results the polymer coating of the nanoparticles significantly improved biocompatibility of the magnetite.

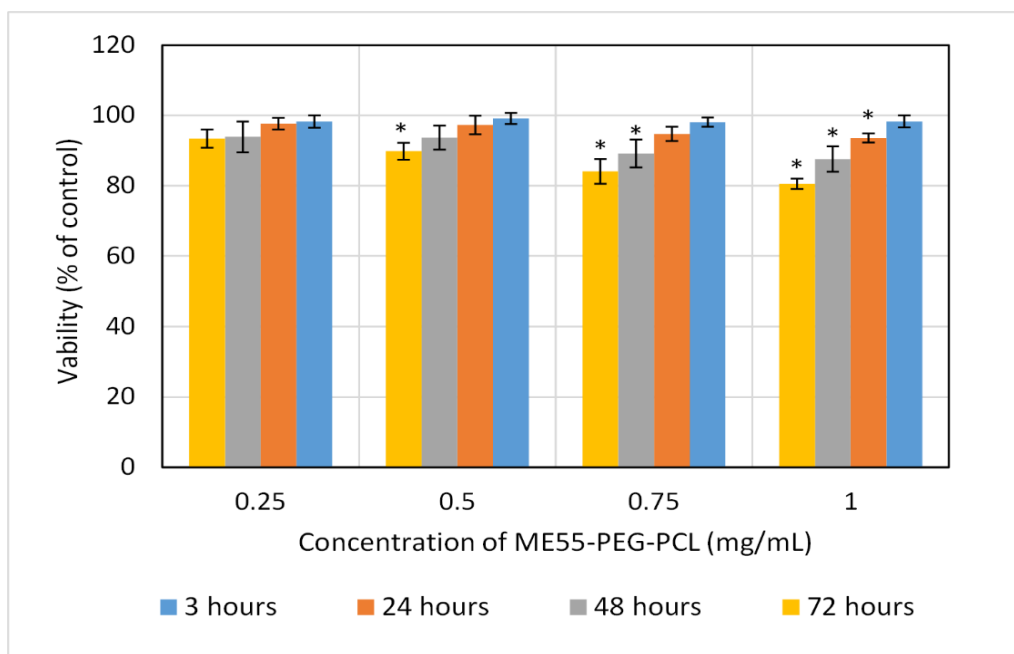


Figure 6-8. Biocompatibility of the PEG-PCL coated magnetite (ME55-PEG-PCL) against U87 cells. Bars marked with * showed statistically significant difference compared to control sample ($P < 0.05$).

It was observed that the biocompatibility of magnetite nanoparticles against U87 cell line were considerably improved with polymer coating of nanoparticles. As shown in Figure 6-8 after 72 hours of incubation with maximum dose of PEG-PCL coated magnetite (1 mg/mL), the survival rate was around 80% viable cells which was clearly improved from 49% viable cells observed for incubation of the cells with uncoated magnetite nanoparticles with the same concentration. The magnetic micelles did not show significant toxicity for up to 0.5 mg/mL after 48 hours of incubation. The toxicity was observed to be time and dose dependant and longer incubation time of 72 hours resulted in increased toxicity.

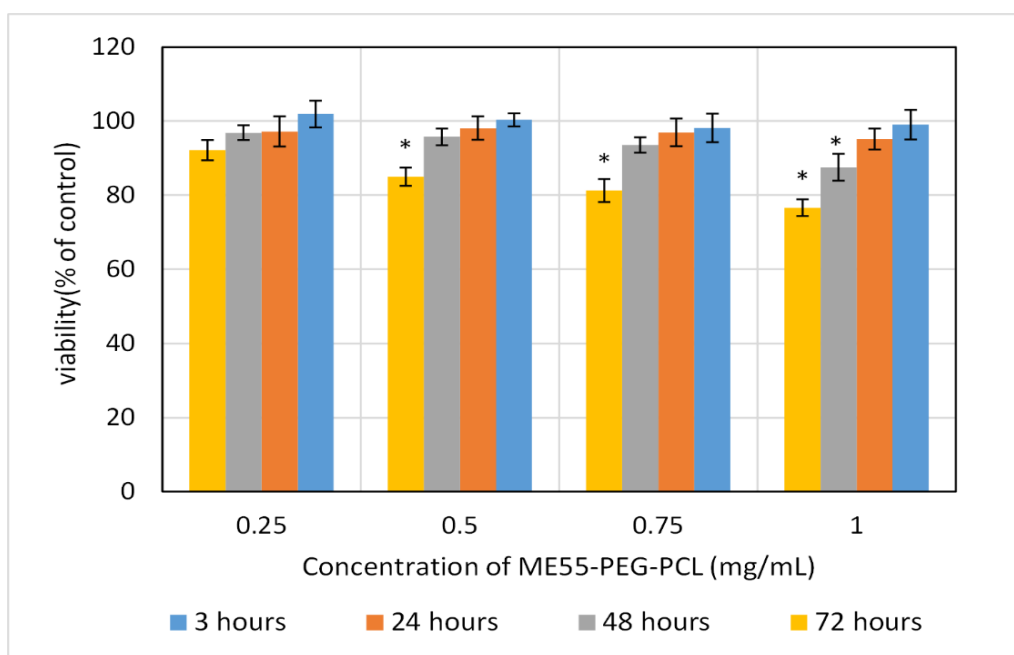


Figure 6-9. Biocompatibility of the PEG-PCL coated magnetite (ME55-PEG-PCL) against MCF7 cells. Bars marked with * showed statistically significant difference compared to control sample ($P < 0.05$).

Similar to U87 cells the MCF7 cells experienced time and dose dependant toxicity. Viability of MCF7 cells incubated with PEG-PCL coated magnetite nanoparticles for 72 hours were significantly higher than cells incubated with uncoated magnetite nanoparticles. MCF7 cells incubated with maximum dose (1 mg/mL) of PEG-PCL coated magnetite showed 76% viable cells compare to 45% viable cells for uncoated magnetite. The magnetic micelles did not show significant cytotoxicity for concentrations up to 0.25 mg/mL even after 72 hours of incubation.

The cytotoxicity study confirmed the biocompatibility of the PEG-PCL coated magnetite nanoparticles for their application as drug delivery system.

6.5.5 ME60

Mesoporous silica coating of magnetite could improve the biocompatibility of the magnetite nanoparticles and the large surface area of mesoporous silica make it attractive for drug delivery applications (Nakamura et al., 2015). To evaluate the possibility of the mesoporous silica nanoparticles to be used in drug delivery systems the cytotoxicity of the nanoparticles were tested against MCF7 and U87 cell lines.

The mesoporous nanoparticles were synthesised as explained in Section 2.4 and characterized with different methods such as BET and TEM. The drug loading capacity of the nanoparticles were evaluated and presented in Section 5.4. Mesoporous nanoparticles exhibited the high drug loading capacities which is advantageous for drug delivery applications. The biocompatibility of the synthesised nanoparticles (ME60) were tested using PrestoBlue assay.

Cells were treated with mesoporous silica coated magnetite nanoparticles (ME60) with different concentration of 0.25 mg/mL, 0.5 mg/mL, 0.75 mg/mL and 1 mg/mL and the viability was

measures after 3, 24, 48 and 72 hours. The results are presented in Figure 6-10 and Figure 6-11 for U87 and MCF7 cell lines. The results are shown as cell viability percentage compare to untreated control cells.

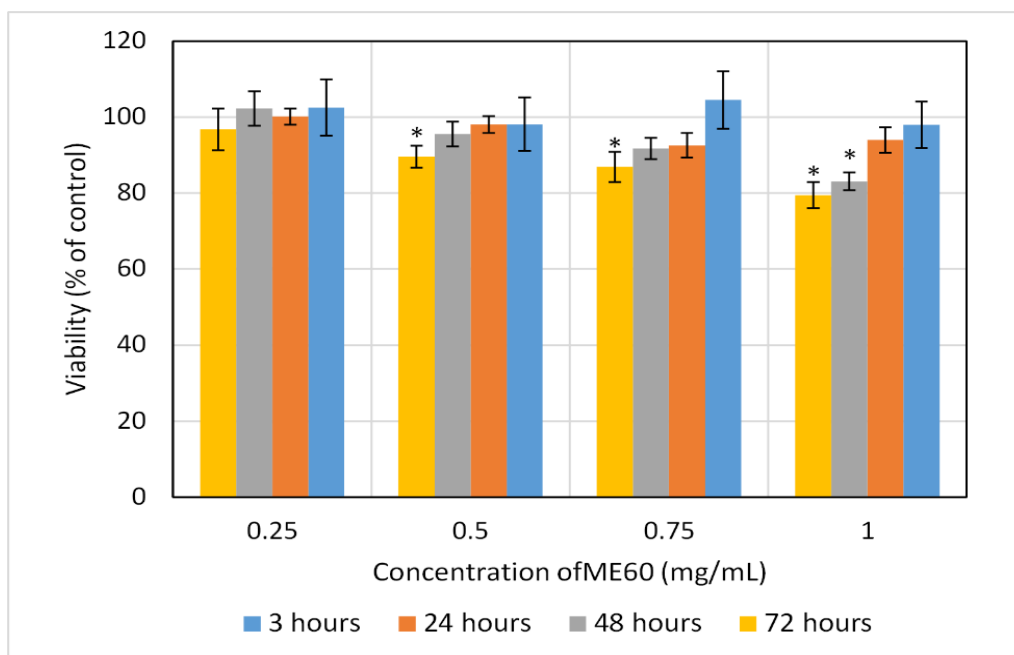


Figure 6-10. Biocompatibility of the mesoporous coated magnetite (ME60) against U87 cells. Bars marked with * showed statistically significant difference compared to control sample ($P < 0.05$).

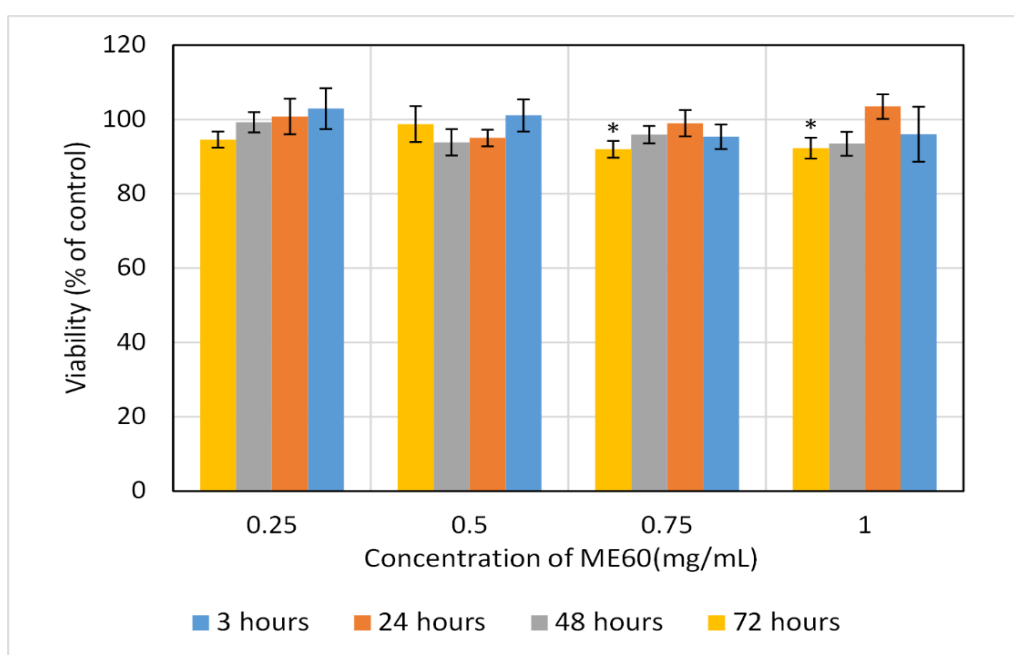


Figure 6-11. Biocompatibility of the mesoporous coated magnetite (ME60) against MCF7 cells. Bars marked with * showed statistically significant difference compared to control sample ($P < 0.05$).

As presented in the figures mesoporous coated magnetic nanoparticles are biocompatible and exhibited very limited toxicity against both cell lines. However the toxicity was observed to be cell dependant which is in agreement with literature (Yu et al., 2011). The mesoporous nanoparticles show higher toxicity toward U87 cell lines than MCF7 cells.

The cellular viability of both cell lines after 72 hours of incubation with maximum dose (1 mg/mL) of mesoporous silica coated magnetite were significantly improved compared to uncoated nanoparticles. The MCF7 cells showed no significant toxicity to 1 mg/mL of mesoporous silica coated nanoparticles even after 48 hours of incubation however, it showed slight toxicity when incubation for 72 hours. Mesoporous coated nanoparticles with concentrations up to 0.5 mg/mL did not show significant change in cell viability even after 72 hours of incubation. In comparison for U87 cell lines the safe dose that did not induce cytotoxicity after 72 hours of incubation was 0.25 mg/mL of mesoporous coated magnetite nanoparticles (ME60). Higher dose of 0.5 and 0.75 mg/mL of mesoporous silica coated nanoparticles (ME60) induced toxicity after 72 hours incubation and 1 mg/mL of nanoparticles induced toxicity in 48 hours. Similar results were reported by Wang *et al.* for MCF7 cell lines incubated with mesoporous silica nanoparticle for 48 hours, they have observed 71.4% cell viability at 1.6 mg/mL and negligible cytotoxicity at concentration of 0.8 mg/mL (Wang et al., 2014).

These data establish the excellent biocompatibility of the mesoporous silica coated magnetic nanoparticles. The data clearly demonstrate the enhanced biocompatibility of the magnetite nanoparticles by silica coating of the nanoparticles.

6.5.6 ME93-PEG-PCL and ME94-PEG-PCL

Mesoporous silica coated nanoparticles have received considerable attention as drug delivery systems however due to the open pore structure there is limited control over drug release from the mesochannels and premature drug release occurs during the delivery (Liu et al., 2014a).

The drug leaking issue was observed during the drug loading and release experiments for magnetic mesoporous silica nanoparticles (ME16, ME32, ME33 and ME60). To overcome this problem the mesoporous silica nanoparticles were octyl-modified and coated with PEG-PCL diblock copolymer (which was shown to be biocompatible (see Section 6.5.3)) as explained in Section 2.25. Surface coating of the mesoporous silica nanoparticles with polymer proved to improve the control over drug release and add temperature and pH triggered drug released properties to the nanoparticles. Furthermore coating the nanoparticles with PEG contained shell could enhance their cellular uptake (Sardan et al., 2014).

Drug loading properties of the polymer capped mesoporous silica nanoparticles were presented in Section 5.7. Cytotoxicity of polymer coated nanoparticles (ME93-PEG-PCL and ME94-PEG-PCL) were tested to evaluate the biocompatibility of the nanoparticles and to determine the possibility to improve the biocompatibility of the nanoparticles by polymer coating of mesoporous silica nanoparticles.

Cells were treated with polymer capped mesoporous silica coated magnetite nanoparticles (ME93-PEG-PCL and ME94-PEG-PCL) with different concentrations for up to 72 hours and the

viability was measured after 3, 24, 48 and 72 hours. The results are presented in Figure 6-12 and Figure 6-13 for U87 cell line and Figure 6-14 and Figure 6-15 for MCF7 cell line. The results are shown as cell viability percentage compared to untreated control cells.

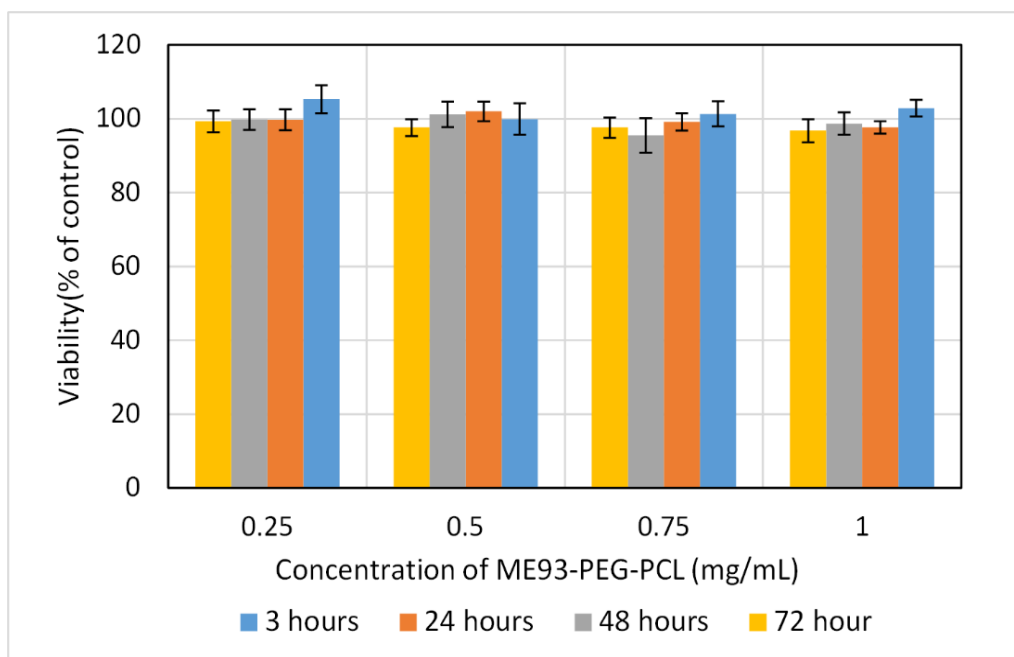


Figure 6-12. Biocompatibility of the polymer capped mesoporous coated magnetite nanoparticles (ME93-PEG-PCL) against U87 cells.

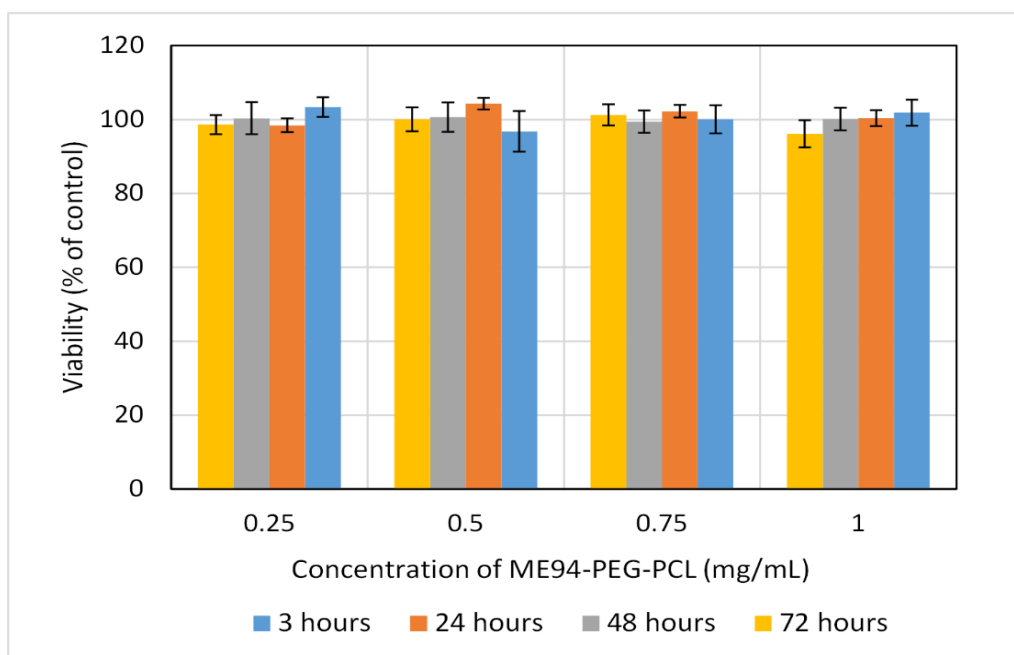


Figure 6-13. Biocompatibility of the polymer capped mesoporous coated magnetite nanoparticles (ME94-PEG-PCL) against U87 cells.

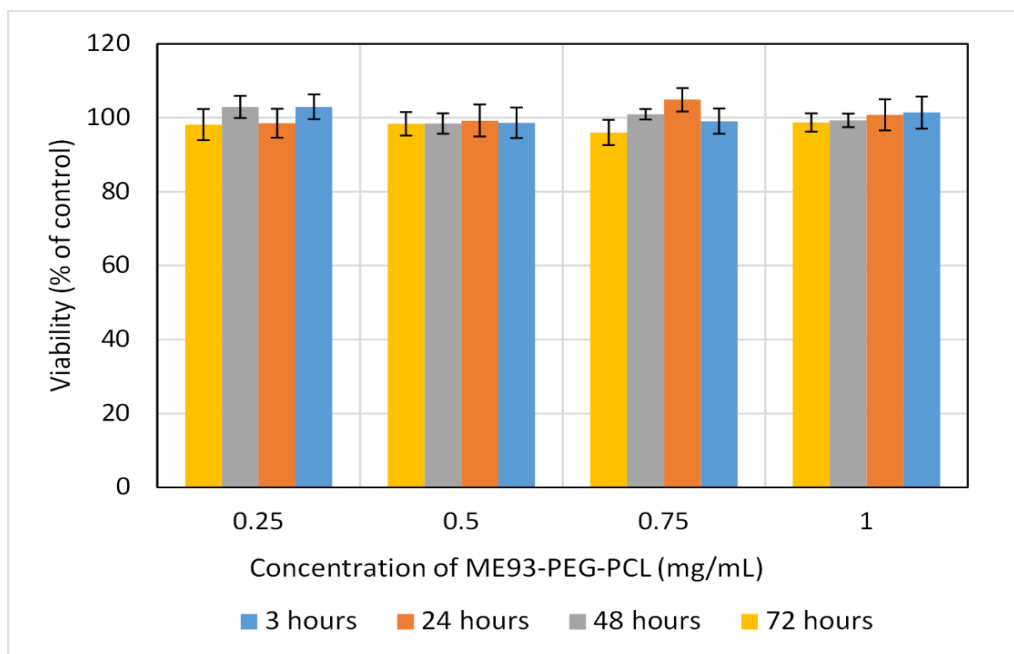


Figure 6-14. Biocompatibility of the polymer capped mesoporous coated magnetite nanoparticles (ME93-PEG-PCL) against MCF7 cells.

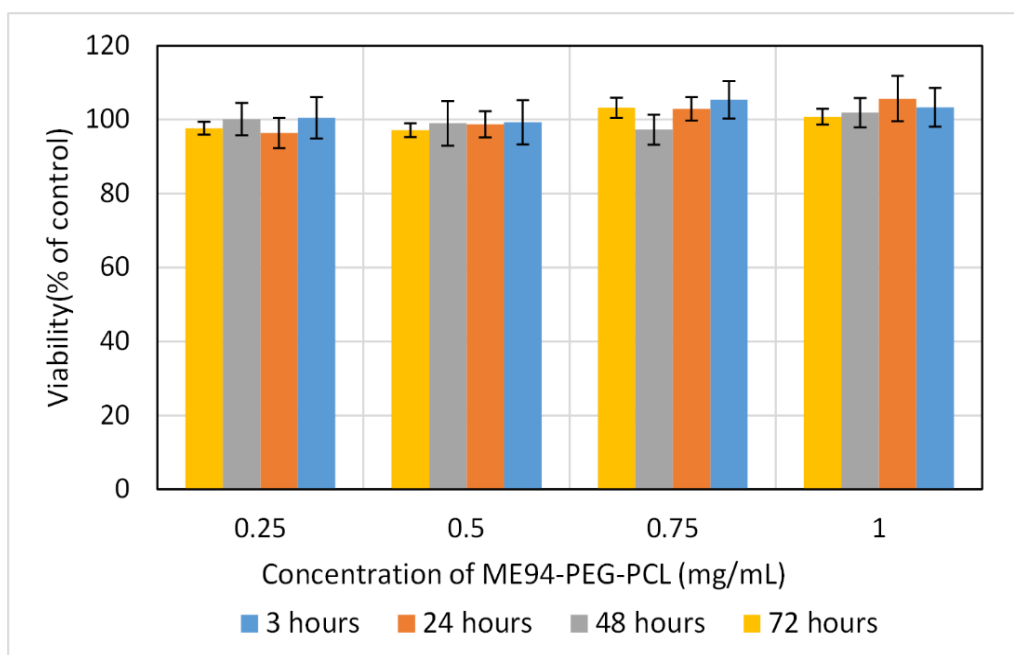


Figure 6-15. Biocompatibility of the polymer capped mesoporous coated magnetite nanoparticles (ME94-PEG-PCL) against MCF7 cells.

As seen from the figures, coating mesoporous silica nanoparticles with polymer have improved the biocompatibility of the nanoparticles. As expected, the viability assays indicated that no evidence of cytotoxicity was observed after cells have been treated with different concentrations of polymer capped particle (0.25 mg/mL to 1 mg/mL) for 72 hours.

Similarly He *et al.* have reported around 90% cell viability for L929 cells after 48 hours of incubation with 1 mg/mL of PEG-PCL polymer coated mesoporous silica particles (polymer

grafting *via* disulphide bonds) (He et al., 2013). Liu *et al.* have reported very limited cytotoxicity of less than 10% for PEGylated magnetic mesoporous nanoparticles at concentration of 1 mg/mL against melanoma MEL-5 and L929 cell lines after 96 hours of incubation (Liu et al., 2014a).

The results suggested that the polymer coated mesoporous nanoparticles are biocompatible and suitable to be used as drug delivery systems.

6.5.7 ME60-L

Liposomes have been widely investigated as drug delivery systems due to their high biocompatibility with the biomimetic membrane. Most recently, a kind of drug carrier based on the combination of mesoporous silica structures and liposome has been reported (Wu et al., 2013b). By coating liposome on the surfaces of mesoporous nanoparticles, the advantages of both mesoporous nanoparticles and liposome can be achieved.

Liposome capped mesoporous silica coated magnetite nanoparticles (ME60-L) were synthesised as explained in Section 2.20. The drug loading and release efficiency of ME60-L were evaluated and presented in Chapter 5. The results showed promising potential for protocells to be used in drug delivery applications. Cells were treated with liposome coated mesoporous silica nanoparticles (ME60-L) with different concentration of 0.25 mg/mL, 0.5 mg/mL, 0.75 mg/mL and 1 mg/mL, the cell viability were measured after 3, 24, 48 and 72 hours. The biocompatibility of the nanoparticles were tested against MCF7 and U87 cell lines and the results are shown in Figure 6-16 and Figure 6-17.

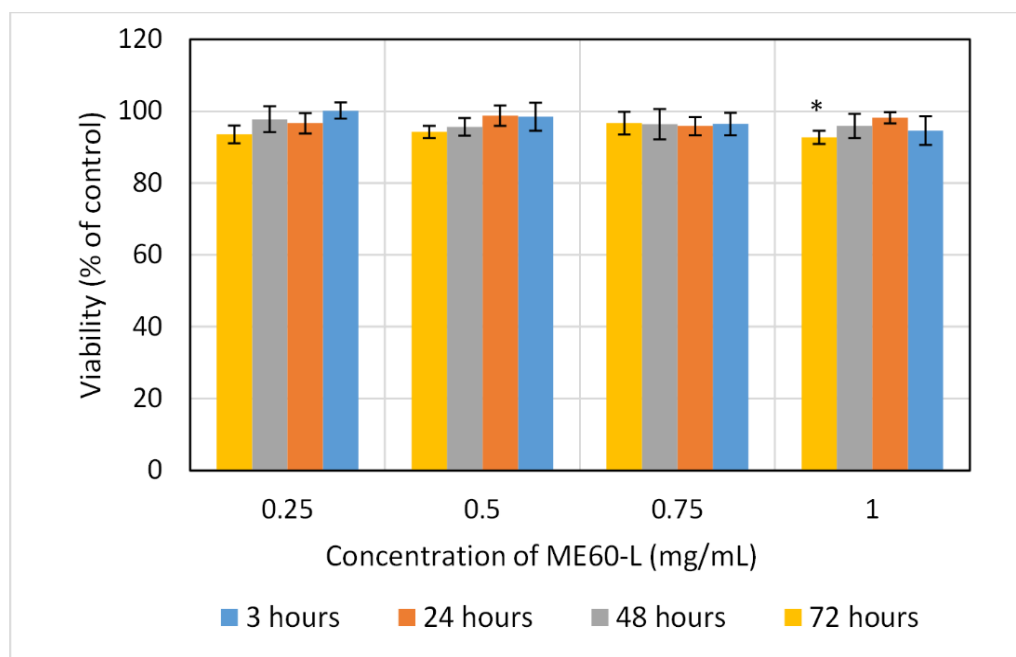


Figure 6-16. Biocompatibility of the SPC liposome capped mesoporous coated magnetite nanoparticles (ME60-L) against U87 cells. Bars marked with * showed statistically significant difference compared to control sample ($P < 0.05$)

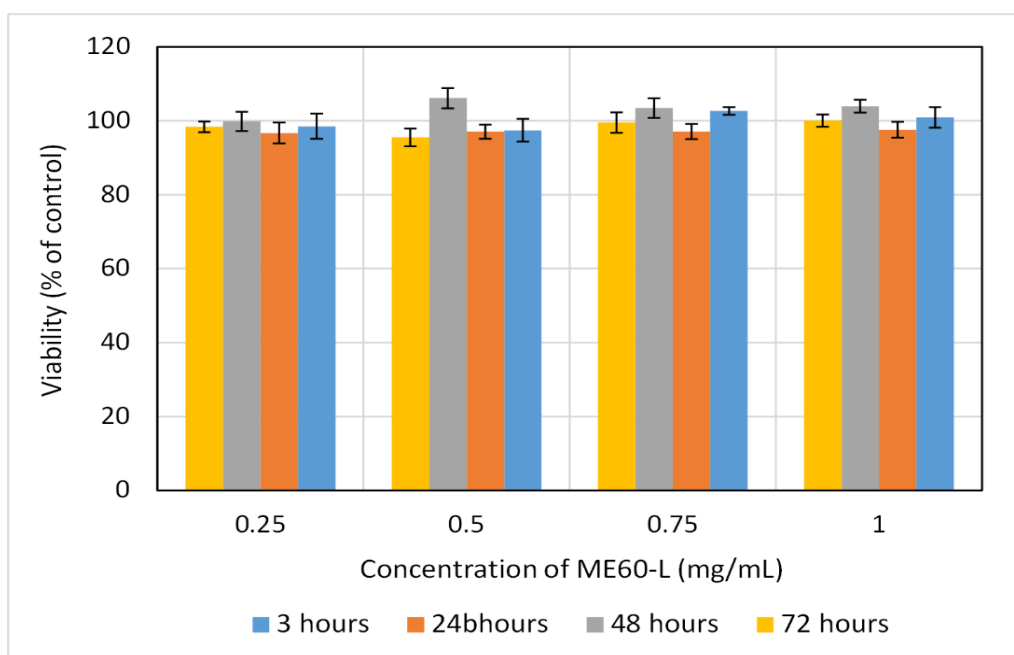


Figure 6-17. Biocompatibility of the SPC liposome capped mesoporous coated magnetite nanoparticles (ME60-L) against MCF7 cells.

As seen in the figures protocoils were biocompatible and exhibited very limited toxicity against both cell lines. However low cytotoxicity was observed for U87 cell lines when incubated for 72 hours with maximum concentration of 1 mg/mL of protocoils. The biocompatibility of the mesoporous nanoparticles were clearly improved by liposome coating of the nanoparticles.

6.5.8 Summary

The biocompatibility of the synthesised nanoparticles were evaluated against two cell lines of MCF7 and U87. The data demonstrated that only bare magnetite nanoparticles induced toxicity in low dosage of 0.25 mg/mL. It was shown that the biocompatibility of the magnetite nanoparticles were significantly improved by surface coatings. The comparison data is demonstrated in Figure 6-18 and Figure 6-19.

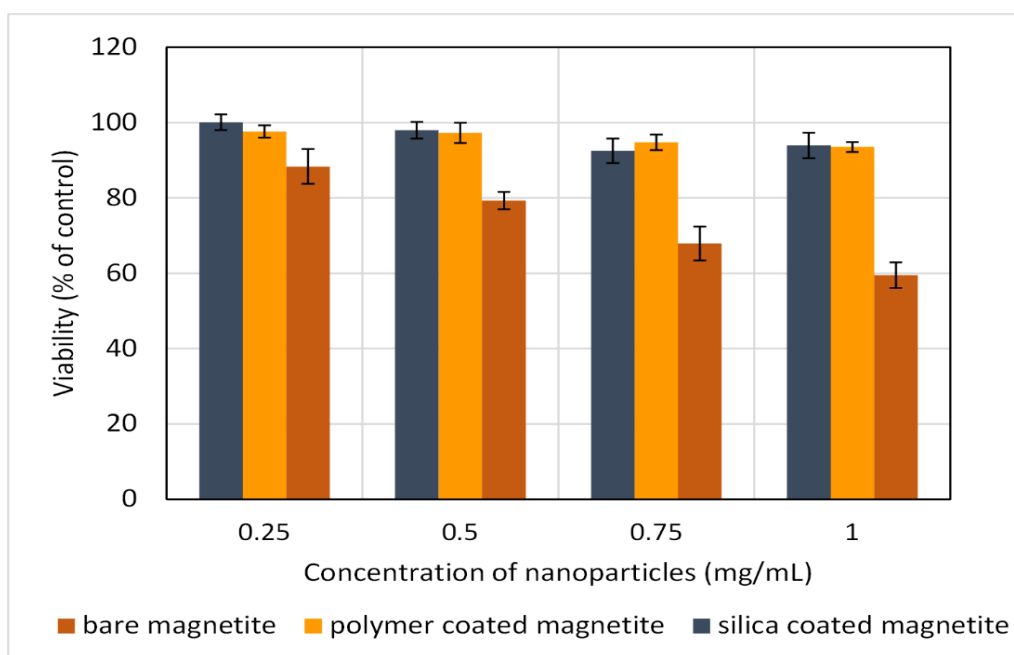


Figure 6-18. Biocompatibility of bare magnetite (ME53), silica coated magnetite (ME60) and polymer coated magnetite (ME55-PEG-PCL) against U87 cells after 24 hours of incubation.

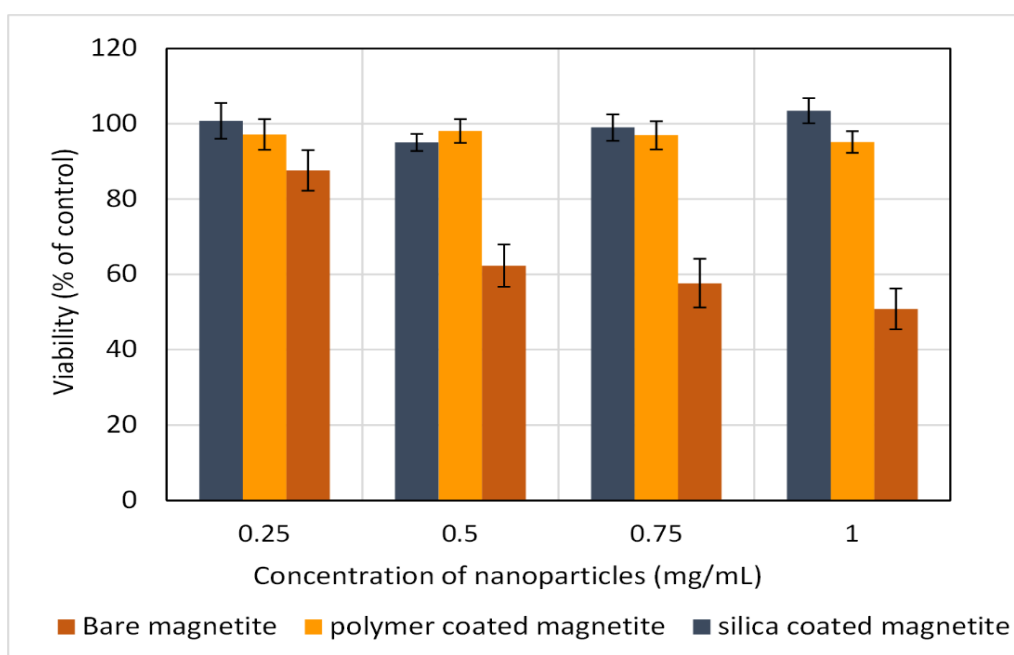


Figure 6-19. Biocompatibility of bare magnetite (ME53), silica coated magnetite (ME60) and polymer coated magnetite (ME55-PEG-PCL) against U87 cells after 24 hours of incubation.

These data demonstrated that coatings of nanoparticles improved the biocompatibility of the bare magnetite.

Mesoporous coated silica nanoparticles showed good biocompatibility against both cell lines, however they exhibited cytotoxicity at high dose or after long incubation period. To further improve the stability and biocompatibility of the silica nanoparticles, and also improve the control over the drug release, the silica coated nanoparticles were surface modified with the

biocompatible polymer or liposomes. The cytotoxicity of the surface modified mesoporous silica nanoparticles compare to bare silica nanoparticles are shown in Figure 6-20 and Figure 6-21.

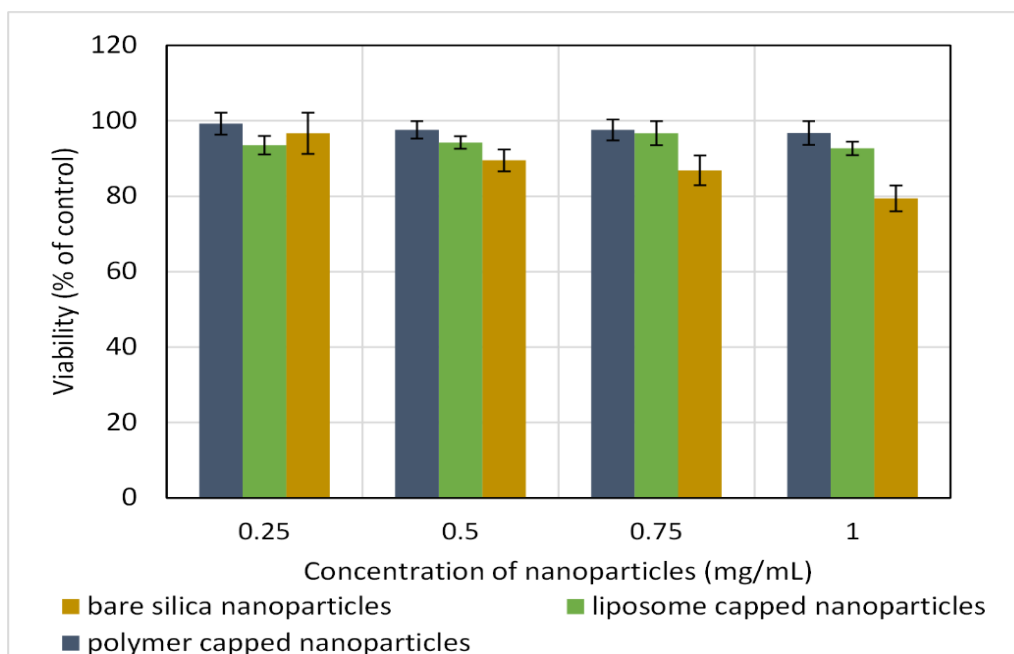


Figure 6-20. Biocompatibility of silica coated magnetite (ME60), liposome capped silica nanoparticles (ME60-L) and polymer capped silica nanoparticles (ME93-PEG-PCL) against U87 cells after 72 hours of incubation.

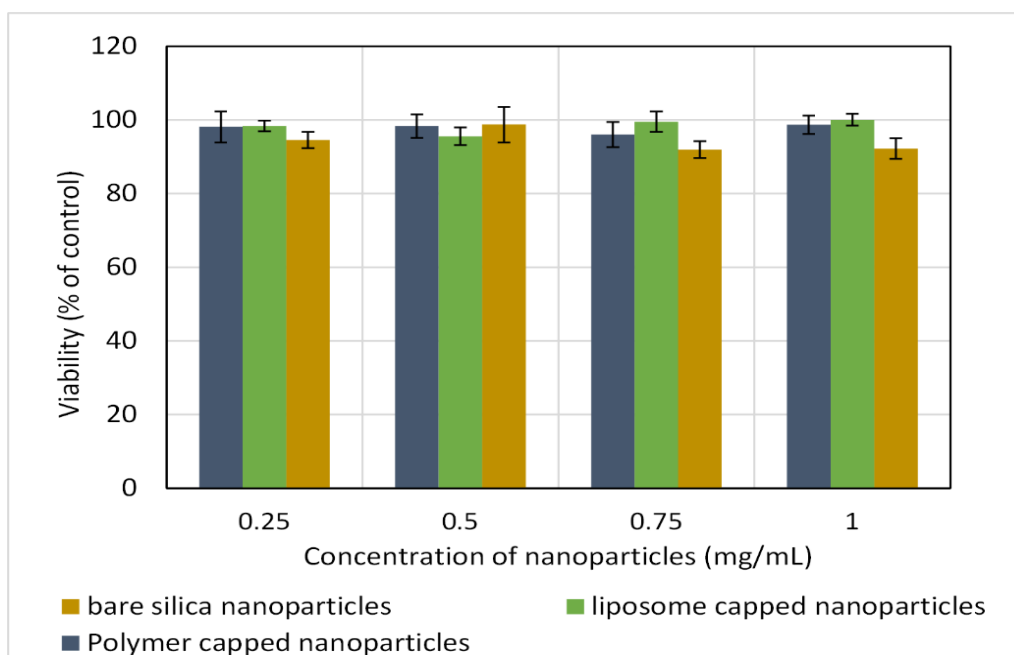


Figure 6-21. Biocompatibility of silica coated magnetite (ME60), liposome capped silica nanoparticles (ME60-L) and polymer capped silica nanoparticles (ME93-PEG-PCL) against MCF7 cells after 72 hours of incubation

The results established that the capped silica nanoparticles exhibit greater biocompatibility than uncoated silica nanoparticles against both cell lines.

6.6 *In vitro* Cytotoxicity Study of Drug Loaded Nanoparticles

After study the biocompatibility of the nanoparticles the efficiency of the nanoparticles as drug delivery systems were evaluated.

Doxorubicin (DOX) an anthracycline antibiotic was used as the model drug in cytotoxicity studies. Cells were incubated with different concentrations of free DOX (2.5, 5, 7.5 and 10 $\mu\text{g}/\text{mL}$ equivalent to 4.31, 8.62, 12.93, 17.24 μM) for up to 72 hours to identify the optimal dose and treatment time for maximum DOX induced cytotoxicity the. The cytotoxicity was measured using PrestoBlue assay. The dose response cytotoxicity charts are shown in Figure 6-22 and Figure 6-23. The cytotoxicity is expressed as percentage of surviving cells compare to untreated control cells.

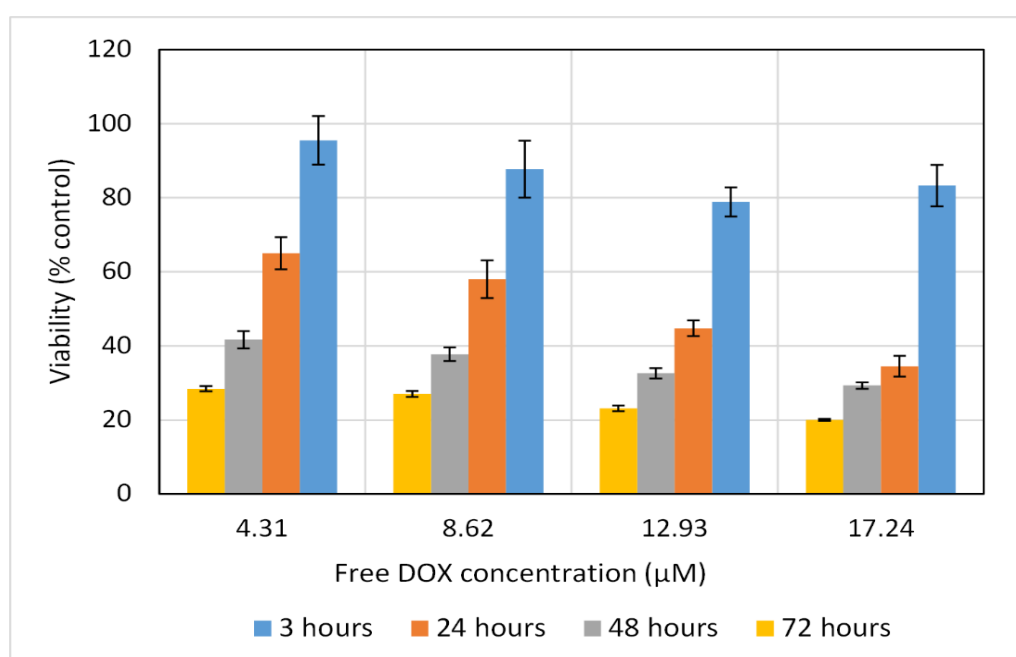


Figure 6-22. DOX induced cytotoxicity against U87 cells for various incubation time

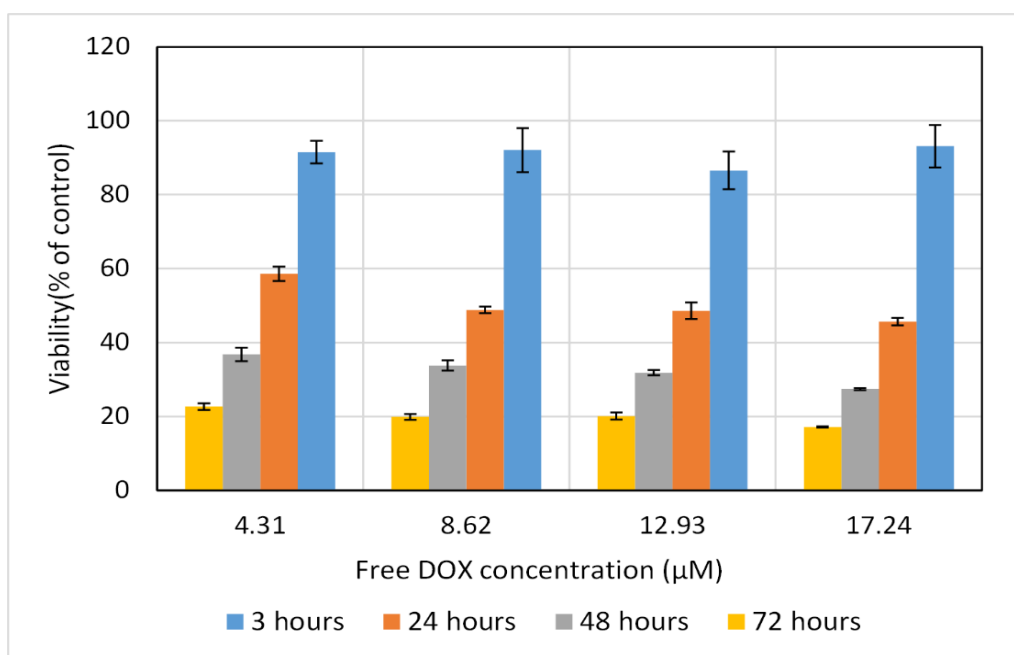


Figure 6-23. DOX induced cytotoxicity against MCF7 cells for various incubation time.

The DOX mediated cytotoxicity exhibited dose-time dependant effects on both cell lines with high initial survival rate after 3 hours of incubation with maximum DOX dose of 10 μg/mL. The cell viability declined significantly with longer incubation times. However, concentrations higher than 5 μM resulted in comparable cytotoxicity for similar incubation times.

DOX IC50 indicates the concentration of DOX required to inhibit the growth of 50% of cells in the given period (Osman et al., 2012). The IC50 was calculated from the dose dependent cytotoxicity curves in the given period based on the equation $y = f(x)$ where $y=50\%$. $f(x)$ was calculated from the fitted polynomial trendlines for each curve. DOX cytotoxicity against MCF7 cells after 24 hours of incubation with different concentration of DOX is shown in Figure 6-24 as an example. In this example,

$$y = f(x) = -0.0357x^3 + 1.2569x^2 - 14.205x + 99.858 \quad \text{Equation 6-2}$$

Where x is the DOX concentration.

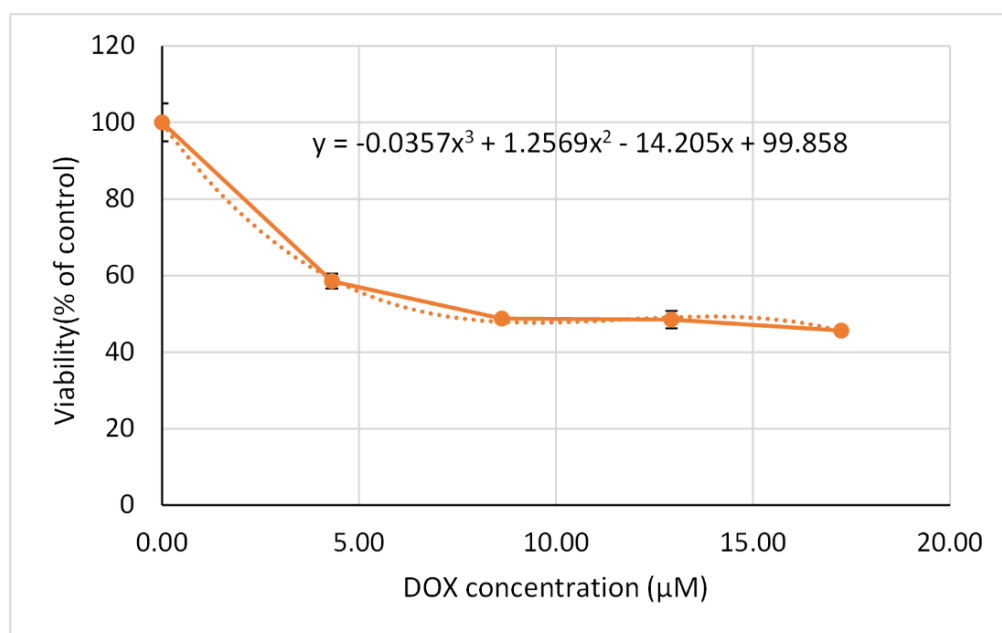


Figure 6-24. DOX induced cytotoxicity against MCF7 cells after 24 hours of incubation with 3rd degree polynomial trendline.

The IC₅₀ of free DOX at different incubation times for both cell lines are shown in Table 6-1.

Table 6-1. IC₅₀ for free DOX at different incubation times

Time (hours)	DOX IC ₅₀ (µM)	
	MCF7	U87
3	>17.24	>17.24
24	6.88	11.39
48	2.56	2.946
72	1.873	2.024

As summarised in the Table 6-1 the IC₅₀ was decreased with increase in incubation time. However there was not much different between 48 hours and 72 hours of incubation. IC₅₀ could not be calculated for less than 24 hours since there was limited cytotoxicity. The results demonstrated that DOX cytotoxicity at lower dose and limited incubation time was cell dependant similar to the reported literature (Lüpertz et al., 2010). Al-Ghamdi has studied the effect of DOX on prostate carcinoma cell line (DU-145), and reported IC₅₀ of 2.2, 0.4, 0.28, and 0.22 µM for DOX incubation periods of 48, 72, 96, and 120 hours respectively. They have observed no effect for incubation times less than 24 hours (Al-Ghamdi, 2008). Kundu *et al.* have observed around 65% U87 viable cells after 24 hours incubation with 25 µM of DOX (Kundu et al., 2015). Osman *et al.* have reported IC₅₀ of 0.7 µM for 48 hours incubation of DOX with MCF7 cells (Osman et al., 2012) and Cuong *et al.* have reported an IC₅₀ of 0.58 µM, and 11.08 µM for free DOX incubated against wild type MCF7 cells and drug resistant MCF7 cells, over 48 hours (Cuong et al., 2012).

The obtained results were in good range with the reported cytotoxicity in the literature, however the small differences could be due to cell culture conditions including differences in the cell medium and the passage number and the toxicity assay which were used.

6.6.1 DOX Loaded ME55-PEG-PCL

DOX was encapsulated in PEG-PCL magnetic micelles following the method explained in Section 2.24. The drug content of the micelles were calculated as explained in Section 5.6 (Table 5-1) to be 69.1 $\mu\text{g}/\text{mg}$. Therapeutic potential of the DOX loaded magnetic micelles were evaluated against cancer cells using PrestoBlue cytotoxicity assay. Cells were incubated with free DOX or DOX loaded nanoparticle solution with an equivalent amount of DOX (4.31, 8.62, 12.93 and 17.34 μM) for up to 72 hours. The amount of nanoparticles added to the cells were calculated based on the drug content of the nanoparticles. For instance 0.14 mg of ME55-PEG-PCL were added to 1 mL of medium to obtain 10 $\mu\text{g}/\text{mL}$ of DOX.

The cytotoxicity of the DOX loaded PEG-PCL magnetic micelles against U87 and MCF7 cells are shown in Figure 6-25 and Figure 6-26.

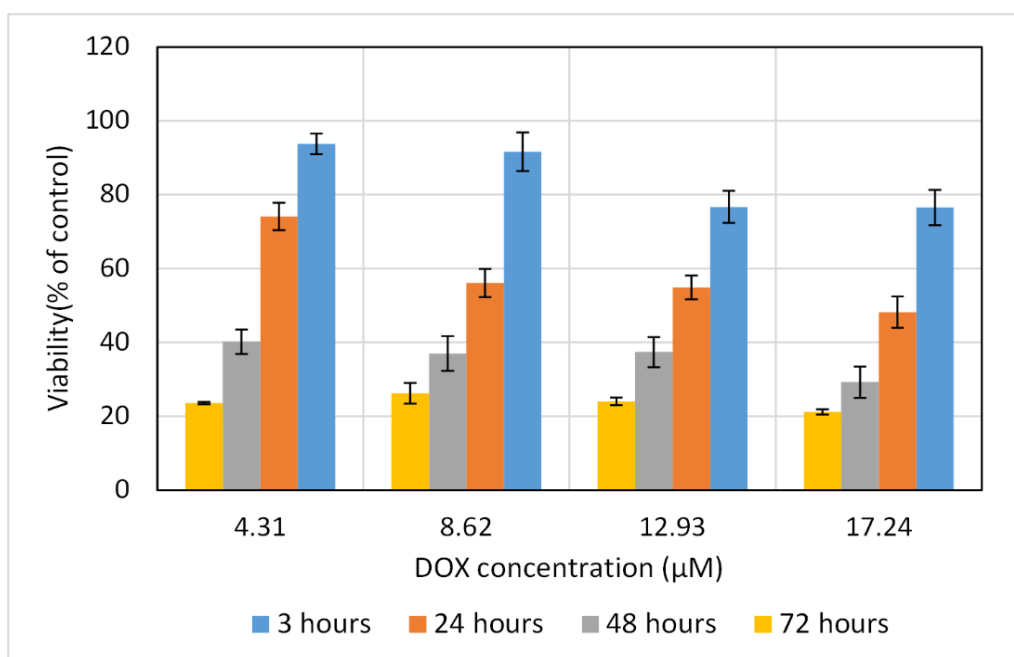


Figure 6-25. Cytotoxicity of DOX-loaded micelles (ME55-PEG-PCL) against U87 cells. The cells were incubated with DOX-loaded micelle with DOX concentration up to 17.24 μM , for 3, 24, 48 and 72h at 37 $^{\circ}\text{C}$

The IC₅₀ of DOX loaded PEG-PCL magnetite micelles against U87 cells were calculated as shown in Table 6-2.

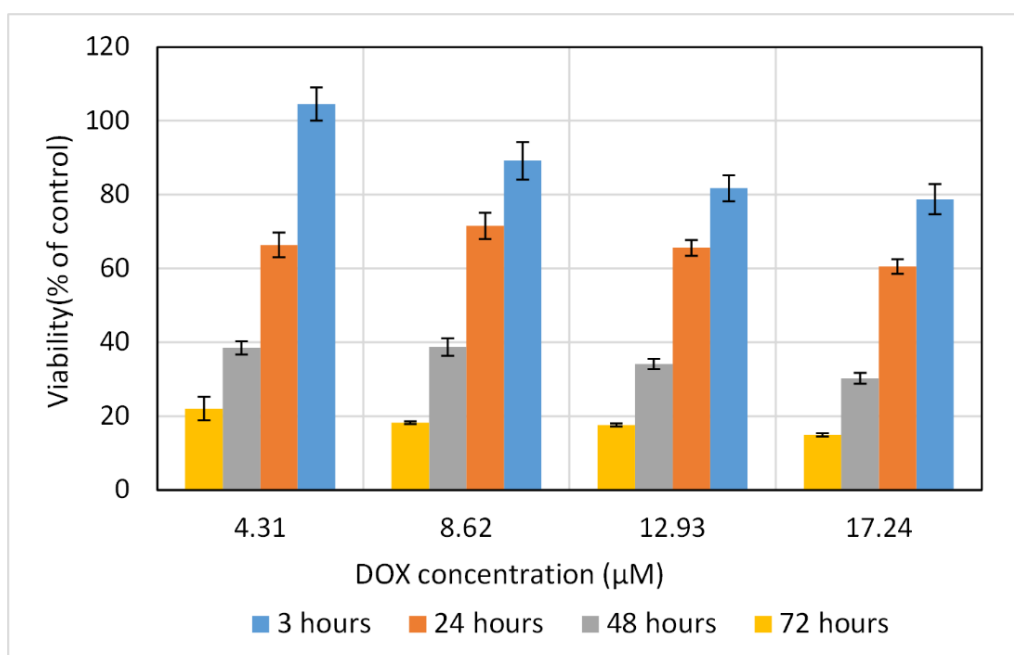


Figure 6-26. Cytotoxicity of DOX-loaded micelles (ME55-PEG-PCL) against MCF7 cells. The cells were incubated with DOX-loaded micelle with DOX concentration up to 17.24 µM, for 3, 24, 48 and 72h at 37 °C

The IC₅₀ values for 48 hours and 72 hours incubation with DOX loaded magnetic micelles were 2.55 and 1.86 for MCF7 cells. Since the highest dose of 17.24 µM did not kill 50% of the cells after 24 hours of incubation the IC₅₀ for MCF7 in 24 hours could not be calculated. The IC₅₀ of DOX loaded magnetic micelles in different periods are listed in Table 6-2

Table 6-2. The IC₅₀ values for DOX loaded magnetic micelles against MCF7 and U87

Time (hours)	DOX IC ₅₀ (µM)	
	MCF7	U87
3	>17.24	>17.24
24	>17.24	16.4
48	2.55	2.9
72	1.86	1.8

Similar to free DOX the cell viability was time dependent and decreased with increase in incubation time. The DOX loaded micelles did not induce high cytotoxicity against either cell lines for the first 3 hours of incubation even at high dose of DOX, however significant increase in cytotoxicity was observed after 48 hours of incubation (cell viability decreased to 30% for MCF7 cells and 29% for U87 cells).

It is suggested that the delayed cytotoxicity of the DOX during the initial hours of treatment could be due to DOX lag phase (Cuong et al., 2010b, Upadhyay et al., 2010). Similarly, Cuong *et al.* have reported limited cytotoxicity for the initial 2 hours incubation of MCF7 cells with DOX loaded polymeric micelles followed by significant decrease in cell viability after 48 hours (Cuong

et al., 2010b). Shuai *et al.* have reported limited cytotoxicity in MCF7 cells incubated with either free or DOX loaded PEG-PCL micelles for DOX concentration of up to 10 μM at the first 24 hours. They have observed for both free DOX and encapsulated DOX, at incubation times longer than 96 hours and DOX concentration higher than 1 μM almost all the cells were killed, however for low DOX concentration of 0.001 to 0.1 μM , free DOX showed higher cytotoxicity (Shuai et al., 2004).

The calculated IC₅₀ for DOX loaded magnetic micelles was higher than free DOX for the first 24 hours indicating higher survival rate, but after 48 hours the values were slightly lower suggesting efficient drug release and cytotoxicity against both cell lines. Similar IC₅₀ trends have been reported by Cuong *et al.* for DOX loaded micelles against MCF7 cells after 48 hours of incubation (Cuong et al., 2012). Cuong *et al.* have reported an IC₅₀ of 0.051 μM for free DOX and 0.375 μM for DOX loaded triblock PEG-PCL-PEG polymer micelles against MCF7 cells for 96 hours incubation, however they have observed similar cytotoxicity for free DOX and DOX loaded micelles in DOX concentrations more than 1 $\mu\text{g/mL}$ (Cuong et al., 2010a). Gao *et al.* have reported an IC₅₀ of 0.102 μM for DOX loaded star shaped PCL-PEG micelles against CT-26 cells (mouse colon carcinoma) which was higher than the value they reported for free DOX (0.028 μM) after 48 hours incubation (Gao et al., 2013).

The higher toxicity of drug loaded nanoparticles rather than free DOX over the 48 hours could be explained by the continues sustained release of DOX from the magnetic micelles. As is it suggested in the literature, continues exposure to lower dosage of DOX would cause higher toxicity than incubating the cells with a single high dose (Upadhyay et al., 2010). In addition, Maysinger group demonstrated that micelles changed the pattern of cellular distribution of DOX and increased the amount of the drug delivered to the cells. They have concluded that the encapsulated DOX were taken up by cells mainly *via* an endocytic pathway and localized in acidic endocytic compartments (Upadhyay et al., 2010).

Cell morphology were visualized after treatment with DOX loaded magnetic micelles by light microscopy where dead cells are clearly observed. The images are presented in Figure 6-27 and Figure 6-28.

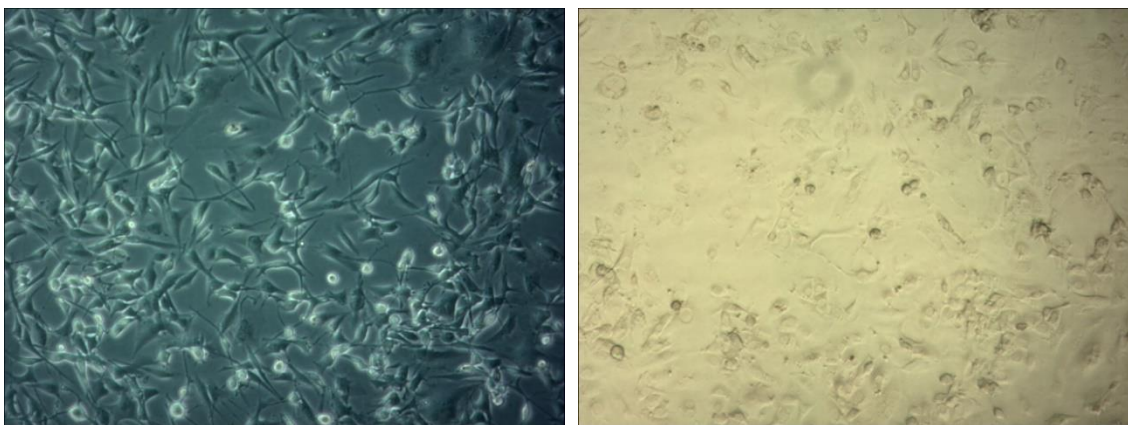


Figure 6-27 The optical microscopy of U87 cell line (left) as control cells and DOX loaded magnetic micelle (ME55-PEG-PCL) treated cells (right).

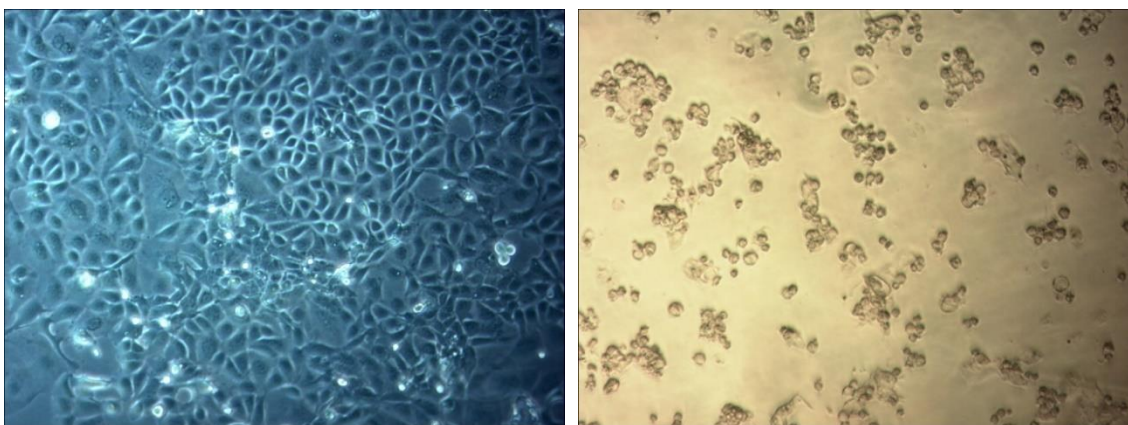


Figure 6-28 MCF7 the optical microscopy of MCF7 cell line (left) as control cells and DOX loaded magnetic micelle (ME55-PEG-PCL) treated cells (right).

The results indicate that the DOX encapsulation in micelles would not significantly improve the cytotoxicity against the MCF7 cells, however many groups have reported enhanced cytotoxicity against drug resistant MCF7 cells (Cuong et al., 2010a). Xu *et al.* have reported similar IC₅₀ values for free DOX and polymersome loaded DOX against MCF7 cells, however they have reported DOX loaded polymersomes improved DOX cytotoxicity against drug resistant MCF7 cells by 12 times (Xu et al., 2014). Furthermore it is suggested in the literature that drug encapsulation could improve the side effects against healthy cells (Yu et al., 2014).

The results confirmed that the cell viability for both cell lines declined with the increase in DOX loaded magnetic micelles concentration which considering the biocompatibility studies of the synthesised PEG-PCL polymer, it could be directly related to DOX concentration encapsulated in the micelles. However the cytotoxicity of the DOX-loaded micelles in the initial 24 hours is much lower than the free DOX.

6.6.2 DOX loaded ME93-PEG-PCL and ME94-PEG-PCL

DOX was encapsulated in PEG-PCL capped silica coated magnetic nanoparticles as explained before in Section 2.25. The drug content of the nanoparticles were calculated as explained in

Section 5.7 (Table 5-1) to be 79.2 $\mu\text{g}/\text{mg}$ and 62.0 $\mu\text{g}/\text{mg}$ for ME93-PEG-PCL and ME94-PEG-PCL. Therapeutic potential of the DOX loaded nanoparticles were evaluated against cancer cells using PrestoBlue cytotoxicity assay. Cells were incubated with free DOX or DOX loaded nanoparticle solution with an equivalent amount of DOX (4.31, 8.62, 12.93 and 17.34 μM) for up to 72 hours. The amount of nanoparticles added to the cells were calculated based on the drug content of the nanoparticles.

The cytotoxicity of the DOX loaded PEG-PCL capped mesoporous silica coated nanoparticles (ME93-PEG-PCL) against U87 and MCF7 are shown in Figure 6-30 and Figure 6-29.

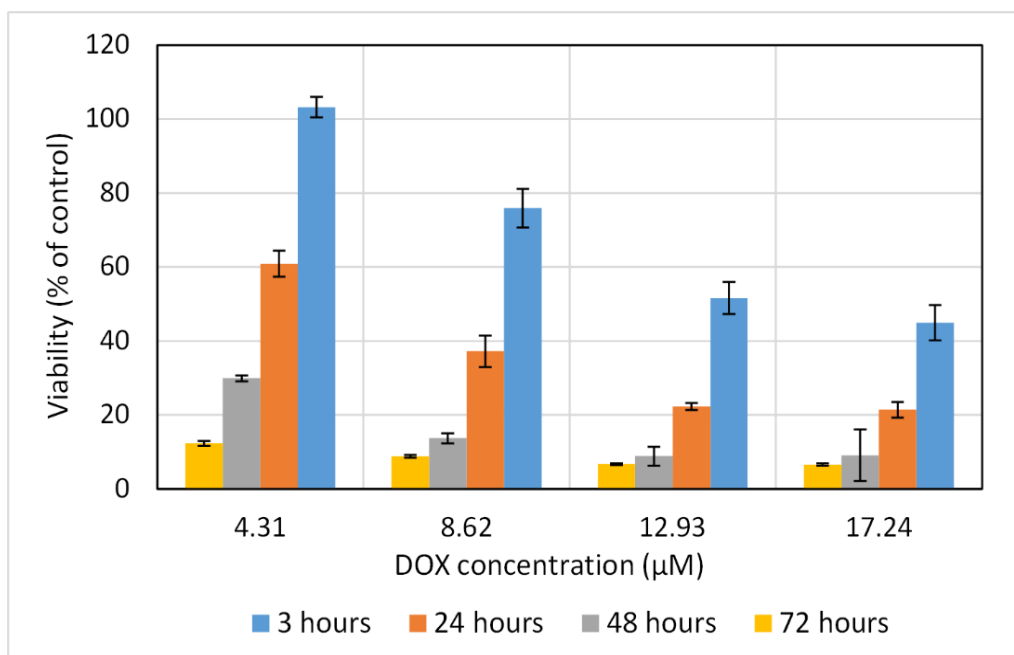


Figure 6-29. Cytotoxicity of DOX-loaded polymer capped nanoparticles (ME93-PEG-PCL) against U87 cells. The cells were incubated with DOX-loaded nanoparticles with DOX concentration up to 17.24 μM , for 3, 24, 48 and 72h at 37°C

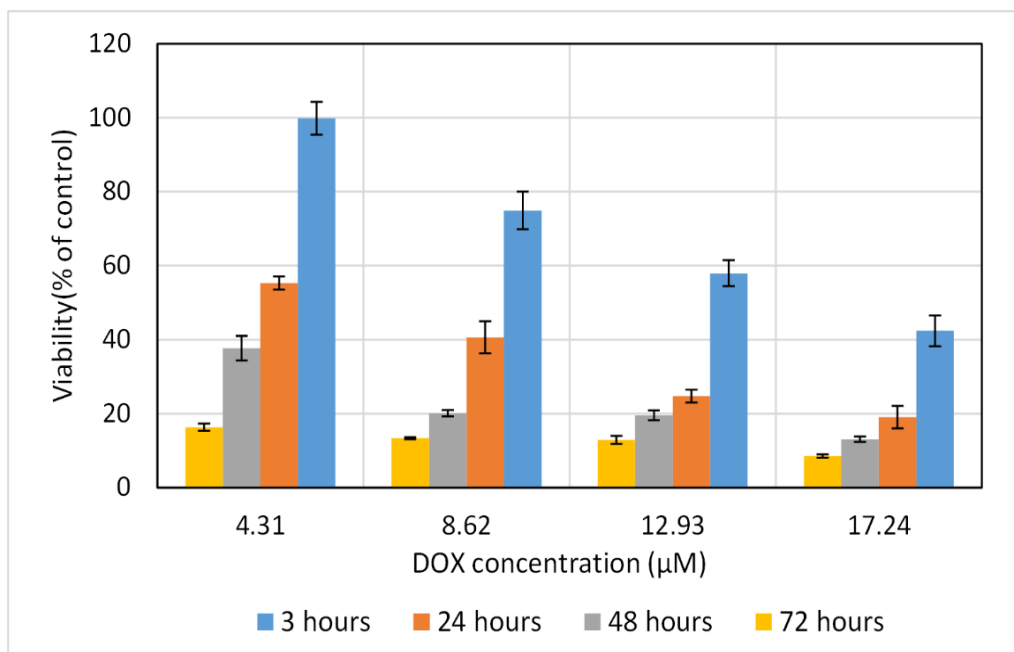


Figure 6-30. Cytotoxicity of DOX-loaded polymer capped nanoparticles (ME93-PEG-PCL) against MCF7 cells. The cells were incubated with DOX-loaded nanoparticles with DOX concentration up to 17.24 µM, for 3, 24, 48 and 72h at 37°C

The cytotoxicity of the DOX loaded PEG-PCL capped mesoporous silica coated nanoparticles (ME94-PEG-PCL) against U87 and MCF7 are shown in. Figure 6-32 and Figure 6-31.

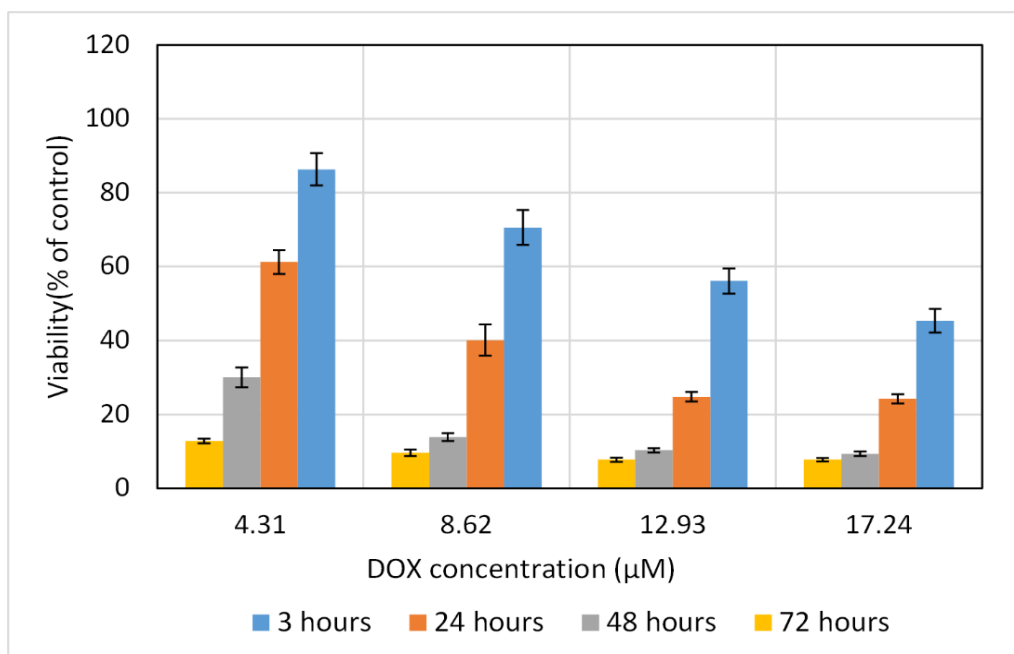


Figure 6-31. Cytotoxicity of DOX-loaded polymer capped nanoparticles (ME94-PEG-PCL) against U87 cells. The cells were incubated with DOX-loaded nanoparticles with DOX concentration up to 17.24 µM, for 3, 24, 48 and 72h at 37 °C

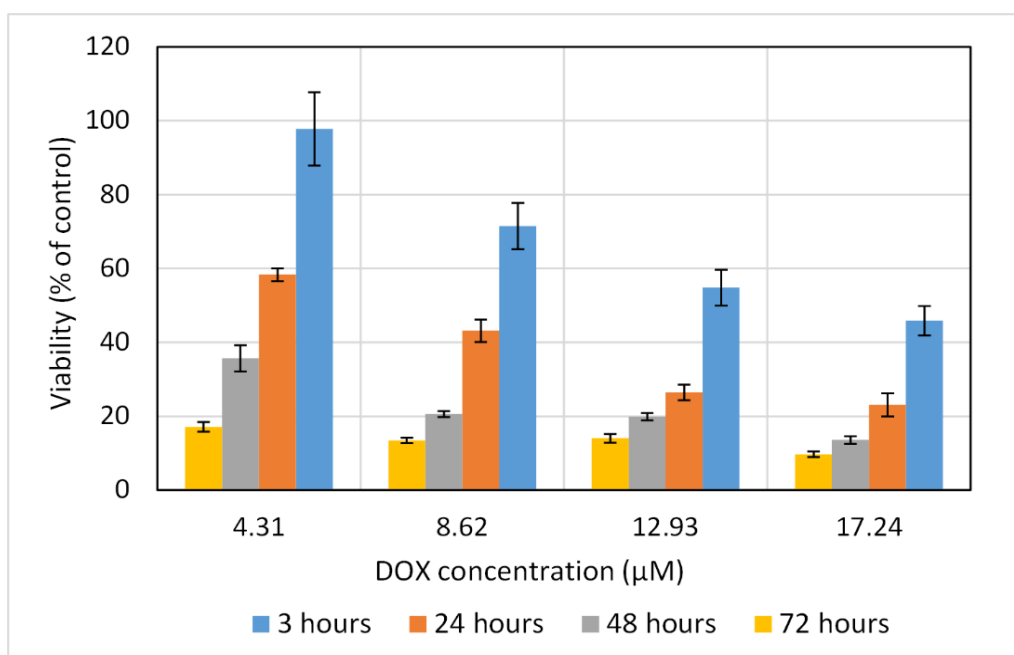


Figure 6-32. Cytotoxicity of DOX-loaded polymer capped nanoparticles (ME94-PEG-PCL) against MCF7 cells. The cells were incubated with DOX-loaded nanoparticles with DOX concentration up to 17.24 µM, for 3, 24, 48 and 72h at 37°C

The results indicated that the cell viability was time dependant and decreased with an increase in incubation time. The DOX loaded polymer capped nanoparticles (both materials) induced high cytotoxicity against both cell lines even after 3 hours of incubation which is higher toxicity than free DOX. Interestingly the highest DOX concentration of encapsulated DOX was able to reduce the cell viability by more than 50% in only 3 hours of incubation. Higher toxicity of drug loaded nanoparticles compare to free DOX was also observed by Tang *et al.* for DOX loaded chitosan/poly (methacrylic acid) coated mesoporous silica nanoparticles incubated with HeLa cells (Tang et al., 2011).

The IC₅₀ of DOX loaded PEG-PCL capped mesoporous silica coated magnetite nanoparticles (ME93-PEG-PCL) against both cell lines are calculated from experimental data and listed in Table 6-3. Similarly the calculated IC₅₀ for DOX loaded ME94-PEG-PCL is presented in Table 6-4.

Table 6-3. The IC₅₀ values for DOX loaded ME93-PEG-PCL against MCF7 and U87

	Time (hours)	DOX IC ₅₀ (µM)	
		MCF7	U87
ME93-PEG-PCL	3	14.303	13.325
	24	5.555	6.056
	48	3.085	2.738
	72	2.094	2.003

Table 6-4. The IC50 values for DOX loaded ME94-PEG-PCL against MCF7 and U87

	Time (hours)	DOX IC50 (μM)	
		MCF7	U87
ME94-PEG-PCL	3	13.71	15.04
	24	6.132	6.254
	48	2.97	2.716
	72	2.112	1.561

Significant increase in cytotoxicity was observed by encapsulating the DOX in polymer capped mesoporous silica nanoparticles. The calculated IC50 for DOX loaded ME93-PEG-PCL and ME94-PEG-PCL were lower than free DOX for the first 24 hours indicating lower survival rate, however after 48 hours the values were comparable.

The increased toxicity in the first 24 hours compare to free drug indicate an increased cellular uptake for the nanoparticle and efficient drug release. He *et al.* have reported an IC50 of 2.31 μM for DOX loaded mesoporous nanoparticles with polymer grafted capes incubated with Hela cells for 24 hours, however it was higher than the value they have reported for free DOX (He et al., 2013).

6.6.3 DOX loaded ME60

DOX was loaded into mesochannels of mesoporous silica coated magnetic nanoparticles as explained before in Section 2.18.2. The drug content of the nanoparticles were calculated as explained in Section 5.4.1 (Table 5-1) to be 103 $\mu\text{g}/\text{mg}$. Therapeutic potential of the DOX loaded nanoparticles were evaluated against cancer cells using PrestoBlue cytotoxicity assay. Cells were incubated with free DOX or DOX loaded nanoparticle solution with an equivalent amount of DOX (4.31, 8.62, 12.93 and 17.34 μM) for up to 72 hours. The amount of nanoparticles added to the cells were calculated based on the drug content of the nanoparticles. 0.097 mg of ME60 were added to 1 mL of medium to obtain 10 $\mu\text{g}/\text{mL}$ of DOX.

The cytotoxicity of the DOX loaded mesoporous silica coated nanoparticles (ME60) against U87 and MCF7 are shown in Figure 6-33 and Figure 6-34.

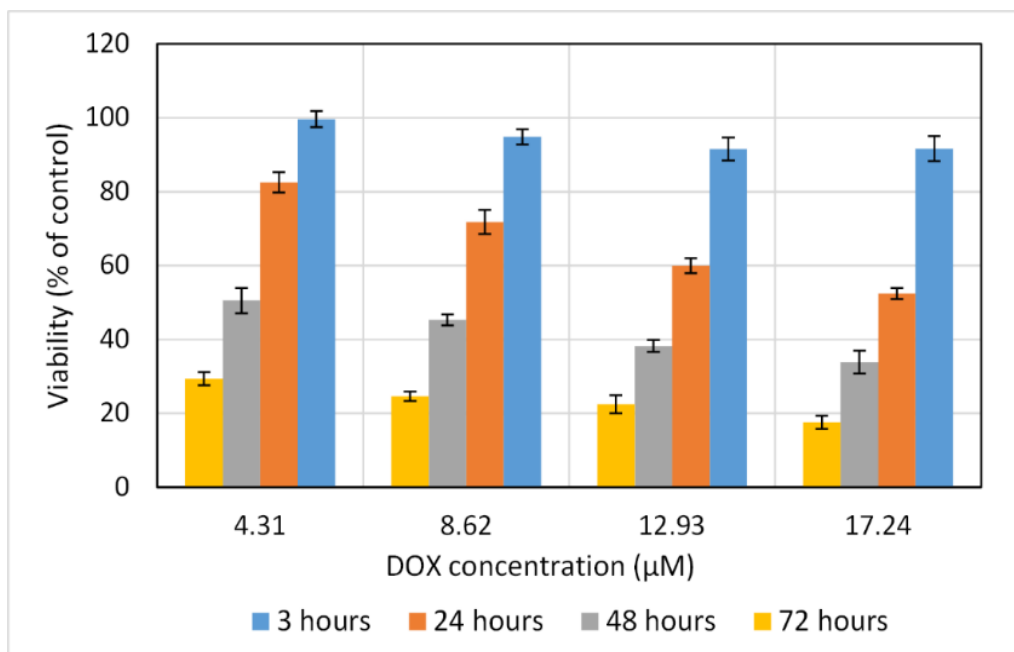


Figure 6-33. Cytotoxicity of DOX-loaded polymer capped nanoparticles (ME60) against U87 cells. The cells were incubated with DOX-loaded nanoparticles with DOX concentration up to 17.24 µM, for 3, 24, 48 and 72h at 37°C

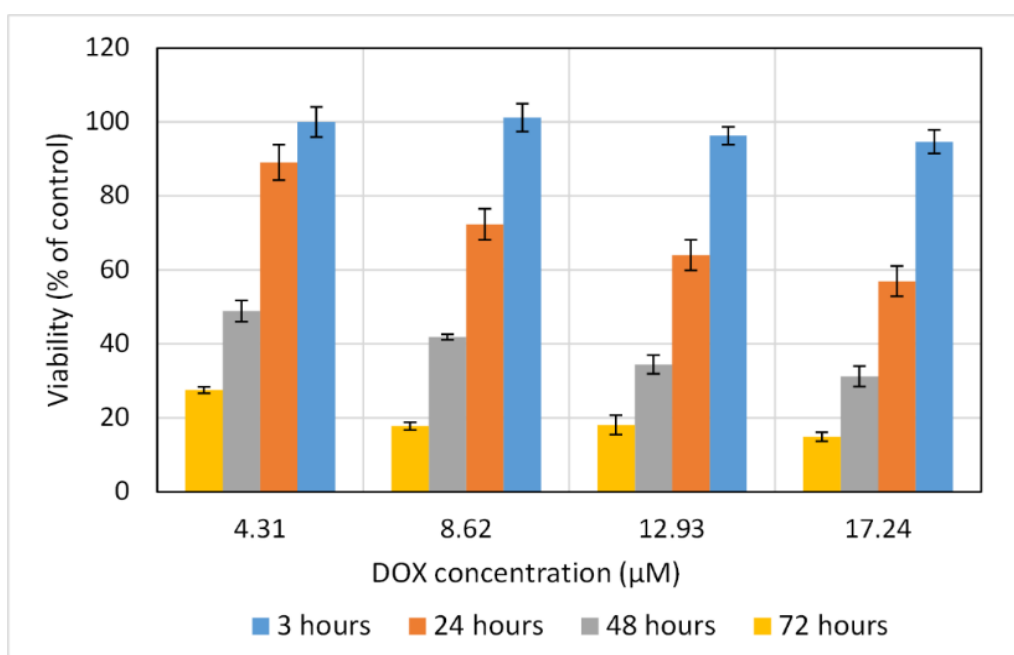


Figure 6-34. Cytotoxicity of DOX-loaded polymer capped nanoparticles (ME60) against MCF7 cells. The cells were incubated with DOX-loaded nanoparticles with DOX concentration up to 17.24 µM, for 3, 24, 48 and 72h at 37°C

As expected the cell viability was time and dose dependant and was decreased with increase in incubation time or DOX concentration. The DOX loaded mesoporous silica coated nanoparticles (ME60) did not induce high cytotoxicity in the first 3 hours of incubation even with the highest dose of 17.24 µM. Significant decrease in cell viability was observed after 48 hours of incubation with DOX loaded ME60, however the cytotoxicity was lower than free DOX. Similar results have been reported in the literature for wild type cells (Xie et al., 2014). Gai *et al.* have reported higher

cytotoxicity for free DOX compare to mesoporous silica coated magnetite at DOX concentrations lower than 10.7 μM (Gai et al., 2011).

The IC50 of DOX loaded mesoporous silica coated magnetite nanoparticles (ME60) against both cell lines are calculated from experimental data and presented in Table 6-5.

Table 6-5. The IC50 values for DOX loaded ME60 against MCF7 and U87

Time (hours)	DOX IC50 (μM)	
	MCF7	U87
3	>17.24	>17.24
24	>17.24	>17.24
48	4.582	4.944
72	2.533	2.658

The calculated IC50 for DOX loaded mesoporous silica-magnetite core shell nanoparticles (ME60) were higher than free DOX during the 48 hours of experiment, indicating higher survival rate. However it was close to IC50 of the free DOX after 72 hours of incubation. These results indicate slow drug release from the mesochannels of the nanoparticles which is in agreement with drug release profiles described earlier in Section 5.4.2. Additionally the delayed drug response could be due to different drug transport path into the cells as free DOX molecules are transported into the cells *via* passive diffusion mechanism while DOX loaded nanoparticles would enter the cells by endocytosis mechanism and the DOX molecules would release gradually inside the cell (Gai et al., 2011, Kim et al., 2008).

The results indicate that the DOX encapsulation in uncapped mesoporous nanoparticles would not improve the cytotoxicity against the MCF7 cells, however it is reported in the literature that drug loaded mesoporous nanoparticles have higher cytotoxicity than free DOX against drug resistant cells (Huang et al., 2011, Wang et al., 2014, Shen et al., 2011).

6.6.4 DOX loaded ME60-L

DOX was loaded into mesochannels of mesoporous silica coated magnetic nanoparticles and the pores were capped with liposomes (ME60-L) as explained before in Section 2.20. The drug content of the nanoparticles were calculated as explained in Section 5.5 (Table 5-1) to be 37.5 $\mu\text{g}/\text{mg}$. Therapeutic potential of the DOX loaded nanoparticles were evaluated against cancer cells using PrestoBlue cytotoxicity assay. Cells were incubated with free DOX or DOX loaded nanoparticle solution with an equivalent amount of DOX (4.31, 8.62, 12.93 and 17.34 μM) for up to 72 hours. The amount of nanoparticles added to the cells were calculated based on the drug content of the nanoparticles. 0.27 mg of ME60-L were added to 1ml of medium to obtain 10 $\mu\text{g}/\text{mL}$ of DOX.

The cytotoxicity of the DOX loaded mesoporous silica coated nanoparticles (ME60-L) against U87 and MCF7 are shown in Figure 6-35 and Figure 6-36.

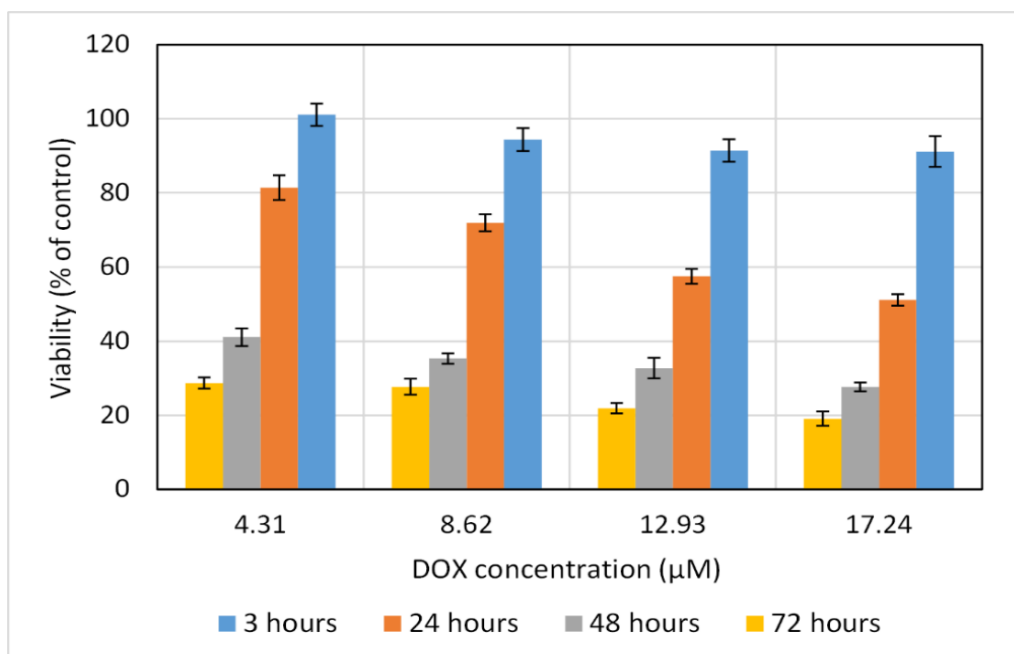


Figure 6-35. Cytotoxicity of DOX-loaded polymer capped nanoparticles (ME60-L) against U87 cells. The cells were incubated with DOX-loaded nanoparticles with DOX concentration up to 17.24 µM, for 3, 24, 48 and 72h at 37 °C

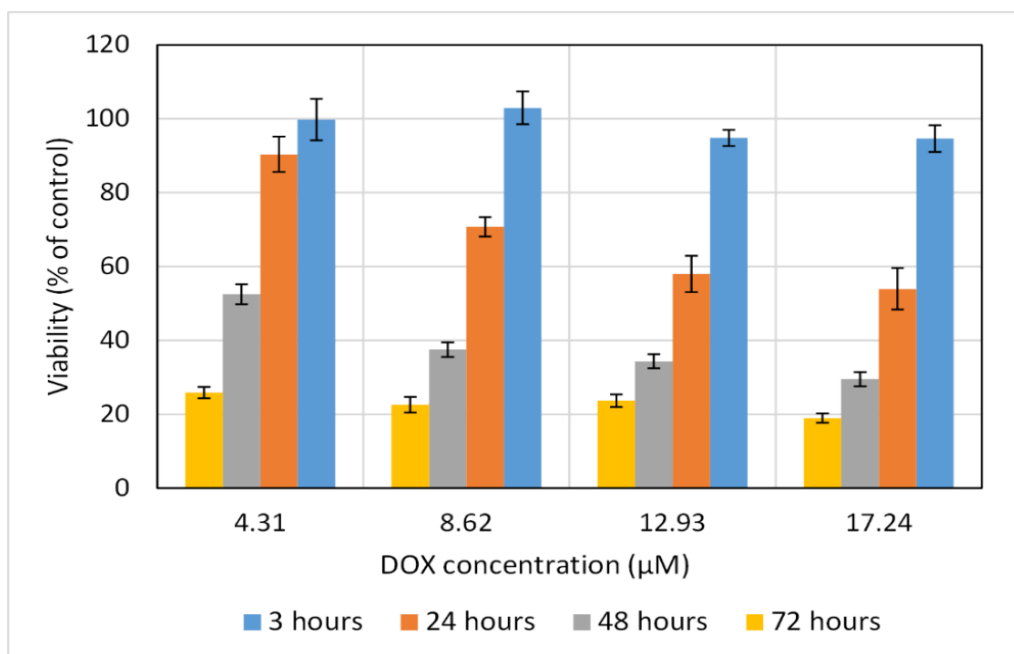


Figure 6-36. Cytotoxicity of DOX-loaded polymer capped nanoparticles (ME60-L) against MCF7 cells. The cells were incubated with DOX-loaded nanoparticles with DOX concentration up to 17.24 µM, for 3, 24, 48 and 72h at 37°C

The results indicated that the cell viability was time and dose dependant and was decreased with increase in incubation time or DOX concentration. The DOX loaded liposome capped mesoporous silica coated nanoparticles (ME60-L) did not induce high cytotoxicity in the first 3 hours of incubation even with the highest dose of 17.24 µM. Cell viability was reduced to 53%

after incubation with highest DOX dose for 24 hours, for both cell lines. Significant decrease in cell viability was observed after 48 hours of incubation with DOX loaded ME60-L. The cytotoxicity was cell dependant and observed to be higher in U87 cells.

The IC50 of DOX loaded mesoporous silica coated magnetite nanoparticles (ME60-L) against both cell lines are calculated from experimental data and presented in Table 6-6.

Table 6-6. The IC50 values for DOX loaded ME60-L against MCF7 and U87

Time (hours)	DOX IC50 (µM)	
	MCF7	U87
3	>17.24	>17.24
24	>17.24	>17.24
48	4.775	3.488
72	2.443	2.694

The calculated IC50 for DOX loaded ME60-L indicate that liposome coated mesoporous silica nanoparticles showed higher cytotoxicity compare to uncapped silica coated nanoparticles which could be due to reduced premature drug release (during the sample preparation) and improved endocytosis (Liu et al., 2009a), however the cytotoxicity was lower than the free DOX.

6.6.5 Summary

Cytotoxicity of the DOX loaded synthesised nanoparticles were evaluated against two cell lines of MCF7 and U87. The data indicate that DOX loaded nanoparticles could induce cytotoxicity toward the cells, however the degree of cell viability was material dependant. Figure 6-37 and Figure 6-38 compare the cytotoxicity induced by the different DOX loaded materials toward MCF7 and U87 cells after 24 hours incubation.

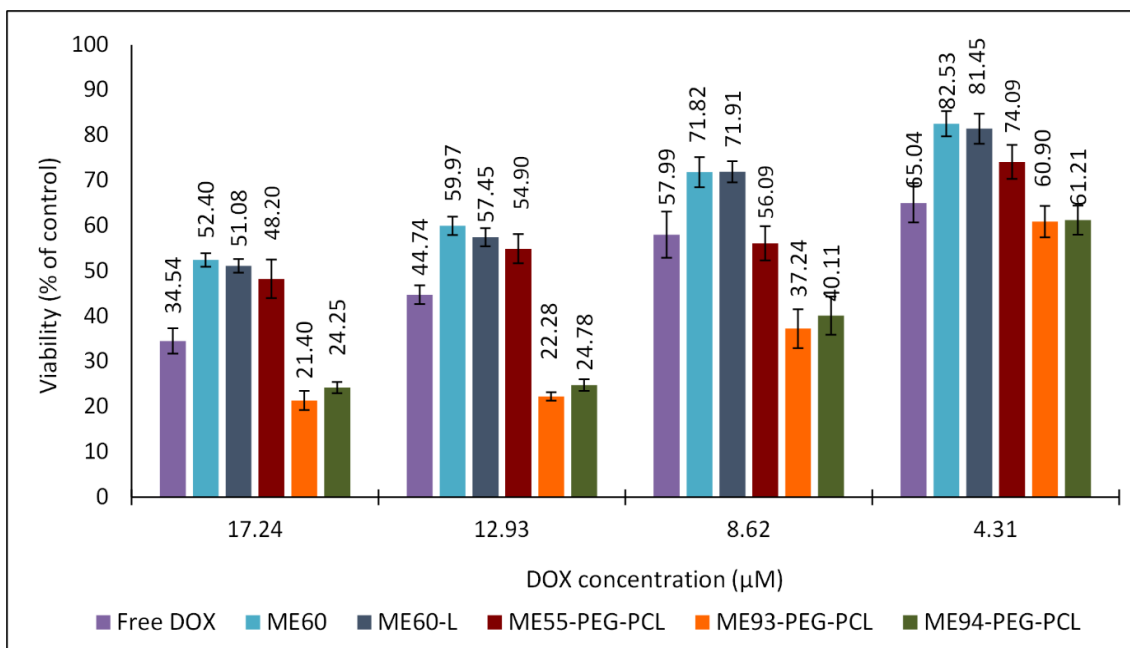


Figure 6-37. Cytotoxicity of different DOX loaded materials toward U87 cells after 24 hours incubation.

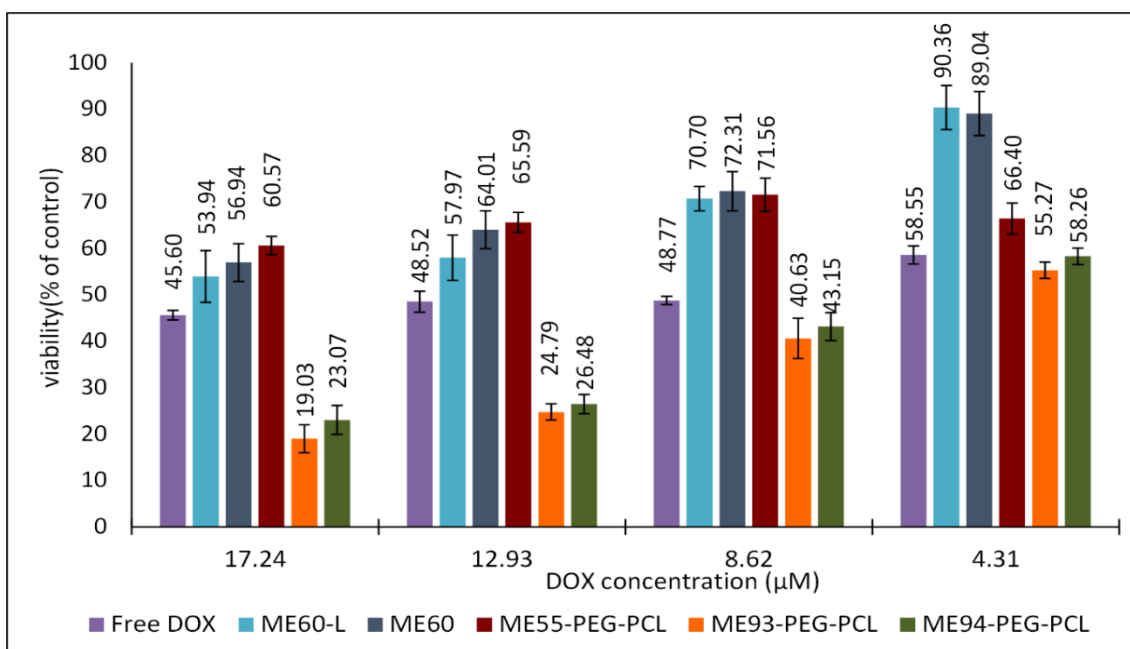


Figure 6-38. Cytotoxicity of different DOX loaded materials toward MCF7 cells after 24 hours incubation.

As shown in the figures ME55-PEG-PCL, ME60 and ME60-L induced cytotoxicity lower than free DOX in the first 24 hours of incubation however after 48 hours they caused comparable cytotoxicity. However ME93-PEG-PCL and ME94-PEG-PCL generated higher cytotoxicity in 24 hours compare to free DOX. The calculated IC₅₀ for different DOX encapsulated materials are summarised in Table 6-7 and Table 6-8.

Table 6-7. Calculated IC50 for different DOX encapsulated materials against U87 cells

Exposure Time (hours)	Materials					
	Free dox	ME55-p	ME60	ME94-p	ME93-p	ME60-l
3	>17.24	>17.24	>17.24	15.04	13.325	>17.24
24	7.17	16.4	>17.24	6.254	6.056	>17.24
48	2.56	2.9	4.944	2.716	2.738	3.488
72	1.87	1.8	2.658	1.561	2.003	2.694

Table 6-8. Calculated IC50 for different DOX encapsulated materials against MCF7

Exposure Time (hours)	Materials					
	Free dox	ME55-PEG-PCL	ME60	ME94-PEG-PCL	ME93-PEG-PCL	ME60-L
3	>17.24	>17.24	>17.24	13.71	14.303	>17.24
24	7.17	>17.24	>17.24	6.132	5.555	>17.24
48	2.56	2.55	4.582	2.97	3.085	4.775
72	1.87	1.86	2.533	2.112	2.094	2.443

These data demonstrated that the drug loaded nanoparticles especially polymer capped silica nanoparticles could effectively improve the chemotherapeutic effects of DOX.

6.7 Effect of Magnetic Hyperthermia on Cell Viability

Tumour tissues are more vulnerable to heat than healthy cells (Ota et al., 2014). Hyperthermia treatment employs elevated temperature in the range of 41-46°C to kill tumour cells (Sadhukha et al., 2013). Hyperthermia treatments in combination with radiotherapy, surgery or chemotherapy have proven to enhance treatment response and survival rates (Johannsen et al., 2005b, Maier-Hauff et al., 2011, Sadhukha et al., 2013, Asín et al., 2012). Magnetic hyperthermia is based on the localized heat generated by placing superparamagnetic iron oxide nanoparticles in an alternating magnetic field to kill tumour cells.

The cell response to hyperthermia were evaluated by placing samples in the AC field for 45 minutes. The temperature was maintained in hyperthermia treatment range by changing the magnetic field strength (experiment details are explained in Chapter 2). The cells viability after hyperthermia treatments were measured 2 hours and 24 hours post treatment using PrestoBlue viability assay. A group of control cells were placed in a water bath at 43°C for 45 mins and the

cell viability was assessed to compare the effect of traditional hyperthermia and magnetic hyperthermia treatments.

Control cells without magnetic nanoparticles were exposed to magnetic field for 45 minutes and did not show any changes in cell viability which indicates that magnetic field exposure will not cause any damage to the cells.

6.7.1 ME53

Cells were incubated with bare magnetite nanoparticles (ME53) with the concentration of 0.1 mg/mL which was shown to be non-toxic against both cell lines. After 24 hours the media was changed to remove the nanoparticles not internalised by the cells. The cells were then exposed to the magnetic field for 45 minutes. The cell viability of the magnetic field exposed cells were compared to water bath hyperthermia treated cells and the control cells treated with the magnetic nanoparticles at 37°C. The results are presented as percentage of viable cells compare to untreated control cells in Figure 6-39 and Figure 6-40.

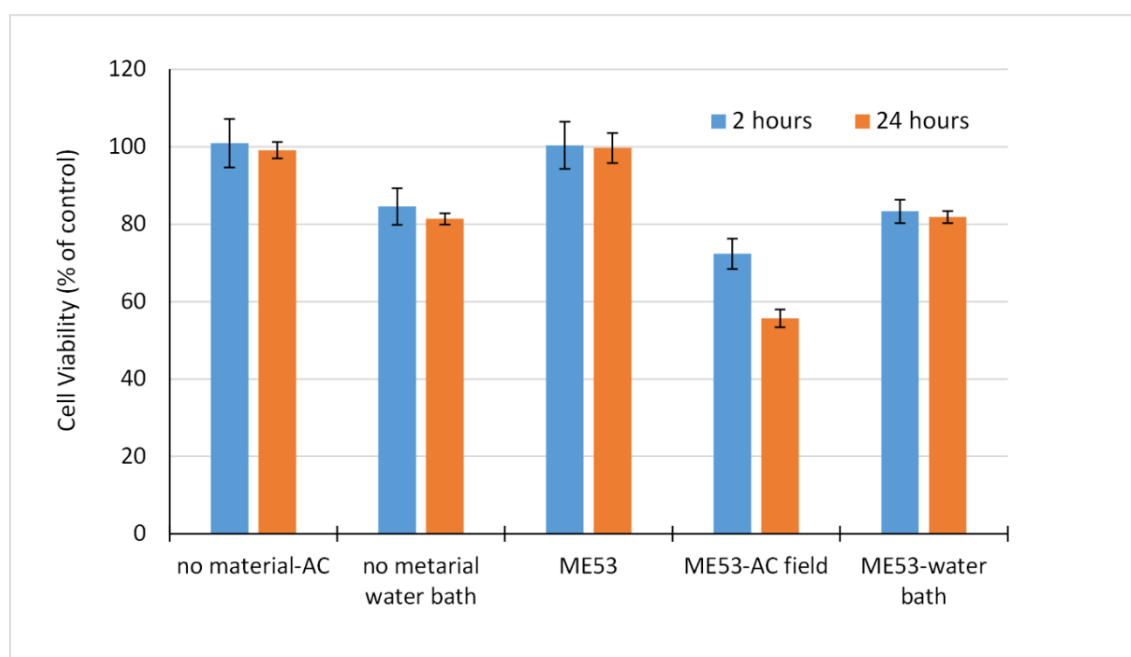


Figure 6-39. Effects of hyperthermia on U87 cells viability, The viability of cells incubated with ME53 and exposed to the magnetic field were compared to water bath hyperthermia treated cells (45 minutes treatment).

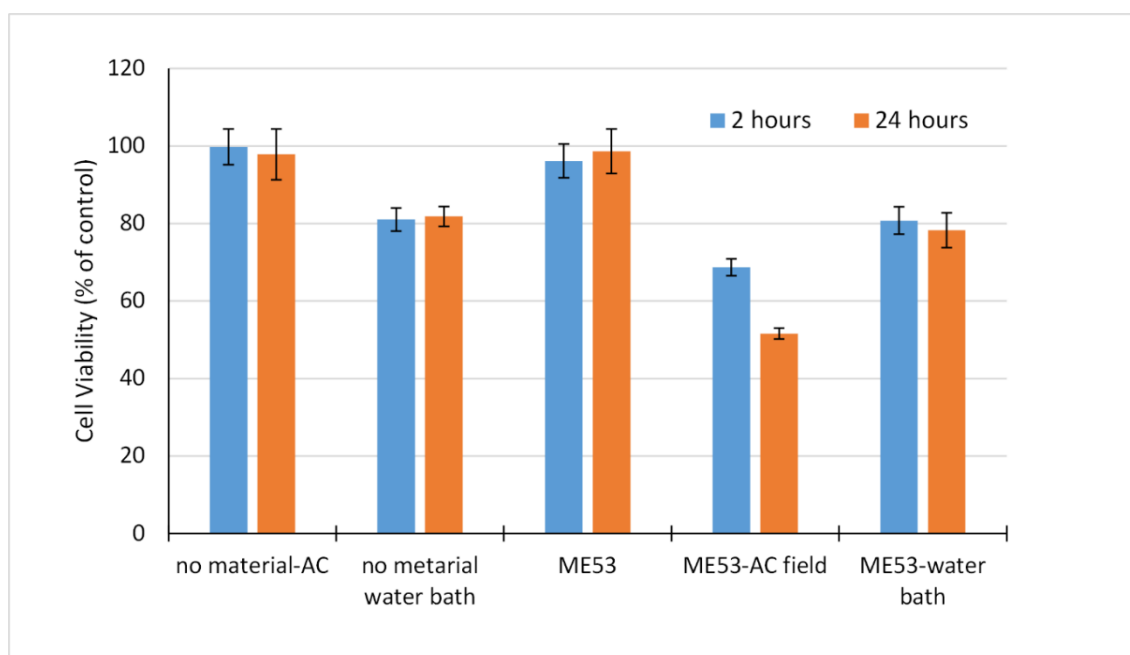


Figure 6-40. Effects of hyperthermia on MCF7 cells viability, The viability of cells incubated with ME53 and exposed to the magnetic field were compared to water bath hyperthermia treated cells (45 minutes treatment).

Three different control samples were used to compare the results; cells without nanoparticles as negative control (100% viable cells), cells with nanoparticles without magnetic field or water bath heating, and cells without nanoparticles exposed to magnetic field.

The results implied that hyperthermia affects both cell lines in a similar pattern, however the cell viability percentage was cell dependant and was slightly different between cell lines, where MCF7 cells showed to be more vulnerable against hyperthermia treatment. Cell type dependant hyperthermia efficacy have been reported in the literature (Jordan et al., 1999).

It was observed that neither magnetic nanoparticles without the magnetic field nor magnetic field alone affected the viability of the cells. As seen from the graphs the results indicated that magnetic hyperthermia caused more cell death than water bath hyperthermia for both cell lines. Hot water hyperthermia resulted in slight decrease in cell viability compared to control sample where magnetic hyperthermia resulted in significant decrease in cell viability. Similar results have been reported by Rodriguez-Luccioni *et al.*, they have reported 85% viable cells for both Caco-2 cells (human epithelial colorectal adenocarcinoma cells) and MCF7 cells after 2 hours water bath hyperthermia and 75% viable Caco-2 cells and 80% MCF7 viable cells after 2 hours of magnetic field hyperthermia (Rodriguez-Luccioni et al., 2011). Sadhukha *et al.* have reported 12% and 10% viable A549 (Human lung adenocarcinoma) and MDA-MB-231 (human mammary adenocarcinoma) cells after 30 minutes of magnetic hyperthermia at 46°C and 90% viable cells in 46°C water bath hyperthermia (Sadhukha et al., 2013).

The higher cell death in magnetic hyperthermia treated cells could be explained by the excess ROS generation during magnetic hyperthermia. As it is reported in the literature that ROS

generation is increased during magnetic hyperthermia while conventional water bath hyperthermia did not increase the ROS generation (Sadhukha et al., 2013).

A change in cell viability was observed when it was measured 2 hours after magnetic hyperthermia treatment and 24 hours after treatment. The cells which were treated with the hot water hyperthermia did not show further reduction in cell viability over 24 hours incubation period, however the cells treated with magnetic hyperthermia showed continues decline in cell viability which is suggested to be a result of cytoskeletal damage of the cells and initiation of apoptosis during the magnetic hyperthermia treatment. Balasubramanian *et al.* have reported morphology change of the cancer cells exposed to alternating magnetic field with disintegrated actin filaments and shrunken morphology. This morphology change is considered as a sign of initiation of cell apoptosis (Balasubramanian et al., 2014).

6.7.2 ME55-PEG-PCL

Cells were incubated with magnetic micelles (ME55-PEG-PCL) with or without DOX. The concentration of 0.14 mg/mL of magnetic micelles were used which was shown to be non-toxic against both cell lines without the drug. The 0.14 mg/mL of drug loaded magnetic micelles contained 17.24 μ M DOX which induced 48.20% and 60.57% cell death against U87 and MCF7 cell lines after 24 hours. Cells were incubated with magnetic micelles for 24 hours after which the media was removed and the cells were exposed to the magnetic field for 45 minutes. The cell viability of the magnetic field exposed cells were compared to water bath hyperthermia cells to quantify the differences between conventional hyperthermia and magnetic hyperthermia. The control cells were treated with magnetic nanoparticles at 37°C. The results are presented in Figure 6-41 and Figure 6-42. The cell viability of the hyperthermia treated samples were compared to cells incubated with free drug as additional control sample.

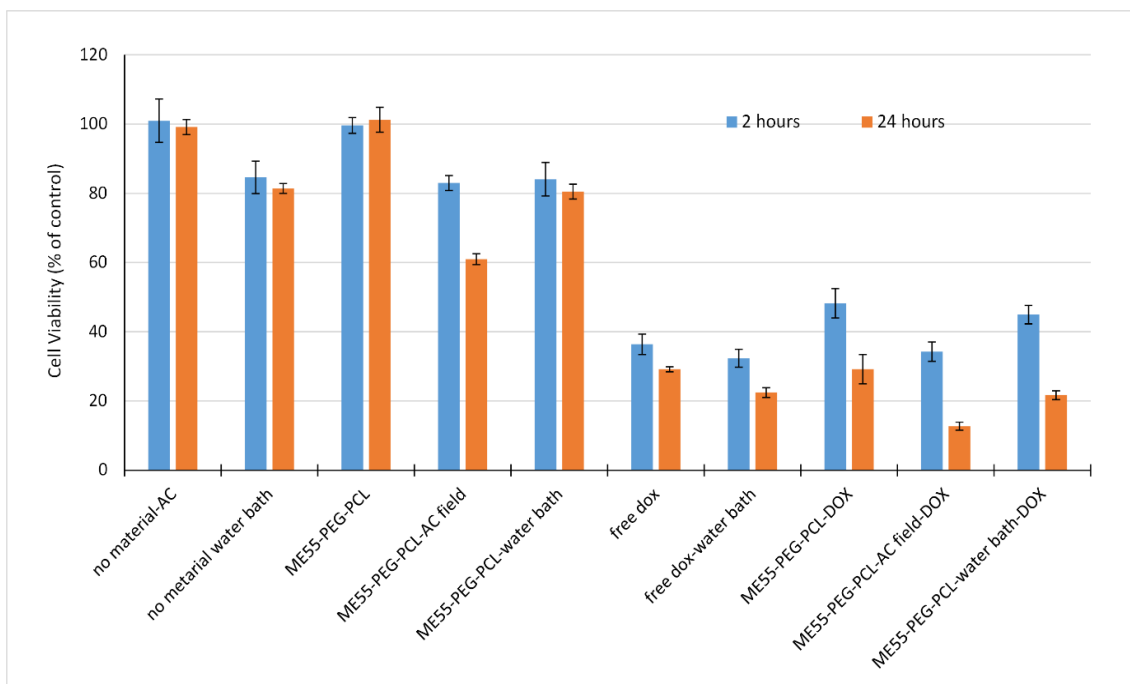


Figure 6-41. Effects of hyperthermia on U87 cells viability, The viability of cells incubated with ME55-PEG-PCL (with and without drug) and exposed to the magnetic field were compared to water bath hyperthermia treated cells (45 minutes treatment).

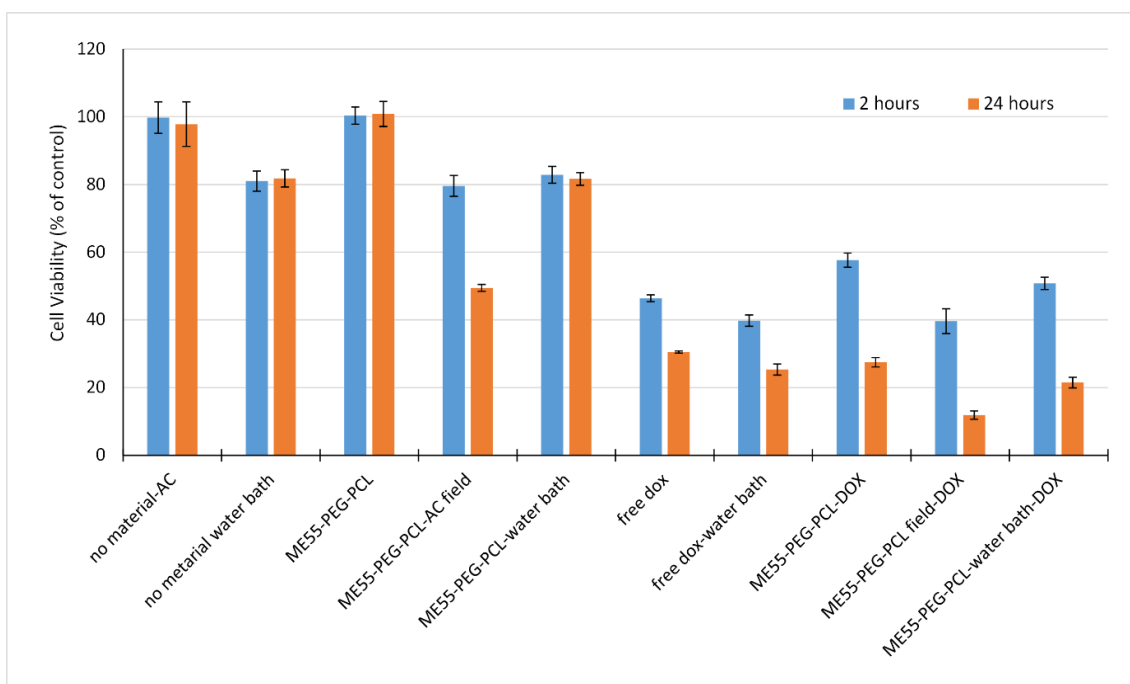


Figure 6-42. Effects of hyperthermia on MCF7 cells viability, The viability of cells incubated with ME55-PEG-PCL (with and without drug) and exposed to the magnetic field were compared to water bath hyperthermia treated cells (45 minutes treatment).

Similar to uncoated magnetite nanoparticles, the results indicated that neither magnetic nanoparticles without the magnetic field nor magnetic field alone affected the viability of the cells.

The viability results of cells treated with magnetic hyperthermia compared with water bath hyperthermia treated cells demonstrated that both methods resulted in similar (around 80%) cell

viability 2 hours post hyperthermia treatments. Viability assay performed after 24 hours indicated that magnetic hyperthermia induced continues decay in cell viability after the treatment, with cell viability reduced from 79.5% to 49.4% for MCF7 cells and 82.9% to 60.9% for U87 cells. Continuous cell death after the treatment could be the result of cytoskeletal changes and apoptosis initiated during the magnetic hyperthermia treatments (Sadhukha et al., 2013, Balasubramanian et al., 2014).

Cytotoxic effects of free DOX in water bath hyperthermia were studied to investigate the effect of heating on DOX efficiency. The results indicated 6.5% and 5% decrease in cell viability after exposure to DOX in heated condition after 2 hours and 24 hours for MCF7 cells and 4% and 7% decrease for U87 cells. An increase in DOX efficiency in elevated temperature has been previously reported by Dorr *et al.* for HEC-1A cells (uterus human adenocarcinoma cells) (Dorr et al., 1985).

Cells viability were studied in the presence of DOX loaded magnetic micelles under hyperthermia condition. Both in water bath and magnetic field induce hyperthermia the results showed an increase in cell death compared to hyperthermia or free DOX, separately. The MCF7 cell viability after 24 hours post magnetic hyperthermia treatment with DOX loaded magnetic micelles was decreased to 11.89% which is much lower than free DOX in the same period. Similarly for U87 cell the viability after 24 hours post magnetic hyperthermia treatment was decreased to 12.74% which is lower than free DOX and water bath hyperthermia treated cells.

As discussed before in Section 5.6.3 the drug release from DOX loaded magnetic micelles were increased with an increase in temperature, and the drug release was faster under magnetically induced hyperthermia compare to the incubator heated samples. Higher DOX release could lead to higher cytotoxicity compare to 37°C condition. Furthermore the effect of hyperthermia itself results in an increased cell death.

These results indicate that DOX loaded magnetic micelles can efficiently provide synergistic effect of hyperthermia and chemotherapy and have great potential to be used as drug delivery systems.

6.7.3 ME93-PEG-PCL and ME94-PEG-PCL

Cells were incubated with polymer capped mesoporous silica coated magnetite nanoparticles (ME93-PEG-PCL and ME94-PEG-PCL) with or without DOX. Nanoparticles concentration were chosen based on the drug loading content of nanocomposites in the way to maintain a drug concentration of 17.24 μM . Concentration of magnetic nanoparticles were 0.126 mg/mL and 0.161 mg/mL for ME93-PEG-PCL and ME94-PEG-PCL which was shown to be non-toxic against both cell lines without the drug.

Cells were incubated with magnetic nanoparticles for 24 hours before the hyperthermia treatment. After which the media was removed and cells were exposed to the magnetic field for 45 minutes. The cell viability were compared to water bath hyperthermia treated cells, free DOX treated cells and control cells which was exposed to magnetic field without presence of the nanoparticles. Another group of control cells were incubated with drug loaded nanoparticles at 37°C. The results are presented in Figure 6-44 and Figure 6-43 for cells incubated with ME93-PEG-PCL and Figure 6-46 and Figure 6-45 for cells treated with ME94-PEG-PCL.

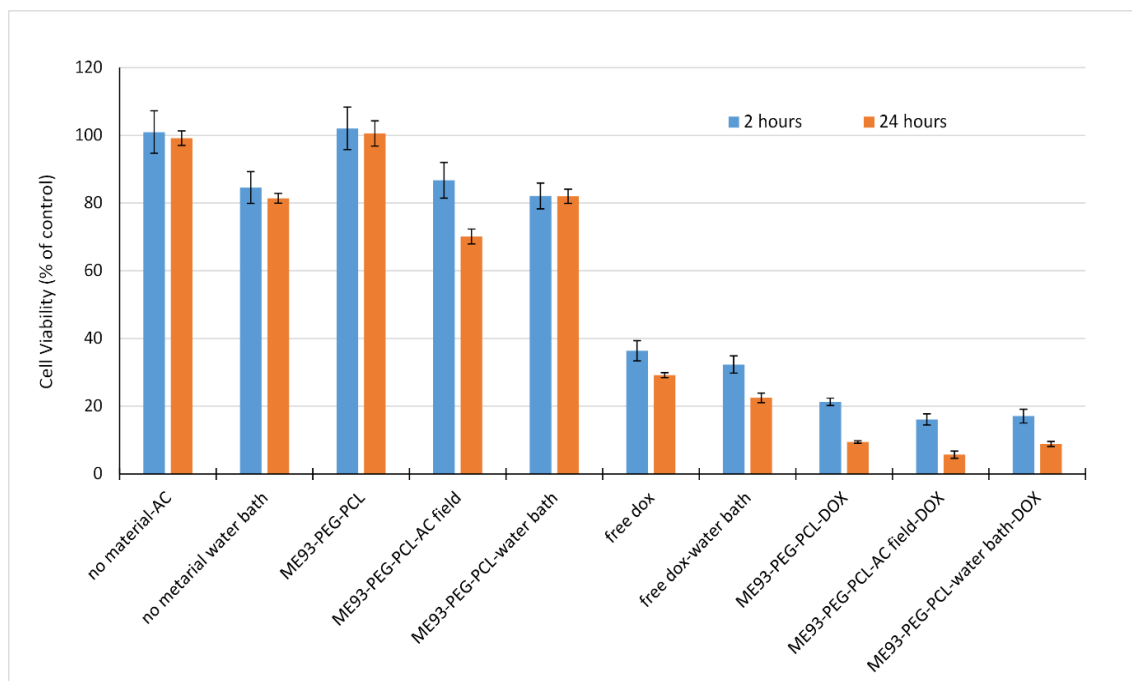


Figure 6-43. Effects of hyperthermia on U87 cells viability, The viability of cells incubated with ME93-PEG-PCL (with and without drug) and exposed to the magnetic field were compared to water bath hyperthermia treated cells (45 minutes treatment).

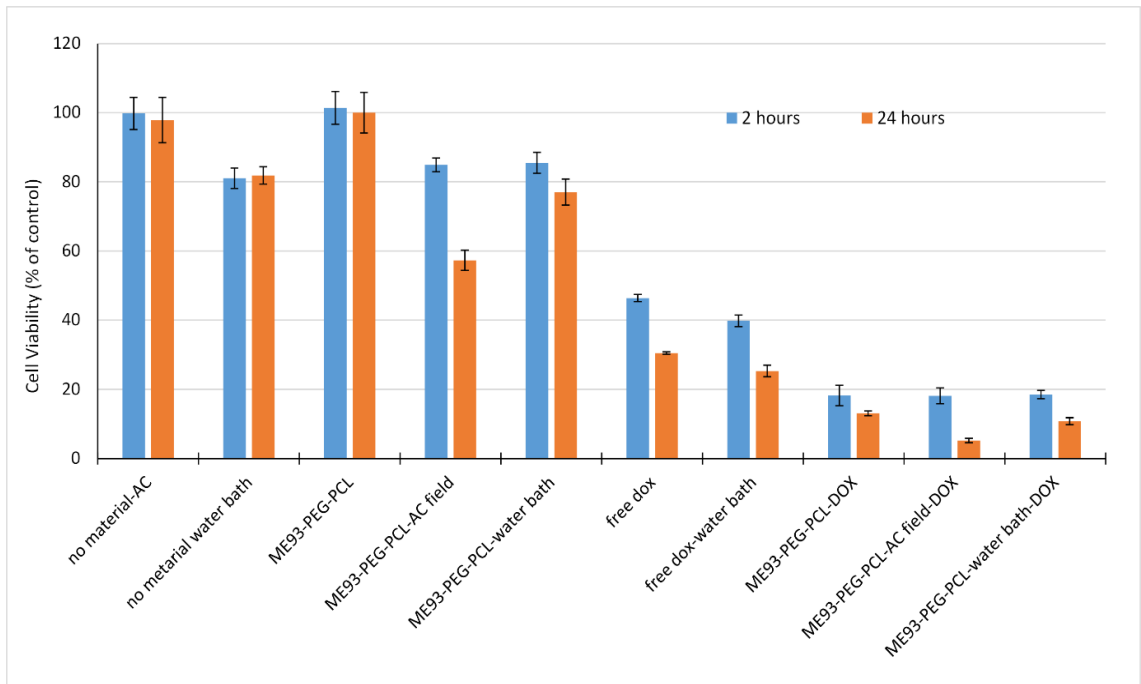


Figure 6-44. Effects of hyperthermia on MCF7 cells viability , The viability of cells incubated with ME93-PEG-PCL (with and without drug) and exposed to the magnetic field were compared to water bath hyperthermia treated cells (45 minutes treatment).

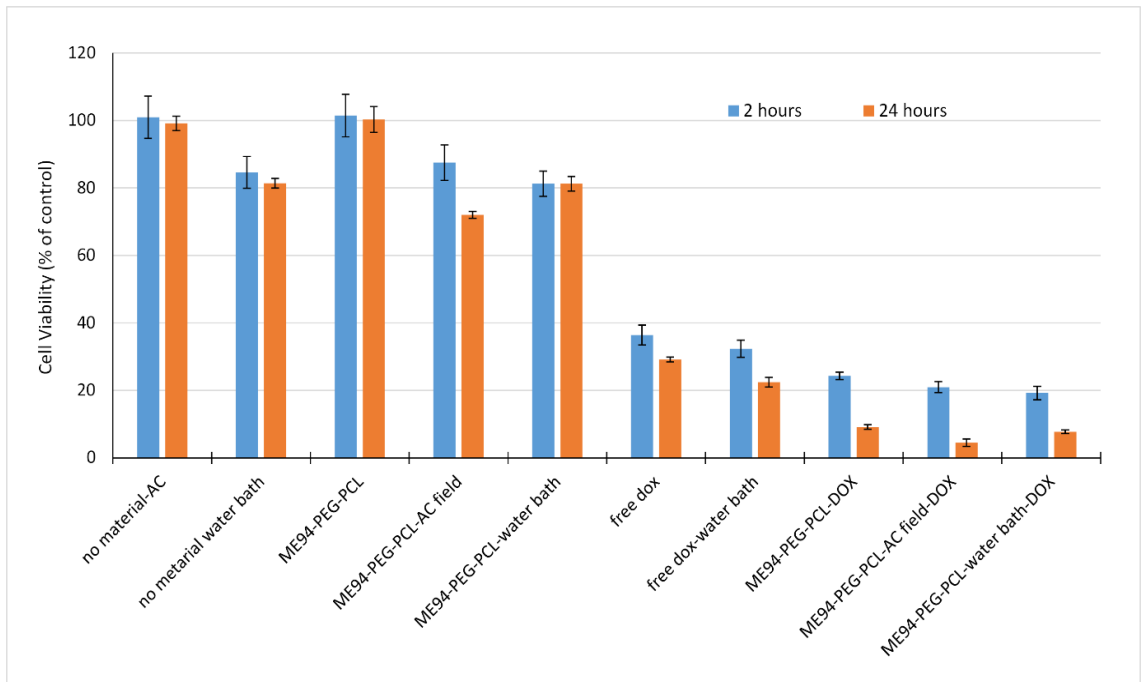


Figure 6-45. Effects of hyperthermia on U87 cells viability , The viability of cells incubated with ME94-PEG-PCL (with and without drug) and exposed to the magnetic field were compared to water bath hyperthermia treated cells (45 minutes treatment).

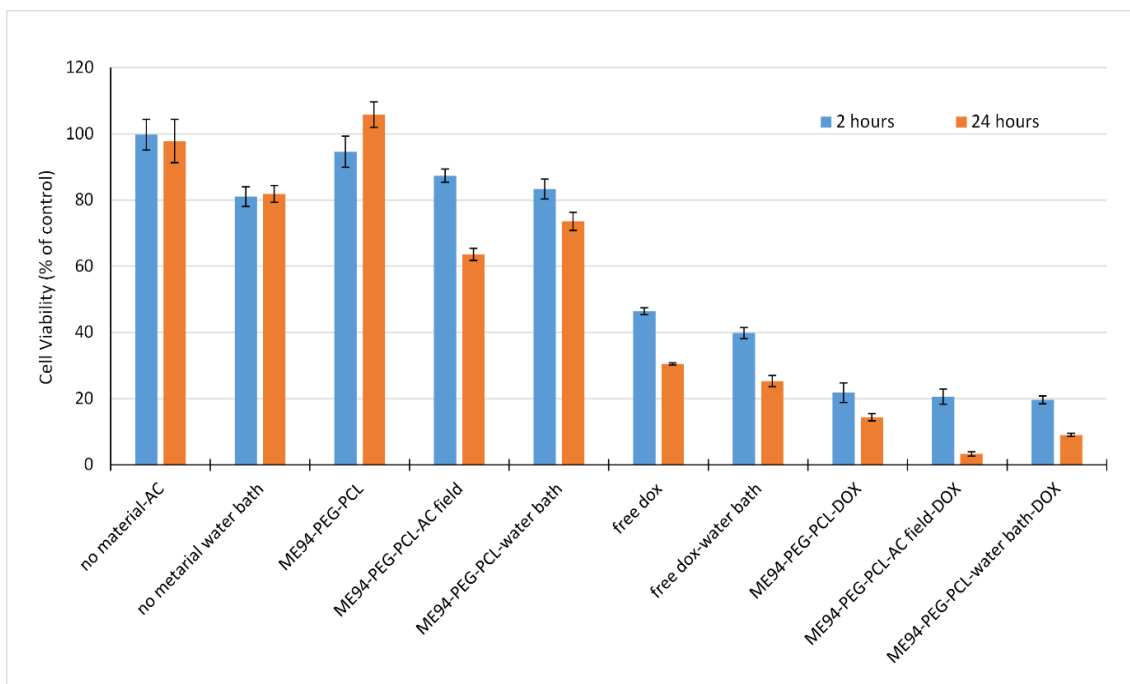


Figure 6-46. Effects of hyperthermia on MCF7 cells viability, The viability of cells incubated with ME94-PEG-PCL (with and without drug) and exposed to the magnetic field were compared to water bath hyperthermia treated cells (45 minutes treatment).

Similar to uncoated magnetite nanoparticles, the results indicated that neither magnetic nanoparticles without the magnetic field nor magnetic field alone affected the viability of the cells.

The viability results of cells treated with magnetic hyperthermia compared to cells treated with water bath hyperthermia demonstrated that both methods resulted in similar cell viability of around 85% viable cells 2 hours post hyperthermia treatments (both nanocomposites). The viability of the cells treated with water bath hyperthermia were slightly lower than AC filed hyperthermia which could be the results of the reduced hyperthermia treatment time due to the nanoparticles lag time, as shown in Section 5.7.3, the polymer capped silica coated nanoparticles need more time to reach the hyperthermia treatment temperature.

Viability assay performed 24 hours post hyperthermia treatment, indicated that magnetic hyperthermia resulted in continues cell death even after the treatment, where cell viability was reduced from 84.9% to 57.2% for MCF7 cells and 86.7% to 70.1% for U87 cells incubated with ME93-PEG-PCL without the drug. In the same way for cells incubated with ME94-PEG-PCL without drug the cell viability was lowered from 87.3% to 63.5% and 87.5% to 72.0% for MCF7 and U87 cells, respectively. Continuous cell death after the treatment could be a result of cytoskeletal damages and apoptosis initiated during the magnetic hyperthermia treatments (Sadhukha et al., 2013, Balasubramanian et al., 2014).

Cells viability were studied in presence of DOX loaded nanoparticles under hyperthermia condition. Treating cells with DOX loaded nanoparticles under hyperthermia condition (Both magnetic field induce hyperthermia and hot water bath hyperthermia) resulted in an increased cell

death compared to either free DOX or hyperthermia, separately. These results indicated significant decrease in cell viability when cells were treated with DOX loaded nanoparticles under magnetic hyperthermia condition. The results showed only 5.3% and 3.3% of the MCF7 cells survived when treated with DOX loaded ME93-PEG-PCL and ME94-PEG-PCL under magnetic hyperthermia condition which is much lower than 57.2% viable cells after hyperthermia treatment alone and 30.5% viable cells after incubating the cells with free DOX. Similar results of 5.7% and 4.4% viable cells were observed for U87 cell line treated with DOX loaded ME93-PEG-PCL and ME94-PEG-PCL and exposed to magnetic hyperthermia, which is much lower compared to 29.1% and 72.0% viable cells after incubating cells with free DOX and hyperthermia treatment alone.

As discussed before in Section 5.7.3, the drug release from DOX loaded nanoparticles were increased with an increase in temperature, and the drug release was faster under magnetically induced hyperthermia compare to incubator which explains the increased cytotoxicity compared to 37°C condition. Furthermore the effect of hyperthermia itself results in increased cell death.

These results demonstrated the potential of the DOX loaded thermosensitive polymer capped mesoporous silica coated magnetite nanoparticles to be used in hyperthermia treatment and heat triggered drug release chemotherapy for cancer therapy.

6.7.4 ME60

Cells were incubated with mesoporous silica coated magnetite nanoparticles (ME60) with and without DOX. Nanoparticles concentration were chosen based on the drug loading content of nanocomposites in the way maintain a drug concentration of 17.24 μM . Concentration of magnetic nanoparticles (ME60) were 0.097 mg/mL which was shown to be non-toxic against both cell lines without the drug.

Cells were incubated with magnetic nanoparticles for 24 hours before the hyperthermia treatment. After which the media was removed and cells were exposed to the magnetic field for 45 minutes. The cell viability were compared to water bath hyperthermia treated cells, free DOX treated cells and control cells which was exposed to magnetic field without presence of the nanoparticles. Another group of control cells were incubated with drug loaded nanoparticles at 37°C. The results are presented in Figure 6-48 and Figure 6-47.

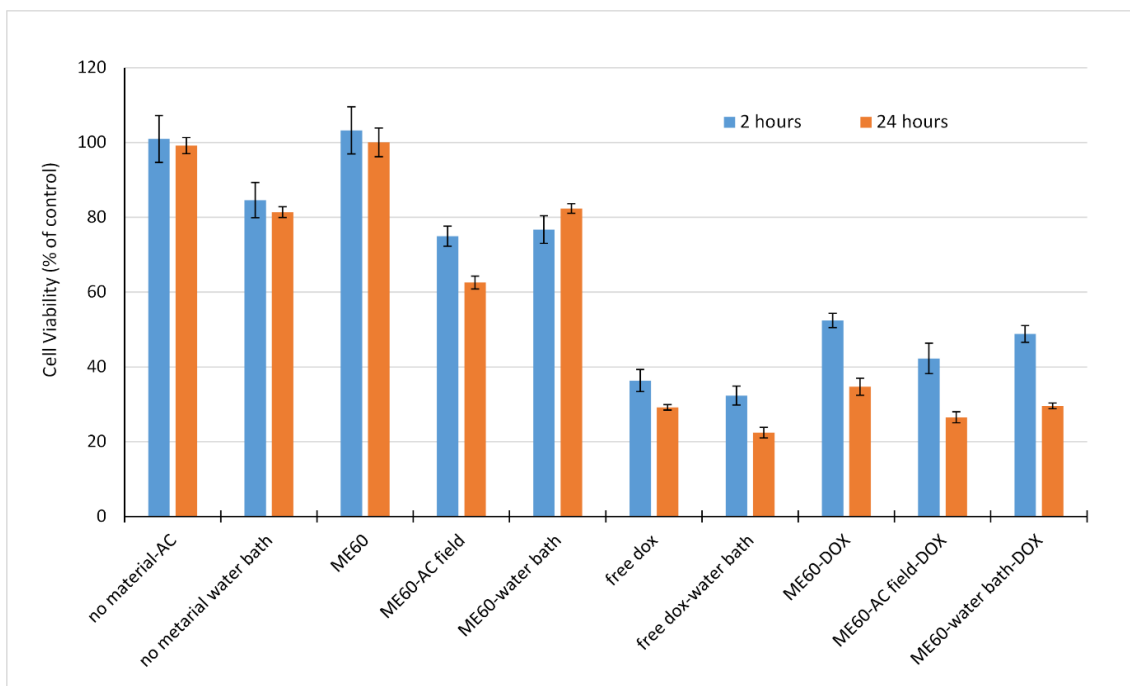


Figure 6-47. Effects of hyperthermia on U87 cells viability, The viability of cells incubated with ME60 (with and without drug) and exposed to the magnetic field were compared to water bath hyperthermia treated cells (45 minutes treatment).

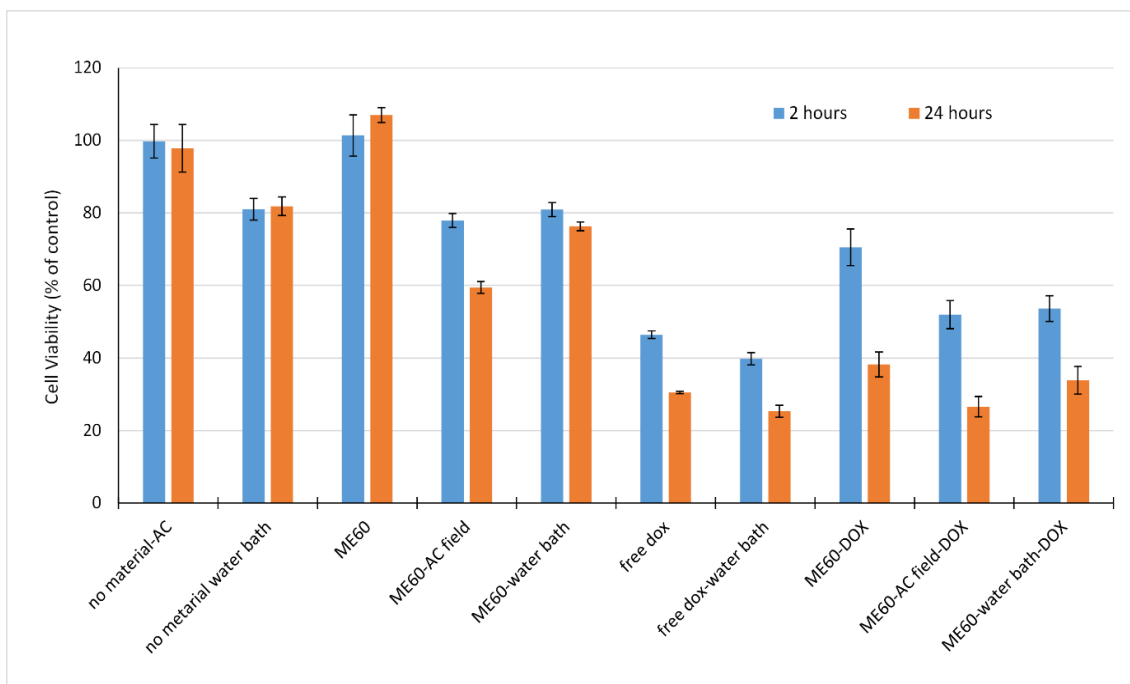


Figure 6-48. Effects of hyperthermia on MCF7 cells viability, The viability of cells incubated with ME60 (with and without drug) and exposed to the magnetic field were compared to water bath hyperthermia treated cells (45 minutes treatment).

Similar to uncoated magnetite nanoparticles, the results indicated that neither magnetic nanoparticles without the magnetic field nor magnetic field alone affected the viability of the cells.

The viability assays performed 2 hours after hyperthermia treatment for magnetic hyperthermia and water bath hyperthermia demonstrated that both methods resulted in a decreased cell viability with the similar survival rate of around 75% to 80% for both cell lines.

Viability assay performed 24 hours later indicated that magnetic hyperthermia induced continues cell viability decay after the treatment and cell viability was reduced from 77.8% to 59.4% for MCF7 cells and 74.9% to 62.5% for U87 cells. However for hot water bath hyperthermia the viability was reduced only from 80.9% to 76.2% for MCF7 cells and was increased slightly from 76.7% to 82.3% for U87 cells.

Cells viability were studied in presence of DOX loaded magnetic nanoparticles under hyperthermia condition. In comparison to either hyperthermia alone or free DOX treatments, a decrease in cell viability was observed under magnetically induced hyperthermia conditions. The MCF7 cell viability 24 hours post magnetic hyperthermia treatment was decreased to 26.5% which is lower than 30.5% for free DOX and 38.25 for DOX loaded nanoparticles without hyperthermia treatment in the same period. Similarly viability of U87 cells 24 hours post magnetic hyperthermia treatment was decreased to 26.5% which is lower than 29.1% viable cells for free DOX treated cells and 34.7% for DOX loaded ME60 treated cells without hyperthermia.

These results indicate that DOX loaded mesoporous silica nanoparticles could provide the synergic effect of hyperthermia and chemotherapy and have great potential to be used in drug delivery applications.

6.7.5 ME60-L

Cells were incubated with liposome capped mesoporous silica coated magnetite nanoparticles (ME60-L) with or without DOX. Nanoparticles concentration were chosen based on the drug loading content of nanocomposites in the way maintain a drug concentration of 17.24 μM . Concentration of magnetic nanoparticles were 0.27 mg/mL which was shown to be non-toxic against both cell lines without the drug.

Cells were incubated with liposome capped nanoparticles with and without the drug for 24 hours before the hyperthermia treatment. After 24 hours the media was removed and cells were exposed to the magnetic field for 45 minutes. The cell viability were compared to water bath hyperthermia treated cells, free DOX treated cells and control cells which were exposed to magnetic field without presence of the nanoparticles. Another group of control cells were incubated with drug loaded nanoparticles at 37°C. The results are presented in Figure 6-50 and Figure 6-49.

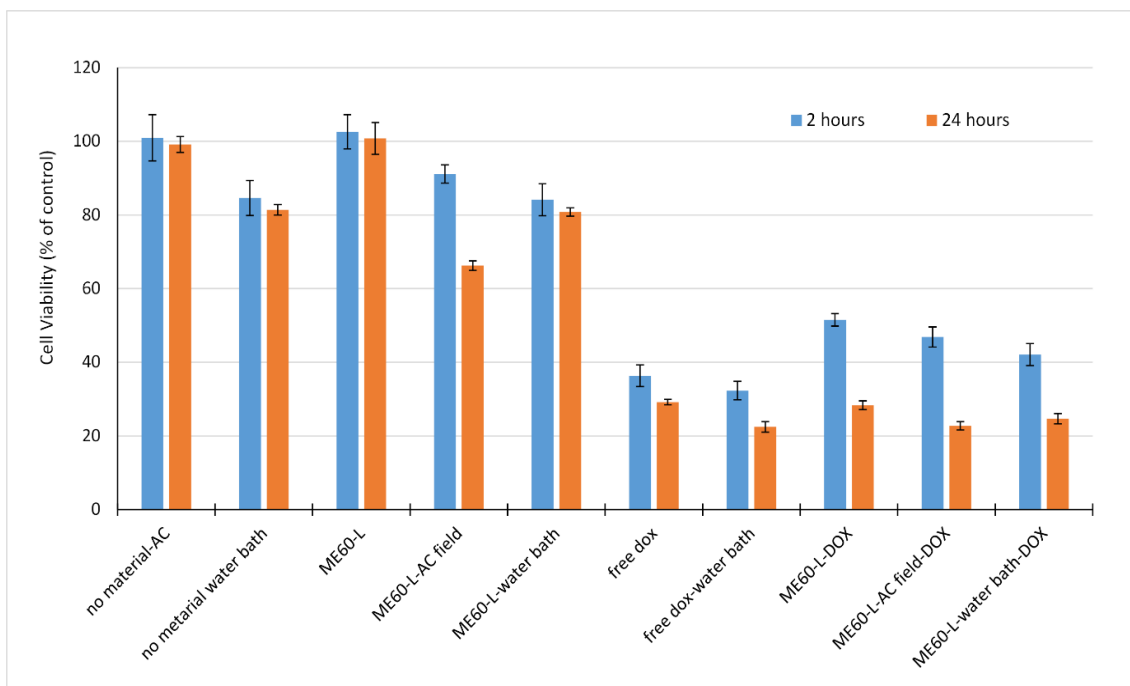


Figure 6-49. Effects of hyperthermia on U87 cells viability , The viability of cells incubated with ME60-L (with and without drug) and exposed to the magnetic field were compared to water bath hyperthermia treated cells (45 minutes treatment).

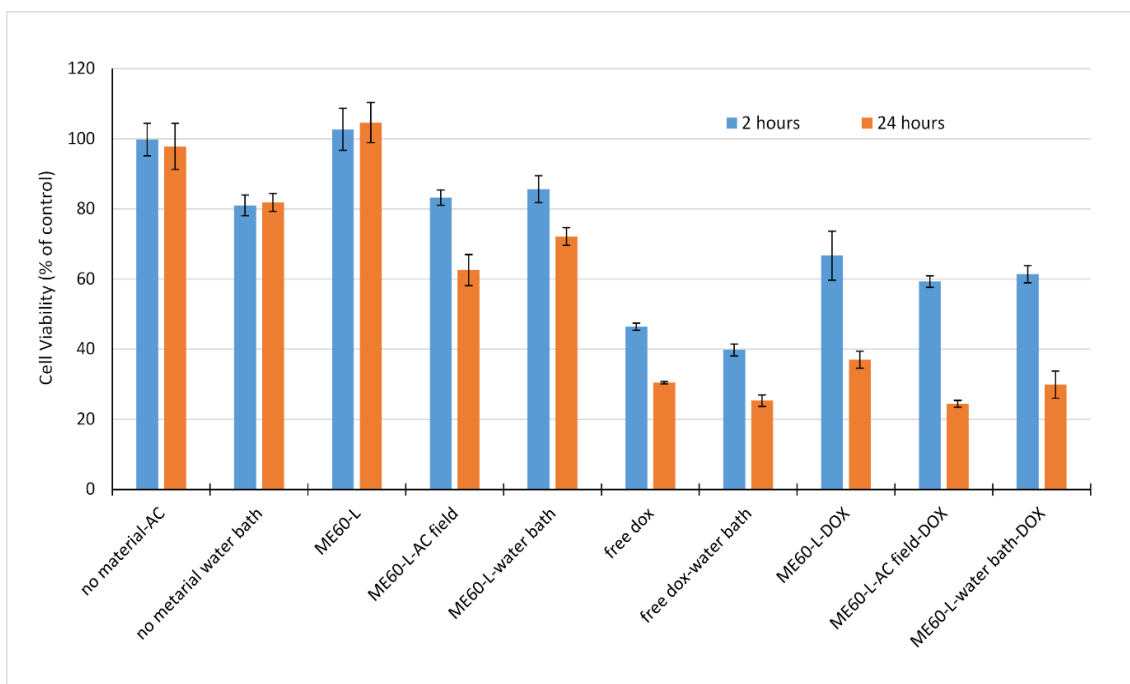


Figure 6-50. Effects of hyperthermia on MCF7 cells viability , The viability of cells incubated with ME60-L (with and without drug) and exposed to the magnetic field were compared to water bath hyperthermia treated cells (45 minutes treatment).

The results indicated that neither magnetic nanoparticles without the magnetic field nor magnetic field alone affected the viability of the cells.

The viability assay for magnetic hyperthermia compared with water bath hyperthermia performed 2 hours after the treatment established that both methods resulted in decreased cell viability, however the cells survival rate after magnetic hyperthermia treatments were higher than survival

rate for cells treated in the same way with uncapped mesoporous silica nanoparticles (ME60). This could be explained by the higher SPA of the uncapped nanoparticles, which result in faster temperature rise (see Section 3.14.2 for SPA calculations).

Viability assay performed 24 hours post hyperthermia treatment indicated that similar to other synthesised magnetic nanoparticles, cells incubated with ME60-L and exposed to magnetic hyperthermia continued to decay even after the treatment. Cell viability were further reduced from 83.2% in 2 hours to 62.5% after 24 hours, for MCF7 cells and similarly from 91.1% to 66.2% for U87 cells.

Viability assays performed for cells incubated with DOX loaded nanoparticles showed an increase in cell death under hyperthermia condition (both hot water bath hyperthermia and magnetic hyperthermia) compare to cells incubated at body temperature. However, the cell viability measured 2 hours after hyperthermia treatments with DOX loaded nanoparticles showed higher survival rates than cells treated with free DOX.

The cell viability measured 24 hours after magnetic hyperthermia treatment with DOX loaded nanoparticles showed further decrease in viable cells. The viability of MCF7 cells was reduced from 59.2% to 24.4% which is lower than free DOX in the same period. The cell viability for U87 measured 24 hours after magnetic hyperthermia treatment was decreased from 46.8% to 22.7% which is also lower than free DOX and water bath hyperthermia treated cells. The increased cell death after hyperthermia treatment could be due to higher drug release due to increased temperature as disused in Section 5.5.3 and the hyperthermia induced damage to the cell structure and apoptosis.

These results indicate that DOX loaded liposome capped mesoporous silica coated magnetite nanoparticles could to be used in drug delivery applications to provide synergistic effect of hyperthermia and chemotherapy.

6.8 Summary

Feasibility of magnetically induced hyperthermia and hyperthermia cell death using synthesised magnetic nanoparticles were investigated. Cells were treated with different magnetic nanoparticles and placed in an AC magnetic field and the viability assays were performed 2 hours and 24 hours post treatments. Figure 6-51 and Figure 6-52 present a summary of the magnetic hyperthermia induced cell death caused by different nanoparticles.

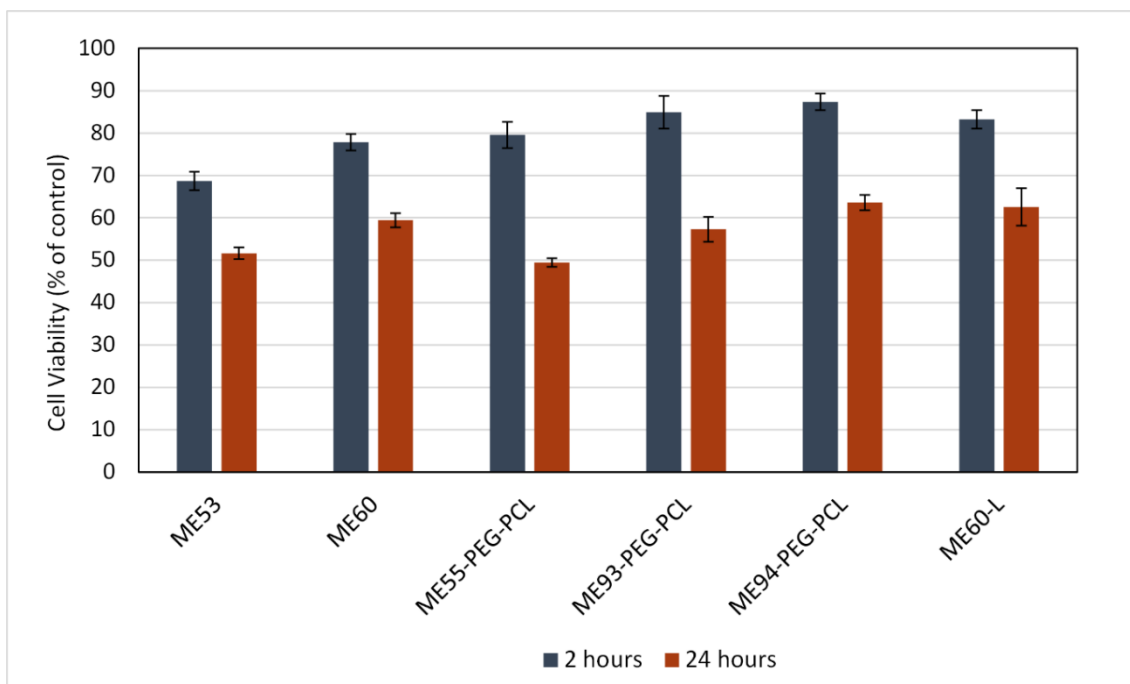


Figure 6-51. Effects of 45 minutes magnetically induced hyperthermia treatment on MCF7 cells viability.

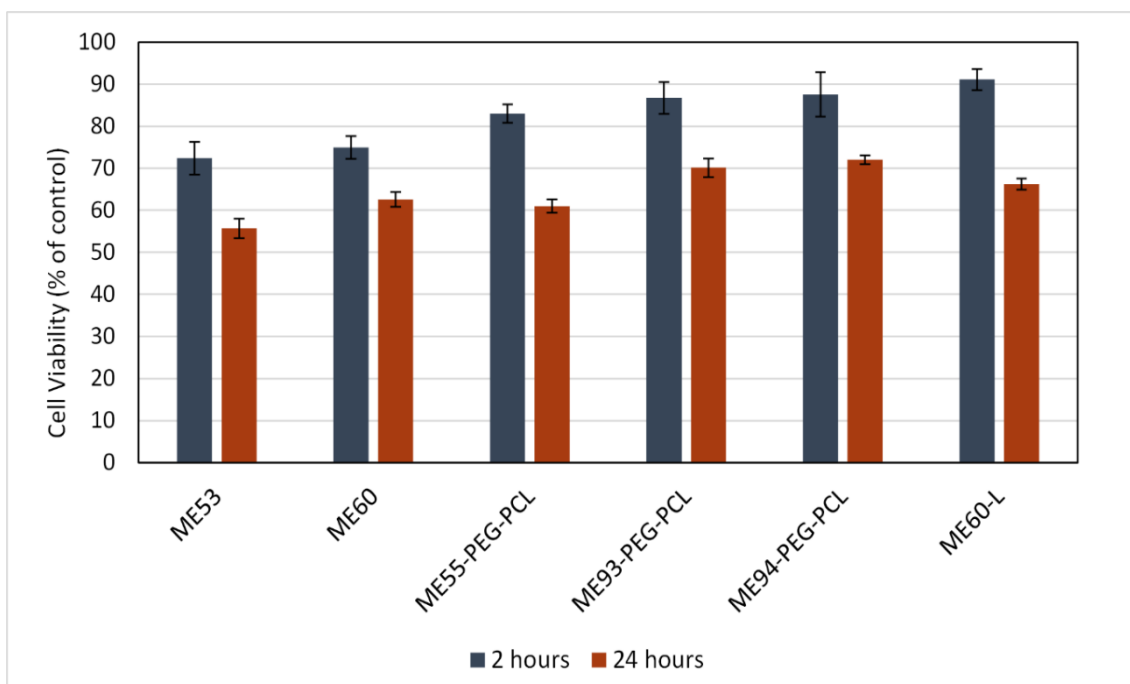


Figure 6-52. Effects of 45 minutes magnetically induced hyperthermia treatment on U87 cells viability

As illustrated in the graphs hyperthermia generated by ME53 (bare magnetite) resulted in the highest cell death followed by ME55-PEG-PCL (polymer coated magnetite nanoparticles) and ME60 (mesoporous silica coated nanoparticles). These results could be due higher SPA and rapid heating of these nanoparticles compared to other polymer capped or liposome capped mesoporous silica coated nanoparticles with lower SPA and saturation magnetization.

The viability testes performed 24 hours after the hyperthermia treatment showed continues cell death after the hyperthermia treatments for all materials. The results for MCF7 cells and U87cells

were slightly different nonetheless both cell lines followed the same pattern for different materials with MCF7 cells being more sensitive to hyperthermia treatment. A minimum of 37% decrease in cell viability for MCF7 cells and 28% for U87cells was observed 24 hours after magnetic hyperthermia treatment. The lowest cell death was induced by ME94-PEG-PCL.

Synergic effects of hyperthermia and DOX was studied by incubating the cells with DOX loaded nanoparticles for 24 hours followed by 45 minutes of hyperthermia treatment. The viability assays were performed 2 hours and 24 hours after treatments. Figure 6-53 and Figure 6-54 present a summary of cells viabilities for cells underwent hyperthermia with different DOX loaded nanoparticles compare to cells treated with DOX loaded nanoparticles without the hyperthermia treatment.

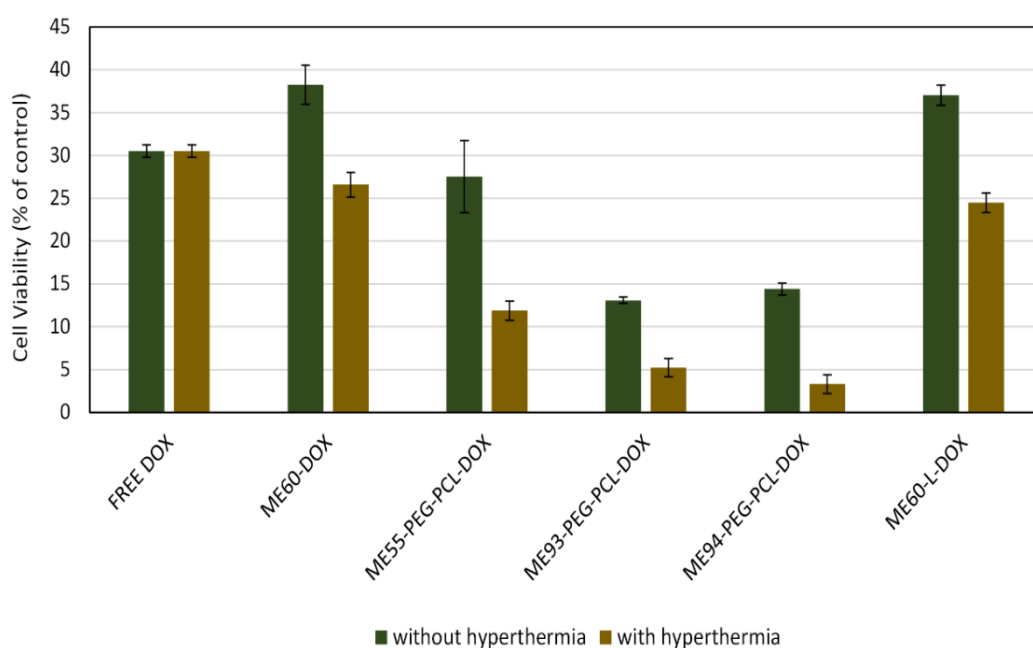


Figure 6-53. Cells viabilities for MCF7 cells treated with DOX loaded nanoparticles with and without additional hyperthermia treatment

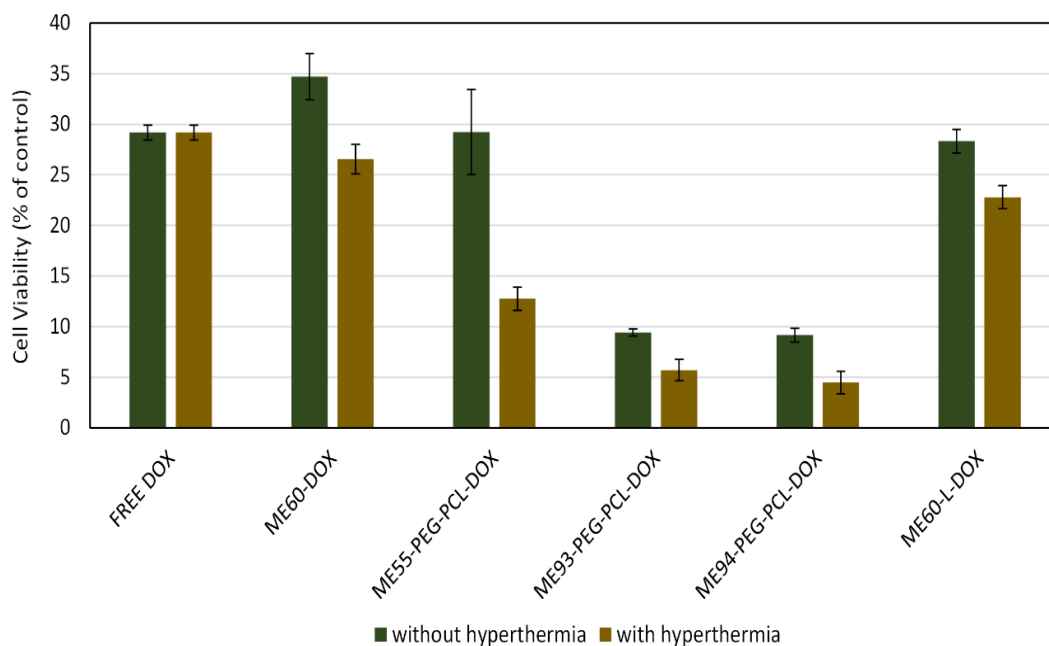


Figure 6-54. Cells viabilities for U87 cells treated with DOX loaded nanoparticles with and without additional hyperthermia treatment

The results established that hyperthermia treatment increased the cell death compared to cells treated with free drug or DOX loaded nanoparticles without hyperthermia. The effect was more obvious for the polymer coated magnetite nanoparticles (ME55-PEG-PCL) as they show significant decrease in cell viability after the hyperthermia treatment. ME60-L showed the least changes in the cell viability which could be due to small changes in drug release with the temperature rise and long lag time for nanoparticles to reach the effective hyperthermia treatment temperature.

The DOX loaded polymer capped mesoporous silica coated magnetite nanoparticles (both ME93-PEG-PCL and ME94-PEG-PCL) showed great potential in decreasing the cell viability. Additionally, when the nanoparticle treated cells underwent hyperthermia treatment the survival rate reduce even lower and only 5% of the cells survived 24 hours after the treatment. In comparison around 30% of the cells treated with the free DOX survived (up to 89% increased cytotoxicity).

These results confirmed the substantial potential of the synthesised DOX loaded nanoparticles to be used for drug delivery application with simultaneously magnetically induced hyperthermia treatment to kill cancer cells and improve the cancer therapy.

CHAPTER 7

CONCLUSION AND FUTURE WORK

7.1 Conclusions

The aims of this thesis were to synthesis iron oxide-based magnetic nanoparticles, characterise the synthesis materials and evaluated the developed nanoparticles as platforms for drug delivery, hyperthermia and catalysis. This project employs several formulations of magnetic nanoparticles, including mesoporous silica- magnetite core-shell nanoparticles, magnetoliposomes and magnetic micelles, for drug delivery and catalysis applications.

The main synthesis routes used to prepare magnetite nanoparticles were chemical co-precipitation of ferrous and ferric chlorides and thermal decomposition of iron (III) acetylacetonate. The magnetite nanoparticle prepared by these methods were used later as core materials to prepare core-shell structures. The nanoparticles prepared by the thermal decomposition methods were surface functionalised and hydrophobic, whereas the magnetite prepared by co-precipitation method were hydrophilic and were required, underwent post synthesise oleic acid modification to become hydrophobic. The synthesised magnetite nanoparticles were characterised using different physio-chemical techniques including TEM, VSM and XRD. From the TEM images it was observed that the nanoparticles prepared by co-precipitation method had a boarder size distribution and larger particles compare to the particles prepared *via* thermal decomposition method. The magnetic heating of the nanoparticles were assessed using commercial magnetic field applicator (DM2 nanoScale Biomagnetics) with a field strength of up to 200 G and frequency of 406 kHz. It was observed that the magnetic nanoparticles prepared by the co-precipitation method possess higher SPA and require less time to increase the temperature of the solution.

Mesoporous silica coating of magnetite nanoparticles were performed by different methods of direct coating of mesoporous silica layer with CTAB as template or coating of the nanoparticles with an amorphous silica layer followed by protected etching of the deposited silica layer. The thickness of the silica shell of the nanoparticles were optimised according to the desired application. The mesoporous silica-magnetite nanoparticles were characterised using different methods including TEM, BET and VSM. The BET isotherms of the silica coated nanoparticles indicated high surface area with mesoporous structure for all developed nanoparticles. The silica coated magnetic nanoparticles were used as enzyme supports and in drug delivery applications.

PEG-PCL di block copolymer were synthesised by ring-opening polymerization of ϵ -caprolactone from the alcohol terminus of poly (ethylene glycol) monomethyl ether using dibutyltin dilaurate as catalyst. The synthesised polymer were characterised using ^1H NMR where the formation of the copolymer was confirmed. The synthesised polymer was used to develop magnetic micelles for drug delivery applications. The magnetic micelles were prepared by self-assembly of the polymer encapsulating the hydrophobic magnetite nanoparticles as core structure. The DSC thermal isotherm of the micelles indicate that the melting temperature of the micelles are in the range of hyperthermia treatment which makes the thermosensitive polymer suitable to

be used in hyperthermia triggered drug release applications. The thermosensitive polymer were also used to cap the mesochannels of the silica nanoparticles to reduce the premature drug release and enhance the control over drug release.

Magnetoliposomes were prepared using SPC and cholesterol following lipid film hydration method, with addition of magnetite nanoparticles followed by ultra-sonication and filtration to obtain a nanoparticles within the size range of 100 nm. The size of the magnetoliposomes were assessed using DLS. The magnetoliposomes were used as drug delivery systems for hydrophilic MMC drug. Furthermore similar to PEG-PCL polymer, liposomes were used to cap the mesochannels of the mesoporous silica nanoparticles to reduce the premature drug release and enhance the control over drug release.

Silica-magnetite core-shell nanoparticles were used as enzymes supports for bio-catalysis reactions. The enzymes (PFL and CRL lipases) were immobilised on silica coated nanoparticles both through physical adsorption and chemical bonding. To immobilise the lipase *via* chemical conjugation the nanoparticles were surface amine functionalised using APTS following two different methods where TPPE method showed higher amine density. Following the surface amine functionalisation, glutaraldehyde was used to convert surface amine groups to aldehyde in order to covalently bond with the NH₂ groups of lipase *via* imine bonding.

The immobilised lipases were used in catalytic reactions of hydrolysis of pNPP and hydrolysis of cis-3,5-diacetoxy-1-cyclopentene to investigate the catalytic activity of the immobilized enzymes compared with the free enzymes. The results indicated that both physically and chemically immobilised lipases retained their activity after immobilisation.

In case of hydrolysis of pNPP the free lipases provided slightly higher conversion than immobilised lipases in the first cycle however the immobilised lipases were easily recycled and reused in sequential cycles which provides higher total yield per mg of lipase. The chemically immobilised lipase exhibited good reusability without loss of its activity for four sequential cycles, however the physically adsorbed lipase showed reduced activity which could be explained by loss of enzyme during recycling between successive reactions. The CRL lipase (free or immobilised) activity in the presence of an AC field were accessed by hydrolysis of pNPP and the results showed that the lipase retained its activity under influenced of an AC magnetic field and interestingly exposure to the AC magnetic field resulted in increased reaction yield.

The hydrolysis of cis-3,5-diacetoxy-1-cyclopentene were performed at two temperatures of 25°C and 37°C where it was observed that both lipases exhibited higher activity at higher temperature which could be due to fact that for PFL and CRL the optimum temperature is close to 37°C. The free lipase showed higher conversion rate compared to immobilised lipases, however the immobilised lipases afford higher ratios of the desired product of (1S,4R)-cis-4-acetoxy-2-cyclopenten-1-ol which conclude that the immobilised lipases provide enhanced control over the

formation of the desired products. Particularly in case of PFL, the free lipase reached its maximum conversion to desired product during the initial 4 hours of the reaction at 25°C or initial hour at 37°C, after which the dihydroxy by-product is formed in an excess amount as the dominant product. The immobilised lipases were used in three successive cycles where it was observed that the chemically immobilised lipases retained their activity during recycling while physically adsorbed lipase displayed a decreased activity in each consecutive cycle indicating lipase loss during the reaction and recycling process.

In this project, different magnetic nanocomposites were developed as for drug delivery systems based on magnetite core-shell structure. Two different model drugs of MMC and DOX were used to study the ability of the synthesised nanoparticles for loading and release of the chemotherapeutic agents. The initial material used as drug delivery systems were silica-magnetite core-shell nanoparticle, which exhibited high drug loss and low control over drug release profile, and magnetoliposomes which showed lower drug loading content compare to silica based nanoparticles. The drug delivery systems were then optimized by combining the liposomes and silica-magnetite core-shell nanoparticle to obtain high drug loading capacity with enhanced control over the drug release profile. Capping the mesopores of the silica nanoparticles with liposomes reduced the drug release (at 37°C after 48 hours) by 52.7%. However, the liposome capped nanoparticles did not exhibit hyperthermia triggered release properties. To improve the drug delivery system and obtain the triggered release characteristics, the mesopores of silica-magnetite core-shell nanoparticle were also capped with heat sensitive PEG-PCL polymer. Coating the silica nanoparticles with polymeric micelles or liposomes prevents the entrapped drug from dissociation upon dilution in the blood stream after intravenous injection and facilitates their extravasations at tumour sites by avoiding renal clearance and non-specific reticuloendothelial uptake (Shuai et al., 2004). Capping the mesopores of the silica nanoparticles with PEG-PCL diblock copolymer reduced the drug release (at 37°C after 48 hours) by 41.5%.

The drug release from nanoparticles were assessed under both pH and temperature stimuli conditions. For pH triggered conditions normal physiological pH (7.4) and acidic pH (5.5) were used and for temperature triggered release body temperature (37°C) and the hyperthermia treatment condition (43°C) were used. The hyperthermia condition were studied using an AC magnetic field and an incubator. The results indicated that all the developed materials were suitable to be used in hyperthermia treatments however polymer capped materials showed higher increase in drug release with the temperature rise compare to liposome capped material. All the developed material showed pH responsive release profiles with increased drug release in lower pH.

The biocompatibility of the synthesised nanoparticles were evaluated against two cell lines of MCF7 and U87 and the data demonstrated that only bare magnetite nanoparticles induced toxicity in low dosage of 0.25 mg/mL. It was shown that the biocompatibility of the magnetite

nanoparticles were significantly improved by surface coatings. Mesoporous coated silica nanoparticles showed good biocompatibility against both cell lines, however they exhibited cytotoxicity at high dose or after long incubation period. Silica coated nanoparticles capped with PEG-PCL polymer or liposomes exhibited greater biocompatibility than uncoated silica nanoparticles against both cell lines.

DOX loaded nanoparticles induced cytotoxicity toward both cell lines, however the degree of cytotoxicity was different between different materials. ME55-PEG-PCL, ME60 and ME60-L induced lower cytotoxicity than free DOX in the first 24 hours of incubation however after 48 hours they caused comparable cytotoxicity. The ME93-PEG-PCL and ME94-PEG-PCL generated higher cytotoxicity compared to free DOX even in the first 24 hours.

In the final part of the project the feasibility of magnetically induced hyperthermia triggered drug release and hyperthermia cell death using synthesised magnetic nanoparticles were investigated. Cells were treated with different magnetic nanoparticles and placed in an AC magnetic field and the viability assays were performed 2 hours and 24 hours post treatments. Hyperthermia generated by bare magnetite resulted in the highest cell death followed by polymer coated magnetite nanoparticles and ME60, respectively. The viability testes performed 24 hours after the hyperthermia treatment showed continues cell death after the hyperthermia treatments for all materials. The results for MCF7 cells and U87cells were slightly different however both cell lines followed the same pattern, with MCF7 cells being more sensitive to hyperthermia treatment. A minimum of 37% decrease in cell viability for MCF7 cells and 28% for U87cells was observed 24 hours after magnetic hyperthermia treatment.

Synergic effects of hyperthermia and DOX was studied by incubating the cells with DOX loaded nanoparticles for 24 hours followed by 45 minutes of hyperthermia treatment. The viability assays were performed 2 hours and 24 hours after treatments. The results established that hyperthermia treatment increased the cell death compare to cells treated with free drug or DOX loaded nanoparticles without hyperthermia. The effect was more obvious for the magnetic micelles. Liposome capped nanoparticles induced the lowest changes in the cell viability. The DOX loaded polymer capped mesoporous silica coated magnetite nanoparticles showed great potential in decreasing the cell viability. Furthermore, when the nanoparticle treated cells underwent hyperthermia treatment the survival rate reduce even lower and only 5% of the cells survived 24 hours after the treatment. In comparison around 30% of the cells treated with the free DOX survived.

These data demonstrated that the drug loaded nanoparticles especially polymer capped silica nanoparticles could effectively improve the chemotherapeutic effects of DOX. The synthesised DOX loaded nanoparticles showed great potential to be used as drug delivery systems with simultaneous magnetically induced hyperthermia to kill cancer cells and improve the cancer therapy.

7.2 Future work

The magnetic nanocomposites were used in this project to utilise the magnetic hyperthermia triggered drug release. On the other hand employing magnetic nanoparticles would offer the advantage of magnetic targeting. Evaluation of the feasibility of magnetic targeting *in silico* using computer modelling and *in vivo* using magnetic probes could benefit from additional advantage of magnetic nanoparticles.

The drug delivery systems developed in this project are based on passive targeting using EPR effect. However, the materials used in this project could easily be functionalised with additional targeting legends such as RDG peptides to selectively target the cancerous cells which increases the cellular uptake and consequently increase the efficiency of the developed drug delivery systems.

Magnetic nanoparticles are established as MRI contrasting agents. Evaluation of the developed nanoparticles as MRI contrast agent would offer the possibility of *in vivo* monitoring of the nanoparticles which adds additional control over the drug delivery system.

This project presented the use of liposomes and polymers in drug delivery systems, where the liposomes offer higher drug encapsulation efficiency and the polymers offer higher thermosensitivity and more efficient hyperthermia release profiles. Development of drug delivery systems with combination of these two could improve the efficiency of the drug delivery system.

The mesoporous silica nanoparticles prepared by protected etching theoretically offer the possibility of encapsulation of two different anticancer agents. It is suggested to explore the feasibility of simultaneous loading and controlled release profile of two anticancer drug.

In case of bio-catalysis, the catalysis reaction was performed under the influence of an AC magnetic field to study the effect of magnetic field on lipase activity and reaction rate. As the next step it is suggested to use the magnetic field during the enantioselective reaction to study the effect of magnetic field on specificity and enantioselectivity of the lipase.

References

- ABOU EL-NOUR, K. M. M., EFTAIHA, A. A., AL-WARTHAN, A. & AMMAR, R. A. A. 2010. Synthesis and applications of silver nanoparticles. *Arabian Journal of Chemistry*, 3, 135-140.
- AI, H., FLASK, C., WEINBERG, B., SHUAI, X., PAGEL, M. D., FARRELL, D., DUERK, J. & GAO, J. 2005a. Magnetite-loaded polymeric micelles as ultrasensitive magnetic-resonance probes. *Advanced Materials*, 17, 1949-1951.
- AI, H., FLASK, C., WEINBERG, B., SHUAI, X. T., PAGEL, M. D., FARRELL, D., DUERK, J. & GAO, J. 2005b. Magnetite-Loaded Polymeric Micelles as Ultrasensitive Magnetic-Resonance Probes. *Advanced Materials*, 17, 1949-1952.
- AKOH, C. C., LEE, G. C. & SHAW, J. F. 2004. Protein engineering and applications of *Candida rugosa* lipase isoforms. *Lipids*, 39, 513-26.
- AL-GHAMDI, S. S. 2008. Time and dose dependent study of doxorubicin induced DU-145 cytotoxicity. *Drug Metab Lett*, 2, 47-50.
- ALEXIOU, C., ARNOLD, W., KLEIN, R. J., PARAK, F. G., HULIN, P., BERGEMANN, C., ERHARDT, W., WAGENPFEIL, S. & LUBBE, A. S. 2000. Locoregional cancer treatment with magnetic drug targeting. *Cancer Res*, 60, 6641-8.
- ALEXIOU, C., JURGONS, R., SCHMID, R. J., BERGEMANN, C., HENKE, J., ERHARDT, W., HUENGES, E. & PARAK, F. 2003. Magnetic drug targeting--biodistribution of the magnetic carrier and the chemotherapeutic agent mitoxantrone after locoregional cancer treatment. *J Drug Target*, 11, 139-49.
- ALLEN, T. M. & CULLIS, P. R. 2013. Liposomal drug delivery systems: From concept to clinical applications. *Advanced Drug Delivery Reviews*, 65, 36-48.
- AMMAR, M., MAZALEYRAT, F., BONNET, J. P., AUDEBERT, P., BROSSEAU, A., WANG, G. & CHAMPION, Y. 2007. Synthesis and characterization of core-shell structure silica-coated Fe 29.5 Ni 70.5 nanoparticles. *Nanotechnology*, 18, 285606.
- AMSTAD, E., KOHLBRECHER, J., MÜLLER, E., SCHWEIZER, T., TEXTOR, M. & REIMHULT, E. 2011. Triggered release from liposomes through magnetic actuation of iron oxide nanoparticle containing membranes. *Nano letters*, 11, 1664-1670.
- ANOBOM, C. D., PINHEIRO, A. S., DE-ANDRADE, R. A., AGUIEIRAS, E. C. G., ANDRADE, G. C., MOURA, M. V., ALMEIDA, R. V. & FREIRE, D. M. 2014. From Structure to Catalysis: Recent Developments in the Biotechnological Applications of Lipases. *BioMed Research International*, 2014, 11.
- ANSORGE-SCHUMACHER, M. B. & THUM, O. 2013. Immobilised lipases in the cosmetics industry. *Chemical Society Reviews*, 42, 6475-6490.
- ANTONELLI, A., SFARA, C., MOSCA, L., MANUALI, E. & MAGNANI, M. 2008. New biomimetic constructs for improved in vivo circulation of superparamagnetic nanoparticles. *Journal of nanoscience and nanotechnology*, 8, 2270-2278.
- ARAVINDAN, R., ANBUMATHI, P. & VIRUTHAGIRI, T. 2007. Lipase applications in food industry. *Indian Journal of Biotechnology*, 6, 141.
- ASHLEY, C. E., CARNES, E. C., PHILLIPS, G. K., PADILLA, D., DURFEE, P. N., BROWN, P. A., HANNA, T. N., LIU, J., PHILLIPS, B., CARTER, M. B., CARROLL, N. J., JIANG, X., DUNPHY, D. R., WILLMAN, C. L., PETSEV, D. N., EVANS, D. G., PARIKH, A. N., CHACKERIAN, B., WHARTON, W., PEABODY, D. S. & BRINKER, C. J. 2011a. The targeted delivery of multicomponent cargos to cancer cells by nanoporous particle-supported lipid bilayers. *Nat Mater*, 10, 389-397.

- ASHLEY, C. E., CARNES, E. C., PHILLIPS, G. K., PADILLA, D., DURFEE, P. N., BROWN, P. A., HANNA, T. N., LIU, J., PHILLIPS, B., CARTER, M. B., CARROLL, N. J., JIANG, X., DUNPHY, D. R., WILLMAN, C. L., PETSEV, D. N., EVANS, D. G., PARIKH, A. N., CHACKERIAN, B., WHARTON, W., PEABODY, D. S. & BRINKER, C. J. 2011b. The targeted delivery of multicomponent cargos to cancer cells by nanoporous particle-supported lipid bilayers. *Nat Mater*, 10, 389-97.
- ASÍN, L., IBARRA, M. R., TRES, A. & GOYA, G. F. 2012. Controlled Cell Death by Magnetic Hyperthermia: Effects of Exposure Time, Field Amplitude, and Nanoparticle Concentration. *Pharmaceutical Research*, 29, 1319-1327.
- ASSANGA, I. & LUJAN, L. 2013. Cell growth curves for different cell lines and their relationship with biological activities. *International Journal of Biotechnology and Molecular Biology Research*, 4, 60-70.
- ATCC 2012. American Type Culture Collection (ATCC)
- ATCC 2015. MCF7 ATCC[®] HTB-22 Homo sapiens mammary gland, breast; deri.
- ATCC 2016. U-87 MG ATCC[®] HTB-14[„]ç Homo sapiens brain glioblastoma; astr.
- AVATI POLAR LIPIDS, I. 2016. Soy PC [Online]. Available: https://www.avantilipids.com/index.php?option=com_content&view=article&id=348&Itemid=256&catnumber=840054.
- AYSUN ADAN GÖKBULUT, A. A. 2013. Purification and biochemical characterization of an extracellular lipase from psychrotolerant *Pseudomonas fluorescens* KE38 Information | Open Access Article | openaccessarticles.com. *Turk J Biol: TURKISH JOURNAL OF BIOLOGY*, 37, 538 to 546.
- AZEVEDO, R. C. S., SOUSA, R. G., MACEDO, W. A. A. & SOUSA, E. M. B. 2014. Combining mesoporous silica–magnetite and thermally-sensitive polymers for applications in hyperthermia. *Journal of Sol-Gel Science and Technology*, 72, 208-218.
- AZUAR, E., MARCOS, M. D., MARTÍNEZ-MÁÑEZ, R., SANCENÓN, F., SOTO, J., AMORÓS, P. & GUILLEM, C. 2009. pH- and Photo-Switched Release of Guest Molecules from Mesoporous Silica Supports. *Journal of the American Chemical Society*, 131, 6833-6843.
- BABA, D., SEIKO, Y., NAKANISHI, T., ZHANG, H., ARAKAKI, A., MATSUNAGA, T. & OSAKA, T. 2012. Effect of magnetite nanoparticles on living rate of MCF-7 human breast cancer cells. *Colloids Surf B Biointerfaces*, 95, 254-7.
- BABAY, S., MHIRI, T. & TOUMI, M. 2015. Synthesis, structural and spectroscopic characterizations of maghemite γ -Fe₂O₃ prepared by one-step coprecipitation route. *Journal of Molecular Structure*, 1085, 286-293.
- BAE, S., SANG WON, L., HIRUKAWA, A., TAKEMURA, Y., YOUN HAENG, J. & SANG GEUN, L. 2009. AC Magnetic-Field-Induced Heating and Physical Properties of Ferrite Nanoparticles for a Hyperthermia Agent in Medicine. *Nanotechnology, IEEE Transactions on*, 8, 86-94.
- BAKER, I., ZENG, Q., LI, W. & SULLIVAN, C. R. 2006. Heat deposition in iron oxide and iron nanoparticles for localized hyperthermia. *Journal of Applied Physics*, 99, 08H106.
- BALASUBRAMANIAN, S., GIRIJA, A. R., NAGAOKA, Y., IWAI, S., SUZUKI, M., KIZHIKILLOT, V., YOSHIDA, Y., MAEKAWA, T. & NAIR, S. D. 2014. Curcumin and 5-Fluorouracil-loaded, folate- and transferrin-decorated polymeric magnetic nanoformulation: a synergistic cancer therapeutic approach, accelerated by magnetic hyperthermia. *International Journal of Nanomedicine*, 9, 437-459.
- BANERJEE, R., KATSENOVICH, Y., LAGOS, L., MCIINTOSH, M., ZHANG, X. & LI, C. Z. 2010. Nanomedicine: Magnetic Nanoparticles and their Biomedical Applications. *Current Medicinal Chemistry*, 17, 3120-3141.
- BAÑOBRE-LÓPEZ, M., TEIJEIRO, A. & RIVAS, J. 2013. Magnetic nanoparticle-based hyperthermia for cancer treatment. *Reports of Practical Oncology & Radiotherapy*, 18, 397-400.

- BAPTISTA, A. L., COUTINHO, P. J., REAL OLIVEIRA, M. E. & GOMES, J. I. 2003. Effect of pH on the control release of microencapsulated dye in lecithin liposomes. II. *J Liposome Res*, 13, 123-30.
- BARNAKOV, Y. A., YU, M. H. & ROSENZWEIG, Z. 2005. Manipulation of the magnetic properties of magnetite-silica nanocomposite materials by controlled Stober synthesis. *Langmuir*, 21, 7524-7527.
- BARROS, M., FLEURI, L. F. & MACEDO, G. A. 2010. Seed lipases: sources, applications and properties - a review. *Brazilian Journal of Chemical Engineering*, 27, 15-29.
- BARROW, M., TAYLOR, A., MURRAY, P., ROSSEINSKY, M. J. & ADAMS, D. J. 2015. Design considerations for the synthesis of polymer coated iron oxide nanoparticles for stem cell labelling and tracking using MRI. *Chemical Society Reviews*, 44, 6733-6748.
- BEAUNE, G., MÉNAGER, C. & CABUIL, V. 2008. Location of magnetic and fluorescent nanoparticles encapsulated inside giant liposomes. *The Journal of Physical Chemistry B*, 112, 7424-7429.
- BEE, A., MASSART, R. & NEVEU, S. 1995. Synthesis of very fine maghemite particles. *Journal of Magnetism and Magnetic Materials*, 149, 6-9.
- BEHDADFAR, B., KERMANPUR, A., SADEGHI-ALIABADI, H., MORALES, M. D. P. & MOZAFFARI, M. 2012. Synthesis of high intrinsic loss power aqueous ferrofluids of iron oxide nanoparticles by citric acid-assisted hydrothermal-reduction route. *Journal of Solid State Chemistry*, 187, 20-26.
- BENJAMIN, S. & PANDEY, A. 1998a. Candida rugosa and its lipases: A retrospect. *Journal of scientific & industrial research*, 57, 1-9.
- BENJAMIN, S. & PANDEY, A. 1998b. Candida rugosa lipases: Molecular biology and versatility in biotechnology. *Yeast*, 14, 1069-1087.
- BENNETT, J. B. 2012. *Magnetic heating of Fe₃O₄ nanoparticles and magnetic micelles for a magnetothermally-triggered drug delivery system for cancer therapy*. UNIVERSITY OF ALABAMA.
- BERRY, C. C. & CURTIS, A. S. G. 2003. Functionalisation of magnetic nanoparticles for applications in biomedicine. *Journal of Physics D-Applied Physics*, 36, R198-R206.
- BERRY, C. C., WELLS, S., CHARLES, S. & CURTIS, A. S. 2003. Dextran and albumin derivatised iron oxide nanoparticles: influence on fibroblasts in vitro. *Biomaterials*, 24, 4551-4557.
- BHARDE, A., RAUTARAY, D., BANSAL, V., AHMAD, A., SARKAR, I., YUSUF, S. M., SANYAL, M. & SASTRY, M. 2006. Extracellular biosynthesis of magnetite using fungi. *Small*, 2, 135-141.
- BHARTI, C., NAGAICH, U., PAL, A. K. & GULATI, N. 2015. Mesoporous silica nanoparticles in target drug delivery system: A review. *International Journal of Pharmaceutical Investigation*, 5, 124-133.
- BLANCO-MANTECÓN, M. & O'GRADY, K. 2006. Interaction and size effects in magnetic nanoparticles. *Journal of Magnetism and Magnetic Materials*, 296, 124-133.
- BONCLER, M., RÓŻALSKI, M., KRAJEWSKA, U., PODSĘDEK, A. & WATALA, C. 2014. Comparison of PrestoBlue and MTT assays of cellular viability in the assessment of anti-proliferative effects of plant extracts on human endothelial cells. *Journal of Pharmacological and Toxicological Methods*, 69, 9-16.
- BONNAUD, C., MONNIER, C. A., DEMURTAS, D., JUD, C., VANHECKE, D., MONTET, X., HOVIUS, R., LATTUADA, M., ROTHEN-RUTISHAUSER, B. & PETRI-FINK, A. 2014. Insertion of nanoparticle clusters into vesicle bilayers. *ACS nano*, 8, 3451-3460.
- BORRELLI, G. M. & TRONO, D. 2015. Recombinant Lipases and Phospholipases and Their Use as Biocatalysts for Industrial Applications. *International Journal of Molecular Sciences*, 16, 20774-20840.
- BOSCOLO, B., TROTTA, F. & GHIBAUDI, E. 2010. High catalytic performances of Pseudomonas fluorescens lipase adsorbed on a new type of cyclodextrin-based nanosponges. *Journal of Molecular Catalysis B: Enzymatic*, 62, 155-161.

- BOTHUN, G. D. & PREISS, M. R. 2011. Bilayer heating in magnetite nanoparticle-liposome dispersions via fluorescence anisotropy. *Journal of Colloid and Interface Science*, 357, 70-74.
- BOYER, C., WHITTAKER, M. R., BULMUS, V., LIU, J. & DAVIS, T. P. 2010. The design and utility of polymer-stabilized iron-oxide nanoparticles for nanomedicine applications. *NPG Asia Mater*, 2, 23-30.
- BRADFORD, M. M. 1976. A rapid and sensitive method for the quantitation of microgram quantities of protein utilizing the principle of protein-dye binding. *Anal Biochem*, 72, 248-54.
- BRÄHLER, M., GEORGIEVA, R., BUSKE, N., MÜLLER, A., MÜLLER, S., PINKERNELLE, J., TEICHGRÄBER, U., VOIGT, A. & BÄUMLER, H. 2006. Magnetite-loaded carrier erythrocytes as contrast agents for magnetic resonance imaging. *Nano letters*, 6, 2505-2509.
- BRAVO-OSUNA, I., PONCHEL, G. & VAUTHIER, C. 2007. Tuning of shell and core characteristics of chitosan-decorated acrylic nanoparticles. *European journal of pharmaceutical sciences*, 30, 143-154.
- BRAZEL, C. S. 2008. Magnetothermally-responsive Nanomaterials: Combining Magnetic Nanostructures and Thermally-Sensitive Polymers for Triggered Drug Release. *Pharmaceutical Research*, 26, 644-656.
- BRAZEL, C. S. 2009. Magnetothermally-responsive nanomaterials: combining magnetic nanostructures and thermally-sensitive polymers for triggered drug release. *Pharm Res*, 26, 644-56.
- BRUCE, I. J. & SEN, T. 2005. Surface modification of magnetic nanoparticles with alkoxysilanes and their application in magnetic bioseparations. *Langmuir*, 21, 7029-7035.
- BRÜSEHABER, E., BÖTTCHER, D., LIEBETON, K., ECK, J., NAUMER, C. & BORNSCHEUER, U. T. 2008. Asymmetric synthesis of cis-3,5-diacetoxycyclopent-1-ene using metagenome-derived hydrolases. *Tetrahedron: Asymmetry*, 19, 730-732.
- CABRERA, L., GUTIERREZ, S., MENENDEZ, N., MORALES, M. P. & HERRASTI, P. 2008. Magnetite nanoparticles: Electrochemical synthesis and characterization. *Electrochimica Acta*, 53, 3436-3441.
- CADIRCI, B. H. & YASA, I. 2010. An organic solvents tolerant and thermotolerant lipase from *Pseudomonas fluorescens* P21. *Journal of Molecular Catalysis B: Enzymatic*, 64, 155-161.
- CAMPOS, E. A., PINTO, D., DE OLIVEIRA, J. I. S., MATTOS, E. D. & DUTRA, R. D. L. 2015. Synthesis, Characterization and Applications of Iron Oxide Nanoparticles - a Short Review. *Journal of Aerospace Technology and Management*, 7, 267-276.
- CARLSSON, N., GUSTAFSSON, H., THÖRN, C., OLSSON, L., HOLMBERG, K. & ÅKERMAN, B. 2014. Enzymes immobilized in mesoporous silica: a physical-chemical perspective. *Adv Colloid Interface Sci*, 205, 339-60.
- CARVALHO, A. C. L. D. M., FONSECA, T. D. S., DE MATTOS, M. C., DE OLIVEIRA, M. D. C. F., DE LEMOS, T. L. G., MOLINARI, F., ROMANO, D. & SERRA, I. 2015. Recent Advances in Lipase-Mediated Preparation of Pharmaceuticals and Their Intermediates. *International Journal of Molecular Sciences*, 16, 29682-29716.
- CHAKRABORTY, K. & PAULRAJ, R. 2009. Purification and biochemical characterization of an extracellular lipase from *Pseudomonas fluorescens* MTCC 2421. *J Agric Food Chem*, 57, 3859-66.
- CHAKRABORTY, M., JAIN, S. & RANI, V. 2011. Nanotechnology: Emerging Tool for Diagnostics and Therapeutics. *Applied Biochemistry and Biotechnology*, 165, 1178-1187.
- CHANG, B., SHA, X., GUO, J., JIAO, Y., WANG, C. & YANG, W. 2011. Thermo and pH dual responsive, polymer shell coated, magnetic mesoporous silica nanoparticles for controlled drug release. *Journal of Materials Chemistry*, 21, 9239-9247.
- CHANG, S.-F., CHANG, S.-W., YEN, Y.-H. & SHIEH, C.-J. 2007. Optimum immobilization of *Candida rugosa* lipase on Celite by RSM. *Applied Clay Science*, 37, 67-73.

- CHANG, S.-W., LEE, G.-C. & SHAW, J.-F. 2006. Codon Optimization of *Candida rugosa* lip1 Gene for Improving Expression in *Pichia pastoris* and Biochemical Characterization of the Purified Recombinant LIP1 Lipase. *Journal of Agricultural and Food Chemistry*, 54, 815-822.
- CHANG, Y., BAI, Y., TENG, B. & LI, Z. 2009. A new drug carrier: Magnetite nanoparticles coated with amphiphilic block copolymer. *Chinese Science Bulletin*, 54, 1190-1196.
- CHASTELLAIN, M., PETRI, A. & HOFMANN, H. 2004. Superparamagnetic iron oxide nanoparticles for biomedical applications: a focus on PVA as a coating. *Quantum Dots, Nanoparticles and Nanowires*, 269-272.
- CHEN, A. M., ZHANG, M., WEI, D., STUEBER, D., TARATULA, O., MINKO, T. & HE, H. 2009a. Co-delivery of Doxorubicin and Bcl-2 siRNA by Mesoporous Silica Nanoparticles Enhances the Efficacy of Chemotherapy in Multidrug-Resistant Cancer Cells. *Small*, 5, 2673-2677.
- CHEN, C. S., FUJIMOTO, Y., GIRDAUKAS, G. & SIH, C. J. 1982. Quantitative analyses of biochemical kinetic resolutions of enantiomers. *Journal of the American Chemical Society*, 104, 7294-7299.
- CHEN, D., JIANG, M., LI, N., GU, H., XU, Q., GE, J., XIA, X. & LU, J. 2010a. Modification of magnetic silica/iron oxide nanocomposites with fluorescent polymethacrylic acid for cancer targeting and drug delivery. *Journal of Materials Chemistry*, 20, 6422-6429.
- CHEN, J., WANG, Y. G., LI, Z. Q., WANG, C., LI, J. F. & GU, Y. J. 2009b. Synthesis and characterization of magnetic nanocomposites with Fe₃O₄ core. *Journal of Physics: Conference Series*, 152, 012041.
- CHEN, S. 2010. *Polymer-coated iron oxide nanoparticles for medical imaging*. PhD, Massachusetts Institute of Technology.
- CHEN, Y., BOSE, A. & BOTHUN, G. D. 2010b. Controlled release from bilayer-decorated magnetoliposomes via electromagnetic heating. *ACS nano*, 4, 3215-3221.
- CHEN, Y., CHEN, H., GUO, L., HE, Q., CHEN, F., ZHOU, J., FENG, J. & SHI, J. 2010c. Hollow/Rattle-Type Mesoporous Nanostructures by a Structural Difference-Based Selective Etching Strategy. *ACS Nano*, 4, 529-539.
- CHEN, Y., CHEN, H., ZENG, D., TIAN, Y., CHEN, F., FENG, J. & SHI, J. 2010d. Core/Shell Structured Hollow Mesoporous Nanocapsules: A Potential Platform for Simultaneous Cell Imaging and Anticancer Drug Delivery. *ACS Nano*, 4, 6001-6013.
- CHENG, D., HONG, G., WANG, W., YUAN, R., AI, H., SHEN, J., LIANG, B., GAO, J. & SHUAI, X. 2011. Nonclustered magnetite nanoparticle encapsulated biodegradable polymeric micelles with enhanced properties for in vivo tumor imaging. *Journal of Materials Chemistry*, 21, 4796-4804.
- CHERAGHIPOUR, E., JAVADPOUR, S. & MEHDIZADEH, A. R. 2012. Citrate capped superparamagnetic iron oxide nanoparticles used for hyperthermia therapy.
- CHERTOK, B., DAVID, A. E. & YANG, V. C. 2010. Polyethyleneimine-modified iron oxide nanoparticles for brain tumor drug delivery using magnetic targeting and intra-carotid administration. *Biomaterials*, 31, 6317-24.
- CHIANG, C.-L., SUNG, C.-S. & CHEN, C.-Y. 2006. Application of silica-magnetite nanocomposites to the isolation of ultrapure plasmid DNA from bacterial cells. *Journal of magnetism and magnetic materials*, 305, 483-490.
- CHIN, A. B. & YAACOB, I. I. 2007. Synthesis and characterization of magnetic iron oxide nanoparticles via w/o microemulsion and Massart's procedure. *Journal of materials processing technology*, 191, 235-237.
- CHIOU, S.-H. & WU, W.-T. 2004. Immobilization of *Candida rugosa* lipase on chitosan with activation of the hydroxyl groups. *Biomaterials*, 25, 197-204.
- CHON, C. H., KIHM, K. D., LEE, S. P. & CHOI, S. U. S. 2005. Empirical correlation finding the role of temperature and particle size for nanofluid (Al₂O₃) thermal conductivity enhancement. *Applied Physics Letters*, 87, 153107.
- CHUNFU, Z., JINQUAN, C., DUANZHI, Y., YONGXIAN, W., YANLIN, F. & JIAJÜ, T. 2004. Preparation and radiolabeling of human serum albumin (HSA)-coated magnetite

- nanoparticles for magnetically targeted therapy. *Applied Radiation and Isotopes*, 61, 1255-1259.
- CINTRA, E., FERREIRA, F., JUNIOR, J. S., CAMPELLO, J., SOCOLOVSKY, L., LIMA, E. & BAKUZIS, A. 2009a. Nanoparticle agglomerates in magnetoliposomes. *Nanotechnology*, 20, 045103.
- CINTRA, E. R., FERREIRA, F. S., JUNIOR, J. L. S., CAMPELLO, J. C., SOCOLOVSKY, L. M., LIMA, E. M. & BAKUZIS, A. F. 2009b. Nanoparticle agglomerates in magnetoliposomes. *Nanotechnology*, 20, 045103.
- CLARES, B., BIEDMA-ORTIZ, R. A., SÁEZ-FERNÁNDEZ, E., PRADOS, J. C., MELGUIZO, C., CABEZA, L., ORTIZ, R. & ARIAS, J. L. 2013. Nano-engineering of 5-fluorouracil-loaded magnetoliposomes for combined hyperthermia and chemotherapy against colon cancer. *European Journal of Pharmaceutics and Biopharmaceutics*, 85, 329-338.
- CLARK, M. J., HOMER, N., O'CONNOR, B. D., CHEN, Z., ESKIN, A., LEE, H., MERRIMAN, B. & NELSON, S. F. 2010. U87MG Decoded: The Genomic Sequence of a Cytogenetically Aberrant Human Cancer Cell Line. *PLoS Genetics*, 6, e1000832.
- CORDEIRO, A. L., LENK, T. & WERNER, C. 2011. Immobilization of Bacillus licheniformis alpha-amylase onto reactive polymer films. *J Biotechnol*, 154, 216-21.
- CORMA, A. 1997. From microporous to mesoporous molecular sieve materials and their use in catalysis. *Chemical Reviews*, 97, 2373-2419.
- CORMA, A., FORNES, V. & REY, F. 2002. Delaminated Zeolites: An Efficient Support for Enzymes. *Advanced Materials*, 14, 71-74.
- COULTHARD, G., ERB, W. & AGGARWAL, V. K. 2012. Stereocontrolled organocatalytic synthesis of prostaglandin PGF₂[agr] in seven steps. *Nature*, 489, 278-281.
- COVALIU, C. I., BERGER, D., MATEI, C., DIAMANDESCU, L., VASILE, E., CRISTEA, C., IONITA, V. & IOVU, H. 2011. Magnetic nanoparticles coated with polysaccharide polymers for potential biomedical applications. *Journal of Nanoparticle Research*, 13, 6169-6180.
- CUMMINGS, J., SPANSWICK, V. J., TOMASZ, M. & SMYTH, J. F. 1998. Enzymology of mitomycin C metabolic activation in tumour tissue: implications for enzyme-directed bio-reductive drug development. *Biochemical pharmacology*, 56, 405-414.
- CUONG, N.-V. & HSIEH, M.-F. 2009. Recent Advances in Pharmacokinetics of Polymeric Excipients Used in Nanosized Anti-Cancer Drugs. *Current Drug Metabolism*, 10, 842-850.
- CUONG, N.-V., HSIEH, M.-F., CHEN, Y.-T. & LIAU, I. 2010a. Synthesis and characterization of PEG-PCL-PEG triblock copolymers as carriers of doxorubicin for the treatment of breast cancer. *Journal of Applied Polymer Science*, 117, 3694-3703.
- CUONG, N.-V., JIANG, J.-L., LI, Y.-L., CHEN, J.-R., JWO, S.-C. & HSIEH, M.-F. 2010b. Doxorubicin-Loaded PEG-PCL-PEG Micelle Using Xenograft Model of Nude Mice: Effect of Multiple Administration of Micelle on the Suppression of Human Breast Cancer. *Cancers*, 3, 61.
- CUONG, N.-V., LI, Y.-L. & HSIEH, M.-F. 2012. Targeted delivery of doxorubicin to human breast cancers by folate-decorated star-shaped PEG-PCL micelle. *Journal of Materials Chemistry*, 22, 1006-1020.
- CUSHEN, M., KERRY, J., MORRIS, M., CRUZ-ROMERO, M. & CUMMINS, E. 2012. Nanotechnologies in the food industry – Recent developments, risks and regulation. *Trends in Food Science & Technology*, 24, 30-46.
- CUSHING, B. L., KOLESNICHENKO, V. L. & O'CONNOR, C. J. 2004. Recent advances in the liquid-phase syntheses of inorganic nanoparticles. *Chemical reviews*, 104, 3893-3946.
- CUYPER, M. & JONIAU, M. Magnetoliposomes. *European Biophysics Journal*, 15, 311-319.
- DAGLAR, B., OZGUR, E., CORMAN, M. E., UZUN, L. & DEMIREL, G. B. 2014. Polymeric nanocarriers for expected nanomedicine: current challenges and future prospects. *RSC Advances*, 4, 48639-48659.
- DANAFAR, H., DAVARAN, S., ROSTAMIZADEH, K., VALIZADEH, H. & HAMIDI, M. 2014. Biodegradable m-PEG/PCL Core-Shell Micelles: Preparation and Characterization as a Sustained Release Formulation for Curcumin. *Advanced Pharmaceutical Bulletin*, 4, 501-510.

- DANG, F., ENOMOTO, N., HOJO, J. & ENPUKU, K. 2008. A Novel Method to Synthesize Monodispersed Magnetite Nanoparticles. *Chemistry Letters*, 37, 530-531.
- DE SOUSA, M. E., FERNÁNDEZ VAN RAAP, M. B., RIVAS, P. C., MENDOZA ZÉLIS, P., GIRARDIN, P., PASQUEVICH, G. A., ALESSANDRINI, J. L., MURACA, D. & SÁNCHEZ, F. H. 2013. Stability and Relaxation Mechanisms of Citric Acid Coated Magnetite Nanoparticles for Magnetic Hyperthermia. *The Journal of Physical Chemistry C*, 117, 5436-5445.
- DEATSCH, A. E. & EVANS, B. A. 2014. Heating efficiency in magnetic nanoparticle hyperthermia. *Journal of Magnetism and Magnetic Materials*, 354, 163-172.
- DENG, Y.-H., WANG, C.-C., HU, J.-H., YANG, W.-L. & FU, S.-K. 2005. Investigation of formation of silica-coated magnetite nanoparticles via sol-gel approach. *Colloids and Surfaces A: Physicochemical and Engineering Aspects*, 262, 87-93.
- DENG, Y., QI, D., DENG, C., ZHANG, X. & ZHAO, D. 2008. Superparamagnetic high-magnetization microspheres with an Fe₃O₄@ SiO₂ core and perpendicularly aligned mesoporous SiO₂ shell for removal of microcystins. *Journal of the American Chemical Society*, 130, 28-29.
- DING, H. L., ZHANG, Y. X., WANG, S., XU, J. M., XU, S. C. & LI, G. H. 2012. Fe₃O₄@SiO₂ Core/Shell Nanoparticles: The Silica Coating Regulations with a Single Core for Different Core Sizes and Shell Thicknesses. *Chemistry of Materials*, 24, 4572-4580.
- DONG, J., XUE, M. & ZINK, J. I. 2013. Functioning of nanovalves on polymer coated mesoporous silica Nanoparticles. *Nanoscale*, 5, 10300-6.
- DORR, R. T., ALBERTS, D. S. & STONE, A. 1985. Cold protection and heat enhancement of doxorubicin skin toxicity in the mouse. *Cancer Treat Rep*, 69, 431-7.
- DRUMMOND, D. C., MEYER, O., HONG, K., KIRPOTIN, D. B. & PAPAHAJIOPOULOS, D. 1999. Optimizing liposomes for delivery of chemotherapeutic agents to solid tumors. *Pharmacol Rev*, 51, 691-743.
- DUAN, H., KUANG, M., WANG, X., WANG, Y. A., MAO, H. & NIE, S. 2008. Reexamining the Effects of Particle Size and Surface Chemistry on the Magnetic Properties of Iron Oxide Nanocrystals: New Insights into Spin Disorder and Proton Relaxivity. *The Journal of Physical Chemistry C*, 112, 8127-8131.
- DUNLOP, D. J. 1990. Developments in rock magnetism. *Reports on Progress in Physics*, 53, 707.
- DYAL, A., LOOS, K., NOTO, M., CHANG, S. W., SPAGNOLI, C., SHAFI, K. V. P. M., ULMAN, A., COWMAN, M. & GROSS, R. A. 2003. Activity of Candida rugosa Lipase Immobilized on γ -Fe₂O₃ Magnetic Nanoparticles. *Journal of the American Chemical Society*, 125, 1684-1685.
- E.Y.TSYMBAL. 2016. *Physics 927 | Physics & Astronomy | University of Nebraska–Lincoln* [Online]. University of Nebraska-Lincoln University of Nebraska-Lincoln Available: <http://unlcms.unl.edu/cas/physics/tsymbal/teaching/SSP-927/index.shtml>.
- EAG 2016. EAG | Energy Dispersive X-Ray Spectroscopy, EDS Analysis, Elemental Analysis.
- EL-BOUBBOU, K., AL-KAYSI, R. O., AL-MUHANNA, M. K., BAHHARI, H. M., AL-ROMAEH, A. I., DARWISH, N., AL-SAAD, K. O. & AL-SUWAIDAN, S. D. 2015. Ultra-Small Fatty Acid-Stabilized Magnetite Nanocolloids Synthesized by In Situ Hydrolytic Precipitation. *Journal of Nanomaterials*, 2015, 11.
- EL-TONI, A., IBRAHIM, M., LABIS, J., KHAN, A. & ALHOSHAN, M. 2013a. Optimization of Synthesis Parameters for Mesoporous Shell Formation on Magnetic Nanocores and Their Application as Nanocarriers for Docetaxel Cancer Drug. *International Journal of Molecular Sciences*, 14, 11496.
- EL-TONI, A. M., IBRAHIM, M. A., LABIS, J. P., KHAN, A. & ALHOSHAN, M. 2013b. Optimization of Synthesis Parameters for Mesoporous Shell Formation on Magnetic Nanocores and Their Application as Nanocarriers for Docetaxel Cancer Drug. *International Journal of Molecular Sciences*, 14, 11496-11509.
- ERNST, O. & ZOR, T. 2010. Linearization of the Bradford Protein Assay. *Journal of Visualized Experiments : JoVE*, 1918.

- ESTELRICH, J., ESCRIBANO, E., QUERALT, J. & BUSQUETS, M. 2015. Iron Oxide Nanoparticles for Magnetically-Guided and Magnetically-Responsive Drug Delivery. *International Journal of Molecular Sciences*, 16, 8070.
- ESTEVANATO, L. L., LACAVA, L. M., CARVALHO, L. C., AZEVEDO, R. B., SILVA, O., PELEGRINI, F., BÁO, S. N., MORAIS, P. C. & LACAVA, Z. G. 2012. Long-term biodistribution and biocompatibility investigation of dextran-coated magnetite nanoparticle using mice as the animal model. *Journal of biomedical nanotechnology*, 8, 301-308.
- FAJAROH, F., SETYAWAN, H., WIDIYASTUTI, W. & WINARDI, S. 2012. Synthesis of magnetite nanoparticles by surfactant-free electrochemical method in an aqueous system. *Advanced Powder Technology*, 23, 328-333.
- FARAJI, M., YAMINI, Y. & REZAEI, M. 2010. Magnetic nanoparticles: synthesis, stabilization, functionalization, characterization, and applications. *Journal of the Iranian Chemical Society*, 7, 1-37.
- FARIA, M. R., CRUZ, M. M., GONÇALVES, M. C., CARVALHO, A., FEIO, G. & MARTINS, M. B. F. 2013. Synthesis and characterization of magnetoliposomes for MRI contrast enhancement. *International Journal of Pharmaceutics*, 446, 183-190.
- FERLAY, J., SHIN, H.-R., BRAY, F., FORMAN, D., MATHERS, C. & PARKIN, D. M. 2010. Estimates of worldwide burden of cancer in 2008: GLOBOCAN 2008. *International Journal of Cancer*, 127, 2893-2917.
- FERLAY, J., SOERJOMATARAM, I., DIKSHIT, R., ESER, S., MATHERS, C., REBELO, M., PARKIN, D. M., FORMAN, D. & BRAY, F. 2015. Cancer incidence and mortality worldwide: Sources, methods and major patterns in GLOBOCAN 2012. *International Journal of Cancer*, 136, E359-E386.
- FERNÁNDEZ-LORENTE, G., PALOMO, J. M., FUENTES, M., MATEO, C., GUISÁN, J. M. & FERNÁNDEZ-LAFUENTE, R. 2003. Self-assembly of *Pseudomonas fluorescens* lipase into bimolecular aggregates dramatically affects functional properties. *Biotechnology and Bioengineering*, 82, 232-237.
- FERRARI, M. 2005. Cancer nanotechnology: Opportunities and challenges. *Nature Reviews Cancer*, 5, 161-171.
- FICKERS, P., MARTY, A. & NICAUD, J. M. 2011. The lipases from *Yarrowia lipolytica*: genetics, production, regulation, biochemical characterization and biotechnological applications. *Biotechnol Adv*, 29, 632-44.
- FORNARI, F. A., RANDOLPH, J. K., YALOWICH, J. C., RITKE, M. K. & GEWIRTZ, D. A. 1994. Interference by doxorubicin with DNA unwinding in MCF-7 breast tumor cells. *Mol Pharmacol*, 45, 649-56.
- FORTIN-RIPOCHE, J.-P., MARTINA, M. S., GAZEAU, F., MÉNAGER, C., WILHELM, C., BACRI, J.-C., LESIEUR, S. & CLÉMENT, O. 2006. Magnetic targeting of magnetoliposomes to solid tumors with MR imaging monitoring in mice: Feasibility 1. *Radiology*, 239, 415-424.
- FOX, P. F. & STEPANIAK, L. 1983. Isolation and some properties of extracellular heat-stable lipases from *Pseudomonas fluorescens* strain AFT 36. *Journal of Dairy Research*, 50, 77-89.
- FRANGER, S., BERTHET, P. & BERTHON, J. 2004. Electrochemical synthesis of Fe₃O₄ nanoparticles in alkaline aqueous solutions containing complexing agents. *Journal of Solid State Electrochemistry*, 8, 218-223.
- FRASCIONE, D., DIWOKY, C., ALMER, G., OPRIESSNIG, P., VONACH, C., GRADAUER, K., LEITINGER, G., MANGGE, H., STOLLBERGER, R. & PRASSL, R. 2012. Ultrasmall superparamagnetic iron oxide (USPIO)-based liposomes as magnetic resonance imaging probes. *International Journal of Nanomedicine*, 7, 2349-2359.
- FREEMAN, M. W., ARROTT, A. & WATSON, J. H. L. 1960. Magnetism in Medicine. *Journal of Applied Physics*, 31, S404-S405.
- FRIMPONG, R. A. & HILT, J. Z. 2010. Magnetic nanoparticles in biomedicine: synthesis, functionalization and applications. *Nanomedicine (Lond)*, 5, 1401-14.

- FRITZE, A., HENS, F., KIMPFLER, A., SCHUBERT, R. & PESCHKA-SÜSS, R. 2006. Remote loading of doxorubicin into liposomes driven by a transmembrane phosphate gradient. *Biochimica et Biophysica Acta (BBA) - Biomembranes*, 1758, 1633-1640.
- GABIZON, A. A., TZEMACH, D., HOROWITZ, A. T., SHMEEDA, H., YEY, J. & ZALIPSKY, S. 2006. Reduced Toxicity and Superior Therapeutic Activity of a Mitomycin C Lipid-Based Prodrug Incorporated in Pegylated Liposomes. *Clinical Cancer Research*, 12, 1913-1920.
- GAI, S., YANG, P., MA, P. A., WANG, D., LI, C., LI, X., NIU, N. & LIN, J. 2011. Fibrous-structured magnetic and mesoporous Fe₃O₄/silica microspheres: synthesis and intracellular doxorubicin delivery. *Journal of Materials Chemistry*, 21, 16420-16426.
- GAIHRE, B., KHIL, M. S., LEE, D. R. & KIM, H. Y. 2009. Gelatin-coated magnetic iron oxide nanoparticles as carrier system: drug loading and in vitro drug release study. *International Journal of Pharmaceutics*, 365, 180-189.
- GAO, F., BOTELLA, P., CORMA, A., BLESÁ, J. & DONG, L. 2009. Monodispersed mesoporous silica nanoparticles with very large pores for enhanced adsorption and release of DNA. *J Phys Chem B*, 113, 1796-804.
- GAO, M., LI, W., DONG, J., ZHANG, Z. & YANG, B. 2011. Synthesis and characterization of superparamagnetic Fe₃O₄@ SiO₂ core-shell composite nanoparticles. *World Journal of Condensed Matter Physics*, 1, 49.
- GAO, S., WANG, Y., DIAO, X., LUO, G. & DAI, Y. 2010. Effect of pore diameter and cross-linking method on the immobilization efficiency of *Candida rugosa* lipase in SBA-15. *Bioresource Technology*, 101, 3830-3837.
- GAO, X., WANG, B., WEI, X., RAO, W., AI, F., ZHAO, F., MEN, K., YANG, B., LIU, X., HUANG, M., GOU, M., QIAN, Z., HUANG, N. & WEI, Y. 2013. Preparation, characterization and application of star-shaped PCL/PEG micelles for the delivery of doxorubicin in the treatment of colon cancer. *International Journal of Nanomedicine*, 8, 971-982.
- GARCIA-JIMENO, S., ESCRIBANO, E., QUERALT, J. & ESTELRICH, J. 2011. Magnetoliposomes prepared by reverse-phase followed by sequential extrusion: characterization and possibilities in the treatment of inflammation. *Int J Pharm*, 405, 181-7.
- GARNIER, B., TAN, S., MIRAUX, S., BLEDE, E. & BRISSON, A. R. 2012. Optimized synthesis of 100 nm diameter magnetoliposomes with high content of maghemite particles and high MRI effect. *Contrast media & molecular imaging*, 7, 231-239.
- GARTMANN, N., SCHÜTZE, C., RITTER, H. & BRÜHWILER, D. 2010. The Effect of Water on the Functionalization of Mesoporous Silica with 3-Aminopropyltriethoxysilane. *The Journal of Physical Chemistry Letters*, 1, 379-382.
- GHARIB, A., FAEZIZADEH, Z., MESBAH-NAMIN, S. A. R. & SARAVANI, R. 2014. Preparation, characterization and in vitro efficacy of magnetic nanoliposomes containing the artemisinin and transferrin. *DARU Journal of Pharmaceutical Sciences*, 22, 44-44.
- GHORPADE, S. R., KHARUL, R. K., JOSHI, R. R., KALKOTE, U. R. & RAVINDRANATHAN *, T. 1999. Desymmetrization of meso-cyclopenten-cis-1,4-diol to 4-(R)-hydroxycyclopent-2-en-1-(S)-acetate by irreversible transesterification using Chirazyme®. *Tetrahedron: Asymmetry*, 10, 891-899.
- GIBSON, L. T. 2014. Mesosilica materials and organic pollutant adsorption: part B removal from aqueous solution. *Chemical Society Reviews*, 43, 5173-5182.
- GILCHRIST, R. K., MEDAL, R., SHOREY, W. D., HANSELMAN, R. C., PARROTT, J. C. & TAYLOR, C. B. 1957. Selective Inductive Heating of Lymph Nodes. *Annals of Surgery*, 146, 596-606.
- GIRI, S., SAMANTA, S., MAJI, S., GANGULI, S. & BHAUMIK, A. 2005. Magnetic properties of α -Fe₂O₃ nanoparticle synthesized by a new hydrothermal method. *Journal of Magnetism and Magnetic Materials*, 285, 296-302.
- GLOVER, A. L., BENNETT, J. B., PRITCHETT, J. S., NIKLES, S. M., NIKLES, D. E., NIKLES, J. A. & BRAZEL, C. S. 2013. Magnetic Heating of Iron Oxide Nanoparticles and Magnetic Micelles for Cancer Therapy. *IEEE transactions on magnetics*, 49, 231-235.
- GLOVER, A. L., NIKLES, S. M., NIKLES, J. A., BRAZEL, C. S. & NIKLES, D. E. 2012. Polymer Micelles with Crystalline Cores for Thermally Triggered Release. *Langmuir*, 28, 10653-10660.

- GOBE, M., KON-NO, K., KANDORI, K. & KITAHARA, A. 1983. Preparation and characterization of monodisperse magnetite sols in WO microemulsion. *Journal of Colloid and Interface Science*, 93, 293-295.
- GOHARDANI, O., ELOLA, M. C. & ELIZETXEA, C. 2014. Potential and prospective implementation of carbon nanotubes on next generation aircraft and space vehicles: A review of current and expected applications in aerospace sciences. *Progress in Aerospace Sciences*, 70, 42-68.
- GOLOVIN, Y. I., GRIBANOVSKII, S. L., GOLOVIN, D. Y., KLYACHKO, N. L. & KABANOV, A. V. 2014a. Single-domain magnetic nanoparticles in an alternating magnetic field as mediators of local deformation of the surrounding macromolecules. *Physics of the Solid State*, 56, 1342-1351.
- GOLOVIN, Y. I., GRIBANOVSKII, S. L., KLYACHKO, N. L. & KABANOV, A. V. 2014b. Nanomechanical control of the activity of enzymes immobilized on single-domain magnetic nanoparticles. *Technical Physics*, 59, 932-935.
- GONTERO, P., SARGENT, J. M., HOPSTER, D. J., LEWANDOWIC, G. M., TAYLOR, C. G., ELGIE, A. W., WILLIAMSON, C. J., SRIPRASAD, S. I. & MUIR, G. H. 2002. Ex vivo chemosensitivity to mitomycin C in bladder cancer and its relationship with P-glycoprotein and apoptotic factors. *Anticancer Res*, 22, 4073-80.
- GONZALEZ-FERNANDEZ, M. A., TORRES, T. E., ANDRÉS-VERGÉS, M., COSTO, R., DE LA PRESA, P., SERNA, C. J., MORALES, M. P., MARQUINA, C., IBARRA, M. R. & GOYA, G. F. 2009. Magnetic nanoparticles for power absorption: Optimizing size, shape and magnetic properties. *Journal of Solid State Chemistry*, 182, 2779-2784.
- GORDON, R. T., HINES, J. R. & GORDON, D. 1979. Intracellular hyperthermia a biophysical approach to cancer treatment via intracellular temperature and biophysical alterations. *Medical Hypotheses*, 5, 83-102.
- GOTTESMAN, M. M., FOJO, T. & BATES, S. E. 2002. Multidrug resistance in cancer: role of ATP-dependent transporters. *Nat Rev Cancer*, 2, 48-58.
- GOU, M. L., QIAN, Z. Y., WANG, H., TANG, Y. B., HUANG, M. J., KAN, B., WEN, Y. J., DAI, M., LI, X. Y., GONG, C. Y. & TU, M. J. 2008. Preparation and characterization of magnetic poly(epsilon-caprolactone)-poly(ethylene glycol)-poly(epsilon-caprolactone) microspheres. *J Mater Sci Mater Med*, 19, 1033-41.
- GREENE, R. F., COLLINS, J. M., JENKINS, J. F., SPEYER, J. L. & MYERS, C. E. 1983. Plasma pharmacokinetics of adriamycin and adriamycinol: implications for the design of in vitro experiments and treatment protocols. *Cancer Res*, 43, 3417-21.
- GROCHULSKI, P., LI, Y., SCHRAG, J., BOUTHILLIER, F., SMITH, P., HARRISON, D., RUBIN, B. & CYGLER, M. 1993. Insights into interfacial activation from an open structure of *Candida rugosa* lipase. *Journal of Biological Chemistry*, 268, 12843-12847.
- GULDHE, A., SINGH, B., RAWAT, I., PERMAUL, K. & BUX, F. 2015. Biocatalytic conversion of lipids from microalgae *Scenedesmus obliquus* to biodiesel using *Pseudomonas fluorescens* lipase. *Fuel*, 147, 117-124.
- GUPTA, A. K. & GUPTA, M. 2005. Synthesis and surface engineering of iron oxide nanoparticles for biomedical applications. *Biomaterials*, 26, 3995-4021.
- GUPTA, A. K. & WELLS, S. 2004. Surface-modified superparamagnetic nanoparticles for drug delivery: preparation, characterization, and cytotoxicity studies. *NanoBioscience, IEEE Transactions on*, 3, 66-73.
- GUPTA, N., RATHI, P. & GUPTA, R. 2002. Simplified para-nitrophenyl palmitate assay for lipases and esterases. *Analytical Biochemistry*, 311, 98-99.
- HÄFELI, U. O., RIFFLE, J. S., HARRIS-SHEKHAWAT, L., CARMICHAEL-BARANAUSKAS, A., MARK, F., DAILEY, J. P. & BARDENSTEIN, D. 2009. Cell uptake and in vitro toxicity of magnetic nanoparticles suitable for drug delivery. *Mol Pharm*, 6, 1417-28.
- HASAN, F., SHAH, A. A. & HAMEED, A. 2006. Industrial applications of microbial lipases. *Enzyme and Microbial Technology*, 39, 235-251.

- HAUL, R. 1982. S. J. Gregg, K. S. W. Sing: Adsorption, Surface Area and Porosity. 2. Auflage, Academic Press, London 1982. 303 Seiten, Preis: \$ 49.50. *Berichte der Bunsengesellschaft für physikalische Chemie*, 86, 957-957.
- HE, H., KUANG, H., YAN, L., MENG, F., XIE, Z., JING, X. & HUANG, Y. 2013. A reduction-sensitive carrier system using mesoporous silica nanospheres with biodegradable polyester as caps. *Physical Chemistry Chemical Physics*, 15, 14210-14218.
- HE, N., WANG, Z. & LI, S. DNA separation and amplification application of (Fe₃O₄/PMMA)/SiO₂ nanoparticles with core-shell structure. ABSTRACTS OF PAPERS OF THE AMERICAN CHEMICAL SOCIETY, 2006. AMER CHEMICAL SOC 1155 16TH ST, NW, WASHINGTON, DC 20036 USA.
- HE, Q., SHI, J., ZHU, M., CHEN, Y. & CHEN, F. 2010. The three-stage in vitro degradation behavior of mesoporous silica in simulated body fluid. *Microporous and Mesoporous Materials*, 131, 314-320.
- HEALTH, D. O. 2015. Department of Health Annual Report and Accounts.
- HELMI RASHID FARIMANI, M., SHAHTAHMASSEBI, N., REZAEI ROKNABADI, M. & GHOWS, N. 2013. Synthesis and study of structural and magnetic properties of superparamagnetic Fe₃O₄@ SiO₂ core/shell nanocomposite for biomedical applications. *Nanomedicine Journal*, 1, 71-78.
- HODGSON, B. 2014. *Immobilisation of Bio-molecules on Magnetisable Solid Supports for Applications in Bio-catalysts and Bio-sensors*. Doctoral, University of Central Lancashire.
- HOFFMANN, F., CORNELIUS, M., MORELL, J. & FRÖBA, M. 2006. Silica-Based Mesoporous Organic–Inorganic Hybrid Materials. *Angewandte Chemie International Edition*, 45, 3216-3251.
- HONG, G.-B., ZHOU, J.-X. & YUAN, R.-X. 2012. Folate-targeted polymeric micelles loaded with ultrasmall superparamagnetic iron oxide: combined small size and high MRI sensitivity. *International Journal of Nanomedicine*, 7, 2863-2872.
- HONG, G., YUAN, R., LIANG, B., SHEN, J., YANG, X. & SHUAI, X. 2008a. Folate-functionalized polymeric micelle as hepatic carcinoma-targeted, MRI-ultrasensitive delivery system of antitumor drugs. *Biomedical Microdevices*, 10, 693-700.
- HONG, G., YUAN, R., LIANG, B., SHEN, J., YANG, X. & SHUAI, X. 2008b. Folate-functionalized polymeric micelle as hepatic carcinoma-targeted, MRI-ultrasensitive delivery system of antitumor drugs. *Biomed Microdevices*, 10, 693-700.
- HONG, R., FISCHER, N. O., EMRICK, T. & ROTELLO, V. M. 2005. Surface PEGylation and ligand exchange chemistry of FePt nanoparticles for biological applications. *Chemistry of materials*, 17, 4617-4621.
- HONGZHANG, Q., BIAO, Y. & CHENGKUI, L. Preparation and magnetic properties of magnetite nanoparticles by sol-gel method. Nanoelectronics Conference (INEC), 2010 3rd International, 3-8 Jan. 2010 2010. 888-889.
- HOU, J., DONG, G., YE, Y. & CHEN, V. 2014. Enzymatic degradation of bisphenol-A with immobilized laccase on TiO₂ sol-gel coated PVDF membrane. *Journal of Membrane Science*, 469, 19-30.
- HOUDE, A., KADEMI, A. & LEBLANC, D. Lipases and their industrial applications. *Applied Biochemistry and Biotechnology*, 118, 155-170.
- HSIEH, M.-F., VAN CUONG, N., CHEN, C.-H., CHEN, Y. T. & YEH, J.-M. 2008. Nano-Sized Micelles of Block Copolymers of Methoxy Poly(ethylene glycol)-Poly(ϵ -caprolactone)-Graft-2-Hydroxyethyl Cellulose for Doxorubicin Delivery. *Journal of Nanoscience and Nanotechnology*, 8, 2362-2368.
- HSU, M.-H. & SU, Y.-C. 2008. Iron-oxide embedded solid lipid nanoparticles for magnetically controlled heating and drug delivery. *Biomedical Microdevices*, 10, 785-793.
- HU, B., PAN, J., YU, H.-L., LIU, J.-W. & XU, J.-H. 2009. Immobilization of *Serratia marcescens* lipase onto amino-functionalized magnetic nanoparticles for repeated use in enzymatic synthesis of Diltiazem intermediate. *Process Biochemistry*, 44, 1019-1024.

- HU, F., WEI, L., ZHOU, Z., RAN, Y., LI, Z. & GAO, M. 2006. Preparation of biocompatible magnetite nanocrystals for in vivo magnetic resonance detection of cancer. *Advanced Materials*, 18, 2553-2556.
- HUANG, C., TANG, Z., ZHOU, Y., ZHOU, X., JIN, Y., LI, D., YANG, Y. & ZHOU, S. 2012. Magnetic micelles as a potential platform for dual targeted drug delivery in cancer therapy. *International Journal of Pharmaceutics*, 429, 113-122.
- HUANG, I. P., SUN, S. P., CHENG, S. H., LEE, C. H., WU, C. Y., YANG, C. S., LO, L. W. & LAI, Y. K. 2011. Enhanced chemotherapy of cancer using pH-sensitive mesoporous silica nanoparticles to antagonize P-glycoprotein-mediated drug resistance. *Mol Cancer Ther*, 10, 761-9.
- INTORASOOT, S., SRIRUNG, R., INTORASOOT, A. & NGAMRATANAPAIBOON, S. 2009. Application of gelatin-coated magnetic particles for isolation of genomic DNA from bacterial cells. *Analytical biochemistry*, 386, 291-292.
- ISHIKAWA, T., KATAOKA, S. & KANDORI, K. 1993. The influence of carboxylate ions on the growth of β -FeOOH particles. *Journal of materials science*, 28, 2693-2698.
- ISHIKAWA, T., TAKEDA, T. & KANDORI, K. 1992. Effects of amines on the formation of β -ferric oxide hydroxide. *Journal of materials science*, 27, 4531-4535.
- ISO, M., CHEN, B., EGUCHI, M., KUDO, T. & SHRESTHA, S. 2001. Production of biodiesel fuel from triglycerides and alcohol using immobilized lipase. *Journal of Molecular Catalysis B: Enzymatic*, 16, 53-58.
- ITO, A., SHINKAI, M., HONDA, H. & KOBAYASHI, T. 2005. Medical application of functionalized magnetic nanoparticles. *Journal of Bioscience and Bioengineering*, 100, 1-11.
- IYER, A. K., KHALED, G., FANG, J. & MAEDA, H. 2006. Exploiting the enhanced permeability and retention effect for tumor targeting. *Drug Discov Today*, 11, 812-8.
- JAEGER, K. E., RANSAC, S., DIJKSTRA, B. W., COLSON, C., HEUVEL, M. & MISSET, O. 1994. Bacterial lipases. *FEMS microbiology reviews*, 15, 29-63.
- JANA, N. R., CHEN, Y. & PENG, X. 2004. Size-and shape-controlled magnetic (Cr, Mn, Fe, Co, Ni) oxide nanocrystals via a simple and general approach. *Chemistry of materials*, 16, 3931-3935.
- JARRETT, B. R., FRENDO, M., VOGAN, J. & LOUIE, A. Y. 2007. Size-controlled synthesis of dextran sulfate coated iron oxide nanoparticles for magnetic resonance imaging. *Nanotechnology*, 18, 035603.
- JENNIE P. MATHER, P. E. R. 2007. *Introduction to Cell and Tissue Culture: Theory and Technique*, Springer Science & Business Media.
- JOHANSEN, M., GNEVECKOW, U., ECKELT, L., FEUSSNER, A., WALDÖFNER, N., SCHOLZ, R., DEGER, S., WUST, P., LOENING, S. & JORDAN, A. 2005a. Clinical hyperthermia of prostate cancer using magnetic nanoparticles: presentation of a new interstitial technique. *International journal of hyperthermia*, 21, 637-647.
- JOHANSEN, M., GNEVECKOW, U., ECKELT, L., FEUSSNER, A., WALDÖFNER, N., SCHOLZ, R., DEGER, S., WUST, P., LOENING, S. A. & JORDAN, A. 2005b. Clinical hyperthermia of prostate cancer using magnetic nanoparticles: Presentation of a new interstitial technique. *International Journal of Hyperthermia*, 21, 637-647.
- JOHANSEN, M., GNEVECKOW, U., TAYMOORIAN, K., THIESEN, B., WALDOFNER, N., SCHOLZ, R., JUNG, K., JORDAN, A., WUST, P. & LOENING, S. A. 2007. Morbidity and quality of life during thermotherapy using magnetic nanoparticles in locally recurrent prostate cancer: results of a prospective phase I trial. *Int J Hyperthermia*, 23, 315-23.
- JOHNSON, A. K., ZAWADZKA, A. M., DEOBALD, L. A., CRAWFORD, R. L. & PASZCZYNSKI, A. J. 2007. Novel method for immobilization of enzymes to magnetic nanoparticles. *Journal of Nanoparticle Research*, 10, 1009-1025.
- JOHNSON, E. A. 2013. Biotechnology of non-Saccharomyces yeasts-the basidiomycetes. *Appl Microbiol Biotechnol*, 97, 7563-77.
- JORDAN, A., SCHOLZ, R., MAIER-HAUFF, K., VAN LANDEGHEM, F. K. H., WALDOEFNER, N., TEICHGRAEBER, U., PINKERNELLE, J., BRUHN, H., NEUMANN, F., THIESEN, B., VON

- DEIMLING, A. & FELIX, R. 2006. The effect of thermotherapy using magnetic nanoparticles on rat malignant glioma. *J Neurooncol*, 78, 7-14.
- JORDAN, A., SCHOLZ, R., WUST, P., SCHIRRA, H., THOMAS, S., SCHMIDT, H. & FELIX, R. 1999. Endocytosis of dextran and silan-coated magnetite nanoparticles and the effect of intracellular hyperthermia on human mammary carcinoma cells in vitro. *Journal of Magnetism and Magnetic Materials*, 194, 185-196.
- JORDAN, A., WUST, P., SCHOLZ, R., TESCHE, B., FÄHLING, H., MITROVICS, T., VOGL, T., CERVÓS-NAVARRO, J. & FELIX, R. 1996. Cellular uptake of magnetic fluid particles and their effects on human adenocarcinoma cells exposed to AC magnetic fields in vitro. *International Journal of Hyperthermia*, 12, 705-722.
- JUANG, J.-H., WANG, J.-J., SHEN, C.-R., KUO, C.-H., CHIEN, Y.-W., KUO, H.-Y., TSAI, Z.-T. & YEN, T.-C. Magnetic resonance imaging of transplanted mouse islets labeled with chitosan-coated superparamagnetic iron oxide nanoparticles. *Transplantation proceedings*, 2010. Elsevier, 2104-2108.
- JULIAN-LOPEZ, B., BOISSIERE, C., CHANEAC, C., GROSSO, D., VASSEUR, S., MIRAUX, S., DUGUET, E. & SANCHEZ, C. 2007. Mesoporous maghemite-organosilica microspheres: a promising route towards multifunctional platforms for smart diagnosis and therapy. *Journal of Materials Chemistry*, 17, 1563-1569.
- JURGONS, R., SELIGER, C., HILPERT, A., TRAHMS, L., ODENBACH, S. & ALEXIOU, C. 2006. Drug loaded magnetic nanoparticles for cancer therapy. *Journal of Physics: Condensed Matter*, 18, S2893.
- KALKAN, N. A., AKSOY, S., AKSOY, E. A. & HASIRCI, N. 2012. Preparation of chitosan-coated magnetite nanoparticles and application for immobilization of laccase. *Journal of Applied Polymer Science*, 123, 707-716.
- KALKOTE, U. R., GHORPADE, S. R., JOSHI, R. R., RAVINDRANATHAN *, T., BASTAWADE, K. B. & GOKHALE, D. V. 2000. A practical and scalable process for 4-(R)-hydroxycyclopent-2-en-1-(S)-acetate by desymmetrization of meso-cyclopent-2-en-1,4-diacetate catalyzed by *Trichosporon beigellii* (NCIM 3326), a cheap biocatalyst†. *Tetrahedron: Asymmetry*, 11, 2965-2970.
- KALLUMADIL, M., TADA, M., NAKAGAWA, T., ABE, M., SOUTHERN, P. & PANKHURST, Q. A. 2009. Suitability of commercial colloids for magnetic hyperthermia. *Journal of Magnetism and Magnetic Materials*, 321, 1509-1513.
- KALO, P., HUOTARI, H. & ANTILA, M. 1989. *Pseudomonas fluorescens* Lipase-catalysed Interesterification of Butter Fat. *Lipid / Fett*, 91, 276-281.
- KANDORI, K., KAWASHIMA, Y. & ISHIKAWA, T. 1992. Effects of citrate ions on the formation of monodispersed cubic hematite particles. *Journal of colloid and interface science*, 152, 284-288.
- KAPSE-MISTRY, S., GOVENDER, T., SRIVASTAVA, R. & YERGERI, M. 2014. Nanodrug delivery in reversing multidrug resistance in cancer cells. *Frontiers in Pharmacology*, 5, 159.
- KÄTZEL, U. 2007. *Dynamic Light Scattering for the Characterization of Polydisperse Fractal Systems by the Example of Pyrogenic Silica*. DEng, Technischen Universität Dresden.
- KAWAI, N., ITO, A., NAKAHARA, Y., HONDA, H., KOBAYASHI, T., FUTAKUCHI, M., SHIRAI, T., TOZAWA, K. & KOHRI, K. 2006. Complete regression of experimental prostate cancer in nude mice by repeated hyperthermia using magnetite cationic liposomes and a newly developed solenoid containing a ferrite core. *Prostate*, 66, 718-27.
- KEDAR, U., PHUTANE, P., SHIDHAYE, S. & KADAM, V. 2010. Advances in polymeric micelles for drug delivery and tumor targeting. *Nanomedicine: Nanotechnology, Biology and Medicine*, 6, 714-729.
- KHALKHALI, M., ROSTAMIZADEH, K., SADIGHIAN, S., KHOEINI, F., NAGHIBI, M. & HAMIDI, M. 2015. The impact of polymer coatings on magnetite nanoparticles performance as MRI contrast agents: a comparative study. *DARU Journal of Pharmaceutical Sciences*, 23, 45.

- KHOEE, S., BAGHERI, Y. & HASHEMI, A. 2015. Composition controlled synthesis of PCL-PEG Janus nanoparticles: magnetite nanoparticles prepared from one-pot photo-click reaction. *Nanoscale*, 7, 4134-4148.
- KHOLLAM, Y., DHAGE, S., POTDAR, H., DESHPANDE, S., BAKARE, P., KULKARNI, S. & DATE, S. 2002. Microwave hydrothermal preparation of submicron-sized spherical magnetite (Fe₃O₄) powders. *Materials Letters*, 56, 571-577.
- KIEVIT, F. M., WANG, F. Y., FANG, C., MOK, H., WANG, K., SILBER, J. R., ELLENBOGEN, R. G. & ZHANG, M. 2011. Doxorubicin loaded iron oxide nanoparticles overcome multidrug resistance in cancer in vitro. *Journal of Controlled Release*, 152, 76-83.
- KIM, D.-H., VITOL, E. A., LIU, J., BALASUBRAMANIAN, S., GOSZTOLA, D. J., COHEN, E. E., NOVOSAD, V. & ROZHKOVA, E. A. 2013. Stimuli-Responsive Magnetic Nanomicelles as Multifunctional Heat and Cargo Delivery Vehicles. *Langmuir*, 29, 7425-7432.
- KIM, D. K., MIKHAYLOVA, M., WANG, F. H., KEHR, J., BJELKE, B., ZHANG, Y., TSAKALAKOS, T. & MUHAMMED, M. 2003. Starch-coated superparamagnetic nanoparticles as MR contrast agents. *Chemistry of Materials*, 15, 4343-4351.
- KIM, E. H., LEE, H. S., KWAK, B. K. & KIM, B.-K. 2005a. Synthesis of ferrofluid with magnetic nanoparticles by sonochemical method for MRI contrast agent. *Journal of Magnetism and Magnetic Materials*, 289, 328-330.
- KIM, J., KIM, H. S., LEE, N., KIM, T., KIM, H., YU, T., SONG, I. C., MOON, W. K. & HYEON, T. 2008. Multifunctional uniform nanoparticles composed of a magnetite nanocrystal core and a mesoporous silica shell for magnetic resonance and fluorescence imaging and for drug delivery. *Angew Chem Int Ed Engl*, 47, 8438-41.
- KIM, K. R., KWON, D. Y., YOON, S. H., KIM, W. Y. & KIM, K. H. 2005b. Purification, refolding, and characterization of recombinant *Pseudomonas fluorescens* lipase. *Protein Expression and Purification*, 39, 124-129.
- KINDSTEDT, P., CARIĆ, M. & MILANOVIĆ, S. 2004. Pasta-filata cheeses. In: PATRICK F. FOX, P. L. H. M. T. M. C. & TIMOTHY, P. G. (eds.) *Cheese: Chemistry, Physics and Microbiology*. Academic Press.
- KIREITSEU, M., TOMLINSON, G. & BASENUK, V. Design and Manufacturing Concepts of Nanoparticle-reinforced Aerospace Materials. Cleantech 2007: the Cleantech Conference, Venture Forum and Trade Show, May 23-24, 2007, Santa Clara, California, USA, 2007. CRC, 238.
- KLEM, M. T., YOUNG, M. & DOUGLAS, T. 2005. Biomimetic magnetic nanoparticles. *Materials Today*, 8, 28-37.
- KLYACHKO, N. L., SOKOLSKY-PAPKOV, M., POTHAYEE, N., EFREMOVA, M. V., GULIN, D. A., POTHAYEE, N., KUZNETSOV, A. A., MAJOUGA, A. G., RIFFLE, J. S., GOLOVIN, Y. I. & KABANOV, A. V. 2012. Changing the Enzyme Reaction Rate in Magnetic Nanosuspensions by a Non-Heating Magnetic Field. *Angewandte Chemie International Edition*, 51, 12016-12019.
- KNEZEVIC, N. Z. & LIN, V. S. 2013. A magnetic mesoporous silica nanoparticle-based drug delivery system for photosensitive cooperative treatment of cancer with a mesopore-capping agent and mesopore-loaded drug. *Nanoscale*, 5, 1544-51.
- KOBAYASHI, T. 2011. Cancer hyperthermia using magnetic nanoparticles. *Biotechnology Journal*, 6, 1342-1347.
- KOBAYASHI, Y., HORIE, M., KONNO, M., RODRÍGUEZ-GONZÁLEZ, B. & LIZ-MARZÁN, L. M. 2003. Preparation and properties of silica-coated cobalt nanoparticles. *The Journal of Physical Chemistry B*, 107, 7420-7425.
- KOMARNENI, S. 2003. Nanophase materials by hydrothermal, microwave-hydrothermal and microwave-solvothermal methods. *CURRENT SCIENCE-BANGALORE*, 85, 1730-1734.
- KOMURA, S., SHIMOKAWA, N. & ANDELMAN, D. 2006. Tension-Induced Morphological Transition in Mixed Lipid Bilayers. *Langmuir*, 22, 6771-6774.
- KONG, J., COOLAHAN, K. & MUGWERU, A. 2013. Manganese based magnetic nanoparticles for heavy metal detection and environmental remediation. *Analytical Methods*, 5, 5128-5133.

- KOUTZAROVA, T., KOLEV, S., GHELEV, C., PANEVA, D. & NEDKOV, I. 2006. Microstructural study and size control of iron oxide nanoparticles produced by microemulsion technique. *physica status solidi (c)*, 3, 1302-1307.
- KULKARNI, S. A., SAWADH, P. & PALEI, P. K. 2014. Synthesis and Characterization of Superparamagnetic Fe₃O₄@ SiO₂ Nanoparticles. *J. Korean Chem. Soc*, 58.
- KULSHRESTHA, P., GOGOI, M., BAHADUR, D. & BANERJEE, R. 2012. In vitro application of paclitaxel loaded magnetoliposomes for combined chemotherapy and hyperthermia. *Colloids Surf B Biointerfaces*, 96, 1-7.
- KUMAR, C. S. S. R. & MOHAMMAD, F. 2011. Magnetic nanomaterials for hyperthermia-based therapy and controlled drug delivery. *Advanced Drug Delivery Reviews*, 63, 789-808.
- KUMARI, A., YADAV, S. K. & YADAV, S. C. 2010. Biodegradable polymeric nanoparticles based drug delivery systems. *Colloids and Surfaces B: Biointerfaces*, 75, 1-18.
- KUNDU, A., NANDI, S., DAS, P. & NANDI, A. K. 2015. Fluorescent graphene oxide via polymer grafting: an efficient nanocarrier for both hydrophilic and hydrophobic drugs. *ACS Appl Mater Interfaces*, 7, 3512-23.
- KWON, G. S. 2003. Polymeric Micelles for Delivery of Poorly Water-Soluble Compounds. 20, 47.
- LACAVA, L., LACAVA, Z., DA SILVA, M., SILVA, O., CHAVES, S., AZEVEDO, R. B. D., PELEGRINI, F., GANSAU, C., BUSKE, N. & SABOLOVIC, D. 2001. Magnetic resonance of a dextran-coated magnetic fluid intravenously administered in mice. *Biophysical Journal*, 80, 2483-2486.
- LACONTE, L. E. W., NITIN, N., ZURKIYA, O., CARUNTU, D., O'CONNOR, C. J., HU, X. & BAO, G. 2007. Coating thickness of magnetic iron oxide nanoparticles affects R2 relaxivity. *Journal of Magnetic Resonance Imaging*, 26, 1634-1641.
- LALL, N., HENLEY-SMITH, C. J., DE CANHA, M. N., OOSTHUIZEN, C. B. & BERRINGTON, D. 2013. Viability Reagent, PrestoBlue, in Comparison with Other Available Reagents, Utilized in Cytotoxicity and Antimicrobial Assays. *International Journal of Microbiology*, 2013, 5.
- LARIOS, A., GARCIA, H. S., OLIART, R. M. & VALERIO-ALFARO, G. 2004. Synthesis of flavor and fragrance esters using *Candida antarctica* lipase. *Appl Microbiol Biotechnol*, 65, 373-6.
- LE, B., SHINKAI, M., KITADE, T., HONDA, H., YOSHIDA, J. U. N., WAKABAYASHI, T. & KOBAYASHI, T. 2001. Preparation of Tumor-Specific Magnetoliposomes and Their Application for Hyperthermia. *JOURNAL OF CHEMICAL ENGINEERING OF JAPAN*, 34, 66-72.
- LEE, H., YU, M. K., PARK, S., MOON, S., MIN, J. J., JEONG, Y. Y., KANG, H.-W. & JON, S. 2007. Thermally cross-linked superparamagnetic iron oxide nanoparticles: synthesis and application as a dual imaging probe for cancer in vivo. *Journal of the American Chemical Society*, 129, 12739-12745.
- LEE, H. Y., LIM, N. H., SEO, J., KHANG, G., KIM, J., LEE, H. & CHO, S. 2005a. Preparation of poly (vinylpyrrolidone) coated iron oxide nanoparticles for contrast agent. *Polymer (Korea)*, 29, 266.
- LEE, J., ISOBE, T. & SENNA, M. 1996. Magnetic properties of ultrafine magnetite particles and their slurries prepared via in-situ precipitation. *Colloids and Surfaces A: Physicochemical and Engineering Aspects*, 109, 121-127.
- LEE, J. E., LEE, N., KIM, H., KIM, J., CHOI, S. H., KIM, J. H., KIM, T., SONG, I. C., PARK, S. P., MOON, W. K. & HYEON, T. 2010. Uniform Mesoporous Dye-Doped Silica Nanoparticles Decorated with Multiple Magnetite Nanocrystals for Simultaneous Enhanced Magnetic Resonance Imaging, Fluorescence Imaging, and Drug Delivery. *Journal of the American Chemical Society*, 132, 552-557.
- LEE, L.-C., YEN, C.-C., MALMIS, C. C., CHEN, L.-F., CHEN, J.-C., LEE, G.-C. & SHAW, J.-F. 2011. Characterization of Codon-Optimized Recombinant *Candida rugosa* Lipase 5 (LIP5). *Journal of Agricultural and Food Chemistry*, 59, 10693-10698.
- LEE, Y., LEE, J., BAE, C. J., PARK, J. G., NOH, H. J., PARK, J. H. & HYEON, T. 2005b. Large-Scale Synthesis of Uniform and Crystalline Magnetite Nanoparticles Using Reverse Micelles as Nanoreactors under Reflux Conditions. *Advanced Functional Materials*, 15, 503-509.

- LEI, L., LING-LING, J., YUN, Z. & GANG, L. 2013. Toxicity of superparamagnetic iron oxide nanoparticles: Research strategies and implications for nanomedicine. *Chinese Physics B*, 22, 127503.
- LEIS, B., ANGELOV, A., MIENTUS, M., LI, H., PHAM, V. T. T., LAUINGER, B., BONGEN, P., PIETRUSZKA, J., GONÇALVES, L. G., SANTOS, H. & LIEBL, W. 2015. Identification of novel esterase-active enzymes from hot environments by use of the host bacterium *Thermus thermophilus*. *Frontiers in Microbiology*, 6, 275.
- LELLOUCHE, J.-P., SENTHIL, G., JOSEPH, A., BUZHANSKY, L., BRUCE, I., BAUMINGER, E. R. & SCHLESINGER, J. 2005. Magnetically responsive carboxylated magnetite-polydipyrrole/polydicarbazole nanocomposites of core-shell morphology. Preparation, characterization, and use in DNA hybridization. *Journal of the American Chemical Society*, 127, 11998-12006.
- LEMKE, A. J., SENFFT VON PILSACH, M. I., LUBBE, A., BERGEMANN, C., RIESS, H. & FELIX, R. 2004. MRI after magnetic drug targeting in patients with advanced solid malignant tumors. *Eur Radiol*, 14, 1949-55.
- LI, C., ZHANG, Y., SU, T., FENG, L., LONG, Y. & CHEN, Z. 2012a. Silica-coated flexible liposomes as a nanohybrid delivery system for enhanced oral bioavailability of curcumin. *International Journal of Nanomedicine*, 7, 5995-6002.
- LI, H., YAN, K., SHANG, Y., SHRESTHA, L., LIAO, R., LIU, F., LI, P., XU, H., XU, Z. & CHU, P. K. 2015a. Folate-bovine serum albumin functionalized polymeric micelles loaded with superparamagnetic iron oxide nanoparticles for tumor targeting and magnetic resonance imaging. *Acta Biomaterialia*, 15, 117-126.
- LI, J., WANG, X., ZHANG, T., WANG, C., HUANG, Z., LUO, X. & DENG, Y. 2015b. A review on phospholipids and their main applications in drug delivery systems. *Asian Journal of Pharmaceutical Sciences*, 10, 81-98.
- LI, X., LI, H., LIU, G., DENG, Z., WU, S., LI, P., XU, Z., XU, H. & CHU, P. K. 2012b. Magnetite-loaded fluorine-containing polymeric micelles for magnetic resonance imaging and drug delivery. *Biomaterials*, 33, 3013-3024.
- LI, Y., WU, H., YANG, X., JIA, M., LI, Y., HUANG, Y., LIN, J., WU, S. & HOU, Z. 2014a. Mitomycin C-Soybean Phosphatidylcholine Complex-Loaded Self-Assembled PEG-Lipid-PLA Hybrid Nanoparticles for Targeted Drug Delivery and Dual-Controlled Drug Release. *Molecular Pharmaceutics*, 11, 2915-2927.
- LI, Y., WU, H., YANG, X., JIA, M., LI, Y., HUANG, Y., LIN, J., WU, S. & HOU, Z. 2014b. Mitomycin C-soybean phosphatidylcholine complex-loaded self-assembled PEG-lipid-PLA hybrid nanoparticles for targeted drug delivery and dual-controlled drug release. *Mol Pharm*, 11, 2915-27.
- LI, Z., SUN, Q. & GAO, M. 2005. Preparation of water-soluble magnetite nanocrystals from hydrated ferric salts in 2-pyrrolidone: mechanism leading to Fe₃O₄. *Angewandte Chemie International Edition*, 44, 123-126.
- LIANG, M.-T., WANG, S.-H., CHANG, Y.-L., HSIANG, H.-I., HUANG, H.-J., TSAI, M.-H., JUAN, W.-C. & LU, S.-F. 2010. Iron oxide synthesis using a continuous hydrothermal and solvothermal system. *Ceramics International*, 36, 1131-1135.
- LIBERMAN, A., MENDEZ, N., TROGLER, W. C. & KUMMEL, A. C. 2014. Synthesis and surface functionalization of silica nanoparticles for nanomedicine. *Surface Science Reports*, 69, 132-158.
- LIEN, Y.-H. & WU, T.-M. 2008. Preparation and characterization of thermosensitive polymers grafted onto silica-coated iron oxide nanoparticles. *Journal of Colloid and Interface Science*, 326, 517-521.
- LIFE-TECHNOLOGIES. 2014. PrestoBlue® Cell Viability Reagent [Online]. life technologies. Available: <http://www.lifetechnologies.com/order/catalog/product/A13261?ICID=cvc-prestoblue-c1t1>.
- LIM, Y. T., LEE, K. Y., LEE, K. & CHUNG, B. H. 2006. Immobilization of histidine-tagged proteins by magnetic nanoparticles encapsulated with nitrilotriacetic acid (NTA)-phospholipids micelle. *Biochemical and Biophysical Research Communications*, 344, 926.

- LIMA, L. N., OLIVEIRA, G. C., ROJAS, M. J., CASTRO, H. F., RÓS, P. C. M., MENDES, A. A., GIORDANO, R. L. C. & TARDIOLI, P. W. 2015. Immobilization of *Pseudomonas fluorescens* lipase on hydrophobic supports and application in biodiesel synthesis by transesterification of vegetable oils in solvent-free systems. *Journal of Industrial Microbiology & Biotechnology*, 42, 523-535.
- LIN-AI, T., PI-JU, T., YU-CHAO, W., YU-JING, W., LEU-WEI, L. & CHUNG-SHI, Y. 2009. Thermosensitive liposomes entrapping iron oxide nanoparticles for controllable drug release. *Nanotechnology*, 20, 135101.
- LINEMANN, T., THOMSEN, L., JARDIN, K., LAURSEN, J., JENSEN, J., LICHOTA, J. & MOOS, T. 2013. Development of a Novel Lipophilic, Magnetic Nanoparticle for in Vivo Drug Delivery. *Pharmaceutics*, 5, 246.
- LINGJIE, W., MING, W., YONGYI, Z., DA, Z., AIXIAN, Z., XIAOLONG, L. & JINGFENG, L. 2015. Multifunctional PEG modified DOX loaded mesoporous silica nanoparticle@CuS nanohybrids as photo-thermal agent and thermal-triggered drug release vehicle for hepatocellular carcinoma treatment. *Nanotechnology*, 26, 025102.
- LINKO, Y. Y. & YAN WU, X. 1996. Biocatalytic production of useful esters by two forms of lipase from *Candida rugosa*. *Journal of chemical technology and biotechnology*, 65, 163-170.
- LIU, F., LIU, S., HE, S., XIE, Z., ZU, X. & JIANG, Y. 2010. Survivin transcription is associated with P-glycoprotein/MDR1 overexpression in the multidrug resistance of MCF-7 breast cancer cells. *Oncol Rep*, 23, 1469-75.
- LIU, H.-L., KO, S. P., WU, J.-H., JUNG, M.-H., MIN, J. H., LEE, J. H., AN, B. H. & KIM, Y. K. 2007. One-pot polyol synthesis of monosize PVP-coated sub-5nm Fe₃O₄ nanoparticles for biomedical applications. *Journal of Magnetism and Magnetic Materials*, 310, e815-e817.
- LIU, J., DETREMBLEUR, C., DE PAUW-GILLET, M.-C., MORNET, S., ELST, L. V., LAURENT, S., JEROME, C. & DUGUET, E. 2014a. Heat-triggered drug release systems based on mesoporous silica nanoparticles filled with a maghemite core and phase-change molecules as gatekeepers. *Journal of Materials Chemistry B*, 2, 59-70.
- LIU, J., JIANG, X., ASHLEY, C. & BRINKER, C. J. 2009a. Electrostatically Mediated Liposome Fusion and Lipid Exchange with a Nanoparticle-Supported Bilayer for Control of Surface Charge, Drug Containment, and Delivery. *Journal of the American Chemical Society*, 131, 7567-7569.
- LIU, J., QIAO, S. Z., CHEN, J. S., LOU, X. W., XING, X. & LU, G. Q. 2011. Yolk/shell nanoparticles: new platforms for nanoreactors, drug delivery and lithium-ion batteries. *Chemical Communications*, 47, 12578-12591.
- LIU, J., STACE-NAUGHTON, A., JIANG, X. & BRINKER, C. J. 2009b. Porous Nanoparticle Supported Lipid Bilayers (Protocells) as Delivery Vehicles. *Journal of the American Chemical Society*, 131, 1354-1355.
- LIU, Q., ZHANG, J., SUN, W., XIE, Q. R., XIA, W. & GU, H. 2012. Delivering hydrophilic and hydrophobic chemotherapeutics simultaneously by magnetic mesoporous silica nanoparticles to inhibit cancer cells. *International Journal of Nanomedicine*, 7, 999-1013.
- LIU, X., GUAN, Y., MA, Z. & LIU, H. 2004a. Surface modification and characterization of magnetic polymer nanospheres prepared by miniemulsion polymerization. *Langmuir*, 20, 10278-10282.
- LIU, X., WANG, Q., LI, C., ZOU, R., LI, B., SONG, G., XU, K., ZHENG, Y. & HU, J. 2014b. Cu₂-xSe@mSiO₂-PEG core-shell nanoparticles: a low-toxic and efficient difunctional nanopatform for chemo-photothermal therapy under near infrared light radiation with a safe power density. *Nanoscale*, 6, 4361-4370.
- LIU, Z. L., WANG, H. B., LU, Q. H., DU, G. H., PENG, L., DU, Y. Q., ZHANG, S. M. & YAO, K. L. 2004b. Synthesis and characterization of ultrafine well-dispersed magnetic nanoparticles. *Journal of Magnetism and Magnetic Materials*, 283, 258-262.

- LIU, Z. L., WANG, X., YAO, K. L., DU, G. H., LU, Q. H., DING, Z. H., TAO, J., NING, Q., LUO, X. P., TIAN, D. Y. & XI, D. 2004c. Synthesis of magnetite nanoparticles in W/O microemulsion. *Journal of Materials Science*, 39, 2633-2636.
- LOPEZ, J. A., GONZÁLEZ, F., BONILLA, F. A., ZAMBRANO, G. & GÓMEZ, M. E. 2010. Synthesis and characterization of Fe₃O₄ magnetic nanofluid. *Revista Latinoamericana de Metalurgia y Materiales*, 30, 60-66.
- LOU, X. W., ARCHER, L. A. & YANG, Z. 2008. Hollow Micro-/Nanostructures: Synthesis and Applications. *Advanced Materials*, 20, 3987-4019.
- LU, A.-H., SALABAS, E. L. & SCHÜTH, F. 2007a. Magnetic Nanoparticles: Synthesis, Protection, Functionalization, and Application. *Angewandte Chemie International Edition*, 46, 1222-1244.
- LU, A. H., SALABAS, E. E. L. & SCHÜTH, F. 2007b. Magnetic nanoparticles: synthesis, protection, functionalization, and application. *Angewandte Chemie International Edition*, 46, 1222-1244.
- LU, A. H., SCHMIDT, W., MATOUSSEVITCH, N., BONNEMANN, H., SPLIETHOFF, B., TESCHE, B., BILL, E., KIEFER, W. & SCHÜTH, F. 2004. Nanoengineering of a magnetically separable hydrogenation catalyst. *Angew Chem Int Ed Engl*, 43, 4303-6.
- LU, C.-W., HUNG, Y., HSIAO, J.-K., YAO, M., CHUNG, T.-H., LIN, Y.-S., WU, S.-H., HSU, S.-C., LIU, H.-M., MOU, C.-Y., YANG, C.-S., HUANG, D.-M. & CHEN, Y.-C. 2006. Bifunctional Magnetic Silica Nanoparticles for Highly Efficient Human Stem Cell Labeling. *Nano Letters*, 7, 149-154.
- LU, C.-W., HUNG, Y., HSIAO, J.-K., YAO, M., CHUNG, T.-H., LIN, Y.-S., WU, S.-H., HSU, S.-C., LIU, H.-M., MOU, C.-Y., YANG, C.-S., HUANG, D.-M. & CHEN, Y.-C. 2007c. Bifunctional Magnetic Silica Nanoparticles for Highly Efficient Human Stem Cell Labeling. *Nano Letters*, 7, 149-154.
- LU, C., BHATT, L. R., JUN, H. Y., PARK, S. H. & CHAI, K. Y. 2012. Carboxyl-polyethylene glycol-phosphoric acid: a ligand for highly stabilized iron oxide nanoparticles. *Journal of Materials Chemistry*, 22, 19806-19811.
- LU, J., LIONG, M., LI, Z., ZINK, J. I. & TAMANOI, F. 2010a. Biocompatibility, Biodistribution, and Drug-Delivery Efficiency of Mesoporous Silica Nanoparticles for Cancer Therapy in Animals. *Small (Weinheim an der Bergstrasse, Germany)*, 6, 1794-1805.
- LU, J., LIONG, M., LI, Z., ZINK, J. I. & TAMANOI, F. 2010b. Biocompatibility, Biodistribution, and Drug-Delivery Efficiency of Mesoporous Silica Nanoparticles for Cancer Therapy in Animals. *Small*, 6, 1794-1805.
- LU, J., LIONG, M., ZINK, J. I. & TAMANOI, F. 2007d. Mesoporous Silica Nanoparticles as a Delivery System for Hydrophobic Anticancer Drugs. *Small*, 3, 1341-1346.
- LUBBE, A. S., BERGEMANN, C., RIESS, H., SCHRIEVER, F., REICHARDT, P., POSSINGER, K., MATTHIAS, M., DORKEN, B., HERRMANN, F., GURTLER, R., HOHENBERGER, P., HAAS, N., SOHR, R., SANDER, B., LEMKE, A. J., OHLENDORF, D., HUHN, W. & HUHN, D. 1996. Clinical experiences with magnetic drug targeting: a phase I study with 4'-epidoxorubicin in 14 patients with advanced solid tumors. *Cancer Res*, 56, 4686-93.
- LUO, S., WANG, L., DING, W., WANG, H., ZHOU, J., JIN, H., SU, S. & OUYANG, W. 2014. Clinical trials of magnetic induction hyperthermia for treatment of tumours. *OA Cancer* 2.
- LÜPERTZ, R., WÄTJEN, W., KAHL, R. & CHOVOLOU, Y. 2010. Dose- and time-dependent effects of doxorubicin on cytotoxicity, cell cycle and apoptotic cell death in human colon cancer cells. *Toxicology*, 271, 115-121.
- LV, Y., LIU, H., WANG, Z., LIU, S., HAO, L., SANG, Y., LIU, D., WANG, J. & BOUGHTON, R. I. 2009. Silver nanoparticle-decorated porous ceramic composite for water treatment. *Journal of Membrane Science*, 331, 50-56.
- MA, M., WU, Y., ZHOU, J., SUN, Y., ZHANG, Y. & GU, N. 2004. Size dependence of specific power absorption of Fe₃O₄ particles in AC magnetic field. *Journal of Magnetism and Magnetic Materials*, 268, 33-39.

- MA, M., ZHANG, Y., YU, W., SHEN, H.-Y., ZHANG, H.-Q. & GU, N. 2003. Preparation and characterization of magnetite nanoparticles coated by amino silane. *Colloids and Surfaces A: Physicochemical and Engineering Aspects*, 212, 219-226.
- MA, Y.-H., WU, S.-Y., WU, T., CHANG, Y.-J., HUA, M.-Y. & CHEN, J.-P. 2009. Magnetically targeted thrombolysis with recombinant tissue plasminogen activator bound to polyacrylic acid-coated nanoparticles. *Biomaterials*, 30, 3343-3351.
- MACRAE, A. & HAMMOND, R. 1985. Present and future applications of lipases. *Biotechnology and Genetic Engineering Reviews*, 3, 193-218.
- MAGDASSI, S., GROUCHKO, M. & KAMYSHNY, A. 2010. Copper Nanoparticles for Printed Electronics: Routes Towards Achieving Oxidation Stability. *Materials*, 3, 4626.
- MAGFORCE 2016. MagForce AG " NanoTherm", Ç.
- MAHMOUDI, M., SANT, S., WANG, B., LAURENT, S. & SEN, T. 2011. Superparamagnetic iron oxide nanoparticles (SPIONs): Development, surface modification and applications in chemotherapy. *Advanced Drug Delivery Reviews*, 63, 24-46.
- MAHMOUDI, M., SIMCHI, A., IMANI, M., MILANI, A. S. & STROEVE, P. 2008. Optimal design and characterization of superparamagnetic iron oxide nanoparticles coated with polyvinyl alcohol for targeted delivery and imaging†. *The Journal of Physical Chemistry B*, 112, 14470-14481.
- MAHMOUDI, M., SIMCHI, A., MILANI, A. & STROEVE, P. 2009. Cell toxicity of superparamagnetic iron oxide nanoparticles. *Journal of colloid and interface science*, 336, 510-518.
- MAIER-HAUFF, K., ROTHE, R., SCHOLZ, R., GNEVECKOW, U., WUST, P., THIESEN, B., FEUSSNER, A., VON DEIMLING, A., WALDOEFNER, N., FELIX, R. & JORDAN, A. 2007. Intracranial thermotherapy using magnetic nanoparticles combined with external beam radiotherapy: results of a feasibility study on patients with glioblastoma multiforme. *J Neurooncol*, 81, 53-60.
- MAIER-HAUFF, K., ULRICH, F., NESTLER, D., NIEHOFF, H., WUST, P., THIESEN, B., ORAWA, H., BUDACH, V. & JORDAN, A. 2011. Efficacy and safety of intratumoral thermotherapy using magnetic iron-oxide nanoparticles combined with external beam radiotherapy on patients with recurrent glioblastoma multiforme. *J Neurooncol*, 103, 317-24.
- MAITYT, D., PRADHAN, P., CHANDRASEKHARAN, P., KALE, S. N., SHUTER, B., BAHADUR, D., FENG, S. S., XUE, J. M. & DING, J. 2011. Synthesis of hydrophilic superparamagnetic magnetite nanoparticles via thermal decomposition of Fe(acac)₃ in 80 vol% TREG + 20 vol% TREM. *J Nanosci Nanotechnol*, 11, 2730-4.
- MAL, N. K., FUJIWARA, M. & TANAKA, Y. 2003. Photocontrolled reversible release of guest molecules from coumarin-modified mesoporous silica. *Nature*, 421, 350-3.
- MALIK, S., CUSIDÓ, R. M., MIRJALILI, M. H., MOYANO, E., PALAZÓN, J. & BONFILL, M. 2011. Production of the anticancer drug taxol in *Taxus baccata* suspension cultures: A review. *Process Biochemistry*, 46, 23-34.
- MALVERN 2011. DYNAMIC LIGHT SCATTERING COMMON TERMS DEFINED. Malvern Instruments Worldwide: Malvern Instruments Worldwide.
- MAMANI, J. B., COSTA-FILHO, A. J., CORNEJO, D. R., VIEIRA, E. D. & GAMARRA, L. F. 2013. Synthesis and characterization of magnetite nanoparticles coated with lauric acid. *Materials Characterization*, 81, 28-36.
- MARSZAŁŁ, M. P. & SIÓDMIĄK, T. 2012. Immobilization of *Candida rugosa* lipase onto magnetic beads for kinetic resolution of (R,S)-ibuprofen. *Catalysis Communications*, 24, 80-84.
- MARTINA, M.-S., FORTIN, J.-P., MÉNAGER, C., CLÉMENT, O., BARRATT, G., GRABIELLE-MADELMONT, C., GAZEAU, F., CABUIL, V. & LESIEUR, S. 2005. Generation of superparamagnetic liposomes revealed as highly efficient MRI contrast agents for in vivo imaging. *Journal of the American Chemical Society*, 127, 10676-10685.
- MASCOLO, M., PEI, Y. & RING, T. 2013. Room Temperature Co-Precipitation Synthesis of Magnetite Nanoparticles in a Large pH Window with Different Bases. *Materials*, 6, 5549.

- MASSART, R. 1981. PREPARATION OF AQUEOUS MAGNETIC LIQUIDS IN ALKALINE AND ACIDIC MEDIA. *Ieee Transactions on Magnetics*, 17, 1247-1248.
- MATEO, C., TORRES, R., FERNANDEZ-LORENTE, G., ORTIZ, C., FUENTES, M., HIDALGO, A., LOPEZ-GALLEGO, F., ABIAN, O., PALOMO, J. M., BETANCOR, L., PESSELA, B. C. C., GUISAN, J. M. & FERNANDEZ-LAFUENTE, R. 2003. Epoxy-amino groups: A new tool for improved immobilization of proteins by the epoxy method. *Biomacromolecules*, 4, 772-777.
- MATHEW, D. S. & JUANG, R.-S. 2007. An overview of the structure and magnetism of spinel ferrite nanoparticles and their synthesis in microemulsions. *Chemical Engineering Journal*, 129, 51-65.
- MATSUMAE, H., FURUI, M. & SHIBATANI, T. 1993. Lipase-catalyzed asymmetric hydrolysis of 3-phenylglycidic acid ester, the key intermediate in the synthesis of diltiazem hydrochloride. *Journal of Fermentation and Bioengineering*, 75, 93-98.
- MATSUMOTO, S., YAMAMOTO, A., TAKAKURA, Y., HASHIDA, M., TANIGAWA, N. & SEZAKI, H. 1986. Cellular Interaction and in Vitro Antitumor Activity of Mitomycin C-Dextran Conjugate. *Cancer Research*, 46, 4463-4468.
- MATSUNAGA, T., OKAMURA, Y. & TANAKA, T. 2004. Biotechnological application of nano-scale engineered bacterial magnetic particles. *Journal of Materials Chemistry*, 14, 2099-2105.
- MCBAIN, S. C., YIU, H. H. P. & DOBSON, J. 2008. Magnetic nanoparticles for gene and drug delivery. *International Journal of Nanomedicine*, 3, 169-180.
- MEDEIROS, S. F., SANTOS, A. M., FESSI, H. & ELAISSARI, A. 2011. Stimuli-responsive magnetic particles for biomedical applications. *International Journal of Pharmaceutics*, 403, 139-161.
- MEDINA, C., SANTOS-MARTINEZ, M. J., RADOMSKI, A., CORRIGAN, O. I. & RADOMSKI, M. W. 2007. Nanoparticles: pharmacological and toxicological significance. *British Journal of Pharmacology*, 150, 552-558.
- MEINCKE, M., SCHLORF, T., KOSSEL, E., JANSEN, O., GLUEER, C.-C. & MENTLEIN, R. 2007. Iron oxide-loaded liposomes for MR imaging. *Frontiers in bioscience: a journal and virtual library*, 13, 4002-4008.
- MENG, H., MAI, W. X., ZHANG, H., XUE, M., XIA, T., LIN, S., WANG, X., ZHAO, Y., JI, Z., ZINK, J. I. & NEL, A. E. 2013. Co-delivery of an Optimal Drug/siRNA Combination Using Mesoporous Silica Nanoparticle to Overcome Drug Resistance in Breast Cancer In Vitro and In Vivo. *ACS nano*, 7, 994-1005.
- MERCER, T. & BISSELL, P. R. 2013. The Observed Linearity and Detection Response of Magnetic Fluid Concentration Magnetometry; A Theoretical and Experimental Description. *Magnetics, IEEE Transactions on*, 49, 3516-3519.
- MERCER, T., BISSELL, P. R. & GILSON, R. G. 2002. Measurement of hindered settling in magnetic dispersions. *Magnetics, IEEE Transactions on*, 38, 3219-3221.
- MERCER, T., BISSELL, P. R., GOTAAS, J. A. & GILSON, R. G. 1999. Hindered settling of particulate dispersions. *Journal of Magnetism and Magnetic Materials*, 193, 284-287.
- MIGNEAULT, I., DARTIGUENAVE, C., BERTRAND, M. J. & WALDRON, K. C. 2004. Glutaraldehyde: behavior in aqueous solution, reaction with proteins, and application to enzyme crosslinking. *Biotechniques*, 37, 790-806.
- MILAŠINOVIĆ, N., JAKOVETIĆ, S., KNEŽEVIĆ-JUGOVIĆ, Z., MILOSAVLJEVIĆ, N., LUČIĆ, M., FILIPOVIĆ, J. & KRUŠIĆ, M. K. 2014. Catalyzed Ester Synthesis Using *Candida rugosa* Lipase Entrapped by Poly(N-isopropylacrylamide-co-itaconic Acid) Hydrogel. *The Scientific World Journal*, 2014, 10.
- MIRANDA, M., URIOSTE, D., ANDRADE SOUZA, L. T., MENDES, A. A. & DE CASTRO, H. F. 2011. Assessment of the Morphological, Biochemical, and Kinetic Properties for *Candida rugosa* Lipase Immobilized on Hydrous Niobium Oxide to Be Used in the Biodiesel Synthesis. *Enzyme Research*, 2011, 10.

- MIZUKI, T., SAWAI, M., NAGAOKA, Y., MORIMOTO, H. & MAEKAWA, T. 2013. Activity of Lipase and Chitinase Immobilized on Superparamagnetic Particles in a Rotational Magnetic Field. *PLoS ONE*, 8, e66528.
- MIZUKI, T., WATANABE, N., NAGAOKA, Y., FUKUSHIMA, T., MORIMOTO, H., USAMI, R. & MAEKAWA, T. 2010. Activity of an enzyme immobilized on superparamagnetic particles in a rotational magnetic field. *Biochemical and Biophysical Research Communications*, 393, 779-782.
- MODY, V., COX, A., SHAH, S., SINGH, A., BEVINS, W. & PARIHAR, H. 2014. Magnetic nanoparticle drug delivery systems for targeting tumor. *Applied Nanoscience*, 4, 385-392.
- MOGHIMI, S. M. & SZEBENI, J. 2003. Stealth liposomes and long circulating nanoparticles: critical issues in pharmacokinetics, opsonization and protein-binding properties. *Progress in lipid research*, 42, 463-478.
- MOHAN, P. & RAPOPORT, N. 2010. Doxorubicin as a Molecular Nanotheranostic Agent: Effect of Doxorubicin Encapsulation in Micelles or Nanoemulsions on the Ultrasound-Mediated Intracellular Delivery and Nuclear Trafficking. *Molecular Pharmaceutics*, 7, 1959-1973.
- MØLLER, A. C. & OLSEN, L. F. 1999. Effect of Magnetic Fields on an Oscillating Enzyme Reaction. *Journal of the American Chemical Society*, 121, 6351-6354.
- MONNIER, C. A., BURNAND, D., ROTHEN-RUTISHAUSER, B., LATTUADA, M. & PETRI-FINK, A. 2014. Magnetoliposomes: opportunities and challenges. *European Journal of Nanomedicine*, 6, 201-215.
- MONNIER CHRISTOPHE, A., BURNAND, D., ROTHEN-RUTISHAUSER, B., LATTUADA, M. & PETRI-FINK, A. 2014. Magnetoliposomes: opportunities and challenges. *European Journal of Nanomedicine*.
- MONTERO, G. 2011. BIODIESEL-FEEDSTOCKS AND PROCESSING TECHNOLOGIES.
- MOON, J. H., SHIN, J. W., KIM, S. Y. & PARK, J. W. 1996. Formation of Uniform Aminosilane Thin Layers: An Imine Formation To Measure Relative Surface Density of the Amine Group. *Langmuir*, 12, 4621-4624.
- MORENO-PEREZ, S., LUNA, P., SENORANS, F. J., GUISAN, J. M. & FERNANDEZ-LORENTE, G. 2015. Enzymatic synthesis of triacylglycerols of docosahexaenoic acid: Transesterification of its ethyl esters with glycerol. *Food Chemistry*, 187, 225-229.
- MORNET, S., LAMBERT, O., DUGUET, E. & BRISSON, A. 2005. The Formation of Supported Lipid Bilayers on Silica Nanoparticles Revealed by Cryoelectron Microscopy. *Nano Letters*, 5, 281-285.
- MORNET, S., VASSEUR, S., GRASSET, F. & DUGUET, E. 2004. Magnetic nanoparticle design for medical diagnosis and therapy. *Journal of Materials Chemistry*, 14, 2161-2175.
- MOTOYAMA, J., HAKATA, T., KATO, R., YAMASHITA, N., MORINO, T., KOBAYASHI, T. & HONDA, H. 2008a. Size dependent heat generation of magnetite nanoparticles under AC magnetic field for cancer therapy. *Biomagnetic Research and Technology*, 6, 4-4.
- MOTOYAMA, J., HAKATA, T., KATO, R., YAMASHITA, N., MORINO, T., KOBAYASHI, T. & HONDA, H. 2008b. Size dependent heat generation of magnetite nanoparticles under AC magnetic field for cancer therapy. *BioMagnetic Research and Technology*, 6, 4.
- MÜLLER, R., HERGT, R., ZEISBERGER, M. & GAWALEK, W. 2005. Preparation of magnetic nanoparticles with large specific loss power for heating applications. *Journal of Magnetism and Magnetic Materials*, 289, 13-16.
- MURRAY, C., KAGAN, C. & BAWENDI, M. 2000. Synthesis and characterisation of monodisperse nanocrystals and close-packed nanocrystal assemblies. *Annu Rev Mater Sci*, 30, 545 - 610.
- NADERI, M. 2015. Chapter Fourteen - Surface Area: Brunauer–Emmett–Teller (BET) A2 - Tarleton, Steve. *Progress in Filtration and Separation*. Oxford: Academic Press.
- NAKAMURA, T., SUGIHARA, F., MATSUSHITA, H., YOSHIOKA, Y., MIZUKAMI, S. & KIKUCHI, K. 2015. Mesoporous silica nanoparticles for ¹⁹F magnetic resonance imaging, fluorescence imaging, and drug delivery. *Chemical Science*, 6, 1986-1990.

- NAMBOODIRI, V. V. & VARMA, R. S. 2001. Microwave-accelerated Suzuki cross-coupling reaction in polyethylene glycol (PEG). *Green Chem.*, 3, 146-148.
- NANO. 2016. *What's So Special about the Nanoscale?* | Nano [Online]. Nano.Gov: Official website of the United States National Nanotechnology Initiative. Available: <http://www.nano.gov/nanotech-101/special>.
- NANOCOMPOSIX 2012. NANOCOMPOSIX'S GUIDE TO DYNAMIC LIGHT SCATTERING MEASUREMENT AND ANALYSIS. nanoComposix.
- NAPPINI, S., BOMBELLI, F. B., BONINI, M., NORDEN, B. & BAGLIONI, P. 2010. Magnetoliposomes for controlled drug release in the presence of low-frequency magnetic field. *Soft Matter*, 6, 154-162.
- NARASIMHAN, B., PRABHAKAR, S., MANOHAR, P. & GNANAM, F. 2002. Synthesis of gamma ferric oxide by direct thermal decomposition of ferrous carbonate. *Materials Letters*, 52, 295-300.
- NARITA, A., NAKA, K. & CHUJO, Y. 2009. Facile control of silica shell layer thickness on hydrophilic iron oxide nanoparticles via reverse micelle method. *Colloids and Surfaces A: Physicochemical and Engineering Aspects*, 336, 46-56.
- NASONGKLA, N., BEY, E., REN, J., AI, H., KHEMTONG, C., GUTHI, J. S., CHIN, S.-F., SHERRY, A. D., BOOTHMAN, D. A. & GAO, J. 2006. Multifunctional Polymeric Micelles as Cancer-Targeted, MRI-Ultrasensitive Drug Delivery Systems. *Nano Letters*, 6, 2427-2430.
- NATALIE, A. F. & SHOUHENG, S. 2010. Magnetic Nanoparticle for Information Storage Applications. *Inorganic Nanoparticles*. CRC Press.
- NAVE, R. 2016. *Hysteresis in magnetic materials* [Online]. Available: <http://hyperphysics.phy-astr.gsu.edu/hbase/solids/hyst.html>.
- NÉEL, L. 1953. Thermoremanent Magnetization of Fine Powders. *Reviews of Modern Physics*, 25, 293-295.
- NEWSMEDICAL 2014. Avastin (Bevacizumab) Price.
- NGUYEN, T. D., TSENG, H. R., CELESTRE, P. C., FLOOD, A. H., LIU, Y., STODDART, J. F. & ZINK, J. I. 2005. A reversible molecular valve. *Proc Natl Acad Sci U S A*, 102, 10029-34.
- NICOLAS, J., MURA, S., BRAMBILLA, D., MACKIEWICZ, N. & COUVREUR, P. 2013. Design, functionalization strategies and biomedical applications of targeted biodegradable/biocompatible polymer-based nanocarriers for drug delivery. *Chemical Society Reviews*, 42, 1147-1235.
- NIMNI, M. E., CHEUNG, D., STRATES, B., KODAMA, M. & SHEIKH, K. 1987. Chemically modified collagen: A natural biomaterial for tissue replacement. *Journal of Biomedical Materials Research*, 21, 741-771.
- NOBUTO, H., SUGITA, T., KUBO, T., SHIMOSE, S., YASUNAGA, Y., MURAKAMI, T. & OCHI, M. 2004. Evaluation of systemic chemotherapy with magnetic liposomal doxorubicin and a dipole external electromagnet. *Int J Cancer*, 109, 627-35.
- NORTHFELT, D. W., DEZUBE, B. J., THOMMES, J. A., MILLER, B. J., FISCHL, M. A., FRIEDMAN-KIEN, A., KAPLAN, L. D., DU MOND, C., MAMELOK, R. D. & HENRY, D. H. 1998. Pegylated-liposomal doxorubicin versus doxorubicin, bleomycin, and vincristine in the treatment of AIDS-related Kaposi's sarcoma: results of a randomized phase III clinical trial. *Journal of clinical oncology*, 16, 2445-2451.
- O'SHAUGHNESSY, J. A. 2003. Pegylated liposomal doxorubicin in the treatment of breast cancer. *Clin Breast Cancer*, 4, 318-28.
- OGINO, H. & ISHIKAWA, H. 2001. Enzymes which are stable in the presence of organic solvents. *Journal of Bioscience and Bioengineering*, 91, 109-116.
- OSMAN, A.-M. M., BAYOUMI, H. M., AL-HARTHI, S. E., DAMANHOURI, Z. A. & ELSHAL, M. F. 2012. Modulation of doxorubicin cytotoxicity by resveratrol in a human breast cancer cell line. *Cancer Cell Int*, 12, 47.
- OTA, S., YAMAZAKI, N., TOMITAKA, A., YAMADA, T. & TAKEMURA, Y. 2014. Hyperthermia Using Antibody-Conjugated Magnetic Nanoparticles and Its Enhanced Effect with Cryptotanshinone. *Nanomaterials*, 4, 319.

- OTSUKA, H., NAGASAKI, Y. & KATAOKA, K. 2003. PEGylated nanoparticles for biological and pharmaceutical applications. *Advanced Drug Delivery Reviews*, 55, 403-419.
- OVERGAARD, J., GONZALEZ GONZALEZ, D., HULSHOF, M. C., ARCANGELI, G., DAHL, O., MELLA, O. & BENTZEN, S. M. 2009. Hyperthermia as an adjuvant to radiation therapy of recurrent or metastatic malignant melanoma. A multicentre randomized trial by the European Society for Hyperthermic Oncology. 1996. *Int J Hyperthermia*, 25, 323-34.
- PADWAL, P., BANDYOPADHYAYA, R. & MEHRA, S. 2014. Polyacrylic Acid-Coated Iron Oxide Nanoparticles for Targeting Drug Resistance in Mycobacteria. *Langmuir*, 30, 15266-15276.
- PAN, J., WAN, D. & GONG, J. 2011. PEGylated liposome coated QDs/mesoporous silica core-shell nanoparticles for molecular imaging. *Chemical Communications*, 47, 3442-3444.
- PANKHURST, Q., CONNOLLY, J., JONES, S. & DOBSON, J. 2003a. Applications of magnetic nanoparticles in biomedicine. *J Phys D: Appl Phys*, 36, R167 - R181.
- PANKHURST, Q. A., CONNOLLY, J., JONES, S. K. & DOBSON, J. 2003b. Applications of magnetic nanoparticles in biomedicine. *Journal of Physics D: Applied Physics*, 36, R167.
- PANKHURST, Q. A., CONNOLLY, J., JONES, S. K. & DOBSON, J. 2003c. Applications of magnetic nanoparticles in biomedicine. *Journal of Physics D-Applied Physics*, 36, R167-R181.
- PANKHURST, Q. A., THANH, N. T. K., JONES, S. K. & DOBSON, J. 2009. Progress in applications of magnetic nanoparticles in biomedicine. *Journal of Physics D: Applied Physics*, 42, 224001.
- PARK, J., AN, K., HWANG, Y., PARK, J.-G., NOH, H.-J., KIM, J.-Y., PARK, J.-H., HWANG, N.-M. & HYEON, T. 2004. Ultra-large-scale syntheses of monodisperse nanocrystals. *Nat Mater*, 3, 891-895.
- PARK, J. H., SARAVANAKUMAR, G., KIM, K. & KWON, I. C. 2010. Targeted delivery of low molecular drugs using chitosan and its derivatives. *Advanced Drug Delivery Reviews*, 62, 28-41.
- PATEL, R. N., BANERJEE, A., KO, R. Y., HOWELL, J. M., LI, W. S., COMEZOGU, F. T., PARTYKA, R. A. & SZARKA, F. T. 1994. Enzymic preparation of (3R-cis)-3-(acetyloxy)-4-phenyl-2-azetidinone: a taxol side-chain synthon. *Biotechnol Appl Biochem*, 20 (Pt 1), 23-33.
- PATEL, R. N., HOWELL, J., CHIDAMBARAM, R., BENOIT, S. & KANT, J. 2003. Enzymatic preparation of (3R)-cis-3-acetyloxy-4-(1,1-dimethylethyl)-2-azetidinone: a side-chain synthon for an orally active taxane. *Tetrahedron: Asymmetry*, 14, 3673-3677.
- PEREIRA, E. B., ZANIN, G. M. & CASTRO, H. F. 2003. Immobilization and catalytic properties of lipase on chitosan for hydrolysis and esterification reactions. *Brazilian Journal of Chemical Engineering*, 20, 343-355.
- PETCHAROEN, K. & SIRIVAT, A. 2012. Synthesis and characterization of magnetite nanoparticles via the chemical co-precipitation method. *Materials Science and Engineering: B*, 177, 421-427.
- PHILIPSE, A. P., VAN BRUGGEN, M. P. & PATHMAMANOCHARAN, C. 1994. Magnetic silica dispersions: preparation and stability of surface-modified silica particles with a magnetic core. *Langmuir*, 10, 92-99.
- PODARU, G., OGDEN, S., BAXTER, A., SHRESTHA, T., REN, S., THAPA, P., DANI, R. K., WANG, H., BASEL, M. T., PRAKASH, P., BOSSMANN, S. H. & CHIKAN, V. 2014. Pulsed Magnetic Field Induced Fast Drug Release from Magneto Liposomes via Ultrasound Generation. *The Journal of Physical Chemistry B*, 118, 11715-11722.
- PRADHAN, P., GIRI, J., BANERJEE, R., BELLARE, J. & BAHADUR, D. 2007. Preparation and characterization of manganese ferrite-based magnetic liposomes for hyperthermia treatment of cancer. *Journal of Magnetism and Magnetic Materials*, 311, 208-215.
- PRADHAN, P., GIRI, J., RIEKEN, F., KOCH, C., MYKHAYLYK, O., DÖBLINGER, M., BANERJEE, R., BAHADUR, D. & PLANK, C. 2010. Targeted temperature sensitive magnetic liposomes for thermo-chemotherapy. *Journal of Controlled Release*, 142, 108-121.
- PURUSHOTHAM, S., CHANG, P. E. J., RUMPEL, H., KEE, I. H. C., NG, R. T. H., CHOW, P. K. H., TAN, C. K. & RAMANUJAN, R. V. 2009. Thermoresponsive core-shell magnetic

- nanoparticles for combined modalities of cancer therapy. *Nanotechnology*, 20, 305101.
- QIU, H., CUI, B., LI, G., YANG, J., PENG, H., WANG, Y., LI, N., GAO, R., CHANG, Z. & WANG, Y. 2014. Novel Fe₃O₄@ZnO@mSiO₂ Nanocarrier for Targeted Drug Delivery and Controllable Release with Microwave Irradiation. *The Journal of Physical Chemistry C*, 118, 14929-14937.
- QIU, X. L., LI, Q. L., ZHOU, Y., JIN, X. Y., QI, A. D. & YANG, Y. W. 2015. Sugar and pH dual-responsive snap-top nanocarriers based on mesoporous silica-coated Fe₃O₄ magnetic nanoparticles for cargo delivery. *Chem Commun (Camb)*, 51, 4237-40.
- QU, L. & TIE, S. 2009. Mesoporous silica-coated superparamagnetic magnetite functionalized with CuO and its application as a desulfurizer. *Microporous and Mesoporous Materials*, 117, 402-405.
- RĂCUCIU, M., CREANGĂ, D. & AIRINEI, A. 2006. Citric-acid-coated magnetite nanoparticles for biological applications. *The European Physical Journal E*, 21, 117-121.
- RAMOS-SÁNCHEZ, L. B., CUJILEMA-QUITIO, M. C., JULIAN-RICARDO, M. C., CORDOVA, J. & FICKERS, P. 2015. Fungal lipase production by solid-state fermentation. *Journal of Bioprocessing & Biotechniques*, 5, 1.
- RATH, D., RANA, S. & PARIDA, K. M. 2014. Organic amine-functionalized silica-based mesoporous materials: an update of syntheses and catalytic applications. *RSC Advances*, 4, 57111-57124.
- RAVINDRA KUMAR, G., SHIVANI, S. & MAHESH CHANDRA, C. 2015. Functionalized Magnetic Nanoparticles for Environmental Remediation. In: SHIVANI, S., AMANDEEP, S. & MRUTYUNJAY, S. (eds.) *Handbook of Research on Diverse Applications of Nanotechnology in Biomedicine, Chemistry, and Engineering*. Hershey, PA, USA: IGI Global.
- RAY, A. 2012. Application of lipase in industry. *Asian Journal of Pharmacy and Technology*, 2, 33-37.
- REBELO, L. P., NETTO, C. G. C. M., TOMA, H. E. & ANDRADE, L. H. 2010. Enzymatic kinetic resolution of (RS)-1-(Phenyl)ethanols by Burkholderia cepacia lipase immobilized on magnetic nanoparticles. *Journal of the Brazilian Chemical Society*, 21, 1537-1542.
- REDDY, L. H., ARIAS, J. L., NICOLAS, J. & COUVREUR, P. 2012. Magnetic Nanoparticles: Design and Characterization, Toxicity and Biocompatibility, Pharmaceutical and Biomedical Applications. *Chemical Reviews*, 112, 5818-5878.
- REIS, P., HOLMBERG, K., WATZKE, H., LESER, M. E. & MILLER, R. 2009. Lipases at interfaces: A review. *Advances in Colloid and Interface Science*, 147-148, 237-250.
- REISS, G. & HUTTEN, A. 2005. Magnetic nanoparticles: Applications beyond data storage. *Nat Mater*, 4, 725-726.
- REN, N., WANG, B., YANG, Y.-H., ZHANG, Y.-H., YANG, W.-L., YUE, Y.-H., GAO, Z. & TANG, Y. 2005. General Method for the Fabrication of Hollow Microcapsules with Adjustable Shell Compositions. *Chemistry of Materials*, 17, 2582-2587.
- RITTIERODT, M. & HARADA, K. 2003. Repetitive doxorubicin treatment of glioblastoma enhances the PGP expression—a special role for endothelial cells. *Experimental and Toxicologic Pathology*, 55, 39-44.
- RODRIGUEZ-LUCCIONI, H. L., LATORRE-ESTEVEZ, M., MENDEZ-VEGA, J., SOTO, O., RODRIGUEZ, A. R., RINALDI, C. & TORRES-LUGO, M. 2011. Enhanced reduction in cell viability by hyperthermia induced by magnetic nanoparticles. *Int J Nanomedicine*, 6, 373-80.
- ROSENHOLM, J. M., PEUHU, E., BATE-EYA, L. T., ERIKSSON, J. E., SAHLGREN, C. & LINDÉN, M. 2010a. Cancer-Cell-Specific Induction of Apoptosis Using Mesoporous Silica Nanoparticles as Drug-Delivery Vectors. *Small*, 6, 1234-1241.
- ROSENHOLM, J. M., SAHLGREN, C. & LINDEN, M. 2010b. Towards multifunctional, targeted drug delivery systems using mesoporous silica nanoparticles—opportunities & challenges. *Nanoscale*, 2, 1870-83.

- ROSENHOLM, J. M., ZHANG, J., SUN, W. & GU, H. 2011. Large-pore mesoporous silica-coated magnetite core-shell nanocomposites and their relevance for biomedical applications. *Microporous and Mesoporous Materials*, 145, 14-20.
- ROVERS, S. A. 2010. *Magnetically induced localized on-demand drug delivery / Stefan Adrianus Rovers*. PhD, Technische Universiteit Eindhoven.
- ROZZELL, D. & LALONDE, J. 2010. Enzymatic Processes for the Production of Pharmaceutical Intermediates. *Enzyme Technologies*. John Wiley & Sons, Inc.
- RSC 2016. Introduction to NMR spectroscopy - Learn Chemistry Wiki.
- RÚA, M. L. & BALLESTEROS, A. 1994. Rapid purification of two lipase isoenzymes from *Candida rugosa*. *Biotechnology Techniques*, 8, 21-26.
- RUBIO-PINO, I. A. S. B. G.-S. A. A. L. L. M. R.-D. A. A.-S. A. L. R.-C. E. E. G. 2013. Cell growth curves for different cell lines and their relationship with biological activities. *International Journal of Biotechnology and Molecular Biology*, 4, 10.
- SABIR, S., ARSHAD, M. & CHAUDHARI, S. K. 2014. Zinc Oxide Nanoparticles for Revolutionizing Agriculture: Synthesis and Applications. *The Scientific World Journal*, 2014, 8.
- SABOKTAKIN, M. R., MAHARRAMOV, A. & RAMAZANOV, M. A. 2009. Synthesis and characterization of superparamagnetic nanoparticles coated with carboxymethyl starch (CMS) for magnetic resonance imaging technique. *Carbohydrate polymers*, 78, 292-295.
- SADHUKHA, T., NIU, L., WIEDMANN, T. S. & PANYAM, J. 2013. Effective Elimination of Cancer Stem Cells by Magnetic Hyperthermia. *Molecular Pharmaceutics*, 10, 1432-1441.
- SAHOO, B., DEVI, K. S., DUTTA, S., MAITI, T. K., PRAMANIK, P. & DHARA, D. 2014. Biocompatible mesoporous silica-coated superparamagnetic manganese ferrite nanoparticles for targeted drug delivery and MR imaging applications. *J Colloid Interface Sci*, 431, 31-41.
- SALATA, O. 2004. Applications of nanoparticles in biology and medicine. *Journal of Nanobiotechnology*, 2, 3.
- SALGADO, C. L., SANCHEZ, E. M. S., ZAVAGLIA, C. A. C. & GRANJA, P. L. 2012. Biocompatibility and biodegradation of polycaprolactone-sebacic acid blended gels. *Journal of Biomedical Materials Research Part A*, 100A, 243-251.
- SALIS, A., BHATTACHARYYA, M. S., MONDUZZI, M. & SOLINAS, V. 2009. Role of the support surface on the loading and the activity of *Pseudomonas fluorescens* lipase used for biodiesel synthesis. *Journal of Molecular Catalysis B: Enzymatic*, 57, 262-269.
- SANGUANSRI, P. & AUGUSTIN, M. A. 2006. Nanoscale materials development – a food industry perspective. *Trends in Food Science & Technology*, 17, 547-556.
- SANSON, C., SCHATZ, C., MEINS, J.-F. L., ALAIN SOUM, J. T., GARANGER, E. & LECOMMANDOUX, S. 2010. A simple method to achieve high doxorubicin loading in biodegradable polymersomes. *Journal of Controlled Release*.
- SANTOS, J. C., NUNES, G. F. M., MOREIRA, A. B. R., PEREZ, V. H. & DE CASTRO, H. F. 2007. Characterization of *Candida rugosa* Lipase Immobilized on Poly(N-methylolacrylamide) and Its Application in Butyl Butyrate Synthesis. *Chemical Engineering & Technology*, 30, 1255-1261.
- SANTRA, S., TAPEC, R., THEODOROPOULOU, N., DOBSON, J., HEBARD, A. & TAN, W. 2001. Synthesis and Characterization of Silica-Coated Iron Oxide Nanoparticles in Microemulsion: The Effect of Nonionic Surfactants. *Langmuir*, 17, 2900-2906.
- SARDAN, M., YILDIRIM, A., MUMCUOGLU, D., TEKINAY, A. B. & GULER, M. O. 2014. Noncovalent functionalization of mesoporous silica nanoparticles with amphiphilic peptides. *Journal of Materials Chemistry B*, 2, 2168-2174.
- SATO, T., IJIMA, T., SEKI, M. & INAGAKI, N. 1987. Magnetic properties of ultrafine ferrite particles. *Journal of Magnetism and Magnetic Materials*, 65, 252-256.
- SCHWERTMANN, U. & CORNELL, R. M. 2007. Iron Oxides in the Laboratory: Preparation and Characterization. *Iron Oxides in the Laboratory*. Wiley-VCH Verlag GmbH.
- SEBASTIANELLI, A., SEN, T. & BRUCE, I. J. 2008. Extraction of DNA from soil using nanoparticles by magnetic bioseparation. *Letters in applied microbiology*, 46, 488-491.

- SEBAUGH, J. L. 2011. Guidelines for accurate EC50/IC50 estimation. *Pharmaceutical Statistics*, 10, 128-134.
- SEN, T. & BRUCE, I. 2012a. Surface engineering of nanoparticles in suspension for particle based bio-sensing. *Scientific Reports*, 2.
- SEN, T. & BRUCE, I. J. 2009. Mesoporous silica–magnetite nanocomposites: Fabrication, characterisation and applications in biosciences. *Microporous and Mesoporous Materials*, 120, 246-251.
- SEN, T. & BRUCE, I. J. 2012b. Surface engineering of nanoparticles in suspension for particle based bio-sensing. *Scientific reports*, 2.
- SEN, T., BRUCE, I. J. & MERCER, T. 2010. Fabrication of novel hierarchically ordered porous magnetic nanocomposites for bio-catalysis. *Chemical Communications*, 46, 6807.
- SEN, T., MAGDASSI, S., NIZRI, G. & BRUCE, I. J. 2006. Dispersion of magnetic nanoparticles in suspension. *Micro & Nano Letters*, 1, 39.
- SEN, T., SHEPPARD, S. J., MERCER, T., EIZADI-SHARIFABAD, M., MAHMOUDI, M. & ELHISSI, A. 2012a. Simple one-pot fabrication of ultra-stable core-shell superparamagnetic nanoparticles for potential application in drug delivery. *RSC Advances*, 2, 5221-5228.
- SEN, T., SHEPPARD, S. J., MERCER, T., ELHISSI, A., SHARIFABAD, M. E. & MAHMOUDI, M. 2012b. Fabrication of lipid bilayer coated stable superparamagnetic core-shell nanoparticles in suspension for in vitro investigation of anticancer drug mitomycin C. *RSC Advances (under Revision)*.
- SENENIG, R., SAPIR, Y., MACDONALD, C., COHEN, S. & POLYAK, B. 2012. Magnetic nanoparticle-based approaches to locally target therapy and enhance tissue regeneration in vivo. *Nanomedicine (London, England)*, 7, 1425-1442.
- SERRA, E., MAYORAL, Á., SAKAMOTO, Y., BLANCO, R. M. & DÍAZ, I. 2008. Immobilization of lipase in ordered mesoporous materials: Effect of textural and structural parameters. *Microporous and Mesoporous Materials*, 114, 201-213.
- SHAH, R. R., DAVIS, T. P., GLOVER, A. L., NIKLES, D. E. & BRAZEL, C. S. 2015. Impact of magnetic field parameters and iron oxide nanoparticle properties on heat generation for use in magnetic hyperthermia. *Journal of Magnetism and Magnetic Materials*, 387, 96-106.
- SHAO, D., WANG, Z., DONG, W. F., ZHANG, X., ZHENG, X., XIAO, X. A., WANG, Y. S., ZHAO, X., ZHANG, M., LI, J., HUO, Q. S. & CHEN, L. 2015. Facile Synthesis of Core-shell Magnetic Mesoporous Silica Nanoparticles for pH-sensitive Anticancer Drug Delivery. *Chem Biol Drug Des*, 86, 1548-53.
- SHAPIRO, B., KULKARNI, S., NACEV, A., MURO, S., STEPANOV, P. Y. & WEINBERG, I. N. 2015. Open challenges in magnetic drug targeting. *Wiley Interdisciplinary Reviews: Nanomedicine and Nanobiotechnology*, 7, 446-457.
- SHARIFABAD, M. E., HODGSON, B., JELLITE, M., MERCER, T. & SEN, T. 2014. Enzyme immobilised novel core-shell superparamagnetic nanocomposites for enantioselective formation of 4-(R)-hydroxycyclopent-2-en-1-(S)-acetate. *Chemical Communications*, 50, 11185-11187.
- SHARMA, D., SHARMA, B. & SHUKLA, A. 2011. Biotechnological approach of microbial lipase: a review. *Biotechnology*, 10, 23-40.
- SHARMA, S. & KANWAR, S. S. 2014. Organic Solvent Tolerant Lipases and Applications. *The Scientific World Journal*, 2014, 15.
- SHAW, J. F., CHANG, C. H. & WANG, Y. J. 1989. Characterization of three distinct forms of lipolytic enzyme in a commercial *Candida* lipase preparation. *Biotechnology Letters*, 11, 779-784.
- SHAY, L. K. & FISHER, T. J. 1991. Enhancing the flavor of protein products derived from microorganisms. Google Patents.
- SHEN, J., HE, Q., GAO, Y., SHI, J. & LI, Y. 2011. Mesoporous silica nanoparticles loading doxorubicin reverse multidrug resistance: performance and mechanism. *Nanoscale*, 3, 4314-4322.

- SHUAI, X., AI, H., NASONGKLA, N., KIM, S. & GAO, J. 2004. Micellar carriers based on block copolymers of poly(ϵ -caprolactone) and poly(ethylene glycol) for doxorubicin delivery. *Journal of Controlled Release*, 98, 415-426.
- SHUAI, X., MERDAN, T., UNGER, F., WITTMAR, M. & KISSEL, T. 2003. Novel Biodegradable Ternary Copolymers hy-PEI-g-PCL-b-PEG: Synthesis, Characterization, and Potential as Efficient Nonviral Gene Delivery Vectors. *Macromolecules*, 36, 5751-5759.
- SIGMA-ALDRICH 2016. Analytical / Chromatography Products.
- SILVA, A. C., OLIVEIRA, T. R., MAMANI, J. B., MALHEIROS, S. M. F., MALAVOLTA, L., PAVON, L. F., SIBOV, T. T., AMARO, E., TANNUS, A., VIDOTO, E. L. G., MARTINS, M. J., SANTOS, R. S. & GAMARRA, L. F. 2011. Application of hyperthermia induced by superparamagnetic iron oxide nanoparticles in glioma treatment. *International Journal of Nanomedicine*, 6, 591-603.
- SINFELT, J. H. & CUSUMANO, J. A. 1977. 1 - Bimetallic Catalysts. In: BURTON, J. J. & GARTEN, R. L. (eds.) *Advanced Materials in Catalysis*. Academic Press.
- SINGH, A., GOEL, Y., RAI, A. K. & BANERJEE, U. C. 2013. Lipase catalyzed kinetic resolution for the production of (S)-3-[5-(4-fluoro-phenyl)-5-hydroxy-pentanoyl]-4-phenyl-oxazolidin-2-one: An intermediate for the synthesis of ezetimibe. *Journal of Molecular Catalysis B: Enzymatic*, 85-86, 99-104.
- SINGH, N., JENKINS, G. J. S., ASADI, R. & DOAK, S. H. 2010. Potential toxicity of superparamagnetic iron oxide nanoparticles (SPION). *Nano Reviews*, 1, 10.3402/nano.v1i0.5358.
- SINHA, V. R., BANSAL, K., KAUSHIK, R., KUMRIA, R. & TREHAN, A. 2004. Poly- ϵ -caprolactone microspheres and nanospheres: an overview. *International Journal of Pharmaceutics*, 278, 1-23.
- SLOWING, I. I., TREWYN, B. G., GIRI, S. & LIN, V. S. Y. 2007a. Mesoporous Silica Nanoparticles for Drug Delivery and Biosensing Applications. *Advanced Functional Materials*, 17, 1225-1236.
- SLOWING, I. I., TREWYN, B. G. & LIN, V. S. Y. 2007b. Mesoporous Silica Nanoparticles for Intracellular Delivery of Membrane-Impermeable Proteins. *Journal of the American Chemical Society*, 129, 8845-8849.
- SOBAL, N. S., HILGENDORFF, M., MÖHWALD, H., GIERSIG, M., SPASOVA, M., RADEVIC, T. & FARLE, M. 2002. Synthesis and structure of colloidal bimetallic nanocrystals: the non-alloying system Ag/Co. *Nano letters*, 2, 621-624.
- SOLLIS, P. M., BISSELL, P. R., MERCER, T., GOTAAAS, J. A. & GILSON, R. G. 1998. Dispersion stability during the settling process. *Journal of Magnetism and Magnetic Materials*, 177-181, Part 2, 892-893.
- SON, M., MOON, Y., OH, M. J., HAN, S. B., PARK, K. H., KIM, J.-G. & AHN, J. H. 2012. Lipase and Protease Double-Deletion Mutant of *Pseudomonas fluorescens* Suitable for Extracellular Protein Production. *Applied and Environmental Microbiology*, 78, 8454-8462.
- SONMEZ, M., GEORGESCU, M., ALEXANDRESCU, L., GURAU, D., FICAI, A., FICAI, D. & ANDRONESCU, E. 2015. SYNTHESIS AND APPLICATIONS OF Fe₃O₄/SiO₂ CORE-SHELL MATERIALS. *Curr Pharm Des*, 21, 5324-35.
- SONNET, P. E. & BAILLARGEON, M. W. 1991. Methyl-branched octanoic acids as substrates for lipase-catalyzed reactions. *Lipids*, 26, 295-300.
- SOSNIK, A. & COHN, D. 2003. Poly(ethylene glycol)-poly(epsilon-caprolactone) block oligomers as injectable materials. *Polymer*, 44, 7033-7042.
- SOUZA, K., ARDISSON, J. & SOUSA, E. 2009a. Study of mesoporous silica/magnetite systems in drug controlled release. *Journal of Materials Science: Materials in Medicine*, 20, 507-512.
- SOUZA, K. C., ARDISSON, J. D. & SOUSA, E. M. B. 2008. Study of mesoporous silica/magnetite systems in drug controlled release. *Journal of Materials Science: Materials in Medicine*, 20, 507-512.

- SOUZA, K. C., MOHALLEM, N. D. S. & SOUSA, E. M. B. 2009b. Mesoporous silica-magnetite nanocomposite: facile synthesis route for application in hyperthermia. *Journal of Sol-Gel Science and Technology*, 53, 418-427.
- SRIVASTAVA, V., GUSAIN, D. & SHARMA, Y. C. 2013. Synthesis, characterization and application of zinc oxide nanoparticles (n-ZnO). *Ceramics International*, 39, 9803-9808.
- STANICKI, D., ELST, L. V., MULLER, R. N. & LAURENT, S. 2015. Synthesis and processing of magnetic nanoparticles. *Current Opinion in Chemical Engineering*, 8, 7-14.
- STÖBER, W., FINK, A. & BOHN, E. 1968. Controlled growth of monodisperse silica spheres in the micron size range. *Journal of colloid and interface science*, 26, 62-69.
- STUPP, R., MASON, W. P., VAN DEN BENT, M. J., WELLER, M., FISHER, B., TAPHOORN, M. J., BELANGER, K., BRANDES, A. A., MAROSI, C., BOGDAHN, U., CURSCHMANN, J., JANZER, R. C., LUDWIN, S. K., GORLIA, T., ALLGEIER, A., LACOMBE, D., CAIRNCROSS, J. G., EISENHAEUER, E. & MIRIMANOFF, R. O. 2005. Radiotherapy plus concomitant and adjuvant temozolomide for glioblastoma. *N Engl J Med*, 352, 987-96.
- SUGIMOTO, T. & MATIJEVIC, E. 1980. FORMATION OF UNIFORM SPHERICAL MAGNETITE PARTICLES BY CRYSTALLIZATION FROM FERROUS HYDROXIDE GELS. *Journal of Colloid and Interface Science*, 74, 227-243.
- SUGIMOTO, T. & MATIJEVIĆ, E. 1980. Formation of uniform spherical magnetite particles by crystallization from ferrous hydroxide gels. *Journal of Colloid and Interface Science*, 74, 227-243.
- SUN, C., VEISEH, O., GUNN, J., FANG, C., HANSEN, S., LEE, D., SZE, R., ELLENBOGEN, R. G., OLSON, J. & ZHANG, M. 2008. In Vivo MRI Detection of Gliomas by Chlorotoxin-Conjugated Superparamagnetic Nanoparticles. *small*, 4, 372-379.
- SUN, J., ZHOU, S., HOU, P., YANG, Y., WENG, J., LI, X. & LI, M. 2007. Synthesis and characterization of biocompatible Fe₃O₄ nanoparticles. *Journal of Biomedical Materials Research Part A*, 80A, 333-341.
- SUN, S. & ZENG, H. 2002. Size-Controlled Synthesis of Magnetite Nanoparticles. *Journal of the American Chemical Society*, 124, 8204-8205.
- SUN, S., ZENG, H., ROBINSON, D. B., RAOUX, S., RICE, P. M., WANG, S. X. & LI, G. 2003. Monodisperse MFe₂O₄ (M = Fe, Co, Mn) Nanoparticles. *Journal of the American Chemical Society*, 126, 273-279.
- SUN, Y.-K., MA, M., ZHANG, Y. & GU, N. 2004. Synthesis of nanometer-size maghemite particles from magnetite. *Colloids and Surfaces A: Physicochemical and Engineering Aspects*, 245, 15-19.
- SUN, Y., DUAN, L., GUO, Z., DUANMU, Y., MA, M., XU, L., ZHANG, Y. & GU, N. 2005. An improved way to prepare superparamagnetic magnetite-silica core-shell nanoparticles for possible biological application. *Journal of Magnetism and Magnetic Materials*, 285, 65-70.
- SUNDARESAN, V., MENON, J. U., RAHIMI, M., NGUYEN, K. T. & WADAJKAR, A. S. 2014. Dual-responsive polymer-coated iron oxide nanoparticles for drug delivery and imaging applications. *International journal of pharmaceuticals*, 466, 1-7.
- SUZUKI, M., AKI, A., MIZUKI, T., MAEKAWA, T., USAMI, R. & MORIMOTO, H. 2015. Encouragement of Enzyme Reaction Utilizing Heat Generation from Ferromagnetic Particles Subjected to an AC Magnetic Field. *PLoS ONE*, 10, e0127673.
- SZAKACS, G., PATERSON, J. K., LUDWIG, J. A., BOOTH-GENTHE, C. & GOTTESMAN, M. M. 2006. Targeting multidrug resistance in cancer. *Nat Rev Drug Discov*, 5, 219-34.
- TA, T. & PORTER, T. M. 2013. Thermosensitive liposomes for localized delivery and triggered release of chemotherapy. *Journal of Controlled Release*, 169, 112-125.
- TALELLI, M., RIJCKEN, C. J. F., LAMMERS, T., SEEVINCK, P. R., STORM, G., VAN NOSTRUM, C. F. & HENNINK, W. E. 2009. Superparamagnetic Iron Oxide Nanoparticles Encapsulated in Biodegradable Thermosensitive Polymeric Micelles: Toward a Targeted Nanomedicine Suitable for Image-Guided Drug Delivery. *Langmuir*, 25, 2060-2067.
- TANG, F., LI, L. & CHEN, D. 2012. Mesoporous Silica Nanoparticles: Synthesis, Biocompatibility and Drug Delivery. *Advanced Materials*, 24, 1504-1534.

- TANG, H., GUO, J., SUN, Y., CHANG, B., REN, Q. & YANG, W. 2011. Facile synthesis of pH sensitive polymer-coated mesoporous silica nanoparticles and their application in drug delivery. *International Journal of Pharmaceutics*, 421, 388-396.
- TENG, Y. & XU, Y. 2007. A modified para-nitrophenyl palmitate assay for lipase synthetic activity determination in organic solvent. *Analytical Biochemistry*, 363, 297-299.
- THANH, N. T. 2012. *Magnetic nanoparticles: from fabrication to clinical applications*, CRC press.
- THEPPALEAK, T., TUMCHARERN, G., WICHAI, U. & RUTNAKORNPITUK, M. 2009. Synthesis of water dispersible magnetite nanoparticles in the presence of hydrophilic polymers. *Polymer Bulletin*, 63, 79-90.
- TIETZE, R., LYER, S., DURR, S., STRUFFERT, T., ENGELHORN, T., SCHWARZ, M., ECKERT, E., GOEN, T., VASYLYEV, S., PEUKERT, W., WIEKHORST, F., TRAHMS, L., DORFLER, A. & ALEXIOU, C. 2013. Efficient drug-delivery using magnetic nanoparticles--biodistribution and therapeutic effects in tumour bearing rabbits. *Nanomedicine*, 9, 961-71.
- TING, W. J., TUNG, K. Y., GIRIDHAR, R. & WU, W. T. 2006. Application of binary immobilized *Candida rugosa* lipase for hydrolysis of soybean oil. *Journal of Molecular Catalysis B: Enzymatic*, 42, 32-38.
- TODAKA, Y., NAKAMURA, M., HATTORI, S., TSUCHIYA, K. & UMEMOTO, M. 2003. Synthesis of ferrite nanoparticles by mechanochemical processing using a ball mill. *Materials Transactions*, 44, 277-284.
- TOMASZ, M. 1995. Mitomycin C: small, fast and deadly (but very selective). *Chemistry & biology*, 2, 575-579.
- TORCHILIN, V. P. 2000. Drug targeting. *European Journal of Pharmaceutical Sciences*, 11, Supplement 2, S81-S91.
- TORCHILIN, V. P. 2005a. Recent advances with liposomes as pharmaceutical carriers. *Nat Rev Drug Discov*, 4, 145-160.
- TORCHILIN, V. P. 2005b. Recent advances with liposomes as pharmaceutical carriers. *Nature reviews Drug discovery*, 4, 145-160.
- TRAN, H. V., DAI TRAN, L. & NGUYEN, T. N. 2010. Preparation of chitosan/magnetite composite beads and their application for removal of Pb (II) and Ni (II) from aqueous solution. *Materials Science and Engineering: C*, 30, 304-310.
- TREICHEL, H., OLIVEIRA, D., MAZUTTI, M. A., LUCCIO, M. & OLIVEIRA, J. V. 2009. A Review on Microbial Lipases Production. *Food and Bioprocess Technology*, 3, 182-196.
- TRESILWISED, N., PITHAYANUKUL, P. & PLANK, C. 2005. Factors Affecting Sizes of Magnetic Particles Formed by Chemical Co-precipitation. *Mahidol University Journal of Pharmaceutical Sciences*, 32, 6.
- TSUBAKI, M., KOMAI, M., ITOH, T., IMANO, M., SAKAMOTO, K., SHIMAOKA, H., TAKEDA, T., OGAWA, N., MASHIMO, K., FUJIWARA, D., MUKAI, J., SAKAGUCHI, K., SATOU, T. & NISHIDA, S. 2014. By inhibiting Src, verapamil and dasatinib overcome multidrug resistance via increased expression of Bim and decreased expressions of MDR1 and survivin in human multidrug-resistant myeloma cells. *Leuk Res*, 38, 121-30.
- TSUZUKI, T. 2009. Commercial scale production of inorganic nanoparticles. *International Journal of Nanotechnology*, 6, 567-578.
- UCL. 2016. *Magnetism* [Online]. Gale Research. Available: <http://www.ucl.ac.uk/EarthSci/people/lidunka/GEOL2014/Geophysics9%20-Magnetism/Useful%20papers/Magnetism.htm>.
- UEMURA, A., NOZAKI, K., YAMASHITA, J.-I. & YASUMOTO, M. 1989. Regioselective deprotection of 3',5'-O-acylated pyrimidine nucleosides by lipase and esterase. *Tetrahedron Letters*, 30, 3819-3820.
- UK, C. R. 2013. *Treatment for glioma (astrocytoma)* [Online]. Cancer Research UK. Available: <http://www.cancerresearchuk.org/about-cancer/type/brain-tumour/treatment/types/treatment-for-glioma#highgrade>.
- UK, C. R. 2015. Cancer incidence statistics.
- UPADHYAY, K. K., BHATT, A. N., MISHRA, A. K., DWARAKANATH, B. S., JAIN, S., SCHATZ, C., LE MEINS, J.-F., FAROOQUE, A., CHANDRAIAH, G., JAIN, A. K., MISRA, A. &

- LECOMMANDOUX, S. 2010. The intracellular drug delivery and anti tumor activity of doxorubicin loaded poly(γ -benzyl L-glutamate)-b-hyaluronan polymersomes. *Biomaterials*, 31, 2882-2892.
- URIBE MADRID, S. I., PAL, U., KANG, Y. S., KIM, J., KWON, H. & KIM, J. 2015. Fabrication of Fe₃O₄@mSiO₂ Core-Shell Composite Nanoparticles for Drug Delivery Applications. *Nanoscale Research Letters*, 10, 217.
- URSACHI, I., VASILE, A., CHIRIAC, H., POSTOLACHE, P. & STANCU, A. 2011a. Magnetic properties of magnetite nanoparticles coated with mesoporous silica by sonochemical method. *Materials Research Bulletin*, 46, 2468-2473.
- URSACHI, I., VASILE, A., IANCULESCU, A., VASILE, E. & STANCU, A. 2011b. Ultrasonic-assisted synthesis and magnetic studies of iron oxide/MCM-41 nanocomposite. *Materials Chemistry and Physics*, 130, 1251-1259.
- UTHAMAN, S., LEE, S. J., CHERUKULA, K., CHO, C.-S. & PARK, I.-K. 2015. Polysaccharide-Coated Magnetic Nanoparticles for Imaging and Gene Therapy. *BioMed Research International*, 2015, 14.
- VAKHLU, J. 2006. Yeast lipases: enzyme purification, biochemical properties and gene cloning. *Electronic Journal of Biotechnology*, 9, 0-0.
- VALLET-REGI, M., RÁMILA, A., DEL REAL, R. P. & PÉREZ-PARIENTE, J. 2001. A New Property of MCM-41: Drug Delivery System. *Chemistry of Materials*, 13, 308-311.
- VAN EWIJK, G., VROEGE, G. & PHILIPSE, A. 1999. Convenient preparation methods for magnetic colloids. *Journal of Magnetism and Magnetic Materials*, 201, 31-33.
- VARANDA, L. C., JÚNIOR, M. J. & JÚNIOR, W. B. 2011. *Magnetic and multifunctional magnetic nanoparticles in nanomedicine: challenges and trends in synthesis and surface engineering for diagnostic and therapy applications*, INTECH Open Access Publisher.
- VEERARAGAVAN, K. & GIBBS, B. F. 1989. Detection and partial purification of two lipases from *Candida rugosa*. *Biotechnology Letters*, 11, 345-348.
- VEISEH, O., GUNN, J. W. & ZHANG, M. 2010. Design and fabrication of magnetic nanoparticles for targeted drug delivery and imaging. *Advanced Drug Delivery Reviews*, 62, 284-304.
- VERMA, N., THAKUR, S. & BHATT, A. 2012. Microbial Lipases: Industrial Applications and Properties (A Review).
- VERWEIJ, J. & PINEDO, H. M. 1990. Mitomycin C: mechanism of action, usefulness and limitations. *Anti-cancer drugs*, 1, 5-14.
- VIJAYAKUMAR, R., KOLTYPIN, Y., FELNER, I. & GEDANKEN, A. 2000. Sonochemical synthesis and characterization of pure nanometer-sized Fe₃O₄ particles. *Materials Science and Engineering: A*, 286, 101-105.
- VOGT, C., TOPRAK, M., MUHAMMED, M., LAURENT, S., BRIDOT, J.-L. & MÜLLER, R. 2010. High quality and tuneable silica shell-magnetic core nanoparticles. *Journal of Nanoparticle Research*, 12, 1137-1147.
- VOIT, W., KIM, D. K., ZAPKA, W., MUHAMMED, M. & RAO, K. V. 2001. Magnetic behavior of coated superparamagnetic iron oxide nanoparticles in ferrofluids. *MRS Online Proceedings Library Archive*, 676, null-null.
- WADAJKAR, A. S., MENON, J. U., TSAI, Y. S., GORE, C., DOBIN, T., GANDEE, L., KANGASNIEMI, K., TAKAHASHI, M., MANANDHAR, B., AHN, J. M., HSIEH, J. T. & NGUYEN, K. T. 2013. Prostate cancer-specific thermo-responsive polymer-coated iron oxide nanoparticles. *Biomaterials*, 34, 3618-25.
- WAHAJUDDIN & ARORA, S. 2012. Superparamagnetic iron oxide nanoparticles: magnetic nanoplatforms as drug carriers. *International Journal of Nanomedicine*, 7, 3445-3471.
- WANG, J., REN, F., YI, R., YAN, A., QIU, G. & LIU, X. 2009. Solvothermal synthesis and magnetic properties of size-controlled nickel ferrite nanoparticles. *Journal of Alloys and Compounds*, 479, 791-796.
- WANG, L.-S., WU, L.-C., LU, S.-Y., CHANG, L.-L., TENG, I. T., YANG, C.-M. & HO, J.-A. A. 2010a. Biofunctionalized Phospholipid-Capped Mesoporous Silica Nanoshuttles for Targeted Drug Delivery: Improved Water Suspensibility and Decreased Nonspecific Protein Binding. *ACS Nano*, 4, 4371-4379.

- WANG, L., NEOH, K.-G., KANG, E.-T., SHUTER, B. & WANG, S.-C. 2010b. Biodegradable magnetic-fluorescent magnetite/poly(dl-lactic acid-co- α,β -malic acid) composite nanoparticles for stem cell labeling. *Biomaterials*, 31, 3502-3511.
- WANG, Q. & LIU, J. 2011. Nanoparticles Enhanced Hyperthermia. 5, 567-598.
- WANG, W.-W., ZHU, Y.-J. & RUAN, M.-L. 2007. Microwave-assisted synthesis and magnetic property of magnetite and hematite nanoparticles. *Journal of Nanoparticle Research*, 9, 419-426.
- WANG, X., TENG, Z., WANG, H., WANG, C., LIU, Y., TANG, Y., WU, J., SUN, J., WANG, H., WANG, J. & LU, G. 2014. Increasing the cytotoxicity of doxorubicin in breast cancer MCF-7 cells with multidrug resistance using a mesoporous silica nanoparticle drug delivery system. *International Journal of Clinical and Experimental Pathology*, 7, 1337-1347.
- WANG, X., ZHUANG, J., PENG, Q. & LI, Y. 2005. A general strategy for nanocrystal synthesis. *Nature*, 437, 121-124.
- WANG, Y., ZHAO, Q., HAN, N., BAI, L., LI, J., LIU, J., CHE, E., HU, L., ZHANG, Q., JIANG, T. & WANG, S. 2015. Mesoporous silica nanoparticles in drug delivery and biomedical applications. *Nanomedicine: Nanotechnology, Biology and Medicine*, 11, 313-327.
- WILLIAM, W. 2004. Synthesis of monodisperse iron oxide nanocrystals by thermal decomposition of iron carboxylate salts. *Chemical Communications*, 2306-2307.
- WILLIS, A. L., TURRO, N. J. & O'BRIEN, S. 2005. Spectroscopic characterization of the surface of iron oxide nanocrystals. *Chemistry of materials*, 17, 5970-5975.
- WILLNER, I. & KATZ, E. 2003. Magnetic Control of Electrocatalytic and Bioelectrocatalytic Processes. *Angewandte Chemie International Edition*, 42, 4576-4588.
- WILSON, M. W., KERLAN, R. K., JR., FIDELMAN, N. A., VENOOK, A. P., LABERGE, J. M., KODA, J. & GORDON, R. L. 2004. Hepatocellular carcinoma: regional therapy with a magnetic targeted carrier bound to doxorubicin in a dual MR imaging/ conventional angiography suite--initial experience with four patients. *Radiology*, 230, 287-93.
- WU, C., ZHOU, G., JIANG, X., MA, J., ZHANG, H. & SONG, H. 2012. Active biocatalysts based on *Candida rugosa* lipase immobilized in vesicular silica. *Process Biochemistry*, 47, 953-959.
- WU, H., LIU, G., ZHANG, S., SHI, J., ZHANG, L., CHEN, Y., CHEN, F. & CHEN, H. 2011. Biocompatibility, MR imaging and targeted drug delivery of a rattle-type magnetic mesoporous silica nanosphere system conjugated with PEG and cancer-cell-specific ligands. *Journal of Materials Chemistry*, 21, 3037-3045.
- WU, J.-H., KO, S. P., LIU, H.-L., KIM, S., JU, J.-S. & KIM, Y. K. 2007. Sub 5 nm magnetite nanoparticles: Synthesis, microstructure, and magnetic properties. *Materials Letters*, 61, 3124-3129.
- WU, P., ZHU, J. & XU, Z. 2004. Template-assisted synthesis of mesoporous magnetic nanocomposite particles. *Advanced Functional Materials*, 14, 345-351.
- WU, S.-H., MOU, C.-Y. & LIN, H.-P. 2013a. Synthesis of mesoporous silica nanoparticles. *Chemical Society Reviews*, 42, 3862-3875.
- WU, S. H., GUO, Z. W. & SIH, C. J. 1990. Enhancing the enantioselectivity of *Candida* lipase-catalyzed ester hydrolysis via noncovalent enzyme modification. *Journal of the American Chemical Society*, 112, 1990-1995.
- WU, X., WANG, Z., ZHU, D., ZONG, S., YANG, L., ZHONG, Y. & CUI, Y. 2013b. pH and Thermo Dual-Stimuli-Responsive Drug Carrier Based on Mesoporous Silica Nanoparticles Encapsulated in a Copolymer-Lipid Bilayer. *ACS Applied Materials & Interfaces*, 5, 10895-10903.
- WUST, P., GNEVECKOW, U., JOHANNSEN, M., BOHMER, D., HENKEL, T., KAHMANN, F., SEHOULI, J., FELIX, R., RICKE, J. & JORDAN, A. 2006. Magnetic nanoparticles for interstitial thermotherapy--feasibility, tolerance and achieved temperatures. *Int J Hyperthermia*, 22, 673-85.
- XIE, M., XU, Y., SHEN, H., SHEN, S., GE, Y. & XIE, J. 2014. Negative-charge-functionalized mesoporous silica nanoparticles as drug vehicles targeting hepatocellular carcinoma. *Int J Pharm*, 474, 223-31.

- XIE, S., ZHANG, B., WANG, L., WANG, J., LI, X., YANG, G. & GAO, F. 2015. Superparamagnetic iron oxide nanoparticles coated with different polymers and their MRI contrast effects in the mouse brains. *Applied Surface Science*, 326, 32-38.
- XU, F., CHENG, C., XU, F., ZHANG, C., XU, H., XIE, X., YIN, D. & GU, H. 2009a. Superparamagnetic magnetite nanocrystal clusters: a sensitive tool for MR cellular imaging. *Nanotechnology*, 20, 405102.
- XU, H., CUI, L., TONG, N. & GU, H. 2006. Development of High Magnetization Fe₃O₄/Polystyrene/Silica Nanospheres via Combined Miniemulsion/Emulsion Polymerization. *Journal of the American Chemical Society*, 128, 15582-15583.
- XU, H., LI, M. & HE, B. 1995. Immobilization of *Candida cylindracea* lipase on methyl acrylate-divinyl benzene copolymer and its derivatives. *Enzyme and Microbial Technology*, 17, 194-199.
- XU, J., YANG, H., FU, W., DU, K., SUI, Y., CHEN, J., ZENG, Y., LI, M. & ZOU, G. 2007. Preparation and magnetic properties of magnetite nanoparticles by sol-gel method. *Journal of Magnetism and Magnetic Materials*, 309, 307-311.
- XU, J., ZHAO, Q., JIN, Y. & QIU, L. 2014. High loading of hydrophilic/hydrophobic doxorubicin into polyphosphazene polymersome for breast cancer therapy. *Nanomedicine*, 10, 349-58.
- XU, L., JIANG, X., YANG, J., LIU, Y. & YAN, Y. 2009b. Cloning of a novel lipase gene, lipJ08, from *Candida rugosa* and expression in *Pichia pastoris* by codon optimization. *Biotechnology Letters*, 32, 269-276.
- XUE, S., WANG, Y., WANG, M., ZHANG, L., DU, X., GU, H. & ZHANG, C. 2014. Iodinated oil-loaded, fluorescent mesoporous silica-coated iron oxide nanoparticles for magnetic resonance imaging/computed tomography/fluorescence trimodal imaging. *International Journal of Nanomedicine*, 9, 2527-2538.
- YANAGISAWA, T., SHIMIZU, T., KURODA, K. & KATO, C. 1990. The Preparation of Alkyltriethylammonium-Kaneinite Complexes and Their Conversion to Microporous Materials. *Bulletin of the Chemical Society of Japan*, 63, 988-992.
- YANAI, A., HAFELI, U. O., METCALFE, A. L., SOEMA, P., ADDO, L., GREGORY-EVANS, C. Y., PO, K., SHAN, X., MORITZ, O. L. & GREGORY-EVANS, K. 2012. Focused magnetic stem cell targeting to the retina using superparamagnetic iron oxide nanoparticles. *Cell Transplant*, 21, 1137-48.
- YANG, C., GUO, W., CUI, L., AN, N., ZHANG, T., GUO, G., LIN, H. & QU, F. 2015. Fe₃O₄@mSiO₂ core-shell nanocomposite capped with disulfide gatekeepers for enzyme-sensitive controlled release of anti-cancer drugs. *Journal of Materials Chemistry B*, 3, 1010-1019.
- YANG, P., QUAN, Z., HOU, Z., LI, C., KANG, X., CHENG, Z. & LIN, J. 2009a. A magnetic, luminescent and mesoporous core-shell structured composite material as drug carrier. *Biomaterials*, 30, 4786-4795.
- YANG, Y., SONG, W., WANG, A., ZHU, P., FEI, J. & LI, J. 2010. Lipid coated mesoporous silica nanoparticles as photosensitive drug carriers. *Physical Chemistry Chemical Physics*, 12, 4418-4422.
- YANG, Z., FONG, D. W. F., YIN, L., WONG, Y. & HUANG, W. 2009b. Liposomes modulate docetaxel-induced lipid oxidization and membrane damage in human hepatoma cells. *Journal of Liposome Research*, 19, 122-130.
- YI, Y., LI, Y., WU, H., JIA, M., YANG, X., WEI, H., LIN, J., WU, S., HUANG, Y., HOU, Z. & XIE, L. 2014. Single-step assembly of polymer-lipid hybrid nanoparticles for mitomycin C delivery. *Nanoscale Res Lett*, 9, 560.
- YILDIRIM, A., DEMIREL, G. B., ERDEM, R., SENTURK, B., TEKINAY, T. & BAYINDIR, M. 2013. Pluronic polymer capped biocompatible mesoporous silica nanocarriers. *Chemical Communications*, 49, 9782-9784.
- YILMAZ, E., CAN, K., SEZGIN, M. & YILMAZ, M. 2011. Immobilization of *Candida rugosa* lipase on glass beads for enantioselective hydrolysis of racemic Naproxen methyl ester. *Bioresource Technology*, 102, 499-506.

- YILMAZ, E., SEZGIN, M. & YILMAZ, M. 2009. Immobilized copper-ion affinity adsorbent based on a cross-linked β -cyclodextrin polymer for adsorption of *Candida rugosa* lipase. *Biocatalysis and Biotransformation*, 27, 360-366.
- YIN, M., LIU, D., XU, F., XIAO, L., WANG, Q., WANG, B., CHANG, Y., ZHENG, J., TAO, X., LIU, G. & ZHANG, L. 2016. A specific antimicrobial protein CAP-1 from *Pseudomonas* sp. isolated from the jellyfish *Cyanea capillata*. *Int J Biol Macromol*, 82, 488-96.
- YIU, H. H. P. & KEANE, M. A. 2012. Enzyme–magnetic nanoparticle hybrids: new effective catalysts for the production of high value chemicals. *Journal of Chemical Technology & Biotechnology*, 87, 583-594.
- YIU, H. H. P., MCBAIN, S. C., LETHBRIDGE, Z. A. D., LEES, M. R., PALONA, I., OLARIU, C. I. & DOBSON, J. 2011. Novel Magnetite-Silica Nanocomposite (Fe(3)O(4)-SBA-15) Particles for DNA Binding and Gene Delivery Aided by a Magnet Array. *Journal of Nanoscience and Nanotechnology*, 11, 3586-3591.
- YONG, Y., BAI, Y.-X., LI, Y.-F., LIN, L., CUI, Y.-J. & XIA, C.-G. 2008. Characterization of *Candida rugosa* lipase immobilized onto magnetic microspheres with hydrophilicity. *Process Biochemistry*, 43, 1179-1185.
- YOUNGIL, L., JUN-RAK, C., KWI JONG, L., NATHAN, E. S. & DONGHOON, K. 2008. Large-scale synthesis of copper nanoparticles by chemically controlled reduction for applications of inkjet-printed electronics. *Nanotechnology*, 19, 415604.
- YU, J., XIE, X., XU, X., ZHANG, L., ZHOU, X., YU, H., WU, P., WANG, T., CHE, X. & HU, Z. 2014. Development of dual ligand-targeted polymeric micelles as drug carriers for cancer therapy in vitro and in vivo. *Journal of Materials Chemistry B*, 2, 2114-2126.
- YU, L. M., KAZAZIAN, K. & SHOICHET, M. S. 2007. Peptide surface modification of methacrylamide chitosan for neural tissue engineering applications. *Journal of Biomedical Materials Research Part A*, 82, 243-255.
- YU, T., MALUGIN, A. & GHANDEHARI, H. 2011. Impact of Silica Nanoparticle Design on Cellular Toxicity and Hemolytic Activity. *ACS Nano*, 5, 5717-5728.
- YUAN, Y. & LEE, T. R. 2013. Contact Angle and Wetting Properties. In: BRACCO, G. & HOLST, B. (eds.) *Surface Science Techniques*. Berlin, Heidelberg: Springer Berlin Heidelberg.
- ZAHR, A. S., DAVIS, C. A. & PISHKO, M. V. 2006. Macrophage Uptake of Core-Shell Nanoparticles Surface Modified with Poly(ethylene glycol). *Langmuir*, 22, 8178-8185.
- ZALOGA, J., JANKO, C., NOWAK, J., MATUSZAK, J., KNAUP, S., EBERBECK, D., TIETZE, R., UNTERWEGER, H., FRIEDRICH, R. P., DUERR, S., HEIMKE-BRINCK, R., BAUM, E., CICHA, I., DÖRJE, F., ODENBACH, S., LYER, S., LEE, G. & ALEXIOU, C. 2014. Development of a lauric acid/albumin hybrid iron oxide nanoparticle system with improved biocompatibility. *International Journal of Nanomedicine*, 9, 4847-4866.
- ZENG, X., MORGENSTERN, R. & NYSTROM, A. M. 2014. Nanoparticle-directed sub-cellular localization of doxorubicin and the sensitization breast cancer cells by circumventing GST-mediated drug resistance. *Biomaterials*, 35, 1227-39.
- ZHANG, D., TONG, Z., LI, S., ZHANG, X. & YING, A. 2008a. Fabrication and characterization of hollow Fe₃O₄ nanospheres in a microemulsion. *Materials Letters*, 62, 4053-4055.
- ZHANG, L.-Y., GU, H.-C. & WANG, X.-M. 2007. Magnetite ferrofluid with high specific absorption rate for application in hyperthermia. *Journal of Magnetism and Magnetic Materials*, 311, 228-233.
- ZHANG, L. & GRANICK, S. 2006. How to stabilize phospholipid liposomes (using nanoparticles). *Nano letters*, 6, 694-698.
- ZHANG, L., GU, F. X., CHAN, J. M., WANG, A. Z., LANGER, R. S. & FAROKHZAD, O. C. 2008b. Nanoparticles in Medicine: Therapeutic Applications and Developments. *Clinical Pharmacology & Therapeutics*, 83, 761-769.
- ZHANG, M. & O'CONNOR, C. J. 2007. Synthesis and Characterization of PMMA Coated Magnetite Nanocomposites by Emulsion Polymerization. *MRS Online Proceedings Library Archive*, 1032, null-null.
- ZHANG, Q., GE, J., GOEBL, J., HU, Y., LU, Z. & YIN, Y. 2009. Rattle-type silica colloidal particles prepared by a surface-protected etching process. *Nano Research*, 2, 583-591.

- ZHANG, Q., GE, J., GOEBL, J., HU, Y., LU, Z. & YIN, Y. 2010a. Rattle-type silica colloidal particles prepared by a surface-protected etching process. *Nano Research*, 2, 583-591.
- ZHANG, Q., ZHANG, T., GE, J. & YIN, Y. 2008c. Permeable Silica Shell through Surface-Protected Etching. *Nano Letters*, 8, 2867-2871.
- ZHANG, T., GE, J., HU, Y., ZHANG, Q., ALONI, S. & YIN, Y. 2008d. Formation of Hollow Silica Colloids through a Spontaneous Dissolution–Regrowth Process. *Angewandte Chemie International Edition*, 47, 5806-5811.
- ZHANG, W., LI, Y., LIU, L., SUN, Q., SHUAI, X., ZHU, W. & CHEN, Y. 2010b. Amphiphilic Toothbrushlike Copolymers Based on Poly(ethylene glycol) and Poly(ϵ -caprolactone) as Drug Carriers with Enhanced Properties. *Biomacromolecules*, 11, 1331-1338.
- ZHANG, X., NIU, H., PAN, Y., SHI, Y. & CAI, Y. 2010c. Chitosan-Coated Octadecyl-Functionalized Magnetite Nanoparticles: Preparation and Application in Extraction of Trace Pollutants from Environmental Water Samples. *Analytical Chemistry*, 82, 2363-2371.
- ZHANG, X., ZHANG, Y., YANG, G., XIE, Y., XU, L., AN, J., CUI, L. & FENG, Y. 2016. Modulation of the thermostability and substrate specificity of *Candida rugosa* lipase1 by altering the acyl-binding residue Gly414 at the α -helix-connecting bend. *Enzyme and Microbial Technology*, 82, 34-41.
- ZHANG, Y. & ZHUO, R.-X. 2005. Synthesis and in vitro drug release behavior of amphiphilic triblock copolymer nanoparticles based on poly (ethylene glycol) and polycaprolactone. *Biomaterials*, 26, 6736-6742.
- ZHAO, B., WANG, X. Q., WANG, X. Y., ZHANG, H., DAI, W. B., WANG, J., ZHONG, Z. L., WU, H. N. & ZHANG, Q. 2013a. Nanotoxicity comparison of four amphiphilic polymeric micelles with similar hydrophilic or hydrophobic structure. *Part Fibre Toxicol*, 10, 47.
- ZHAO, C.-X., YU, L. & MIDDELBERG, A. P. J. 2013b. Magnetic mesoporous silica nanoparticles end-capped with hydroxyapatite for pH-responsive drug release. *Journal of Materials Chemistry B*, 1, 4828-4833.
- ZHAO, F., ZHANG, B. & FENG, L. 2012. Preparation and magnetic properties of magnetite nanoparticles. *Materials Letters*, 68, 112-114.
- ZHAO, F., ZHANG, B., WANG, J. & TU, Z. 2013c. Synthesis and Properties of Magnetite Nanoparticles Coated with Poly(ethylene glycol) and Poly(ethylene imine). *Journal of Nanoscience and Nanotechnology*, 13, 6793-6797.
- ZHAO, H., SAATCHI, K. & HÄFELI, U. O. 2009. Preparation of biodegradable magnetic microspheres with poly(lactic acid)-coated magnetite. *Journal of Magnetism and Magnetic Materials*, 321, 1356-1363.
- ZHAO, L.-Y., LIU, J.-Y., OUYANG, W.-W., LI, D.-Y., LI, L., LI, L.-Y. & TANG, J.-T. 2013d. Magnetic-mediated hyperthermia for cancer treatment: Research progress and clinical trials. *Chinese Physics B*, 22, 108104.
- ZHAO, W., GU, J., ZHANG, L., CHEN, H. & SHI, J. 2005. Fabrication of uniform magnetic nanocomposite spheres with a magnetic core/mesoporous silica shell structure. *Journal of the American Chemical Society*, 127, 8916-8917.
- ZHAO, X., SHI, Y., WANG, T., CAI, Y. & JIANG, G. 2008. Preparation of silica-magnetite nanoparticle mixed hemimicelle sorbents for extraction of several typical phenolic compounds from environmental water samples. *Journal of Chromatography A*, 1188, 140-147.
- ZHENG, Y.-H., CHENG, Y., BAO, F. & WANG, Y.-S. 2006. Synthesis and magnetic properties of Fe₃O₄ nanoparticles. *Materials Research Bulletin*, 41, 525-529.
- ZHOU, S., DENG, X. & YANG, H. 2003. Biodegradable poly(ϵ -caprolactone)-poly(ethylene glycol) block copolymers: characterization and their use as drug carriers for a controlled delivery system. *Biomaterials*, 24, 3563-3570.
- ZHU, S., ZHOU, Z., ZHANG, D., JIN, C. & LI, Z. 2007. Design and synthesis of delivery system based on SBA-15 with magnetic particles formed in situ and thermo-sensitive PNIPA as controlled switch. *Microporous and Mesoporous Materials*, 106, 56-61.
- ZOU, J., PENG, Y.-G. & TANG, Y.-Y. 2014. A facile bi-phase synthesis of Fe₃O₄@SiO₂ core-shell nanoparticles with tunable film thicknesses. *RSC Advances*, 4, 9693-9700.

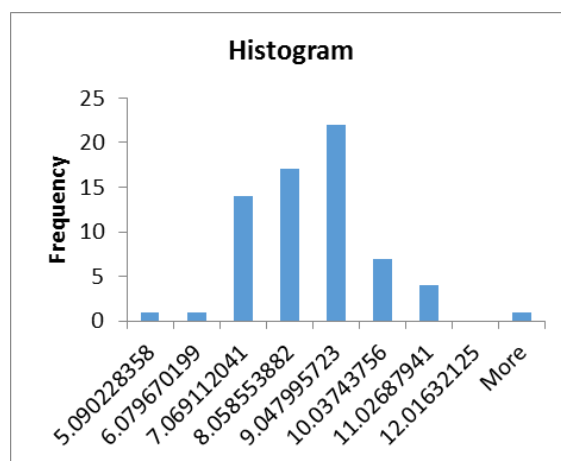
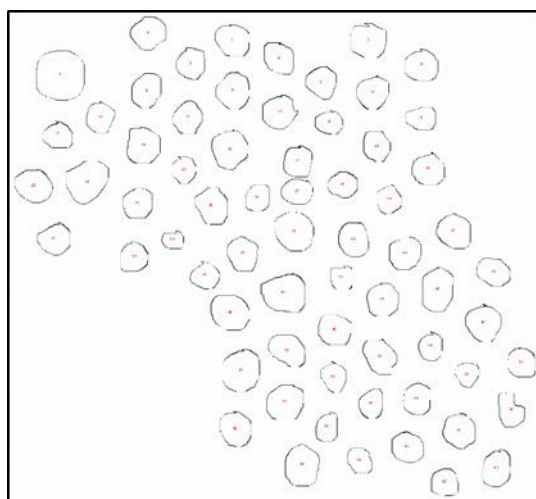
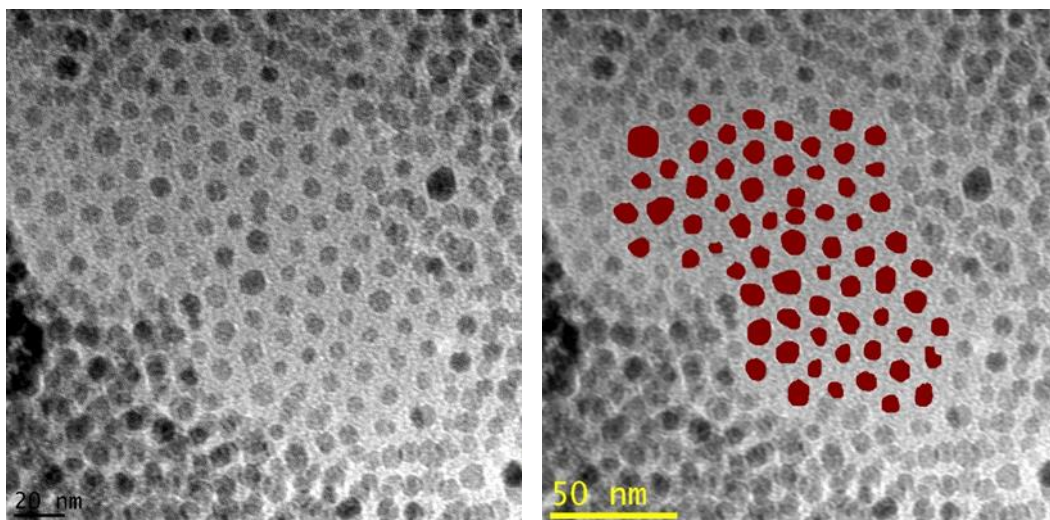
ZULLO, B. A. & CIAFARDINI, G. 2008. Lipolytic yeasts distribution in commercial extra virgin olive oil. *Food Microbiol*, 25, 970-7.

APPENDICES

Appendix A

Image analysis in order to obtain particles size distribution from TEM images were performed using Imagej image processing software. Two examples are presented here.

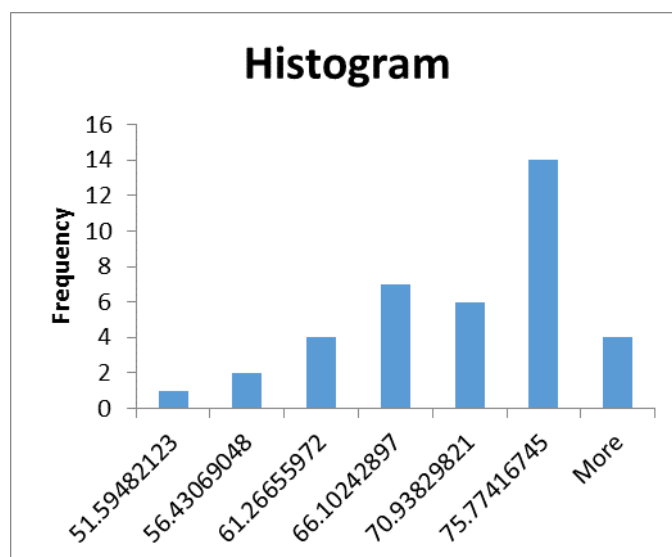
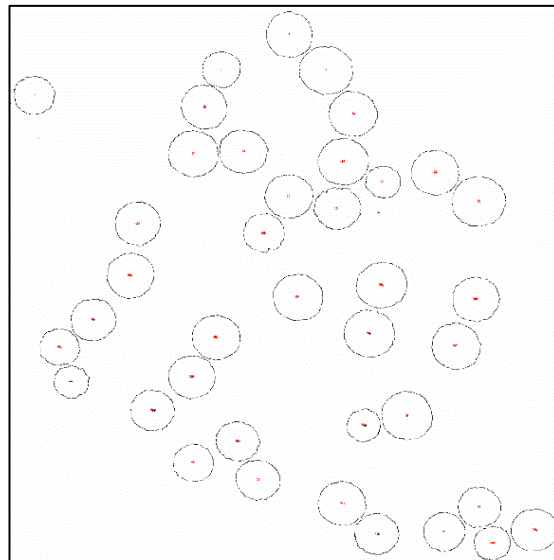
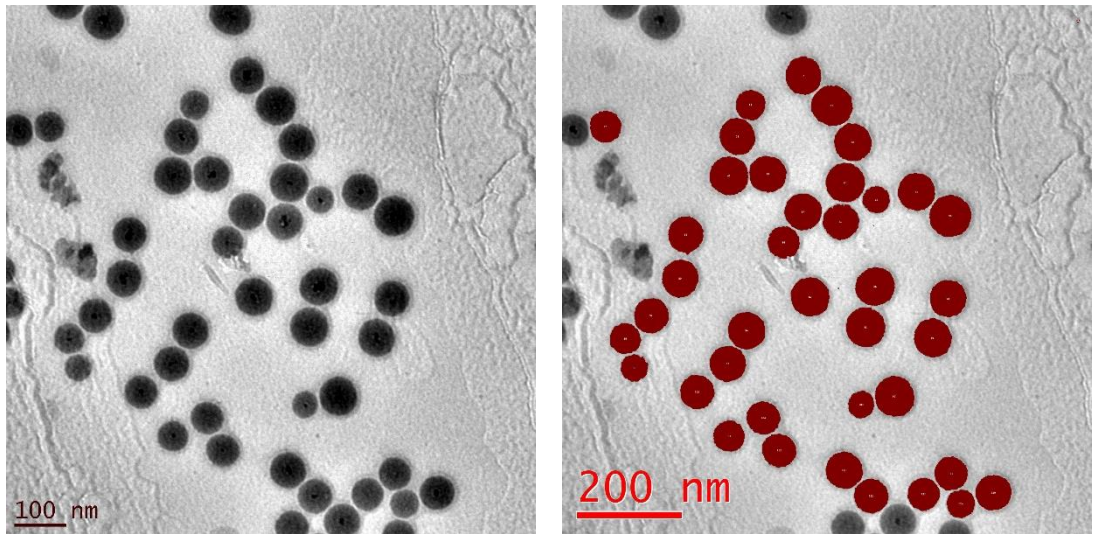
ME59 size distribution:



	Area (nm ²)	d (nm)
1	57.09	8.525799
2	66.09	9.173244
3	57.67	8.568998
4	49.97	7.976452
5	45.76	7.633049
6	54.12	8.301068
7	132.85	13.00576
8	47.7	7.793172
9	62.43	8.915624
10	53.6	8.261092
11	53.19	8.229436
12	56.86	8.508607
13	47.65	7.789086
14	43.76	7.46438
15	36.64	6.83019
16	32.78	6.460402
17	38.96	7.043111
18	64.65	9.072758
19	70.24	9.456868
20	43.05	7.403578
21	46.99	7.734955
22	51.75	8.117275
23	33.44	6.525115
24	88.04	10.58754
25	62	8.884866
26	38.5	7.001409
27	41.72	7.288316
28	35.54	6.726881
29	35.04	6.679395
30	60.88	8.80425
31	47.4	7.768626
32	79.71	10.07422
33	59.9	8.733101
34	49.94	7.974057
35	54.88	8.35915

Id	Area (nm ²)	d (nm)
36	20.35	5.090228
37	53.08	8.220922
38	54.71	8.346193
39	42.67	7.37083
40	48.11	7.826593
41	37.48	6.90804
42	28.22	5.994232
43	73.28	9.659347
44	88.01	10.58574
45	55.54	8.409264
46	72.14	9.583919
47	63.77	9.010798
48	55.08	8.374368
49	34.26	6.604634
50	58.7	8.645181
51	56.46	8.478626
52	44.17	7.499266
53	83.16	10.28993
54	36.49	6.816195
55	29.16	6.093248
56	46.18	7.667999
57	69.7	9.420446
58	36.54	6.820863
59	43.16	7.41303
60	56.98	8.517581
61	33.53	6.53389
62	56.86	8.508607
63	50.61	8.027369
64	74.13	9.715207
65	32.83	6.465327
66	54.21	8.307967
67	39.55	7.09624
average	8.08	
STD	1.28	

ME56 size distribution



Id	Area (nm ²)	d (nm)
1	3997	71.3382
2	4884.25	78.8595
3	2604.5	57.58604
4	2938.75	61.1697
5	3806.25	69.61514
6	4107.25	72.31537
7	3970	71.09684
8	4385	74.72052
9	4481.5	75.53822
10	4095.25	72.20965
11	2090.75	51.59482
12	3957	70.98034
13	5103.5	80.61004
14	3665.25	68.31355
15	3718	68.80338
16	2956.5	61.35416
17	3991.5	71.2891
18	4404.25	74.88435
19	4407.5	74.91197
20	3958.25	70.99155
21	3569.75	67.4177

Id	Area (nm ²)	d (nm)
22	4538	76.0129
23	4061.5	71.91149
24	4242.25	73.49422
25	2751.75	59.19153
26	3783.75	69.40908
27	2104.25	51.76113
28	3370.75	65.51162
29	4673	77.13526
30	2033.25	50.88039
31	3203	63.86068
32	2842.5	60.15965
33	3309.5	64.91368
34	3954	70.95343
35	3233.5	64.16401
36	3727.25	68.88891
37	3018.75	61.99671
38	3381.75	65.61843
39	2309.75	54.22974
Average	67.58	
STD	7.51	

Appendix B

LIST OF PUBLICATIONS

1. **Maneea Eizadi Sharifabad**, Tim Mercer, and Tapas Sen “Drug-loaded liposome-capped mesoporous core-shell magnetic nanoparticles for cellular toxicity study”. *Nanomedicine*, Vol. 11, No. 21, 2757-2767, 2016.
2. **Maneea Eizadi Sharifabad**, Tim Mercer and Tapas Sen “The fabrication and characterization of stable core-shell superparamagnetic nanocomposites for potential application in drug delivery”. *Journal of Applied Physics*, 117 (17), 17D139, 2015.
3. **Maneea Eizadi Sharifabad**, Ben Hodgson, Mourad Jellite, Tim Mercer and Tapas Sen “Enzyme immobilised novel core-shell superparamagnetic nanocomposites for enantioselective formation of 4- (R)-hydroxycyclopent-2-en-1- (S)-acetate”. *Chemical Communications*, 50 (76), 11185-11187, 2014.
4. Tapas Sen , Sarah J. Sheppard , Tim Mercer , **Maneea Eizadi sharifabad** , Morteza Mahmoudi and Abdelbary Elhissi “Simple one-pot fabrication of ultra-stable core-shell superparamagnetic nanoparticles for potential application in drug delivery” *RSC Adv.*,2, 5221-5228, 2012.
5. Y. Patil-Sen, **M Eizadi sharifabad**, H. Bux, T. Mercer, G. Bond and T. Sen “Thermally responsive lipid coated superparamagnetic nanoparticles for frequency triggered drug delivery” *NSTI Nanotech 2015*, CRC press, Taylor & Francis group
6. **Maneea Eizadi Sharifabad**, Tim Mercer and Tapas Sen “Mesoporous Nanoparticle Supported Liposomes For Magnetic Hyperthermia Triggered Drug Delivery” 61st annual conference on magnetism and magnetic materials (MMM) October 31st to November 4th, 2016
7. **Maneea Eizadi Sharifabad**, Tim Mercer and Tapas Sen “The fabrication and characterization of stable core-shell superparamagnetic nanocomposites for potential application in drug delivery” Annual Conference on Magnetism and Magnetic Materials (MMM) Hawaii, USA, 3rd to 7th November 2014
8. **Maneea Eizadi Sharifabad**, and Tapas Sen “Enantioselective desymmetrization of meso-cyclopent-2-en-1,4-diacetate to 4- (R)-hydroxycyclopent-2-en-1- (S)-acetate using enzyme immobilized superparamagnetic nanocomposites” International Conference in Nanoscience and Nanotechnology (NSTI 2014) Washington DC, USA, 15th to 18th June 2014
9. **Maneea Eizadi Sharifabad**, Tim Mercer and Tapas Sen “Fabrication of Stable Bio-Compatible Mesoporous Silica and Core-Shell Silica-Magnetite Nanoparticles for Potential Application In Drug Delivery” International Conference in Nanoscience and Nanotechnology (NSTI 2013) Washington DC, USA, 12th to 14th May 2013

